On the 70th Anniversary
of Academician Jaures Ivanovich Alferov,
Vice-President of the Russian Academy of Sciences

Jaures Ivanovich Alferov turned 70 on March 15, 2000

The Editorial Board of *Physics of the Solid State* heartily congratulate Academician Alferov on this occasion. We apologize for the long delay, for which there is no good excuse. We are just late. When we met, the stream of journal issues had already passed. Everything should be done in due time, especially in such a dynamic business as publishing periodicals.

We shall not list in this brief tribute all his ranks, awards, prizes, high posts, and memberships of many academies and scientific societies all over the world. This was also avoided when outstanding physicists such as Petr Leonidovich Kapitza or Lev Davidovich Landau were congratulated because the made names for themselves through their contribution to science, not through a collection of titles or memberships.

The name of Jaures Alferov is familiar to a very broad circle of scientists due to his famous works on the development of the first heterolasers on semiconducting crystals. The social and political activity of Academician Alferov, who is a member of the Russian parliament, has brought him recognition in still wider circles of society.

In the 1960s, a tremendous amount of foresight and courage were required to leave the well-trodden route of the physics of semiconducting homojunctions to turn to the unbeaten track of heterojunctions, on which nothing remarkable had been discovered before Alferov's investigations.

The first double-heterostructure laser, continuously operating at room temperature, was designed by Alferov and his young collaborators on the basis of the well-known semiconducting couple GaAs–GaAlAs. The discovery of this couple paved the way for the development of ultrahigh technologies for obtaining quantum-dimensional semiconducting structures. An ensemble of quantum dots (quasi-atoms) is a material "speck of dust" which is capable, however, of emitting luminous flux having a power of tens of watts and even higher. The amazing thing is that, as well as the fact that in spite of all difficulties encountered in the evolution of science in our country (especially in recent years), Alferov succeeded in establishing a supreme research and technological base at the Ioffe Physicotechnical Institute for developing heterolasers and continued obtaining record-high results in this rapidly progressing branch of optoelectronics, which opened immense prospects for the application of various-range lasers in diversified fields of technology from medical to military engineering.

The personality of Jaures Alferov is extremely multifaceted. It is difficult to mention many things in a short greeting communication, but we must mention the creation of the Scientific and Educational Center at the Physicotechnical Institute. At this center, school-age pupils become university students, and students are converted into young scientists. The exuberant energy and precise mind of Jaures Ivanovich have been manifested most brilliantly during the construction of the center. The scale of this institution constructed in recent years in a "blank space" by the efforts of a lone scientist—not an oil magnate—impresses our foreign guests, town governors, and even businessmen.

We sincerely wish our colleague and outstanding person Jaures Ivanovich Alferov preservation good spirits, health, and success for many years.

Editorial Board

===== **REVIEW** =====

Effects of Strong Electron Correlations in X-ray and Electron Spectra of High-T_c Superconductors

P. V. Avramov and S. G. Ovchinnikov

Kirenskiĭ Institute of Physics, Siberian Division, Russian Academy of Sciences,
Akademgorodok, Krasnoyarsk, 660036 Russia

e-mail: paul@post.krascience.rssi.ru

Abstract—The current state of theoretical and experimental studies on the electronic structure of high-T_c superconductors is analyzed. The agreement between the theory and experimental spectroscopic data is shown to be rather poor in certain cases. The reason is that the X-ray and electronic spectra reveal strong electron correlations. At the same time, no realistic model has been developed up to now in which both one-electron and multielectron mechanisms of the formation of the spectra could be described in a unified way in compounds containing transition and rare-earth elements. In this paper, particular attention is paid to a sudden-perturbation model, by which it has been possible to describe or interpret some X-ray and electronic spectra, including both one-electron and multielectron effects. © 2000 MAIK "Nauka/Interperiodica".

INTRODUCTION

It can now be confidently said that the discovery of high-T_c superconductivity (HTSC) has given vigorous impetus to the development of many areas of both experimental and theoretical physics. Particularly striking is the development of high-resolution electron spectroscopy and the theory of strong electron correlations. The first attempts to elucidate the features of the electronic structure of high-T_c superconductors and to correlate them with the nature of the HTSC were made almost immediately after the discovery of these compounds [1]. It became clear that the spectral data obtained by X-ray and electron spectroscopy methods could not be unambiguously interpreted. The reason was that the atomic and electronic band structures of the HTSC materials were complicated and also that the spectra showed the effects of strong electron correlations [2–4].

Detailed analysis of the literature concerned with experimental and theoretical studies on high-T_c superconductors shows that a great deal of information on their electronic structure has been accumulated to date. This information was obtained mainly by experimental methods, namely, by X-ray electron and photoelectron spectroscopy, X-ray spectroscopy, X-ray emission spectroscopy, X-ray absorption spectroscopy, and optical spectroscopy.

Photoelectron spectroscopy of core electron states allowed one to obtain some information about more general characteristics of the electronic structure, such as the oxidation levels of copper and the occupancies of multielectron configurations due to strong electron correlations. The X-ray absorption spectra (XASs) also suggest that strong electron correlations affect the electronic structures of high-T_c superconductors, in particular, the structure of unoccupied electronic states in them.

Also, theoretical one-electron calculations of the electronic structure of key objects were made, which were not accompanied, as a rule, by the theoretical modeling of relevant spectroscopic experiments. Only some features of physical experiments, predominantly of those on metallic phases, were adequately described in terms of the theoretical one-electron models developed thus far.

On the other hand, multielectron models of HTSC (the Anderson model, several versions of the Hubbard model, the t–J model, etc.) undoubtedly gave some insight into the role of strong electron correlations. However, one-electron excitations of a system were not theoretically treated in these models, which does not allow one to directly compare the theory with the great bulk of the experimental data.

In fact, the view of the electronic structure of high-T_c superconductors has been fragmentary up to now; some effects have been investigated only in one-electron models and others only in multielectron ones. No realistic model was developed, in terms of which one could interpret a great body of experimental data revealing both one-electron and multielectron effects (for example, X-ray absorption spectra and various electronic spectra).

1. BASIC DATA ON THE ELECTRONIC STRUCTURE OF HIGH-T_c SUPERCONDUCTORS

1.1. Electronic Spectra of Superconductors

Analysis of the literature [3, 5–13] shows that Cu2p X-ray photoelectron spectra (Cu2p-XPSs) of copper were investigated the most, because they can be experimentally measured quite easily. From these spectra, one can obtain some information about the valence and charge states of copper in compounds. Figure 1 shows typical Cu2p-XPSs of compounds CuO, La$_{2-x}$Sr$_x$CuO$_4$ ($x = 0, 0.15$), and Cu$_2$O [3, 5]. In the spectra of CuO and La$_{2-x}$Sr$_x$CuO$_4$, in contrast to those of Cu$_2$O, there are two intense peaks, which the authors of [3, 5] associate with transitions to $3d^{10}$ and $3d^9$ states, respectively. The $3d^9$ peak has a complex structure due to the Coulomb interaction of $2p$ and $3d$ vacancies in the final state; this peak is nearly rectangular in shape for "good" samples (fabricated under certain conditions). In the process of physical degradation of the samples, the $3d^9$ peak first becomes asymmetric and then less intense.

The satellite structure of Cu2p-XPSs was widely used to estimate the charge distribution in the ground state [14, 15]. Most of the estimations, made in the Anderson model (described in [16–22]) using experimental data, show that, in CuO and La$_{2-x}$Sr$_x$CuO$_4$ oxides, the weight of the $3d^9$ configuration does not exceed 50–60% and only a moderate contribution is observed from the $3d^8$ configuration.

There are a number of papers in which the Cu2p-XPSs are misinterpreted. In most of the papers, it was concluded that the Cu(+3) ions make a considerable contribution to the chemical bond. Theoretically, we believe that the spectra of the ions in the NaCuO$_2$ compound [23] (Fig. 2), in which the local structural parameters of the environment of the copper ion (CuO$_4$ cluster) are close to those in the HTSC compounds under study, are of greatest interest. There are two fundamental distinctions between the Cu2p-XPS of NaCuO$_2$ and those of La$_2$CuO$_4$ and CuO: a noticeable shift of the principal peak and its satellite to shorter wavelengths and the emergence of an additional long-wavelength satellite at an energy of 937.5 eV.

The presence of a complex satellite structure in all the X-ray electron spectra mentioned above is an unambiguous manifestation of strong valence electron correlations in high-T_c superconductors.

1.2. X-ray Absorption Spectra of High-T_c Superconducting Compounds

The best understood X-ray absorption (XAFS) spectra of HTSC compounds are CuK spectra. They are observed when X-rays induce transitions of $1s$ electrons of copper to unoccupied Cup orbitals. In copper oxides, there are no vacant Cup states up to the ionization threshold. For this reason, in this energy range, there are no intense lines in all CuK spectra of HTSC
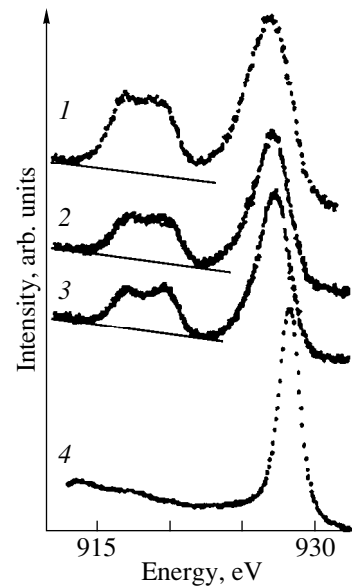

Fig. 1. Cu2$p_{3/2}$ X-ray photoelectron spectra [3, 5] of compounds (*1*) CuO, (*2*) La$_{1.85}$Sr$_{0.15}$CuO$_4$, (*3*) La$_2$CuO$_4$, and (*4*) Cu$_2$O.
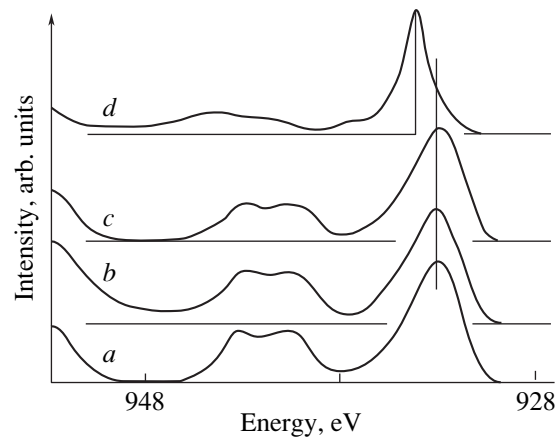

Fig. 2. Cu2$p_{3/2}$ X-ray photoelectron spectra [23] of compounds (*a*) CuO, (*b*) La$_2$CuO$_4$, (*c*) YBa$_2$Cu$_3$O$_7$, and (*d*) NaCuO$_2$. The half-width of the spectral line Γ(eV) is (*a*) 3.25, (*b*) 3.30, (*c*) 3.20, and (*d*) 1.60.

compounds and related oxides. Historically [1], the CuK absorption spectra were used, first of all, for determining the oxidation level of copper in high-T_c superconductors. In fact, it was on the basis of these spectra that the erroneous inference was first made that Cu(III) ions are of considerable importance in forming the electronic structure of La$_2$CuO$_4$. Later, the nature of the principal peaks of the near-range fine structure of X-ray absorption spectra was elucidated on the basis of one-electron calculations [24–27]. The features of the spectra were identified that are associated with the scatter-
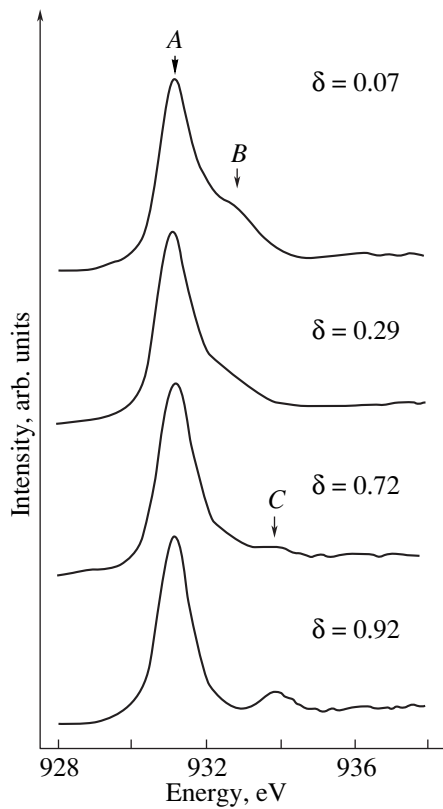
Fig. 3. Experimental CuL_3 X-ray absorption spectra [31] of the $YBa_2Cu_3O_{7-\delta}$ compound for different values of δ.

ing of photoelectrons by the atoms of the first coordination shell [1, 24] and by more distant atoms [25–27].

Noteworthy is the paper by Li *et al.* [26], in which the experimental spectrum was compared with theoretical one-electron calculations of polarized CuK spectra for an extended cluster and the conclusion was drawn that the peak 7 eV higher than the principal peak in the *z*-polarized spectrum has a multielectron nature. However, this hypothesis was not substantiated in [26], not even qualitatively. The CuK spectra are well reproduced, and hence, their variations with composition and under different conditions can be determined with a high degree of accuracy. In the experimental work by Kosugi *et al.* [28], owing to this property of CuK spectra, the spectra of two-hole Cup states were first obtained for doped $La_{2-x}Sr_xCuO_4$ and $YBa_2Cu_3O_7$ compounds. It should be emphasized that work was very important, because only the method proposed in [28] made it possible to separate the spectra corresponding to the electronic states produced by doping.

Another experimentally well studied spectrum of HTSC compounds is the CuL_3 spectrum. The CuL_3 X-ray absorption spectra are associated with the transition of an electron, excited by an X-ray quantum, from the 2*p* energy level of copper either to a *d*-type bound state or to the *s* or *d* orbital in the positive-energy range (after which the electron leaves the system).

Up to now, the mechanism of the formation of CuL_3 X-ray absorption spectra of high-T_c superconductors has been studied either by a method based on the one-electron approximation and multiple-scattering theory (see, e.g., [2, 27]) or by a multielectron treatment based on the Anderson model [29]. The former approach ignores the effects of strong electron correlations, which are important in forming these spectra, while the latter gives a very rough picture of X-ray absorption, reducing the entire spectrum to a single white line and not allowing one to describe the intricate part of the spectrum above the ionization threshold. Nevertheless, some interesting results were obtained using even this much-simplified multielectron description of the formation of CuL_3 X-ray absorption spectra. In [29], the modeling of the white line (transitions to vacant Cud bound states from the core $Cu2p$ orbitals) of CuL_3 absorption spectra was performed for both one-hole and two-hole configurations of the CuO_4 cluster in terms of the three-band *p–d* model. It was shown that the *z*-polarized spectrum becomes noticeably more intense after doping. A comparison between the results obtained in [29] and [30] shows that the theory agrees well with the experimental X-ray absorption data; hence, the conclusion is substantiated that the density of Cud_{z^2} states becomes significantly higher after doping.

Nowadays, there is a great body of experimental data [29, 31] suggesting that, in copper-containing HTSC oxides, the mechanisms of the formation of $CuL_{2,3}$ spectra are essentially different from those described by a one-electron, crystal-field model. First of all, the experimental spectra indicate that there occur electron transitions, known as nondiagrammatic, to the states that cannot be described by this model. These transitions are associated either with strong electron correlations or with photoelectron scattering on possible potential barriers produced by surrounding atoms and chemical bonds in the compounds under discussion. The discrepancies were best demonstrated in [31] in the CuL_3 spectrum of $YBa_2Cu_3O_{7-\delta}$ (Fig. 3).

In [31], the fundamental peak *A* of the white line was attributed to the transition $Cu2p^63d^9 \longrightarrow Cu2p^53d^{10}$ for any value of δ, while the peak *B* for $\delta = 0.07$–0.30 was ascribed to the transition $Cu2p^63d^9\underline{L} \longrightarrow Cu2p^53d^{10}\underline{L}$, accompanied by strong electron-correlation effects, which agrees with the theoretical results obtained in [32], where X-ray absorption due to transitions from the core 2*p* energy level of copper was investigated in the $YBa_2Cu_3O_{7-\delta}$ compound using the Anderson model. When δ is increased (causing the electron vacancy concentration to decrease), the intensity of the peak *B* falls to zero and a peak *C* appears at a distance of 2.8 eV from it. The peak *C* was attributed in [31] (taking into account the position of the fundamental peak in the CuL_3 spectrum of

Cu$_2$O [33]) to copper ions with the (+1) oxidation level. Undoubtedly, this interpretation of the peak C deserves attention, but the mechanism of the formation of the CuL_3 spectrum of univalent copper was not discussed in [31] and [33]. Moreover, the absolute values of the absorption oscillator strengths for the $2p$ orbital of copper in YBa$_2$Cu$_3$O$_{7-\delta}$ and Cu$_2$O were not presented in [33], which does not allow one to correctly analyze the CuL_3 spectrum of the complex YBa$_2$Cu$_3$O$_{7-\delta}$ system, which is a combination of the spectra of copper ions with +1, +2, and +3 oxidation levels. Thus, it looks as if, even with allowances made for the multielectron effects, one cannot explain all features of the CuL_3 spectra of copper-containing HTSC materials.

According to [32], in the undoped system (with one electron vacancy per formula unit), X-rays can induce only transition $2p^6 d^9_{x^2-y^2} \longrightarrow 2p^5 d^{10}$, even though in the initial state there are two d^9 and two $d^{10}\underline{L}$ configurations, due to the hybridization of the vacant states. In doped systems (with more than one vacancy per formula unit), there appear contributions from the Cud^8, Cu$d^9\underline{L}$, and Cu$d^{10}\underline{LL}$ configurations and, hence, the multielectron effects are much stronger. For this reason, the CuL_3 spectra of dopant-produced electronic states of doped compounds noticeably differ from the spectra for undoped ones; in particular, there appear shakeup satellites near the white line [2, 32, 33].

1.3. X-ray Spectra of Core Energy Levels

Nowadays, there is a great body of spectral data available in the literature (see, e.g., [34, 35]) on CuK_α X-ray spectra (transitions from the Cu$2p$ to the Cu$1s$ orbital ionized by an X-ray quantum). In most of the papers dealing with the theoretical and experimental investigation of these spectra, some spectral features are explained in terms of the Anderson model or the two-band Hubbard model. The mechanisms of the formation of the spectra are commonly discussed for the one-hole configuration, and no account is taken of the contribution from the two-hole configuration, for which the correlation effects are of fundamental importance.

The authors of papers [36, 37] considered the energy shift of the principal peak in the CuK_α spectra that is caused by the phase transition from the nonsuperconducting to the superconducting state in HTSC oxides, among them La$_{2-x}$Sr$_x$CuO$_4$. It was shown that only in YBa$_2$Cu$_3$O$_7$, the principal peak of the CuK_α spectrum is shifted by 0.35 eV, due to a change of the leading configuration. Theoretically calculated spectra of systems with a one-hole configuration were described in detail in [36, 37]. A low-intensity satellite was shown to exist which depends on the density of states of the Cud^9 configurations and whose position is

higher by 0.4 eV than that of the principal peak; the latter depends on the density of the Cu$d^{10}\underline{L}$ state in the $1s$ and $2p$ hole configurations. It was shown in [37] that the shift of the K_α line of copper cannot be measured without separating out the contributions of the satellite structure. Hence, analysis of these spectra cannot be performed without resorting to multielectron methods.

1.4. One-Electron Calculations of the Electronic Structure of Cuprates

Even the first attempts to describe the electronic structure of copper-containing HTSC materials by nonempirical, cluster, and band, one-electron methods were accompanied, as a rule, by comparing the calculations and experimental photoelectron and X-ray emission spectra of these compounds (see, e.g., [1–7, 38–43]). These calculations gave practically the same picture of the electronic structure formed by the Cu$3d$ and O$2p$ orbitals (see Fig. 4 and, e.g., [44, 45]).

However, it immediately became obvious that there are fundamental limitations to such calculations when applied to HTSC materials.

(1) First of all, the one-electron calculations give zero magnetic moment for copper ions, whereas the experiment shows that all undoped HTSC compounds are antiferromagnets, with the copper ion magnetic moment being equal to $\mu \sim 0.5\mu_B$, and although the high-T_c superconductors themselves possess no long-range antiferromagnetic order, they show strong spin fluctuations [46].

(2) The experimental photoelectron spectra are shifted to lower energies by about 1–2 eV as compared
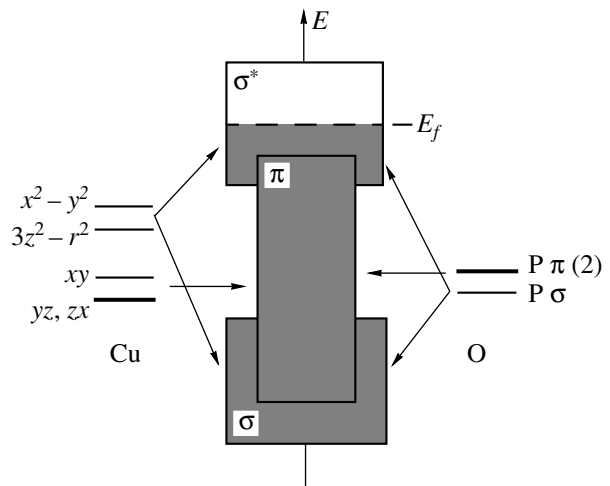

Fig. 4. Schematic diagram of the electronic states of the Cu$3d$ and O$2p$ orbitals of the CuO$_2$ plane in terms of the crystal-field theory and its interpretation in terms of the LCAO–LDA method [44, 45]. The hatching shows the occupied states; $\sigma^{(*)}$ and π designate (anti)bonding $pd\sigma$ states.

to the band calculations for both $La_{2-x}Sr_xCuO_4$ and $YBa_2Cu_3O_{7-\delta}$.

(3) The one-electron calculations predict a metallic behavior for the ground state of undoped oxides such as La_2CuO_4 and $YBa_2Cu_3O_6$, whereas the experiment shows that they are insulators.

(4) The one-electron models offer no explanation of X-ray electron spectra and X-ray spectra of the core energy levels of copper and oxygen, because they have a complex satellite structure.

(5) A comparison of the theory and the experiment showed that a number of features of the X-ray absorption spectra of copper also cannot be explained in terms of a simple one-electron model.

In more recent papers [47–49], an attempt has been made to improve the one-electron approach by introducing a vacant-state potential correction. In effect, such a correction to the potential is analogous to the introduction of the parameter U_d in the Hubbard model, which will be discussed below.

This improved approach allowed one to qualitatively explain the forbidden gap, the shift of the photoelectron spectra to lower energies, and the magnetic moment of copper atoms in the ground state of undoped oxides, such as La_2CuO_4, $CaCuO_2$, $Sr_2CuO_2Cl_2$, and $YBa_2Cu_3O_6$. The nature of the electronic states of the top of the valence band and the bottom of the conduction band was also adequately described and the results agreed with the most reliable experimental and theoretical data. Unfortunately, in those papers, modeling of the X-ray and photoelectron spectra was not conducted and a comparison of the calculations and the experimental data was made only indirectly, which does not allow one to definitively judge the adequacy of this approach.

1.5. Strong Electron Correlations

As mentioned above, the one-electron models cannot describe the features of the electronic structure of undoped cuprates and some of their physical and spectral properties associated with strong electron correlations. To take these correlations into account, two methods were used in the literature. One of them is based on models like the Hubbard or the Anderson model, and the other is an *ab initio* approach, such as the configuration interaction (CI) method or the multiconfiguration self-consistent field (MC SCF) approximation.

Model calculations are the simplest and physically most illustrative method for taking strong electron correlations into account. The simplest of them is the tight-binding model, which describes the electronic structure of the CuO_2 plane and takes into account only the atomic orbitals of the CuO_4 cluster (two occupied $p_{x,y}$ orbitals of oxygens and one half-filled $Cu d_{x^2-y^2}$

orbital). The corresponding model Hamiltonian has the form

$$H_{3bd}^0 = \varepsilon_d \sum_{i,\sigma} d_{i\sigma}^+ d_{i\sigma} + \varepsilon_p \sum_{j,\sigma} p_{j\sigma}^+ p_{j\sigma}$$

$$+ \sum_{\langle i,j \rangle \sigma} t_{pd}^{ij}(d_{i\sigma}^+ p_{j\sigma} + \text{H.c.}) + \sum_{\langle i,j \rangle \sigma} t_{pp}^{jj'}(p_{j\sigma}^+ p_{j\sigma} + \text{H.c.}).$$

Here, the summation is carried out over atoms in the cluster, $\langle i, j \rangle$ means that the summation is performed over its nearest neighbors, and σ is a spin index. In this model, there are three bands containing five electrons. In actual practice, however, this Hamiltonian is written in the hole representation, in which the state $Cu3d^{10}2O2p^6$ is taken as the vacuum state. In the case of one vacancy, the electronic structure of the CuO_2 plane is reduced to one Hubbard band $Cu3d^9 2O2p^6$. As is customary in this model, $d_{i\sigma}^+$ and $p_{j\sigma}^+$ are the creation operators for holes at d and p orbitals, respectively, of copper and oxygen atoms in the CuO_2 plane. The charge-transfer gap Δ equals the difference between the energies of the p and d states of oxygen and copper ($\Delta \equiv \varepsilon_p - \varepsilon_d$) and is positive in the hole representation. The hopping integrals t_{pd}^{ij} and $t_{pp}^{jj'}$ are parameters of the system, determined either from the experimental data or from some nonempirical calculations. The signs of these parameters are dictated by the symmetry of the system, and their absolute values are much less than Δ (t_{pd}^{ij}, $t_{pp}^{jj'} \ll \Delta$).

This model ignores one of the main features of the strongly localized d orbitals of copper, their strong Coulomb interaction. The Emery model is not subjected to this drawback. It is a three-band analog of the one-band Hubbard model,

$$H_{3bd} = H_{3bd}^0 + U_d \sum_i n_{i\uparrow}^d n_{i\downarrow}^d$$

$$+ U_p \sum_j n_{j\uparrow}^p n_{j\downarrow}^p + U_{pd} \sum_{\langle i,j \rangle} n_i^d n_j^p,$$

where $n_{i\sigma}^d = d_{i\sigma}^+ d_{i\sigma}$ and $n_{j\sigma}^p = p_{j\sigma}^+ p_{j\sigma}$ are the densities of $Cu3d$ and $O2p$ holes, respectively. The quantities U_d and U_p are the Hubbard interaction parameters at the same orbitals for copper and oxygen, respectively, and U_{pd} characterizes the copper–oxygen interaction. In the hole representation, these quantities are positive and correspond to repulsion. The quantity U_d is dominant in the formation of the electronic structure and because of this, the transition $Cu3d^9 \longrightarrow Cu3d^8$ is suppressed.

The limit case where all three Hubbard interaction parameters are zero ($U_d = U_p = U_{pd} = 0$) corresponds to one-electron calculations. In this case, the upper σ^*

band (Fig. 4) is twofold degenerate (in terms of this model) and, hence, half-filled.

As the Hubbard repulsion parameter U_d increases, the degeneracy of the σ^* band is lifted and there appear the lower (LHB) filled and the upper (UHB) vacant Hubbard bands [50]. When $U_d < \Delta$, the electronic structure corresponds to a Mott–Hubbard insulator, with the filled upper band being composed of the Cud-type states. When $U_d > \Delta$, we have a charge-transfer insulator. In the latter case, the lower Hubbard band is situated below the oxygen subband, and a minimal electron excitation energy is required for the electron charge transfer to occur from the oxygen sublattice to copper centers.

Magnetism of individual copper atoms in undoped cuprates is simply and naturally explained in terms of the three-band Hubbard model. Indeed, when the copper d band is split into two Hubbard bands, corresponding to the $d^9 \longrightarrow d^8$ and $d^{10} \longrightarrow d^9$ excitations, the number of the remaining electrons per formula unit is even, which explains the insulating behavior of these compounds. Since the d^9 configuration corresponds to a magnetic ion, it is not surprising that magnetism occurs [51, 52].

The long-range antiferromagnetic order in such compounds is due to the spin superexchange between copper centers having one vacancy. It can be described by performing a unitary transformation that reduces the three-band model to the two-dimensional Heisenberg model [53]

$$H = J_{CC} \sum_{\langle i, j \rangle} (S_i S_j - 1/4 n_i^d n_j^d),$$

where J_{CC} is the exchange coupling constant and S_i is the spin operator of a copper center. We have

$$J_{CC} = (4t_{pd}^4/\Delta)(1/U_d + 2/(2\Delta + U_p)).$$

A lower experimental estimate of this constant is $J_{CC} \cong 0.15$ eV.

Another evident success of Hubbard-type models in studying undoped high-T_c superconductors is the fact that, using this approach, it has been possible to qualitatively describe CuK_α X-ray spectra and Cu2p X-ray electron spectra (Cu2p-XPSs) of these compounds [52, 54–57]. However, in most of those papers, only the mechanisms of the formation of spectra for a one-hole configuration were discussed, ignoring the contribution from two-hole configurations, for which electron correlations are of fundamental importance.

For a two-hole configuration of the structural unit of a high-T_c superconductor, this problem was first solved by Zhang and Rice [58]. One would think that, in a charge-transfer insulator, an extra hole should be situated in the oxygen subband, which is just below the upper Hubbard band. However, Zhang and Rice argued against this point of view. They demonstrated that the

covalent mixing of atomic states of copper and oxygen (due to which, in the band theory, the π band is basically of an oxygen nature, see Fig. 4) leads to the formation of a triplet and a singlet (Zhang–Rice singlet) in the Cu3d^9O2p^5 states through Hubbard splitting of occupied states in the one-electron π band. According to their calculations, the singlet is the highest of the occupied states (in the electron representation) and it is the first to be occupied by an extra vacancy produced in the process of doping.

In terms of the one-band Hubbard model, this means that both the Zhang–Rice singlet and the Cu3d^{10} vacuum state are nondegenerate and similar in behavior to the upper and lower Hubbard bands. Hence, they can be described in terms of an effective Hubbard model with a half-filled band,

$$H = -t \sum_{\langle i, j \rangle}^{nn} (c_{i\sigma}^+ c_{j\sigma} + \text{H.c.})$$
$$- t' \sum_{\langle i, j \rangle \sigma}^{nnn} (c_{i\sigma}^+ c_{j\sigma} + \text{H.c.}) + U \sum_i n_{i\uparrow} n_{i\downarrow},$$

where $n_{i\sigma} = c_{i\sigma}^+ c_{i\sigma}$ is the electron density for spin σ and $U \approx \Delta$. In addition to the hopping integral t between nearest neighbors (equal to 430 meV), this model involves the hopping integral on atoms of the next coordination shell ($t' = -70$ meV) [53].

In a CuO$_4$ cluster, the single oxygen state that is mixed with a copper d state is described by the totally symmetric combination $P_{B\sigma}^+ = (1/2) \sum_i p_{i\sigma}^+$. The other three oxygen states $P_{NB\alpha\sigma}^+$ are not binding states. In the half-filled state, the cluster has one vacancy with spin down. When one more hole is added (in the process of doping), we have the problem of two holes for four states interacting with the copper states.

Thus, we have the following five configurations (basis wave functions): the Cud^8O2p^6 configuration, represented by the state $|d_{j\uparrow}^+ d_{j\downarrow}^+\rangle$; the Cu$d^{10}$O2$p^4$ configuration, represented by $|P_{B\uparrow}^+ P_{B\downarrow}^+\rangle$; the Cu$d^9$O2$p^5$ configurations of the first type represented by the singlet $|S\rangle = (|P_{B\uparrow}^+ d_{j\downarrow}^+\rangle + |d_{j\uparrow}^+ P_{B\downarrow}^+\rangle)/\sqrt{2}$ and the triplet $|T\rangle = (|P_{B\uparrow}^+ d_{j\downarrow}^+\rangle - |d_{j\uparrow}^+ P_{B\downarrow}^+\rangle)/\sqrt{2}$. The Cu$d^9$O2$p^5$ configurations of the second type are represented by the states involving the nonbinding oxygen states, such as $|P_{NB\alpha\uparrow}^+ d_{j\downarrow}^+\rangle$.

The Hamiltonian of this model is not difficult to diagonalize. In the case of a charge-transfer insulator, the ground state is found to be the Zhang–Rice singlet, whereas the triplet is 2–4 eV higher and plays no part in the phenomenon in question at low temperatures. In this model, the Zhang–Rice singlet represents an effec-

tive spinless hole (in the doubly occupied-state subspace) moving through the two-dimensional spin lattice.

The other approach that allows one to consider strong electron correlations is multiconfiguration *ab initio* calculations (CI method and MC SCF approximation). For Cu(II) oxide systems, these calculations demonstrate strong localization of valence band top electrons (see, e.g., [59, 60]), which substantiates the applicability of Hubbard-type models. The most detailed study, in our opinion, was carried out in [60], where it was shown that the process of ionization of both core and valence orbitals is accompanied by a strong screening effect, which leads to the emergence of multielectron shakedown satellites in electronic spectra associated with the charge transfer from the occupied $O2p$ to vacant $Cu3d\sigma$ orbitals.

Of the papers in which the *ab initio* MC SCF method was used to investigate doped copper oxide [formally, Cu(III)] systems, of special note is that by Eto and Kamimura [61]. In that paper, the electronic structures of compounds La–Se–Cu–O and Nd–Ce–Cu–O were calculated by a multiconfiguration variational method in a cluster approximation. Calculations were performed for the CuO_6, CuO_4, Cu_2O_{11}, and Cu_2O_7 clusters. It was shown that, at the hole concentration close to the superconducting value, the ground state of the hole-doped CuO_6 cluster changes over from $^1A_{1g}$ to $^3B_{1g}$ when the copper–apical-oxygen internuclear distance is varied. The ground state of the electron-doped CuO_4 cluster was shown to be $^3B_{1g}$ and the dopant electron was at the $Cu4s$ orbital. Eto and Kamimura also adequately described the antiferromagnetic ordering in the Cu_2O_{11} and Cu_2O_7 clusters and showed that doping suppresses antiferromagnetism in both p-type (Cu_2O_{11} cluster) and n-type (Cu_2O_7 cluster) systems, though the mechanisms of these processes are different.

1.6. A multielectron Model for the CuO₂ Plane

In a multielectron approach, the Hamiltonian of the multi-band p–d model, describing the valence state of copper and oxygen, can be written in the hole representation as [62–64]

$$H = H_d + H_p + H_{pp} + H_{pd},$$

$$H_d = \sum_r H_d(r),$$

$$H_d(r) = \sum_{\lambda\sigma} [(\varepsilon_{d\lambda} - \mu)d^+_{r\lambda\sigma}d_{r\lambda\sigma} + (1/2)U_d n^\sigma_{r\lambda} n^{-\sigma}_{r\lambda}]$$

$$+ \sum_{\sigma\sigma'} (V_d n^\sigma_{r1} n^{\sigma'}_{r2} - J_d d^+_{r1\sigma}d_{r1\sigma}d^+_{r2\sigma'}d_{r2\sigma}),$$

$$H_p = \sum_i H_p(i),$$

$$H_p(r) = \sum_{\alpha\sigma} [(\varepsilon_{p\alpha} - \mu)p^+_{i\alpha\sigma}p_{i\alpha\sigma} + (1/2)U_p n^\sigma_{i\alpha} n^{-\sigma}_{i\alpha}]$$

$$+ \sum_{\sigma\sigma'} (V_p n^{\sigma'}_{i1} n^{\sigma'}_{i2} - J_p p^+_{i1\sigma}p_{i1\sigma'}p^+_{i2\sigma'}p_{i2\sigma}),$$

$$H_{pd} = \sum_{i,r} H_{pd}(i, r),$$

$$H_{pd}(i, r) = \sum_{\lambda\alpha}\sum_{\sigma\sigma'} (T_{\lambda\alpha}p^+_{i\alpha\sigma}d_{r\lambda\sigma} + \text{H.c.}$$

$$+ V_{\lambda\alpha} n^\sigma_{r\lambda} n^{\sigma'}_{i\alpha} - J_{\lambda\alpha}d^+_{r\lambda\sigma}d_{r\lambda\sigma'}p^+_{i\alpha\sigma'}p_{i\alpha\sigma}),$$

$$H_{pp} = \sum_{(i,j)\alpha\beta\sigma} (t_{\alpha\beta}p^+_{i\alpha\sigma}p_{j\beta\sigma} + \text{H.c.}), \tag{1}$$

where $\varepsilon_{p\alpha}$ and $\varepsilon_{d\lambda}$ are the one-particle energies of p- and d-hole orbitals α and λ, respectively; U_p and U_d are the Hubbard correlation parameters; V_p and V_d are the matrix elements of the intraatomic Coulomb repulsion at the same and different orbitals of oxygen and copper; J_p and J_d are the Hund exchange integrals at oxygen and copper atoms, respectively; $T_{\lambda\alpha}$ and $t_{\lambda\alpha}$ are the matrix elements of p–d and p–p hopping, respectively, between their nearest neighbors; $V_{\lambda\alpha}$ and $J_{\lambda\alpha}$ are the matrix elements of the Coulomb and exchange interactions, respectively, between nearest copper–oxygen neighbors; and μ is the self-consistently calculated chemical potential, situated in the insulator energy gap of the undoped system. Obviously, the correctness of the results obtained in this model depends on the basis functions chosen for calculations. For this reason, one should include at least the $d_{x^2-y^2}$ and d_{z^2} orbitals of copper, as well as the p_x and p_y orbitals for all oxygen atoms. The energy of the $d_{x^2-y^2}$ orbital was taken to be ε_d, the energy of the d_{z^2} orbital was $(\varepsilon_d + \Delta_d)$, and the energy of the $p_{x,y}$ orbitals was ε_p.

In (1), the first two terms describe intraatomic interactions, including the Hubbard correlations U_p and U_d, the Coulomb interaction between holes at different orbitals and the Hund exchange. The last two terms in (1) correspond to interatomic p–p and p–d hopping and Coulomb interaction. The values of the parameters of the Hamiltonian (1) are taken from the experiment; they were determined by matching the electronic structure of the ground state of La_2CuO_4 to the optical and magnetic data [65]

$$V_p = 3 \text{ eV}, \quad V_d = 4.5 \text{ eV},$$

$$J_p \ = \ J_d \ = \ 0.5 \ \text{eV},$$

$$T_{\lambda\alpha} \ = \ 1.5 \ \text{eV}, \quad t_{\lambda\alpha} \ = \ 0.2 \ \text{eV},$$

$$V_{\lambda\alpha} \ = \ 0.6 \ \text{eV}, \quad J_{\lambda\alpha} \ = \ 0.2 \ \text{eV},$$

$$\varepsilon_d \ = \ 0, \quad \Delta_d \ = \ 1.5 \ \text{eV}, \quad \varepsilon_3 \ = \ 2 \ \text{eV}.$$

The dependence of the results on the choice of U_p and U_d is discussed below. The parameters U_p and U_d are assumed to be infinite, unless otherwise specified.

1.7. The Ground State of the CuO$_4$ Cluster

Let us consider localized states with no hopping between unit cells. Figure 5 shows the local bases for (a) the Hubbard model and (b) a multi-band p–d model; in the latter case, only several excited states with $n = 1$ and $n = 2$ [65, 66] are shown for a particular unit cell in which a quasiparticle is created. In the hole representation of the Hubbard model (Fig. 5a), the top of the valence band consists only of two quasiparticles [67] (in terms of the multielectron approach), corresponding to the upper and lower Hubbard bands with energies

$$\Omega_+ \ = \ E_0(2, S) - E_0(1) \ = \ E_0(1) + U$$

and

$$\Omega_- \ = \ E_0(1) - E_0(0) \ = \ E_0(1),$$

where $E_0(0)$, $E_0(1)$, and $E_0(2, S)$ are the energies of the ground states of the cluster in the zero-, one-, and two-particle subspaces of the Hilbert space. The $S = 1/2$ state with the energy $E_0(1)$ is degenerate due to spin, whereas the state with $E_0(2, S)$ may be a singlet ($S = 0$) or a triplet ($S = 1$). Dispersion in the system [$\Omega_S \longrightarrow \Omega_S(k)$] is associated with intercluster hopping. The dispersion relation varies with different values of S; hence, the X-ray spectra will be different for systems differing in spin.

In a many-band model, the number of different transitions between states in which the numbers of electrons (or holes) differ by unity is much larger (Fig. 5b). It is much more convenient to describe the localized particles, introduced in these models, in terms of the Hubbard operators

$$X^{pq} \ = \ |p\rangle|q\rangle,$$

which are constructed for a complete set of localized multielectron states. Here, as indicated above, the states of one unit cell, that is, multielectron molecular orbitals, are implied.

In terms of the three-band p–d model, in the case where $T_{\lambda\alpha} \ll \Delta, U_p, U_d$ ($T_{\lambda\alpha}$ is the p–d hopping parameter and $\Delta = \varepsilon_d - \varepsilon_p$ is the charge-transfer energy), the effective exchange integral $J_{\text{Cu–O}}$ can be written as [53]

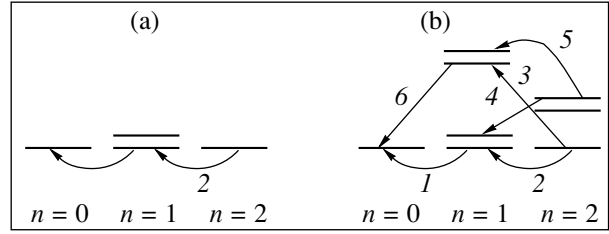$$J_{\text{Cu–O}} \ = \ 8T_{\lambda\alpha}^2(1/(\Delta + U_p) + 1/(D_d - \Delta)).$$

Fig. 5. Local bases of (a) the one-band Hubbard model and (b) the multiband p–d model. Only some of the excited terms are shown in the one-hole and two-hole subspaces of the Hilbert space in the multiband model. Arrows show the processes of quasiparticle annihilation.

In the limit of $U_p = U_d = \infty$, the exchange integral $J_{\text{Cu–O}}$ is zero and the singlet and triplet are degenerate. However, at finite U_p and U_d, the value of $J_{\text{Cu–O}}$ becomes large; for typical values of parameters $U_d = 10 \ \text{eV}$, $U_p = 6 \ \text{eV}$, $T_{\lambda\alpha} = 1$–$1.5 \ \text{eV}$, and $\Delta = 2$–$3 \ \text{eV}$, we have $J_{\text{Cu–O}} = 2 \ \text{eV}$. Therefore, in order to correctly evaluate the effective exchange integral, one should take into account the finiteness of the intraatomic Coulomb repulsion parameters U_p and U_d.

The state of two holes in the CuO$_4$ unit cell may be a Zhang–Rice singlet [58] or a triplet [68]. When calculating the spectra, the energies of the singlet (ε_S) and the triplet (ε_T) were determined by exactly diagonalizing the Hamiltonian of the CuO$_4$ cluster at $U_p = U_d = \infty$. Relatively small variations in the values of parameters may result in the crossover between the singlet and triplet, that is, in the change of sign of the level splitting $\Delta\varepsilon = \varepsilon_T - \varepsilon_S$. In our case, at $\Delta = \varepsilon_p - \varepsilon_d = 2 \ \text{eV}$, the ground state of two holes is a triplet ($\varepsilon_T = -0.93$ and $\varepsilon_S = -0.82$), while at $\Delta = 1.5 \ \text{eV}$, the ground state is a singlet ($\varepsilon_T = -1.52$ and $\varepsilon_S = -1.54$).

When the values of the Hubbard repulsion parameters are finite, the picture becomes somewhat different. Figure 6 shows calculated level splitting [69] in the multiband p–d model for $U_d = 12 \ \text{eV}$, $U_p = 8 \ \text{eV}$, $T_{\lambda\alpha} = 1.5 \ \text{eV}$, and $\Delta = 3 \ \text{eV}$ (curve 1). This curve corresponds to a minimal set of parameters, which is arbitrarily called "three-band model plus d_{z^2} orbital," because all parameters that are not involved in the three-band model are taken to be zero. The calculations for this set explicitly show the effect of the d_{z^2} orbital when its energy is lowered to its actual values.

As Δ_d is decreased, the effect of the Coulomb interaction between orbitals increases, as seen from curve 2, for which we have taken $V_d = 4.5 \ \text{eV}$. Curve 3 corresponds to the case where all the parameters we used to completely calculate the CuO$_2$ layer are taken to be nonzero.

It is seen from Fig. 6 that the exchange splitting $\Delta\varepsilon$ decreases as the energies of the $d_{x^2-y^2}$ and d_{z^2} orbitals
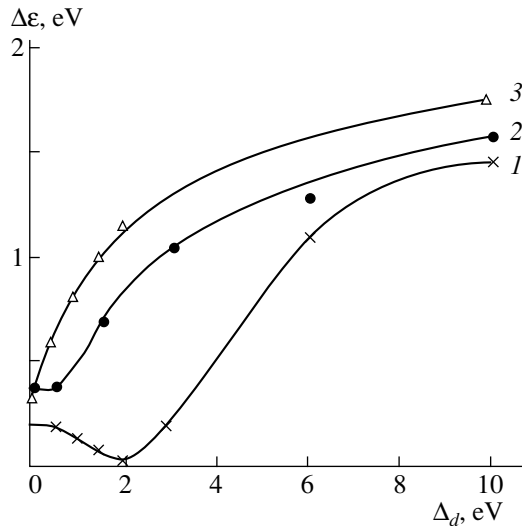
Fig. 6. Dependence of the triplet–singlet splitting energy $\Delta\varepsilon = \varepsilon_T - \varepsilon_S$ for the two-hole states of the CuO_4 cluster on the crystal-field parameter $\Delta_d = \varepsilon d_{z^2} - \varepsilon d_{x^2-y^2}$. The model parameters are (eV): (1) $U_d = 12$, $U_p = 8$, $\Delta = 3$, $T_{\lambda\alpha} = 1.5$, and other parameters are zero; (2) $V_d = 4.5$ and the other parameters as for curve 1; and (3) $U_d = 12$, $U_p = 8$, $\Delta = 2$, $T_{\lambda\alpha} = 1.5$, $t_{\alpha\beta} = 0.2$, $V_d = 4.5$, $V_p = 3$, $V_{pd} = 0.6$, $J_p = J_d = 0.5$, and $J_{pd} = 0.2$.

approach each other. Virtual transitions to orbitally nondegenerate states lead to antiferromagnetic exchange and stabilize the singlet, whereas virtual transitions to degenerate states lead to ferromagnetic exchange and stabilize the triplet. The latter is due to the fact that, according to the Stoner criterion, the density of states at the Fermi surface increases in proportion to the degeneracy.

Thus, the transition from the three-band to the multiband p–d model with finite values of the Hubbard correlation parameters leads to a decrease in $\Delta\varepsilon$, from 2–4 eV in the former case to 0.1 eV in the latter. The introduction of other small parameters into the many-band model may lead to the inversion of the singlet and triplet states. For instance, these may be oxygen–oxygen hopping parameters $t_{\lambda\alpha}$ [68], interatomic Coulomb and exchange p–d integrals V_{pd} and J_{pd}, or the contribution from apical oxygen atoms.

1.8. General Characterization of the Electronic Structure of the HTSC Oxides

Thus, on the basis of the data obtained by various experimental and theoretical methods and presented above, the following current view of the electronic structure of high-T_c superconductors was formed [53].

The Hubbard repulsion removes the degeneracy of the upper half-filled one-electron band σ^* (Figs. 4, 7a), splitting it into the lower and upper Hubbard bands (LHB and UHB, respectively) depending on the relative values of the parameters t_{pp}, t_{pd}, U_d, and Δ (Figs. 7b, 7c). According to the classification by Zaanen, Sawatzky, and Allen [50], there are three types of electronic structures (Fig. 7): (a) d-type metal, corresponding to $U_d = 0$ (this case was discussed in Subsection 1.4); (b) the Mott–Hubbard insulator, where t_{pp}, $t_{pd} <$
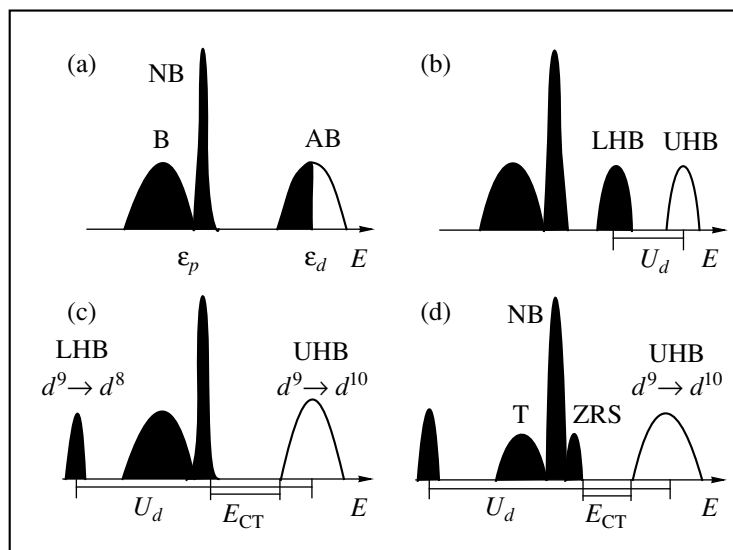

Fig. 7. (a–c) Zaanen–Sawatzky–Allen classification [50] of the one-particle spectra of transition-metal compounds: (a) metal, (b) Mott–Hubbard insulator, and (c) charge-transfer insulator (CTI); and (d) CTI with Zhang–Rice singlet–triplet splitting. Shaded regions indicate occupied states, (N)[A]B are (non)[anti]bonding states, L(U)HB are lower (upper) Hubbard bands, ZRS is the Zhang–Rice singlet, T is the triplet, E_{CT} is the renormalized charge-transfer gap, and E is the energy.

$U_d \ll \Delta$ and (c) the charge-transfer insulator, where t_{pp}, $t_{pd} < \Delta < U_d$.

The experimental resonance photoelectron spectroscopy data, which allow one to determine the partial contributions from the O2p and Cu3d states, suggest that the electronic structure of high-T_c superconductors corresponds to a charge-transfer insulator. Measurements showed [70–72] that, in the La$_{2-x}$Sr$_x$CuO$_4$, YBa$_2$Cu$_3$O$_{7-\delta}$, and Nd$_{2-x}$Ce$_x$CuO$_4$ compounds, the parameter U_d of the three-band Hubbard model is much larger than Δ. It was found, while making a comparison of the experimental data and cluster calculations [70–72], that U_d ranged in magnitude from 7.3 to 10.5 eV.

In the one-electron π subsystem, the Hubbard repulsion manifests itself in the same way, splitting it into a triplet and a singlet state. According to [58], among the occupied states in undoped high-T_c superconductors, the singlet has the highest energy and, in terms of the Hubbard model, it is an analog of the UHB, whereas the triplet has a lower energy and corresponds to the LHB.

This last case of the electronic structure calculated for the undoped superconductors in the Hubbard model is shown in Fig. 7d. The ZRS peak corresponds to the Zhang–Rice singlet, which is the ground state among the two-hole states [58].

2. A SUDDEN-PERTURBATION (SP) MODEL AND A SCHEME FOR CALCULATING SPECTRAL CHARACTERISTICS

2.1. The Theoretical Fundamentals of X-ray Spectroscopy (Sudden-Perturbation Model)

The formation of X-ray (absorption and emission) spectra and of X-ray electron spectra is associated with a one-electron and a one-photon process; that is, the electronic system interacts with one X-ray quantum, and one electron makes a transition from some core or valence orbital to a highly excited state. Other (say, Auger) processes that accompany or follow this process noticeably differ in transition energy (which allows one to resolve them) and, in addition, the particles emitted or absorbed in them differ in nature. The processes of the interaction of X-rays with the matter we consider here obey the energy conservation law, and all channels of excitation and decay of highly excited states in these processes are known.

Since the early 1930s, the theory of the interaction of X-rays with matter has been based on the sudden-perturbation (SP) approximation, which was successfully employed to treat the processes in the electron shell of an atom that accompany the α, β^-, and β^+ decay of nuclei, K-capture, and multiple ionization of atoms [73–77]. Later, this approximation was extended to all cases of inelastic interaction of X-rays with matter.

The SP model is based on the assumption that, due to some interaction, the Hamiltonian of the system is suddenly changed [78, 79] as compared with the over-all duration of the corresponding process or the lifetime of the system. This is true in the case of K-capture or β decay. Indeed, the lifetime of the excited state of the electronic system with a vacancy at the 1s orbital (from which an electron has fallen on the nucleus), as evaluated from the experimental X-ray line widths ($\Delta E = \Gamma \approx$ 1 eV) and the Heisenberg uncertainty relation, is of the order of $\tau^* = \Delta t > \hbar/\Delta E \approx 10^{-15}$ s. At the same time, the time τ_K it takes for the electron to "fall" on the nucleus can be estimated as the ratio of the effective orbit radius R_{1s} (~0.1 au) to the effective velocity v_{1s} of an electron moving in this orbit. The latter can be evaluated from the virial theorem (the kinetic electron energy is obtained to be about 10^3–10^4 eV) and, hence, the time τ_K is of the order of ~10^{-19}–10^{-18} s, which is far shorter than the lifetime (10^{-15} s) of the ionized excited state of the atom with the charge of its nucleus changed by unity. Thus, in the case of the K-capture, one can assume that the Hamiltonian of the system suddenly changes in comparison with the lifetime of the final highly excited state with an electron vacancy at the 1s orbital. In the case of the β decay, the change in the charge of the nucleus occurs even more quickly, because the radius of the atomic nucleus is much smaller than that of the electron shells.

The applicability of the SP model is also well founded for the X-ray spectroscopy of inner shells. For example, it can be used to describe K_α spectra, which are associated with transitions from 2p states to the ionized 1s state (the transition energy is of the order of 10^4 eV for elements in the middle of the periodic system). Such spectra are commonly measured for excitation energies 3–5 times higher than the K-shell energy E_K, because in this case the line strength ceases to depend on the excitation energy, which is due to the nature of vacant states with energies of the order of 10^4 eV (above the ionization threshold). Hence, one can take the energy of an exciting photon to be $\hbar\bar{\omega} \gg E_K$. In the SP model, it is assumed that an 1s electron is so quickly removed that the potential for 2p electrons changes suddenly. Hence, the time it takes for the 1s electron to go out of the L shell should be small in comparison with the revolution period of 2p electrons,

$$r_{2p}/v_{1s} \ll 2\pi r_{2p}/v_{2p},$$

here, r_{2p} is the orbit radius of 2p electrons (0.25 au for copper). Taking the excitation energy to be ~10^4–10^5 eV and using the virial theorem, one obtains $v_{1s} \sim 3 \times 10^9$–$10^{10}$ cm/s and $v_{2p} \sim 5 \times 10^7$–$10^8$ cm/s for elements in the middle of the periodic table. Thus, the condition for suddenness is fulfilled and mixing of the 1s electron with the 2p shell does not occur.

However, a more detailed consideration of the formation of even these high-energy X-ray spectra, associated with inner shells, raises some questions. Undoubtedly, the effective nucleus charge, as it does for the 2p shell, Z_{2p}, changes suddenly, but the 2p shell
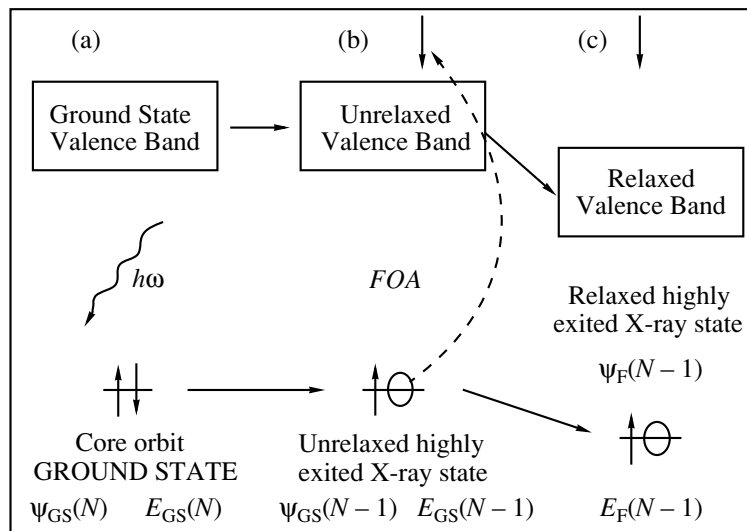
Fig. 8. Process of excitation of the electron system by an X-ray quantum (schematic): (a) the ground state of the system before absorption of an X-ray quantum $\hbar\omega$; (b) the final state of the electron system in the frozen-orbital approximation (*FOA*), described by the wave function Ψ_0^* and energy E_0^*, with a hole at the core energy level, a photoelectron in the continuum, and with the unrelaxed valence band; and (c) the final quasi-stationary state of the relaxed electron system with the X-ray hole, described by the wave function Ψ^* and energy E^*.

itself will be affected by the electron going through and out of the electron system (a distance of roughly 2 au). This increases the duration of the system perturbation by at least an order of magnitude (up to 10^{-17}–10^{-18} s) and becomes comparable to the revolution period of $2p$ electrons (about 10^{-17} s). Furthermore, considering this process formally, we should add a time-dependent perturbation term to the initial Hamiltonian of the system.[1] Therefore, in terms of quantum mechanics, the energy is not conserved in this process.

It is here that a hidden paradox arises when one discusses the applicability of the SP model in the context of X-ray spectroscopy theory. On the one hand, the process of the electron going out of the system causes a perturbation finite in time, which must lead to the violation of the energy conservation. On the other hand, no other particles (quanta or electrons) are emitted or absorbed, and they are not involved directly in the formation or decay of highly excited states; hence, energy must be strictly conserved.

For the valence shell, the revolution period of electrons, as evaluated from the effective radius ($R_{vs} \approx 3$ au) and their energy ($E_{vs} \approx 5$ eV), is of the order of 5×10^{-16} s, which is close to the lifetime (10^{-15} s) of a highly excited state. Hence, the valence electrons have no time to make a sufficient number of revolutions about the nucleus during the lifetime of the excited state. Due to

this fact, it is commonly assumed in X-ray spectroscopy [80] that the transition of an electron system, induced by an X-ray quantum, from the ground state with a wave function $\Psi_{GS}(N)$ and an energy $E_{GS}(N)$ to a final quasi-stationary highly excited state with an X-ray hole at a core orbital [with a wave function $\Psi_F(N-1)$ and an energy $E_F(N-1)$], proceeds via a transient, "unrelaxed," highly excited state $\Psi_{GS}(N-1)$ with an energy of $E_{GS}(N-1)$. In this transient state, the hole is already created at a core orbital, but the other part of the electron system has not yet adapted itself to it (has not relaxed, in terms of X-ray spectroscopy, see Fig. 8). In this scheme, it is assumed that the rearrangement time of the valence shell τ_r is longer than the duration of the perturbation or, what is the same, longer than the time it takes for the electron to leave the core, $\tau_c = a/v \approx$ $a/\sqrt{2\hbar\overline{\omega}/m_e}$, where a is the effective distance the electron travels before it leaves the system (which is roughly 2–3 au), v is the velocity of the electron at which it goes out of the system, and $\hbar\overline{\omega}$ is the energy of the absorbed quantum.

The currently available methods for studying matter that are based on the excitation by X-rays are used, first of all, to investigate the valence shell of the electron structure, the effective radius of which is 2–5 au. In these methods (X-ray absorption spectroscopy, X-ray emission spectroscopy, and some other techniques, by which the specified channels of the creation and decay of highly excited X-ray states are investigated), significantly lower excitation energies are used, 10^3–10^2 eV, which are often close to the ionization thresholds of

---

[1] In fact, the photoelectron no longer belongs to the system in question and, hence, its exit from the system affects the latter, giving rise to a time-dependent perturbation or, in terms of X-ray spectroscopy, to the time-dependent process of "relaxation" of the electron energy levels.

core states. Let us evaluate the time it takes for an electron to leave the system and travel a distance (about 10 au) at which the photoelectron no longer affects the electronic structure of the X-ray cation. We will take the energy E_i of the core state from which an electron is knocked to be 1000 eV ($2p$ state of copper) and the energy of exciting radiation $\hbar\overline{\omega}$ to be equal to the ionization threshold (also 1000 eV).

For the core state before the absorption of an X-ray quantum, the virial theorem holds; hence, $E_i = T_i + V$ and $E_i = -T_i$. Immediately after the absorption (the initial instant), the potential energy of the system is not changed (because the nucleus charge and the electron charge distribution remain the same), but the total energy of the electron at the initial instant $E_f(t = 0)$ becomes equal to $(E_i + \hbar\overline{\omega})$. Under these conditions, the kinetic energy of the photoelectron at the initial instant is $T_f(t = 0) = -2E_i$ and at the infinitely long time $t \longrightarrow \infty$, it is equal to zero. Therefore, we can evaluate the effective velocity of the photoelectron; it is obtained as $(\nu_p(t_0) = 2.5 \times 10^8$ cm/s at the initial instant and $\nu_p(t_\infty) = 0$ at the final instant. Accordingly, the average velocity is 10^8 cm/s, whereas the time it takes for the photoelectron to move a distance of 10 au (5×10^{-8} cm) is $\tau_p = 5 \times 10^{-16}$ s.

At the present time, X-ray methods are being developed in which the effective time it takes for an electron to leave the system can be longer by several orders of magnitude than the estimate made above. For example, in X-ray absorption spectroscopy, the case is rather common where many-center scattering of a photoelectron occurs by nearest-neighbor atoms (XANES range of X-ray absorption spectra); or a photoelectron resides near the absorbing atom for an anomalously long time, because around this atom there is a high positive barrier due to vacant electron states with a large l (giant-resonance spectra in lanthanides and actinides); or a photoelectron, being several atomic units away from the positively charged X-ray hole, is attracted to it (X-ray excitons).

Thus, it is seen that the lifetime of highly excited X-ray states and the time it takes for a photoelectron to leave the system, as well as the revolution period of valence shell electrons, are of the same order of magnitude in the case of the formation of spectra associated with the structure of valence states.

In spite of this, the SP model adequately describes X-ray processes of various types. In the process of absorption of an X-ray quantum, the total energy of the system is changed by the quantum energy $\hbar\overline{\omega}$ and the final energy of the highly excited state is $E_f = (E_i + \hbar\overline{\omega}) = $ const. Thus, it is seen that the energy conservation law is strictly obeyed in the process of interaction of X-ray quanta with matter.

Taking into account that $E_f = (E_i + \hbar\overline{\omega}) = $ const, we can write the wave function of the final state in the form

$$\Psi_F^n(x, t) = \exp\left(-\frac{i}{\hbar}E_F^n t\right)\Phi_F^n(x),$$

which is a solution to the time-dependent Schrödinger equation

$$i\hbar\frac{\partial\Psi_F^n(x, t)}{\partial t} = H\exp\left(-\frac{i}{\hbar}E_F^n t\right)\Phi_F^n(x),$$

where H is the Hamiltonian of the system. Analogously, the initial (ground) state of the system can be written as

$$\Psi_{GS}(x, t) = \exp\left(-\frac{i}{\hbar}E_{GS}t\right)\Phi_{GS}(x).$$

According to quantum mechanics, the probability of the dipole transition from the initial to the final state is given by the formula

$$I_F^n(x, t)$$

$$\approx \left|\int\exp\left(\frac{i}{\hbar}E_{GS}t\right)\Phi_{GS}^*(x)r\exp\left(-\frac{i}{\hbar}E_F^n t\right)\Phi_F^n(x)dx\right|^2$$

$$= \left|\left(\exp\left(\frac{i}{\hbar}E_{GS}t\right)\exp\left(-\frac{i}{\hbar}E_F^n t\right)\right)\int\Phi_{GS}^*(x)r\Phi_F^n(x)dx\right|^2.$$

The total energies of the initial and final states are very large; for individual atoms and molecules, we have $E_{GS} \approx E_F^n \approx 10^4$–$10^5$ eV, while for a solid, in which the effective volume in which the interaction of an electromagnetic quantum with matter takes place may comprise as many as 10 atoms, we have $E_{GS} \approx E_F^n \approx 10^5$–$10^6$ eV. At the initial instant, the time-dependent factors in both the initial and final states are equal to unity and, in addition, the continuity condition for the wave function is fulfilled

$$\exp\left(-\frac{i}{\hbar}E_{GS}t_{(t = 0)}\right)\Phi_{GS}(x) = \exp\left(-\frac{i}{\hbar}E_F^n t_{(t = 0)}\right)\Phi_F^n(x),$$

$$\Phi_{GS}(x)_{(t = 0)} \equiv \Phi_F^n(x)_{(t = 0)}.$$

Therefore, for the probability of dipole transitions, we have a conventional formula

$$I_F^n(x) = \left|\int\Phi_{GS}^*(x)r\Phi_F^n(x)dx\right|^2.$$

Thus, the only process that is associated with the formation of X-ray spectra and proceeds "in a moment" is the interaction of the X-ray quantum with a core electron. Therefore, in the SP model, the Hamiltonian of the system in a highly excited X-ray state can be written as

$$H_{ex} = H_0 + H_{c, d}, \tag{2}$$

where H_0 is the Hamiltonian of the unperturbed system (1) and $H_{c,d}$ is the term describing the interaction of a core hole with the other part of the electron system,

$$H_{c,d} = V_{c,h} \sum d^{+}_{r\lambda\sigma} d_{r\lambda\sigma} n_c,$$

where $n_c = \sum_{\sigma} n_{c\sigma}$ is the number operator of X-ray-produced vacancies at a core orbital.

It follows from the above consideration that the state with $\Psi_{GS}(N-1)$ and $E_{GS}(N-1)$ does not occur; instead, an X-ray quantum induces the transition of the system from the stationary ground state (Ψ_{GS}, E_{GS}) to the final (for the process in question) quasi-stationary state (Φ_F, E_F) with the lifetime τ^* via the transient state $[\Phi_T(N, t) E_T(N, t)]$, the lifetime of which is equal to τ_c (the time it takes for the core electron to leave the system); hence, the duration of the rearrangement of the electron system is $\tau_r = \tau_c$. The change in energy of the electron shells in the process of relaxation associated with the X-ray-created hole is of the order of 1–10 eV, whereas the total excitation energy of the system is $\hbar\overline{\omega} \sim 1000$ eV; that is, the change in energy associated with the relaxation of the valence shell during X-ray processes is a small perturbation of the system.

2.2. The Influence of Strong Electron Correlations on the Spectrum Structure

When studying the X-ray and electron spectra of copper oxide high-T_c superconductors, one should take multielectron states into account, because the core hole strongly interacts with Cu3d electrons. Let us consider the absorption spectrum in the case where an inner-shell 1s or 2p hole is created. In one-electron calculations, the SP approximation in this case is better known as the Larson model [81–84]. The interaction of vacant electron states with X-ray-produced core 2p and 1s vacancies is described by the Coulomb matrix elements $V^p_{c,d} = 7.5$ eV and $V^s_{c,d} = 7$ eV, respectively.

It should be noted that, in the formation of X-ray absorption spectra, the final states may have no holes at copper atoms (transitions $2p \longrightarrow d^{10}$, $d^{10}\underline{L}$, $d^{10}\underline{L}s(\varepsilon)$, $d^{10}\underline{LL}s(\varepsilon)$ and $1s \longrightarrow d^{10}\underline{L}$, $d^{10}\underline{LL}$), one hole (transitions $2p \longrightarrow d^9 s(\varepsilon)$, $d^9\underline{L}s(\varepsilon)$, d^9 and $1s \longrightarrow d^9$, $d^9\underline{L}$), or two holes at copper atoms (transitions $2p \longrightarrow d^8 s(\varepsilon)$ and $1s \longrightarrow d^8$).

Before the creation of a hole at a core orbital of copper, the multielectron wave function of the system can be written as

$$\psi_{in} = \varphi_c^n \psi^{(pd)}_{in,0},$$ (3)

where φ_c^n is the wave function of the core electron, n is the occupation number of the core orbital, and $\psi^{(pd)}_{in,0}$ is

the wave function of the ground state of the valence electron system of copper and oxygen with the energy $E^{(pd)}_{in,0}$, described by the Hamiltonian (1) under the condition $n_d + n_p = n_h = $ const, where n_d and n_p are the concentrations of holes in d states of copper and p states of oxygen, respectively, and n_h is the number of holes in a unit cell, being equal to 1 or 2, depending on the doping.

The wave function of the system in the final state with the unchanged number of vacancies in the valence shell (excluding the process of formation of the white line of the CuL_3 spectrum, in which the number of Cu3d vacancies is decreased by unity) and with one photoelectron in the s, p, or d continuum far beyond the ionization threshold can be written in the form

$$\Psi^{(m)}_f = \varphi_c^{n-1} \varphi_l \psi^{(pd)}_{f,m},$$ (4)

where φ_l is the wave function of the photoelectron in the l state with an energy ε_l, to which this electron makes a transition after excitation, and $\psi^{(pd)}_{f,m}$ is the wave function of the mth term of the system of p and d electrons in the final state with the energy $E^{(pd)}_{f,m}$. The index m enumerates all eigenstates of the Hamiltonian $(1 + 2)H + H_{c,d}$ [given by (1) and (2)] that have a vacancy at a core orbital.

The energies of the initial and final states are

$$E_{in} = n\varepsilon_c + E^{(pd)}_{in,0},$$
$$E_{f,m} = (n-1)\varepsilon_c + \varepsilon_l + E^{(pd)}_{f,m},$$ (5)

respectively, where $E^{(pd)}_{f,m}$ is the energy of the mth term of the final highly excited state. In the approximation where strong electron correlations and the formation of the white line of the CuL_3 spectrum are ignored, the energy of the absorbed X-ray quantum equals

$$\hbar\omega_0 = \varepsilon_l - \varepsilon_c.$$ (6)

When strong electron correlations are taken into account, the energy of the absorbed X-ray quantum is

$$\hbar\omega = \varepsilon_l - \varepsilon_c + \Delta E_m,$$
$$\Delta E_m = E^{(pd)}_{f,m} - E^{(pd)}_{in,0}.$$ (6a)

Thus, in the one-electron approximation, we can write the energy of this quantum as $\hbar\omega_0 = \hbar\omega - \Delta E_m$.

X-ray absorption is described by the Hamiltonian

$$H_{X\text{-ray}} = \sum_k I^{(0,k)} c^+ l_k,$$

where $I^{(0,k)} = |\langle\varphi_c|\mathbf{er}|\varphi_k\rangle|^2$ is the one-electron dipole matrix element, c^+ is the creation operator of a hole at a core orbital, and l_k is the annihilation operator of a hole in the valence shell or in the continuum. In the case

where the number of d holes remains unchanged (transitions to s or p orbitals), the intensity of an X-ray-induced transition is

$$I_m(\hbar\omega) = \left|\langle\varphi_{\text{in}}|\mathbf{er}|\psi_f^{(m)}\rangle\right|^2 = \left|\langle\varphi_c(\varepsilon_c)|\mathbf{er}|\varphi_l(\varepsilon_l)\rangle\right|^2 \\ \times\left|\langle\psi_{\text{in},0}^{(pd)}(E_{\text{in},0}^{(pd)})|\psi_{f,m}^{(pd)}(E_{f,m}^{(pd)})\rangle\right|^2. \quad (7)$$

In the absence of strong Coulomb interaction between the hole at an inner-shell orbital and valence vacancies ($V_{c,d} = 0$), the functions $\psi_{\text{in},0}^{(pd)}(E_{\text{in},0}^{(pd)})$ and $\psi_{f,m}^{(pd)}(E_{f,m}^{(pd)})$ are mutually orthogonal and, hence, the last factor in (7), $I^{(c,m)}(\Delta E_m) = |\langle\psi_{\text{in},0}^{(pd)}(E_{\text{in},0}^{(pd)})|\psi_{f,m}^{(pd)}(E_{f,m}^{(pd)})\rangle|^2$, is equal to $\delta_{m,0}$. In this case, the transition probability is determined only by the matrix element $I^{(0,l)}(\hbar\omega_0) = \langle\varphi_c(\varepsilon_c)|\mathbf{er}|\varphi_l(\varepsilon_l)\rangle$, which is calculated in the one-electron approximation.

If the Coulomb interaction (2) is not ignored, the states of valence p and d electrons (holes) before and after photoionization cease to be orthogonal and, therefore, both the ground term and various excited terms of the final state contribute to the absorption spectrum.

The formation of the white line of the $CuL_{2,3}$ spectrum is more difficult to analyze, because the number of holes in the d shell decreases. The wave function in this process can be written in the form

$$\Psi_f^{(m)} = \varphi_c^{n-1}\psi_{f,m}^{(pd)}(n_h - 1), \quad (8)$$

where $\psi_{f,m}^{(pd)}(n_h - 1)$ is the multielectron function in the $(n_h - 1)$-particle subspace of the Hilbert space. The energy of the final state is equal to

$$E_{f,m} = (n-1)\varepsilon_c + E_{f,m}^{(pd)}(n_h - 1) \quad (9)$$

while the energy of the absorbed X-ray quantum is

$$\hbar\omega = -\varepsilon_c + \Delta E_m. \quad (10)$$

The one-electron energies ε_d of the d orbitals of the initial and final states are included in the multielectron energies $E_{\text{in},0}^{(pd)}$ and $E_{f,m}^{(pd)}$; their values, as obtained by X_α calculations and used in treating the processes of this type, are roughly –2 to –3 eV.

In the absence of the strong Coulomb interaction with the X-ray hole (and, hence, in the absence of the relaxation of the electron system associated with the creation of this hole), the energies of the initial and final states of the d shells can be written as $E_{\text{in}}^0 = n\varepsilon_c + (10 - n_h)\varepsilon_d$ and $E_f^0 = (n-1)\varepsilon_c + (10 - n_h + 1)\varepsilon_d$, respectively. In this case, the one-electron transition energy is

$$E_f^0 - E_{\text{in}}^0 = \hbar\omega_0 = \varepsilon_d - \varepsilon_c$$

and, in addition,

$$\hbar\omega_0 = \hbar\omega - \Delta E_m.$$

Therefore, the intensity of the white line (associated with a decrease of the number of d holes by unity) can be written in the form

$$I_m(\hbar\omega) = \left|\langle\psi_{\text{in}}|\mathbf{er}|\psi_f^{(m)}\rangle\right|^2 = \left|\langle\varphi_c(\varepsilon_c)|\mathbf{er}|\varphi_d(\varepsilon_d)\rangle\right|^2 \\ \times\left|\langle\psi_{\text{in},0}^{(pd)}(E_{\text{in},0}^{(pd)})|d_{r\lambda\sigma}|\psi_{f,m}^{(pd)}(E_{f,m}^{(pd)}, n_h - 1)\rangle\right|^2. \quad (11)$$

As in (7), we designate the one-electron contribution as $I^{(c,m)}(\Delta E_m)$ and the multielectron one as $I^{(0,l)}(\hbar\omega_0)$.

Summing (7) and (11) over multielectron transitions, we obtain an expression describing the whole spectrum,

$$I(\hbar\omega) = \sum_m I_m(\hbar\omega) \\ = \sum_m I^{(0,l)}(\hbar\omega - \Delta E_m)I^{(c,m)}(\Delta E_m). \quad (12)$$

Thus, the total absorption spectrum $I(\hbar\omega)$ consists of a set of one-electron spectra, the intensity of the principal line of which is proportional to the multielectron factor $I^{(c,m)}(\Delta E_m)$ with $m = 0$, given by (7) and (11), and satellites, separated from the principal line by $\Delta E_m = E_{f,m}^{(pd)} = E_{\text{in},0}^{(pd)}$ and having an intensity determined by multielectron factors (7) and (11) with $m \neq 0$. As is seen, the X-ray absorption spectrum of the strongly correlated electron system is the discrete convolution of two spectra: the discrete spectrum $I^{(c,m)}(\Delta E_m)$ of transitions between p and d states of electrons (holes) and the one-electron spectrum $I^{(0,l)}(\hbar\omega - \Delta E_m^{(h)})$ of transitions from $1s$ and $2p$ core orbitals to vacant electron states situated both below and above the ionization threshold.

2.3. A One-Electron Model for Calculating X-ray Absorption Spectra

The problem of choosing a cluster for calculating the one-electron structure and spectra of high-T_c superconductors has long been solved [27]. The one-electron profiles of X-ray absorption spectra both below and above the ionization threshold were calculated in the self-consistent-field approximation for X_α scattered waves (SCF X_αSW) [85]. By now, the range of applicability of this approximation is well known. In this paper, the electronic structure of clusters CuO_6^{10-} and CuO_6^{9-} ($La_{2-x}Sr_xCuO_4$), corresponding to the (+2) and (+3) formal copper states, was calculated employing the X_α-OMEGA program complex [86], while the calculations of the electronic wave functions and one-electron X-ray dipole transition intensities in all energy range were performed using the X_α-CONTINUOUS program [87]. The cluster parameters were chosen

in accord with the internuclear spacing presented in [88, 89].

2.4. The Structure of the Final Spectra

The final spectra include both the effects of the density of vacant one-electron states and the doping of the $La_{2-x}Sr_xCuO_4$ compound and the effects of strong correlations in doped and undoped unit cells. These spectra are obtained by summing the one-electron spectra in accordance with (12). The xy-polarized CuL_3 spectrum of undoped La_2CuO_4 represents the (only possible) one-electron transition from the Cud^9 to the Cud^{10} configuration with an intensity of 0.3428 and an energy of 2.03 eV; the profile of the spectral line is obtained using the calculated profiles of one-electron spectral lines of the CuO_6^{10-} cluster by the SCF-X_αSW method. The polarized spectra of unit cells with two vacancies in the triplet ground state are more complex; for instance, the xy component is formed by transitions from the ground two-hole state to four configurations of the final state with a vacancy at the $Cu2p$ core orbital (in the one-hole subspace) with weighting factors 0.0560, 0.2241, 0.0037, and 0.0285, while the z component is formed by the same transitions with weights of 0.2238, 0.0000, 0.0148, and 0.0000. The energies of these four configurations are 1.9405, 2.1424, 9.8151, and 10.3131 eV, respectively. The profiles of these spectral lines are calculated by the SCF-X_αSW method for the CuO_6^{9-} cluster, which corresponds to the (+3) copper state in the one-electron approximation. The integrated intensity of the polarized lines below the ionization threshold depends only on the occupancies of the corresponding (in accord with the Δm selection rules) vacant d orbitals ($x^2 - y^2$ or z^2) in the initial state, whereas the number of multielectron transitions depends on the number of configurations in the final state. In our model, the orthorhombic distortion of the CuO plane is not taken into account, which leads to the absence of the white line in the z component of the spectra of the undoped compound, because the d_{z^2} orbital makes no contribution to the initial state; the emergence of the white line in the spectra of the doped compound is due to the mixing of the states $d^8(d_{x^2-y^2} + d_{z^2})$ and $d^9L(d_{z^2})$ with weights $(0.38)^2$ and $(-0.46)^2$, respectively.

The CuL_3 spectra of the singlet state are found by the same procedure. In the xy-polarized spectrum, the intensities of transitions to the final configurations are 0.222, 0.001, 0.042, and 0.000, whereas in the z-polarized spectrum, they are 0.000, 0.005, 0.000, and 0.002, with the energies of the configurations being 2.139, 2.280, 10.363, and 10.956 eV, respectively. Thus, in the singlet state, as is seen from these data, the density of vacant bound d_{z^2} states is practically zero.

The CuK spectra are also calculated from (7) and (12). For example, the spectrum of undoped La_2CuO_4 is formed from the one-electron spectrum of the $Cud^{10}\underline{L}$ configuration with a weighting factor of 0.765 and an energy of 2.7 eV and the one-electron spectrum of the Cud^9 configuration with a weight of 0.235 and an energy of 10.6 eV. The spectrum of $LaSrCuO_4$ with the singlet two-hole ground state is also formed from the spectra of two configurations: $Cud^{10}\underline{LL}$ with a weight of 0.849 and an energy of 2.3 eV and $Cud^9\underline{L}$ with a weight of 0.144 and an energy of 12.1 eV. The spectrum of $LaSrCuO_4$ with the triplet two-hole ground state is formed from the spectra of three configurations: $Cud^{10}\underline{LL}$ with a weight of 0.630 and an energy of 3.425 eV, $Cud^9\underline{L}$ (of an $x^2 - y^2$ character) with a weight of 0.151 and an energy of 11.7 eV, and a combination of $Cud^9\underline{L}$ (of a z^2 character) and Cud^8, with a weight of 0.219 and an energy of 16.5 eV.

2.5. Low-Concentration Approximation (Independent-Center Model)

In a doped $La_{2-x}Sr_xCuO_4$ crystal, one part of the unit cells has a single hole, while the other part has two holes. The spectra of these partly doped superconductors are calculated under the assumption that the highly correlated two-hole states produced by dopant atoms do not interact with each other, because their concentration is low. In this case, the weighting factors of the one- and two-hole components of the spectra of compounds $La_{2-x}Sr_xCuO_4$ ($x = 0.2$) are taken in accordance with the degree of doping. For example, the spectrum of $La_{1.8}Sr_{0.2}CuO_4$ is formed from the spectrum of La_2CuO_4 with a weight of 0.8 and the spectrum of (singlet or triplet) $LaSrCuO_4$ with a weight of 0.2. The halfwidths of the Lorentzian and Gaussian broadening of the CuK_α- and $Cu2p$-XPS spectra are taken to be 0.3 eV.

3. MANIFESTATION OF THE EFFECTS OF STRONG ELECTRON CORRELATIONS IN X-RAY AND ELECTRON SPECTRA

3.1. The Cu2p X-ray Photoelectron Spectra of La_2CuO_4-Type Compounds

As indicated in Section 1, the multiplet structure of the spectra of copper oxides with the Cud^9 configuration is well understood in terms of the multielectron Anderson model and described in detail (see, e.g., [58]). Nonetheless, we would like to cite the typical experimental $Cu2p$-XPS spectra of compounds Cu_2O, CuO, La_2CuO_4, $La_{1.85}Sr_{0.15}CuO_4$ (Fig. 1) [3, 5], and $NaCuO_2$ (Fig. 2) [23].

Figure 9 shows the $Cu2p$-XPS spectra of (a) the one-hole configuration and (b) two-hole configuration

calculated in the extended p–d model. According to the calculations, the principal peaks of these two spectra correspond to Cu^{+1}. For example, in the one-hole configuration (Fig. 9a), the occupancy of the Cu$d^{10}\underline{L}$ configuration is $(0.91)^2$, and that of Cud^9 is $(0.42)^2$. In the two-hole configuration, the occupancy of Cu$d^{10}\underline{LL}$ is even somewhat higher, $(0.92)^2$; the weight factor of the Cud^8 configuration is negligible, at $(0.05)^2$, while the weights of the two Cu$d^9\underline{L}$ configurations are $(0.37)^2$ and $(0.11)^2$.

It is seen from Fig. 9 that the addition of one more hole leads to the appearance of an extra short-wavelength satellite near 18 eV, associated with transitions to the two Cu$d^9\underline{L}$ configurations with weights $(0.12)^2$ and $(0.81)^2$ and the Cud^8 configurations with a weight of $(0.56)^2$. Thus, these calculations qualitatively support both a growth of the short-wavelength part of the $3d^9$ peak with a doping of La$_2$CuO$_4$ and the appearance of an extra satellite in the spectrum of the NaCuO$_2$ compound. The significant differences in the positions of the peaks in NaCuO$_2$ are likely to be due to the fact that the Cud^8 configurations are practically absent in NaCuO$_2$ [90] and only the Cu$d^9\underline{L}$ configuration is responsible for the formation of the principal peak; hence, copper is in the bivalent state in this compound. As for the energy spacing between these two satellites in La$_2$CuO$_4$, its overestimation by roughly 3 eV is due, in our opinion, to the rather inexact determination of the p–d-model parameters.

If the spin–orbit splitting of the core $2p$ energy level and the effect of doping on the spectra in the independent-center approximation (Fig. 10) are taken into account, then, in the spectrum of La$_{1.8}$Sr$_{0.2}$CuO$_4$, the principal peak depending on the occupancy of the Cu$d^{10}\underline{L}$ configuration has a feebly marked (in proportion to the degree of doping) asymmetric short-wavelength structure (with a peak at 17 eV) associated with the energy separation of the Cu$d^{10}\underline{L}$ and Cu$d^{10}\underline{LL}$ cluster configurations with the formal (+2) and (+3) oxidation levels of copper. In our opinion, a comparison of our results and the experimental spectrum [3] (Figs. 1, 2) lends credence to this prediction.

For the most part, the results we obtained are similar to the calculations of the Cu$2p$ XPS in [58], with the essential difference being that the high-energy satellite separated by 14 eV from the principal line is absent in [58], which is due, in our opinion, to the fact that we perform the complete diagonalization of the Hamiltonian, including all two-particle states, whereas in [58], the diagonalization is carried out numerically in a given, less complete, basis.
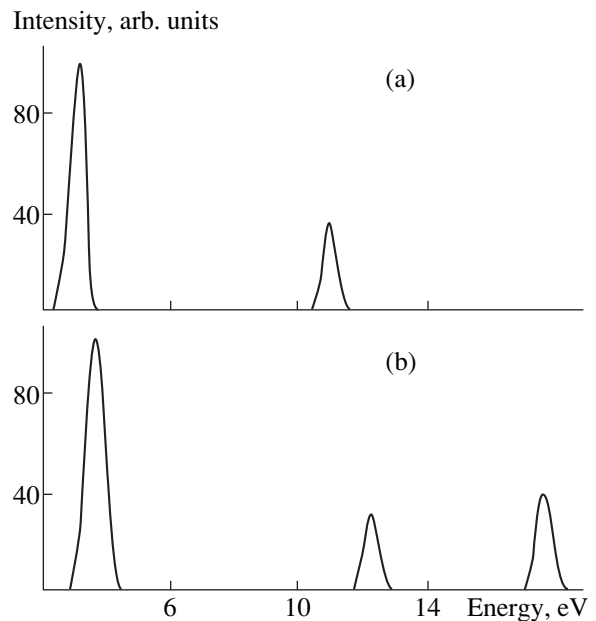

Fig. 9. Theoretical Cu$2p$ X-ray photoelectron spectra of compounds (a) La$_2$CuO$_4$ and (b) LaSrCuO$_4$ without spin–orbit splitting of the Cu$2p$ orbital.

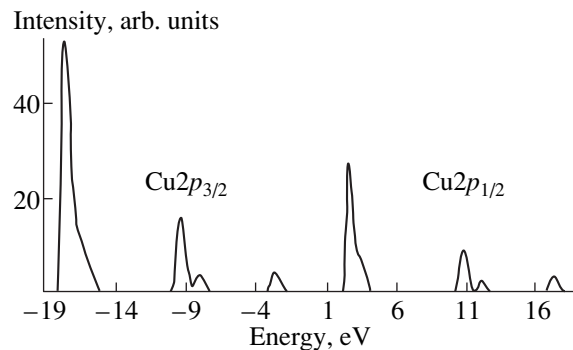**Fig. 10.** Theoretical Cu$2p$ X-ray photoelectron spectrum of the La$_{1.8}$Sr$_{0.2}$CuO$_4$ compound (including the spin–orbit splitting of the $2p$ orbital of copper, $\Delta_\varepsilon = 20$ eV), calculated in the independent-center approximation.

3.2. The CuK$_\alpha$ Spectra of La$_2$CuO$_4$-Type Compounds

As mentioned in Section 1, the theoretical spectra of systems with one hole are described in detail in [36, 37]. In these spectra, there is a faint satellite depending on the density of the Cud^9 configurations and lying 0.4 eV above the principal peak, which depends on the density of Cu$d^{10}\underline{L}$ state in the 1s- and 2p-hole configurations. As shown in [37], the shift of the K_α line of copper cannot be measured, using the Larson model, without separating the satellite structure configurations.

In our case, the addition of one more hole to the cluster leads to the change in the nature of the principal peak (Fig. 11), which now depends, for the most part,
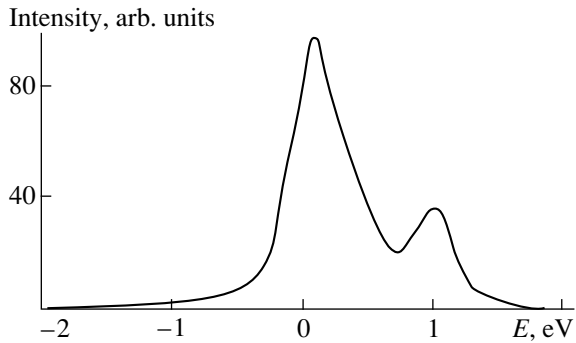
Intensity, arb. units

Fig. 11. Theoretical CuK_α spectrum of the two-hole configuration corresponding to the LaSrCuO$_4$ compound.
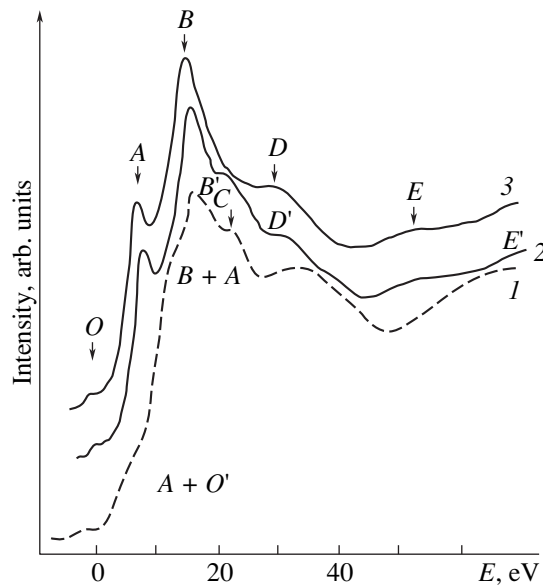

Fig. 12. Experimental [28] (*1*), theoretical CuK (including multielectron effects) (*2*), and theoretical one-electron (*3*) absorption spectra of La$_2$CuO$_4$. Peaks O, A, B, D, and E correspond to the principal spectral line (configuration $d^{10}\underline{L}$), while peaks O', A', B', D', and E' correspond to the shake-up satellite (configuration d^9), separated from the principal line by 7.8 eV.

on the density of the Cu$d^{10}\underline{LL}$ configurations of the ground, intermediate, and final 1s and 2p hole states. The faint satellite lying 0.4 eV above the principal peak now reflects the density of the Cu$d^9\underline{L}$ configurations, while the new short-wavelength intense satellite at 1 eV is due to the two Cu$d^9\underline{L}$ configurations and the one Cud^8 configuration with a weight of $(0.56)^2 + (0.57)^2$. When the spin–orbit splitting of the core 2p orbital of copper and the superposition of the two-hole and one-hole spectra (in the independent-center model) are taken into account, there appear asymmetry and a faint

shoulder on the short-wavelength side of the principal peak.

3.3. The Ground Terms of the Initial and Final X-ray States of the CuO$_4$ Cluster

The weights of the d^9 and $d^{10}\underline{L}$ configurations of the undoped CuO$_4$ unit cell in La$_2$CuO$_4$ are 69 and 31%, respectively. Thus, the copper ion in this cell is basically in the common Cu^{+2} oxidation state. Doping does not change this picture; the dominant configuration of the CuO$_4$ unit cell of the completely doped LaSrCuO$_4$ compound is the $d^9\underline{L}$ configuration with a weight of 57% (the contribution from the $d_{x^2-y^2}$ state is 36% and that from the d_{z^2} state is 21%), while the weight of the $d^9\underline{LL}$ configuration is 28% and that of d^8 is 14%.

The creation of an X-ray core (1s or 2p) hole leads to a dramatic rearrangement of the electronic structure of both doped and undoped unit cells. In this case, the weights of the d^9 and $d^{10}\underline{L}$ configurations of the undoped CuO$_4$ unit cell of La$_2$CuO$_4$ are 18 and 82%, respectively. Thus, the oxidation level of copper is changed and equals +1. The same picture takes place in doped CuO$_4$ unit cells, in which the weight of the $d^{10}\underline{LL}$ configuration is 85%, while that of $d^9\underline{L}$ is 15% (14% of $d_{x^2-y^2}$ and 1% of d_{z^2}). The weight of the d^8 configuration is negligible, only 0.3%.

3.4. The CuK Absorption Spectra of La$_{2-x}$Sr$_x$CuO$_4$

There is some direct experimental evidence that strong electron correlations affect the CuK X-ray absorption spectra of La$_2$CuO$_4$ [91]. The mechanism of the formation of these spectra was investigated in detail by using various versions of the nonempirical one-electron multiple-scattering method [24–27], and all features were adequately described, except for the peak C, which lies 7 eV above the principal peak. The former peak appeared only in the xy-polarized spectra when the cluster size was as large as 50–60 atoms [25–27], whereas, experimentally, this feature is also observed in the z polarization [91].

When one more vacancy per unit cell is added by doping, contributions from the Cud^8, Cu$d^9\underline{L}$, and the Cu$d^{10}\underline{LL}$ configurations appear. This leads to significantly more complicated CuK absorption spectra associated with the electronic states produced by doping of HTSC compounds [28].

In order to study the effect of strong electron correlations on the CuK X-ray absorption spectra, we completely diagonalize the multiband p–d-model Hamiltonian of the CuO$_4$ cluster in the sudden-perturbation approximation described in Section 2. The matrix ele-

ments of X-ray-induced transitions $1s \longrightarrow p(\varepsilon)$ are calculated for the CuO_6^{10-} and CuO_6^{9-} clusters by the non-empirical SCF-X_αSW method. The final spectra are constructed using the spectral line profiles as calculated by the one-electron method and the weight factors and energies of configurations as calculated in the many-band p–d model. The spectrum of completely doped LaSrCuO$_4$ is calculated for both the singlet and triplet two-hole states.

3.5. Discussion of Results

Figure 12 shows the experimental [28] and theoretical one-electron CuK spectra of La$_2$CuO$_4$. It is seen that both the positions and the relative intensities of the peaks of the calculated spectrum, including multielectron effects, correlate well with those of the experimental spectrum, excepting perhaps the long-wavelength range of the spectra near peak A. It has been pointed out in the literature that some discrepancy in this range is due to the small size of the CuO_6^{10-} cluster for which the theoretical peak A was calculated [25–27].

The calculations showed that the principal spectral line in the CuK spectrum corresponds to the $d^{10}\underline{L}$ configuration with a weight of $(0.88)^2$ (peaks O, A, B, D, and E), whereas the single intense short-wavelength shake-up satellite (peak C in the experimental spectrum and peak B' in the theoretical one in Fig. 12), separated by an energy of 7.8 eV from the principal peak, is associated with the d^9 configuration (peaks O', A', B', D', and E'). Therefore, the experimental peak C should be correlated with the theoretical peak B'. This peak is due to photoelectron scattering by surrounding atoms in La$_2$CuO$_4$, as is indicated in the literature [25–27], and is also associated with the Cud^9 configuration in this compound.

The shape of the experimental CuK spectrum of dopant-produced states in LaSrCuO$_4$ ("trivalent copper") is significantly more complex [28] (Fig. 13). A comparison of the experimental [28] (curve 1) and theoretical CuK spectra of LaSrCuO$_4$ with the singlet (curve 3) and triplet (curve 2) ground states shows that the two-hole ground state of LaSrCuO$_4$ in the doped La$_{2-x}$Sr$_x$CuO$_4$ system is the triplet. The principal line in this spectrum (peaks O, A, B, D, and E) is associated with the $d^{10}\underline{LL}$ configuration with a weight of $(0.91)^2$ mixed with small amounts of states $d^9\underline{L}$ ($x^2 - y^2$, with a weight of $(0.39)^2$, and z^2 with a weight of $(0.12)^2$). The first satellite (peaks O', A', B', D', and E') is principally associated with the $d^9\underline{L}$ state of an $x^2 - y^2$ character with a weight of $(0.90)^2$, mixed with a small amount of $d^{10}\underline{LL}$ (with a weight of $(0.39)^2$). The second satellite (peaks O'', A'', B'', D'', and E'') depends on the density of configurations $d^9\underline{L}$ (z^2), having a weight of $(0.81)^2$,
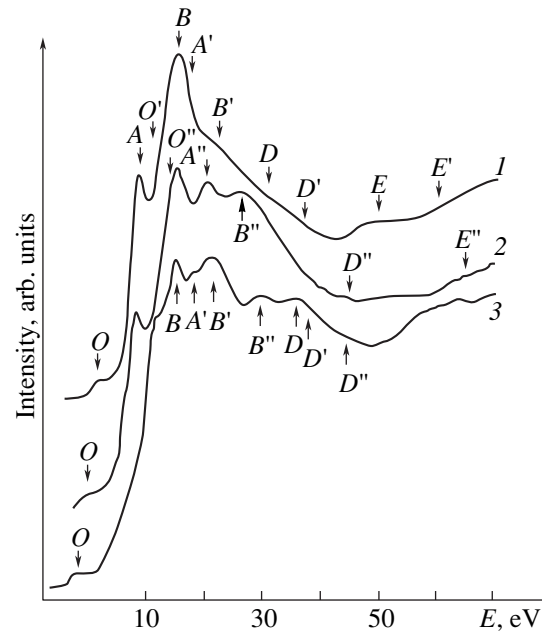

Fig. 13. Experimental [28] (*1*) and theoretical CuK X-ray absorption spectra for dopant-produced two-hole states with the triplet (*2*) and singlet (*3*) ground states. Peaks O, A, B, D, and E correspond to the principal spectral line (the $d^{10}\underline{LL}$ state); peaks O', A', B', D', and E' correspond to the first satellite (the $d^9\underline{L}$ ($x^2 - y^2$) state); and peaks O'', A'', B'', D'', and E'' correspond to the second satellite (the $d^9\underline{L}$ (z^2) and d^8 states).

and d^8, having a weight of $(0.57)^2$, mixed with a small amount of $d^9\underline{L}$ ($x^2 - y^2$) with a weight of $(0.12)^2$. The symbols above the experimental curve in Fig. 13 indicate the correspondence between peaks and configurations. Some discrepancies observed for the relative intensities and positions of peaks A' and B' are associated with the overestimation of the relative intensity of peak A in the one-electron calculation, which leads to some distortion of the final spectrum.

3.6. The Influence of Strong Electron Correlations of the CuL_3 X-ray Absorption Spectra of La$_{2-x}$Sr$_x$CuO$_4$

The scheme for calculating the CuL_3 absorption spectra was described in detail in Section 2. In the La$_{2-x}$Sr$_x$CuO$_4$ system with $x = 0$ (with one electron vacancy per formula unit), as was shown in [32], there occurs only one X-ray-induced transition, $2p^6 d^9_{x^2 - y^2} \longrightarrow 2p^5 d^{10}$, although the initial state consists of two d^9-type and two $d^{10}\underline{L}$-type configurations by virtue of the hybridization of vacant states. In the case of $x > 0$, there appear contributions from the Cud^8, Cu$d^9\underline{L}$, and Cu$d^{10}\underline{LL}$ configurations, due to which the multielectron effects become much stronger and the CuL_3 spec-
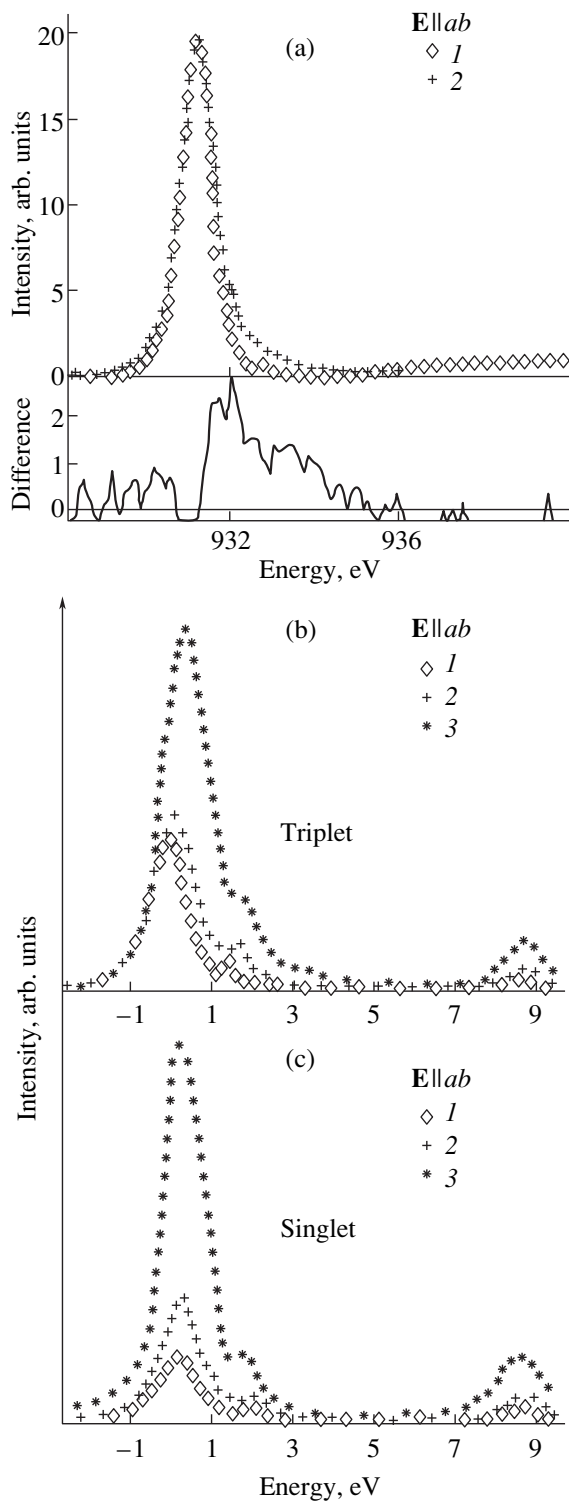
Fig. 14. (a) Experimental *xy*-polarized CuL_3 X-ray absorption spectra of (*1*) La$_2$CuO$_4$ and (*2*) La$_{1.92}$Sr$_{0.08}$CuO$_4$ [2]; (b) theoretical *xy*-polarized spectra of compounds (*1*) La$_2$CuO$_4$, (*2*) La$_{1.92}$Sr$_{0.08}$CuO$_4$, and (*3*) LaSrCuO$_4$ for when the two-hole ground state is the triplet; and (c) theoretical *xy*-polarized spectra of compounds (*1*) La$_2$CuO$_4$, (*2*) La$_{1.92}$Sr$_{0.08}$CuO$_4$, and (*3*) LaSrCuO$_4$ for when the two-hole state is the singlet; **E** ∥ *ab*.
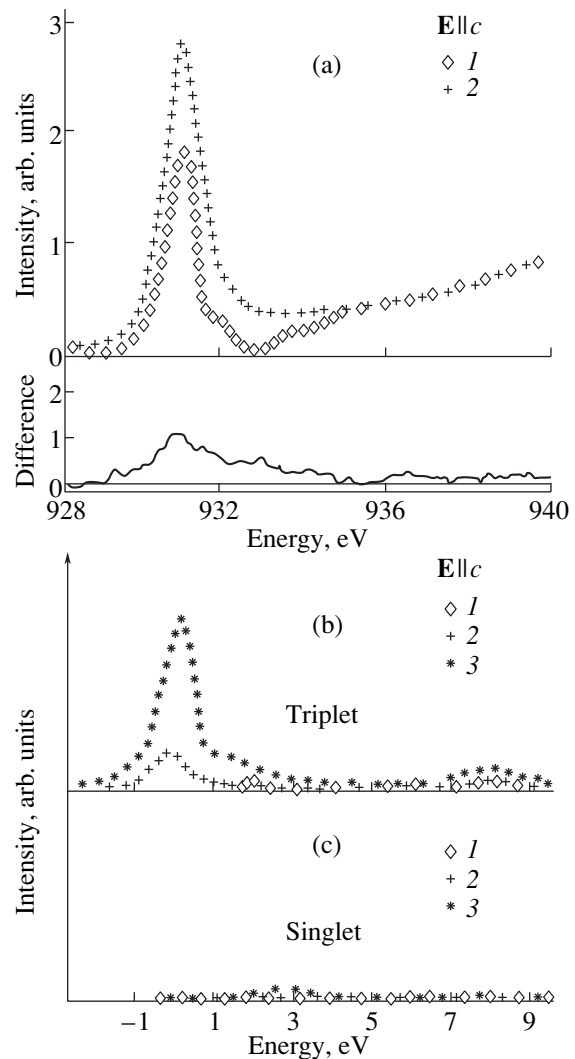
Fig. 15. (a) Experimental *z*-polarized CuL_3 X-ray absorption spectra of (*1*) La$_2$CuO$_4$ and (2) La$_{1.92}$Sr$_{0.08}$CuO$_4$ [2]; (b) theoretical *z*-polarized spectra of compounds (*1*) La$_2$CuO$_4$, (2) La$_{1.92}$Sr$_{0.08}$CuO$_4$, and (*3*) LaSrCuO$_4$ for when the two-hole ground state is the triplet; and (c) theoretical *z*-polarized spectra of compounds (*1*) La$_2$CuO$_4$, (*2*) La$_{1.92}$Sr$_{0.08}$CuO$_4$, and (*3*) LaSrCuO$_4$ for when the two-hole ground state is the singlet; **E** ∥ *c*.

tra of dopant-produced electronic states of doped compounds differ noticeably from those of undoped ones (in particular, shake-up satellites appear near the white line [2, 32, 33]).

Figure 14a presents the experimental CuL_3 spectra of La$_2$CuO$_4$ and La$_{1.92}$Sr$_{0.08}$CuO$_4$ [2] for the *xy* polarization, while the theoretical *xy*-polarized spectra of the La$_2$CuO$_4$, LaSrCuO$_4$, and La$_{1.92}$Sr$_{0.08}$CuO$_4$ compounds are shown in Fig. 14b for when the two-hole ground state is the triplet, and in Fig. 14c for when this state is the singlet.

Figure 15a presents the experimental CuL_3 spectra of La_2CuO_4 and $La_{1.92}Sr_{0.08}CuO_4$ [2] for the z polarization, while the theoretical z-polarized spectra of the La_2CuO_4, $LaSrCuO_4$, and $La_{1.92}Sr_{0.08}CuO_4$ compounds are shown in Fig. 15b for the case where the two-hole ground state is the triplet and in Fig. 15c for the case where this state is the singlet.

In both the experimental and theoretical xy-polarized spectra of the undoped La_2CuO_4 compound (Fig. 14), there are no nondiagram spectral lines (the electronic transitions that cannot be described in terms of the crystal-field theory in the first approximation) below the ionization threshold. However, in the experimental z-polarized spectrum (Fig. 15), a fairly intense white line is observed, which is absent in the corresponding theoretical spectrum. This difference is due to the fact that, in this paper, no account is taken of the orthorhombic distortion of the CuO_2 plane, which, as was shown in [92], is responsible for this effect. The shape of the line above the ionization threshold in both the z- and xy-polarized spectra is described adequately, as in the case of the spectra calculated in the one-electron approximation [27].

The principal difference between the experimental spectra of doped and undoped compounds is that, in the former case, the intensity of the white line becomes much higher in the z polarization (Fig. 15). The absence of the white line in the theoretical z-polarized spectrum of a doped compound with the singlet ground state and its presence in the case of the triplet ground state (Fig. 15) suggests that, in the unit cell with two electron vacancies, the ground state is the triplet. In this case, the white line is associated with transitions from the ground state to a final state with a $Cu2p$ vacancy and with appreciably populated d_{z^2} states of the $d^8(d_{x^2-y^2} + d_{z^2})$ and $d^9\underline{L}(d_{z^2})$ orbitals (with weights of $(0.38)^2$ and $(-0.46)^2$, respectively) with a transition energy of 1.94 eV and an intensity of 0.2238. The transition intensity of the white line with the z polarization for the configuration being next in energy is equal to zero.

Our model adequately describes the faint long-wavelength satellite in the xy polarization, which is associated with the lowest energy configuration of the final state with a core $2p$ vacancy (the transition intensity 0.0560) and is situated 0.4 eV below the white line in the experimental spectrum (Fig. 14) [2]. The xy-polarized white line for the triplet state is associated with the configuration that is next in energy and for which the transition energy is 2.14 eV and the intensity is 0.2241. The transition intensities to the next two high-energy configurations (for which the transition energies are 9.82 and 10.31 eV, respectively) are virtually zero in these spectra, and the corresponding white lines are practically absent above the ionization threshold. In the range above the threshold, the spectra are largely composed of the lines due to the first two configurations. The small energy separation between these

spectral lines and the large (compared to that of the white line) half-widths of the features lead to some flattening of the spectra in the positive energy range. In our calculations, in contrast to those in [30], the peak corresponding to the s states (at about 8 eV) in the range above the ionization threshold has a noticeable intensity, which is due, in our opinion, to the cluster effect.

CONCLUSIONS

Analysis of the literature showed that a great body of experimental data give evidence of the rather dramatic effect of strong electron correlations on the electronic structure of high-T_c superconductors and, in particular, on the structure of vacant electronic states. For example, the investigation of the X-ray absorption spectra allowed one to separate out two-particle contributions due to doping, and it was shown that one dopant atom interacts with two copper centers and produces vacant electronic states of a $Cu\,d_{z^2}$ character.

Theoretical one-electron and multielectron calculations of the electronic structure of the key objects were performed, but, as a rule, they were not accompanied by theoretical modeling of the available spectroscopic measurements. It became clear that most of the experimental X-ray and electron spectra could not be directly and unambiguously interpreted. This was due to the fact that the principal features of the electronic structure of high-T_c superconductors are determined by strong electron correlations. Only some experimental data have been adequately described in terms of the current theoretical models. These data were obtained, for the most part, for insulating phases, whereas no spectra of dopant-produced two-hole states have been theoretically investigated up to now. For treating the spectral properties of a material with a strongly correlated electron system, a multielectron theory of X-ray and X-ray electron spectra has been developed on the basis of the sudden-perturbation model. This theory allowed one to describe a number of key spectral characteristics of the compounds in question in a unified way. The X-ray and electronic spectra were represented in the form of convolution of the spectrum of one-electron transitions to vacant orbitals both below and above the ionization threshold and the spectrum of multielectron transitions within the system of valence electrons.

In all the spectra investigated (except for the CuL_3 absorption spectrum), the principal spectral lines correspond either to the $Cud^{10}\underline{L}$ (for the undoped unit cell) or to the $Cud^{10}\underline{LL}$ (for the doped unit cell) configuration. In the spectra of undoped centers, the satellite structures are determined by the contributions from the Cud^9 configurations. Doping leads to more complicated spectra, which contain satellites depending on the density of the $Cud^9\underline{L}$ configurations. In all cases considered, the contribution from the Cud^8 two-hole con-

figurations is small. The white line of the CuL_3 spectrum of undoped and doped unit cells corresponds to the Cud^9 and Cu$d^9\underline{L}$ configurations, respectively. Doping leads to an increase in the occupancy of the Cud_{z^2} orbitals, which in turn results in an increase of the intensity of the z-polarized CuL_3 spectrum.

ACKNOWLEDGMENTS

REFERENCES

1. E. E. Alp, G. K. Shenoy, D. G. Hinks, *et al.*, Phys. Rev. B **35**, 7199 (1987).
2. M. Pompa, C. Li, A. Bianconi, *et al.*, Physica C **184**, 51 (1991).
3. J. Fuggle, J. Fink, and N. Nucker, Int. J. Mod. Phys. B **5**, 1185 (1988).
4. A. Fujimori, E. Takayama-Myromachi, Y. Uchida, *et al.*, Phys. Rev. B **35**, 8814 (1987).
5. F. Al Shamma and J. C. Fuggle, Physica C **169**, 325 (1990).
6. A. Bianconi, J. Budnik, B. Chamberland, *et al.*, Physica C **153**–**155**, 115 (1988).
7. N. Nucker, J. Fink, B. Renker, *et al.*, Z. Phys. B **67**, 9 (1987).
8. P. Steiner, J. Albers, V. Kinsinger, *et al.*, Z. Phys. B **66**, 275 (1987).
9. P. Steiner, R. Courth, V. Kinsinger, *et al.*, Appl. Phys. A **44**, 75 (1987).
10. D. D. Sarma, Phys. Rev. B **37**, 7948 (1988).
11. D. E. Ramaker, N. H. Turner, J. S. Murday, *et al.*, Phys. Rev. B **36**, 5672 (1987).
12. A. Ueda, Y. Okamoto, and T. Imanaka, Chem. Express **3**, 723 (1988).
13. H. Ishii, T. Koschizawa, H. Kataura, *et al.*, Jpn. J. Appl. Phys. **28**, L1952 (1989).
14. G. van der Laan, C. Westra, C. Haas, *et al.*, Phys. Rev. B **23**, 4369 (1981).
15. G. van der Laan, G. A. Sawatzky, C. Haas, *et al.*, Phys. Rev. B **20**, 4287 (1979).
16. R. Manne and T. Aberg, Chem. Phys. Lett. **7**, 282 (1970).
17. A. Kotani and Y. Toyozawa, Jpn. J. Phys. **35**, 1073 (1973).
18. A. Kotani and Y. Toyozawa, Jpn. J. Phys. **37**, 912 (1974).
19. O. Gunnarsson and K. Schönhammer, Phys. Rev. Lett. **50**, 604 (1983).
20. O. Gunnarsson and K. Schönhammer, Phys. Rev. B **28**, 4315 (1983).
21. O. Gunnarsson and K. Schönhammer, Phys. Rev. B **31**, 4815 (1985).
22. J. C. Fuggle, M. Campagna, Z. Zolnierek, *et al.*, Phys. Rev. Lett. **45**, 1597 (1980).
23. P. Steiner, V. Kinsinger, I. Sander, *et al.*, Z. Phys. B: Condens. Matter **67**, 467 (1987).
24. P. V. Avramov, A. V. Kondratenko, S. Ph. Ruzankin, *et al.*, Preprint No. 89-05 (Inst. of Inorg. Chem., Acad. of Sci. of the USSR, Siberian Branch, 1989).
25. J. Guo, D. E. Ellis, G. L. Goodman, *et al.*, Phys. Rev. B **41**, 82 (1990).
26. C. Li, M. Pompa, A. C. Castellano, *et al.*, Physica C **175**, 369 (1991).
27. P. V. Avramov, S. Ph. Ruzankin, and G. M. Zhidomorov, Phys. Rev. B **46**, 6495 (1992).
28. N. Kosugi, Y. Tokura, H. Takagi, *et al.*, Phys. Rev. B **41**, 131 (1990).
29. Y. Seino, A. Kotani, and A. Biankoni, J. Phys. Soc. Jpn. **59**, 815 (1990).
30. M. Pompa, P. Castricci, C. Li, *et al.*, Physica C **184**, 102 (1991).
31. O. Strebel, G. Kaindl, A. Kolodziejcyk, *et al.*, J. Magn. Magn. Mater. **76**–**77**, 597 (1988).
32. Y. Seino, K. Okada, and A. Kotani, J. Phys. Soc. Jpn. **59**, 1384 (1990).
33. A. Bianconi, A. C. Castellano, M. De Santis, *et al.*, Solid State Commun. **63**, 1009 (1987).
34. S. Kishida, H. Tokutaka, S. Nakanishi, *et al.*, Jpn. J. Appl. Phys. **28**, L949 (1989).
35. E. Z. Kurmaev, V. I. Nefedov, and L. D. Finkelstain, Int. J. Mod. Phys. B **2**, 393 (1988).
36. M. S. Osadchiĭ, V. V. Murakhtanov, É. S. Fomin, *et al.*, Zh. Éksp. Teor. Fiz. **101**, 1259 (1992) [Sov. Phys. JETP **74**, 674 (1992)].
37. L. N. Mazalov, D. M. Tolstyakov, V. V. Murakhtanov, *et al.*, Zh. Strukt. Khim. **30**, 78 (1989).
38. J. Redinger, Yu. J. Freeman, and A. J. Weinberg, Phys. Lett. A **124**, 463 (1987).
39. B. Reihl, T. Reisesterer, J. D. Bednorz, *et al.*, Phys. Rev. B **35**, 8804 (1987).
40. J. C. Fuggle, P. J. W. Weijs, R. Schoorl, *et al.*, Phys. Rev. B **37**, 123 (1988).
41. H. Chen, J. Callaway, and P. K. Misra, Phys. Rev. B **36**, 8863 (1987).
42. V. I. Anisimov, V.R. Galakhov, V. A. Gubanov, *et al.*, Fiz. Met. Metalloved. **65**, 204 (1988).
43. W. M. Temmerman, G. M. Stocks, P. J. Durham, *et al.*, Preprint No. DL/SCI/P551T (Daresbury Lab., UK, 1987).
44. L. F. Mattheis, Phys. Rev. Lett. **58**, 1028 (1987).
45. J. Fink, N. Nucker, H. A. Romberg, *et al.*, J. Res. Develop. **33**, 372 (1989).
46. S. Ushida, Int. J. Mod. Phys. B **2**, 181 (1988).
47. V. I. Anisimov, M. A. Korotin, and I. V. Afanasyev, Physica C **161**, 59 (1989).
48. V. I. Anisimov, M. A. Korotin, and E. Z. Kurmaev, J. Phys.: Condens. Matter **2**, 3973 (1990).
49. M. A. Korotin, V. I. Anisimov, S. M. Butorin, *et al.*, Mater. Lett. **10**, 34 (1990).
50. J. Zaanen, G. A. Sawatzky, and J. W. Allen, Phys. Rev. Lett. **55**, 418 (1985).
51. I. I. Mazin, Usp. Fiz. Nauk **158**, 155 (1989) [Sov. Phys. Usp. **32**, 469 (1989)].
52. J. Zaanen, O. Jepsen, O. Gunnarsson, *et al.*, Physica C **153**–**155**, 1636 (1988).

53. W. Brenig, Phys. Rep. **251**, 153 (1995).

54. K. Okada and A. Kotani, J. Phys. Soc. Jpn. **58**, 1095 (1989).

55. A. Fujimori, Phys. Rev. B **39**, 793 (1989).

56. D. Sarma and S. G. Ovchinnikov, Phys. Rev. B **42**, 6817 (1990).

57. M. S. Osadchiĭ, V. V. Murakhtanov, É. S. Fomin, *et al.*, Zh. Strukt. Khim. **30**, 78 (1989).

58. F. C. Zhang and T. M. Rice, Phys. Rev. B **37**, 3759 (1988).

59. R. A. Bair and W. A. Goddard III, Phys. Rev. B **22**, 2767 (1980).

60. A. V. Kondratenko and L. S. Cederbaum, Phys. Rev. B **43**, 10595 (1991).

61. M. Eto and H. Kamimura, J. Phys. Soc. Jpn. 60, 2311 (1991).

62. V. J. Emery, Phys. Rev. Lett. **58**, 2794 (1987).

63. C. M. Varma, S. Schmitt-Rink, and E. Abrahams, Solid State Commun. **62**, 681 (1987).

64. Yu. B. Gaididei and V. B. Loktev, Phys. Status Solidi **147**, 308 (1988).

65. S. G. Ovchinnikov, Zh. Éksp. Teor. Fiz. **102**, 127 (1992) [Sov. Phys. JETP **75**, 67 (1992)].

66. S. G. Ovchinnikov, Usp. Fiz. Nauk **167**, 1043 (1997) [Phys. Usp. **40**, 1095 (1997)].

67. S. G. Ovchinnikov and I. S. Sandalov, Physica C **161**, 607 (1989).

68. S. G. Ovchinnikov, Mod. Phys. Lett. B **5**, 531 (1991).

69. P. V. Avramov and S. G. Ovchinnikov, Physica C **278**, 94 (1997).

70. Z.-X. Shen, J. W. Allen, J. J. Yeh, *et al.*, Phys. Rev. B **36**, 8414 (1987).

71. R. Zanoni, Y. Chang, M. Tang, *et al.*, Phys. Rev. B **38**, 11832 (1988).

72. H. Namatame, A. Fujimori, Y. Tokura, *et al.*, Phys. Rev. B **41**, 7205 (1990).

73. F. Bloch, Phys. Rev. **48**, 187 (1935).

74. R. D. Richtmyer, Phys. Rev. **49**, 1 (1936).

75. F. L. Feinberg, Phys. **IV**, 423 (1941).

76. A. J. Migdal, Phys. **IV**, 449 (1941).

77. V. P. Sachenko and V. F. Demekhin, Zh. Éksp. Teor. Fiz. **49**, 765 (1965).

78. L. D. Landau and E. M. Lifshitz*, Quantum Mechanics: Nonrelativistic Theory* (Fizmatgiz, Moscow, 1963).

79. D. I. Blokhintsev, *Principles of Quantum Mechanics* (Nauka, Moscow, 1976).

80. L. N. Mazalov, V. D. Yumatov, and V. V. Murakhtanov, *X-ray Spectra of Molecules* (Nauka, Novosibirsk, 1977).

81. S. Larson, Chem. Phys. Lett. **32**, 401 (1975).

82. S. Larson, Chem. Phys. Lett. **40**, 362 (1976).

83. S. Larson, Phys. Scripta **21**, 558 (1980).

84. S. Larson and M. Braga, Chem. Phys. Lett. **48**, 596 (1977).

85. F. W. Kutzler, C. R. Natoli, D. K. Misemer, *et al.*, J. Chem. Phys. **73**, 3274 (1980).

86. S. F. Ruzankin, Zh. Strukt. Khim. **20**, 953 (1979).

87. S. F. Ruzankin, V. I. Nemanova, and A. V. Kondratenko, Zh. Strukt. Khim. **27**, 162 (1986).

88. J. D. Jorgensen, H.-B. Schüttler, and D. G. Hinks, Phys. Rev. Lett. **58**, 1024 (1987).

89. P. Bordet, C. Chailont, J. J. Capponi, *et al.*, Nature **327**, 687 (1987).

90. D. Khomskii, *The International Conference on Strongly Correlated Electron Systems 68* (Amsterdam, 1994).

91. H. Oyanagi, K. Oka, H. Unoki, *et al.*, Physica B **158**, 436 (1989).

92. S. G. Ovchinnikov, Fiz. Tverd. Tela (Leningrad) **35**, 617 (1993) [Phys. Solid State **35**, 315 (1993)].

Translated by Yu. Epifanov

Transport Properties of HTSC + Ba(Pb, Met)O$_3$ Composites as Functions of the Electrical and Magnetic Characteristics of Nonsuperconducting Components

M. I. Petrov, D. A. Balaev, S. V. Ospishchev, and K. S. Aleksandrov

Kirenskiĭ Institute of Physics, Siberian Division, Russian Academy of Sciences, Akademgorodok, Krasnoyarsk, 660036 Russia
e-mail: smp@iph.krasnoyarsk.su
Received in final form October 26, 1999

Abstract—Composites simulating a network of weak metallic links and consisting of a classic 1–2–3 HTSC and a BaPbO$_3$ metal oxide with incorporated Sn, Ni, and Fe impurities have been prepared. Experimental resistivity, magnetic, and Mössbauer studies of the BaPb$_{0.9}$Met$_{0.1}$O$_3$ nonsuperconducting components are presented. The transport properties of the HTSC + BaPb$_{0.9}$Met$_{0.1}$O$_3$ composites have been investigated. The superconducting properties of the composites are observed to be suppressed, both when the carrier mean free path in nonsuperconducting components with tin impurities decreases, and as a result of an additional interaction of the magnetic moments of (Fe, Ni) impurities with the spins of supercurrent carriers. The experimental temperature dependences of the composite critical current are analyzed in terms of the de Gennes theory for the superconductor–normal metal–superconductor structures. © 2000 MAIK "Nauka/Interperiodica".

As shown in our earlier experimental study [1], HTSC + BaPbO$_3$ composites are equivalent to an *S–N–S* weak-link network (*S* stands here for a superconductor, and *N*, for a normal metal) in the "clean" limit. Indeed, the mean free path *l* in BaPbO$_3$ is substantially longer than the coherence length ξ_0 in HTSCs, and this accounts for the fact that the theory [2], including in the clean limit the tunneling, the proximity effect, and Andreev scattering, provides a good description of the transport properties of these composites. The part played by weak links in an *S–N–S* structure can, however, be varied by properly varying not only the effective thickness of the *N* layer (a subject of study in [1, 3]), but the mean free path of carriers in the normal metal *N* as well.

The dependence of the critical current of *S–N–S* junctions on the thickness of the *N* layer, as well as on the carrier mean free path in it, was studied comprehensively for low-temperature superconductors [4]. The mean free path and the nature of interaction of impurities with Cooper pairs were varied by introducing impurities, both nonmagnetic and paramagnetic, into the *N* metal. The BCS-based theory was found to agree with the experiment; however, one did not measure and, hence, analyze the temperature dependences of the critical current.

By analogy with [4], we have made an attempt to carry out a similar study on HTSC-based *S–N–S* structures. Unfortunately, the absence of a reproducible technology of manufacturing single junctions forced us to study HTSC + normal metal composites. As already mentioned, such composites are equivalent to a weak-link network characterized by some distribution func-

tion of the *S–N–S* junctions (links) in this network in their geometrical parameters. However, if the technology of composite preparation is followed with a good enough reproducibility, it appears logical to expect the distribution function to be reproducible and to associate all variations in the transport properties with the interaction of supercurrent carriers tunneling through a metal with various impurities.

The specific difficulties involved in the preparation of HTSC-based composites are considered partially in [1, 3]. One of them, namely, the oxidation of the *N* metal, was overcome by using the BaPbO$_3$ metal oxide, which exhibits only a weak chemical interaction with 1–2–3 HTSCs [1, 3]. Our preliminary experiments [5] showed that incorporating impurities in BaPbO$_3$ brings about a noticeable additional degradation of the superconducting properties of the *S–N–S* weak-link network in HTSC + BaPbO$_3$ composites.

This work presents detailed experimental data on a study of the effect of magnetic (Fe, Ni) and nonmagnetic (Sn) impurities introduced into BaPbO$_3$ on the transport properties of HTSC + Ba(Pb, Met)O$_3$ composites.

1. PREPARATION AND PHYSICAL PROPERTIES OF NONSUPERCONDUCTING COMPONENTS

The nonsuperconducting components of the composites were prepared of the BaO$_2$, PbO, NiO, Fe$_2^{57}$O$_3$, and Sn^{119}O$_2$ oxides at 880°C by ceramic technology. Using the hematite enriched in the Fe^{57} isotope to 90%

made monitoring the solubility of iron in $BaPbO_3$ by Mössbauer spectroscopy (Fig. 1) possible. Annealing for two weeks, alternating with grinding, is seen to result in the disappearance of the six-line spectrum of the $Fe_2^{57}O_3$ hematite, which is evidence of its "dissolution" in $BaPbO_3$. To increase the reliability still further, the synthesis was prolonged for one more week. The $BaPb_{0.9}Ni_{0.1}O_3$ and $BaPb_{0.9}Sn_{0.1}O_3$ sample were prepared by the technique used to synthesize the iron-containing $BaPbO_3$. The "dissolution" of tin in $BaPbO_3$ was also checked by Sn^{119} Mössbauer spectroscopy. The absence of a spectrum characteristic of SnO_2 argues for complete "dissolution" of tin in $BaPbO_3$. There is nothing strange in this, because Sn^{4+} is an electronic analog of Pb^{4+}. X-ray diffraction analysis performed on $BaPb_{0.9}Met_{0.1}O_3$ samples revealed the $BaPbO_3$ perovskite phase, with no foreign reflections evident within the analytical accuracy.

Figure 2 presents temperature dependences of the electrical resistivity $\rho(T)$ of $BaPb_{0.9}Met_{0.1}O_3$ and $BaPbO_3$ samples measured by the four-point probe method. Partial substitution of lead makes the $\rho(T)$ curves only weakly dependent on temperature (with a slight increase of ρ, with decreasing temperature observed for the $BaPb_{0.9}Fe_{0.1}O_3$ sample), and results in an increase of ρ in an absolute magnitude, it being the largest for the iron impurities (see the table). This is not at odds with the classical mechanism of carrier interaction with magnetic and nonmagnetic impurities [6].

Figure 3 illustrates magnetic measurements made on samples with Ni and Fe impurities. The measurements were carried out on a vibrating-sample magnetometer [7]. A comparison of the experimental magnetization curve $M(H)$ with the Brillouin function permitted determination of the magnetic moments per impurity atom. The best-fit figures are 3.6 μB for Fe and 0.13 μB for Ni ions (μB is the Bohr magneton). The value for the iron ions is slightly smaller than the nominal value for Fe^{4+} [8], if one assumes that the cations of iron to substitute for those of lead in the $BaPbO_3$ structure. As for nickel, one may conjecture Ni to also occupy the lead sites in $BaPbO_3$, which makes +4 its formal valence state. In this case, the electronic configuration of the Ni^{4+} cation should be $3d^6$. Assuming this configuration, the low-spin state (no high-spin state was ever observed for Ni^{4+} [9]) yields zero spin magnetic moment. By contrast, the experimental value is 0.13 μB. A possible reason for the nonzero magnetic moment of Ni could be a covalent admixture to the nickel $3d$ levels. Thus, the magnetic moment for both the iron and nickel in the metal oxide is seen to deviate from the nominal value, which is in marked contrast with the behavior of magnetodielectrics, where this agreement is much better [8].

The magnetization of the samples drops with increasing temperature by the $1/T$ law, which argues for
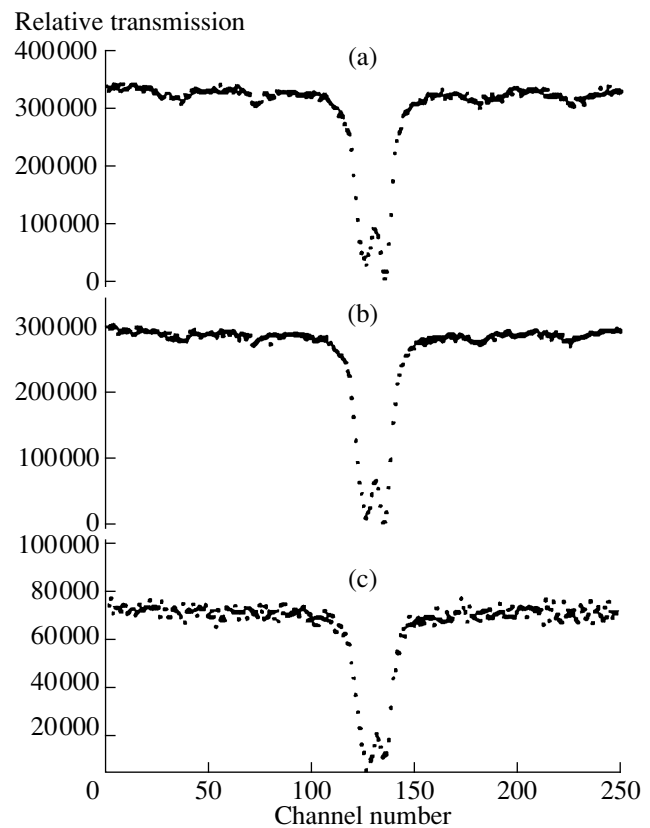
Relative transmission

Fig. 1. Mössbauer spectra of $BaPb_{0.9}Fe_{0.1}^{57}O_3$. (a) After one weak of synthesis, (b) after two weeks, (c) after three weeks.
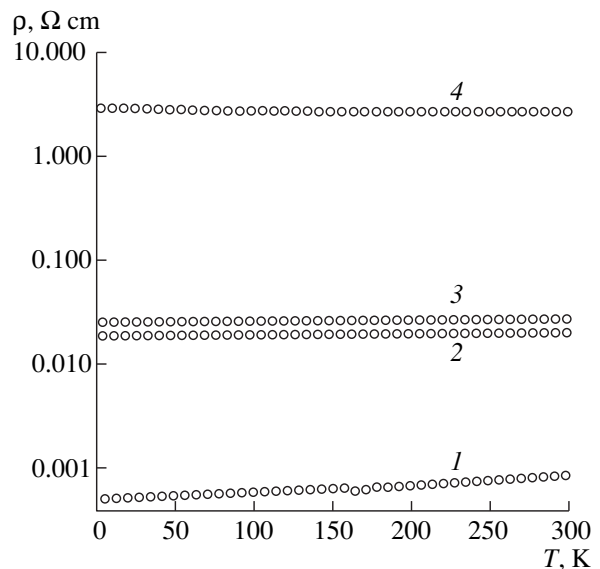

Fig. 2. Experimental $\rho(T)$ relations for the nonsuperconducting components of the composites plotted on a semilogarithmic scale. (1) $BaPbO_3$, (2) $BaPb_{0.9}Sn_{0.1}O_3$, (3) $BaPb_{0.9}Ni_{0.1}O_3$, (4) $BaPb_{0.9}Fe_{0.1}O_3$.
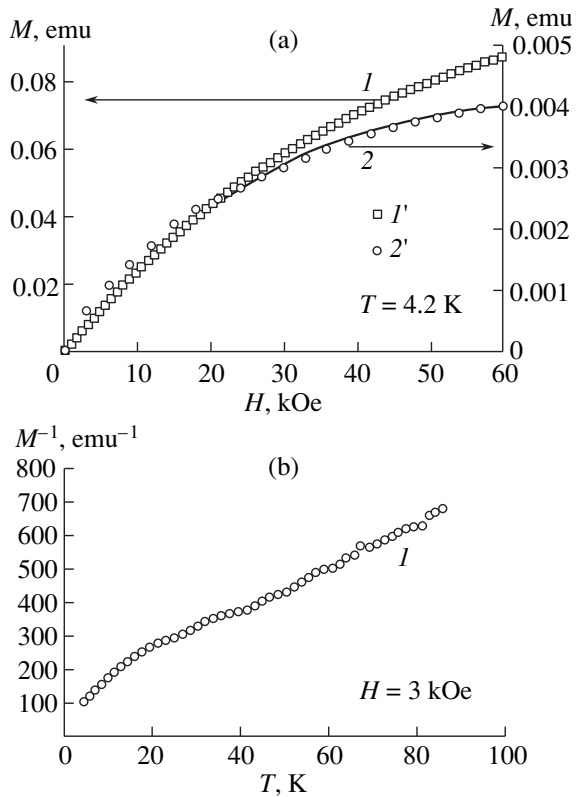
Fig. 3. Magnetic measurements on nonsuperconducting components of the composites (*1'*) $BaPb_{0.9}Fe_{0.1}O_3$ ($m =$ 96 mg) and (*2'*) $BaPb_{0.9}Ni_{0.1}O_3$ ($m =$ 112 mg). (a) Field dependences (for $T = 4.2$ K), (b) temperature dependences (for $H = 3$ kOe) of the magnetization M. Solid curves represent calculations made using the Brillouin function with (*1*) $J = 1$ for $BaPb_{0.9}Fe_{0.1}O_3$ and (*2*) $J = 2$ for $BaPb_{0.9}Ni_{0.1}O_3$.

the compounds being paramagnetic (see Fig. 3). The absence of a hysteresis in the field dependences bears out this assumption. The deviation of the $M^{-1} = f(T)$ relation from a linear course in the low-temperature domain suggests that one should take into account pairwise exchange interactions; however, this work does not deal with a study of the various aspects of the magnetism of these compounds, but rather of the effect of magnetic scattering centers on the transport properties of composites containing them.

2. PREPARATION AND TRANSPORT PROPERTIES OF THE HTSC + Ba(Pb, Met)O_3 COMPOSITES

The superconducting component of the composites, $Y_{0.75}Lu_{0.25}Ba_2Cu_3O_7$, was prepared by the standard ceramic technology. The composites were synthesized by fast sintering [1, 3]. The composite components, mixed thoroughly in the ratio 85 vol % HTSC with 15 vol % $BaPb_{0.9}Met_{0.1}O_3$ (Met = Sn, Ni, Fe), were pressed into pellets, placed onto preheated boats, and introduced for five minutes into a furnace heated to 950°C. Because a 1–2–3 HTSC inevitably loses oxygen at this temperature, the composite samples were transferred from this high-temperature furnace to another furnace maintained at 400°C in order to restore the oxygen stoichiometry, where they were kept for six hours, which is long enough to reach oxygen saturation [1].

To learn the effect of various impurities present in the nonsuperconducting component on the transport properties of the composites, the results obtained were compared with the data for a reference composite that did not contain impurities in $BaPbO_3$.

X-ray diffraction analysis of the composites revealed the presence of two phases only, the 1–2–3 HTSC and the perovskite. No other reflections were detected within the analytical errors.

Denote the composite samples by $S + 15N$, $S + 15N(Sn10)$, $S + 15N(Ni10)$, and $S + 15N(Fe10)$. Here S stands for the superconductor, N, for the impurity-free $BaPbO_3$, and $N(Sn10)$, $N(Ni10)$, $N(Fe10)$, for $BaPb_{0.9}Met_{0.1}O_3$ with Met = Sn, Ni, and Fe, respectively.

The temperature dependences of the composite magnetization, $M(T)$, measured in a field of 200 Oe, showed the presence of one superconducting phase at temperatures below 93.5 K. The $M(T)$ relations are similar in pattern to those quoted in [10] for the HTSC + $BaPbO_3$ composites.

Figure 4 illustrates the effect of the various impurities in $BaPbO_3$ on the I–V characteristics of the composites at $T = 4.2$ K. The I–V relations were measured by the four-point probe technique, with the sample placed directly into a helium bath for efficient heat

Some parameters of the composite nonsuperconducting components

N-metal	μ, μ_0	$\rho(5\ K)$, Ω cm	R_N, Ω cm	l, Å	T_{pb}, K
$BaPbO_3$	–	0.0005	0.0022	>100	0
$BaPb_{0.9}Sn_{0.1}O_3$	–	0.019	0.0089	4.4 ± 1.0	0
$BaPb_{0.9}Ni_{0.1}O_3$	0.13	0.026	0.0098	4.0 ± 0.5	20 ± 5
$BaPb_{0.9}Fe_{0.1}O_3$	3.6	3.0	0.0524	4.0 ± 0.5	50 ± 5

Note: μ is the magnetic moment per impurity atom, ρ is the electrical resistivity, R_N is the normal resistance of composites with the corresponding components at $T = 4.2$ K. The values of l and T_{pb} were derived from the best fit of the experimental $J_c(T)$ relations for the composites to the de Gennes theory (see Sect. 3).

removal (for more details, see [11, 12]). The I–V characteristics shown in Fig. 4 exhibit an extra current, which is typical of *S–N–S* structures [13]. The table lists the normal resistances R_N of the composites, derived from the linear part of the I–V characteristics at $T = 4.2$ K. The values of ρ of the components correlate clearly with R_N.

Figure 5 presents normalized temperature dependences of the electrical resistance $R(T)$ of the composites, measured by the four-point probe technique for a transport current of $\sim 0.01 \times J_c(5$ K$)$ [$J_c(5$ K$)$ is the critical current at 5 K]. The jump in the electrical resistance at 93.5 K corresponds to the HTSC grains undergoing the superconducting transition in the composite. The fact that this temperature is the same for all the composite samples argues against diffusion of chemical elements from the nonsuperconducting components into the HTSC grains. The smooth tail in the $R(T)$ relations seen below 93.5 K is due to the weak links [1, 3, 10, 14–16]. The characteristic temperature at which the resistance of a composite sample becomes zero depends on the nature of the impurity introduced in $BaPbO_3$ (see Fig. 5). The $R(T)$ curve for the composites containing magnetic impurities has a segment below the T_c of the HTSC grains, extended in temperature, within which the resistance varies only weakly, with a subsequent transition to the superconducting state. Such $R(T)$ behavior was observed in $YBa_2Cu_3O_7/Pr_{0.7}Sr_{0.3}MnO_3/Ag$ and $YBa_2Cu_3O_7/Pr_{0.7}Sr_{0.3}MnO_3/YBa_2Cu_3O_7$ sandwiches with a ferromagnetic interlayer [14], as well as in HTSC + CuO-insulator composites with magnetic scattering centers (Ni) [15]. This behavior is apparently accounted for by the interaction of carrier pairs with magnetic moments in the interlayers.

The temperature dependences of the critical current density $J_c(T)$ of the composites measured by the four-point probe technique based on a standard 1 μV/cm criterion [17] (with the method employed described in detail in [1, 10]) are displayed in Fig. 6. Note certain features in the experimental $J_c(T)$ relations. Although the curves follow the same pattern for all the samples, the absolute values of $J_c(5$ K$)$ for the composites depend strongly on the character of the impurity (Sn, Ni, Fe) and correlate with the electrical resistance data. For high temperatures, the experimental values of $J_c(T)$ become extremely small, and at a finite measuring-current density [$\sim 0.01 \times J_c(5$ K$)$] a nonzero voltage drop appears (Figs. 5, 6).

3. ANALYSIS OF THE TEMPERATURE BEHAVIOR OF CRITICAL CURRENT FOR THE HTSC + Ba(Pb, Met)O₃ COMPOSITES

As shown by an analysis of the $J_c(T)$ relations for the HTSC + $BaPbO_3$ composites [1, 10], a composite sample can be characterized by an average geometrical
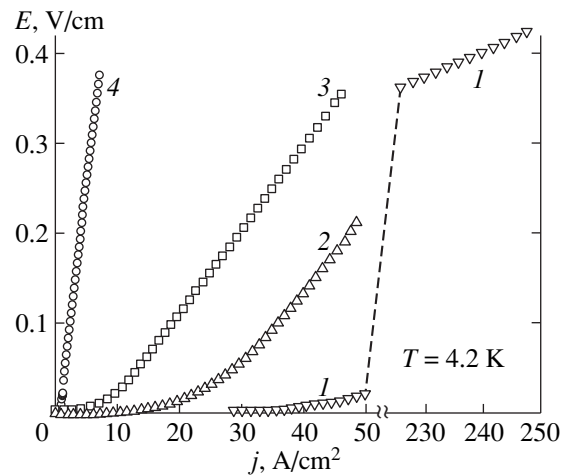

Fig. 4. Experimental I–V characteristics of composite samples obtained at $T = 4.2$ K. (*1*) $S + 15N$, (*2*) $S + 15N$(Sn10), (*3*) $S + 15N$(Ni10), (*4*) $S + 15N$(Fe10).

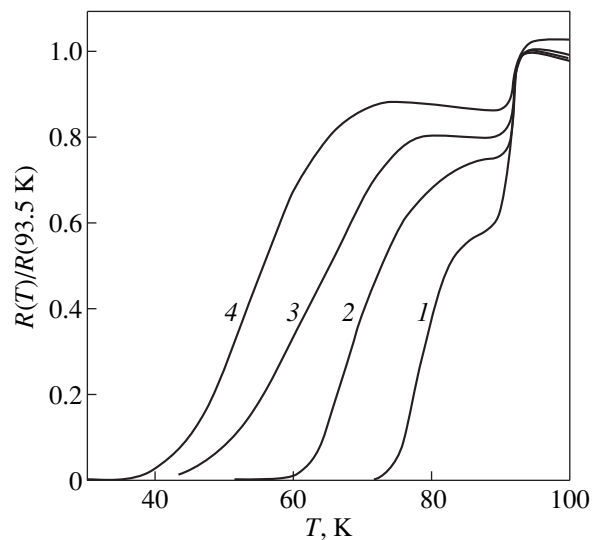**Fig. 5.** Experimental temperature dependences of the electrical resistance of the samples. (*1*) $S + 15N$, (*2*) $S + 15N$(Sn10), (*3*) $S + 15N$(Ni10), (*4*) $S + 15N$(Fe10).

weak-link length d. For the 15 vol % $BaPbO_3$ samples, this value, estimated by the theory of [2], was found to be ~ 100 Å. It was natural to expect that the value of d for the composites with impurities in $BaPbO_3$, prepared by the same technology and with the same content of the nonsuperconducting component, would be the same.

Unfortunately, there is presently no microscopic theory applicable to the temperature dependence of the critical current for the crossover from the "clean" limit ($l > d_{eff}$, where d_{eff} is the effective weak-link length [18]) to the "dirty" one ($l \ll d_{eff}$ [18]), like this was done for the I–V characteristics of *S–N–S* junctions [19, 20]. Therefore we are going to present here the results of a
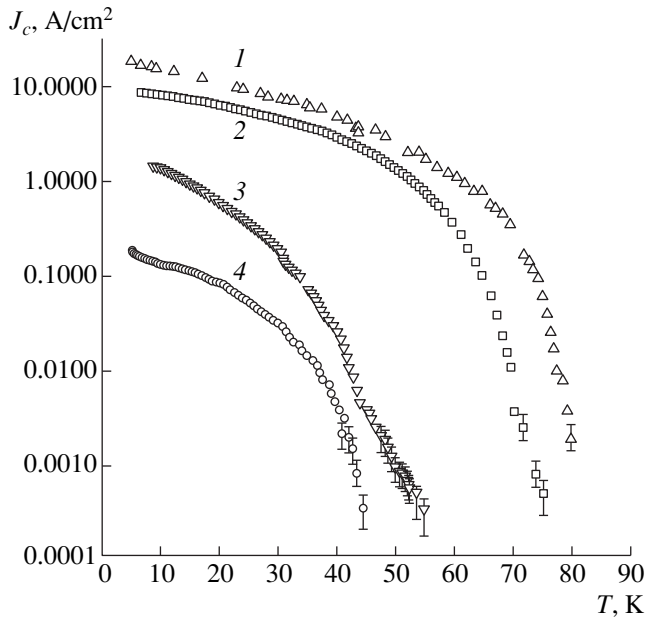
J_c, A/cm^2

Fig. 6. Experimental temperature dependences of the critical current density of composites drawn on a semilogarithmic scale. (*1*) $S + 15N$, (*2*) $S + 15N(\text{Sn}10)$, (*3*) $S + 15N(\text{Ni}10)$, (*4*) $S + 15N(\text{Fe}10)$.
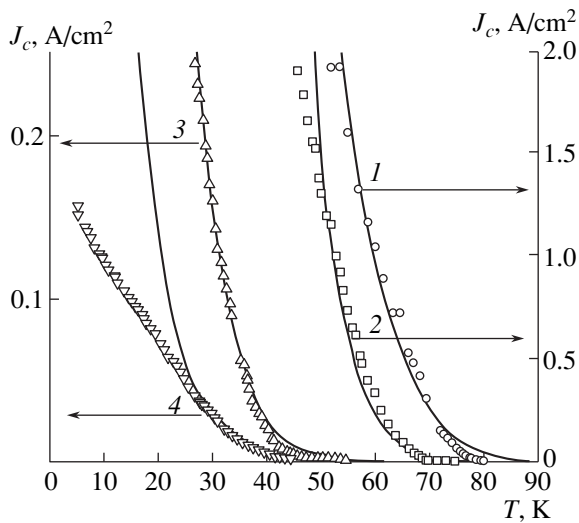

Fig. 7. Temperature dependences of the critical current. (*1*) $S + 15N$, (*2*) $S + 15N(\text{Sn}10)$, (*3*) $S + 15N(\text{Ni}10)$, (*4*) $S + 15N(\text{Fe}10)$. Solid curves are fits plotted by the de Gennes theory (see text and the table).

treatment of the experimental $J_c(T)$ relations made on the basis of the de Gennes proximity theory [21].

At temperatures not too far from T_c, the de Gennes theory yields for the critical current of a S–N–S junction [17, 22, 23]

$$J_c(T) = C(1 - T/T_c)^2 \frac{d/\xi N}{\sinh(d/\xi N)}, \qquad (1)$$

where C is a constant that depends on the contact geometry, which for a three-dimensional network of Josephson junctions with some distribution function for the geometric parameters plays the part of a normalization factor, d is the geometric width of the N interlayer, which is an effective quantity for composites, and ξ_N is the coherence length in the N metal or the pair penetration depth into the N metal, which for a "dirty" N metal is defined as [17, 22]

$$\xi_N = (\hbar V_f l/6\pi k_B T)^{1/2}, \qquad (2)$$

where $\hbar$ is the Planck constant, k_B is the Boltzmann constant, and V_f is the Fermi velocity in the N metal. If the N interlayer is not a "clean" metal, ξ_N does not depend on the mean free path and is defined as [22]

$$\xi_N = \hbar V_f/2\pi k_B T. \qquad (3)$$

The fitting parameters for experimental $J_c(T)$ curves are d and l; besides, one should also know V_f. The best fit of the theory to the experiment was reached for $V_f \approx 1.8 \times 10^7$ cm/s, the value derived from the relation $V_f = \hbar \times 3^{1/3}\pi^{2/3} n^{1/3}$ m^{-1} (m is the electron mass) for $n = 1.4 \times 10^{20}$ cm^{-3} quoted in [24] for BaPbO$_3$.[1]

The best-fit curve for the experimental $J_c(T)$ relation obtained for the $S + 15N$ sample (curve *1* in Fig. 7) within the 55–80-K temperature interval was calculated using (3) and (1) for $d = 100$ Å.

The curve for the case of nonmagnetic impurities was calculated from (2) and (1). We tried to fit the experimental data for the sample $S + 15N(\text{Sn}10)$ (curve *2* in Fig. 7) to the theory in the high-temperature region [15–20 K below the temperature at which $J_c(T)$ becomes practically zero] by varying the mean free path in (2). The best fit was reached at a surprisingly small value of 4.4 ± 1 Å. At the same time, straightforward calculations show that at a tin concentration $x = 0.125$, the most probable distance between scattering centers (Sn atoms) in BaPb$_{l \times x}$Sn$_x$O$_3$ is equal to the lattice constant 4.268 Å; for $x = 0.1$, it is 4.6 Å, which is close to the estimate of l obtained here.

While the de Gennes theory could formally be used to treat the $J_c(T)$ curves for samples with magnetic impurities in BaPbO$_3$ (in Fig. 7, these relations extend to lower temperatures), and the mean free paths thus obtained would obviously be substantially less than the lattice constant, which is an unphysical result. This is a consequence of the fact that the de Gennes theory does not include the mechanism of Cooper pair interaction with the magnetic moments of the N interlayer. In our opinion, an original way out of this problem was pro-

---

[1] In the case of the Sn $\longrightarrow$ Pb substitution, there are no grounds to expect n to change, because tin has the same electronic configuration as lead. The change in n caused by a nickel and iron substitution should not apparently be larger than that for BaPb$_{1-x}$BiO$_3$ [24–26] and, because of the $V_f(n) \sim n^{1/3}$ dependence being weak, should only slightly affect the results of the fitting given in the table.

posed in [22], where the mean lifetime τ of a pair inside the N interlayer is modified to become

$$\tau = \tau + \tau_{pb} = (\hbar/2\pi k_B)(1/T + 1/T_{pb}) \qquad (4)$$

(we are using here the notation accepted in [22]). The effect of this mechanism on the critical current consists in substituting $T + T_{pb}$ for T in (3). Curves *3* and *4* in Fig. 7, which are the best fits to $J_c(T)$ for the samples $S + 15N$(Ni10) and $S + 15N$(Fe10), were calculated using expressions (1), (2), and (4) with the parameters given in the table.

At low temperatures, one observes a noticeable discrepancy between the experiment and the de Gennes theory, which is illustrated in Fig. 7 for the $S + 15N$(Fe10) sample. Similar cases were reported by other authors as well [22, 23], which is hardly surprising, because, as already pointed out above, the theory of the proximity effect was developed for the high-temperature domain [21, 22].

Summing up the results obtained in this work, we note that magnetic impurities degrade the transport properties of composites more strongly than nonmagnetic ones do. This degradation is more pronounced in the case where the impurity is the iron atoms, whose magnetic moment is substantially higher than that of the nickel atoms. The degradation of superconductivity in $BaPbO_3$ having a tin impurity can be associated only with a decrease of the carrier mean free path in the N layer. In the case of composites with $BaPbO_3$ containing magnetic impurities, this degradation of the superconducting properties can be related to one more mechanism of Cooper pair breaking, namely, through the exchange interaction at impurity magnetic moments [4].

This Cooper-pair breaking by impurities can be connected with inelastic processes, such as magnetic scattering in conventional *s*-type superconductors. In *d*-type superconductors, however, strong elastic scattering can also bring about pair breaking, as this was pointed out in [23].

REFERENCES

1. M. I. Petrov, D. A. Balaev, S. V. Ospishchev, *et al.*, Phys. Lett. A **237**, 85 (1997).
2. U. Gunsenheimer, U. Schüssler, and R. Kümmel, Phys. Rev. B **49**, 6111 (1994).
3. M. I. Petrov, D. A. Balaev, S. V. Ospishchev, *et al.*, Fiz. Tverd. Tela (St. Petersburg) **39** (3), 418 (1997) [Phys. Solid State **39**, 362 (1997)].
4. J. Niemeyer and G. von Minnegerode, Z. Physik B **36**, 57 (1979).
5. M. I. Petrov, D. A. Balaev, S. V. Ospishchev, *et al.*, Physica C **282**–**287**, 2447 (1997).
6. A. A. Abrikosov, *Introduction to the Theory of Normal Metals* (Nauka, Moscow, 1972).
7. A. D. Balaev, Yu. V. Boyarshinov, M. M. Karpenko, *et al.*, Prib. Tekh. Éksp. **3**, 167 (1985).
8. S. Krupićka, *Physik der Ferrite und der verwandten magnetischen Oxide* (Academia, Prague, 1973; Mir, Moscow, 1976), Vol. 1.
9. F. A. Cotton and G. Wilkinson, *Advanced Inorganic Chemistry* (Wiley, New York, 1966), Vols. 1–3.
10. M. I. Petrov, D. A. Balaev, B. P. Khrustalev, *et al.*, Sverkhprovod.: Fiz., Khim., Tekh. **8** (1), 53 (1995).
11. M. I. Petrov, S. N. Krivomasov, B. P. Khrustalev, *et al.*, Solid State Commun. **82**, 453 (1992).
12. M. I. Petrov, D. A. Balaev, D. M. Gohfeld, *et al.*, Physica C **314**, 51 (1999).
13. G. E. Blonder, M. Tinkham, and T. M. Klapwijk, Phys. Rev. B **25**, 4515 (1982).
14. G. C. Xiong, G. J. Lian, J. F. Kang, *et al.*, Physica C **282**–**287**, 693 (1997).
15. M. I. Petrov, D. A. Balaev, K. A. Shaĭkhutdinov, *et al.*, Fiz. Tverd. Tela (St. Petersburg) **40** (9), 1599 (1998) [Phys. Solid State **40**, 1451 (1998)].
16. A. Gerber, T. Grenet, M. Cyrot, *et al.*, Phys. Rev. Lett. **65**, 3201 (1990).
17. A. Barone and G. Paterno, *Physics and Applications of the Josephson Effect* (Wiley, New York, 1982; Mir, Moscow, 1984).
18. K. K. Likharev, Rev. Mod. Phys. **51** (1), 101 (1979).
19. R. Kümmel, B. Huckestein, and R. Nicolsky, Solid State Commun. **65**, 1567 (1988).
20. R. Kümmel, U. Gunsenheimer, and R. Nicolsky, Phys. Rev. B **42**, 3992 (1990).
21. P. G. de Gennes, Rev. Mod. Phys. **36**, 225 (1964).
22. L. Antogonazza, S. J. Berkowitz, T. H. Geballe, *et al.*, Phys. Rev. B **51** (13), 8560 (1995).
23. K. Char, Physica C **282**–**287**, 419 (1997).
24. K. Kitazawa, A. Katsui, A. Toriumi, *et al.*, Solid State Commun. **52**, 459 (1984).
25. T. D. Thanh, A. Koma, and S. Tanaka. Appl. Phys. **22**, 205 (1980).
26. D. P. Moiseev, S. K. Uvarova, and M. B. Fenik, Fiz. Tverd. Tela (Leningrad) **23** (8), 2347 (1981) [Sov. Phys. Solid State **23**, 1371 (1981)].

Translated by G. Skrebtsov

METALS
AND SUPERCONDUCTORS

Luminescence Spectra and Crystal Structure of High-Temperature Superconductors

V. V. Eremenko, T. V. Sukhareva, and V. N. Samovarov

Verkin Institute for Low Temperature Physics and Engineering, Academy of Sciences of Ukraine, Kharkov, 310164 Ukraine
e-mail: eremenko@ilt.kharkov.ua
Received November 4, 1999

Abstract—A study is reported of the effect of temperature ($4.2\ K \leq T \leq 150\ K$), the content of weakly bonded oxygen [$6.1 \leq (7 - \delta) \leq 6.9$], illumination [$E_{exc} = 3.4$ eV, $(\Phi t)_{max} \sim 1.5 \times 10^{20}$ photon cm^{-2}], and substitution (Cu $\longrightarrow$ Ag, Cr, Fe, Mn) on the luminescence spectra of the high-T_c superconductor $YBa_2Cu_3O_{7-\delta}$. Only two bands with $E_{lum} \sim 2.4$ and ~ 2.8 eV were observed in the luminescence spectra in all these cases. A clearly pronounced correlation between the electronic and structural changes in $YBa_2Cu_3O_{7-\delta}$, caused by the influence of temperature, illumination, doping with oxygen or metal ions, and the spectral parameters (peak position E_{lum}, width $\Delta\lambda_{lum}$, and intensity I_{lum} of the luminescence bands), has been established. It is shown that luminescence spectra of HTSCs can be employed as a fairly reliable optical probe to study the electronic processes occurring in these substances, in particular, the electron (hole) transfer between the CuO_2 plane and the $CuO_{1-\delta}$ chain plane serving as a charge reservoir. © 2000 MAIK "Nauka/Interperiodica".

Right now, it has been reliably established that the luminescence spectra (LS) of high-temperature superconductors (HTSC) $YBa_2Cu_3O_{7-\delta}$, $Bi_2Sr_2CaCu_2O_{8\pm\delta}$, $Bi_2Sr_2Ca_2Cu_3O_{10\pm\delta}$, $YBa_2Cu_4O_{8\pm\delta}$ and others are characterized by the presence of two principal bands peaking at $E_{lum} \sim 2.4$ and ~ 2.8 eV [1–10]. The intensity ratio of these bands ($I_{lum} = I_{\sim 2.8\ eV}/I_{\sim 2.4\ eV}$) and their spectral position (E_{lum}) depend on the specific features of the HTSC crystal structure. Interestingly, the intense luminescence band with $E_{lum} \sim 2.8$ eV is typically observed in the HTSCs whose lattice contains a $CuO_{1-\delta}$ chain plane ($YBa_2Cu_3O_{7-\delta}$, $YBa_2Cu_4O_{8\pm\delta}$) or a $BiO_{1\pm\delta}$ plane with an excess oxygen ion ($Bi_2Sr_2CaCu_2O_{8\pm\delta}$, $Bi_2Sr_2Ca_2Cu_3O_{10\pm\delta}$) [1, 2]. On the other hand, the luminescence spectra of the La_2Cu_4 HTSC, whose lattice contains copper ions only in the CuO_2 planes, does not have the $E_{lum} \sim 2.8$ eV band [1].

It may be suggested that the band at $E_{lum} \sim 2.4$ eV acts in the luminescence spectroscopy of high-temperature superconductors as an optical probe for electronic processes in the active (charge transfer) CuO_2 plane, whereas that at $E_{lum} \sim 2.8$ eV, if one considers specifically the $YBa_2Cu_3O_{7-\delta}$ HTSC, could serve to optically probe the electronic processes occurring in the charge reservoirs [11], i.e., the $CuO_{1-\delta}$ chain planes. In other words, these two bands belong to two different electronic and structural subsystems of the $YBa_2Cu_3O_{7-\delta}$ HTSC unit cell.

This work was aimed at studying the intensity redistribution between the luminescence bands and the variation of their spectral characteristics caused by external or internal factors acting on the electronic and structural state of $YBa_2Cu_3O_{7-\delta}$. With this in mind, we investigated the evolution of the luminescence spectrum of the $YBa_2Cu_3O_{7-\delta}$ HTSC initiated by chemical doping, illumination, and temperature.

Because the two electronic and structural subsystems are coupled primarily by a charge transfer between the $CuO_{1-\delta}$ and CuO_2 planes, there are grounds to suggest that such studies could yield information on the charge redistribution between these subsystems induced by a variation of temperature, chemical composition, or illumination. Obtaining such information would undoubtedly be important for establishing the nature of high-temperature superconductivity. We are not aware of any previous investigations of this kind.

The choice of the $YBa_2Cu_3O_{7-\delta}$ HTSC as an object for the study was motivated by the fact that the content of the so-called weakly bonded oxygen in its O4 and O5 sites can vary within the largest limits found thus far, namely, from $(7 - \delta) \sim 7$ (orthorhombic structure O-I, metallic phase, superconductor with $T_c \sim 90$ K, nearly all oxygen sites in the…–Cu1–O4–Cu1–… chains along the **b** axis are occupied, almost all O5 sites in the…–Cu1–O5–Cu1–… chains along the **a** axis are vacant) to $(7 - \delta) \sim 6$ (tetragonal structure T, insulator, the O4 and O5 oxygen sites are vacant), including the "semiconducting"[1] orthorhombic O-II phase [$(7 - \delta) \sim$

---

[1] The O-II phase of $YBa_2Cu_3O_{7-\delta}$ is certainly not semiconducting in the true sense of the word, and the temperature dependence of its electrical resistivity ρ takes on an unusual shape close to the $\rho(T)$ relation for semiconductors only at low temperatures.

6.5] with $T_c \sim 60$ K. It is essential also that $YBa_2Cu_3O_{7-\delta}$ is a very well studied representative of the HTSC class, and that the nature of the structural changes (as well as of the critical temperature of the superconducting transition, critical magnetic fields, and macroscopic properties) this compound undergoes when subjected to various internal and external factors is, as a rule, fairly well known.

This investigation was focused on the following points: the effect of the content of weakly bonded lattice oxygen within $6.1 \leq 7 - \delta \leq 6.9$ on the luminescence spectra of single crystals $YBa_2Cu_3O_{7-\delta}$; the luminescence of HTSC ceramics with copper being replaced by atoms of other $3d$ metals (Me) in the lattice, $(YBa_2Cu_3O_{7-\delta} \longrightarrow YBa_2Cu_{3-x}Me_xO_{7-\delta})$;[2] the effect of illumination up to the maximum fluence $(\Phi t)_{max} \sim 1.5 \times 10^{20}$ photon cm^{-2} (excitation energy $E_{exc} = 3.4$ eV) on the luminescence of $YBa_2Cu_3O_{7-\delta}$ single crystals; and the luminescence of the $YBa_2Cu_3O_{\sim 6.95}$ single-crystal composition ($T_c \sim 92$ K) in the temperature range of 4.2–150 K.

Thus, this work takes the specific example of the $YBa_2Cu_3O_{7-\delta}$ superconductor to establish whether there is a correlation between the spectral characteristics (position E_{lum}, peak width $\Delta\lambda_{lum}$, and intensity I_{lum} of the luminescence bands) and the evolution of the electronic energy spectrum induced by a variation of temperature, doping by oxygen or metal ions, and illumination fluence.

1. EXPERIMENTAL TECHNIQUE

The techniques used to excite and measure HTSC luminescence spectra were described elsewhere [1]. The luminescence was excited in all experiments by a DRSh-500 continuously pumping mercury vapor lamp (with the excitation energy used in the study $E_{exc} = 3.4$ eV, the light flux incident on the sample $\Phi \sim 10^{16}$ photon cm^{-2} s^{-1}). Note that the energy $E_{exc} = 3.4$ eV corresponds to the maximum of absorption in the CuO_2 plane and is in excess of the optical gap $h\nu \sim 2$ eV separating in the $YBa_2Cu_3O_{7-\delta}$ HTSC the valence band, where the carriers (holes) appear, from the upper (empty) Hubbard band [3]. Thus, when photons with $E_{exc} = 3.4$ eV excite the luminescence, the electron is ejected into the upper Hubbard band by transferring from the oxygen to the copper ion $O^{2-}Cu^{2+} \longrightarrow O^-Cu^+$ in the CuO_2 plane. Note also that the excitation energy $E_{exc} = 3.4$ eV lies at the right-hand wing of the absorption band peaking at ~ 4 eV, which belongs to the $CuO_{1-\delta}$ chain structure. Therefore, direct chain excitation by 3.4-eV photons is also possible.

The luminescence was studied in reflection, with the secondary radiation projected on the slit of an MDR-3 scanning monochromator with a 1200 line/mm grating providing a wavelength resolution $\delta\lambda_{lum}$ of not worse than 2 nm. The luminescence was detected by a liquid-nitrogen-cooled FEU-79 PM tube operating in the photon counting mode.

To study the luminescence of the $YBa_2Cu_3O_{\sim 6.95}$ HTSC at low temperatures, the samples were placed in a helium cryostat [13]. The sample temperature in the cryostat could be maintained in the 4.2–300 K range to within 0.5 K with an electronic control unit.

The computer-based methods of luminescence spectra processing used in this work permitted the determination of the position, width, and integrated intensity of spectral bands and of the errors of all the measured quantities by the minimum χ^2 fitting [1].

2. RESULTS OF THE STUDY

2. 1. Effect of Oxygen Content on the Luminescence Spectra

This part of the work deals with the luminescence of a series of single crystals cut from the same single-crystal block of the $YBa_2Cu_3O_{7-\delta}$ HTSC and subjected to special heat treatments to obtain samples with different oxygen indices $(7 - \delta)$. The samples were cut in the plane perpendicular to the ab basal plane,[3] a geometry that allows one to determine the value of $(7 - \delta)$ from Raman scattering (RS) spectra. The RS line most sensitive to the oxygen content is at 502 cm^{-1}; it is associated with the A_g vibrational mode of the apex oxygen at the O1 site, and its intensity for the zz component of the scattering tensor is proportional to $(7 - \delta)$ [15].

Within a broad concentration range of the weakly bound oxygen, $6.1 \leq (7 - \delta) \leq 6.9$, one observes only two luminescence bands peaking at $E_{lum} \sim 2.4$ and ~ 2.8 eV. The shape of the luminescence spectra depends substantially on the $(7 - \delta)$ oxygen parameter, namely, for $(7 - \delta) \longrightarrow 7$ (i.e., in the ortho-I phase), the band with $E_{lum} \sim 2.8$ eV is fairly intense for $(7 - \delta) \sim 6.5$ (in the ortho-II phase[4]), and this band all but disappears against the background of the band with $E_{lum} \sim 2.4$ eV; for $(7 - \delta) \longrightarrow 6$ (i.e., in the tetra-phase), the ~ 2.8-eV band intensifies again.

---

[2] The use of polycrystalline samples was motivated in this case by the fact that the $YBa_2Cu_{3-x}Me_xO_{7-\delta}$ HTSCs cannot, in practice, be prepared in single-crystal form [12].

[3] We are stressing this point, because in the work a clearly pronounced anisotropy of the spectral characteristics has been observed (we have in mind the anisotropy of I_{lum}, i.e., of the band luminescence yield). The dependence of the nature of HTSC luminescence spectra on single-crystal orientation was apparently first revealed by Stankevitch et $al.$ [6]. The existence of this effect is in qualitative agreement with modern concepts of the anisotropy of HTSC optical properties (see, e.g., [14]).

[4] Recall that the lattice of the O-II phase of $YBa_2Cu_3O_{7-\delta}$ differs from that of the O-I-type in that for an ideal composition, $(7 - \delta) = 6.5$, the copper–oxygen chains …–Cu1–O4–Cu1–… of the former, aligned with the b axis of the orthorhombic lattice, alternate with the "defective" chains …–Cu1–□–Cu1–…, where □ is the oxygen vacancy.
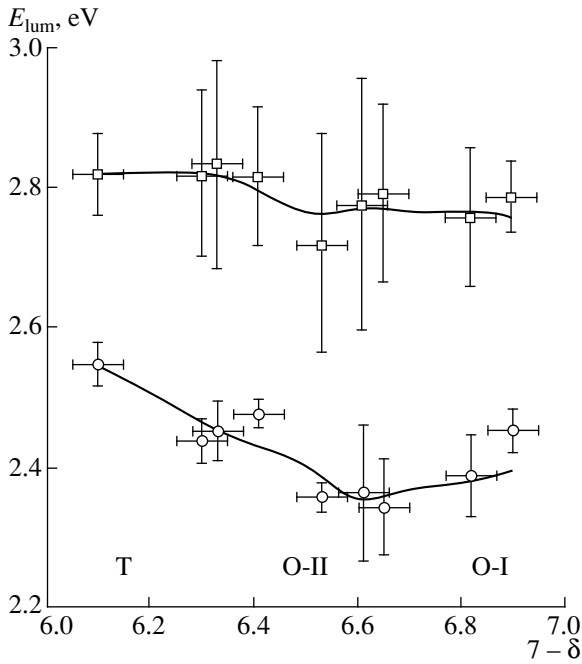
Fig. 1. Position of the luminescence bands of $YBa_2Cu_3O_{7-\delta}$ HTSC single crystal *vs* oxygen index $(7-\delta)$.

Fig. 2. Luminescence band intensity ratio $I_{lum}(T) = I_{\sim 2.8\,eV}/I_{\sim 2.4\,eV}$ of $YBa_2Cu_3O_{7-\delta}$ HTSC single crystal *vs* oxygen index $(7-\delta)$.

Figure 1 presents the energy position of the bands with $E_{lum} \sim 2.4$ and ~ 2.8 eV as a function of the oxygen index $(7-\delta)$; Fig. 2, the band integrated-intensity ratio, $I_{lum} = I_{\sim 2.8\,eV}/I_{\sim 2.4\,eV}$.

The dependences of the LS parameters on the content of weakly bound oxygen $(7-\delta)$ are clearly non-monotonic, with the bends in the $E_{lum}(7-\delta)$ and $I_{lum}(7-\delta)$ curves coinciding approximately in position with the boundaries separating the O-I, O-II, and T phases in the $(7-\delta)$–T diagram at room temperature [16]. The width of the spectral bands $\Delta\lambda_{lum}$ depends only weakly on the oxygen index.

Depending on the actual doping level in various parts of the phase diagram, one observes different trends in the intensity variation of both luminescence bands:

(i) In the region of the insulating (T) phase, $(7-\delta) < 6.5$, $I_{\sim 2.8\,eV}$ decreases, and $I_{\sim 2.4\,eV}$ increases with increasing oxygen doping level, where the holes appearing in the valence band remain localized.

(ii) In the "semiconducting" O-II phase, where the holes in the valence band may be already considered to be itinerant, one observes opposite trends in the variation of the luminescence bands in intensity ($I_{\sim 2.8\,eV}$ increases, and $I_{\sim 2.4\,eV}$ decreases).

(iii) In the metallic O-I phase and under optimum doping, the intensities of the $E_{lum} \sim 2.8$ and ~ 2.4 eV bands exhibit a trend to saturation.
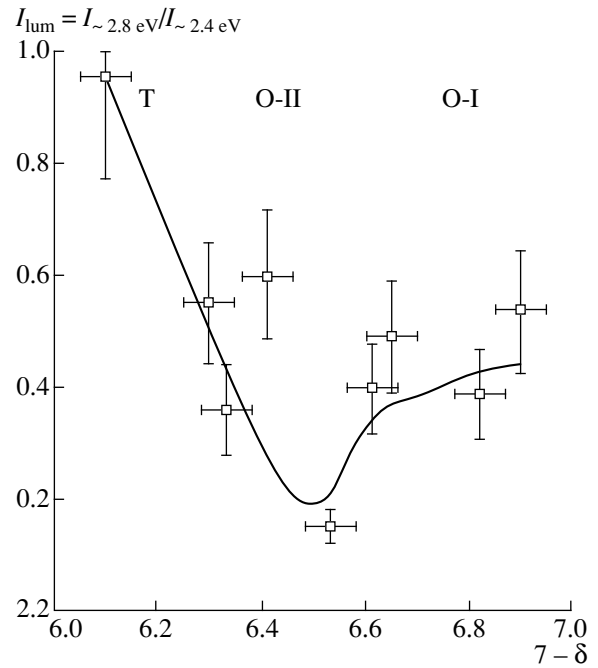
2. 2. Effect of Substitution on the Luminescence Spectra

A study of the influence of copper replacement in the HTSC lattice by atoms of other elements by the following scheme $YBa_2Cu_3O_{7-\delta} \longrightarrow YBa_2Cu_{3-x}Me_xO_{7-\delta}$ ($Me = Mn, Cr, Ag, Fe$; $x_{max} \sim 0.3$) on LS did not reveal any qualitative effects; indeed, no new bands appeared in the spectra, despite the insertion into the lattice of strongly luminescing ions (for example, of chromium and manganese ions in different valence states). Moreover, the corresponding change in the LS parameters (E_{lum}, $\Delta\lambda_{lum}$, and I_{lum}), if any, was not outside the probable measurement error.[5]

It should be stressed that the negative result obtained here, i.e., the absence of a noticeable effect of substitution on the LS parameters, is at odds with the reports [18, 19] on the observation of impurity-ion luminescence bands in $YBa_2Cu_3O_{7-\delta}$ at about the same doping level.

2. 3. Effect of Illumination on the Luminescence Spectra

To establish the nature of the effect of illumination on the luminescence of high-temperature superconduc-

---

[5] Note that the presence of impurity ions in the $YBa_2Cu_3O_{7-\delta}$ HTSC lattice was evidenced by a systematic detection of changes in the lattice parameters and the superconducting transition temperature depending on the species (Me) and concentration (x) of the substituting ions (see, e.g., [17], where the $YBa_2Cu_{3-x}Me_xO_{7-\delta}$ system is studied).
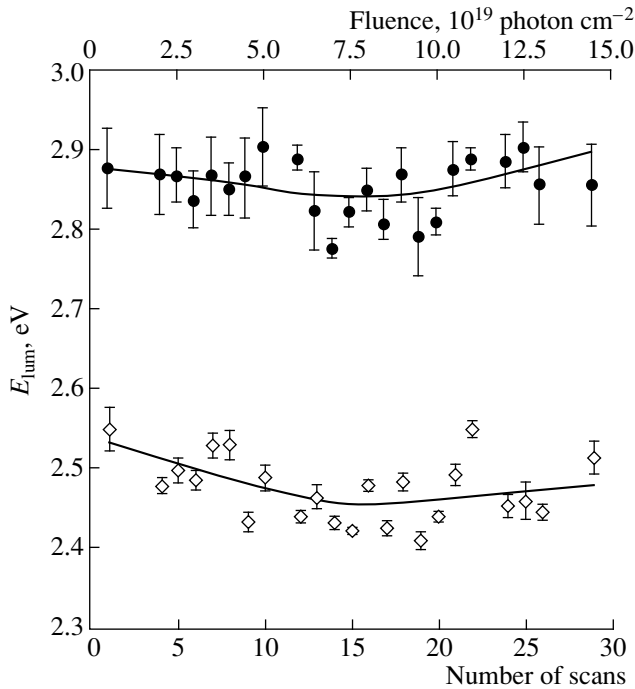
Fluence, 10^{19} photon cm^{-2}

Fig. 3. Position of the luminescence bands of $YBa_2Cu_3O_{\sim6.41}$ HTSC single crystal *vs* the number of scans and illumination fluence.

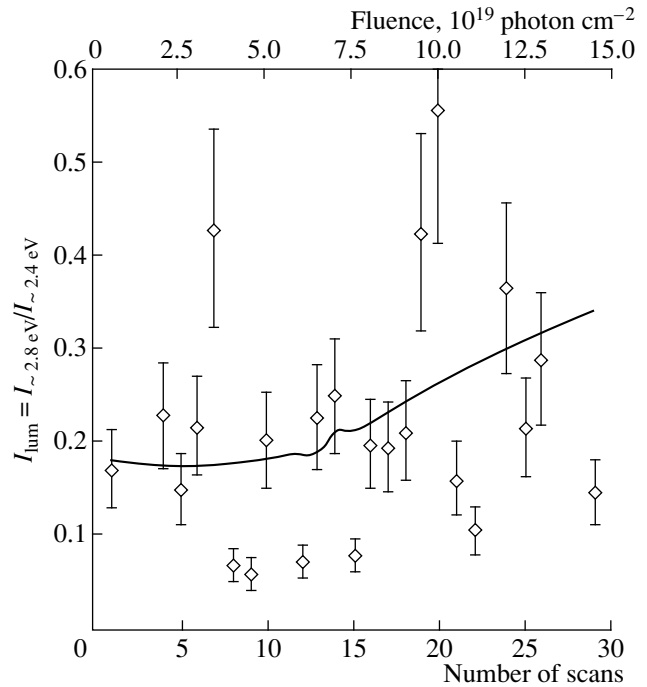**Fig. 4.** Luminescence band intensity ratio $I_{lum}(T) = I_{\sim2.8\,eV}/I_{\sim2.4\,eV}$ of $YBa_2Cu_3O_{\sim6.41}$ HTSC single crystal *vs* the number of scans and illumination fluence.

tors, we repeatedly measured the luminescence spectra from the surface of $YBa_2Cu_3O_{7-\delta}$ HTSC single crystals in different electronic and structural states [we used samples with the values of $(7 - \delta)$, respectively, 6.1 (the T phase), 6.41 (the O-II phase), and 6.9 (the O-I phase), see 2. 1]. The maximum illumination fluence accumulated in 30 cycles can be estimated as $(\Phi t)_{max} \sim 1.5 \times 10^{20}$ photon cm^{-2}.

The LS parameters were determined for each illumination cycle.[6] The spectral position of the luminescence bands E_{lum} and their relative intensity $I_{lum}(T) = I_{\sim2.8\,eV}/I_{\sim2.4\,eV}$ for the $YBa_2Cu_3O_{7-\delta}$ samples in the insulator T or the metallic O-I phase ($T_c \sim 90$ K) virtually do not depend on illumination.

The pattern is different for the $YBa_2Cu_3O_{6.41}$ sample (the "semiconducting" O-II phase at the insulator–metal transition) (Figs. 3, 4). Illumination produces weak, but statistically significant effects in the LS evolution; indeed, illumination in up to ~15–20 cycles (a fairly rough estimate of Φt yields 6×10^{19} photon cm^{-2}) exhibits a trend pointing to a decrease in E_{lum} of both bands, while the band intensity ratio $I_{lum}(T) = I_{\sim2.8\,eV}/I_{\sim2.4\,eV}$ remains practically constant; for $\Phi t \gtrsim 6 \times 10^{19}$ photon cm^{-2}, one observes a trend to an increase

---

[6] The accuracy of determination of the LS parameters (E_{lum}, $\Delta\lambda_{lum}$, and I_{lum}) for any one spectrum is naturally lower than that of averaged spectra, which are obtained, as a rule, by repeated scanning in λ_{lum}.

in E_{lum} of both bands; the magnitude of I_{lum} increases sharply and substantially. We note immediately that a comparison of Figs. 3 and 4 with Figs. 1 and 2 shows the LS parameters undergoing the same changes with increasing content of weakly bound oxygen, from the "starting" value $(7 - \delta) = 6.41$ to $(7 - \delta)_{max} \sim 6.9$.

Thus, as the pumping dose and, hence, the number of electrons injected into the conduction band increase, the behavior of the luminescence bands as to intensity and position in weakly doped samples approximately follows a scenario close to the metallization of the spectrum through chemical doping, i.e., an increase of the content of weakly bonded oxygen in the …–Cu1–O4–Cu1–… chains (see Subsection 2.1). The threshold for the light-induced metallization effects to appear in samples with $(7 - \delta) = 6.41$ is a fluence of $\sim 6 \times 10^{19}$ photon cm^{-2}.

2. 4. Effect of Temperature on the Luminescence Spectra

The sample studied in this part of the work was a $YBa_2Cu_3O_{\sim6.95}$ single crystal with $T_c \sim 92$ K cut along the **ab** basal plane. The luminescence spectra measured throughout the temperature range covered, 4.2 to 150 K, contained only the bands with $E_{lum} \sim 2.4$ and ~2.8 eV, i.e., the same as at room temperature.

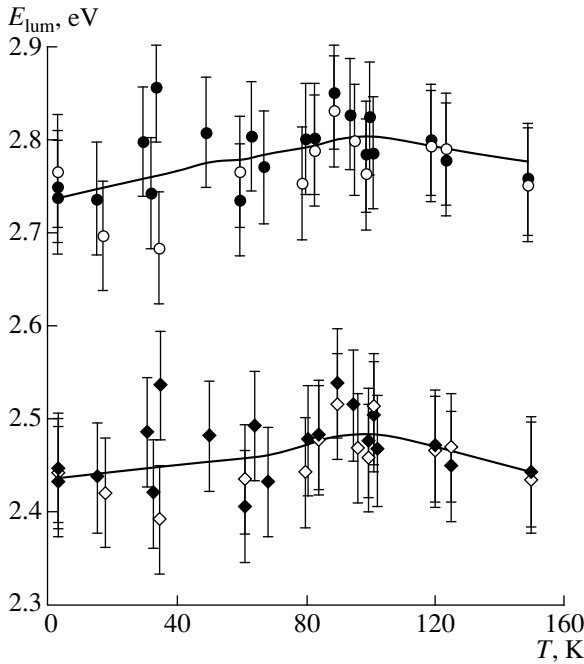Figures 5 and 6 illustrate the determination of the position of the E_{lum} centers and of the luminescence-

Fig. 5. Temperature dependence of the position of the luminescence bands of $YBa_2Cu_3O_{\sim 6.95}$ HTSC single crystal ($T_c \sim 92$ K).

band intensities [Fig. 6a presents the temperature dependences of the absolute band intensities, $I_{\sim 2.8\,eV}(T)$ and $I_{\sim 2.4\,eV}(T)$, and Fig. 6, the ratio of the integrated intensities of these bands, $I_{lum}(T) = I_{\sim 2.8\,eV}/I_{\sim 2.4\,eV}$.[7]

For $T > T_c$, the relative intensity of the band with $E_{lum} \sim 2.8$ eV is observed to decrease with the temperature. The band with $E_{lum} \sim 2.4$ eV varies little in terms of absolute intensity. As the temperature decreases in the region of the existence of the normal phase, the ratio $I_{lum}(T) = I_{\sim 2.8\,eV}/I_{\sim 2.4\,eV}$ decreases because of the variation in intensity of the band with $E_{lum} \sim 2.8$ eV.

Near T_c, both the absolute and relative luminescence-band intensities become sensitive to the superconducting transition. For $T < T_c$, even the half-width of the bands varied, namely, the band with $E_{lum} \sim 2.4$ eV became narrower, while that with $E_{lum} \sim 2.8$ eV broadened. Below T_c, the intensity of the luminescence band with $E_{lum} \sim 2.4$ eV follows a temperature-dependent pattern, whereas the integrated intensity of the band with $E_{lum} \sim 2.8$ eV is practically independent of temperature for $T < T_c$. At the superconducting transition temperature, the relative intensity $I_{lum}(T) = I_{\sim 2.8\,eV}/I_{\sim 2.4\,eV}$ increases.

In short, while in the case of oxygen doping the break of the $I_{lum}(7 - \delta)$ curve was the point of the concentration-driven insulator–metal phase transition, this

---

[7] The data relate to two series of measurements denoted in Figs. 5 and 6 by different symbols.

singular point in the temperature dependence of I_{lum} coincides with the superconducting transition temperature. Note that the sensitivity of luminescence spectra to the superconducting transition was first revealed in [20].

The decrease of E_{lum} for $T < T_c$ is observed in both luminescence bands.

It should be stressed that while the errors of individual measurements of the spectral characteristics are fairly large (in the figures, they are shown by bars), the change of the pattern of their temperature dependence in the vicinity of T_c is statistically significant. Indeed, accepting the rough approximation of the photon energy in the band with $E_{lum} \sim 2.8$ eV depending linearly on temperature, i.e.,

$$E_{lum}(T) = E_{lum}(0) + dE_{lum}/dT \times T,$$

we have $E_{lum}(0) = 2.918 \pm 0.029$ eV, $dE_{lum}/dT = -(10.90 \pm 2.46) \times 10^{-4}$ eV/K for $T > T_c$, and $E_{lum}(0) = 2.736 \pm 0.019$ eV, $dE_{lum}/dT = (7.60 \pm 3.37) \times 10^{-4}$ eV/K for $T < T_c$.

3. DISCUSSION OF RESULTS

Consider the results obtained from the standpoint of the concept postulating charge redistribution between the CuO_2 charge-transfer plane and the $CuO_{1-\delta}$ chain plane, the "charge reservoir." It is known (see, e.g., [2, 3, 21–23]) that insertion in chemical doping of an extra oxygen in the …–Cu1–O4–Cu1–… chains (to be precise, in the "defective" chains of the type …–Cu1–□–Cu1–O4–Cu1–…) brings about the trapping of an electron from the CuO_2 plane to leave a hole there. The holes forming in the CuO_2 plane in the insulator T phase for $(1 - \delta) < 0.4$ are localized, because the Fermi level remains above the hole mobility edge [23]. For $(1 - \delta) \sim 0.4$, the Fermi level crosses the mobility edge, and $YBa_2Cu_3O_{7-\delta}$ transfers to the conducting state. This opens the channel for the transfer of normal electrons through the apex oxygen ion at the O1 site from the Fermi level of CuO_2 to the $CuO_{1-\delta}$ chain plane, which increases the number of mobile holes. In the "metallic" state [$(1 - \delta) \longrightarrow 1$], when the doping level increases, the width of the hole band of mobile carriers is ~ 0.1 eV [23].

Accepting the traditional reasoning, the luminescence band with $E_{lum} \sim 2.4$ eV belonging to the CuO_2 plane can be assigned in the insulating phase to the recombination luminescence of electrons from the upper band with localized holes. As for the appearance of the luminescence band with $E_{lum} \sim 2.8$ eV in the insulating (T), "semiconducting" (O-II), and metallic (O-I) phases, it is related to the luminescence of the F centers forming in the $CuO_{1-\delta}$ chain planes at oxygen vacancies [1]. These F centers can become populated through the transfer of both the normal electrons from the CuO_2 planes and excited electrons to the Hubbard band.

The increase in the relative intensity of the luminescence band with $E_{lum} \sim 2.4$ eV, with increasing doping level in the observed regions where the insulating phase exists, implies that the intensity of recombination luminescence in the CuO_2 plane grows with the increasing number of localized holes. At the same time, the F-center luminescence intensity decreasing natural way as a result of the decrease of the number of oxygen vacancies in the …–Cu1–O4–Cu1–… chains with increasing concentration of the weakly bound oxygen. When the metallic phase forms, i.e., when mobile holes appear, one observes a distinct break of the $I_{\sim 2.8 \, eV}/I_{\sim 2.4 \, eV}(7 - \delta)$ dependence (see Fig. 2), and as the doping index $(7 - \delta)$ increases, the intensity of the band with $E_{lum} \sim 2.8$ eV begins to increase, and that of the band with $E_{lum} \sim 2.4$ eV, to decrease. This behavior of the $I_{\sim 2.8 \, eV}/I_{\sim 2.4 \, eV}(7 - \delta)$ relation suggests a sharp decrease in the recombination in the CuO_2 plane, i.e., a strong decrease in the probability of radiative recombination luminescence between an electron (in the upper band) and a mobile hole.

In this connection, note the following two points.

(i) Metallization creates density-of-states tails in the optical gap separating the two bands, thus increasing the probability of nonradiative recombination of the electron and the hole.

(ii) The decrease in the probability of recombination luminescence occurring can also be connected with selection rules in the wave vector **k** for mobile holes in the valence band.

The saturation of the $I_{lum}(7 - \delta)$ dependence for $(7 - \delta) \longrightarrow 7$ is apparently due to the saturation of the number of holes and the completion of the formation of the hole band.

The change in the luminescence intensity of the $E_{lum} \sim 2.8$-eV band observed when doping in the region where the metallic O-I phase exists should obviously be insignificant, which is in full agreement with the experimental data (Fig. 2). As seen from Fig. 1, when the doping index $(7 - \delta)$ is increased in the insulating phase, the band with $E_{lum} \sim 2.4$ eV is redshifted. Generally speaking, this indicates a shift of the mobility edge in the CuO_2 plane, at which the excited electron and hole recombine. The redshift implies that the separation between the upper band and the mobility edge decreases upon doping, i.e., the Fermi level and the mobility edge come closer.

Experiments involving light-induced doping of a sample with the oxygen index $(7 - \delta) = 6.41$ (Figs. 3, 4), i.e., of a sample close to the insulator–metal transition, reveal the formation of an illumination threshold $\Phi t \sim 6 \times 10^{19}$ photon cm^{-2}, above which the dependence of $I_{lum} = I_{\sim 2.8 \, eV}/I_{\sim 2.4 \, eV}$ on illumination fluence behaves similar to that on the oxygen index in the region of metallization obtained under chemical doping (Figs. 1, 2). Thus, illumination to fluences higher than the threshold may be classed among the light-induced doping phe-
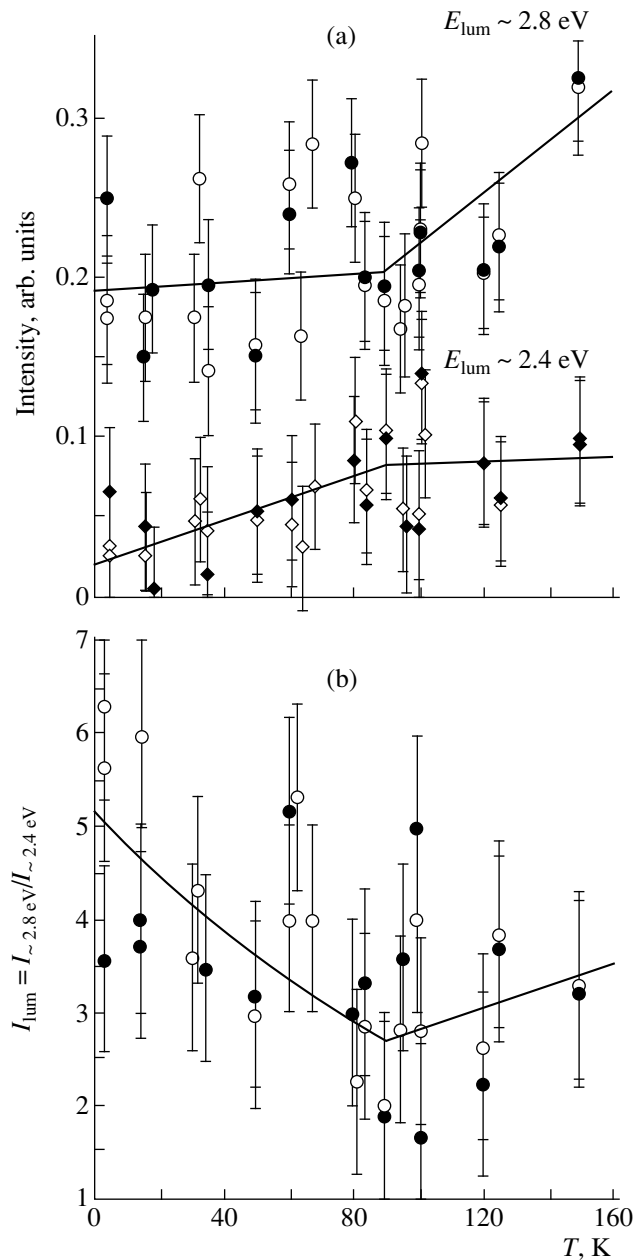
Fig. 6. Temperature dependence of the luminescence band intensity of $YBa_2Cu_3O_{\sim 6.95}$ HTSC single crystal. (a) Temperature dependences of the absolute band intensities; (b) temperature dependence of the luminescence band intensity ratio $I_{lum}(T) = I_{\sim 2.8 \, eV}/I_{\sim 2.4 \, eV}$.

nomena. Considered in terms of the charge transfer between the CuO_2 and $CuO_{1-\delta}$ planes, this means that photoexcitation to a threshold fluence gives rise to changes in the chain structure, which opens the metallization channel through the transfer of normal electrons to the $CuO_{1-\delta}$ chain plane. This channel becomes open as a result of a buildup of the illumination fluence, which requires invoking an analysis of electron-stimulated chain-lengthening processes. Recall that metalli-

zation is accompanied by an increase in chain length [21]. Because the chain lengthening is connected with oxygen attaching to Cu–O dangling bonds, the electron-stimulated chain lengthening is equivalent to the electron-stimulated diffusion of weakly bound oxygen. It may be conjectured that the energy of an excited electron released in a chain in its localization favors overcoming the oxygen-diffusion barrier, which is about 1 eV [11].

The very large change of the $I_{lum} = I_{\sim 2.8\,eV}/I_{\sim 2.4\,eV}$ ratio under light-induced doping (by nearly a factor two) is comparable to the effect of chemical doping, where $(7 - \delta)$ changes from 6.5 to 6.9. In a very rough approximation, this may mean that illumination of an HTSC with a composition $YBa_2Cu_3O_{\sim 6.41}$ to a fluence $\Phi t \sim 6 \times 10^{19}$ photon cm^{-2} with a photon energy $E_{exc} \sim$ 3.4 eV is equivalent to a transfer of a negative charge of 0.5 atomic units from a CuO_2 plane to a $CuO_{1-\delta}$ chain. Calculating the number of unit cells in the illuminated HTSC volume (the depth of light penetration into $YBa_2Cu_3O_{7-\delta}$ was measured in [24] to be ~700 Å) shows that this charge transfer corresponds approximately to an illumination fluence of ~1 photon/unit cell (similar estimates were obtained in [21]).

Thus, the totality of the results obtained in the work suggests a clearly pronounced relationship between the evolution of the crystalline structure [the concentration-driven transformations $T \longrightarrow$ O-II $\longrightarrow$ O-I, the intensification of rhombic distortions $(b - a)/(b + a)$, etc.; see, e.g., [25, 26] (the effect of the oxygen index and illumination)], metallization of the electron energy spectrum (the concentration-driven insulator $\longrightarrow$ semiconductor $\longrightarrow$ metal transitions, the increase in the electrical conductivity in the normal state, the growth of the superconducting transition temperature, etc.), and the exolution of the luminescence spectrum with an increasing content of the weakly bound oxygen or other factors resulting in the formation and enhanced stability of the …–Cu1–O4–Cu1–… chains [11], which act as charge reservoirs.[8]

Let us turn now to the temperature dependences of the LS parameters obtained for the samples with optimum doping at illuminations below the threshold fluence. As seen from Figs. 6a and 6b, above T_c the integrated intensity of the $E_{lum} \sim 2.4$-eV band remains practically constant, whereas that of the band with $E_{lum} \sim$ 2.8 eV varies strongly, and this accounts for the temperature behavior of the relative intensity of these bands. The absence of any intensity redistribution between the luminescence bands indicates that there is no redistribution of normal electrons (holes) between the CuO_2 and $CuO_{1-\delta}$ sublattices with decreasing temperature. Thus, temperature-induced doping on the CuO_2 plane does not occur at low temperatures, which, in its turn,

implies that the thermally stimulated transfer of normal electrons from the CuO_2 plane is hindered. This conclusion appears very significant in connection with the discussion of a probable existence of a strong thermally stimulated doping channel for the CuO_2 plane in HTSCs, which opens with decreasing temperature. In particular, some theories [27] suggest that a decrease of temperature may give rise to a noticeable electron transfer from the CuO_2 plane to the $CuO_{1-\delta}$ chain structure. Our result is the only evidence of the weak influence of temperature on the number of holes in the CuO_2 plane.

The temperature dependence of the $E_{lum} \sim 2.8$-eV band intensity for $T < T_c$ is governed by the processes taking place on the $CuO_{1-\delta}$ chain plane itself and is related to the temperature-induced variation of the extent to which the competing channels of radiative and nonradiative deexcitation are operating. As seen from Fig. 6, below T_c the temperature dependences of the intensities of these bands change their pattern, namely, the intensity of the band at $E_{lum} \sim 2.4$ eV becomes temperature dependent, while that at $E_{lum} \sim 2.8$ eV no longer depends on temperature. The decrease of the integrated intensity of the band at $E_{lum} \sim 2.4$ eV for $T < T_c$ coincides with its weakening under metallization of the spectrum. In other words, below the superconducting transition temperature, recombination of an excited electron with the superconducting condensate is hindered, which may be assigned to the most distinct manifestation of the selection rule in the wave vector **k**, the conditions where recombination with band holes is less efficient than that with the localized ones.

As follows from the above results, with $YBa_2Cu_3O_{7-\delta}$ acted upon by different factors (an increase of oxygen content in the regions of existence of the O-II and O-I phases, under illumination of the sample in the O-II phase), one observes the same, qualitatively identical effect in the evolution of the emission spectrum. We have in mind a noticeable growth of the relative intensity of the band at $E_{lum} \sim 2.8$ eV and a change in intensity of the $E_{lum} \sim 2.4$-eV band, which gives one grounds to maintain that the charge transfer between the sublattices has the same nature, which accounts for the associated integrated intensity redistribution between the bands at $E_{lum} \sim 2.4$ and ~2.8 eV.

The absence of any pronounced effects in the luminescence spectra of $YBa_2Cu_3O_{7-\delta}$ under the Cu $\longrightarrow$ Me substitution (see Subsect. 2. 2) is accounted for by the fact that these substitutions do not affect the structure of the …Cu1–O4–Cu1… chains strongly enough, nor, correspondingly, the probability of the processes occurring in these chains, as well as the electron exchange between the $CuO_{1-\delta}$ chain and CuO_2 charge-transfer planes.

Thus, an analysis of the results obtained in this work argues convincingly for the existence of a distinct correlation between the structural changes in the

---

[8] The acting factor in this work is illumination and, naturally, the superconducting transition, but (despite the negative result obtained here) one cannot rule out the influence of substitution.

$YBa_2Cu_3O_{7-\delta}$ high-T_c superconductor, which are induced by internal or external factors acting on its crystal lattice and the parameters of luminescence spectra (the spectral position E_{lum}, width $\Delta\lambda_{lum}$, and intensity I_{lum} of the luminescence bands). We have in mind here not only the differences between the LS parameters of the various structural modifications of $YBa_2Cu_3O_{7-\delta}$ (O-I, O-II, and T), but some finer effects of a correlated variation of I_{lum}, E_{lum}, and (partially) $\Delta\lambda_{lum}$, on the one hand, and of the extent of metallization (including the onset of the superconducting transition) of the $YBa_2Cu_3O_{7-\delta}$ electronic spectrum, on the other.

It should be stressed that the redistribution of integrated intensity of the luminescence bands originating from different electronic and structural subsystems (the CuO_2 charge-transfer and $CuO_{1-\delta}$ chain planes) permits one to investigate the processes governing charge transfer between the subsystems, and the temperature dependences of the parameters of these bands offer the possibility of studying localization and delocalization in each of these subsystems.

The establishment of a correlation between the electronic and structural properties, on the one hand, and the optical parameters of $YBa_2Cu_3O_{7-\delta}$, on the other hand, paves the way for using the luminescence spectra of high-T_c superconductors as an efficient optical probe of electronic processes occurring in these substances.

ACKNOWLEDGMENTS

REFERENCES

1. T. V. Sukhareva and V. V. Eremenko, Fiz. Tverd. Tela (St. Petersburg) **39** (10), 1739 (1997) [Phys. Solid State **39**, 1548 (1997)].
2. I. Fugol, C. Politis, A. Rathner, *et al.*, J. Lumin. **62**, 291 (1994).
3. I. Ya. Fugol, V. N. Samovarov, Yu. I. Rybalko, *et al.*, Modern Phys. Lett. B **4** (12), 803 (1990).
4. T. V. Sukhareva, Funct. Mater. **4** (3), 430 (1997).
5. T. V. Sukhareva, Funct. Mater. **4** (4), 467 (1997).
6. V. G. Stankevitch, N. Yu. Svechnikov, K. V. Kaznacheev, *et al.*, Phys. Rev. B **47** (2), 1024 (1993).
7. A. A. Avdeenko, V. V. Eremenko, P. V. Zinov'ev, *et al.*, Ukr. Fiz. Zh. **39** (9–10), 961 (1994).
8. A. A. Avdeenko, V. V. Demirskiy, V. V. Eremenko, *et al.*, Funct. Mater. **3** (2), 183 (1996).
9. A. A. Avdeenko, P. V. Zinov'ev, N. B. Silaeva, *et al.*, Zh. Prikl. Spektrosk. **58** (3–4), 404 (1993).
10. S. H. Pawar and B. M. Todkar, Indian J. Pure Appl. Phys. **30**, 562 (1992).
11. J. D. Jorgansen, Phys. Today **44** (6), 34 (1991).
12. V. A. Finkel', *High-Temperature Superconductors: Materials Science, Technologies, Applications* (Kiev, 1993).
13. A. A. Avdeenko, V. V. Eremenko, P. V. Zinov'ev, *et al.*, in *Abstracts of Papers to the 30th Meeting on Low-Temperature Physics* (Dubna, 1994), Vol. 1, p. 3.
14. S. N. Rasshkeev, E. G. Maksimov, S. Yu. Savrasov, *et al.*, Zh. Éksp. Teor. Fiz. **97** (5), 1688 (1990) [Sov. Phys. JETP **70**, 952 (1990)].
15. D. Mihailovic and C. M. Foster, Solid State Commun. **74** (4), 753 (1990).
16. G. Ceder, M. Asta, W. C. Carter, *et al.*, Phys. Rev. B **41** (13), 8698 (1990).
17. R. F. Jardim, S. Gama, O. F. de Lima, *et al.*, Phys. Rev. B **38** (7), 4580 (1988).
18. Z. Song, L. Zhang, H. Liu, *et al.*, Chinese Science Bull. **35** (6), 479 (1990).
19. Z. Song, L. Zhang, J. Wang, *et al.*, Lanthanide & Actinide Research **3**, 63 (1989).
20. V. V. Eremenko, I. Ya. Fugol', and V. N. Samovarov, Pis'ma Zh. Éksp. Teor. Fiz. **47**, 529 (1988) [JETP Lett. **47**, 618 (1988)].
21. V. I. Kudinov, I. L. Chaplygin, A. I. Kirilyuk, *et al.*, Phys. Rev. B **47** (14), 9017 (1993).
22. G. Uimin, Mod. Phys. Lett. B **6**, 2291 (1992).
23. I. Ya. Fugol', A. M. Ratner, V. N. Samovarov, *et al.*, Fiz. Nizk. Temp. **20** (6), 520 (1994) [Low Temp. Phys. **20**, 410 (1994)].
24. I. Bozovik, K. Char, and S. J. B. Yoo, Phys. Rev. B **38** (7), 5077 (1988).
25. V. A. Finkel', V. M. Arzhavitin, A. A. Blinkin, *et al.*, Physica C **235–240**, 303 (1994).
26. D. Lederman, J. Hasen, I. K. Schuller, *et al.*, Appl. Phys. Lett. **64** (5), 652 (1994).
27. D. Khomskii and F. Kusmartsev, Phys. Rev. B **46**, 14245 (1992).

Translated by G. Skrebtsov

Effect of Coulomb Correlation on Hopping Conductivity

V. D. Kagan

Ioffe Physicotechnical Institute, Russian Academy of Sciences, Politekhnicheskaya ul. 26, St. Petersburg, 194021 Russia
e-mail: victor_kagan@pop.rssi.ru
Received September 14, 1999

Abstract—The analysis of hopping conductivity requires a complete quantum-statistical description of a pair of sites between which an electron jump takes place. This description includes a double-charged energy level, the energy being increased by the Coulomb repulsion of the charges. The inclusion of this level changes the occupation numbers of single-charge states essential for hopping conductivity. Such an indirect influence of Coulomb repulsion is referred to as Coulomb correlation. It leads to a modification of Mott's law in the case of conductivity with variable range hopping. The concept of a Coulomb gap is not required for the characterization of this modification. © 2000 MAIK "Nauka/Interperiodica".

In compensated semiconductors at low temperatures, conduction takes place through electron jumps from filled donors to empty ones, the number of which is equal to the number of acceptors. These jumps are not classical ones of a particle from one potential well to another, but proceed by quantum tunneling between two states of a pair of donors containing one electron. The energies of electrons located at donors having coordinates r_i and r_j are characterized by a random spread over a wide range and generally do not coincide ($\varepsilon_i \neq \varepsilon_j$); hence, electron tunneling is impossible without the participation of phonons, whose energy must compensate the difference in the electron energies. A quantum-mechanical description of the hopping process is given in the well-known paper by Miller and Abrahams [1], which is a starting point for all the theories of hopping conductivity. In that paper, the hopping conductivity was calculated, which exhibited a natural exponential dependence on the distance noticeably exceeding the electron localization radius a at a donor:

$$w_{ij} = w_{ij}^0 \exp\left(-2\frac{r_{ij}}{a}\right), \qquad (1)$$

where $r_{ij} = |r_i - r_j|$.

The probability w is proportional to the square of the overlap integral $J_{ij} = J_0\exp(-r_{ij}/a)$.

However, the statistical description given in [1] for a pair of energy levels between which the hopping occurs is not quite satisfactory, and the present paper aims to correct this drawback. The presence of the overlap integral of a pair of donors leads to the collectivization of one-electron levels with energies ε_i and ε_j, as a result of which the energies assume the values

$$E_{1,2} = \frac{\varepsilon_i + \varepsilon_j}{2} \pm \sqrt{\left(\frac{\varepsilon_i - \varepsilon_j}{2}\right)^2 + J_{ij}^2}. \qquad (2)$$

According to Shklovskiĭ and Éfros [2], this two-center system has, in addition to one-electron levels, two more energy levels: a level without electrons with zero energy, and a two-electron level with the energy

$$E_3 = \varepsilon_i + \varepsilon_j + \frac{e^2}{kr_{ij}} = E_1 + E_2 + \frac{e^2}{kr_{ij}}. \qquad (3)$$

Here, e is the electron charge and k is the static permittivity of the semiconductor. All four levels should be taken into account in a statistical description of the filling of the states in the two-center system, and this statistics differs significantly from the Fermi statistics. Proceeding from the conventional equilibrium exponential expression for the probability of level filling and from the probability normalization requirement, we obtain the following expression for the equilibrium occupation numbers:

$$n_s^{(0)} = A^{-1}\exp[(\mu - E_s)/T]. \qquad (4)$$

The normalization factor A is given by

$$A = 1 + \exp[(\mu - E_1)/T] + \exp[(\mu - E_2)/T] + \exp[(2\mu - E_3)/T]. \qquad (5)$$

Here, T is the temperature in energy units. Note that, for the states with E_1 and E_2, in which there is only one electron and a Coulomb repulsion is ruled out, the occupation numbers have higher values (in view of the normalization condition) than in the hypothetical case of electrons having zero electric charge. This is just the Coulomb correlation discovered in [2]. The chemical potential μ is determined by solving the averaged problem and is an independent parameter for an isolated pair of energy levels.

Let us consider justifying the inclusion of the Coulomb repulsion energy to the energy of the third two-electron level, although the energies of an electron at the ith site are self-consistently determined, taking into

account the action exerted by electrons located at all the remaining sites. Naturally, this can be done in the amorphous semiconductor model, where random energy values ε_i are due to fluctuations of the atomic arrangement at lattice sites, as well as valence forces of a non-Coulomb origin. However, one can assume that expression (3) for the energy of a two-electron level also holds in the model of a classical impurity band, where random values ε_i are determined just by the Coulomb interactions with all the charges of the semiconductor, and the application of this expression does not take into account the Coulomb interaction between the electrons at sites i and j twice. All calculations are carried out in the thermodynamic limit, where the total volume of the semiconductor, as well as the number of any impurities, tends to infinity, while their ratio, i.e., impurity concentration, is assumed to be finite. In this case, the contribution of an individual impurity j to the quantity ε_i is negligibly small. Mathematically, this is reflected in the fact that a finite contribution to ε_i comes from the integral of the concentration of all the impurities, in which the contribution of the given impurity is an infinitely small quantity. On the contrary, the contribution of the Coulomb repulsion to the energy of two individual impurities is finite.

The hopping process can be described as the balance of transitions between the energy levels E_1 and E_2, accompanied by the emission (w_e) or absorption (w_a) of a phonon:

$$w_a = w_{ij}N(E_2 - E_1), \quad w_e = w_{ij}[N(E_2 - E_1) + 1],$$
$$N(\varepsilon) = \frac{1}{e^{\varepsilon/T} - 1}. \tag{6}$$

Here, $N(E)$ is the Planck equilibrium distribution function for phonons.

Further discussion follows the scheme of paper [1], modified to use the pair statistics. The current I_{ij} includes the difference of the numbers of transitions between the levels E_1 and E_2:

$$I_{ij} = er_{ij}(w_a n_1 - w_e n_2). \tag{7}$$

In equilibrium, the current is zero as expected. In the presence of an electric field E, two changes should be introduced into expression (6) for the current. First, the electron energy at a site in the expressions for the probabilities acquires a correction

$$\delta\varepsilon_i = eEr_i + \sum_s K_{is}\delta f_s, \tag{8}$$

where K_{is} is an interaction function, taking into account the effect of the one-particle distribution function on the energy level, and δf_s is the change in the equilibrium one-particle distribution function. Second, equilibrium pair distribution functions should be replaced by the corresponding nonequilibrium functions. However, the

nonequilibrium pair distribution function for an independent pair of donors in the electric field would be reduced to the equilibrium function, depending on modified energies. The total current in this case would remain equal to zero. Apart from the change in the energy at a site, for the system of interacting pairs, one has to introduce a change in the energies $E_{1,2}$ in the form of local voltages U_{ij}:

$$\delta E_{1,2} = \pm eU_{ij}. \tag{9}$$

These local voltages should be calculated for the complete system of all pairs, taking into account the boundary condition according to which the total voltage drop across the entire system is equal to the potential difference applied to the entire sample.

Considering the current linear in the electric field, we can solve the problem of the network of random resistances in the field of random potential differences:

$$I_{ij} = R_{ij}^{-1}U_{ij}. \tag{10}$$

Here,

$$R_{ij}^{-1} = 2\frac{e^2 r_{ij}w_{ij}}{T}N(E_2 - E_1)n_1. \tag{11}$$

At low temperatures, the Planck distribution function is transformed into the Wien distribution function and, besides, we can neglect the third term in the normalization factor, i.e.,

$$R_{ij}^{-1} = 2\frac{e^2 r_{ij}w_{ij}}{T}$$
$$\times \frac{e^{-\frac{E_2 - E_1}{T}}e^{\frac{\mu - E_1}{T}}}{1 + e^{\frac{\mu - E_1}{T}} + e^{\frac{\mu - E_2}{T}} + e^{\frac{2\mu - (e^2/kr_{ij}) - E_2 - E_1}{T}}}. \tag{12}$$

The currents in the resistor network must be summed over all energy values at the sites and over the distances between the sites. Since the pairs mainly have large energies, in the expressions for energies we can neglect the overlap integral, i.e.,

$$E_{1,2} = \frac{\varepsilon_i + \varepsilon_j}{2} \pm \frac{|\varepsilon_i - \varepsilon_j|}{2},$$
$$E_2 - E_1 = |\varepsilon_i - \varepsilon_j|. \tag{13}$$

Nevertheless, we do not arrive at the Miller–Abrahams expressions just in view of the difference between the pair statistics and the Fermi statistics. Following [1], we write the expression for the resistance at extremely low temperatures in an equivalent form:

$$R_{ij}^{-1} = \gamma_{ij}e^{-2\frac{r_{ij}}{a} - \frac{\varepsilon_{ij}}{T}}, \tag{14}$$

$$\varepsilon_{ij} = \frac{1}{2}(|\mu - E_1| + |\mu - E_2 - e^2/kr_{ij}| \qquad (15)$$

$$+ |\varepsilon_i - \varepsilon_j| - e^2/kr_{ij}).$$

Pay attention to the case when the two energies ε_i and ε_j belong to the interval between μ and $\mu - \dfrac{e^2}{kr_{ij}}$; in this case, the activation energy is equal to $|\varepsilon_i - \varepsilon_j|$. This case is not encountered in the Miller–Abrahams network.

If we disregard the Coulomb repulsion energy e^2/kr_{ij}, expression (15) is transformed into the Miller–Abrahams formula.

The random resistor network used for solving various problems in the percolation theory for the conductivity with a constant jump length (nearest neighbor hopping, NNH), as well as for the conductivity with a variable jump length (variable range hopping, VRH) [3]. The modification of the Miller–Abrahams network makes it possible to take into account the influence of the Coulomb interaction on all types of hopping conductivity. Shklovskiĭ and Efros [3] believed that this effect must be taken into consideration by proceeding from the ideas concerning the presence of a "soft" Coulomb gap in the spectrum of one-particle states. However, the Coulomb gap has nothing to do with problems of collective processes, including the problem of conduction. The entire interaction is taken into account in formula (15).

According to Ambegaokar et al. [4], for the percolation problem in which the conductivity should be determined, the connectivity condition has the form

$$2\frac{r_{ij}}{a} + \frac{|\varepsilon_i - \varepsilon_j|}{T} \le \xi, \qquad (16)$$

where the quantity ξ defines the magnitude of the exponent in the electrical conductivity. Going over to an analysis of VRH, we introduce dimensionless variables $x_{ij} = 2\dfrac{r_{ij}}{a\xi}$ and $y_i = \dfrac{\varepsilon_i}{T\xi}$, for which the percolation problem is formulated in a dimensionless form with the unit connectivity condition. The percolation criterion for this problem is

$$g\left(\frac{a}{2}\right)^3 T\xi^4 \ge n_c. \qquad (17)$$

Here, g is the (constant) density of states and the number n_c is known from the literature [3]. The conventional solution of the Mott problem corresponds to the equality sign in formula (17), which defines the quantity $\xi_c = \left(\dfrac{2n_c}{gTa^3}\right)^{1/4}$.

While solving this problem, we simplified expression (15) for the activation energy, neglecting the Coulomb repulsion energy in it. This could be done only provided that

$$T\xi_c \ge 2\frac{e^2}{ka\xi_c}\beta, \quad \beta \le 1. \qquad (18)$$

Condition (18) sets a limit on the application of Mott's law at low temperatures:

$$T \gg ga\left(\frac{e^2}{k}\right)^2. \qquad (19)$$

As the temperature decreases further, Mott's law for VRH becomes inapplicable. We must now use inequality (18) and the inequality opposite to (19). We choose the activation energy in the Coulomb energy range specified above; for this purpose, we use the equality sign in formula (18). With this choice, inequality (17) is equivalent to the inequality opposite to (19), which confirms the applicability of the new law just in the temperature range in which Mott's law is not valid. Thus, the Coulomb activation energy has led to the well-known law for the electrical conductivity:

$$\sigma = \exp\left(-\sqrt{\frac{2\beta(e^2/ka)}{T}}\right). \qquad (20)$$

This law is thought to be associated with the Coulomb gap in the one-particle density of states [3]. However, the Coulomb gap has nothing in common with the conduction process involving two-particle states subject to the two-particle statistics (4), (5), which just determines the law (20).

The VRH process can occur only under the condition when the average hopping range $\dfrac{a\xi_c}{2}$ is much larger than the average hopping range r_0 in the NNH process, which is approximately equal to the average separation $N^{-1/3}$ between majority impurities, where N is the concentration of majority impurities. This leads to the following criterion for the applicability of Mott's law:

$$\left(\frac{a}{gT}\right)^{1/4} \ll r_0, \qquad (21)$$

while the applicability of dependence (20) is determined by the inequality

$$\left(\frac{e^2}{kT}a\right)^{1/2} \ll r_0. \qquad (22)$$

These inequalities set the upper limit on the temperature at which the VRH conductivity laws are observed; this agrees with the experimental results at low temperatures. It should be recalled, however, that, in accordance with (19), the temperature at which Mott's law holds is also limited from below; i.e., Mott's law is observed in a certain temperature range.

Inequalities (18)–(22) determine what we shall refer to as a "phase diagram," i.e., the ranges of temperatures and concentrations of majority and minority impurities in which different temperature dependences of conductivity are observed. The change of the inequalities for the corresponding equalities determines the boundaries of these regions. The boundary separating the regions where Mott's law and equality (20) are satisfied is determined by the equation

$$T = c_1 a g \frac{e^4}{k^2}, \tag{23}$$

while the boundary separating the regions of applicability of Mott's law and the NNH law is defined as

$$T = c_2 \frac{a}{g r_0^4}, \tag{24}$$

and the boundary between the regions where law (20) and the NNH law are satisfied can be described as

$$T = c_3 \frac{e^2 a}{k r_0^2}. \tag{25}$$

Unfortunately, we are not in a position to determine the constants in these equalities, and our phase diagram only shows the general form of the regions, rather than their exact boundaries. It should be recalled that the density of states is proportional to the concentration n of minority impurities, i.e.,

$$g = \frac{n}{A}, \tag{26}$$

where A is the characteristic spread of random energies. The difficulty lies in that the phase diagram depends on two concentrations, namely, on those of the majority and minority carriers.

Figures 1a–1c depict phase diagrams in the space of temperatures T and the minority carrier concentrations n for a given concentration of majority carriers. The law (20) is observed in region I, Mott's law in region II, and the exponential temperature dependence of the NNH conductivity in region III. Figure 1a corresponds to a special degenerate case which is possible only for an accidental relation between the constants appearing in the equations that define the boundaries of the regions:

$$c_3 = \sqrt{c_1 c_2}. \tag{27}$$

The characteristic feature of all the diagrams is the existence of a critical concentration of minority carriers above which Mott's law is not observed.

Figures 2a–2c show phase diagrams in the space of temperatures T and concentrations of majority carriers N for a fixed concentration of minority carriers. Finally, Figs. 3a–3c show phase diagrams in the space of temperatures T and concentrations of majority carriers N
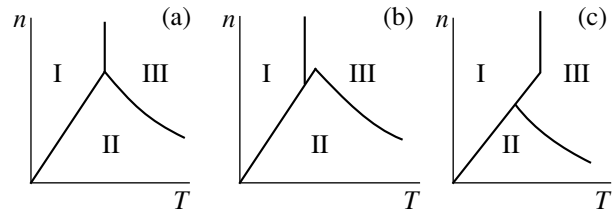

Fig. 1. Temperature and concentration regions for minority carriers, in which different laws of electrical conductivity are observed for a fixed concentration of majority carriers.

Fig. 2. Temperature and concentration regions for majority carriers, in which different laws of electrical conductivity are observed for a fixed concentration of minority carriers.
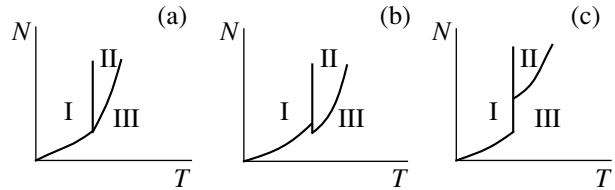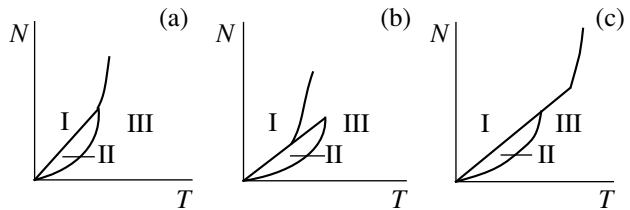

Fig. 3. Temperature and concentration regions for majority carriers, in which different laws of electrical conductivity are observed for a fixed degree of compensation.

for a fixed degree of compensation $K = \frac{n}{N}$. Figures 2a and 3a correspond to the accidental relation (27). All the diagrams demonstrate the existence of the critical concentration of carriers above which Mott's law does not hold.

On the side of high temperatures, the phase diagram of hopping conductivity should be supplemented by a region corresponding to conduction through delocalized states, which can considerably reduce the range of the NNH conductivity. This effect is apparently manifested in experiments with doped germanium [5].

Let us consider the problem on VRH in a strong magnetic field of strength H, in which the magnetic length $\lambda = \sqrt{\frac{ch}{eH}}$ is smaller than the localization radius. In this case, the wave function of the localized state falls off along the magnetic field in the distance $a_H = a \ln(H/H_0)$, which differs from a only slightly, while

across the magnetic field it falls of in a much smaller distance λ. Consequently, we must replace inequality (17) by the inequality

$$g\lambda^2 a_H T\xi^4 \geq n_c, \tag{28}$$

and inequality (18) by the inequality

$$T\xi \geq 2\frac{e^2}{k\sqrt{a_H^2 + 2\lambda^2\xi}}\beta. \tag{29}$$

In (29), the term with λ can be neglected, after which this inequality coincides with (18). Having determined now the activation energy from this condition, we find that it does not depend on the magnetic field. The magnetic field determines the range of low temperatures defined by inequality (28), in which the law (20) is observed. Consequently, a strong magnetic field considerably modifies Mott's law, but does not affect the law (20). This conclusion basically differs from that associating the law (20) with the Coulomb gap; according to this law, a strong dependence on the magnetic field takes place (ξ_c is proportional to $H^{1/5}$) [3].

The pair statistics was used for describing transport phenomena in rf fields [2]. The main idea of the present paper is that the same statistics should be used for describing transport phenomena in a static field. However, this necessitates considerable changes in the theory, namely, a modification of the random resistor network. We have demonstrated some consequences of such a modification. It is likely that all the effects emerging as a result of electrons hopping between localized states in a semiconductor must be revised on the basis of the two-particle statistics and the modified random resistor network.

ACKNOWLEDGMENTS

REFERENCES

1. A. Miller and E. Abrahams, Phys. Rev. **120** (3), 745 (1960).
2. B. I. Shklovskiĭ and A. L. Éfros, Zh. Éksp. Teor. Fiz. **81** (1), 406 (1981) [Sov. Phys. JETP **54**, 218 (1981)].
3. B. I. Shklovskii and A. L. Efros, *Electronic Properties of Doped Semiconductors* (Springer, Berlin, 1984).
4. V. Ambegaokar, B. I. Halperin, and J. S. Langer, Phys. Rev. B **4** (8), 2612 (1971).
5. A. G. Zabrodskiĭ, A. G. Andreev, and A. V. Alekseenko, Fiz. Tekh. Poluprovodn. **26** (3), 431 (1992) [Sov. Phys. Semicond. **26**, 244 (1992)].

Translated by N. Wadhwa

Properties of Erbium Luminescence in Bulk Crystals of Silicon Carbide

R. A. Babunts, V. A. Vetrov, I. V. Il'in, E. N. Mokhov, N. G. Romanov, V. A. Khramtsov, and P. G. Baranov

Ioffe Physicotechnical Institute, Russian Academy of Sciences, Politekhnicheskaya ul. 26, St. Petersburg, 194021 Russia
e-mail: ivan.ilyin@pop.ioffe.rssi.ru
Received October 25, 1999

Abstract—The infrared luminescence of Er^{3+} ions has been studied in bulk crystals of silicon carbide $6H$-SiC doped with erbium in the process of their growth. The erbium centers of different symmetry in the crystals are revealed by the EPR technique. A number of intense luminescence bands of erbium ions are observed at a wavelength of about 1.54 μm. The luminescence can be excited by the light with quantum energies above and below the band gap of SiC. It is found that the luminescence exhibits unusual temperature behavior: as the temperature increases, the luminescence intensity abruptly rises starting with 77 K, passes through a maximum at ~240 K, and, in the vicinity of ~400 K, decreases down to the values observed at 77 K. The activation energies for the flare-up and quenching of the Er^{3+} luminescence are estimated at $E_A \approx 130$ and ≈ 350 meV, respectively. The mechanisms of the flare-up and quenching of the Er^{3+} luminescence in SiC are discussed. © *2000 MAIK "Nauka/Interperiodica".*

1. INTRODUCTION

In recent years, the search for new semiconducting materials doped with rare-earth elements and their studies have been actively pursued with the aim of creating new optoelectronic devices. Of special interest are the Er^{3+} erbium ions, because the $^4I_{13/2} \longrightarrow {}^4I_{15/2}$ transition observed within the $4f$ shell of these ions at a wavelength of about 1.54 μm corresponds to the minimum absorption of silica-based optical fiber systems. Since the infrared (IR) luminescence in the range of 1.54 μm is due to the transitions within the $4f$ shell, which is efficiently shielded by outer filled shells, the interaction between the erbium ion and the surrounding matrix is weakened, and the luminescence wavelength is virtually independent of the semiconductor material. It is expected that the semiconductor laser diodes and optical amplifiers operating at the $^4I_{13/2} \longrightarrow {}^4I_{15/2}$ transition of the Er^{3+} ions will be less sensitive to temperature variations as compared to the devices based on the band-to-band recombination. There are many works concerned with the investigation into the luminescence properties of rare-earth elements in the A_3B_5 systems and silicon [1–3]. The main impediment to the use of these materials in optoelectronic devices is a rather low luminescence yield at room temperature. The temperature quenching of IR luminescence of erbium decreases with an increase in the energy gap of a semiconductor [4]. In this respect, it is supposed that silicon carbide SiC as a wide-gap semiconductor is a promising material for the excitation of an intense high-temperature luminescence of Er^{3+} ions. On the other hand, it seems likely that silicon carbide can be directly used in silicon

microelectronics. Moreover, at present, semiconductor devices based on SiC are finding expanding applications.

The erbium luminescence in SiC at a wavelength of about 1.54 μm was first observed in ion-implanted layers [5]. The main problem arising in the ion implantation is the radiation damage of semiconductors upon exposure to large doses of accelerated ions penetrating to a rather small depth. In the limiting case, this can lead to the loss of crystallinity (amorphization) of a material. For the SiC-type crystals capable of crystallizing in different polytypes, a change in the polytype is also possible. The electron paramagnetic resonance (EPR) technique is the most informative method for determining the structure of impurity centers in semiconductors. However, the maximum depth of erbium penetration into the SiC ion-implanted layers was very small (~0.3 μm), and the Er^{3+} ions was not revealed by the EPR technique. As a consequence, the structure of erbium centers was not determined. Therefore, it was necessary to devise a method providing the introduction of Er^{3+} ions into the SiC bulk crystals.

The problem of introducing the Er^{3+} ions into the SiC bulk crystals in the course of their growth was solved in [6]. For these crystals, the intense EPR signals of different-type Er^{3+} centers were recorded for the first time [6], and the IR photoluminescence was observed at a wavelength of 1.54 μm [7]. According to the preliminary analysis, the temperature behavior of this luminescence substantially differs from that of the luminescence observed in the SiC ion-implanted layers
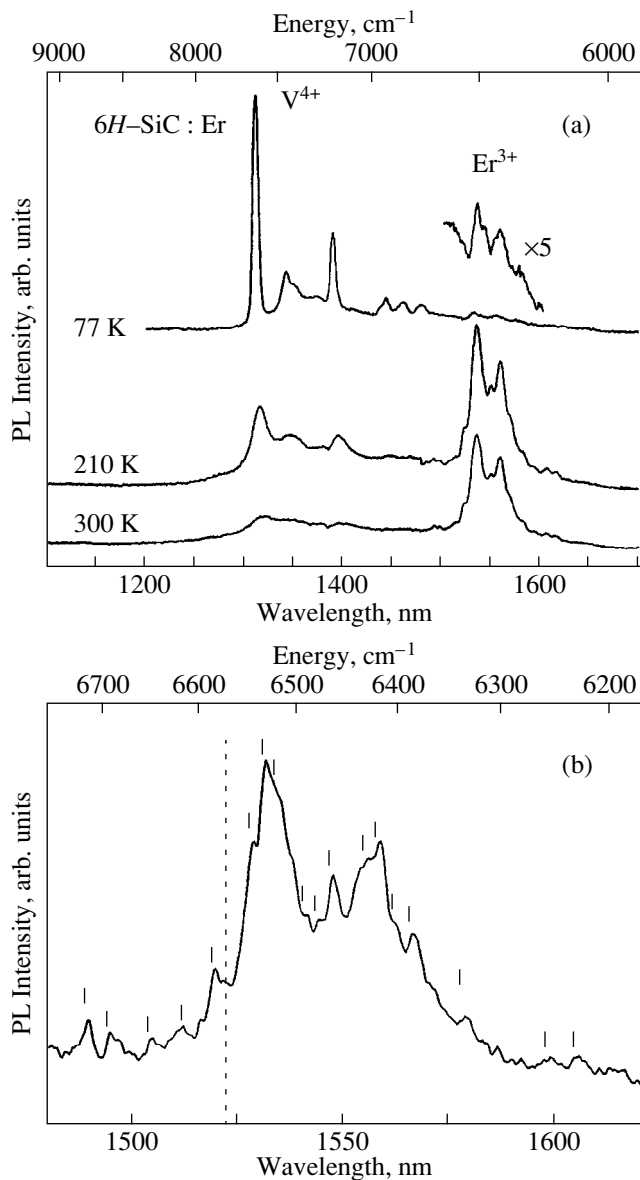
Fig. 1. Photoluminescence spectra of the *6H*-SiC : Er crystal and the EPR signals of the Er^{3+} ions. (a) Spectra in the range 1.1–1.7 μm at temperatures of 77, 210, and 300 K. Photoluminescence was excited by the visible light of a mercury lamp (400–650 nm). (b) The photoluminescence spectrum of Er^{3+} ions on an enlarged scale. Vertical marks indicate selected bands. The vertical dashed line conventionally separates the transitions from the low-lying Stark level of the excited term $^4I_{13/2}$.

[5], which is apparently due to the structural difference of defects in ion-implanted layers and bulk materials.

The present paper reports the results of investigations into the properties of the IR luminescence at a wavelength of 1.54 μm in the SiC bulk crystals whose photoluminescence spectra exhibit the EPR signals of the Er^{3+} centers characterized by the different local symmetry.

2. EXPERIMENTAL TECHNIQUE

The *6H*-SiC bulk crystals were grown by the sublimation sandwich technique [8] under vacuum at temperatures of 1850–1900°C and doped with erbium in the course of their growth. Metallic erbium placed in a tantalum crucible was used as a dopant source. The grown crystals possessed the *n*-type conductivity due to the presence of nitrogen donors. The employment of the tantalum crucible made it possible to reduce the concentration of nitrogen donors down to 10^{16} cm^{-3}. In order to prepare the *p*-type crystals, a number of the *6H*-SiC : Er samples were doped with boron through diffusion at a temperature of 2200°C.

The samples were obtained in the form of plates 3×4 mm in size and about 0.5 mm in thickness with the plane perpendicular to the hexagonal crystal axis *c*. The luminescence was excited by argon (488 and 514 nm) and krypton (647.1 nm) lasers and also by mercury and xenon lamps. Photoluminescence signals were recorded using a Hamamatsu InGaAs *p–i–n* diode (IR range) and a photoelectric multiplier. The luminescence was studied at temperatures in the range from 77 to 400 K.

The EPR spectra were taken on a Jeol production-type spectrometer operating in the *X* band (9.3 GHz) in the temperature range 4–300 K.

3. RESULTS

The luminescence at a wavelength of about 1.54 μm was revealed in the *6H*-SiC : Er crystals, which showed the EPR spectra for several types of Er^{3+} centers with different local symmetry [6, 7]. The EPR signals for at least seven Er^{3+} centers (designated as Ax_1–Ax_7 [6, 7]) with an axial symmetry relative to the hexagonal crystal axis *c* were recorded in these crystals. In addition to the axial centers, the EPR spectra displayed signals of the Er^{3+} ions (denoted as LS_1, LS_2, and LS_3 [6, 7]) characterized by an orthorhombic symmetry. For the centers with the orthorhombic symmetry, the local *z*-axis coincides with one of six directions of the Si–C bonds forming an angle of ~70° with the *c*-axis. For the orthorhombic centers and a number of axial centers, the EPR spectra showed a hyperfine structure owing to the interaction with the ^{167}Er nucleus, which made it possible to directly identify the erbium ions and, furthermore, to establish that the structure of each center involves only one erbium ion.

Figure 1a displays the photoluminescence spectra of the *6H*-SiC : Er crystal in the wavelength range 1.1–1.7 μm at three temperatures (77, 210, and 300 K). It is seen that the photoluminescence spectra exhibit the EPR signals of the Er^{3+} ions. The photoluminescence was excited by the visible light (400–650 nm) of a mercury lamp. The spectrum in the range of 1.54 μm is typical of the $^4I_{13/2} \longrightarrow {}^4I_{15/2}$ transition within the 4*f* shell of the Er^{3+} ions. The photoluminescence spectrum in

the range of 1.54 μm at a temperature of 300 K is depicted on an enlarged scale in Fig. 1b. About 20 photoluminescence bands can be separated in this spectrum, and the most intense bands are located at wavelengths of about 1.53 and 1.56 μm. The erbium photoluminescence can be excited over a wide range of wavelengths from 320 to 600 nm; in this case, no substantial changes in the relative intensities of particular photoluminescence bands of the Er^{3+} ions were observed in the range of 1.54 μm.

In the range 1.3–1.4 μm, three luminescence bands correspond in location to the luminescence bands of the vanadium ions V^{4+} in the 6H-SiC crystal [9]. Vanadium is a typical uncontrollable impurity in silicon carbide.

The main feature of the observed photoluminescence of erbium is the unusual temperature dependence of its intensity. This dependence for the photoluminescence band of erbium at a wavelength of 1.531 μm is depicted by dark circles in Fig. 2a. As the temperature increases beginning with 77 K, the intensity of erbium photoluminescence rapidly increases and reaches a maximum value at approximately 240 K. With a further increase in the temperature, the intensity of erbium photoluminescence decreases and becomes equal to about 50% of the maximum value at a temperature of 300 K. The photoluminescence is reliably recorded up to ~400 K. Figure 2a also demonstrates the temperature dependence of the intensity for the high-energy band of the luminescence of vanadium (open circles). In this case, an increase in the temperature starting with 77 K is accompanied with a drastic decrease in the luminescence intensity. As can be seen from Fig. 2a, an increase in the intensity of the erbium photoluminescence and a decrease in the intensity of the vanadium luminescence are observed in about the same range of temperatures. Moreover, it should be mentioned that the temperature dependence of the intensity of the donor–acceptor photoluminescence observed in the visible range for the 6H-SiC : Er crystals has about the same shape as the corresponding dependence for the IR photoluminescence of vanadium.

The temperature flare-up and the temperature quenching of the photoluminescence of erbium can be described by the known formula

$$I = \frac{I_0}{1 + A \exp\left(-\dfrac{E_A}{kT}\right)}, \qquad (1)$$

where E_A is the activation energy of the process, I_0 is the intensity of luminescence without quenching (at ~240 K), and A is the constant depending on the probability of radiative recombination and the constant in the Boltzmann relation. Formula (1) enables one to determine the activation energies for the flare-up and quenching of the luminescence from the slope of the straight line on the $\ln(I_0/I)$–1/T coordinates. The temperature dependences of the photoluminescence inten-
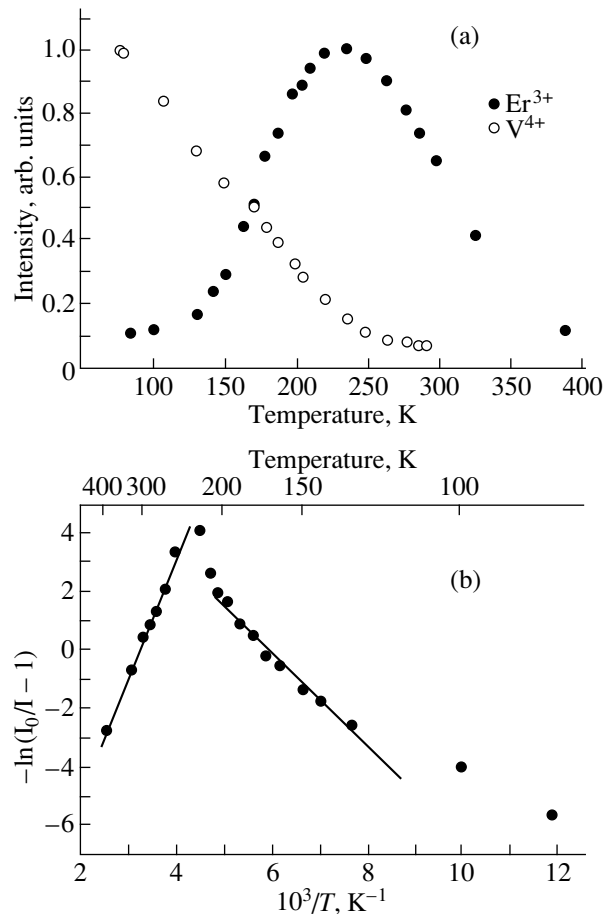

Fig. 2. (a) Temperature dependences of the intensity of photoluminescence for the 1531-nm band of erbium and the high-energy band of vanadium in the 6H-SiC : Er crystals. (b) Dependences shown in Fig. 2a for erbium but constructed on the $\ln(I_0/I - 1)$–1/T coordinates for two temperature ranges corresponding to the flare-up and quenching of the photoluminescence.

sity on these coordinates for two temperature ranges corresponding to the flare-up and quenching of the erbium photoluminescence are displayed in Fig. 2b. The activation energies E_A for the flare-up and quenching of the Er^{3+} luminescence are evaluated to be equal to ≈130 ± 20 and ≈350 ± 20 meV, respectively. The theoretical dependences calculated according to formula (1) with the use of the activation energies given above are depicted by solid lines in Fig. 2b. In the description of the above processes, we proceeded from rough estimates and approximated each process by only one exponent, even though, in principle, it is not improbable that the process is more complex and should be described by the sum of exponents with several activation energies; in the latter case, the activation energies given above correspond to the averaged energies.

Moreover, we investigated the photoluminescence in the 6H-SiC : Er crystals, which were doped with boron through high-temperature diffusion. As a result
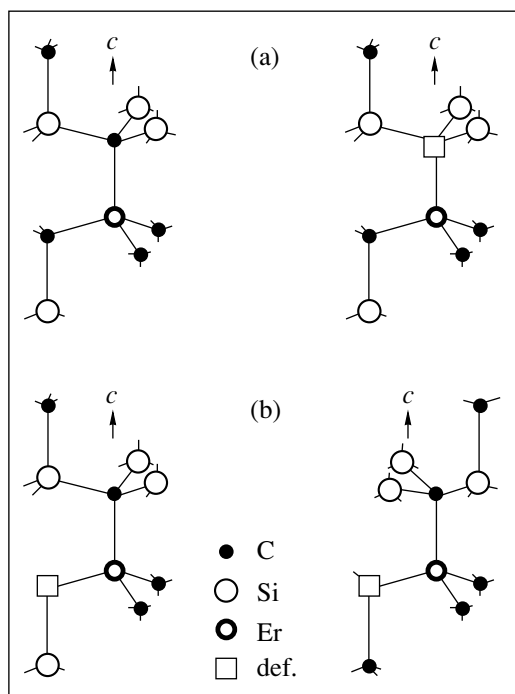
Fig. 3. Possible structures of different Er^{3+} centers according to the EPR data [6, 7]: (a) axial centers (hexagonal site) and (b) orthorhombic centers (hexagonal and quasi-cubic sites).

of this doping, the conductivity of the crystals changed to the *p* type. After the introduction of boron, the intensity of the EPR spectra of Er^{3+} ions became virtually zero, whereas the intensity of the photoluminescence of these ions did not considerably change. Prior to the introduction of boron, the 6*H*-SiC : Er crystals possessed the *n*-type conductivity and their EPR spectra exhibited signals of all the aforementioned erbium centers. The diffusion of boron brought about certain changes in the relative intensities of the photoluminescence of erbium and vanadium: the relative intensity of the erbium luminescence in the *p*-type crystals somewhat decreased. The relative intensities of particular photoluminescence bands of the Er^{3+} ions and the temperature dependences of the photoluminescence intensity for these ions virtually do not change.

4. DISCUSSION

As already mentioned, the IR luminescence of the Er^{3+} ions was observed in the crystals, which, according to the data of our earlier works [6, 7], showed the EPR spectra for several types of Er^{3+} centers characterized by the different symmetry. As uniquely follows from the observation of the hyperfine structure of erbium, the EPR spectra correspond to the single Er^{3+} ions, which are not involved in the impurity clusters (for example, the Er–Er pairs). Reasoning from comparison between the ionic radius of three-valent erbium

and the ionic radii of silicon and carbon, it was concluded that erbium most likely occupies the silicon sites in SiC. Figure 3 demonstrates the models proposed for the erbium centers in 6*H*-SiC on the basis of the EPR data [6]. In the axial centers, erbium replaces silicon and occupies the site in the regular lattice (the hexagonal site in the lattice is shown in Fig. 3a). The differences in the EPR parameters of the three centers are due to the presence of three possible erbium sites in the 6*H*-SiC crystals, namely, the hexagonal and two quasi-cubic sites. The orthorhombic Er^{3+} centers have a more complex structure displayed for the hexagonal and quasi-cubic sites in Fig. 3b. It seems likely that these centers involve another defect in the carbon site near erbium. The presence of three types of these centers is also explained by the hexagonal and two quasi-cubic erbium sites in the lattice. It is quite possible that, in the orthorhombic centers, the Er^{3+} ion forms the complex with one oxygen atom or carbon vacancy in such a way that the line connecting them coincides with one of the Si–C bonds, making an angle of ~70° with the hexagonal axis *c*. A part of the axial centers can also be associated with the complexes whose composition involves the erbium ions; in this case, the defect (for example, the oxygen atom or carbon vacancy) is located so that the line connecting the erbium ion and the defect coincides with the Si–C bond aligned along the *c*-axis (Fig. 3a).

The experimental results obtained in the present work do not permit us to directly assign the photoluminescence bands to the specific (axial or orthorhombic) erbium centers, which manifest themselves in the EPR spectra. It should only be remarked that the photoluminescence was observed solely in the crystals that showed the EPR spectra of the Er^{3+} centers (including the crystals for which the EPR spectra were observed prior to the introduction of boron). The symmetry of all the Er^{3+} centers in the 6*H*-SiC crystal is lower than the cubic symmetry. Therefore, all these centers can contribute to the luminescence (in the octahedral complex, the intracenter luminescence of the Er^{3+} ions cannot be observed, because the *f–f* transitions are parity-forbidden). The ground state $^4I_{15/2}$ in the crystal field of this symmetry is split into the eight doubly degenerate Stark levels (Kramers doublets), and, hence, at least eight luminescence bands should be observed for each erbium center. Taking into account the fact that, according to the EPR data, there are about ten different Er^{3+} centers, a large number of luminescence bands should be observed for the $^4I_{13/2} \longrightarrow {}^4I_{15/2}$ transition in the Er^{3+} ions. Since all the luminescence bands are located in a narrow spectral range, their large number apparently results in considerable widths of the photoluminescence bands (Fig. 1) at temperatures above 77 K and the spectral resolution provided by the instrument employed. For the symmetry lower than the cubic symmetry, the first excited term $^4I_{13/2}$ is split into seven doubly degenerate energy levels. At sufficiently low tem-

peratures (when the thermal energy is less that the splitting of energy levels by the crystal field), only the transitions from the lowest-lying state of the $^4I_{13/2}$ excited term can occur, and eight photoluminescence bands should be observed for each erbium center. The higher-lying states of the $^4I_{13/2}$ term split by the crystal field are not involved in the luminescence process at low temperatures. The higher-lying states of the luminescent levels can be filled with an increase in the sample temperature. The filling of these levels should lead to the appearance of additional photoluminescence bands on the high-energy side of each band observed at low temperatures [10]. A number of these bands can be seen on the high-energy side of the most intense bands corresponding to the transitions in the Er^{3+} ions (Fig. 1b), because a temperature of 77 K is high enough for the Stark levels of the $^4I_{13/2}$ term to be filled. These bands are conventionally separated by the vertical dashed line in Fig. 1b.

Let us now discuss the possible mechanisms of excitation, temperature flare-up, and temperature quenching of the photoluminescence of erbium ions in SiC. The luminescence of erbium (and other rare-earth element) ions can be excited in semiconductors through a number of mechanisms. The simplest mechanism involves the direct optical excitation of the $4f$ shell, followed by the radiative relaxation from the excited state to the ground state. However, the probability of this mechanism is low, and it is of no interest for applications involving the electric excitation of the luminescence. According to our experimental data, the temperature behavior of the erbium photoluminescence virtually does not depend on the excitation quantum energy, so that, apparently, the direct excitation is of little importance in the excitation of the erbium photoluminescence.

Another mechanism explaining the excitation of the luminescence of a rare-earth ion involves the energy transfer from the electron–hole pair (excited, for example, upon interband absorption of the light) to the ion. This mechanism can be efficient when an energy level (or several energy levels), which is related to the rare-earth ion, occurs in the forbidden gap of a semiconductor. In the case when the rare-earth ion gives rise to the energy level in the forbidden gap of the semiconductor, the excitation of carriers from the valence band (conduction band) to this level can produce a bound electron–hole pair or a bound exciton with the subsequent transfer of the recombination energy to the $4f$ shell of the rare-earth ion. The most probable mechanism of this energy transfer is the so-called impurity Auger recombination. The intracenter luminescence corresponds to the transitions between the $4f$ levels lying outside the forbidden gap. The $4f$ electrons are tightly bound to the ion, and their states can be treated as the internal states independent of the band structure of the matrix. In the absence of tight binding, the energy transfer between electronic states of the crystal and

strongly localized states of the $4f$ electrons is determined by the Coulomb interaction. The theoretical treatment of the excitation suggests that the intracenter Auger process provides the energy transfer to the $4f$ electrons through the dipole and exchange interactions. The efficiency of this process drastically increases if the state (related to the rare-earth center) in the forbidden gap allows the localization of energy in the form of bound excitons (or bound electron–hole pairs).

In order to elucidate the nature of these levels, we perform a qualitative analysis of the model according to which a rare-earth ion replaces the silicon atom in the SiC crystal. Let us consider the so-called "vacancy" model, which was elaborated for transition metal ions in semiconductors [11]. According to this model, the elimination of a host crystal atom (for example, a silicon atom in the Si or SiC crystal) from a semiconductor lattice leads to the formation of a vacancy with a certain set of energy levels and wave functions. When an impurity atom occupies this vacancy, the set of energy levels and wave functions, as a rule, changes but not too strongly to lose their identity. The impurity atom gives rise to its intrinsic levels; however, these levels are usually located below the top of the valence band. A similar model for rare-earth elements in the crystals A_3B_5 and silicon was advanced in [12]. As a result of the removal of an atom from the host semiconductor lattice, the vacancy states characterized by the a_1 and t_2 symmetries are formed in the forbidden gap of the crystal. The next stage involves the formation of the substituting rare-earth element center, which can be treated as the interaction between the rare-earth atom and the vacancy. The rare-earth atom shows the $4f^n6s^2$ electronic structure. The ground state of the $4f$ electrons can have three groups of energy levels transformed according to the a_2, t_1, and t_2 irreducible representations of the T_d group, and the $6s$ shell is characterized by the a_1 symmetry. Therefore, the interaction between the $6s$ shell of the rare-earth atom and the a_1 state of the vacancy leads to the formation of the bonding and antibonding states. Note that the lower-lying bounding state is occupied and most likely occurs in the valence band, whereas the higher-lying antibonding state (related to the rare-earth atom) is unoccupied, can lie near the conduction band, and can serve as an electron trap. It is assumed that, for erbium in SiC, this state is almost completely formed by the $6s$ shell of erbium and the $2s$ and $2p$ valence electrons of carbon. For simplicity, let us consider the set of erbium energy levels in cubic SiC. The state of the Er^{3+} ion in SiC corresponds to the A^- state; i.e., it is negatively charged. Hence, it is necessary to consider the negatively charged silicon vacancy with five electrons, whereas six electrons are required for the filling of the t_2 state. Reasoning from the experimentally found charge state of Er^{3+} in SiC, we should assume that one of the $4f$ electrons of erbium transfers to the t_2 level. As a result, we have the completely occupied level, which is located near the bottom
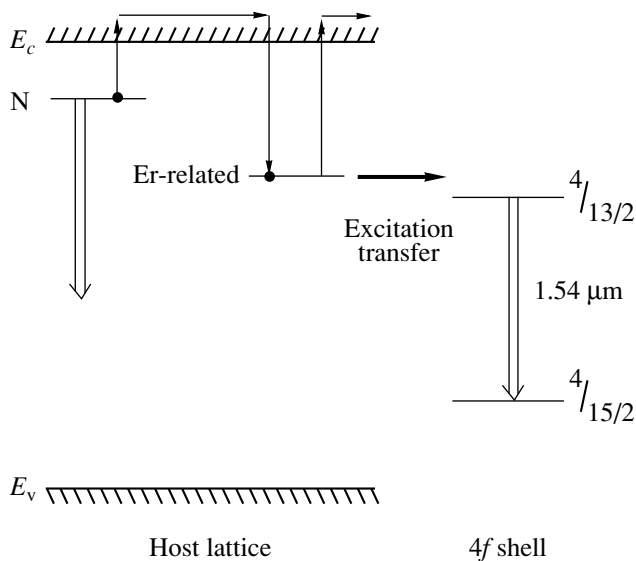
E_c

N

Er-related

Excitation
transfer

$^4I_{13/2}$

1.54 μm

$^4I_{15/2}$

E_v

Host lattice   4*f* shell

Fig. 4. Possible scheme of the energy levels and mechanisms of energy transfer in the 6*H*-SiC : Er crystals. Single arrows show thermal release of electrons from the donor level, retrapping in the erbium-related level, and thermal detrapping of electrons from the erbium level. Double arrows demonstrate radiative transitions, and the heavy arrow indicates the excitation transfer from the erbium-related level to the 4*f* shell of Er^{3+} ion.

of the valence band and, apparently, can serve as a specific hole trap.

The temperature dependence of the photoluminescence intensity in the 6*H*-SiC : Er crystal is characterized by two main ranges (Fig. 2). In the low-temperature range (77–240 K), the efficiency of excitation of the erbium luminescence increases with an increase in the temperature. In the high-temperature range (240–400 K), an increase in the temperature is accompanied by the quenching of the erbium luminescence. Similar dependences were also observed for erbium in silicon but at substantially lower temperatures [13].

The flare-up of the erbium luminescence can be roughly described by formula (1). The experimentally observed activation energy E_A of luminescence in this process is equal to ≈130 ± 20 meV. Since this energy approximately corresponds to the location of donor nitrogen levels with respect to the conduction band, it is reasonable to suppose that an increase in the erbium luminescence is associated with the thermal ionization of nitrogen donors with the subsequent trapping of electrons in the deeper erbium-related levels.

A possible scheme of energy levels in the 6*H*-SiC : Er crystal is depicted in Fig. 4. We believe that, at low temperatures, the carriers are more efficiently trapped in the usual donor levels (most likely, nitrogen donors in our experiments), followed by the recombination. This is corroborated by the intense donor–acceptor luminescence at low temperatures. This luminescence is quenched in about the same temperature range in

which the flare-up of the erbium luminescence takes place. As the temperature increases, the electrons undergo a thermal release from the donor levels and are retrapped in the deeper erbium-related levels with the subsequent transfer of energy to the 4*f* shell of the Er^{3+} ion (see scheme in Fig. 4).

Now, let us dwell briefly on the quenching of the erbium luminescence at high temperatures. First and foremost, we should note that our results obtained for the temperature quenching of photoluminescence in the SiC bulk crystals at high temperatures are in qualitative agreement with the experimental data on the luminescence in ion-implanted layers [5]. This indicates that the processes of photoluminescence quenching occur through similar mechanisms. The quenching of photoluminescence is caused by the fact that the excitation of luminescence is accompanied by competing processes—the release of carriers (most likely, electrons) from the erbium-related levels followed by the nonradiative recombination. The experimentally observed activation energy for the luminescence quenching $E_A \approx$ 350 meV apparently corresponds to the energy of the erbium-related level. The mechanism of the high-temperature quenching is not conclusively elucidated. It can be assumed that, after the ionization of the erbium-related level, the nonradiative recombination at high temperatures occurs at the expense of the Auger recombination with free carriers. As was noted by a number of researchers, this process represents the predominant nonradiative recombination channel for rare-earth impurities in semiconductors. The merits of wide-gap semiconductors are evident owing to the presence of the deeper erbium-related levels and, hence, the higher temperatures of the luminescence quenching. A similar approach can also be applied in describing the quenching of the vanadium luminescence and the donor–acceptor recombination luminescence in the temperature range 77–240 K with the activation energy $E_A \sim$ 130 meV. It should be emphasized that, in silicon crystals, the high quantum yield of luminescence was observed only in the case when the Er^{3+} ion was in a strong negative electric field of ligands (for example, oxygen or fluorine). Moreover, it was noted that this field plays an essential role in an increase in the optical activity of Si : Er [14]. It is reasonable that, in the case of SiC, this role can be played by carbon, because the SiC crystal possesses a considerable degree of ionicity; i.e., in actual fact, we are dealing with the Si^+C^- crystal. Therefore, the advantages of SiC also reside in the fact that the Er^{3+} ion should be surrounded by a negative ligand field in a natural way. This implies that, unlike the silicon crystal, there is no need for an additional doping with oxygen.

ACKNOWLEDGMENTS

REFERENCES

1. V. F. Masterov, Fiz. Tekh. Poluprovodn. (S.-Peterburg) **27**, 1435 (1993) [Semicond. **27**, 791 (1993)] and references cited therein.

2. J. Michel, J. L. Benton, R. F. Ferrante, *et al.*, J. Appl. Phys. **70**, 2672 (1991).

3. A. Polman, J. Appl. Phys. **82**, 1 (1997).

4. W. Jantsch and H. Przybylinska, in *Proceedings of Twenty-Third International Conference on the Physics of Semiconductors, Berlin, Germany, July 21–26, 1996*, Ed. by M. Schefler and R. Zimmermann (World Scientific Publishing Company, Singapore, 1996), p. 3025.

5. W. J. Choyke, R. P. Devaty, L. L. Clemen, *et al.*, Appl. Phys. Lett. **65**, 1668 (1994).

6. P. G. Baranov, I. V. Ilyin, and E. N. Mokhov, Solid State Commun. **103**, 291 (1997); P. G. Baranov, I. V. Il'in, E. N. Mokhov, *et al.*, Fiz. Tverd. Tela (S.-Peterburg) **41**, 865 (1999) [Phys. Solid State **41**, 783 (1999)].

7. P. G. Baranov, I. V. Il'in, E. N. Mokhov, *et al.*, Fiz. Tverd. Tela (S.-Peterburg) **41**, 38 (1999) [Phys. Solid State **41**, 32 (1999)].

8. Yu. A. Vodakov, E. N. Mokhov, M. G. Ramm, *et al.*, Krist. Tech. **5**, 729 (1979).

9. M. Kunzer, H. D. Müller, and U. Kaufmann, Phys. Rev. B **48**, 10846 (1993).

10. W. I. Choyke, P. R. Devaty, M. Yoganathan, G. Pensl, and J. A. Edmond, in *Proceedings of International Conference on Shallow-Level Centers in Semiconductors, Amsterdam, the Netherlands, 17–19 July, 1996*, Ed. by C. A. J. Ammerlaan and B. Pajot (World Scientific Publishing Company, 1997), p. 297.

11. G. D. Watkins, Fiz. Tverd. Tela (S.-Peterburg) **41** (5), 826 (1999) [Phys. Solid State **41** (5), 746 (1999)] and references cited therein.

12. N. P. Il'in and V. F. Masterov, Fiz. Tekh. Poluprovodn. (S.-Peterburg) **29**, 1591 (1995) [Semicond. **29**, 828 (1995)]; N. P. Il'in and V. F. Masterov, Fiz. Tekh. Poluprovodn. (S.-Peterburg) **31**, 1037 (1997) [Semicond. **31**, 886 (1997)].

13. H. Przybylinska, W. Jantsch, Yu. Suprun-Belevitch, *et al.*, Phys. Rev. B **54**, 2532 (1996).

14. L. S. Kimerling, K. D. Kolenbrander, J. Michel, *et al.*, Solid State Phys. **50**, 333 (1996).

Translated by O. Borovik-Romanova

Intracenter Luminescence of Mn²⁺ in Cd₁₋ₓMnₓTe and Cd₁₋ₓ₋ᵧMnₓMgᵧTe under Intense Optical Pumping

V. F. Agekyan, N. N. Vasil'ev, A. Yu. Serov, and N. G. Filosofov

Institute of Physics (Petrodvorets Branch), St. Petersburg State University,
Petrodvorets, 198904 Russia
Received September 7, 1999; in final form, October 28, 1999

Abstract—A comparative analysis of the kinetic properties of intracenter $3d$ luminescence of Mn²⁺ ions in the dilute magnetic superconductors Cd₁₋ₓMnₓTe and Cd₁₋ₓ₋ᵧMnₓMgᵧTe is carried out. The influence of relative concentrations of the cation components on the position of the intracenter luminescence peak indicates that the introduction of magnesium enhances crystal field fluctuations. As a result, the processes facilitating nonlinear quenching of luminescence are suppressed. The kinetics of $3d$-luminescence quenching in Cd₁₋ₓMnₓTe are accelerated considerably upon elevation of optical excitation level due to the evolution of cooperative processes in the system of excited manganese ions. © *2000 MAIK "Nauka/Interperiodica".*

The optical and magnetic properties of semiconducting solid solutions of group II–VI elements with a magnetic component from the iron group and heterostructures on their basis have been studied intensely during the last two decades (see, for example, [1–3]). These materials are dilute magnetic semiconductors (DMS) which attract attention due to their clearly manifested magnetic properties determined by a high concentration of ions with a large magnetic moment of the unfilled $3d$ electron shell. The ion–ion exchange interaction results in a magnetic ordering in pairs and clusters of magnetic ions. The exchange interaction of holes and electrons with magnetic ions leads to the formation of magnetic polarons. The aligning of the magnetic moments of ions in an external field significantly enhances the magnetic field in the bulk of the sample by magnetizing free carriers through the exchange mechanism and giving rise to giant magnetooptical effects.

The most thoroughly studied objects are DMS Cd₁₋ₓMnₓTe and heterostructures CdTe/Cd₁₋ₓMnₓTe. One of the most remarkable properties of DMS is the existence of two mechanisms of excitation and relaxation of the electron system, i.e., the conventional band mechanism and the intracenter one through the energy levels of the $3d$ shell of Mn²⁺. In Cd₁₋ₓMnₓTe, the energy gap at $T = 77$ K is $E_g(x) = (1.59 + 1.55x)$ eV, the excitation threshold for the intracenter transitions being $E_t = 2.15$ eV [the concentration dependence of E_t is weaker than $E_g(x)$]. Thus, $E_g(x) > E_t$ for $x > 0.4$, and the energy states of the $3d$ shell are the lowest-lying excited states. The absorption spectrum for the $3d$ shell is due to transitions from the ground state ⁶$A_1(S)$ to the excited states ⁴$T_1(G)$, ⁴$T_2(G)$, ⁴$A_1(G)$, and ⁴$E(G)$. The broad intracenter luminescence band [transition ⁴$T_1(G)$–⁶$A_1(S)$] has a peak near 2.0 eV, and hence, the Stokes losses are significant. This bright luminescence can also be excited by a nonoptical method through the injection of carriers, which makes the wide-gap Mn-containing crystals of group II–VI elements applicable in electroluminescence devices [4].

The study of the $3d$ luminescence of Cd₁₋ₓMnₓTe and other DMS under a strong optical pumping is important for a comparison with the injection-type saturation of electroluminescence devices. The spectroscopy of intracenter transitions is also of interest in other respects. In structures with quantum wells, where Cd₁₋ₓMnₓTe with $x > 0.4$ is a barrier substance, the barrier-type $3d$-luminescence affects the kinetics of radiative relaxation in the quantum well of CdTe. Transitions in the $3d$ shell are of the intercombination type, and the moment of the Mn²⁺ ion decreases during its excitation from 5/2 to 3/2, suppressing accordingly the internal field and exchange interactions. In turn, this leads to a photo-induced change in magnetic and magnetooptical properties.

Other aspects of spectroscopic studies of intracenter processes include the saturation of absorption and optical bistability in $3d$-absorption bands, which are significant in the case of a strong optical excitation [5], as well as the properties of nanocrystals of group II–VI compounds containing Mn [6].

In recent years, considerable attention was paid to the group belonging to II–VI semiconductors containing light elements and the heterostructures on their basis in connection with the interest in the advance to the short-wavelength spectral range. New multicomponent DMS, like Cd₁₋ₓ₋ᵧMnₓMgᵧTe [7], have also been synthesized to be used in heterostructures with various combinations of magnetic and nonmagnetic quantum wells and barriers [8]. Trication DMS make it possible to control independently the value of E_g, which is a

function of x and y [$E_g(x, y) = (1.59 + 1.55x + 1.80y)$ eV for $Cd_{1-x-y}Mn_xMg_yTe$, and the magnetic properties determined by the value of x. This laid the basis for the development of superlattices in which the potential profile appears only in an external magnetic field and depends on the orientation of spin moments of electrons and holes [9].

Earlier [10], we reported on the concentration and temperature dependences of saturation in intracenter $3d$-luminescence in $Cd_{1-x}Mn_xTe$ with an elevated level of optical pumping. In the present work, we analyzed the effect of pumping level on the kinetics of the $3d$ luminescence in $Cd_{1-x}Mn_xTe$ and its features in the trication DMS $Cd_{1-x-y}Mn_xMg_yTe$.

1. EXPERIMENT

Single crystals of $Cd_{1-x}Mn_xTe$ ($x = 0.4$–0.75) and $Cd_{1-x-y}Mn_xMg_yTe$ ($x = 0.05$–0.55, $y = 0.25$–0.55) were grown according to the Bridgman–Stockbarger technique. The integrated intensity of the 2-eV $3d$-luminescence band was measured on fresh cleaves in the dc mode with a time resolution of 100 ns at $T = 4$ and 77 K. Optical pumping was carried out by the second harmonic of the Nd^{3+} : YAG laser (photon energy, 2.34 eV; pulse duration, 0.15 µs; repetition frequency, 1 kHz; the number of photons per pulse, up to 10^{13}). The excitation energy density I_e at the pulse peak reached 9 kW cm^{-2}. In experiments with a weak pumping up to 50 W cm^{-2}, an Ar^+ laser was used. The value of I_e was measured by electrooptical scanning in a modulator ML-102A. Photoconductivity measurements were made in pulsed electric fields up to 10 kV cm^{-1}.

2. RESULTS

For the sake of comparison with the results of investigation of $Cd_{1-x}Mn_xTe$ [10], we plotted the luminescence intensity I_l as a function of I_e for the DMS $Cd_{1-x-y}Mn_xMg_yTe$. The integral intensity values were measured at the peak of the luminescence pulse over a 2-eV band. Figure 1 shows the results obtained for two samples $Cd_{0.5}Mn_{0.5}Te$ and $Cd_{0.25}Mn_{0.5}Mg_{0.25}Te$ with the same concentration of Mn. It can be seen that the introduction of Mg significantly suppressed the effect of saturation. The variation of the Mn concentration x over a wide range from 0.05 to 0.55 does not affect noticeably the $I_l(I_e)$ dependence. A decrease in the nonlinearity of this dependence for the trication DMS can be due to the enhancement of crystal field fluctuations in the solid solution, which should be expected after the introduction into it of Mg^{2+} whose ionic radius (0.74 Å) is much smaller than the ionic radii of Cd^{2+} (0.99 Å) and Mn^{2+} (0.91 Å). An increase in the spread of the values of local fields surrounding Mn^{2+} ions suppresses the migration of excitation and makes the linear radiative relaxation
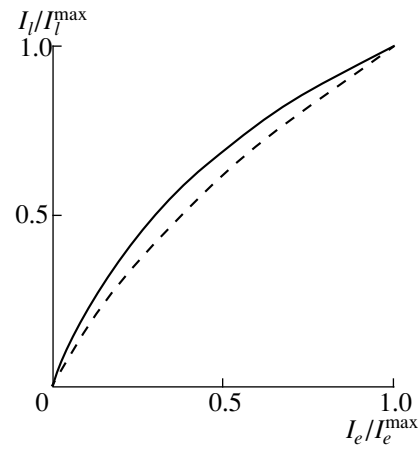
Fig. 1. Peak values of luminescence pulses I_l in the DMS $Cd_{0.5}Mn_{0.5}Te$ (solid curve) and $Cd_{0.25}Mn_{0.5}Mg_{0.25}Te$ (dashed curve) as a function of optical pumping intensity I_e, $I_e^{max} = 2$ kW cm^{-2}, $T = 77$ K.
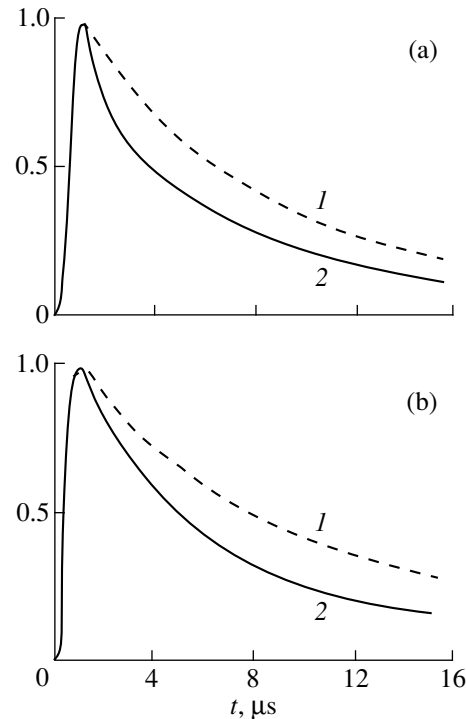
Fig. 2. Kinetics of attenuation of the 2-eV emission band for the minimum and maximum pulsed pumping intensities (1) $I_e^{min} = 0.1$ kW cm^{-2} and (2) $I_e^{max} = 9$ kW cm^{-2} in (a) $Cd_{0.5}Mn_{0.5}Te$ and (b) $Cd_{0.25}Mn_{0.5}Mg_{0.25}Te$ DMS.

in Mn^{2+} (2-eV band) more probable than possible nonlinear processes.

Figure 2 illustrates the kinetics of attenuation of the 2-eV luminescence band for various pulsed pumping levels. An increase in I_e strongly changes the attenua-
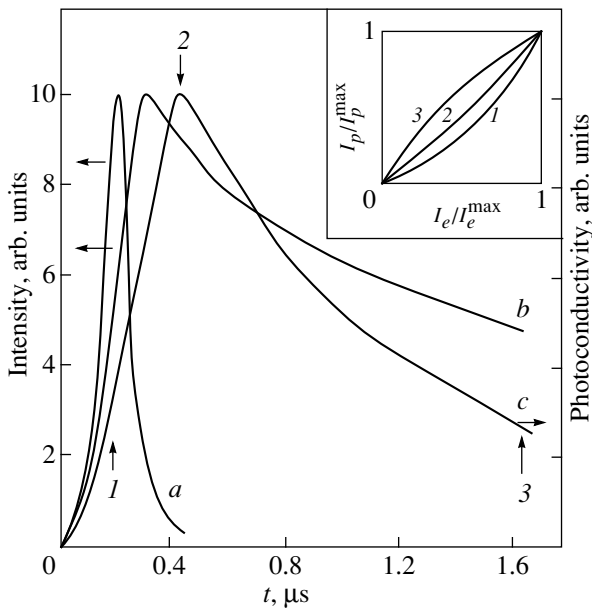
Fig. 3. Pulses of (*a*) laser radiation, (*b*) luminescence, and (*c*) photoconduction in the DMS $Cd_{0.5}Mn_{0.5}Te$, $T = 77$ K (the curves are normalized). The inset shows the photocurrent I_p as a function of I_e for various instants of recording t relative to the photoconduction peak (indicated by arrows). $I_e^{max} = 9$ kW cm^{-2}.
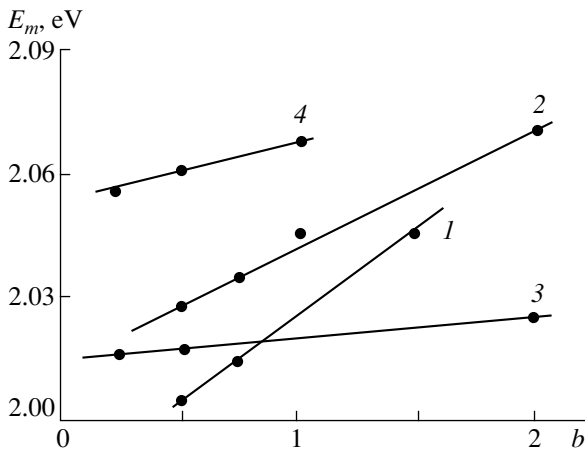
Fig. 4. Effect of relative concentrations of the cation components on the position of the intracenter luminescence peak E_m of the Mn^{2+} ion in the DMS $Cd_{1-x-y}Mn_xMg_yTe$: (*1*) $b = y/(1-x-y)$, $x = 0.375$ (Mg–Cd substitution), (*2*) $b = y/x$, $1-x-y = 0.25$ (Mg–Mn substitution), (*3*) $b = x/(1-x-y)$, $y = 0.25$ (Mn–Cd substitution), and (*4*) $b = x/(1-x-y)$, $y = 0.5$ (Mn–Cd substitution). The lines are drawn for better visualization.

tion rate of intracenter luminescence in $Cd_{0.5}Mn_{0.5}Te$, while the attenuation curve for $Cd_{0.25}Mn_{0.5}Mg_{0.25}Te$ at $I_e = 9$ kW cm^{-2} corresponds to the attenuation curve for $Cd_{0.5}Mn_{0.5}Te$ for smaller values of I_e by an order of

magnitude. This is in accord with the attenuation of luminescence saturation due to the introduction of magnesium into the solid solution.

The obtained results demonstrate the evolution of a certain effective mechanism of nonlinear quenching in $Cd_{1-x}Mn_xTe$ at high levels of I_e, which limits radiative relaxation, and the suppression of this mechanism as a result of introduction of magnesium into the solid solution.

The photocurrent pulse I_p (Fig. 3) was obtained as a result of pumping of the DMS $Cd_{0.5}Mn_{0.5}Te$ with $E_g(0.5) = 2.38$ eV by a light pulse with a photon energy of 2.34 eV; i.e., the interband transition does not take place, and the pumping occurs only to the absorption band of the $3d$ shell of Mn^{2+} ions. The inset in Fig. 3 shows the $I_p(I_e)$ dependences for various instants of recording the photocurrent relative to its maximum value. This dependence is superlinear for the recording at the instant of pumping of the crystal by the laser pulse; i.e., it is typical of the two-photon (two-stage) formation of free carriers as a result of pumping of the $3d$ shell.

The effect of cation substitution on the position of the peak value E_m of the Mn^{2+} intracenter luminescence on the energy scale can serve as an indicator of variation in the crystal field. The measurements made on a batch of $Cd_{1-x-y}Mn_xMg_yTe$ samples with various values of x and y show that the Mn–Cd substitution at a fixed Mg concentration affects the value of E_m only slightly, but an increase in y under the Mg–Cd and Mg–Mn substitutions noticeably shifts the value of E_m to the short-wavelength range (Fig. 4). Thus, the assumption concerning the enhancement of fluctuations of the local field acting on Mn^{2+} ions as a result of the introduction of Mg is confirmed, and this should significantly affect the nonlinear properties of intracenter luminescence in $Cd_{1-x-y}Mn_xMg_yTe$. An increase in the concentration of defects accompanying the complication of the solid solution composition also contributes to the change in the properties of Mn^{2+} intracenter luminescence in the trication DMS. Among other things, the formation of these defects decreases the quantum yield of luminescence as compared to $Cd_{1-x}Mn_xTe$.

3. DISCUSSION

In our previous publication [10], we noted that the nonlinearity of the relation $I_l(I_e)$ is determined to a considerable extent by the transfer of excitation from a Mn^{2+} ion to a similar excited ion. Such a mechanism of cooperative quenching, which is presented schematically in Fig. 5, was used, for example, for crystals activated by rare-earth ions [11]. The population of

excited states of Mn^{2+} is described by the following equations:

$$dn_1/dt = G(t) - w_1 n_1 - 2q_1 n_1^2 + w_{21} n_2,$$

$$dn_2/dt = q_1 n_1^2 - w_{21} n_2 - w_2 n_2, \qquad (1)$$

$$G(t) = \alpha I_e(t)/h\nu,$$

where three of the four parameters w_1, q_1, w_{21}, and w_2 are independent.

The quantum $h\nu = 2.34$ eV transforms the Mn^{2+} ion from state 0 (energy level $^6A_1$) to state 1 (level $^4T_1$). Level 1 is characterized by the concentration n_1, the rate of linear relaxation w_1 to state 0, which has both radiative and nonradiative components, and the cooperative quenching rate $w^+ = 2q_1 n_1$ (q_1 is the coupling constant). The value of w^+ is determined by the probability of the event $(1 + 1) \longrightarrow (0 + 2)$ in which two adjacent Mn^{2+} ions occupying the excited state 1 are transformed into a unexcited ion (state 0) and an ion excited to state 2 (see Fig. 5). The cooperative process is also determined by the efficiency of migration of Frenkel-type excitons over Mn^{2+} ions. In turn, the migration depends on the manganese concentration, temperature, crystal field fluctuations, and the rate of the linear relaxation $1 \longrightarrow 0$, the introduction of magnesium changing the two last parameters. Equation (1) also contains the following quantities: the coefficient of absorption α at the frequency $h\nu$; the pulsed pumping intensity $I_e(t)$; and the concentration n_2 of Mn^{2+} ions in state 2, which is determined by the following components: (1) the cooperative excitation rate w^+, (2) the rate w_{21} of linear relaxation from state 2 to state 1, and (3) the rate w_2 of linear (radiative and nonradiative) relaxation from state 2 to any state except state 1.

Thus, the contribution of the cooperative process to nonlinear quenching is determined by the relation between the rates w_1, w_2, and w_{21}. In the weak pumping approximation disregarding quadratic terms, we have $dn_1/dt = \alpha I_e/h\nu - w_1 n_1$; this relation specifies the linear relaxation rate, which determines the intensity and kinetics of the attenuation of the 2-eV intracenter emission band (transition $1 \longrightarrow 0$). An analysis of the experimental data obtained at $T = 77$ K gives $w_1 = 7 \times 10^4$ s^{-1} for the DMS $Cd_{0.5}Mn_{0.5}Te$ (the attenuation time $\tau_1 = 15$ µs). As expected, the value of w_1 for $Cd_{0.25}Mn_{0.5}Mg_{0.25}Te$ is larger and amounts to 4×10^5 s^{-1}.

The migration of the excitation corresponding to state 1 of the Mn^{2+} ion is enhanced by crystal heating. Numerous experiments indicate a considerable decrease in the difference of configuration coordinates for states 0 and 1 in the temperature range of 80 K and above [12, 13]. Thus, the elevation of temperature not only intensifies the processes involving photons, but also lowers the energy barrier for excitation hopping. The migration acquires more pronounced "resonant"
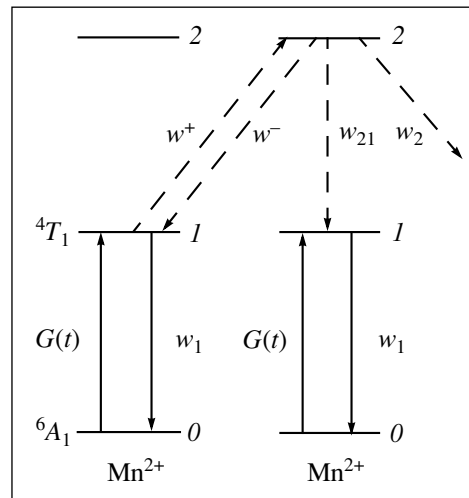
Fig. 5. Three-level diagram of Mn^{2+} ions in the DMS $Cd_{0.5}Mn_{0.5}Te$, illustrating the mechanisms of cooperative excitation and its relaxation (see text for notation).

features, where considerable changes in the ligand coordinates are not required for the excitation of manganese ion. As regards the dynamics of the cooperative process, the $1 \longrightarrow 0$ transition is accompanied at low temperatures by considerable Stokes losses, while the configuration coordinate in the $1 \longrightarrow 2$ transition changes insignificantly. This means that the cooperative process even at low temperatures does not require a considerable vibrational relaxation in the environment of an already excited Mn^{2+} ion (state 1) during the transfer of the second portion of excitation to it.

Linear relaxation from state 2 is described by the rate w_2 and can occur via the following routes: (1) the transfer of excitation from level 2 of a Mn^{2+} ion to band states, followed by the return of excitation from the bottom of the conduction band to level 1 of the Mn^{2+} ion, and (2) radiative or nonradiative $2 \longrightarrow 1$ relaxation within a manganese ion. The probability of self-ionization from state 2 to the band should be considerably higher than the intraionic relaxation probability, since level 2 is in the region of a high density of states of the conduction band. The transfer of an electron to the conduction band results in its rapid relaxation to the bottom of the band, which is accompanied by the emission of optical phonons. This state can be described by the second equation from system (1). After this, either the formation of a Wannier exciton and its radiative recombination at the rate w_2 (interband emission) take place, or the electron returns to the $3d$ levels of manganese at rate w_{21}. The ratio w_2/w_{21} can be estimated by comparing the intensities of interband and intraionic luminescence, whose ratio depends on the mutual positions of the bottom of the conduction band and the excitation threshold for the $3d$ luminescence of Mn^{2+}. The interband exciton luminescence is known to decrease rap-

idly upon an increase in x (starting from $x = 0.4$), and hence, in the $Cd_{0.5}Mn_{0.5}Te$ sample, it is an order of magnitude weaker than the intraionic luminescence of manganese. This mechanism explains the low photosensitivity of CdMnTe and CdMnMgTe crystals. Electrons appear in the conduction band as a result of the cooperative process and leave it for energy levels of manganese upon rapid cooling. Under these conditions, the photocurrent pulse should be proportional to $n_1^2(t)$. The results of processing of the $n_1(t)$ dependence (kinetics of intracenter luminescence) and of the photocurrent pulse are in accord with this dependence.

The proposed model correctly describes the experimentally measured kinetics of 2-eV band attenuation for the pumping levels of $Cd_{0.5}Mn_{0.5}Te$, which are close to the minimum and maximum levels for the following parameters: $w_1 = 7 \times 10^4$ s^{-1} ($\tau = 15$ μs), $q = 4 \times 10^{-13}$ s^{-1} cm^3, $w_{21} = 5 \times 10^4$ s^{-1}, and $w_2 = 2 \times 10^4$ s^{-1}.

For the maximum pumping levels, the rate of the cooperative process is $qn_1^{max} = 4 \times 10^5$ s^{-1}, which is an order of magnitude higher than the linear relaxation rate w_1. The maximum pumping corresponds to the following populations of levels *1* and *2*: $n_1 = 9 \times 10^{17}$ and $n_2 = 2 \times 10^{17}$ cm^{-3}. For moderate pumping levels, the experimental results are in accord with the model only for slightly different values of the parameters, which calls for the refinement of the model.

Another reason behind the nonlinearity of $I_l(I_e)$ can be the two-stage (or two-photon) absorption of the light in an individual Mn^{2+} ion. In this case, the equations determining the kinetics of population of levels *1* and *2* can be written as

$$dn_1/dt = G(t) - w_1 n_1 - \sigma I_e(t) n_1 + w_{21} n_2,$$

$$dn_2/dt = \sigma I_e(t) n_1 - w_{21} n_2 - w_2 n_2,$$

$$G(t) = \alpha I_e/h\nu,$$

where σ is the cross-section of the two-state absorption $0 \longrightarrow 2$ via level *1*. In this case, the process can also be described by four parameters from which three are independent. An analysis of our experimental results proves that such a mechanism cannot satisfy our data on the kinetics of the 2-eV band even at the maximum pumping level. The fundamental difference from the model of cooperative process lies in that the two-photon and two-stage mechanisms are limited in time by the duration of a laser pulse.

Thus, we have analyzed the nonlinearity of intracenter luminescence of Mn^{2+} ions in DMS $Cd_{0.5}Mn_{0.5}Te$, which is associated with cooperative quenching, and estimated the factors suppressing the nonlinearity as a result of introduction of the third cationic component (magnesium) into this DMS.

REFERENCES

1. O. Goede and W. Heimbrodt, Phys. Status Solidi B **146**, 11 (1988).
2. J. K. Furdyna, J. Appl. Phys. **64**, R29 (1988).
3. P. A. Wolff, in *Semiconductors and Semimetals*, Ed. by J. K. Furdyna and J. Kossut (Academic, London, 1988), Vol. 25.
4. A. Fuh, R. P. Gallinger, and O. Caporaletti, Can. J. Phys. **65**, 1060 (1987).
5. K. Dou, S. H. Huang, J. Q. Yu, *et al.*, Solid State Commun. **76**, 1165 (1990).
6. Y. Oka and K. Yanata, J. Lumin. **70**, 21 (1996).
7. V. F. Aguekian, L. K. Gridneva, and A. Yu. Serov, Solid State Commun. **87**, 635 (1993).
8. R. Hellman, A. Euteneuer, E. O. Gobel, *et al.*, J. Cryst. Growth **159**, 976 (1996).
9. M. von Ortenberg, Phys. Rev. Lett. **49**, 1041 (1982).
10. V. F. Agekian, N. N. Vasil'ev, and A. Yu. Serov, Fiz. Tverd. Tela (S.-Peterburg) **41**, 49 (1999) [Phys. Solid State **41**, 41 (1999)].
11. V. V. Ovsyankin and P. P. Feofilov, Opt. Spektrosk. **37**, 262 (1973).
12. J. Watanabe, H. Arai, T. Nouchi, *et al.*, J. Phys. Soc. Jpn. **61**, 2227 (1992).
13. J. E. MacKay, W. M. Becker, J. Spalek, *et al.*, Phys. Rev. B **42**, 1743 (1990).

Translated by N. Wadhwa

EPR Spectra of the Excited Nitrogen State in 6H-SiC

E. N. Kalabukhova*, S. N. Lukin**, and E. N. Mokhov***

* Institute of Semiconductors, National Academy of Sciences of Ukraine,
Kiev, 252028 Ukraine

** Donetsk Physicotechnical Institute, National Academy of Sciences of Ukraine,
Donetsk, 340114 Ukraine

*** Ioffe Physicotechnical Institute, Russian Academy of Sciences,
Politekhnicheskaya ul. 26, St. Petersburg, 194021 Russia

e-mail: katia@phisic.kiev.ua

Received July 9, 1999; in final form, November 12, 1999

Abstract—A study is reported of donor EPR spectra in compensated 6H-SiC crystals with donor concentrations $(N_D - N_A)$ varied from 8×10^{17} to 5×10^{16} cm^{-3}, performed within a temperature interval from 77 to 170 K at a frequency of 37 GHz. A second paramagnetic state of nitrogen in silicon carbide has been found to exist, and it is associated with its excited $1S(E)$ state becoming paramagnetic after thermal ionization of the donor electrons from the $1S(A_1)$ to $1S(E)$ level. The EPR spectrum of nitrogen in the $1S(E)$ state is a single line with an anisotropic width because of the unresolved hyperfine structure. A light-induced charge transfer between the ground, $1S(A_1)$, and excited, $1S(E)$, nitrogen states has been observed. The valley-orbit splitting and the energy required to ionize donor electrons from the $1S(E)$ to higher lying excited states have been determined for the cubic nitrogen sites. The parameters of a structural defect, characteristic of n-type 6H-SiC compensated crystals, have been established. © 2000 MAIK "Nauka/Interperiodica".

Our previous study [1] of the EPR spectra of donors in 6H-SiC with $N_D - N_A$ varied from 2×10^{18} to 1×10^{16} cm^{-3} was performed in a broad temperature range from 4.2 to 160 K at a frequency of 9 GHz, and at $T = 4.2$ K at 140 GHz. The high-temperature EPR spectrum consisted of a single line (I_{Nk}), while the spectrum obtained at a low temperature featured two triplets of hyperfine (HF) EPR lines of nitrogen at two cubic lattice sites (I_{k1}, I_{k2}), which coincide in g factor at 9 GHz, and a single line (I_h) due to nitrogen in the hexagonal position coinciding with the central line of the triplet at the frequency of 9 GHz.

The EPR spectrum of nitrogen measured at $T = 4.2$ K and a nitrogen concentration $(N_D - N_A) \approx 3 \times 10^{17}$ cm^{-3} saturated, which permitted one to detect, by properly increasing the microwave power, a single line I_D, which coincided with the central line of the nitrogen triplet at 9 GHz. It was found to be impossible, however, to isolate the I_D line and to perform studies in an intermediate temperature range because of its overlapping with the higher intensity EPR nitrogen lines. At the same time, when the nitrogen EPR lines begin to weaken in intensity, a single line coinciding with I_D at 9 GHz appears again in the EPR spectrum. This permitted the conclusion that the low-temperature line I_D and the high-temperature one I_{Nk} belong to the same paramagnetic center responsible for the second donor state in silicon carbide.

Because the single EPR line I_{Nk} was observed at higher temperatures than the nitrogen EPR spectrum, it was argued that this line belongs to a donor with a deeper level than that of nitrogen. However, the ionization energy derived from the high-temperature falloff of the I_{Nk} line, 60 meV, which is lower than the nitrogen ionization energy, could not be reconciled with the above conclusion.

To establish the nature of the low-temperature, I_D, and the high-temperature, I_{Nk}, lines in the donor EPR spectrum, a study has been carried out of donor EPR spectra in silicon carbide samples of the 6H polytype, with donor concentrations $N_D - N_A$ varying from 8×10^{17} to 5×10^{16} cm^{-3} and different compensation ratios, within a temperature range of 77 to 170 K and at a frequency of 37 GHz. The use of an EPR radio spectrometer with a higher operating frequency of 37 GHz made it possible to resolve the nitrogen EPR spectra due to the three inequivalent lattice sites, to determine the parameters of the I_D and I_{Nk} single lines, and to establish that the I_D line observed at high power levels and the I_{Nk} line appearing in the EPR spectrum at high temperatures are of a different nature.

1. SAMPLES AND EXPERIMENTAL TECHNIQUE

A study was made on compensated samples of the 6H-SiC polytype grown by the Lely and sublimation-sandwich methods at 1900°C, which had an uncompensated donor concentration $N_D - N_A$ that varied from 8×10^{17} to 5×10^{16} cm^{-3}.
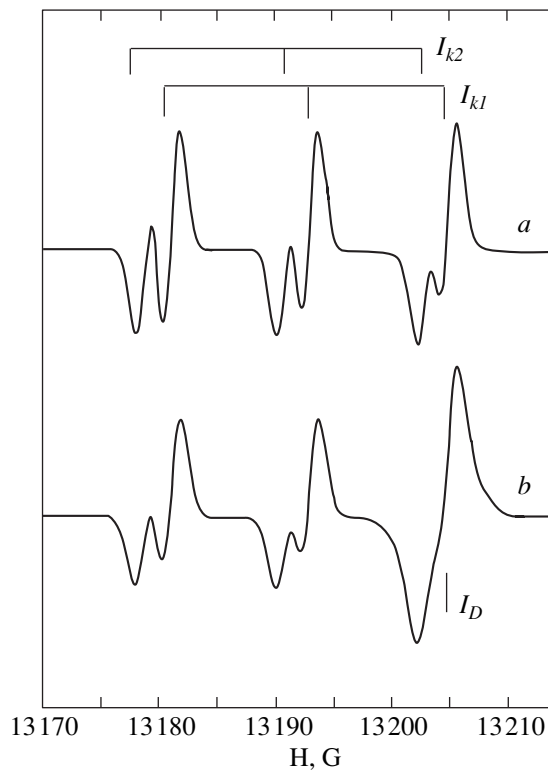
Fig. 1. EPR spectrum of donors in 6*H*-SiC with $(N_D - N_a) \approx$ 4×10^{17} cm^{-3} obtained at two microwave power levels differing by 30 dB, $P_a < P_b$. $\nu = 37$ GHz, $T = 77$ K, **H** ∥ **c**.

The measurements were carried out within a temperature interval of 77 to 170 K on an EPR radiospectrometer with an operating frequency of 37 GHz.

The temperature was controlled by means of a resistive heater mounted on the resonator. The sample temperature, measured with a germanium transducer, was maintained to no less than 0.3 K. The UV light to illuminate a sample was supplied from a DRSh-250 lamp through a UFS-1 color filter. The light was fed into the resonator through a lightguide, with the sample attached to its face end.

EPR spectral parameters of donors in *n*-type 6*H*-SiC

Spectra	$g_{\parallel}$	$g_{\perp}$	$A, \Delta H, G$
I_h	2.0048 ± 0.0002	2.0028 ± 0.0002	$\Delta H_{\parallel} = 2.5$ $\Delta H_{\perp} = 1.8$
I_{k1}	2.0040 ± 0.0002	2.0026 ± 0.0002	11.8
I_{k2}	2.0037 ± 0.0002	2.0030 ± 0.0002	12.0
I_{Nk}	2.0038 ± 0.0002	2.0028 ± 0.0002	$\Delta H_{\parallel} = 6.0$ $\Delta H_{\perp} = 4.5$
I_D	2.0020 ± 0.0002	2.0029 ± 0.0002	$\Delta H_{\parallel} = 4.0$ $\Delta H_{\perp} = 3.0$

2. TEMPERATURE BEHAVIOR OF THE EPR SPECTRA OF DONORS IN 6*H*-SiC

Figure 1 presents an EPR spectrum of donors in 6*H*-SiC obtained at a frequency of 37 GHz at $T = 77$ K using different power levels. At low power levels, the EPR spectrum is actually a sum of two spectra, due to the two nitrogen cubic sites. As the power level increases, an additional single EPR line, I_D, appears, which can be isolated from the 37-GHz nitrogen spectrum and has the parameters listed in the table. As seen from the table, the anisotropy sign of the *g* factor of the additional line ($g_{\perp} > g_{\parallel}$) is opposite to that observed with donor states in silicon carbide, and its width is anisotropic. This gives one grounds to assign the observed line with an unresolved HF structure (HFS) to a structural defect of an acceptor nature.

Figure 2 displays a donor EPR spectrum of 6*H*-SiC measured at 37 GHz within the temperature range from 77 to 140 K. As the temperature increases, the nitrogen EPR line triplets fall in intensity, a process accompanied by a growth of the single line I_{Nk} at the center of the EPR spectrum, with parameters different from those of the I_D (see table), which argues for the I_D and I_{Nk} lines having a different nature.

An analysis of the temperature behavior of the donor EPR spectra carried out at 37 GHz showed that not only the intensity and width of the EPR lines, but also their HF splitting, are sensitive to temperature. As seen from Fig. 3, as the temperature increases, the EPR triplet lines due to the nitrogen cubic positions decrease in intensity and broaden, and their HF splitting decreases. Note that the HFS remains isotropic. This process is accompanied by the appearance of a single broad line I_{Nk}, which grows in intensity and decreases in width. On reaching the maximum intensity and minimum width, the line begins to behave like that of a conventional paramagnetic center, whose signal broadens and drops in amplitude with increasing temperature (see Fig. 2).

A temperature-dependent behavior of the HF splitting of nitrogen EPR lines was observed earlier for nitrogen states with small valley-orbit splittings in 6*H*-SiC [2] and 3*C*-SiC [3]. The HF splitting of the nitrogen triplet was found to decrease at temperatures from 30 to 60 K in 6*H*-SiC for the hexagonal nitrogen, and from 11 to 40 K in 3*C*-SiC; this was accompanied by the formation of a single line in the high-temperature region.

The decrease of the HF splitting was explained as being due to a thermally induced electron transfer from the $1S(A_1)$ to the closest excited $1S(E)$ state separated by the valley-orbit splitting. The temperature dependences of the hyperfine splittings were used to determine the valley-orbit splittings between the $1S(A_1)$ and $1S(E)$ nitrogen states in cubic silicon carbide, and for the hexagonal position of nitrogen in 6*H*-SiC.
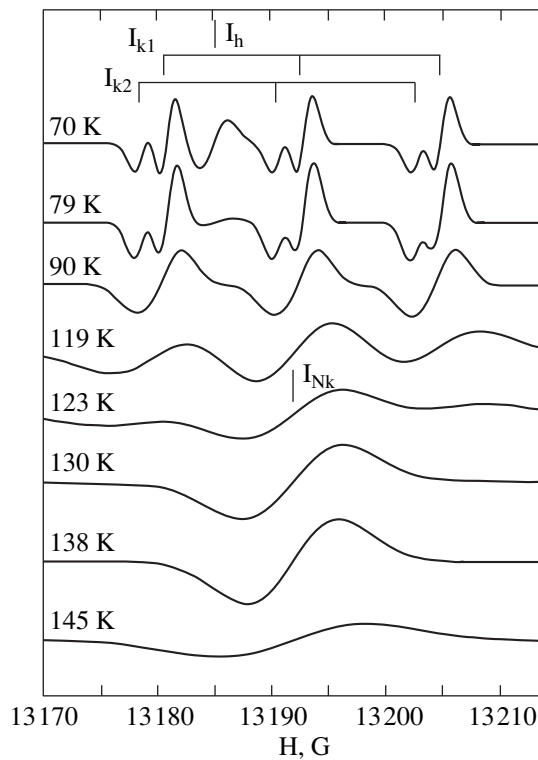
Fig. 3. Temperature behavior of the EPR hyperfine structure of nitrogen occupying cubic lattice sites in *6H*-SiC. $(N_D - N_A) \approx 4 \times 10^{17}$ cm^{-3}, $\nu = 37$ GHz, **H** ∥ **c**.

Fig. 2. Temperature behavior of a donor EPR spectrum in *6H*-SiC. $(N_D - N_A) \approx 4 \times 10^{17}$ cm^{-3}, $\nu = 37$ GHz, **H** ∥ **c**.

These data served as a basis for the assumption [4] that the same pattern should also be observed for the cubic nitrogen positions, but at higher temperatures because of the substantially higher energies of their ionization and the valley-orbit splittings. This assumption has not, however, been supported thus far by the experimental evidence.

The appearance and temperature behavior of the I_{Nk} linewidth, as well as the decrease of the hyperfine splitting of the nitrogen triplets at cubic lattice sites with increasing temperature can be interpreted in the following way.

Within the temperature interval of 100 to 140 K, electrons are thermally transferred from the $1S(A_1)$ singlet to the $1S(E)$ doublet nitrogen state, where the electron has zero probability of being located near the nucleus. This results, on the one hand, in a decrease of the hyperfine splitting of the nitrogen triplets corresponding to the $1S(A_1)$ nitrogen state, and on the other, in the appearance of single lines with an anisotropic width that correspond to nitrogen triplets in the $1S(E)$ state, with the HFS remaining unresolved because of its small magnitude. When operating at 37 GHz, the single lines due to the two cubic nitrogen positions coincide, and the EPR spectrum features one I_{Nk} line with a *g* fac-

tor intermediate between those corresponding to the two cubic nitrogen positions in the $1S(A_1)$ ground state (see table). As the temperature increases, the intensity of the single I_{Nk} line increases, while its width and, hence, the magnitude of the unresolved HFS, reach a minimum value and the largest anisotropy, where the donor electrons already reside in the $1S(E)$ excited state. The table gives the minimum width of the I_{Nk} line for two magnetic-field orientations derived for *6H*-SiC with $(N_D - N_A) \approx 4 \times 10^{17}$ cm^{-3} for a temperature $T = 140$ K. As the temperature is increased still more, the I_{Nk} line broadens and decreases in intensity starting from 140 K, due to the donor electrons being ionized from $1S(E)$ to higher lying excited states or to the conduction band.

It should be pointed out that the temperature intervals where the donor electrons are thermally ionized from the $1S(A_1)$ and $1S(E)$ states will change, depending on the compensation ratio of the crystal under study. For example, as the compensation ratio increases, the electrons will become ionized at progressively higher temperatures [1].

An analysis of the temperature dependences of the nitrogen triplet HF splittings in the $1S(A_1)$ and $1S(E)$ states and of the I_{Nk} linewidth permitted one to obtain a

Fig. 4. Temperature dependence of the hyperfine splitting A of nitrogen at cubic sites of the 6H-SiC lattice. The slope of the curve is fitted by the exp($-E_D$/kT) function with E_D = 10 meV.

Fig. 5. Temperature dependence of the I_{Nk} EPR linewidth in 6H-SiC obtained for **H** ∥ **c**. The three different slopes of the curve are fitted by the exp($-E_D$/kT) function with E_{D1} = 21, E_{D2} = 34, and E_{D3} = 60 meV.

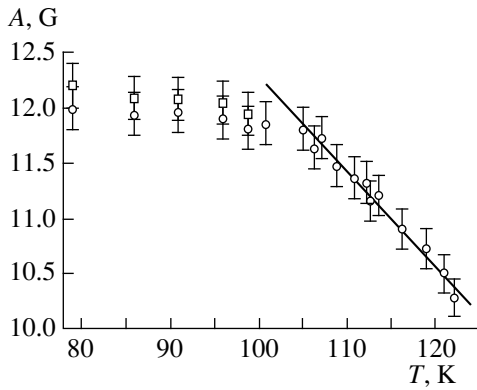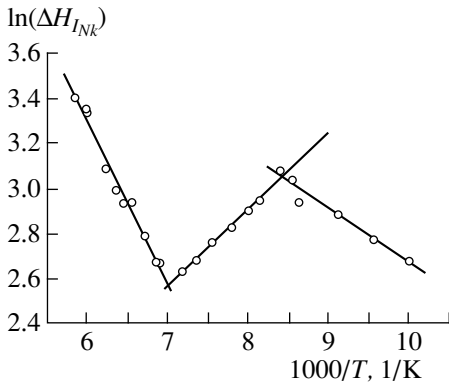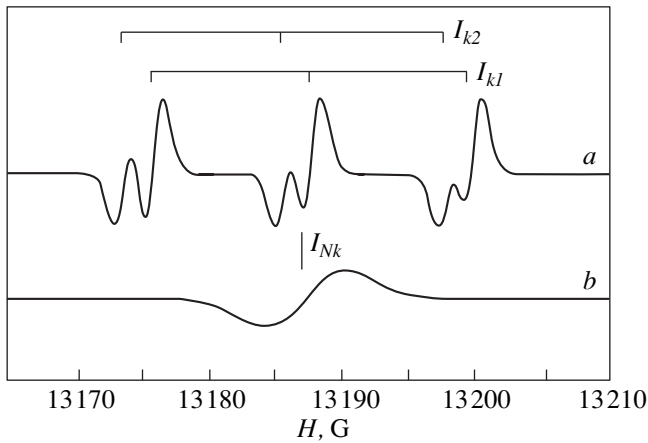**Fig. 6.** EPR spectrum of donors in n-type 6H-SiC crystals obtained at T = 77 K after cooling a sample (*a*) in the dark and (*b*) under UV illumination.

number of energy characteristics of nitrogen donors, in both the ground and excited states.

Figure 4 presents the temperature dependence of the HF splitting of nitrogen occupying cubic lattice sites in the $1S(A_1)$ state measured in the temperature interval from 100 to 120 K. The observed decrease in the hyperfine splitting can be fitted by the following expression

$$A = A_0(1 - e^{-E_D/kT}) \tag{1}$$

with E_D = 10 meV, where A_0 is the hyperfine splitting of the $1S(A_1)$ state, and E_D is the electron ionization energy from the $1S(A_1)$ level.

Presented in Fig. 5 is the temperature dependence of the I_{Nk} linewidth, which can be divided in three sections in the region from 100 to 170 K. Within the 100–120 K interval, the main contribution to this linewidth is due to the broadening of the nitrogen triplet components in the $1S(E)$ state, which becomes manifest in the broadening of the I_{Nk} line, whereas from 120 to 140 K the dominant contribution is due to the decrease of the hyperfine splitting of the nitrogen triplets in the $1S(E)$ state, which will bring about a narrowing of the I_{Nk} line. The two different slopes of the temperature dependence of the I_{Nk} linewidth can be fitted by an exp($-E_D$/kT) function with E_D = 34 and 21 meV, respectively, which add up to give the electron ionization energy from the $1S(A_1)$ to the $1S(E)$ state separated by the valley-orbit splitting: $E_{v.-0.}$ = 34 + 21 = 55 meV. This value agrees with the magnitude of the valley-orbit splitting derived [1] from the temperature dependences of the EPR line intensities of nitrogen occupying the cubic lattice sites.

The ionization energy obtained from the slope of the temperature dependence of the I_{Nk} linewidth in the 140–170 K interval, where electrons are ionized from the $1S(E)$ state to higher lying excited $2p$ states or to the conduction band, is 60 meV; this value agrees with the ionization energies derived [1] from the high-temperature slope of the temperature dependence of the I_{Nk} line intensity in samples with different compensation ratios.

Thus, computer analysis of the temperature behavior of EPR spectra of nitrogen in cubic lattice positions and of the corresponding energy characteristics permits the conclusion that, above 120 K, donor electrons are ionized from the $1S(A_1)$ to the $1S(E)$ level, and that the observed high-temperature I_{Nk} EPR line is due to nitrogen atoms in the $1S(E)$ excited state.

3. LIGHT-INDUCED CHARGE TRANSFER IN NITROGEN PARAMAGNETIC STATES

The above conclusions can be complemented by a study of the charge transfer in nitrogen paramagnetic states in n-type 6H-SiC samples illuminated by light in the intrinsic absorption region. Figure 6 presents a donor EPR spectrum obtained on n-type 6H-SiC samples at T = 77 K after their cooling in the dark and under

UV illumination. One readily sees that crystals cooled in the dark at $T = 77$ K produce two triplets of hyperfine EPR lines due to nitrogen occupying the two cubic positions. When the samples are cooled under UV illumination, the EPR spectrum obtained at $T = 77$ K represents a single line with a g factor coinciding with that of the I_{Nk} line. After switching off the UV light at the low temperature, the EPR spectrum does not change, and only after the crystal has started to warm up in the absence of UV illumination does the single line begin to drop in intensity, with its width varying by the law characteristic of the I_{Nk} line (see Fig. 5), to finally disappear above 200 K.

The observed behavior of the donor EPR spectra obtained on crystals cooled under UV illumination indicates that the nonequilibrium electrons created by as interband light at a high temperature ($T > 140$ K) are trapped by ionized nitrogen atoms to the $1S(E)$ level, to remain frozen-out on this level as the temperature is lowered still more. This can be explained by the fact that, for $T > 120$ K, donor electrons are already capable of localizing at the $1S(E)$ level, whereas their trapping by the $1S(A_1)$ level can only occur at a lower temperature. The trapping of electrons to the $1S(A_1)$ level can only take place when they are thermally ionized from the $1S(E)$ level, but not when the temperature is lowered.

Thus UV illumination can be used for optical recharging of the ground and excited nitrogen states.

REFERENCES

1. E. N. Kalabukhova, S. N. Lukin, Yu. S. Gromovoǐ, *et al.*, Fiz. Tverd. Tela **40**, 1824 (1998) [Phys. Solid State **40**, 1653 (1998)].
2. J.-M. Spaeth, S. Greulich-Weber, M. März, *et al.*, Mater. Science Forum **239**–**241**, 149 (1997).
3. W. E. Carlos, in *Properties of Silicon Carbide*, Ed. by G. L. Harris (IEE, 1995), p. 42.
4. S. Greulich-Weber, Phys. Status Solidi A **162**, 95 (1997).

Translated by G. Skrebtsov

Electron–Electron Correlations in the Model
of Mobile Electron Shells

Yu. D. Panov and A. S. Moskvin

Ural State University, pr. Lenina 51, Yekaterinburg, 620083 Russia

e-mail: yuri.panov@usu.ru

Received July 8, 1999

Abstract—A variational method is proposed that allows one to take into account electron–electron correlations. The variational parameters are the coordinates of the center of a one-particle atomic orbital. The displacement introduced in this way also makes it possible to graphically describe the redistribution of the electron density under an anisotropic external action in terms of a finite initial basis. A generalization of the traditional MO-LCAO scheme in the framework of the model proposed is considered. © *2000 MAIK "Nauka/Interperiodica".*

The description of electron correlations is a fundamental problem in the theory of atoms, molecules, and solids. This problem is especially important for systems with a high density of excited states, in which even a small perturbation may lead to a radical rearrangement of the energy spectrum, as well as to a modification of the ground state, in particular, to the formation of a strongly correlated state. In such a situation, a satisfactory description of the ground state of the system in terms of the initial unperturbed basis requires a large number of functions, and hence is difficult to be implemented in practice and not very informative. This also applies to atomic systems for which a description of some specific correlation effects in the Hartree–Fock approximation requires a large number of configurations. A version of the variational method for the search of the energy and the wave function of the ground state of the system may serve as an alternative approach in this case.

In this paper, we consider a direct variational procedure in which the variational parameters are the coordinates of the center of a one-particle atomic orbital as one such version for a many-electron atom or a cluster. The displacement introduced in this way provides a visual interpretation of the change in the electron density distribution, which allows one to use symmetry arguments for constructing a trial wave function. In the traditional MO-LCAO scheme with a limited set of one-particle functions, displaced electron shells make it possible to take into account additional multipole–multipole interactions and to obtain new states with unique properties.

By way of an example demonstrating the potentialities of the model, we consider, in the first part of this work, a two-electron configuration located in a central Coulomb field and constructed from *s*-type one-particle functions displaced from the center of the field. In order to illustrate physically simple features of the model

with the help of specific analytic calculations, avoiding the use of a large number of variational parameters, we choose the simplest form of the radial dependence of the one-particle function (6) with a single variable parameter Z playing the role of the effective charge. An analysis of the energy functional leads to the conditions in which the energy minimum corresponds to an electron configuration with nonzero displacements. In a certain situation, the minimum energy corresponds to several different directions of displacement. In this case, in analogy with the description of the collective motion of nucleons in nuclei [1] and the effects of nonadiabaticity in molecular spectroscopy [2], correlated physical states are introduced in the form of a superposition of displaced biorbitals degenerate in energy. Such states can make a correlated contribution to the orbital current. In the last section, a generalization of the traditional MO-LCAO scheme in the model of mobile electron shells is considered.

1. GENERAL ANALYSIS
OF A TWO-ELECTRON CONFIGURATION

Let us consider the problem of two electrons in a given atomic potential, i.e., the simplest situation in which electron–electron correlations appear. The orbital part of the singlet two-electron wave function formed from displaced one-particle orbitals can be written as

$$\Psi(\mathbf{r}_1, \mathbf{r}_2; \boldsymbol{\alpha}, \boldsymbol{\beta})$$
$$= \eta^{-1}[\psi(\mathbf{r}_1 - \boldsymbol{\alpha})\psi(\mathbf{r}_2 - \boldsymbol{\beta}) + \psi(\mathbf{r}_1 - \boldsymbol{\beta})\psi(\mathbf{r}_2 - \boldsymbol{\alpha})], \quad (1)$$

where $\boldsymbol{\alpha}$ and $\boldsymbol{\beta}$ are the displacement vectors of one-particle orbitals (Fig. 1), and η is the normalization factor. Henceforth, we shall consider only real one-particle functions of the *s*-type. In this case, we have

$$\eta^2 = 2(1 + S^2(\boldsymbol{\alpha}, \boldsymbol{\beta})), \quad (2)$$

where $S(\boldsymbol{\alpha}, \boldsymbol{\beta})$ is the overlap integral for one-particle orbitals. The Hamiltonian of the problem, written in atomic units ($\varepsilon_0 = me^4/\hbar^2 = e^2/a_0$, $a_0 = \hbar^2/me^2$), has the form

$$\hat{H} = -\frac{\Delta_1}{2} - \frac{\Delta_2}{2} - \frac{Z_0}{r_1} - \frac{Z_0}{r_2} + \frac{1}{|\mathbf{r}_1 - \mathbf{r}_2|}. \qquad (3)$$

The variational procedure is carried out for the total energy functional of the system

$$E\{\Psi\} \equiv \langle \Psi|\hat{H}|\Psi\rangle = E(\boldsymbol{\alpha}, \boldsymbol{\beta}). \qquad (4)$$

Taking into account expression (1), we obtain

$$E(\boldsymbol{\alpha}, \boldsymbol{\beta}) = \frac{1}{1 + S^2(\boldsymbol{\alpha}, \boldsymbol{\beta})}[2t(\boldsymbol{\alpha}, \boldsymbol{\alpha}) \\ - Z_0(u(\boldsymbol{\alpha}, \boldsymbol{\alpha}) + u(\boldsymbol{\beta}, \boldsymbol{\beta})) + 2S(\boldsymbol{\alpha}, \boldsymbol{\beta})t(\boldsymbol{\alpha}, \boldsymbol{\beta}) \\ - 2Z_0 S(\boldsymbol{\alpha}, \boldsymbol{\beta})u(\boldsymbol{\alpha}, \boldsymbol{\beta}) + c(\boldsymbol{\alpha}, \boldsymbol{\beta}) + a(\boldsymbol{\alpha}, \boldsymbol{\beta})], \qquad (5)$$

where the following matrix elements have been introduced: $t(\boldsymbol{\alpha}, \boldsymbol{\alpha})$ for the kinetic energy of an electron between the functions of the same center, $u(\boldsymbol{\alpha}, \boldsymbol{\alpha})$ for the interaction of an electron with the central atomic field between the functions of the same center, $t(\boldsymbol{\alpha}, \boldsymbol{\beta})$ for the kinetic energy of an electron between the functions of different centers, $u(\boldsymbol{\alpha}, \boldsymbol{\beta})$ for the interaction of an electron with the central field between the functions of different centers, and $c(\boldsymbol{\alpha}, \boldsymbol{\beta})$ and $a(\boldsymbol{\alpha}, \boldsymbol{\beta})$ are the direct and exchange components of the electron–electron interaction, respectively. The expression for $t(\boldsymbol{\alpha}, \boldsymbol{\alpha})$ is a one-center integral, whereas $S(\boldsymbol{\alpha}, \boldsymbol{\beta})$, $u(\boldsymbol{\alpha}, \boldsymbol{\alpha})$, $t(\boldsymbol{\alpha}, \boldsymbol{\beta})$, $c(\boldsymbol{\alpha}, \boldsymbol{\beta})$, and $a(\boldsymbol{\alpha}, \boldsymbol{\beta})$ are two-center integrals and $u(\boldsymbol{\alpha}, \boldsymbol{\beta})$ is a three-center integral.

In the subsequent analysis, for one-particle orbitals we shall take the Slater functions characterized by the index k and the effective charge Z:

$$\psi(\mathbf{r}) = N_{Z,k} r^k e^{-Zr}, \qquad (6)$$

where the normalization factor has the form

$$N_{Z,k} = \frac{(2Z)^{k+3/2}}{\sqrt{4\pi(2k+2)!}}. \qquad (7)$$

The expressions for matrix elements are given in Table 1.

Reasoning only from expression (5) and the form of the matrix elements, we can formulate some statements concerning the extreme values of the vectors $\boldsymbol{\alpha}$ and $\boldsymbol{\beta}$. Introducing the vectors

$$\mathbf{q}_+ = \frac{1}{2}(\boldsymbol{\alpha} + \boldsymbol{\beta}), \quad \mathbf{q}_- = \frac{1}{2}(\boldsymbol{\alpha} - \boldsymbol{\beta}) \qquad (8)$$
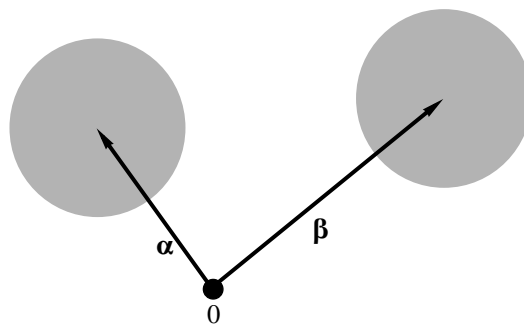

Fig. 1. Displacement vectors $\boldsymbol{\alpha}$ and $\boldsymbol{\beta}$ that characterize the position of the centers of one-particle orbitals relative to the atomic center.

and using a coordinate system with the center at $\mathbf{q}_+ = 0$, we note that $\mathbf{q}_-$ appears only in the expressions for $u(\boldsymbol{\alpha}, \boldsymbol{\alpha}) + u(\boldsymbol{\beta}, \boldsymbol{\beta})$ and $u(\boldsymbol{\alpha}, \boldsymbol{\beta})$:

$$u(\boldsymbol{\alpha}, \boldsymbol{\alpha}) + u(\boldsymbol{\beta}, \boldsymbol{\beta}) \\ = \int \frac{d\mathbf{r}}{|\mathbf{r} - \mathbf{q}_+|}(\psi^2(\mathbf{r} - \mathbf{q}_-) + \psi^2(\mathbf{r} + \mathbf{q}_-)), \qquad (9)$$

$$u(\boldsymbol{\alpha}, \boldsymbol{\beta}) = \int \frac{d\mathbf{r}}{|\mathbf{r} - \mathbf{q}_+|}\psi(\mathbf{r} - \mathbf{q}_-)\psi(\mathbf{r} + \mathbf{q}_-).$$

These expressions are invariant to inversion in the space of displacement vectors, and hence $\mathbf{q}_+ = 0$ is a singular point in the space of the vectors $\mathbf{q}_+$. If the one-particle function ψ is of the s-type, the surfaces $E\{\Psi\} = $ const in the space of the vectors $\mathbf{q}_+$ are spheres, and the point $\mathbf{q}_+ = 0$ is either a minimum or a maximum. In the general case of an arbitrary angular dependence of the one-particle function ψ, the point $\mathbf{q}_+ = 0$ can also be a saddle point.

It is clear from physical considerations why we single out the point $\mathbf{q}_+ = 0$: if $\boldsymbol{\alpha} = -\boldsymbol{\beta}$, such a configuration can minimize the electron–electron repulsion for the given interaction with the central field. This is confirmed by the results of numerical minimization of the energy functional for the $1s^2$ configuration ($k = 0$) presented in Tables 2 and 3. Thus, we can restrict our consideration to the function

$$\Psi(\mathbf{r}_1, \mathbf{r}_2; \mathbf{q}) \\ = \eta^{-1}[\psi(\mathbf{r}_1 - \mathbf{q})\psi(\mathbf{r}_2 + \mathbf{q}) + \psi(\mathbf{r}_1 + \mathbf{q})\psi(\mathbf{r}_2 - \mathbf{q})], \qquad (10)$$

which reduces the number of variational parameters considerably. For the functions (6), the total energy functional depends only on $q = |\mathbf{q}|$ and not on the direction of $\mathbf{q}$.

The parameter Z played the role of a free parameter in the above calculations. This parameter is responsible for the additional mechanism of the electron density redistribution, along with displacements of electron shells. In the case of an isolated atom, Z can also be naturally regarded as a variational parameter since, in this

Table 1. Explicit form of calculated matrix elements involving displaced orbitals

	Definition	Matrix elements for one-particle states $\psi_k(\mathbf{r}) = N_{z,k} r^k e^{-Zr}$, where $N_{Z,k} = \dfrac{(2Z)^{k+3/2}}{\sqrt{4\pi(2k+2)!}}$
$t(\boldsymbol{\alpha}, \boldsymbol{\alpha})$	$\int d\mathbf{r}\, \psi_k(\mathbf{r})\left(-\dfrac{\Delta}{2}\right)\psi_k(\mathbf{r})$	$\dfrac{Z^2}{2(2k+1)}$
$u(\boldsymbol{\alpha}, \boldsymbol{\alpha})$	$\int \dfrac{d\mathbf{r}}{r}\psi_k^2(r-\boldsymbol{\alpha})$	$Z\left[\dfrac{1}{\tilde{a}} - \dfrac{e^{-2\tilde{a}}\tilde{a}^{2k+1}}{\tilde{a}}\displaystyle\sum_{l=0}\left(1-\dfrac{l}{2k+2}\right)\dfrac{(2\tilde{a})^l}{l!}\right]$, where $\tilde{\alpha} = Z\alpha$
$S(\boldsymbol{\alpha}, \boldsymbol{\beta})$	$\int d\mathbf{r}\, \psi_k(r-\boldsymbol{\alpha})\psi_k(r-\boldsymbol{\beta})$	$\dfrac{e^{-\rho}}{(2k+2)!}\displaystyle\sum_{s=0}^{2k+2} C_s^{(k,k)}\rho^s$, where $\rho = Z|\boldsymbol{\alpha}-\boldsymbol{\beta}|$, $A_j^{(n,n')} = \displaystyle\sum_{l=\max\{0,2j-n-1\}}^{\min\{2j,n'+1\}}(-1)^l\dbinom{n+1}{2j-1}\dbinom{n'+1}{l}$, $\dbinom{a}{b} = \dfrac{a!}{b!(a-b)!};\; C_s^{(n,n')} = \displaystyle\sum_{j=0}^{\left[\frac{s}{2}\right]}\dfrac{A_j^{(n,n')}}{2j+1}\dfrac{(n+n'+2-2j)!}{(s-2j)!}$ are the expansion coefficients $\dfrac{2^{n+n'+3}}{4\pi}\int|\mathbf{x}-\boldsymbol{\alpha}|^n e^{-|\mathbf{x}-\boldsymbol{\alpha}|}|\mathbf{x}-\boldsymbol{\beta}|^{n'}e^{-|\mathbf{x}-\boldsymbol{\beta}|}d\mathbf{x} = e^{-\rho}\displaystyle\sum_{s=0}^{n+n'+2}\rho^s C_s^{(n,n')}$
$t(\boldsymbol{\alpha}, \boldsymbol{\beta})$	$\int d\mathbf{r}\, \psi_k(r-\boldsymbol{\alpha})\left(-\dfrac{\Delta}{2}\right)\psi_k(r-\boldsymbol{\beta})$	$-Z^2\dfrac{e^{-\rho}}{2(2k+2)!}\left[\displaystyle\sum_{s=0}^{2k+2}\rho^s C_s^{(k,k)} - 4(k+1)\displaystyle\sum_{s=0}^{2k+1}\rho^s C_s^{(k,k-1)} + 4k(k+1)\displaystyle\sum_{s=0}^{2k}\rho^s C_s^{(k,k-2)}\right]$
$c(\boldsymbol{\alpha}, \boldsymbol{\beta})$	$\int \dfrac{d\mathbf{r}_1 d\mathbf{r}_2}{|\mathbf{r}_1 - \mathbf{r}_2|}\psi_k^2(\mathbf{r}_1-\boldsymbol{\alpha})\psi_k^2(\mathbf{r}_2-\boldsymbol{\beta})$	$Z\left[\dfrac{1}{\rho} - \dfrac{e^{-2\rho}}{(2k+2)\rho}\displaystyle\sum_{l=0}^{2k+1}\rho^l\dfrac{2^l(2k+2-1)}{l!} - \dfrac{e^{-2\rho}}{2^{2k+2}(k+1)(2k+2)!}\displaystyle\sum_{l=0}^{4k+2}\rho^l G_l^{(k)}\right]$, where $G_l^{(k)} = 2^l\displaystyle\sum_{j=\max\{0,l-2k-1\}}^{2k+1}\dfrac{(2k+2-j)}{2^j j!}C_l^{(2k,j-1)}$

Table 1. (Contd.)

Definition	Matrix elements for one-particle states $\psi_k(\mathbf{r}) = N_{z,k} r^k e^{-Zr}$, where $N_{Z,k} = \dfrac{(2Z)^{k+3/2}}{\sqrt{4\pi(2k+2)!}}$
$a(\boldsymbol{\alpha}, \boldsymbol{\beta})$ $\displaystyle\int \frac{d\mathbf{r}_1 d\mathbf{r}_2}{\|\mathbf{r}_1 - \mathbf{r}_2\|} \psi_k(\mathbf{r}_1 - \boldsymbol{\alpha})\psi_k(\mathbf{r}_2 - \boldsymbol{\beta})$ $\times \psi_k(\mathbf{r}_1 - \boldsymbol{\beta})\psi_k(\mathbf{r}_2 - \boldsymbol{\alpha})$	$\displaystyle Z\frac{\rho^{4k+5}}{[(2k+2)!]^2}\sum_{s=0}^{k+1}(4s+1)\sum_{n=0}^{2k+2}\rho^n F_{s,n}^{(k+1)}(\rho)\{e^{-\rho}\Sigma_{s,0}^{(k+1)}(\rho) - \Sigma_{s,n}^{(k+1)}(2\rho)\}$,

where $\displaystyle F_{s,n}^{(m)}(\rho) = \frac{1}{n!}\sum_{j=\frac{n+1}{2}}^{m} B_j^{(m,s)}\frac{(2j)!}{\rho^{2j+1}}$; $\displaystyle B_j^{(m)} = \sum_{r=\max\{0,j-s\}}^{\min\{j,m-s\}} a_r^{(m,s)} b_{j-r}^{(s)}$; $\displaystyle \Sigma_{s,n}^{(m)}(x) = \tilde{\Sigma}_{s,n}^{(m)}(x) - \frac{e^{-x}}{x^{n+2}}\tilde{\tilde{\Sigma}}_{s,n}^{(m)}(x,1)$;

$$\tilde{\tilde{\Sigma}}_{s,n}^{(m)}(x,\xi) = \sum_{i=0}^{m-1}\frac{(2i+n+1)!}{x^{2i}}\tilde{D}_i^{(m,s)}\sum_{t=0}^{2i+n+1}\frac{(x\xi)^t}{t!};$$

$$\tilde{\Sigma}_{s,n}^{(m)}(x) = \frac{e^{-x}}{2x}\sum_{i=0}^{m-s} a_i^{(m,s)}\sum_{l=0}^{2s+2i+n}\frac{\sigma_{2i+n,l}^{(s)}(1)}{x^l}$$

$$\times\left[\ln 2\gamma x - S_{0,l} - (-1)^{l+n}e^{2x}Ei(-2x) + (-1)^{l+n}\sum_{h=0}^{l-1}\frac{(2x)^h}{h!}S_{h,l}\right];$$

$$\tilde{D}_i^{(m,s)} = \sum_{l=\max\{0,i-s+1\}}^{\min\{i,m-s\}} a_l^{(m,s)} D_{i-l}^{(s)}; \quad a_l^{(m,s)} = (-1)^{m-1}\binom{m}{l}\frac{2^{2s+2}(2m-2l)!(m-l+s+1)!}{(m-l-s)!(2m-2l+2s+2)!};$$

$$\sigma_{t,l}^{(s)}(\xi) = \sum_{r=\max\left\{0,\frac{l-t+1}{2}\right\}}^{s} b_r^{(s)}\frac{(2r+t)!}{(2r+t-l)!}\xi^{2r+t}; \quad S_{h,l} = \sum_{t=h+1}^{l}\frac{1}{t}; \quad \gamma = 1.78107; \quad Ei(-x) = -\int_x^\infty\frac{e^{-t}}{t}dt;$$

coefficients $b_l^{(s)}$ and $D_l^{(s)}$ define the Legendre polynomials $P_{2s}(x)$:

$$P_{2s}(x) = \sum_{l=0}^{s} b_l^{(s)} x^{2l}, \quad b_l^{(s)} = \frac{(-1)^{s-l}}{2^{2s}}\frac{(2s+2l)!}{(s-l)!(s+l)!(2l)!} \quad \text{and the second-order Legendre functions } Q_{2s}(x):$$

$$Q_{2s}(x) = \frac{1}{2}\ln\frac{x+1}{x-1}P_{2s}(x) - \sum_{l=0}^{s-1} D_l^{(s)} x^{2l+1}; \quad D_l^{(s)} = \frac{(-1)^l}{(2l+1)!}\sum_{t=l}^{s-1}\frac{(-1)^t(4t+3)(2t+2l+2)!}{2^{2t+1}(2s-2t-1)(s+t+1)(t-l)!(t+l+1)!}$$

Table 1. (Contd.)

	Definition	Matrix elements for one-particle states $\psi_k(\mathbf{r}) = N_{z,k} r^k e^{-Zr}$, where $N_{Z,k} = \dfrac{(2Z)^{k+3/2}}{\sqrt{4\pi(2k+2)!}}$
$u(\boldsymbol{\alpha}, \boldsymbol{\beta})$	$\displaystyle\int\frac{dr}{r}\,\psi_k(\mathbf{r}-\boldsymbol{\alpha})\psi_k(\mathbf{r}-\boldsymbol{\beta})$	$\displaystyle Z\frac{\rho^{2k+2}}{(2k+2)!}\sum_{s=0}^{k+1}(4s+1)P_{2s}(\eta)\Bigg\{Q_{2s}(\eta)\sum_{n=0}^{2k+2}[e^{-\rho}\rho^n - e^{-\rho\xi}(\rho\xi)^n]F_{s,n}^{(k+1)}(\rho) - P_{2s}(\xi)\frac{e^{-\rho\xi}}{\rho^2}\widetilde{\Sigma}_{s,0}^{(k+1)}(x,\xi) + \frac{P_{2s}(\xi)}{2}^{k+1-s}\sum_{i=0}^{}a_i^{(k+1,s)}$

$$\times\left[\frac{e^{-\rho\xi}}{\rho}\ln\frac{\xi_+}{\xi_-}\sum_{l=0}^{2s+2i}\frac{\sigma_{2(i,l)}^{(s)}(\xi)}{(\rho\xi)^l} + \sum_{l=0}^{2s+2i}\frac{\sigma_{2(i,l)}^{(s)}}{2^{l+1}}\left((-1)^{l+1}e^{\rho}Ei(-\rho\xi_+) + e^{-\rho}Ei(-\rho\xi_-) - e^{-\rho\xi}\sum_{h=0}^{l-1}\frac{\rho^h}{h!}S_{h,l}((-1)^{l+1}\xi_+^h + \xi_i^h)\right)\right]\Bigg\},$$

where $\displaystyle\xi = \frac{\alpha+\beta}{|\boldsymbol{\alpha}-\boldsymbol{\beta}|}$, $\eta = \frac{\alpha-\beta}{|\boldsymbol{\alpha}-\boldsymbol{\beta}|}$, $\xi_\pm = \xi\pm1$

case, the atomic potential is the only factor forming the electron density profile:

$$E\{\Psi\} = E(q, Z) \equiv (\boldsymbol{\alpha} = \mathbf{q}, \boldsymbol{\beta} = -\mathbf{q}; Z). \qquad (11)$$

It should be noted, however, that a correlated state of the type of displaced electron shells can be formed with a high probability in a crystal from the given set of functions with a definite value of Z (e.g., with that minimizing the energy of an isolated atom) to minimize a given crystal potential characterized by a parameter Z_0. It is also obvious that the variation of the parameter Z leads only to a certain isotropic variation of the electron density. Consequently, in the case of an anisotropic perturbation, it is impossible to describe the rearrangement of the electron density just by the variation of the effective charge. On the other hand, this problem can in principle be solved easily by using the displacement $\mathbf{q}$ without resorting to a large number of configurations.

2. EXPANSION OF TOTAL ENERGY FUNCTIONAL

The function (10) possesses the following property: its expansion in powers of q near $q = 0$ contains no linear term. Indeed, since

$$\left.\frac{\partial\psi(\mathbf{r} - \mathbf{q})}{\partial q}\right|_{q=0} = -\left.\frac{\partial\psi(\mathbf{r} + \mathbf{q})}{\partial q}\right|_{q=0}, \qquad (12)$$

the first derivative of the function (10) vanishes at $q = 0$. Consequently, the functional $E(q, Z)$ defined on the functions (10) has an extremum at $q = 0$, whose type is determined by the sign of the quadratic term $E^{(2)}$ in the expansion of $E(q)$ in powers of q:

$$E(q) \approx E^{(0)} + E^{(2)}q^2. \qquad (13)$$

For the functions (6), the total energy functional is independent on the direction of $\mathbf{q}$, and hence we can assume that displacements occur along the z-axis. The expansion of function (6) in powers of q has the form

$$\psi(\mathbf{r} - \mathbf{q}) \approx a(\mathbf{r}) - b(\mathbf{r})q - \frac{1}{2}c(\mathbf{r})q^2, \qquad (14)$$

where

$$a(\mathbf{r}) = \psi(\mathbf{r} - \mathbf{q})|_{q=0} = N_{Z,k}r^k e^{-Zr}, \qquad (15)$$

$$b(\mathbf{r}) = \left.\frac{\partial\psi(\mathbf{r} - \mathbf{q})}{\partial z}\right|_{q=0} \qquad (16)$$
$$= N_{Z,k}(kr^{k-1} - Zr^k)e^{-Zr}\cos\theta,$$

$$c(\mathbf{r}) = \left.\frac{\partial^2\psi(\mathbf{r} - \mathbf{q})}{\partial z^2}\right|_{q=0} = N_{Z,k}[kr^{k-2} - Zr^{k-1} \qquad (17)$$
$$+ (k(k-2)r^{k-2} - Z(2k-1)r^{k-1} + Z^2r^k)\cos^2\theta]e^{-Zr},$$

Table 2. Results of minimization of the energy functional $E(\alpha, \beta)$ for $Z = Z_0$

Z	α	β	φ	$E(\alpha, \beta)$
1.5	0.078	0.078	3.1415	–1.3140
1.6	0.068	0.068	3.1415	–1.5614
1.7	0.059	0.059	3.1415	–1.8287
1.8	0.051	0.051	3.1415	–2.116
1.9	0.046	0.046	3.1415	–2.4236
2.0	0.043	0.043	3.1415	–2.7510
2.1	0.041	0.041	3.1415	–3.0984
2.2	0.038	0.038	3.1415	–3.4658
2.3	0.036	0.036	3.1415	–3.8533
2.4	0.034	0.034	3.1415	–4.2608
2.5	0.033	0.033	3.1415	–4.6882

Note: $\alpha = |\boldsymbol{\alpha}|$, $\beta = |\boldsymbol{\beta}|$, and φ is the angle between the vectors $\boldsymbol{\alpha}$ and $\boldsymbol{\beta}$.

Table 3. Results of the minimization of the energy functional $E(\alpha, \beta)$ for Z and $Z_0 = 2.0$

Z	α	β	φ	$E(\alpha, \beta)$
1.5	0.0	0.0	–	–2.8125
1.6	0.0	0.0	–	–2.8400
1.7	0.0	0.0	–	–2.8475
1.8	0.0	0.0	–	–2.8350
1.9	0.011	0.011	3.1415	–2.8026
2.0	0.043	0.043	3.1415	–2.7510
2.1	0.065	0.065	3.1415	–2.6809
2.2	0.084	0.084	3.1415	–2.5931
2.3	0.102	0.102	3.1415	–2.4877
2.4	0.118	0.118	3.1415	–2.3650
2.5	0.132	0.132	3.1415	–2.2253

Note: $\alpha = |\boldsymbol{\alpha}|$, $\beta = |\boldsymbol{\beta}|$, and φ is the angle between the vectors $\boldsymbol{\alpha}$ and $\boldsymbol{\beta}$.

the angle θ being measured from the z-axis. Table 4 contains the expansion in powers of q of various matrix elements, as well as the quantities $E^{(0)}$ and $E^{(2)}$ to within quadratic terms.

The expression for $E^{(2)}$ allows us to formulate a criterion for a nonzero displacement of the electron shell for the case when the one-particle state is chosen in the form of an $1s$-function ($k = 0$). The displacement differs from zero if $Z > Z_0 - 3/16$; otherwise, the displacements of the electron shell from the atomic center are equal to zero. This agrees with the numerical results presented in Table 3.

Thus, for hydrogen-like $1s$-functions (for $Z = Z_0$), the electron configuration with $q = 0$ gives an energy gain as compared to the initial undisplaced configuration. When Z is assumed to be a variable parameter,

Table 4. Expansion of various matrix elements and of the energy functional $E(Z, q)$ in powers of displacements of the electron shells to within quadratic terms

General formula	Explicit form of the expansion accurate to q^2
$S(\mathbf{q}, -\mathbf{q}) \approx 1 - q^2 2\int d\mathbf{r}\, b^2$	$1 - q^2 \dfrac{2Z^2}{3(2k+1)}$
$t(\mathbf{q}, \mathbf{q}) = -\dfrac{1}{2}\int d\mathbf{r}\, a\Delta a$	$\dfrac{Z^2}{2(2k+1)}$
$u(\mathbf{q}, \mathbf{q}) \approx \int \dfrac{d\mathbf{r}}{r} a^2 + q^2 \int \dfrac{d\mathbf{r}}{r}(b^2 + ac)$	$Z - q^2 \dfrac{2Z^3}{3}, \; k = 0$ $\dfrac{Z}{k+1}, \; k \neq 0$
$t(\mathbf{q}, -\mathbf{q}) \approx -\dfrac{1}{2}\left[\int d\mathbf{r}\, a\Delta a + q^2 \int d\mathbf{r}\, c\Delta a\right]$	$\dfrac{Z^2}{2} - q^2 \dfrac{5Z^4}{3}, \; k = 0$ $\dfrac{Z^2}{2(2k+1)} - q^2 \dfrac{Z^4}{4k^2 - 1}, \; k \neq 0$
$u(\mathbf{q}, -\mathbf{q}) \approx \int \dfrac{d\mathbf{r}}{r} a^2 + q^2 \int \dfrac{d\mathbf{r}}{r}(-b^2 + ac)$	$Z - q^2 \dfrac{4Z^3}{3}, \; k = 0$ $\dfrac{Z}{k+1} - q^2 \dfrac{2Z^3}{3(2k+1)(k+1)}, \; k \neq 0$
$c(\mathbf{q}, -\mathbf{q}) \approx \int \dfrac{d\mathbf{r}_1 d\mathbf{r}_2}{r_{12}} a_1^2 a_2^2 + q^2 2\int \dfrac{d\mathbf{r}_1 d\mathbf{r}_2}{r_{12}}$ $\times (-2a_1 b_1 a_2 b_2 + a_1^2 b_2^2 + a_1^2 a_2 c_2)$	$Z\left(\dfrac{1}{k+1} - \dfrac{(4k+3)!}{2^{4k+2}[(2k+2)!]^2}\right) - q^2 Z^3 \dfrac{(4k+2)!}{3 \times 2^{4k-1}[(2k+2)!]^2}$
$a(\mathbf{q}, -\mathbf{q}) \approx \int \dfrac{d\mathbf{r}_1 d\mathbf{r}_2}{r_{12}} a_1^2 a_2^2 + q^2 2\int \dfrac{d\mathbf{r}_1 d\mathbf{r}_2}{r_{12}}(-a_1^2 b_2^2 + a_1^2 a_2 c_2)$	$Z\left(\dfrac{1}{k+1} - \dfrac{(4k+3)!}{2^{4k+2}[(2k+2)!]^2}\right) + q^2 Z^3$ $\times\left(-\dfrac{4}{3(2k+1)(k+1)} + \dfrac{(4k+2)!}{3 \times 2^{4k-1}[(2k+2)!]^2}\right)$
$E^{(0)} = -\int d\mathbf{r}\, a\Delta a - 2Z_0 \int \dfrac{d\mathbf{r}}{r} a^2 + \int \dfrac{d\mathbf{r}_1 d\mathbf{r}_2}{r_{12}} a_1^2 a_2^2$	$Z^2 - 2Z_0 Z + \dfrac{5}{8}Z, \; k = 0$ $\dfrac{Z^2}{2k+1} - \dfrac{2ZZ_0}{k+1} + Z\left(\dfrac{1}{k+1} - \dfrac{(4k+3)!}{2^{4k+2}[(2k+2)!]^2}\right), \; k \neq 0$
$E^{(2)} = -\int d\mathbf{r}\, c\Delta a - \int d\mathbf{r}\, a\Delta a \int d\mathbf{r}\, b^2 - 2Z_0$ $\times\left(\int \dfrac{d\mathbf{r}}{r} ac + \int \dfrac{d\mathbf{r}}{r} a^2 \int d\mathbf{r}\, b^2\right) + 2\int \dfrac{d\mathbf{r}_1 d\mathbf{r}_2}{r_{12}}$ $\times [a_1^2 a_2 c_2 - a_1 b_1 a_2 b_2 + a_1^2 a_2^2 \int d\mathbf{r}\, b^2]$	$-\dfrac{4Z^3}{3}\left(Z - Z_0 + \dfrac{3}{16}\right), \; k = 0$ $-Z^4 \dfrac{4(k+1)}{3(4k^2-1)} - Z^3 \dfrac{(4k+3)!}{3 \times 2^{4k+1}(2k+1)[(2k+2)!]^2}, \; k \neq 0$

Note: Here $\mathbf{r}_{12} = |\mathbf{r}_1 - \mathbf{r}_2|$, and the subscript i on the functions a, b, and c indicates the dependence on $\mathbf{r}_i$.

the minimum of the functional $E(Z, q)$ for $k = 0$ is attained at the point $q_{min} = 0$ and $Z_{min} = Z_0 - 5/16$, which agrees with the well-known result obtained by the direct variational method in the theory of a helium atom [3].

The expression for $E^{(2)}$ also implies that, for any Z_0 and Z, the total energy functional on the functions (10) with one-particle ns-states (6) with $k = 0$ has a minimum for $\mathbf{q} \neq 0$; that is, the displacement of electron shells is always nonzero for states of the form indicated above.

The expression for $E^{(0)}$ allows us to determine the effective charge Z minimizing the total energy of the ns^2-configuration for $q = 0$:

$$Z_{min} = Z_0 \frac{2k+1}{k+1}$$

$$-\left(\frac{2k+1}{2k+2} - \frac{(2k+1)(4k+3)!}{2^{4k+3}[(2k+2)!]^2}\right), \quad k \neq 0. \tag{18}$$

This expression tends to $Z_{min}^{\infty} = 2Z_0 - 1$ as $k \longrightarrow \infty$.

The results presented in Table 4 clarify the reason behind the different behavior of the electron shells with $k = 0$ and $k \neq 0$ as they are displaced from the atomic center. A one-particle function with $k \neq 0$ basically differs from that with $k = 0$ in that the former vanishes at the point $r = 0$ (Fig. 2). The interaction energy of the electrons with the central field is the most sensitive in this respect. Owing to this energy and to the fact that the wave function with $k = 0$ is nonzero at $r = 0$, the total energy of the system sharply increases as the electron shell is displaced from the atomic center. In contrast, the vanishing of the wave function with $k \neq 0$ at $r = 0$ leads to a considerably weaker dependence of the interaction energy with the atomic center on the electron displacement, which is manifested in the vanishing of the quadratic term in the expansion of $u(\mathbf{q}, -\mathbf{q})$. The case of $k = 0$ is also not covered by the expressions with $k \neq 0$ for the integral $t(\mathbf{q}, -\mathbf{q})$ describing the relative motion of electron shells. The integrals associated only with the overlapping of electron shells ($S(\mathbf{q}, -\mathbf{q})$, $c(\mathbf{q}, -\mathbf{q})$, and $a(\mathbf{q}, -\mathbf{q})$) are described by a universal formula applicable to both cases of $k = 0$ and $k \neq 0$. Summarizing what has been said above, we can state that, for $k \neq 0$, the gain in the electron–electron interaction energy upon a displacement of electron shells is not compensated by the loss in the energy of interaction with the atomic center, as in the case $k = 0$, where the electron density is nonzero at the center.

It is intuitively clear that the emergence of a nonzero electron density at the center of the potential must also give a gain in energy. This allows us to indicate the most favorable directions in the displacement of the electron shells in the case of an anisotropic wave function with zero at $r = 0$: for example, this must be the z axis for the p_z orbital and x and y directions for the $d_{x^2-y^2}$ orbital. Since the gains in the energy of interac-
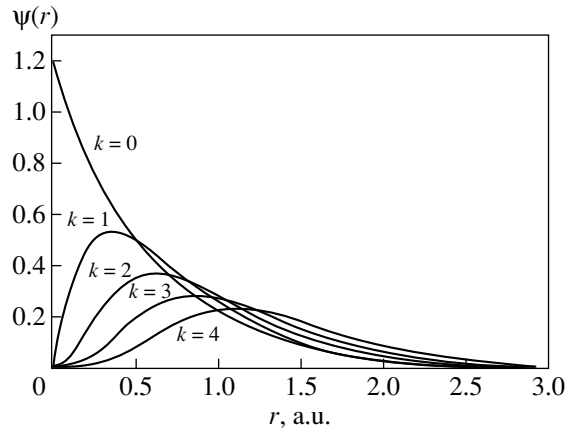

Fig. 2. Slater orbitals $\psi(r)$ (expression (6)) for several first integer values of k; $Z = Z_{min}^{(k)}$ (Table 5).

tion between electrons and with the atomic center are added in this case, this may lead to rather deep minima on the energy surface $E(q, Z)$, located at considerable distances from the point $q = 0$. This is confirmed by the results of numerical minimization of the total energy functional presented in [4] for the np^2 configuration.

3. THE FORM OF THE TOTAL ENERGY FUNCTIONAL $E(q, Z)$

The general expressions of matrix elements for an electron configuration with $\boldsymbol{\alpha} = \mathbf{q}$ and $\boldsymbol{\beta} = -\mathbf{q}$ can be obtained from the formulas given in Table 1, if we consider that $\rho = 2Zq$ and $\tilde{\alpha} = Zq$. In the expression for $u(\boldsymbol{\alpha}, \boldsymbol{\beta})$, we must go to the limit $\xi \longrightarrow 0$ and $\eta \longrightarrow 0$. In terms of the variable $\rho = 2Zq$, this expression assumes the form

$$u(\mathbf{q}, -\mathbf{q}) = Z\frac{\rho^{2k+2}}{(2k+2)!} \sum_{s=0}^{2k+2} (4s+1)b_0^{(s)}\Sigma_{s,0}^{(k+1)}(\rho). \tag{19}$$

For $k = 0$, the expressions for the matrix elements coincide with the well-known results for the helium atom and the hydrogen molecule [5, 6].

The results of minimization of the functional $E(q, Z)$ for several first integer values of k ($k = 0,\ldots, 4$) are given in Table 5. The behavior of the total energy func-

Table 5. Results of minimization of the energy functional $E_k(Z, q)$

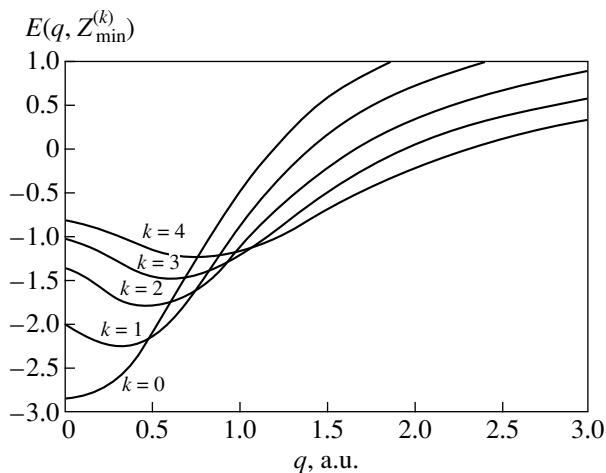| k	E_{min}	q_{min}	Z_{min}	$E_{min}(q = 0) - E_{min}$	$Z_{min}(q = 0) - Z_{min}$
0	−2.84766	0.0	1.6875	0	0
1	−2.22965	0.3437	2.7110	0.2205	−0.2559
2	−1.79140	0.5061	3.2084	0.3463	−0.5204
3	−1.48131	0.6385	3.4999	0.3638	−0.7030
4	−1.25036	0.7644	3.6778	0.3424	−0.8192

Fig. 3. Plots of the total energy functional $E(q, Z)$ for $Z = Z_{\min}^{(k)}$ (Table 5).
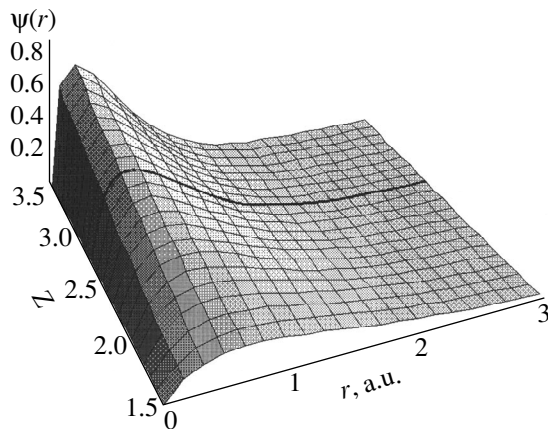

Fig. 4. Variation of the shape of the one-particle function $\psi(r)$ for $k = 1$ with parameter Z. The bold curve on the surface corresponds to the radial profile of the one-particle function for $Z = Z_{\min}^{(1)}$.
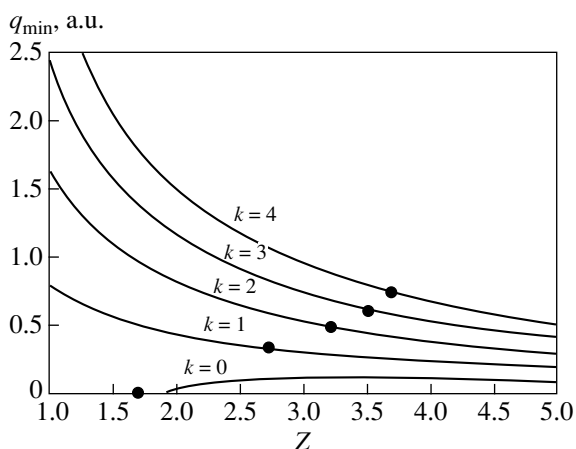

Fig. 5. Dependence of the displacement q of an electron shell minimizing the total energy on the preset parameter Z. Points correspond to the minimum values of the total energy for a given k.

tional as a function of q for $Z = Z_{\min}^{k}$ is illustrated in Fig. 3.

For $k \neq 0$, a displacement of the atomic shells takes place. The decrease in energy relative to the minimum possible value in the absence of displacements of the electron shells and the displacement itself are quite significant (0.22–0.36 a.u. for energy and 0.34–0.76 a.u. for $q_{\min}$. The dependence of the parameters corresponding to the global minimum of the total energy functional, i.e., $q_{\min}$ and $Z_{\min}$, on the number k is fully explained by the form of the electron density distribution for functions with various values of k. It can be seen from Fig. 2 that, as the number k increases, the one-particle functions (10) become more delocalized and the value of the electron density in the neighborhood of $r = 0$ increases. The gain in the system energy can be due to a decrease in the intensity of the electron–electron interaction (decrease of the positive contribution from $t(\mathbf{q}, -\mathbf{q})$, $c(\mathbf{q}, -\mathbf{q})$, and $a(\mathbf{q}, -\mathbf{q})$) and due to an increase in the electron interaction with the atomic center (an increase in the magnitude of the negative contribution from $u(q, q)$ and $u(q, -q)$). The increase in $q_{\min}$ with the number k is associated with the delocalization of $\psi_k(r)$ upon an increase in k; a smaller overlapping and, accordingly, a weaker interaction between the electrons are observed for larger values of q. Another mechanism ensuring the decrease in overlapping is associated with an increase in the parameter Z, which corresponds to a stronger localization of $\psi(r)$. Figure 4 shows the variation of the wave function upon an increase in the parameter Z on the example of the function $\psi(r)$ with $k = 1$. With increasing Z, the magnitude of the negative contribution to the total energy from the interaction with the atomic center also increases; however, the positive contributions, including the kinetic energy, increase as well, resulting in the attainment of a certain compromising value. Consequently, the increase in this parameter with k is also associated with a decrease in the localization of $\psi(r)$ with increasing k. Figure 5 shows the dependence of the displacement minimizing the total energy on the preset parameter Z.

4. DYNAMIC DISPLACEMENTS OF ELECTRON SHELLS

Figure 6 shows the form of the electron density distribution for $k = 1$ in the absence of displacements and in their presence; in both cases, the wave functions minimizing the total energy are used. The symmetry of the displaced electron density distribution ($C_\infty h$) violates the initial spherical symmetry of the system, which can be restored if we take into account configurations equivalent in energy but having other directions of the displacement vector.

The total energy functional can possess a continuum of equivalent minima in the space of displacement vectors. In this respect, we can speak of variational degeneracy in the system. The existence, as well as the shape

and other parameters of the continuum of minima, depends only on one-particle states and the parameters of the central field. In the case of the ns^2 configuration considered above, we fixed only the difference in the displacement vectors for the one-particle orbitals: $|\boldsymbol{\rho}| = |\boldsymbol{\alpha} - \boldsymbol{\beta}| = 2q$ (for $\boldsymbol{\alpha} = \mathbf{q}$ and $\boldsymbol{\beta} = -\mathbf{q}$), and, hence, the continuum is a sphere in the space of vectors $\mathbf{q}$. This restores the spherical symmetry of the problem. Analogous to the description of the collective motion in nuclei [1] and the "method of generating coordinates" in molecular spectroscopy [2], we can construct linear combinations of the biorbitals Ψ with various vectors $\mathbf{q}_{min}$,

$$\overline{\Psi}_f = (\mathbf{r}_1, \mathbf{r}_2) = \int \Psi(\mathbf{r}_1, \mathbf{r}_2; \mathbf{q}, -\mathbf{q}) f(\Omega) d\Omega, \quad (20)$$

where the integration is carried out over a sphere in the $\mathbf{q}$ space. Such a combination may have a lower energy due to "nondiagonal" (in $\mathbf{q}$) contributions to the total energy functional, which take into account the "interaction" of biorbitals. The variational procedure with functions (20) leads to the following integral equation for the function $f(\Omega)$:

$$\int d\Omega f(\Omega)[K(\mathbf{q}, \mathbf{q}') - E I(\mathbf{q}, \mathbf{q}')] = 0, \quad (21)$$

where

$$K(\mathbf{q}, \mathbf{q}') = \langle \Psi(\mathbf{q}, -\mathbf{q}) | \hat{H} | \Psi(\mathbf{q}', -\mathbf{q}') \rangle,$$
$$I(\mathbf{q}, \mathbf{q}') = \langle \Psi(\mathbf{q}, -\mathbf{q}) | \Psi(\mathbf{q}', -\mathbf{q}') \rangle.$$

A symmetry argument [1, 2] leads to trivial solutions to (21) in the case of an ns^2 configuration:

$$f(\Omega) = Y_{LM}(\theta, \varphi). \quad (22)$$

In other words, for an ns^2 configuration with displaced shells, we can introduce a set of orthogonal states

$$\tilde{\Psi}_{LM} = N_{LM} \int Y_{LM}(\Omega) \Psi(\mathbf{q}, -\mathbf{q}) d\Omega, \quad (23)$$

transforming according to irreducible representations of the rotational group. Such states can be referred to as dynamic states, since they might be responsible for the correlation contribution to the orbital current. The spectrum of these states may have nothing in common with that of a spatial rotator. It should also be noted that the electric (dipole, quadrupole) or magnetic susceptibility in the states corresponding to dynamic displacements of the electron shells can be abnormally large, their magnitude being determined by the electron–electron correlation effects.

5. MO-LCAO METHOD FOR DISPLACED ATOMIC ORBITALS

A generalization of the standard MO-LCAO method proposed in [7] presumes the inclusion in the variational procedure for a cluster, instead of the traditional set of molecular orbitals (MOs) $\varphi_{\Gamma_0 \gamma_0}(\mathbf{r}, 0)$, i.e., sym-
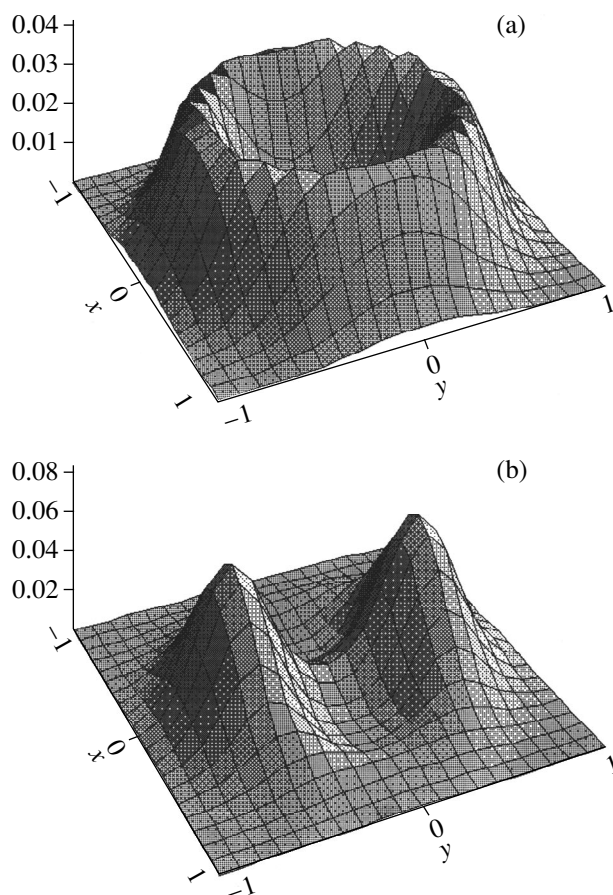

Fig. 6. Two-electron density distribution in the plane $z = 0$ in the state $\Psi(\mathbf{r}_1, \mathbf{r}_2; \mathbf{q}, -\mathbf{q})$ for $k = 1$ and $Z_0 = 2$: (a) with no displacement of the electron shells ($Z = Z_{min}^{(1)}$ for $\mathbf{q} = -0$ (a); and (b) with displacements, $Z = Z_{min}^{(1)}$, $\mathbf{q} = (q_{min}^{(1)}, 0, 0)$.

metrized combinations of atomic functions centered at equilibrium positions of the nuclei ($\mathbf{q}_{\Gamma\gamma} = 0$), of a new set of displaced MO of the type

$$\varphi_{\Gamma_0 \gamma_0}(\mathbf{r}, \mathbf{q}_{\Gamma\gamma}) = \hat{T}_{\mathbf{q}_{\Gamma\gamma}} \varphi_{\Gamma_0 \gamma_0}(\mathbf{r}, 0), \quad (24)$$

where $\mathbf{q}_{\Gamma\gamma}$ is a symmetrized displacement coordinate of atomic shells in the cluster and $\hat{T}_{\mathbf{q}_{\Gamma\gamma}}$ is the symmetrized displacement operator. Such an approach is a natural generalization of the model of displaced electron shells to a cluster comprising many atoms. Other methods of constructing MOs from displaced atomic orbitals are indicated in [7].

The symmetry group of the wave function (24) is the intersection of the kernels of the representations Γ_0 and G. In contrast to symmetrized coordinates of nuclear vibrations in the cluster, the vector $\mathbf{q}_{\Gamma\gamma}$ is fixed and specifies a certain distorted distribution of the electron density. If $\Gamma \neq A_1$, the function (24) will not possess "good" transformational properties (i.e., it will not

belong to a certain irreducible representation of the symmetry group of the undistorted cluster). This situation is similar to the case of a single center, in which a displacement of one electron from the center lowers the system symmetry to the minimum possible (axial) symmetry.

Assuming that the minimum energy corresponds to a configuration minimizing the electron–electron interaction under equal other conditions, we can introduce, analogous to the case of a single center, the following wave function for a two-particle configuration:

$$\Psi_{\Gamma_0\gamma_0;\,\Gamma\gamma}(\mathbf{r}_1, \mathbf{r}_2; \mathbf{q}_{\tilde{\Gamma}\tilde{\gamma}})$$
$$= N(1 \pm \hat{P}_{12})\hat{T}^{(1)}_{\mathbf{q}_{\tilde{\Gamma}\tilde{\gamma}}}\hat{T}^{(2)}_{-\mathbf{q}_{\tilde{\Gamma}\tilde{\gamma}}}\varphi_{\Gamma_0\gamma_0}(\mathbf{r}_1, 0)\varphi_{\Gamma_0\gamma_0}(\mathbf{r}_2, 0), \quad (25)$$

where N is the normalization factor, $\hat{P}_{12}$ is the transposition operator for the electron coordinates, and $\hat{T}^{(i)}_{\mathbf{q}_{\tilde{\Gamma}\tilde{\gamma}}}$ is the operator of a symmetrized displacement $\mathbf{q}_{\tilde{\Gamma}\tilde{\gamma}}$, which is transformed according to an irreducible representation $\tilde{\Gamma}\tilde{\gamma}$ and acts in the space of the coordinates of the ith electron. The upper sign corresponds to the singlet wave function and the lower sign, to the triplet function. The transformational properties $\Gamma\gamma$ of the two-particle wave function (25) are determined by the product $\Gamma\gamma = \Gamma_0\gamma_0 \times [\tilde{\Gamma}\tilde{\gamma}]^2$ for the singlet and by $\Gamma\gamma = \Gamma_0\gamma_0 \times \tilde{\Gamma}\tilde{\gamma}$ for the triplet.

In conclusion, let us record the main features of the model of mobile electron shells. The inclusion of electron correlations often involves a large number of functions in the zeroth approximation. We have demonstrated that, in some cases, the redistribution of the electron density in a system can be described by using a variational procedure in which the coordinates of the center of one-particle functions are varied. The physical clearness of this variational parameter enables one, among other things, to simulate the response of the system to an anisotropic perturbation in a basically simple way without resorting to a large number of configurations. We have considered specific correlated states that can make a correlation contribution to orbital current. A generalization of the MO-LCAO scheme with a limited set of one-particle functions, which makes it possible to take into account additional multipole–multipole interactions in a cluster, is also considered.

REFERENCES

1. J. J. Griffin and J. A. Wheeler, Phys. Rev. **108** (2), 311 (1957).
2. L. Lathouwers, Phys. Rev. A **18** (5), 2150 (1978).
3. L. D. Landau and E. M. Lifshitz, *Quantum Mechanics* (Nauka, Moscow, 1989).
4. A. S. Moskvin, V. A. Korotaev, Yu. D. Panov, *et al.*, Physica C **282**–**287**, 1735 (1997).
5. A. Sommerfeld, *Atomic Structure and Spectra* (GITTL, Moscow, 1956), Vol. 2.
6. Y. Sugiura, Z. Phys. **45** (5), 484 (1927).
7. A. S. Moskvin, Preprint, UrGU (Ural State University, Yekaterinburg, 1995).

Translated by N. Wadhwa

Luminescence of Impurity 3d and 4f Metal Ions in Different Crystalline Forms of Al_2O_3

A. B. Kulinkin, S. P. Feofilov, and R. I. Zakharchenya

Ioffe Physicotechnical Institute, Russian Academy of Sciences, Politekhnicheskaya ul. 26, St. Petersburg, 194021 Russia

Received October 11, 1999

Abstract—The ^2E–$^4A_2$ luminescence spectra of Cr^{3+} ions in Al_2O_3 are investigated in the course of transitions between the structural forms γ–δ–θ–α. The spectral lines observed are assigned to Cr^{3+} ions in these structural forms, which are identified by an X-ray powder diffraction analysis. The lifetimes of the Cr^{3+} excited states in transient forms of Al_2O_3 are measured. Investigations of the luminescence spectra of $Al_2O_3 : Eu^{3+}$ demonstrate that the Eu^{3+} ions can form regular centers only in α-Al_2O_3 and, unlike the Cr^{3+} ions, give no rise to similar centers in moderately ordered θ-Al_2O_3. © 2000 MAIK "Nauka/Interperiodica".

1. INTRODUCTION

It is known that aluminum oxide under normal conditions can occur in different crystalline forms (also referred to as phases). It is conventional to denote these forms by the Greek letters α, β, γ, δ, η, κ, χ, and θ. The α form of Al_2O_3, namely, corundum or sapphire, has received the most study. On the other hand, other metastable crystalline forms—the so-called transient forms—are also of considerable interest. The reason is that many of them are used in practice (adsorbents, catalysts, coatings, and abrasives). In particular, β-Al_2O_3 : Na is the superionic conductor. All transient forms of Al_2O_3 have a disordered crystal lattice and represent more complex objects than α-Al_2O_3 [1]. The structure of all these different forms can be considered a disordered spinel structure with a various degree of distortion. The unit cell of the AB_2O_4 spinel (where $A = M^{2+}$ and $B = Me^{3+}$) contains 32 O^{2-} ions, which comprise a cubic close packing, and 24 cation sites including 16 octahedral and 8 tetrahedral ones. For transient forms of Al_2O_3, the unit cell contains 21 1/3 Al^{3+} ions, which occupy the possible cation sites with a various degree of disorder [1]. This inhomogeneous distribution of cations over the sites and also the distortion of oxygen sublattice, which leads to the lowering of its symmetry, are responsible for the variety of Al_2O_3 transient forms. The transitions between crystalline forms of Al_2O_3 are irreversible and proceed at certain temperatures. The structural transformations of Al_2O_3 also depend on the choice of the starting material [1].

The spectroscopy of impurity rare-earth ions and ions of the iron group in dielectrics provides information on the structure and dynamic processes in crystals. The spectra of impurity ions can be used in determination of the phase composition in different dielectric materials, specifically, in Al_2O_3 [2]. However, no systematic investigations into the spectra of rare-earth ions and iron group ions in different forms of Al_2O_3 were performed. Mention should be made of the only work [3], in which the measurements were carried out with a low spectral resolution. In the present work, the spectra and kinetics of luminescence of the impurity ions Cr^{3+}, Eu^{3+}, and Mn^{4+} were investigated in the course of structural transformations in Al_2O_3.

The problem of incorporating rare-earth ions into the corundum lattice at a large difference in ionic radii has attracted particular interest [4–9]. In the majority of works, the incorporation of rare-earth ions into corundum was investigated by the ion implantation method [4–6]. There is also evidence for applying a more "standard" method of crystal growth [7]. However, rare-earth ions do not necessarily form regular centers in the corundum lattice, which bring about the appearance of narrow lines in the spectra. Based on the performed calculations, Verdozzi *et al.* [8] made the inference that the rare-earth ions substitute for aluminum in corundum, and in this case, the rare-earth ions are strongly shifted (by 0.5 Å) with respect to the Al^{3+} site. According to [8], the shift is observed along the trigonal axis of the crystal toward the octahedral cavity, which is not occupied by the Al^{3+} ion, and causes a strong distortion of the local structure. In our earlier work [9], α-Al_2O_3 : RE^{3+} was obtained from γ-Al_2O_3 : RE^{3+}, which was prepared by the "sol–gel" technology through a series of structural transformations. One of the purposes of the present work was to reveal the stage of the structural transformations of Al_2O_3, at which the Eu^{3+} ions form regular centers.

2. EXPERIMENTAL TECHNIQUE

The samples of high-porosity nanocrystalline transparent γ-Al_2O_3, which was obtained by the sol–gel procedure described in [10, 11], served as the starting materials. A small additive (0.05–1 at. %) of the rare-
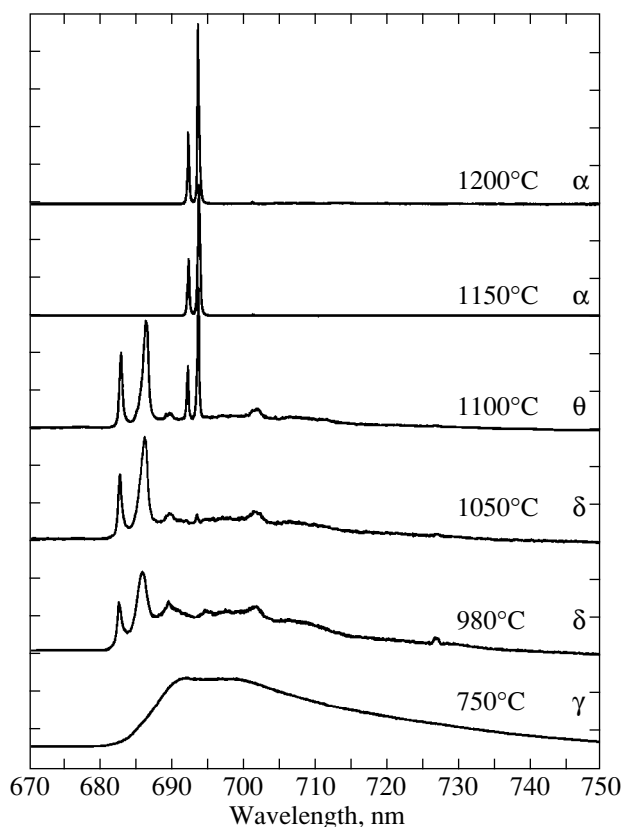
Fig. 1. Luminescence spectra of Al_2O_3 : 0.05 at. % Cr^{3+} annealed at different temperatures. The annealing temperature T_{ann} and dominant crystalline phase in the sample (according to the X-ray scattering data) are indicated at the curves. Conditions: excitation by an Ar laser, λ_{exc} = 514.5 nm, T = 77 K.

earth ions or iron group ions was introduced into the samples in the process of the sol–gel synthesis. Then, the samples were annealed at different temperatures T_{ann} in air for 1 h. The crystal structure was determined by an X-ray diffraction technique. The fluorescence spectra of the impurity ions were investigated by using a double grating monochromator at T = 77 K with excitation by an Ar laser or a Hg lamp. The luminescence decay kinetics was measured by the mechanical modulation of the exciting Ar laser beam and the recording of the luminescence with time resolution.

3. RESULTS AND DISCUSSION

The $^2E–^4A_2$ spectra of Cr^{3+} luminescence in the course of structural transformations are displayed in Fig. 1. The annealing temperatures T_{ann} are given at the curves. The Greek letter near each spectrum denotes the dominant crystalline phase in the sample, which was annealed at the given temperature. The phases were identified from the X-ray scattering data. The spectrum corresponding to γ-Al_2O_3 was described in [12]. The

extremely strong inhomogeneous broadening (150 cm^{-1}) of the $^2E–^4A_2$ (R-line) electron transition is observed, which masks the splitting of the excited ^2E state. The long-wavelength part of the spectrum corresponds to the vibronic transitions. Similar spectra are characteristic of the Cr^{3+} ions in a strong crystal field in a disordered environment, for example, in disordered crystals [13] and glasses [14]. Annealing of the samples leads to radical changes in the luminescence spectra, which manifest themselves in the appearance of narrower doublets, first, at wavelengths of 682 and 686 nm and, second, at 692 and 693.5 nm. After the annealing at T_{ann} = 1200°C, the spectrum contains only the second doublet—the known lines of chromium in ruby. The spectra corresponding to T_{ann} = 980–1100°C directly demonstrate the coexistence of different phases in the samples. Indeed, the strongly inhomogeneously broadened spectra and narrow doublets are observed simultaneously. Analysis of the X-ray scattering data and the luminescence spectra permits us to conclude that the doublet 682 and 686 nm corresponds to the R-lines ($^2E–^4A_2$) of Cr^{3+} in θ-Al_2O_3. Actually, this phase is more ordered compared to the γ and δ phases: the sublattice of the Al^{3+} ions, which occupy tetrahedral sites, is ordered in θ-Al_2O_3 [1]. A similar identification was made in [2] for oxide films on the metal surface. No characteristic features that could be attributed to Cr^{3+} in δ-Al_2O_3 were observed in the spectra. This is likely due to the fact that the degree of disorder in δ-Al_2O_3 is equal to that for γ-Al_2O_3. In actual fact, a strong disorder leads to a strong inhomogeneous broadening and makes the Cr^{3+} spectra for the γ and δ phases indistinguishable.

Figure 2 depicts the curves of Cr^{3+} luminescence decay, which correspond to the different lines in the spectra shown in Fig. 1. The luminescence decay in the 682- and 686-nm lines is strictly exponential and corresponds to the radiation lifetime of the excited ^2E state, i.e., τ_R = 12 ms. This decay suggests a larger degree of ordering of the matrix involving the ions responsible for these lines and, thus, provides additional support for the assignment of these lines to the Cr^{3+} ions in θ-Al_2O_3. The luminescence decay in the region of the broad inhomogeneously broadened spectrum, which is attributed to the strongly disordered γ- and δ-Al_2O_3 phases, exhibits a nonexponential behavior. This corresponds to the contribution of the centers with different lifetimes of the ^2E state. For comparison, the luminescence decay in the "ruby R-lines" at 692 and 693.5 nm (τ_R = 5.8 ms) is also shown in Fig. 2.

Of special interest are the spectroscopic studies of Eu^{3+} ions in the course of structural transformations. Actually, the ionic radius of Eu^{3+} (0.95 Å) substantially exceeds the ionic radius of Cr^{3+} (0.51 Å). Incorporation of Eu^{3+} into disordered γ-Al_2O_3, which contains vacancies, should involve no particular problems, whereas
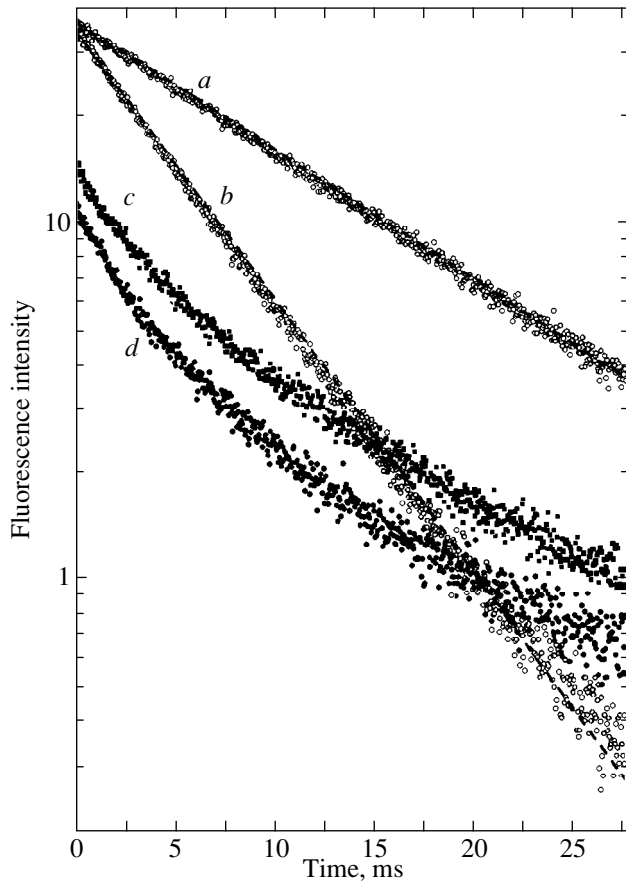
Fig. 2. Luminescence decay of $Al_2O_3 : Cr^{3+}$ for different lines in the spectra shown in Fig. 1. Conditions: excitation by an Ar laser, $\lambda_{exc} = 514.5$ nm, $T = 77$ K. (*a*) $\lambda = 686$ nm (R_1-line of Cr^{3+} in the θ phase), $\tau_R = 12$ ms; (*b*) $\lambda = 693.5$ nm (R_1-line of Cr^{3+} in the α phase), $\tau_R = 5.8$ ms; (*c*) $\lambda = 697.5$ nm; and (*d*) $\lambda = 710$ nm (R-lines of Cr^{3+} and their vibronic wings in the disordered γ and δ phases).

Fig. 3. The $^5D_0-^7F_n$ luminescence spectra of the Cr- and Mn-doped $Al_2O_3 : Eu^{3+}$ samples annealed at different temperatures T_{ann}. Conditions: excitation by an Hg lamp, $\lambda_{exc} = 350$–420 nm, $T = 77$ K.

the Eu^{3+} regular centers in α-Al_2O_3 (corundum) represent a notably unusual object. In the earlier work [9], we demonstrated that α-$Al_2O_3 : Eu^{3+}$, in which Eu^{3+} ions give rise to the single-type regular centers with an axial symmetry, can be obtained upon annealing of γ-$Al_2O_3 : Eu^{3+}$ prepared by the sol–gel technique. In this respect, it is reasonable to raise the questions as to how such formation of the Eu^{3+} centers in α-Al_2O_3 proceeds during annealing of the samples and as to which centers are formed by the Eu^{3+} ions in relatively ordered θ-Al_2O_3. The $^5D_0-^7F_n$ luminescence spectra of the $Al_2O_3 : Eu^{3+}$ samples annealed at different temperatures are shown in Fig. 3. It is seen that the annealing leads to the appearance of narrow lines of α-$Al_2O_3 : Eu^{3+}$ instead of the inhomogeneously broadened spectrum of γ-$Al_2O_3 : Eu^{3+}$. The sample composition can be evaluated from the luminescence spectra of Cr^{3+}, which

are also present in some amounts in the samples. It can be seen that at $T_{ann} = 1200$–1300°C, the sample contains a considerable amount of θ-Al_2O_3. At the same time, the only series of narrow lines corresponding to Eu^{3+} in the samples are the lines attributed to α-$Al_2O_3 : Eu^{3+}$ [9]. Thus, it is evident that, unlike the Cr^{3+} ions, Eu^{3+} gives no rise to regular centers in θ-Al_2O_3. The regular centers are formed only upon the θ–α transitions when the distorted cubic packing of the oxygen sublattice transforms to the hexagonal one. It is also possible that the Eu^{3+} ions in the θ phase form the local surrounding typical of Eu^{3+} in α-Al_2O_3 and, thus, contribute to the narrow lines of Eu^{3+}, which are characteristic of corundum [9].

The luminescence spectra shown in Fig. 3 also exhibit narrow lines at 672 and 676 nm, which are attributed to the Mn^{4+} ions in corundum [15]. These lines indicate that the manganese impurity is present in the samples. A close examination of the luminescence spectra of the Mn-containing samples annealed at dif-

ferent temperatures did not reveal narrow doublets that could be assigned to Mn^{4+} in θ-Al_2O_3. This can be reasonably explained by the fact that the Mn ions in θ-Al_2O_3 occur in other charge states (2+ or 3+), do not give rise to narrow lines in the spectra, and transform into the 4+ state only in the α phase. In contrast, the occurrence of the Mn^{4+} ions in corundum without charge compensation is an unusual property of α-Al_2O_3 : Mn, which was obtained using the sol–gel technology [16]. In the standard crystal growth technique, the charge compensation is required to produce α-Al_2O_3 : Mn^{4+}, for example, by introducing the Mg^{2+} ions [15].

It should be noted that the influence of impurity ions on the temperatures of transitions between the structural forms is seen from Figs. 1 and 3. For pure Al_2O_3, the transitions take place at temperatures of 900°C (γ–δ), 1100°C (δ–θ), and 1150°C (θ–α).

The structural transformations γ–δ–θ–α in Al_2O_3, which was obtained by the sol–gel technology, clearly manifest themselves in the spectra of Cr^{3+} ions. The results of our experiments permit the trustworthy identification of the lines in the luminescence spectra of different crystalline forms containing Cr^{3+}. Therefore, the spectroscopy of Cr^{3+} ions can be used to determine the structural composition of Al_2O_3. The investigations into the spectra of Eu^{3+} in the course of structural transformations demonstrated that the formation of Eu^{3+} regular centers occurs at the stage of the θ–α transition.

ACKNOWLEDGMENTS

REFERENCES

1. R.-S. Zhou and R. L. Snyder, Acta Crystallogr., Sect. B **47**, 617 (1991).

2. D. M. Lipkin, H. Schaffer, F. Adar, *et al.*, Appl. Phys. Lett. **70**, 2550 (1997).

3. Y. Hirai, T. Fukuda, Y. Kobayashi, *et al.*, Solid State Commun. **62**, 637 (1987).

4. E. Alves, M. F. Da Silva, G. N. van den Hoven, *et al.*, Nucl. Instrum. Methods Phys. Res., Sect. B **106**, 429 (1995).

5. N. Can, P. D. Townsend, D. E. Hole, *et al.*, J. Appl. Phys. **78**, 6737 (1995).

6. K. Aono and M. Iwaki, Nucl. Instrum. Methods Phys. Res., Sect. B **141**, 518 (1998).

7. S. Geschwind and J. P. Remeika, Phys. Rev. **122**, 757 (1961).

8. C. Verdozzi, D. R. Jennison, P. A. Schultz, *et al.*, Phys. Rev. Lett. **80**, 5615 (1998).

9. A. A. Kaplyanskiĭ, A. B. Kulinkin, A. B. Kutsenko, *et al.*, Fiz. Tverd. Tela (S.-Peterburg) **40**, 1442 (1998) [Phys. Solid State **40**, 1310 (1998)].

10. B. E. Yoldas, J. Appl. Chem. Biotechnol. **23**, 803 (1973); Am. Ceram. Soc. Bull. **54**, 286 (1975).

11. R. I. Zakharchenya and T. N. Vasilevskaya, J. Mater. Sci. **29**, 2806 (1994).

12. S. P. Feofilov, A. A. Kaplyanskii, and R. I. Zakharchenya, J. Lumin. **66**–**67**, 349 (1995).

13. S. A. Basun, P. Deten, S. P. Feofilov, *et al.*, J. Lumin. **45**, 115 (1990).

14. F. J. Bergin, J. F. Donegan, T. J. Glynn, *et al.*, J. Lumin. **34**, 307 (1986).

15. S. Geschwind, P. Kisliuk, M. P. Klien, *et al.*, Phys. Rev. **126**, 1684 (1962).

16. S. P. Feofilov, A. B. Kulinkin, A. B. Kutsenko, *et al.*, J. Lumin. **76**–**77**, 217 (1998).

Translated by N. Korovin

SEMICONDUCTORS
AND DIELECTRICS

Effect of Vanadium Doping on the Electrical Properties
of $Bi_{12}GeO_{20}$ Crystals

A. Yu. Kudzin, S. N. Plyaka, and G. Kh. Sokolyanskiĭ

Dnepropetrovsk State University, Dnepropetrovsk, 320625 Ukraine
Received August 19, 1999; in final form, October 22, 1999

Abstract—A study is reported of the temperature dependences of the dc and ac electrical conductivities, as well as of *I–V* characteristics of pure and vanadium-doped germanosillenite crystals. It has been established that the charge carriers in $Bi_{12}GeO_{20}$ are electrons and holes. Doping with vanadium gives rise to a strong dependence of the conductivity and its activation energy on the dopant concentration. Within the model, the results explain the hopping-charge transfer in doped, closely compensated semiconductors. © *2000 MAIK "Nauka/Interperiodica".*

Photorefractive germanium and silicon sillenites are wide-gap materials with a high resistivity and a low carrier mobility [1, 2]. A number of publications deal with the investigation of the charge transport mechanism in these crystals [3–5]. Within the 20–400°C region, the conduction occurs through electron (hole) hopping over localized states with a broad energy spectrum. The hopping takes place both over states near the Fermi level and at the density-of-states maximum. Impurities substantially affect the conductivity and its activation energy [2, 6, 7], so that the latter can vary in the high-temperature region from 1.8 eV in crystals with a Mn impurity to 0.45 eV in Al-doped crystals. The reason for such high activation energies is still unclear. There is considerable scatter in determining the type of dark carriers. Thermopower studies [1, 2] suggest that the dark conduction in $Bi_{12}GeO_{20}$ (BGO) and $Bi_{12}SiO_{20}$ (BSO) is of the *p*-type, while in photoinduced transport, electrons are involved. Grebmeier and Oberschmid [8] established by the same method the dark conduction in undoped BGO and BSO to be of the *n*-type. In his studies of the *I–V* characteristics on BGO samples with an electronic contact, Gudaev [7] comes to the conclusion that both the dark and photoinduced conduction is of the *n*-type. Investigation of photoinduced transport in BGO single crystals showed that when photoexcitation takes place in the impurity region, both electrons and holes are mobile [9]. The studies of dark *I–V* characteristics in [3, 6] were performed on samples with two injecting electrodes, thus precluding the determination of the contribution of electrons and holes to the electrical conductivity of the sillenites.

It is known that hopping conduction over localized states can occur only under compensation. But the compensation ratio in BGO and BSO crystals was not determined.

This work was aimed at studying the effect of the vanadium dopant on the electrical conductivity, its activation energy, and compensation ratio of $Bi_{12}GeO_{20}$ single crystals.

1. EXPERIMENTAL TECHNIQUES

A study has been carried out of the temperature dependence of dc and ac electrical conductivity, *I–V* characteristics under monopolar injection, and of optical absorption spectra.

One studied BGO single crystals grown by the Czochralski technique from ultrapure reagents. The V_2O_5 dopant was introduced into the batch in concentrations of 0.2–1 mol %. The contacts used in measuring the *I–V* characteristics were made of different materials. One of the contacts was made of platinum deposited in vacuum. A thin layer of silicate glass (Na_2SiO_3) served as the second electrode. The electrical conductivity in such glasses is ionic [10] and, as shown by our measurements, exceeds by several orders of magnitude that of the samples under study. Using this layer permits one to obtain a sample with one injecting electrode (platinum), i.e., to exclude double injection. The discrimination coefficient may serve as a criterion making possible the separation of monopolar from double injection [11]. In our case, it is greater than unity, which is characteristic of monopolar injection.

The studies of dc *I–V* characteristics were made in fields of 100 to 10 000 V/cm at temperatures ranging from 150 to 400°C. The field was applied to a sample during 5 min. The temperature dependences of dc and ac electrical conductivity were measured in weak fields corresponding to the Ohmic part of the *I–V* curves in the same interval. Low dc currents were measured with a VK2-16 electrometer. A VM-311G Q-meter was used to measure conductivities at a frequency of 20 MHz.

Transmission spectra were measured on a double-beam spectrophotomer SPECORD M-40 at room temperature according to the technique described in [12].

2. EXPERIMENTAL RESULTS AND THEIR DISCUSSION

The temperature dependences of the conductivity of $Bi_{12}GeO_{20}$ crystals measured in the 120–350°C region is presented graphically in Fig. 1. The measurements were performed in a weak dc field (curves *1–3*) corresponding to the Ohmic segment of the *I–V* characteristics on samples with two (curve *1*) and one (curves *2* and *3*) injecting electrodes, as well as in an ac mode at 20 MHz (curve *4*).

The activation energy of ac conduction is constant within the whole temperature range covered and constitutes approximately 0.05 eV. The dc conductivity and its activation energy are practically independent of electrode type and of the polarity of the electric field applied. Two activation energies are observed within the temperature interval studied, namely, 0.62 eV below 200°C, and 1.35 eV at higher temperatures.

Doping the crystal with vanadium does not change the pattern of the temperature behavior of electrical conduction. However, the absolute magnitude of the conductivity and its activation energy depend strongly on the dopant concentration (Table 1). The latter is characteristic of hopping conduction (ε_3 conduction)
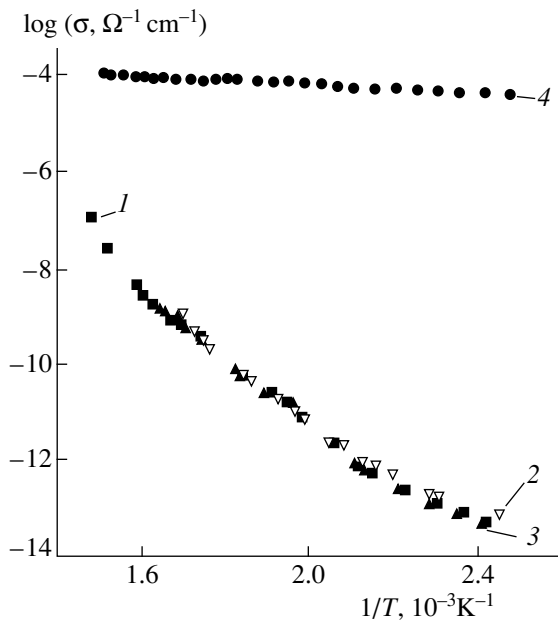

Fig. 1. Temperature dependences of the electrical conductivity of $Bi_{12}GeO_{20}$: (*1*)–(*3*) dc measurements, (*4*) 20 MHz.

[13–15]. In this case, the resistivity is a function of the concentration of donors N_d (or of acceptors N_a):

$$\rho_3 = \rho_{03} \exp(f(N_d)). \qquad (1)$$

By [15],

$$f(N_d) = \frac{\eta}{N_d^{1/3} a}, \qquad (2)$$

where a is the Bohr radius and η is a parameter depending on the compensation ratio [15]

$$K = N_d/N_a. \qquad (3)$$

On the other hand, the temperature dependence of the resistivity in hopping conduction can be written as [13, 15]

$$\rho = \rho_3 \exp\left[\frac{E_3}{kT}\right], \qquad (4)$$

where E_3 is the hopping conduction (HC) activation energy. The finite HC activation energy E_3 in compensated semiconductors is associated with the energy spread of the donor (acceptor) levels. In a general case, the dependence of the HC activation energy on the concentration of the majority impurity N_D has the form [13, 15]

$$E_3 = E_0 F(K), \qquad (5)$$

where $E_0 = \dfrac{e N_D^{1/3}}{\varepsilon \varepsilon_0}$ is the characteristic Coulomb energy of interaction with impurity centers, ε is the relative permittivity of crystals, and $F(K)$ is a function of the compensation ratio. The analytic form of $F(K)$ was found only for the limiting cases of close ($K \longrightarrow 1$) and light ($K \longrightarrow 0$) compensation [13]. It was shown that the $F(K)$ function should grow as $(1 - K)^{-1/3}$ for close compensation. Relations (1)–(5) can be used to derive the following expression for the ε_3 conductivity:

$$\sigma = \sigma_{03} \exp\left[-\left(\frac{\alpha}{N_d^{1/3} a} - \frac{e}{\varepsilon \varepsilon_0} \frac{N_d^{1/3}}{(1 - K)^{1/3} kT}\right)\right]. \qquad (6)$$

This relation is characterized by a strong increase of the activation energy E_3 and a decrease of the conductivity σ for $K \longrightarrow 1$. Our data obtained on vanadium-doped BGO crystals show that when the batch contains 0.5 mol % V_2O_5, the conductivity passes through a minimum, and its activation energy, through a maximum (Table 1). This possibility of controlling the electrical properties of amorphous semiconductors by doping, up to inversion of conduction type, is described by LeComber and Spear [16] and Tawada [17]. Shklovskiĭ and Éfros [18] came to the conclusion that closely compensated crystalline semiconductors with randomly distributed donors and acceptors are so close in electrophysical properties to amorphous semiconductors that they could serve as a model for the latter. As seen from

Table 1. Parameters of the crystals at 200°C

Crystal	σ, Ω^{-1} cm^{-1}	μ_p, cm^2 V^{-1} s^{-1}	μ_n, cm^2 V^{-1} s^{-1}	E_3, eV
Bi$_{12}$GeO$_{20}$	1.51×10^{-12}	2.1×10^{-1}	2.1×10^{-2}	1.35
Bi$_{21}$GeO$_{20}$ + 0.2 mol % V$_2$O$_5$	1.7×10^{-10}	2.82×10^{-1}	3.3×10^{-2}	0.62
Bi$_{21}$GeO$_{20}$ + 0.5 mol % V$_2$O$_5$	5.26×10^{-11}	3.5×10^{-2}	6.4×10^{-2}	0.82
Bi$_{21}$GeO$_{20}$ + 1.0 mol % V$_2$O$_5$	1.85×10^{-10}	–	7.4×10^{-2}	0.52

Table 1, the activation energy is maximal for intermediately doped crystals. This suggests that, by varying the vanadium concentration, one can change the type of conduction in germanosillenites. The activation energy of conduction in an undoped BGO crystal (1.35 eV) shows that its Fermi level E_f lies close to midgap, i.e., that it is closely compensated.

A quantitative comparison of the theory with the experimental data obtained requires the knowledge of N_d and K. Solving the coupled equations (3) and (5) for N_D, with due account of the fact that in the case of close compensation, the free carrier concentration $n = N_D - N_A$, yields

$$N_D = \left(\frac{E_3 \varepsilon \varepsilon_0}{e}\right)^{3/2} n^{1/2}. \qquad (7)$$

As seen from (7), in order to determine the concentration of the majority impurity, one has to know the HC activation energy, the excess carrier concentration n, and the permittivity ε. The HC activation energy E_3 is derived from the temperature dependence of electrical conductivity (Table 1). The relative permittivity ε was found from conductivity measurements at 20 MHz. The concentration n can be determined either using the relation

$$n = \sigma/e\mu \qquad (8)$$

or, by studying the $I–V$ characteristics of space-charge limited currents [19], from the voltage V_Ω at which a crossover occurs from the Ohmic to quadratic $I(U)$ dependence:

$$n = \frac{\varepsilon \varepsilon_0 V_\Omega}{ed^2}. \qquad (9)$$

The results of studies of steady-state $I–V$ characteristics are presented graphically in Fig. 2. Curve *1* was obtained using the injecting platinum electrode as the anode, and curve *2*, when it was the cathode. The $I–V$ curves (Fig. 2) exhibit segments with different $I \sim U^\gamma$ dependences, where γ varies from 1 to 10. The presence of segments with $\gamma \geq 2$ in curves *1* and *2* (Fig. 2) suggests the injection of both electrons and holes from the contacts into the sample [19]. The equilibrium carrier concentrations n and p derived from (9) turn out to be very low 10^{10}–10^{12} cm^{-3} compared with the concentrations of both the intrinsic defects and of the dopant. It should be pointed out that if a voltage step is applied

when measuring a steady-state $I–V$ curve in the weak-field region, where there is no noticeable injection, the current is observed to fall off with time. Measurements of "dynamic" $I–V$ characteristics yield somewhat higher carrier concentrations. This may be due to the fact that at the temperatures used in the experiments, the hopping transport of a charge occurs in the samples over clusters of a finite size; i.e., no infinite percolation cluster has yet formed in these conditions [20]. The charge builds up at cluster ends to create a certain space-charge-type (interlayer) sample polarization. The possibility of carriers migrating over finite clusters to contribute to the permittivity of random-field semiconductors was pointed out in [21]. This phenomenon was observed experimentally in silicosillenites [22]. Finite clusters were detected in sillenites in studies of the temperature dependence of electrical conductivity at various frequencies [4, 5]. Thus, $n(p)$ can be determined with a higher accuracy from (8) using the values of the ac conductivity measured at high frequencies, where practically all carriers participate in charge
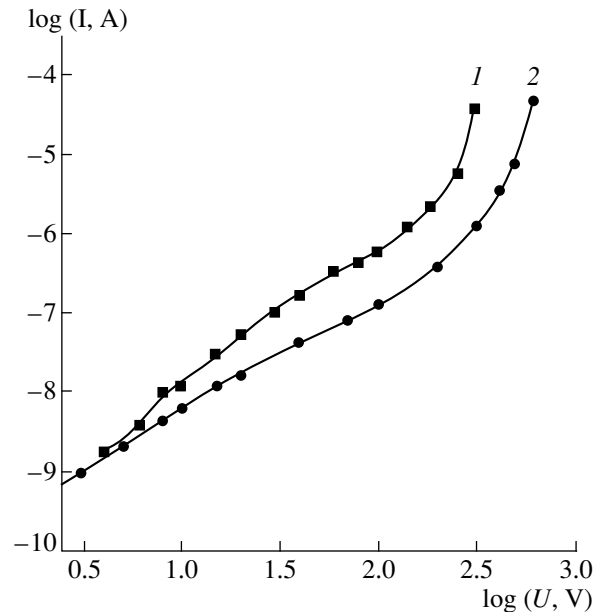

Fig. 2. $I–V$ characteristics of a germanosillenite crystal with nonsymmetrical electrodes. The platinum electrode is used as anode (curve *1*) or cathode (curve *2*).

Table 2. Calculated crystal parameters

Crystal	$N_d \times 10^{-18}$, cm^{-3}	$N_a \times 10^{-18}$, cm^{-3}	K	$n \times 10^{-15}$, cm^{-3}	$p \times 10^{-15}$, cm^{-3}
$Bi_{12}GeO_{20}$	–	3.13	0.99952	–	1.5
$Bi_{21}GeO_{20}$ + 0.2 mol % V_2O_5	7.011	7.021	0.99868	–	9.96
$Bi_{21}GeO_{20}$ + 0.5 mol % V_2O_5	6.906	6.902	0.99944	3.89	–
$Bi_{21}GeO_{20}$ + 1.0 mol % V_2O_5	5.14	5.132	0.99836	8.446	–

transport. The values of the mobility needed to determine n and p were found from the quadratic segments of the *I–V* characteristics using the relation $\mu = \dfrac{8d^3 J}{9\varepsilon\varepsilon_0 U^2}$
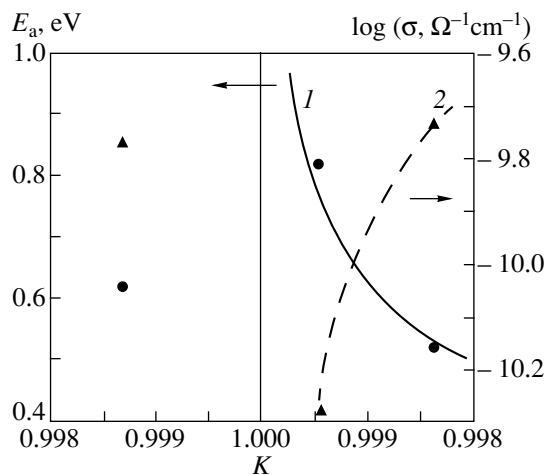

Fig. 3. Activation energy (curve *1*) and electrical conductivity (curve *2*) versus compensation ratio. The points refer to experimental results.
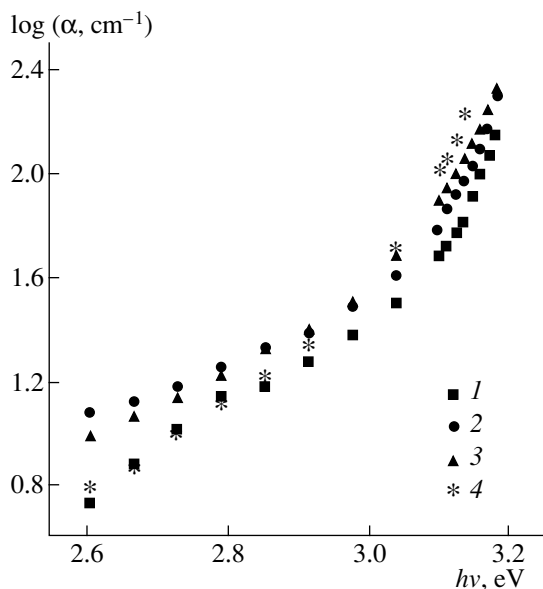

Fig. 4. Spectral response of the absorption coefficient of germanosillenite crystals: (curve *1*) nominally pure and (curves *2–4*) V_2O_5-doped $Bi_{12}GeO_{20}$ crystals.; mol % V_2O_5: (*2*) 0.2, (*3*) 0.5, (*4*) 1.0.

(Table 1). The values of n and p calculated in this way are listed in Table 2.

The majority carriers in BGO were found to be holes [1, 2]. Studies of the incorporation of vanadium into the $Bi_{12}TiO_{20}$ crystal and of its effect on the optical and photoelectric properties suggest [23, 24] that this impurity occupies the tetrahedral positions in the titanosillenite lattice in the 5+ charge state; i.e., it acts as a donor. Because BTO and BGO crystals are isomorphic, it may be conjectured that in germanosillenite one has a similar situation. The low concentration of vanadium (0.2 mol % V_2O_5 in the batch) does not change the type of conduction. Because at 1 mol % V_2O_5, the activation energy is lower than that at 0.5 mol % V_2O_5. In this case the crystals may be assumed already to be of the *n*-type. If we assume that crystals with 0.5 mol % V_2O_5 are also of the *n*-type, equations (5) and (7) can be used to find N_d (N_a) and the compensation ratio of the crystals (Table 2). Note that the value of N_a for a pure $Bi_{12}GeO_{20}$ crystal agrees well with the data quoted in [24] ($N_a \approx 6 \times 10^{18}$ cm^{-3}). As follows from Table 2, the donor concentration decreases with increasing vanadium concentration. A similar decrease of N_d and the associated drop in the photocurrent observed in [24] is associated with the fact that doping the BTO crystal with pentavalent vanadium noticeably reduces the oxygen vacancy concentration, which should bring about a decrease in the donor concentration. It should also be mentioned that the parameter $E_0 = eN_d^{1/3}/\varepsilon\varepsilon_0$ remains practically the same for samples with 0.5 and 1 mol % V_2O_5 in the batch. By contrast, in a crystal with 0.2 mol % V_2O_5, it is different. This provides additional evidence for the crystals with 0.5 and 1 mol % V_2O_5 having the same type of conduction. The dependence of the conductivity and of its activation energy is plotted in Fig. 3 versus compensation ratio for BGO : V using the data of Tables 1 and 2. The same figure displays a calculated $E_3(K)$ dependence with E_0 as a parameter (curve *1*).

As evident from Fig. 3 and Table 2, both pure and vanadium-doped germanosillenite crystals are closely compensated. Such materials are characterized by a shoulder in the absorption spectra, which was exactly what was observed in our experiments (Fig. 4). It should be pointed out that the value of α for $h\nu = 2.8$ eV in the $Bi_{12}GeO_{20}$ crystal is close to that quoted in [25]. Doping with vanadium results in an increase of

absorption in the $2.8 < h\nu < 3.17$ eV region compared to a pure crystal. As the impurity concentration increases, for $h\nu < 3.0$ eV the crystals become more transparent, and for $h\nu > 3.0$ eV, darken. The decrease in absorption in the 2.6–2.8 eV band is probably caused by a decrease in the concentration of intrinsic defects in the crystal, similar to what was observed in [24].

Thus, our experiments suggest that both electrons and holes act as mobile carriers in BGO and BGO:V crystals. One observes a strong dependence of the conductivity and of its activation energy on impurity concentration, and the crystals themselves are closely compensated. Vanadium doping in concentrations below 1 mol % V_2O_5 (in the batch) permits one to properly control the magnitude and type of the dark conduction in $Bi_{12}GeO_{20}$ single crystals. Doping with vanadium changes the compensation ratio and the associated spectral response of the absorption coefficient in the region of the absorption shoulder.

REFERENCES

1. A. A. Ballman, J. Cryst. Growth **1** (3), 37 (1967).

2. R. E. Aldrich, S. L. Hou, and M. L. Harvill, J. Appl. Phys. **42** (1), 493 (1971).

3. V. P. Avramenko, L. P. Klimenko, A. Yu. Kudzin, *et al.*, Fiz. Tverd. Tela (Leningrad) **19** (4), 1201 (1977) [Sov. Phys. Solid State **19**, 702 (1977)].

4. V. P. Avramenko, A. Yu. Kudzin, and G. Kh. Sokolyanskiĭ, Fiz. Tverd. Tela (Leningrad) **22** (10), 3149 (1980) [Sov. Phys. Solid State **22**, 1839 (1980)].

5. V. P. Avramenko, A. Yu. Kudzin, and G. Kh. Sokolyanskiĭ, in *Physics of Active Insulators* (DSU, Dnepropetrovsk, 1980).

6. V. P. Avramenko, A. Yu. Kudzin, T. V. Panchenko, *et al.*, in *Semiconductors-Ferroelectrics* (RSU, Rostov, 1984).

7. O. A. Gudaev, Avtometriya **1**, 106 (1980).

8. B. G. Grebmeier and R. Oberschmid, Phys. Status Solidi A **96**, 199 (1986).

9. S. N. Plyaka and G. Kh. Sokolyanskiĭ, Fiz. Tverd. Tela (S.-Peterburg) **40**, 2054 (1998) [Phys. Solid State **40**, 1859 (1998)].

10. G. I. Skanavi, *Physics of Dielectrics (Weak-Field Region)* (Fizmatgiz, Moscow, 1949).

11. A. N. Zyuganov and S. V. Svechnikov, *Injection Contact Phenomena in Semiconductors* (Naukova Dumka, Kiev, 1981).

12. A. Yu. Kudzin, G. Kh. Sokolyanskiĭ, and A. S. Yudin, Fiz. Tverd. Tela (Leningrad) **30** (6), 1864 (1988) [Sov. Phys. Solid State **30**, 1074 (1988)].

13. B. I. Shklovskiĭ and A. L. Éfros, Fiz. Tekh. Poluprovodn. **14** (5), 825 (1980) [Sov. Phys. Semicond. **14**, 487 (1980)].

14. B. I. Shklovskiĭ, Fiz. Tekh. Poluprovodn. **6** (7), 1197 (1972) [Sov. Phys. Semicond. **6**, 1053 (1972)].

15. B. I. Shklovskiĭ and A. L. Éfros, *Electronic Properties of Semiconductors* (Nauka, Moscow, 1975).

16. P. G. LeComber and W. E. Spear, in *Amorphous Semiconductors*, Ed. by M. H. Brodsky, Topics in Applied Physics, Vol. 36 (Springer, Heidelberg, 1979; Mir, Moscow, 1982).

17. Y. Tawada, in *Amorphous Semiconductors: Technologies & Devices*, Ed. by Y. Hamakawa (North-Holland, Amsterdam, 1983; Metallurgiya, Moscow, 1986).

18. B. I. Shklovskiĭ and A. L. Éfros, Zh. Éksp. Teor. Fiz. **62** (3), 1156 (1972) [Sov. Phys. JETP **35**, 610 (1972)].

19. K. Kao and W. Hwang, *Electrical Transport in Solids, with Particular Reference to Organic Semiconductors* (Pergamon, Oxford, 1981; Mir, Moscow, 1983).

20. V. V. Bryksin and G. Yu. Yashin, Fiz. Tverd. Tela **23** (10), 3063 (1981) [Sov. Phys. Solid State **23**, 1785 (1981)].

21. V. L. Bonch-Bruevich, in *Abstracts VI Intern. Conference on Amorphous and Liquid Semiconductors* (Leningrad, 1976), p. 16.

22. V. P. Avramenko, A. Yu. Kudzin, L. P. Klimenko, *et al.*, in *Active Dielectrics* (Dnepropetrovsk, 1984), p. 71.

23. V. V. Volkov, Yu. F. Khomich, P. I. Perov, *et al.*, Izv. Akad. Nauk SSSR, Neorg. Mater. **25** (5), 827 (1989).

24. A. V. Egorysheva, V. V. Volkov, and M. V. Skorikov, Neorg. Mater. **31** (3), 377 (1995).

25. R. Oberschmid, Phys. Status Solidi A **89**, 263 (1985).

Translated by G. Skrebtsov

Symmetry and Anisotropic Optical Spectrum of Charge-Transfer Excitons in the Model of CuO$_2$ Plane

V. I. Cherepanov, E. N. Kondrashov, and A. S. Moskvin

Ural State University, pr. Lenina 51, Yekaterinburg, 620083 Russia
Received July 15, 1999; in final form, November 24, 1999

Abstract—A method of group-theoretical classification of excitonic states with a charge transfer from a unit cell to neighboring ones is suggested in a tetragonal two-dimensional model of a CuO$_2$ plane. The orientation (anisotropy) and polarization (pleochroism) dependences of the intensities of excitonic dipole-forbidden optical transitions are determined. The phenomenon of initiating dipole-forbidden transitions in an external electric field is theoretically considered. General dependences of the probabilities of such transitions on the value and direction of the electric field and on the light wave polarization are found. The dependences obtained can be used to identify weak absorption bands in dielectric cuprates containing CuO$_2$ planes. © *2000 MAIK "Nauka/Interperiodica".*

Tetragonal two-dimensional (2D) CuO$_2$ layers are fragments of the structures of high-temperature superconductors, such as La$_2$CuO$_{4+y}$, La$_{2-x}$Sr$_x$CuO$_4$, etc. That is why the investigation of electronic (including excitonic) excitations in a 2D model of CuO$_2$ is of great interest. A number of experimental [1–5], as well as theoretical [6–12], articles are dedicated to this question.

In the 2D model of CuO$_2$, a unit cell contains one copper atom and two oxygen atoms. There is one hole per unit cell in the ground state; according to different theoretical estimations, the state of the hole is 70–80% Cu3$d_{x^2-y^2}$ state. Light may initiate the transfer of the hole to a neighboring cell, which leads to the emergence of an empty hole state in the cell and a two-hole singlet state in a neighboring one. Electrostatic interaction binds these two states, and the translational symmetry of the lattice determines the movement of such a singlet pair through the crystal (the so-called charge-transfer exciton [12]). Overhauser [13] was the first to consider the charge-transfer exciton. No current accompanies translational exciton movement.

Since there is a spectrum of energies of two-hole states of a cell and different charge-transfer excitons will appear, depending on the type of the two-hole state generated after the crystal excitation. As a result of the transfer of a hole to one of the four neighboring cells of CuO$_2$ plane being possible, there is an additional degeneracy, which is removed due to *dp*-hybridization and electrostatic interactions. One of the goals of the present paper is to determine the symmetry of excitonic charge-transfer states, which originate at a given symmetry of the "two-hole" state Γ ($\overline{\Gamma}$ is an irreducible rep-

resentation of the $\mathcal{D}_{4h}$ point symmetry group of the 2D lattice with a copper atom in the center). Besides, it is necessary to notice that excitons connected with electronic transitions within a unit cell can exist. Such excitons are similar to Frenkel excitons in crystals and differ from the "two-cell" excitons we consider in this article.

As usual, phototransitions from the ground state of a crystal to the excitonic one can be divided into dipole-allowed and dipole-forbidden transitions. In the 2D model, the probabilities of the former transitions depend on the direction of light polarization, while those of the latter ones are also determined by the light propagation direction. The determination of the dependences of the dipole-forbidden transition probabilities on the direction of polarization (pleochroism) and light propagation (anisotropy) is another purpose of the present paper. Despite the electric quadrupole and magnetic dipole phototransition probabilities being much smaller than those of electric dipole phototransitions, they have been observed in some cases [3, 6]. Besides, the dipole-forbidden phototransitions can be investigated by means of the effect of their enhancement in the external electric field [14–18]. Recently, this effect has been found for two weak absorption peaks at 1.4 and 1.6 eV in La$_2$CuO$_{4+y}$ [18]. In Section 3 of the present paper, the orientation dependence (on the electric field direction) and the polarization dependence (on the direction of the light wave polarization) of the enhanced dipole-forbidden exciton phototransition probabilities of all types are derived in the 2D model of a CuO$_2$ layer.

1. TYPES OF SYMMETRY OF SINGLET EXCITONIC CHARGE-TRANSFER STATES IN THE 2D MODEL

The two-dimensional lattice of a CuO_2 layer possesses the symmetry group $\mathcal{D}_{4h} \times T$, where T is the group of discrete translations $\mathbf{t}_{nm} = n\mathbf{a}_x + m\mathbf{a}_y$. Here, $\mathbf{a}_x$, $\mathbf{a}_y$ are the basis vectors and n, m are integers. An example of a singlet excitonic state with the transfer of a hole from one cell to another is schematically shown in the figure. The hole transfers from the state $\psi_\uparrow^{B_{1g}}(\mathbf{R})$ (for example, it can be $Cu3d_{x^2-y^2}$ state) to a neighboring cell, and, as a result, there appears a two-hole state $\chi_M^\Gamma(\mathbf{R} + \mathbf{a}_x)$ (the structure of the last state is of no importance in what follows) and an empty-hole state $\phi^{A_{1g}}(\mathbf{R})$ corresponding to the closed-shell configuration. In the zeroth approximation, the wave-functions of the four degenerate excitonic states with the transfer of a hole from the cell $\mathbf{R}$ to the cell $\mathbf{R} + \boldsymbol{\tau}$ can be written as

$$\Psi_M^k(\boldsymbol{\tau}) = \frac{1}{\sqrt{N}}\sum_{\mathbf{R}}\exp(i\mathbf{k}\mathbf{R})\phi^{A_{1g}}(\mathbf{R})$$
$$\times\left[\chi_M^\Gamma(\mathbf{R} + \boldsymbol{\tau})\prod_{\boldsymbol{\tau}'\neq\boldsymbol{\tau}}\psi_\downarrow^{B_{1g}}(\mathbf{R} + \boldsymbol{\tau}')\right]\dots,$$

(1)

where $\boldsymbol{\tau} = \pm\mathbf{a}_x, \pm\mathbf{a}_y$. In (1), we have omitted the products of four functions $\psi_\downarrow^{B_{1g}}$ or $\psi_\uparrow^{B_{1g}}$ corresponding to the other coordination shells of the cell $\mathbf{R}$. The products for each shell are invariant with the crystal transformation under the action of the elements $\hat{g}$ of the point group $\mathcal{D}_{4h}$ with the center at an arbitrary site $\mathbf{R}$ and, therefore, can be omitted in the consideration of the symmetry properties of the functions $\Psi_M^k(\boldsymbol{\tau})$. The index Γ in (1) denotes the irreducible representation of the $\mathcal{D}_{4h}$ group with the center at the point $\mathbf{R} + \boldsymbol{\tau}$ and M enumerating the functions belonging to this representation. Considering the action of the operator $\hat{g}$ on function (1) yields

$$\hat{g}\Psi_M^k(\boldsymbol{\tau}) = [X^{B_{1g}}(\hat{g})]^3\sum_{M'}\mathcal{D}_{M'M}^{(\Gamma)}(\hat{g})\Psi_{M'}^{\hat{g}\mathbf{k}}(\hat{g}\boldsymbol{\tau}),$$

where $X^{B_{1g}}$ are the characters of the irreducible representation B_{1g}, and $\mathcal{D}^{(\Gamma)}$ are the matrices of the irreducible representation Γ of the group $\mathcal{D}_{4h}$. Since $X^{B_{1g}}(\hat{g}) = \pm 1$, we can write

$$\hat{g}\Psi_M^k(\boldsymbol{\tau}) = X^{B_{1g}}(\hat{g})\sum_{M'}\mathcal{D}_{M'M}^{(\Gamma)}(\hat{g})\Psi_{M'}^{\hat{g}\mathbf{k}}(\hat{g}\boldsymbol{\tau}). \quad (2)$$

For the elements of the point group of the wave vector $\tilde{\mathfrak{S}}_k$, we have $\hat{g}\mathbf{k} = \mathbf{k} \pm \mathbf{b}$ (where $\mathbf{b}$ is a reciprocal lattice vector); therefore, in the reduced wave-vector scheme, we can write

$$\hat{g}\Psi_M^k(\boldsymbol{\tau}) = X^{B_{1g}}(\hat{g})\sum_{M'}\mathcal{D}_{M'M}^{(\Gamma)}(\hat{g})\Psi_{M'}^{\mathbf{k}}(\hat{g}\boldsymbol{\tau}). \quad (3)$$
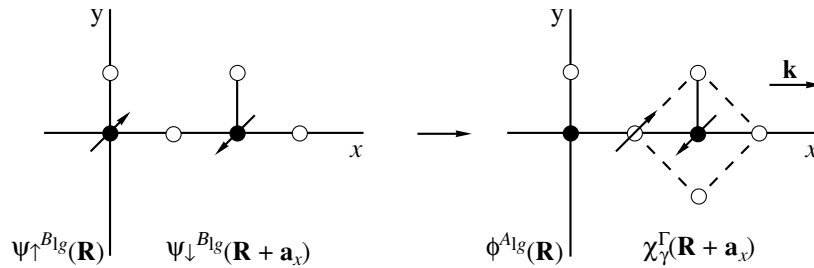
Hence, the characters of the representation Γ_{ex} constructed in terms of the basis functions (1) are

$$X^{\Gamma_{ex}}(\hat{g}) = X^{B_{1g}}(\hat{g})X^\Gamma(\hat{g})\sum_{\boldsymbol{\tau}}\delta_{\hat{g}\boldsymbol{\tau};\,\boldsymbol{\tau}}. \quad (4)$$

The sum in (4) is

$$\sum_{\boldsymbol{\tau}}\delta_{\hat{g}\boldsymbol{\tau};\,\boldsymbol{\tau}} = \begin{cases} 4, & \text{for} \quad \hat{g} = E, IC_{4z}^2 \\ 2, & \text{for} \quad \hat{g} = U_{2x}, U_{2y}, IU_{2x}, IU_{2y} \\ & \text{for the other elements} \\ 0, & \text{of the group } \mathcal{D}_{4h}. \end{cases}$$

The center of the Brillouin zone $\mathbf{k} = 0$, for which we have $\tilde{\mathfrak{S}}_{\mathbf{k}=0} = \mathcal{D}_{4h}$, is particularly interesting. Determining the characters of Γ_{ex} with the aid of (4) and reducing

$$\psi_\uparrow^{B_{1g}}(\mathbf{R}) \qquad \psi_\downarrow^{B_{1g}}(\mathbf{R} + \mathbf{a}_x) \qquad \phi^{A_{1g}}(\mathbf{R}) \qquad \chi_\gamma^\Gamma(\mathbf{R} + \mathbf{a}_x)$$

The formation of a charge-transfer exciton. A hole transfers between the ions of copper and oxygen. The empty hole and two-hole states of the neighboring cells are coupled and move through the lattice. The black circle corresponds to copper; the light one, to oxygen. The ground state is on the left, and the excitonic state is on the right.

Γ_{ex} into a set of irreducible representations of the group $\mathcal{D}_{4h}$, we find the types of excitonic states with $\mathbf{k} = 0$

$$\Gamma = A_{1g}, B_{1g}: \Gamma_{ex} = A_{1g} + B_{1g} + E_u;$$

$$\Gamma = A_{2g}, B_{2g}: \Gamma_{ex} = A_{2g} + B_{2g} + E_u;$$

$$\Gamma = E_g: \Gamma_{ex} = A_{1u} + A_{2u} + B_{1u} + B_{2u} + 2E_g;$$

$$\Gamma = A_{1u}, B_{1u}: \Gamma_{ex} = A_{1u} + B_{1u} + E_g; \qquad (5)$$

$$\Gamma = A_{2u}, B_{2u}: \Gamma_{ex} = A_{2u} + B_{2u} + E_g;$$

$$\Gamma = E_u: \Gamma_{ex} = A_{1g} + A_{2g} + B_{1g} + B_{2g} + 2E_u.$$

Using (4), it is easy to carry out the group-theoretical classification of the states for any symmetry point in the Brillouin zone. Besides, the level splitting caused by a displacement from a more symmetric to a less symmetric point can be easily determined. For example, the following level splitting takes place as a result of a displacement from the zone center along a C_{2v} axis: $A_{1g}(B_{1g}) \longrightarrow A_1$, $A_{2g}(B_{2g}) \longrightarrow B_1$, $E_g \longrightarrow A_2 + B_2$, $A_{1u}(B_{1u}) \longrightarrow A_2$, $A_{2u}(B_{2u}) \longrightarrow B_2$, and $E_u \longrightarrow A_1 + B_1$ (the irreducible representations of the group of the wave vector C_{2v} are indicated on the right-hand side).

The proper wave functions of the excitonic states are linear combinations of functions (1):

$$\Psi_{\tilde{M}}^{\tilde{\Gamma}}(\mathbf{k}) = \frac{1}{\sqrt{N}} \sum_\tau \sum_M C_{\tilde{M}M,\tau}^{\tilde{\Gamma}\Gamma}(\mathbf{k}) \sum_\mathbf{R} \exp(i\mathbf{k}\mathbf{R})$$

$$\times \phi^{A_{1g}}(R) \left[\chi_M^\Gamma(\mathbf{R}+\boldsymbol{\tau}) \prod_{\tau' \neq \tau} \psi_\downarrow^{B_{1g}}(\mathbf{R}+\boldsymbol{\tau}') \right] \dots . \qquad (6)$$

The coefficients C can be determined only by diagonalizing the Hamiltonian. In what follows, we shall not need explicit expressions of the functions $C_{\tilde{M}M,\tau}^{\tilde{\Gamma}\Gamma}(\mathbf{k})$. In the particular case of an excitation like $b_{1g\uparrow}$, $b_{1g\downarrow} \longrightarrow b_{1g}^0 ({}^1A_{1g})$, $b_{1g}^2 ({}^1A_{1g})$ which leads to the formation of the Zhang–Rice singlet ${}^1A_{1g}$, one can derive from (5) that $\Gamma_{ex} = A_{1g} + B_{1g} + E_u$. This coincides with the result of [12], where these states are denoted $S + D + (P_1, P_2)$, respectively. However, aside from ${}^1A_{1g}$, other "two-hole" singlet states of the CuO_4 system are possible, in particular, ${}^1A_{2g}$, ${}^1B_{1g}$, ${}^1B_{2g}$, ${}^1E_g$, etc. (see [18]). For each of them, according to the reduction (5), a set of excitonic energy levels must exist at $\mathbf{k} = 0$. In accordance with the calculations in [11], excitonic states of the type $\tilde{\Gamma} = A_{2g}$, B_{1g}, and E_u must be within the charge-transfer gap. Besides, current-free exciton-like excitations above the charge-transfer gap were observed in electron energy loss experiments on $Sr_2Cl_2CuO_2$ [4, 12].

2. ANISOTROPY AND PLEOCHROISM OF EXCITONIC PHOTOTRANSITIONS

The wave function of the ground state of the system is

$$\Psi_0 = \psi_\uparrow^{B_{1g}}(\mathbf{R}) \left[\prod_\tau \psi_\downarrow^{B_{1g}}(\mathbf{R}+\boldsymbol{\tau}) \right] \dots, \qquad (7)$$

where we have omitted the products of the functions $\psi_\uparrow^{B_{1g}}$ and $\psi_\downarrow^{B_{1g}}$ for more distant copper atoms relative to the lattice site $\mathbf{R}$. Obviously, the wave function Ψ_0 is transformed on B_{1g} under the action of $\hat{g} \in \mathcal{D}_{4h}$. The probability of the optical transition from the ground to the excitonic state of the $\tilde{\Gamma}(\mathbf{k})$ type is defined by the expression

$$W(0 \longrightarrow \tilde{\Gamma}(\mathbf{k})) = \alpha(\omega) \sum_{\tilde{M}} \left| \langle \Psi_{\tilde{M}}^{\tilde{\Gamma}}(\mathbf{k}) | \hat{H}_{eR} | \Psi_0 \rangle \right|^2, \qquad (8)$$

where $\alpha(\omega) = (2\pi/\hbar)\rho(\omega)$, $\rho(\omega)$ is the density of states for the transition frequency ω, and $\hat{H}_{eR}$ is

$$\hat{H}_{eR} = -\frac{e}{mc} \sum_j (\mathbf{A}(\mathbf{r}_j)\hat{\mathbf{p}}_j) \qquad (9)$$

in the linear approximation in $\mathbf{A}$. Here, $\mathbf{A}$ is the vector potential of the electromagnetic field and $\hat{\mathbf{p}}_j$ is the momentum operator of electron j of the system. We suppose that

$$\mathbf{A}(\mathbf{R}) = A_0 \exp(i\mathbf{q}\mathbf{R})\boldsymbol{\xi}, \qquad (10)$$

where $\boldsymbol{\xi}$ is the unit polarization vector of the light wave. Substituting (6), (9), and (10) into the matrix element (8) yields

$$\langle \Psi_{\tilde{M}}^{\tilde{\Gamma}}(\mathbf{k}) | \hat{H}_{eR} | \Psi_0 \rangle = -\frac{e}{mc} A_0 \frac{1}{\sqrt{N}} \sum_\tau \sum_M \sum_\mathbf{R} C_{\tilde{M}M,\tau}^{*\tilde{\Gamma}\Gamma}(\mathbf{k})$$

$$\times \exp(-i\mathbf{k}\mathbf{R}) \Big\langle \phi^{A_{1g}}(R) \Big[\chi_M^\Gamma(\mathbf{R}+\boldsymbol{\tau})$$

$$\times \prod_{\tau' \neq \tau} \psi_\downarrow^{B_{1g}}(\mathbf{R}+\boldsymbol{\tau}') \Big] \dots \Big| \sum_j \exp(i\mathbf{q}\mathbf{r}_j)(\boldsymbol{\xi}\hat{\mathbf{p}}_j) \Big| \Psi_0 \Big\rangle.$$

It should be noted that, on the left- and right-hand sides of this expression, multielectron wave functions are involved that depend on the electron coordinates $\mathbf{r}_j$ (the function $\phi^{A_{1g}}(\mathbf{R})$, which in turn depend on the differences $(\mathbf{r}_j - \mathbf{R})$. Similarly, the function $\chi_M^\Gamma(\mathbf{R}+\boldsymbol{\tau})$ depends on $(\mathbf{r}_j - (\mathbf{R}+\boldsymbol{\tau}))$. Making the substitution of

variable ($\mathbf{r}_j \longrightarrow \mathbf{r}_j + \mathbf{R}$) and taking into account the invariance of Ψ_0 under translation by $\mathbf{R}$ yields

$$\langle \Psi_{\tilde{M}}^{\tilde{\Gamma}}(\mathbf{k})|\hat{H}_{eR}|\Psi_0\rangle = \frac{B}{\sqrt{N}}\sum_{\mathbf{R}}\exp(i(\mathbf{q}-\mathbf{k})\mathbf{R})$$

$$\times \sum_{\tau}\sum_{M}C_{\tilde{M}M,\tau}^{*\tilde{\Gamma}\Gamma}(\mathbf{k})\left\langle \phi^{A_{1g}}(0)\left[\Psi_M^{\Gamma}(\tau)\right.\right.$$

$$\times \prod_{\tau'\neq\tau}\psi_{\downarrow}^{B_{1g}}(\tau')\right]\ldots\left|\sum_j\exp(i\mathbf{q}\mathbf{r}_j)(\xi\hat{\mathbf{p}}_j)\left|\Psi_0\right\rangle,$$

where $B = -(eA_0)/(mc)$. The sum $\sum_{\mathbf{R}}\exp(i(\mathbf{q}-\mathbf{k})\mathbf{R}) = N\delta_{\mathbf{k};\mathbf{q}}$ leads to the phototransition selection rule: $\mathbf{k} = \mathbf{q}$.

Taking into consideration the condition $q \ll 1/a$ for visible and IR region and expanding the exponent in power series in $\mathbf{q}$ up to terms of the first order, we find

$$\langle \Psi_{\tilde{M}}^{\tilde{\Gamma}}(\mathbf{k})|\hat{H}_{eR}|\Psi_0\rangle = B\sqrt{N}\delta_{\mathbf{k};\mathbf{q}}\sum_{\tau}\sum_{M}C_{\tilde{M}M,\tau}^{*\tilde{\Gamma}\Gamma}(\mathbf{q})$$

$$\times \left\langle \phi^{A_{1g}}(0)\left[\Psi_M^{\Gamma}(\tau)\prod_{\tau'\neq\tau}\psi_{\downarrow}^{B_{1g}}(\tau')\right]\ldots|(\xi\hat{\mathbf{P}})\right. \tag{11}$$

$$+ i\sum_j(\mathbf{q}\mathbf{r}_j)(\xi\hat{\mathbf{p}}_j)|\Psi_0\rangle,$$

where $\hat{\mathbf{P}} = \sum_j\hat{\mathbf{p}}_j$. After common mathematical manipulation (see, e.g., [19, 20]), we obtain

$$\langle \Psi_{\tilde{M}}^{\tilde{\Gamma}}(\mathbf{k})|\hat{H}_{eR}|\Psi_0\rangle = -i\frac{m\omega}{e}B\delta_{\mathbf{k};\mathbf{q}}$$

$$\times \left\langle \Psi_{\tilde{M}}^{\tilde{\Gamma}}(\mathbf{q})\left|\sum_{\alpha}\xi_{\alpha}\mathscr{D}_{\alpha} + i\sum_{\alpha\beta}q_{\alpha}\xi_{\beta}Q_{\alpha\beta}\right. \tag{12}$$

$$+ \frac{e}{2m\omega}\sum_{\alpha}[q\times\xi]_{\alpha}\hat{\mathcal{M}}_{\alpha}\left|\Psi_0\right\rangle,$$

where $\mathscr{D} = -e\sum_j\mathbf{r}_j$ is the electric dipole moment, $Q_{\alpha\beta} = -(e/2)\sum_j r_{j\alpha}r_{j\beta}$ is the electric quadrupole moment, and $\hat{\mathcal{M}} = \sum_j\hat{\mathcal{M}}_j$ is the magnetic moment of the system. In deriving (12), we have taken into account that the matrix element does not depend on the choice of the zeroth lattice site 0; that is, it is possible to replace 0 by $\mathbf{R}$ and introduce the summation $(1/N)\sum_{\mathbf{R}}$.

Since the condition $q \ll (1/a)$ takes place, we can replace $\delta_{\mathbf{k};\mathbf{q}}$ by $\delta_{\mathbf{k};0}$, thus obtaining from (8) and (12)

$$W(0 \longrightarrow \tilde{\Gamma}(0)) = \gamma(\omega)\sum_{\tilde{M}}\left|\left\langle \Psi_{\tilde{M}}^{\tilde{\Gamma}}(0)\right|\sum_{\alpha}\xi_{\alpha}\mathscr{D}_{\alpha}\right.$$

$$+ i\sum_{\alpha\beta}q_{\alpha}\xi_{\beta}Q_{\alpha\beta} + \frac{e}{2m\omega}\sum_{\alpha}[q\times\xi]_{\alpha}\hat{\mathcal{M}}_{\alpha}\left|\Psi_0^{B_{1g}}\right\rangle\right|^2, \tag{13}$$

where $\gamma(\omega) = \alpha(\omega)\omega^2(A^2/c^2)$. Although the function $\Psi_{\tilde{M}}^{\tilde{\Gamma}}(\mathbf{q})$ is generally not analytic at the point $q = 0$, it can be expanded in powers of q at a given q direction. It is easy to prove that the sum in (13) does not depend on the direction of q as it tends to zero.

2.1. Electric Dipole Transitions

In view of the fact that $\mathscr{D}_x$ and $\mathscr{D}_y$ transform according to E_u, and $\mathscr{D}_z$ according to A_{2u}, the electric dipole transitions from the B_{1g}-type ground state are possible only to the state $\tilde{\Gamma} = E_u$ or B_{2u}. Retaining only the electric dipole contribution, we obtain from (13) the formulas

$$W(0 \longrightarrow E_u(0)) = \gamma(\omega)C_2^2(\xi_x^2 + \xi_y^2);$$
$$W(0 \longrightarrow B_{2u}(0)) = \gamma(\omega)C_1^2\xi_z^2, \tag{14}$$

where

$$C_1 = |\langle B_{2u}(0)|\mathscr{D}_z|B_{1g}\rangle|,$$
$$C_2 = |\langle E_u(0)\|\mathscr{D}\|B_{1g}\rangle|.$$

2.2. Dipole-Forbidden Transitions

Introducing the irreducible components $Q^{A_{1g}} = Q_{zz}$, $Q^{A_{1g}'} = Q_{xx} + Q_{yy}$, $Q^{B_{1g}} = Q_{xx} - Q_{yy}$, $Q^{B_{2g}} = Q_{xy}$, $Q_{1,2}^{E_g} = (Q_{xz}, Q_{yz})$, $M^{A_{2g}} = M_z$, and $M_{1,2}^{E_g} = (M_x, M_y)$ we find

$$\sum_{\alpha\beta}q_{\alpha}\xi_{\beta}Q_{\alpha\beta} = \frac{1}{2}q_x\xi_x(Q^{A_{1g}'} + Q^{B_{1g}})$$

$$+ \frac{1}{2}q_y\xi_y(Q^{A_{1g}'} - Q^{B_{1g}}) + q_z\xi_zQ^{A_{1g}} + (q_x\xi_y + q_y\xi_x)Q^{B_{2g}}$$

$$+ (q_x\xi_z + q_z\xi_x)Q_1^{E_g} + (q_y\xi_z + q_z\xi_y)Q_2^{E_g}.$$

We also have

$$\sum_{\alpha}[\mathbf{q}\times\xi]_{\alpha}\hat{\mathcal{M}}_{\alpha} = (q_y\xi_z - q_z\xi_y)\hat{\mathcal{M}}_x^{E_g}$$

$$+ (q_z\xi_x - q_x\xi_z)\hat{\mathcal{M}}_y^{E_g} + (q_x\xi_y - q_y\xi_x)\hat{\mathcal{M}}_z^{A_{2g}}.$$

Applying the Wigner–Eckart–Koster theorem and using the tables of Clebsch–Gordan coefficients for the group $\mathscr{D}_{4h}$ yields

$$W(0 \longrightarrow A_{1g}(0)) = \gamma(\omega)\frac{C_3^2}{4}(q_x\xi_x - q_y\xi_y)^2;$$

$$W(0 \longrightarrow A_{2g}(0)) = \gamma(\omega)C_4^2(q_x\xi_y + q_y\xi_x)^2;$$

$$W(0 \longrightarrow B_{1g}(0)) = \gamma(\omega)\left|\frac{C_5}{2}(q_x\xi_x + q_y\xi_y) + C_6 q_z\xi_z\right|^2;$$

$$W(0 \longrightarrow B_{2g}(0)) = \gamma(\omega)\left(\frac{e}{2m\omega}\right)^2 C_7^2(q_x\xi_y - q_y\xi_x)^2; \quad (15)$$

$$W(0 \longrightarrow E_g(0)) = \gamma(\omega)\{C_{11}^2[(q_x\xi_z + q_z\xi_x)^2$$

$$+ (q_y\xi_z + q_z\xi_y)^2] + \left(\frac{e}{2m\omega}\right)^2 |C_{10}|^2$$

$$\times [(q_x\xi_z - q_z\xi_x)^2 + (q_y\xi_z - q_z\xi_y)^2]\},$$

where $C_{11}^2 = C_8^2 + C_9^2$. The constants C_7^2 and $|C_{10}|^2$ contain only the magnetic dipole (MD) contribution, and the other constants C_i^2 involve only the electric quadrupole (EQ) one. We do not quote the explicit expressions for these constants here. In calculating $W(0 \longrightarrow E_g(0))$, we have neglected the mixed EQ–MD contribution.

The above formulas describe the orientation dependence (on the **q** direction) and polarization dependence (on the **ξ** direction) of the probabilities of the dipole-forbidden phototransitions of all types, $E_0(B_{1g}) \longrightarrow E_{\tilde{T}}(0)$. It can be seen from (15) that various types of transitions have different orientation and polarization dependences. Therefore, the formulas we obtained here can be used in spectroscopic investigations to identify the transitions.

3. THE EFFECT OF AN EXTERNAL ELECTRIC FIELD ON DIPOLE-FORBIDDEN PHOTOTRANSITIONS

Electric dipole transitions from the B_{1g}-type ground state to even-parity excitonic states $\tilde{\Gamma}(0) = \Gamma_g(0)$ are forbidden. However, in an external electric field $\mathscr{E}$, the odd states $\Psi_{M'}^{\Gamma_u}(0)$ are mixed with the excitonic $\Psi_M^{\Gamma_g}(0)$ and the ground state $\Psi_0^{B_{1g}}$. In the first order perturbation theory, we have

$$\Psi_M = \Psi_M^{\Gamma_g}(0) + \sum_{\Gamma_u M'} \frac{\langle\Gamma_u M'|e\mathscr{E}\mathbf{R}|\Gamma_g M\rangle}{\Delta(\Gamma_u; \Gamma_g)}\Psi_{M'}^{\Gamma_u}(0),$$

$$\Psi_0 = \Psi_0^{B_{1g}} + \sum_{\Gamma_u M'} \frac{\langle\Gamma_u M'|e\mathscr{E}\mathbf{R}|0B_{1g}\rangle}{\delta(\Gamma_u; 0)}\Psi_{M'}^{\Gamma_u}(0),$$

where

$$\Delta(\Gamma_u; \Gamma_g) = E_{\Gamma_u}(0) - E_{\Gamma_g}(0),$$

$$\delta(\Gamma_u; 0) = E_{\Gamma_u}(0) - E_0,$$

$$\mathbf{R} = \sum_j \mathbf{r}_j.$$

In the first order in $\mathscr{E}$, the electric-dipole transition matrix element is

$$\langle\Psi_M|\mathscr{E}\mathfrak{D}|\Psi_0\rangle = -e\langle\Psi_M|\xi\mathbf{R}|\Psi_0\rangle$$

$$= -e^2\sum_{\Gamma_u M'}\left[\frac{\langle\Gamma_g M|\mathscr{E}\mathbf{R}|\Gamma_u M'\rangle\langle\Gamma_u M'|\xi\mathbf{R}|0B_{1g}\rangle}{\Delta(\Gamma_u; \Gamma_g)}\right.$$

$$\left.+ \frac{\langle\Gamma_g M|\xi\mathbf{R}|\Gamma_u M'\rangle\langle\Gamma_u M'|\mathscr{E}\mathbf{R}|0B_{1g}\rangle}{\delta(\Gamma_u; 0)}\right].$$

Using the Wigner–Eckart–Koster theorem, for the electric-dipole transition probabilities

$$W(0 \longrightarrow \Gamma_g(0)) = \gamma(\omega)\sum_M\left|\langle\Psi_M|\xi\mathfrak{D}|\Psi_0^{B_{1g}}\rangle\right|^2,$$

we obtain the following expressions:

$$W(0 \longrightarrow A_{1g}(0)) = \gamma(\omega)\frac{e^4}{2}J_1^2(A_{1g})(\mathscr{E}_x\xi_x - \mathscr{E}_y\xi_y)^2,$$

$$W(0 \longrightarrow A_{2g}(0)) = \gamma(\omega)\frac{e^4}{2}J_2^2(A_{2g})(\mathscr{E}_x\xi_y + \mathscr{E}_y\xi_x)^2,$$

$$W(0 \longrightarrow B_{1g}(0)) = \gamma(\omega)e^4$$

$$\times\left[\frac{J_3(B_{1g})}{\sqrt{2}}(\mathscr{E}_x\xi_x + \mathscr{E}_y\xi_y) + K(B_{1g})\mathscr{E}_z\xi_z\right]^2,$$

$$W(0 \longrightarrow B_{2g}(0)) = \gamma(\omega)\frac{e^4}{2}J_5^2(B_{2g})(\mathscr{E}_x\xi_y - \mathscr{E}_y\xi_x)^2,$$

$$W(0 \longrightarrow E_g(0)) = \gamma(\omega)e^4[J_6^2\mathscr{E}_z^2(\xi_x^2 + \xi_y^2) \quad (16)$$

$$+ J_7^2(\mathscr{E}_x^2 + \mathscr{E}_y^2)\xi_z^2 + 2J_8\mathscr{E}_z\xi_z(\mathscr{E}_x\xi_x + \mathscr{E}_y\xi_y)],$$

where

$$J_i(\Gamma_g) = \sum_{E_u}F(\Gamma_g; E_u)\left[\frac{1}{\Delta(E_u; \Gamma_g)} \pm \frac{1}{\delta(E_u; 0)}\right]$$

("+" $i = 1, 2, 3, 4$; "−" $i = 5$),

$$F(\Gamma_g; E_u) = \langle\Gamma_g\|\mathbf{R}\|E_u\rangle\langle E_u\|\mathbf{R}\|0B_{1g}\rangle,$$

$$K(B_{1g}) = \sum_{B_{2u}} F(B_{1g}; B_{2u}) \left[\frac{1}{\Delta(B_{2u}; B_{1g})} \pm \frac{1}{\delta(B_{2u}; 0)} \right],$$

$$F(B_{1g}; B_{2u}) = \langle B_{1g} \| \mathbf{R} \| B_{2u} \rangle \langle B_{2u} \| \mathbf{R} \| 0 B_{1g} \rangle.$$

We do not present the expressions for the parameters J_6, J_7, and J_8, because they are cumbersome. The results for some particular configurations of $\mathscr{E}$ and ξ are listed in the table. It should be noted that, when calculating $W(0 \longrightarrow E_g(0))$, we neglected the splitting of the energy level $E_g(0)$ in the electric field; that is, the total intensity of the splitting components was determined.

The transition probabilities presented in the table are consistent with the selection rules established in [18], but the transition to the A_{2g}-type excitonic state was neglected in that paper. With reference to theoretical calculations [21], the authors of [18] believed that the transition to the A_{2g} state is out of the charge-transfer gap and, therefore, cannot be observed. However, various theoretical calculations lead to different results. For example, the calculation in the six-band Habbard model [11] shows that it is the A_{2g} state that must be the lowest excitonic state below the edge of the charge-transfer band. Thus, the transition $0 \longrightarrow A_{2g}(0)$ should not be excluded from consideration.

An enhancement of two absorption peaks in the electric field at 1.4 eV (at $\mathscr{E} \perp C_4$) and 1.6 eV (at $\mathscr{E} \| C_4$), found by the electroreflection method, was reported in [18] for La_2CuO_{4+y} ($y = 0.016$). The authors of that paper unambiguously identified these peaks with the transitions $B_{1g} \longrightarrow B_{2g}$ and $B_{1g} \longrightarrow E_g$, respectively. However, the first identification is questionable, because there are two allowed transitions, $B_{1g} \longrightarrow B_{2g}$ and $B_{1g} \longrightarrow A_{2g}$, at $\mathscr{E} \| x, \xi \| y$ (or at $\mathscr{E} \| y, \xi \| x$).

In order to distinguish these two transitions, we suggest making an experiment in which the electric field $\mathscr{E}$ is directed along the bisectrix between the x and y axes and the plane of polarization is rotated around the z axis (the light beam must be perpendicular to the CuO_2 planes). For this case, we obtain from (16)

$$W(0 \longrightarrow A_{2g}(0)) = \frac{e^4}{2} \gamma(\omega) J_2^2 \mathscr{E}^2 \cos^2(\phi);$$

$$W(0 \longrightarrow B_{2g}(0)) = \frac{e^4}{2} \gamma(\omega) J_5^2 \mathscr{E}^2 \sin^2(\phi),$$

where ϕ is the angle between ξ and $\mathscr{E}$. Therefore, the polarization dependences for A_{2g} and B_{2g} are different.

Thus, we performed a symmetry analysis of the singlet excitonic states for a two-dimensional CuO_2 crystal transferring a hole from one unit cell to the nearest neighboring ones, which leads to the formation of "two-hole" states in the cells. A group-theoretical method is suggested for describing excitonic singlet

The probabilities of dipole-forbidden phototransitions $E_0(B_{1g}) \longrightarrow E_{\Gamma_g}(0)$ induced by an electric field $\mathscr{E}$ ($\Phi = (1/2)\gamma(\omega)e^4$)

$\mathscr{E}\xi$	ξ_x	ξ_y	ξ_z
$\mathscr{E}_x$	$W(A_{1g}) = \Phi J_1^2 \mathscr{E}^2$	$W(A_{2g}) = \Phi J_2^2 \mathscr{E}^2$	$W(E_g) = 2\Phi J_7^2 \mathscr{E}^2$
	$W(B_{1g}) = \Phi J_3^2 \mathscr{E}^2$	$W(B_{2g}) = \Phi J_5^2 \mathscr{E}^2$	
$\mathscr{E}_y$	$W(A_{2g}) = \Phi J_2^2 \mathscr{E}^2$	$W(A_{1g}) = \Phi J_1^2 \mathscr{E}^2$	$W(E_g) = 2\Phi J_7^2 \mathscr{E}^2$
	$W(B_{bg}) = \Phi J_5^2 \mathscr{E}^2$	$W(B_{1g}) = \Phi J_3^2 \mathscr{E}^2$	
$\mathscr{E}_z$	$W(E_g) = 2\Phi J_6^2 \mathscr{E}^2$	$W(E_g) = 2\Phi J_6^2 \mathscr{E}^2$	$W(B_{1g}) = 2\Phi J_4^2 \mathscr{E}^2$

Note: Small EQ and MD contributions, which do not depend on the field $\mathscr{E}$, are omitted.

states for an arbitrary wave vector $\mathbf{k}$. This method allows one to qualitatively examine calculations of the positions and dispersion of the charge-transfer exciton energy bands in a 2D model. The formulas derived in this paper for the dependences of the probabilities of the dipole-forbidden phototransitions to the excitonic states of different symmetry on the propagation and polarization direction of the light wave can be used for the unambiguous identification of these transitions.

The influence of an external electric field on dipole-forbidden phototransitions is theoretically considered, and the orientation and polarization dependences of various enhanced transitions are determined in the 2D model. These dependences are not the same for different types of the transitions. It is shown that the identification of the enhanced absorption peak at 1.4 eV in La_2CuO_4, with the transition $B_{1g} \longrightarrow B_{2g}$ made in [18], is ambiguous. A modification of the experiment, allowing to distinguish the transition $B_{1g} \longrightarrow B_{2g}$ from $B_{1g} \longrightarrow A_{2g}$, is suggested.

Although the present work is dedicated to charge-transfer excitons, the polarization and orientation dependences obtained in Sections 2 and 3 have a more general meaning, because they are dictated only by the symmetry of excitonic states. In particular, these dependences are valid for one-cell Frenkel excitons.

When interpreting spectroscopic data in La_2CuO_4 and other compounds containing CuO_2 planes, the formulas derived in this paper will enable one to identify the excitonic excitations more completely and exactly.

REFERENCES

1. J. P. Falck, A. Levy, M. A. Kastner, *et al.*, Phys. Rev. Lett. **69**, 1109 (1992).
2. J. D. Perkins, J. M. Graybeal, M. A. Kastner, *et al.*, Phys. Rev. Lett. **71**, 1621 (1993).
3. R. Liu, D. Salamon, M. V. Klein, *et al.*, Phys. Rev. Lett. **71**, 3709 (1993).

4. Y. Y. Wang, F. C. Zhang, V. P. Dravid, *et al.*, Phys. Rev. Lett. **77**, 1809 (1996).

5. J. Fink, R. Neudert, H. C. Schmelz, *et al.*, Physica B (Amsterdam) **237**–**238**, 93 (1997).

6. F. C. Zhang and T. M. Rice, Phys. Rev. B **37**, 3759 (1988).

7. C.-X. Chen, H.-B. Schüttler, and A. J. Fedro, Phys. Rev. B **41**, 2581 (1990).

8. J. Wagner, W. Hanke, and D. Scalapino, Phys. Rev. B **43**, 10517 (1991).

9. V. I. Belinicher, A. L. Chernyshev, and L. V. Popovich, Phys. Rev. B **50**, 13768 (1994).

10. C. Vermeulen and W. Barford, Cond-mat/9502096, 23 Feb. (1995).

11. M. E. Simon, A. A. Aligia, C. D. Batista, *et al.*, Phys. Rev. B **54**, R3780 (1996).

12. F. C. Zhang and K. K. Ng, Cond-mat/9804072, 6 Apr. (1998).

13. A. W. Overhauser, Phys. Rev. **101**, 1702 (1956).

14. V. I. Cherepanov, Fiz. Tverd. Tela (Leningrad) **3**, 2183 (1961) [Sov. Phys. Solid State **3**, 1583 (1961)]; V. I. Cherepanov, V. V. Druzhinin, Yu. A. Kargapolov, *et al.*, Fiz. Tverd. Tela (Leningrad) **3**, 2987 (1961) [Sov. Phys. Solid State **3**, 2179 (1961)].

15. S. A. Moskalenko and A. I. Bobrysheva, Fiz. Tverd. Tela (Leningrad) **4**, 1994 (1962) [Sov. Phys. Solid State **4**, 1994 (1962)].

16. E. F. Gross, B. P. Zaharchenya, and L. M. Kanskaya, Fiz. Tverd. Tela (Leningrad) **3**, 972 (1961) [Sov. Phys. Solid State **3**, 706 (1961)].

17. J. L. Deiss, A. Daunois, and S. Nikitine, Solid State Commun. **8**, 521 (1970); J. L. Deiss and A. Daunois, Surf. Sci. **37**, 804 (1973).

18. J. P. Falck and J. D. Perkins, Phys. Rev. B **49**, 6246 (1994).

19. D. I. Blokhintsev, *Fundamentals of Quantum Mechanics* (Nauka, Moscow, 1983).

20. A. G. Zhilich, V. I. Cherepanov, and Yu. A. Kargapolov, Fiz. Tverd. Tela (Leningrad) **3**, 1812 (1961) [Sov. Phys. Solid State **3**, 1317 (1961)].

21. H. Eskes, L. H. Tjeng, and G. A. Sawatzky, Phys. Rev. B **41**, 288 (1990).

Translated by A. Pushnov

Anisotropy and Scale Effect in the Microhardness of Crystals of Bi-Based Superconducting Phases

V. N. Osipov, V. N. Gurin, L. I. Derkachenko, and I. N. Zimkin

Ioffe Physicotechnical Institute, Russian Academy of Sciences, Politekhnicheskaya ul. 26, St. Petersburg, 194021 Russia
Received July 12, 1999; in final form, October 18, 1999

Abstract—Microhardness studies are carried out on the (001) plane of faceted crystals of the $Bi_2Sr_2CuO_6$ (2201) and $Bi_2Sr_2CaCu_2O_8$ (2212) phases with the help of a Knoop indenter. Peculiarities in the effect produced on the microhardness by the indenter orientation relative to crystal faces, the presence of lead in the structure, and the force applied to the indenter (scale effect) are detected. It is found that crystals of the 2212 phase exhibit the strongest dependence of the microhardness on the above factors. © 2000 MAIK "Nauka/Interperiodica".

The number of publications devoted to physical and mechanical properties of high-T_c superconducting (HTSC) crystals based on bismuth is much smaller than that in which the properties associated with superconductivity are studied. The strength characteristics can be helpful for studying the physical and mechanical properties of complex compounds, such as conductors of the composition $Bi_2Sr_2Ca_2Cu_3O_{10}/Ag$ (2223/Ag) or devices based on HTSC crystals. On the other hand, the values of these characteristics may correlate with the state of the structure [1].

The method of microhardness is a widely used tool for studying physical and mechanical properties. It is especially helpful for small-sized objects (such as HTSC crystals) for which it is difficult to measure strength parameters by using other methods. The microhardness of HTSC materials was studied mainly on Y- and Bi-based superconductors with the help of a Vickers pyramid [2–6].

In the microhardness measurements in the range of small loads, the scale effect, i.e., the dependence of microhardness on the load, is observed. A possible reason behind the scale effect is the elastic relaxation of the material (elastic restoration of the imprint), since hardness is usually calculated from the diagonal of the indenter imprint after the removal of loading. On the other hand, the microhardness under small loads can be affected by strengthening of the material as a result of plastic deformation under the indenter.

In the present communication, the microhardness H_K, the polar anisotropy P_K (type I anisotropy) of microhardness, and the scale effect are studied on the (001) plane of faceted (idiomorphic) crystals of the superconducting Bi-based phases $Bi_2Sr_2CuO_6$ (2201) and $Bi_2Sr_2CaCu_2O_8$ (2212) (the BSCCO system) with the help of a Knoop pyramid, since in this case microhardness is most sensitive to the anisotropy of physical and mechanical properties of the crystal structure [7,

8]. The microhardness anisotropy of $Bi_2Sr_2Ca_2Cu_3O_{10}$ crystals was investigated in [9].

1. EXPERIMENTAL TECHNIQUE

We synthesized the crystals of the HTSC phases of the BSCCO system from a solution in a KCl melt by using the preliminarily formed compounds (precursors) and isothermal holding conditions [10]. The second precursor for obtaining 2201 crystals was CuO.

The phase composition of the synthesis products and the crystal lattice parameters of superconducting phases were determined from the results of analyzing X-ray diffraction patterns obtained on a DRON-2.0 X-ray diffractometer ($FeK_\alpha = 1.937$ Å) by a standard method [11].

The microhardness of crystals selected with the help of an optical microscope was studied on a PMT-3 instrument by measuring the longer diagonal of the imprint made by the Knoop pyramid [12] and having the shape of a rhombus extended along one of its diagonals. The maximum load applied to the indenter was $\cong 0.03N(3g)$ in view of a low microhardness and small sizes of the crystals of the superconducting phases, while the minimum load was $0.01N(1g)$. The time of drawing the indenter to the surface was 15 s and the time of holding under the load was 10 s. The imprints were made so that the longer diagonal lied in the (001) plane of the crystal at angles 0, 45°, and 90° to the {100} faces of the crystals of the 2201 and 2212 phases.

2. DISCUSSION OF RESULTS

The data presented in Table 1 show that when a part of Bi is replaced by Pb, the values of the crystal lattice parameters a and b for the superconductors of the 2201 and 2212 phases become closer. This is apparently due to the lowering of the distortion level of the crystal lat-

Table 1. Crystal lattice parameters for superconducting phases of the BSCCO system depending on the composition and the presence of lead in the structure

Phase	Presence of Pb	a (Å)	b (Å)	c (Å)
2201	–	5.396	5.434	24.64
	+	5.372	5.383	24.52
2212	–	5.390	5.403	30.84
	+	5.377	5.384	30.75

tice of the HTSC phases. This assumption is also confirmed by an analysis of the structure of Bi-based HTSC phases with the help of a high-resolution microscope [13, 14]. It was found that a partial substitution of lead for bismuth leads to a decrease in the intensity of the modulation of the atomic spacing observed in the crystal lattice of this family of HTSC crystals, down to its complete suppression.

The results of microhardness measurements are presented in Table 2. According to these results, the value of H_K of crystals belonging to the BSCCO system is affected by the phase composition and partial substitution of lead for bismuth. For a load equal to 0.03N, the microhardness of the crystals of the 2212 phase is close to the values obtained in [2, 7] for large loads applied to the indenter. The maximum changes in H_K introduced by the addition of lead are observed for crystals of the 2212 phase, which is apparently due to the considerable effect of substitution on the increase in the activation energy for the motion of dislocations in spite of a decrease in the distortion of the structure. Shen

et al. [15] observed edge and screw dislocations, as well as combinations of these dislocations in the structure of the 2212 phase of the BSCCO system. Shen *et al.* [15] considered the double planes of Bi atoms, as well as the planes between Ca- and CuO layers as slip planes.

The data presented in Table 2 point to the existence of polar anisotropy in the microhardness of crystals, which is especially strong for crystals of the 2212 phase. The introduction of lead to the structure of the 2212 phase results in a change in the orientation of the indenter for which the microhardness H_K has the minimum values, while the direction for H_K^{min} remains unchanged upon the introduction of lead into the structure of the 2201 phase. This is apparently due to a change in the slip direction and in the form of the interaction of dislocations under the deformation of the 2212 structure. A partial substitution of lead for bismuth changes not only the value of H_K, but also the polar anisotropy coefficient $P_K = H_K^{\mathrm{max}} / H_K^{\mathrm{min}}$ [16]. For the 2212 phase free of Pb, $P_K = 1.5$, while the value of P_K with Pb is 1.4; for the 2201 phase, $P_K = 1.1$ without Pb and $P_K \cong 1.0$ with Pb. The change in P_K is associated with a more intense increase in the microhardness for directions corresponding to the minimum values of H_K, which therefore leads to a decrease in the degree of anisotropy.

In the range of small loads, the microhardness of BSCCO crystals increases with a decreasing load applied to the indenter, which is attributed to the scale effect [8, 17]. The scale effect can be arbitrarily divided

Table 2. Microhardness H_K (GPa) of crystals of the 2201 and 2212 phases for various angles φ of the indenter orientation relative to the [100] direction

Phase	Load (N)	Microhardness of crystals without Pb			Microhardness of crystals with Pb	
		0	45°	90°	0(90°)	45°
2201	0.03	0.42 ± 0.03	0.36 ± 0.02	0.39 ± 0.03	0.53 ± 0.03	0.50 ± 0.04
	0.02	0.41 ± 0.04	0.40 ± 0.03	–	0.59 ± 0.05	0.56 ± 0.04
	0.01	0.59 ± 0.06	0.59 ± 0.05	–	0.73 ± 0.06	0.67 ± 0.05
2212	0.03	0.96 ± 0.07	0.91 ± 0.08	0.66 ± 0.04	1.12 ± 0.05	0.86 ± 0.05
	0.02	1.28 ± 0.07	–	0.77 ± 0.06	1.40 ± 0.09	1.16 ± 0.08
	0.01	1.88 ± 0.09	–	0.84 ± 0.08	2.57 ± 0.08	1.62 ± 0.08

Table 3. Coefficients C_1 and C_2 for various angles φ of the indenter orientation relative to the [100] direction

Phase	2201				2212			
Presence of Pb	–	–	+	+	–	–	+	+
φ (deg)	0	45	0(90)	45	0	90	0(90)	45
C_1 (N/mm)	0.036	0.040	0.029	0.040	0.087	0.040	0.110	0.089
$C_2 \times 10^4$ (N/mm^2)	16.8	14.3	25.3	22.2	25.8	35.3	19.4	19.2

into the effect of elastic restoration of the surface region (the reduction in the imprint size after the removal of loading) and the effect of work hardening in the plastically deformed volume under the imprint on the change in microhardness [17–19].

It has been established experimentally that the load P applied to the indenter acting on various materials (polycrystals, ceramics, and crystals) is balanced by the resistance offered by the material, which can be presented in the form [17, 20, 21]

$$P = P_1 h + R_2 h^2, \qquad (1)$$

where h is the imprint depth and R_1 and R_2 are proportionality factors.

We assume that the first term on the right-hand side of equation (1) characterizes the contribution of the deformed surface, while the second term describes the contribution of the deformed volume to the resistance offered by the material to the intrusion of the indenter. Equation (1) can be written in the form

$$P = C_1 d + C_2 d^2, \qquad (2)$$

$$P/d = C_1 + C_2 d, \qquad (3)$$

where C_1 and C_2 are new constants and d is the longer diagonal of the imprint.

The figure shows the dependences of P/d on d for crystals of the superconducting phases of the BSCCO system with lead partially substituted for bismuth and without lead. The coefficients C_1 and C_2 for various crystals are given in Table 3. Since, according to [17, 18, 21], elastic restoration is associated with C_1 and strengthening of the region under the indenter is connected with C_2, these coefficients enable us to estimate the variation of the contributions of elastic restoration and strengthening to the scale effect.

According to the data in Table 3, the coefficients C_1 and C_2 differ most strongly (depending on the direction of the longer diagonal of the imprint left by the Knoop pyramid) for the 2212 phase free of Pb, indicating a strong anisotropy of elastic restoration and plastic properties of the crystal lattice of this phase. On the other hand, the closeness of the values of C_1 and C_2 for different orientations in the 2201 phase indicates the similarity of the scale effect in the structure of this HTSC phase.

It can be seen from the figure (curves 5–8 and Table 3) that the change in the scale effect in the 2201 structure is associated with a change in the extent of strengthening of the material under the indenter. The strongest influence on the change in the scale effect is produced by doping with lead of the structure having the 2212 composition, which increases the coefficient C_1 by a factor of 1.5 or 2.5 depending on the orientation of the indenter (see curves 1–4 and Table 3). An increase in C_1 results in a change in the scale effect and, besides, reduces the plasticity of the structure of the
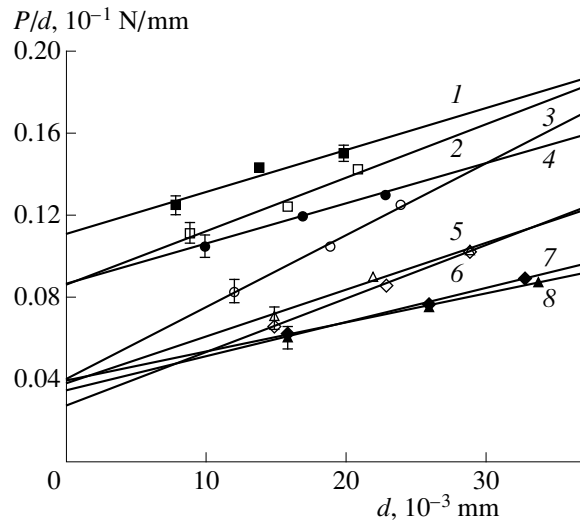
Dependence of P/d on d for crystals of the 2212 and 2201 phases (curves 1–4 and 5–8, respectively) for various orientations of the diagonal of the indenter imprint relative to the [100] direction: (1, 6) with Pb, parallel to [100]; (2, 7) without Pb, parallel to [100]; (3) without Pb, at 90° to [100]; (4, 5) with Pb, at 45° to [100]; and (8) without Pb, at 45° to [100].

2212 phase after the introduction of Pb [8]. At the same time, the difference between the coefficients C_1, as well as C_2, for different orientations decreases, which indirectly confirms the decrease in the anisotropy of this structure upon a partial substitution of Pb for Bi.

Thus, the values of microhardness H_K and the polar anisotropy P_K of microhardness of crystals having the 2201 and 2212 compositions are different. The maximum values of H_K and P_K are observed for crystals of the 2212 phase. A decrease of loading of the indenter leads to an increase in the Knoop microhardness of HTSC crystals belonging to the BSCCO system (scale effect). A change in the orientation of the Knoop indenter leads to a change in the scale effect for crystals with the 2212 structure (scale-effect anisotropy). The data reflecting the influence of the indenter orientation on the scale effect indirectly confirm the existence of polar anisotropy both in the elasticity and in the plasticity of the structure of Bi-based HTSC crystals.

A partial substitution of lead for bismuth in the structure of superconducting phases of the BSCCO system leads to a change in H_K and P_K of the crystals of the phases 2212 and 2201.

The observed strong anisotropy in the microhardness of crystals of the 2212 phase decreases after the introduction of lead into the structure, which is accounted for by a decrease in the distortion of the crystal lattice of this phase. The change observed in the scale effect in crystals of the 2212 phase upon a partial substitution of lead for bismuth is associated with a change in the elastic restoration of the imprint, as well

as with a change in the degree of strengthening of the structure under the indenter.

REFERENCES

1. B. I. Smirnov, T. S. Orlova, and V. V. Shpeizman, J. Mech. Behav. Mater. **5**, 325 (1994).

2. T. S. Orlova, B. I. Smirnov, and V. V. Shpeizman, Fiz. Tverd. Tela (Leningrad) **32** (10), 3165 (1990) [Sov. Phys. Solid State **32**, 1838 (1990)].

3. I. F. Kononyuk, L. V. Makhnach, S. V. Lubenets, *et al.*, in *Abstracts of Papers to the IIIrd All-Union Conf. on High-Temperature Superconductivity* (Kharkov, 1991), Vol. 3, p. 75.

4. S. V. Lubenets, V. D. Natsik, L. S. Fomenko, *et al.*, in *Abstracts of Papers to the IIIrd All-Union Conf. on High-Temperature Superconductivity* (Kharkov, 1991), Vol. 3, p. 76.

5. V. S. Bobrov, G. A. Emel'chenko, A. N. Izotov, *et al.*, in *Abstracts of Papers to the IIIrd All-Union Conf. on High-Temperature Superconductivity* (Kharkov, 1991), Vol. 3, p. 9.

6. L. S. Fomenko, S. V. Lubenets, V. D. Natsik, *et al.*, in *Abstracts of Papers to the IIIrd All-Union Conf. on High-Temperature Superconductivity* (Kharkov, 1991), Vol. 11, p. 11.

7. T. B. Tang and S. C. Fung, Solid State Commun. **87**, 325 (1993).

8. Yu. S. Boyarskaya, D. Z. Grabko, and M. S. Kats, *Physics of Microindentation Processes* (Shtinitsa, Kishinev, 1986).

9. V. N. Osipov, L. I. Derkachenko, Yu. G. Nosov, *et al.*, Solid State Commun. **97**, 377 (1996).

10. V. N. Osipov, I. N. Zimkin, V. N. Gurin, *et al.*, Fiz. Tverd. Tela (S.-Peterburg) **39** (2), 219 (1997) [Phys. Solid State **39**, 192 (1997)].

11. N. N. Kachanov and L. I. Mirkin, *X-ray Diffraction Analysis (Polycrystals)* (Gos. Nauchno-Tekhnich. Izd. Mashinostroit. Lit., Moscow, 1960).

12. B. V. Mott, *Microhardness Tests Using Microindentation* (Metallurgizdat, Moscow, 1960).

13. C. H. Chen, D. J. Werder, G. P. Espinosa, *et al.*, Phys. Rev. B **39** (7), 4686 (1989).

14. Y. P. Lin, J. Barbier, J. E. Greedan, *et al.*, Physica C **158** (1/2), 241 (1989).

15. Z. Li, H. Shen, Y. Qin, *et al.*, Philos. Mag. Lett. **60** (4), 123 (1989).

16. *Methods of Investigation of Minerals*, Ed. by A. I. Ginzburg (Nedra, Moscow, 1985).

17. F. Frohlich, P. Graw, and W. Grellmann, Phys. Status Solidi A **42**, 79 (1977).

18. E. O. Bernhard, Z. Metallkd. **33**, 135 (1941).

19. S. I. Bulychev, Zh. Tekh. Fiz. **69** (7), 42 (1999).

20. K. Hirao and M. Tomozawa, J. Am. Ceram. Soc. **70**, 497 (1987).

21. C. Veerender, V. R. Dumke, and M. Nagabhooshanam, Phys. Status Solidi A **144**, 299 (1994).

Translated by N. Wadhwa

DEFECTS, DISLOCATIONS, AND PHYSICS OF STRENGTH

Effect of Electric Current on Starting Characteristics and Activation Parameters of Short Dislocations in Si Crystals

V. A. Makara, L. P. Steblenko, V. V. Obukhovskiĭ, N. Ya. Gorid'ko, and V. V. Lemeshko

Shevchenko State University, Kiev, 252033 Ukraine
e-mail: makara@hq.ups.kiev.ua
Received July 26, 1999; in final form, November 9, 1999

Abstract—It is shown that the passage of an electric current through crystalline silicon may lead to the so-called galvanoplasticization, as well as the galvanostrengthening, effect. It is found that the effect is sensitive to the temperature regime of deforming and to the preliminary high-temperature treatment of the samples. The motion delay time for short dislocations and starting stresses are significantly affected by the current. The relation of these effects to the change in the electric state of the Cottrell atmosphere as a result of the passage of the current through the crystal is considered. © 2000 MAIK "Nauka/Interperiodica".

The excitation of the electron subsystem of a crystal is known to result in a change in the mobility of dislocations under mechanical loading [1–3]. The excitation can be due to the effect of an electric field, irradiation by a light or electron beam, as to an well as injection current.

The stimulating effect of a current on the mobility of short dislocations ($L \leq 100$ μm) in crystalline Si was studied experimentally in [4–6]. Peculiarities in the behavior of individual dislocations observed in [4–6] agree well with the conclusions later drawn by Aliev *et al.* [7], who studied the electroplastic deformation of silicon samples.

Typical features in the behavior of short dislocation segments in Si crystals are the existence of starting stresses σ_{st} and delay times t_{del} of dislocation movements. Earlier experiments proved that these starting parameters depend on the conditions of bringing dislocations to starting positions, the regimes of thermal treatment of the samples, the experimental temperature, and the state of the surface [8, 9]. One can assume that the emergence of σ_{st} and t_{del} is associated with the formation of a region with an elevated concentration of point defects (Cottrell atmosphere) around dislocations.

In the present communication, we analyze the effect of a direct electric current on the starting characteristics of short dislocations and on the activation parameters determining the depinning of dislocations from the Cottrell atmosphere (the energy of activating the dislocation detachment from pinning centers and the activation volume of the depinning process).

High-temperature treatment (HTT) of samples (in particular, in oxygen atmosphere) is known to be an effective method for changing the concentration and structure of microscopic defects in silicon [10, 11]. For this reason, we studied the effect of electric current on the interaction of dislocations with point defects by using both the initial Si samples and the samples subjected to additional high-temperature treatment in air (3-h annealing at $T = 1300$ K). The layer of oxygen formed during such a thermal treatment was etched by hydrofluoric acid prior to the passage of current.

The sources of dislocation half-loops were stress concentrators drawn in the [110] direction on the (111) surface. The motion of dislocations was induced by bending about the [112] axis (four-support method). The sample size was $20 \times 4 \times 0.4$ mm in the [110], [112], and [111] directions, respectively. The relative error in determining the shear stress was 5%. The initial and final positions of the ends of the half-loops were fixed by the chemical etching method. The dislocation path lengths were measured on a BIOLAM-M microscope with the help of an eye-piece micrometer to within ≈0.3 μm.

We studied the effect of an electric current on the dynamics of dislocations by the method of four-support bending differing from the traditional technique in that the role of two lower supports was played by cylindrical tungsten electrodes to which voltage was supplied. This allowed us to pass the electric current through the samples directly during their mechanical deformation.

The effect of a direct current on the dislocation path lengths was studied in the temperature range $T = 650$–1000 K under mechanical stresses $\sigma = 11$–110 MPa for the current densities $J = 1 \times 10^2$–1×10^6 A/m².

It is well known that, in the low-temperature region ($T < 800$ K), dislocations in initial Si crystals are immobile. In this paper, we prove that the passage of an electric current through the Si samples initiates the motion of dislocations at much lower temperatures than in the initial crystals.

It was found to be expedient to divide the entire temperature interval under investigation into two parts: the
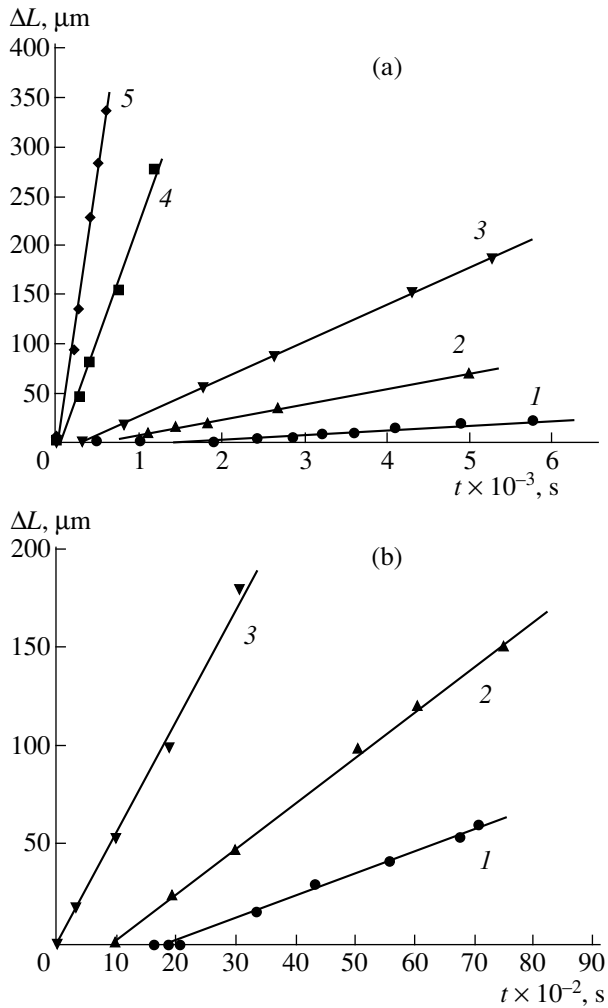
Fig. 1. Effect of current and temperature on the dislocation kinetics for (a) $\sigma = 34$ MPa, $T = 823$ K, and different values of $J \times 10^{-5}$ A/m^2: (*1*) 0, (*2*) 1, (*3*) 2, (*4*) 5, and (*5*) 10; and (b) $\sigma = 110$ MPa, $J = 2 \times 10^5$ A/m^2, and various values of T(K): (*1*) 673, (*2*) 723, and (*3*) 773. Under the same conditions, dislocations remain stationary for $J = 0$.

high-temperature region $\Delta T_1 = 800$–1000 K (which was studied in detail earlier [4–6, 8, 9]) and the low-temperature region $\Delta T_2 = 650$–800 K.

The starting stresses σ_{st} and delay times t_{del} were determined experimentally directly from the linearized dependences of the average dislocation path lengths $\Delta L(t)$ on the time of loading t. Typical time dependences of dislocation path lengths ΔL under various mechanical stresses in the samples carrying an electric current in the regions ΔT_1 and ΔT_2 are shown in Fig. 1. Figure 1a shows that, for a fixed temperature T and a mechanical stress σ, the delay time t_{del} for crystals excited by the current is longer than in the initial Si crystals, with the delay time decreasing and ultimately vanishing upon an increase in the current density J. We found (Fig. 2) that the starting delay time is inversely

proportional to the length of a moving dislocation segment ($t_{del} \approx \text{const}/L$). For fixed σ and J, the delay time is a function of temperature T of the sample (Fig. 1b).

It was found that the temperature dependence of the delay time t_{del} in the initial samples, as well as in the samples carrying current, is of the exponential type:

$$t_{del} \approx t_{del\,0}\exp[V(\sigma)/kT]F(\sigma)/L\nu, \qquad (1)$$

where $t_{del\,0}$ is a certain approximation parameter, $V(\sigma)$ is the activation energy for the depinning of a dislocation from the Cottrell atmosphere, k is the Boltzmann constant, $F(\sigma)$ is a coefficient depending on stress, L is the length of the dislocation segment, and ν is the attempt frequency of depinning of the dislocation segment from the points of its fixation [12–14].

The values of $V(\sigma)$ were calculated from the temperature dependence of delay times for the entire range of working stresses. It was found that the $V(\sigma)$ dependence is linear and can be described by the formula

$$V = V_0 - \gamma\sigma, \qquad (2)$$

where V_0 is the height of the barrier preventing the thermal depinning of dislocations from impurity centers in the absence of external stresses acting on the crystal (this quantity can be assumed to be equal to the energy of dislocation depinning from such centers) and γ is the so-called activation volume of the depinning of a unit-length dislocation [9, 15]. The values of the experimentally determined activation parameters V_0 and γ are given in the table.

The information contained in the table shows that the passage of a current through crystalline silicon reduces the height of the initial barrier V_0 for the depinning of dislocations by 0.6–0.7 eV in the high temperature regions (800–1000 K). At low temperatures (650–800 K), the values of V_0 were determined only for currents of density $J = 2 \times 10^5$ A/m^2. For currents $J < 2 \times 10^5$ A/m^2, dislocations remained at rest in this temperature range during the real time of the experiment. In both temperature regions, there was practically no delay time at the beginning of the motion of dislocations for $J \geq 5 \times 10^5$ A/m^2, and hence the activation parameters of short dislocations for these current densities were not determined.

The noticeable decrease in the barrier height V_0 under the action of the current can be interpreted as the result of a decrease in the energy of interaction of dislocations with pinning centers. It is well known [11,16,17] that, in the temperature intervals ΔT_1 and ΔT_2, dislocations in silicon are charged and are surrounded by spatial charge regions (Read cylinders) in order to satisfy the electroneutrality condition. The atmosphere of point defects around dislocations also includes pinning centers that have to be overcome by a dislocation at the beginning of its movement. The passage of current changes the charge state of the pinning centers, due to their partial or complete neutralization,

thus ensuring the lowering of the potential barrier associated with the Coulomb interaction. Thus, if we assume that a dislocation interacts with pinning centers not only through elastic forces, but also through electric forces, the decrease in the barrier height V_0 in current-excited Si crystals may serve as indirect evidence of the change in the charge state of dislocations and point defects as a result of the passage of current.

In contrast to the dislocation depinning energy, which changes significantly as a result of the passage of current through Si crystals, the activation volume (and, hence, the concentration of pinning centers holding a dislocation in its starting position) is insignificantly affected by current flowing through the sample. It should be noted that this result holds for the high-temperature region. The situation changes drastically as we go over to the range of low temperatures, in which the coefficient γ for excited crystals decreases strongly (approximately by a factor of four) as compared to the activation volume in the high-temperature range. This may indicate that the concentration and structure of pinning centers in the low-temperature region differ from the concentration and structure of similar centers in the range of high temperatures.

Our investigations proved that the characteristics of long and short dislocations in silicon differ qualitatively. Long dislocation segments ($L \gg 300$ μm) have no starting time delay ($t_{del} = 0$), but for a fixed σ only a part of dislocations starts moving.

A qualitatively different situation is realized for short dislocation loops ($L < 100$ μm) in the same Si crystals. For a fixed σ, short dislocations either start almost simultaneously, or all of them remain at rest. The effect of starting time delay is typical just of short dislocations. The delay time itself is a function of stress: $t_{del} = t_{del}(\sigma)$ (Fig. 3).

The dependence $t_{del}(\sigma)$ presented in Fig. 3 corresponds to the high-temperature region (ΔT_1). The rela-
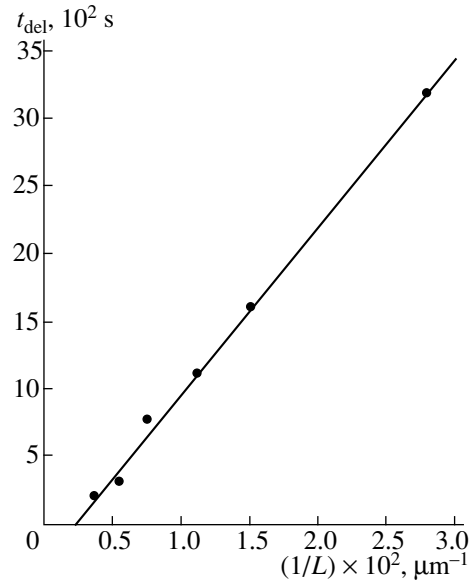

Fig. 2. Dependence of the delay time t_{del} of the beginning of dislocation motion on the length L of dislocation segments in Si crystals for $\sigma = 63$ MPa, $T = 823$ K, $J = 0$.

tion between the delay time and the stress has a typical form

$$\sigma_{st}^* = V_0 - kT \ln(t_{del}/t_{del\,0})\gamma^{-1}, \qquad (3)$$

where $t_{del\,0}$ is a certain approximation parameter.

The stress $\sigma_{st}^A(J, T)$ at which dislocations are set in motion simultaneously (i.e., to $t_{del} = 0$, see Fig. 3) will henceforth be called the absolute start stress. For $\sigma_{st}^* < \sigma_{st}^A(J, T)$, short dislocations are set in motion with a delay ($t_{del} > 0$). Besides, there exists a threshold stress $\sigma_{st}^0 < \sigma_{st}^A(J, T)$ for which dislocations remain at rest irrespective of the time of action of the external agency (rest boundary of a dislocation).

Activation parameters of depinning of short dislocations from pinning centers in Si single crystals

No.	Sample type	$J \times 10^{-4}$, A/m^2	Temperature range			
			$\Delta T_1 = 800–1000$ K		$\Delta T_2 = 650–800$ K	
			V_0, eV	$\gamma \times 10^{27}$, m^3	V_0, eV	$\gamma \times 10^{27}$, m^3
1	Initial Si	0	2.2 ± 0.1	1.0 ± 0.1	*	*
2	Si	1.0	1.6 ± 0.1	0.9 ± 0.1	*	*
3	Si	2.0	1.5 ± 0.1	0.8 ± 0.1	0.8 ± 0.1	0.2 ± 0.1
4	Annealed Si**	0	1.9 ± 0.1	3.5 ± 0.1	*	*
5	Annealed Si**	1.0–10.0	*	*	*	*

* Marks conditions under which the motion of dislocations is not observed, ** corresponds to an annealing temperature of 1300 K and annealing time of 3 h.
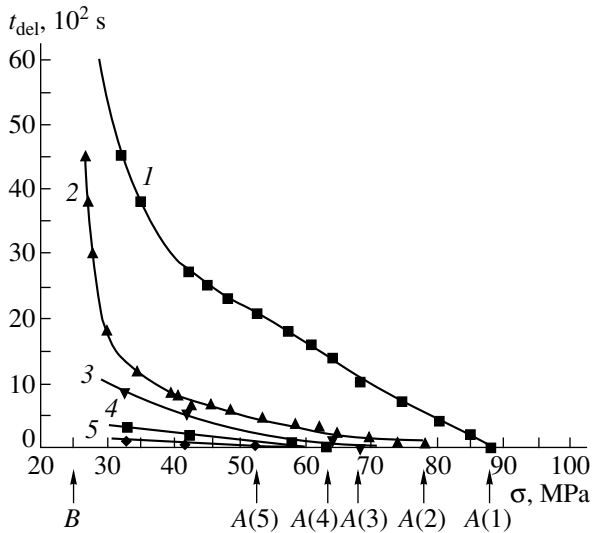
Fig. 3. Starting characteristics of motion of short dislocations in the temperature range ΔT_1. The arrows on the letters *A* (*1–5*) indicate the corresponding values of the absolute start loading, and *B* is the rest boundary for dislocations: (*1*) $J = 0$, $T = 823$ K, (*2*) $J = 0$, $T = 873$ K, (*3*) $J = 1 \times 10^5$ A/m^2, $T = 823$ K, (*4*) $J = 1 \times 10^5$ A/m^2, $T = 873$ K, (*5*) $J = 1 \times 10^5$ A/m^2, $T = 923$ K.
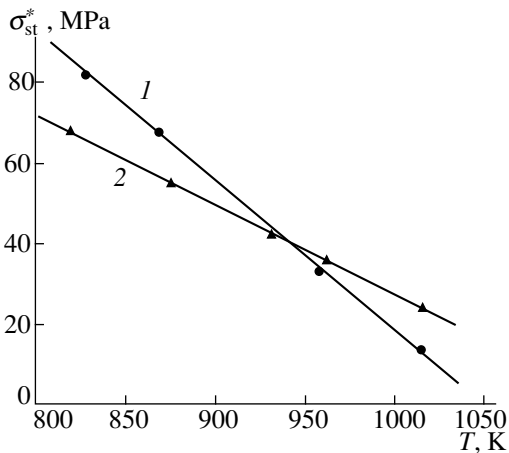

Fig. 4. Temperature dependence of starting stress σ_{st}^* for a fixed value of the delay time $t_{del} = 300$ s and different values of J, A/m^2: (*1*) 0, (*2*) 1×10^5.

The boundaries σ_{st}^0 and σ_{st}^A of the start regions in the initial, as well as galvanoexcited, samples depend on the sample temperature, decreasing upon heating. For a fixed temperature, the values of stresses σ_{st}^A and σ_{st}^0 in galvanoexcited Si crystals are lower than in the initial crystals. For example, for a current with $J \geq 2 \times 10^5$ A/m^2, σ_{st}^0 is smaller than the initial value by

approximately a factor of three. The values of σ_{st}^A and σ_{st}^0 in galvanoexcited samples were functions of the current density, decreasing upon an increase in *J*.

It should be emphasized that the start characteristics t_{del}, σ_{st}^A, σ_{st}^*, and σ_{st}^0 have the above-mentioned peculiarities only in the temperature range $T < 973$ K. However, in the region $T \geq 973$ K, the galvanostrengthening effect can be observed, in which the values of starting characteristics of Si samples differs significantly as a result of the passage of a current, namely, the values of starting stresses in galvanoexcited crystals are higher than the starting stresses of motion of short dislocations in the initial Si crystals (Fig. 4). It should be noted that the $\sigma_{st}^*(T)$ dependence depicted in Fig. 4 was measured for a fixed starting delay time equal to 300 s.

The results described above lead to the conclusion that the passage of a current produces a plasticizing effect on the surface layers of Si only for $T < 973$ K. It was found that the effect of current on the motion of dislocations depends not only on the temperature range under investigation, but also on the previous history of the sample, in particular, on the preliminary HTT of samples. For example, the passage of a current through the samples subjected to a preliminary HTT does not induce the motion of dislocations in any temperature range under investigation. On the other hand, the motion of dislocations was observed in Si samples subjected to HTT, but carrying no current, which allowed us to determine the activation parameters of dislocation depinning from impurity centers in samples subjected to annealing in air (see table).

Thus, the effect of a current on the starting parameters and dynamic behavior of dislocations strongly depends on the previous history of the samples, which is clearly manifested in Si samples subjected to thermal treatment (annealed in air). In this case, the passage of current pins dislocations in their starting positions, which can be explained by a change in the charge state of structural defects in such samples. According to Shimura [18], annealing of silicon at high temperatures $T \sim 1300$ K leads to oxygen diffusion to the bulk of the material along dislocations and slip planes and to the formation of coarser pinning centers. It was proved in [17, 18] that dislocations surrounded by an atmosphere of impurities lose their electrical activity as a result of such a thermal treatment; i.e., they become electrically neutral.

The electroneutrality of the atmosphere can only account for the decrease in the delay time and the increase in the velocity of dislocations that we observed [15] in samples annealed at a high temperature ($T \sim$ 1300 K). At the same time, the passage of a current changes the state of the Cottrell atmosphere around a dislocation, namely, the initially neutral atmosphere becomes charged. We can assume that the coarser charge centers formed as a result of the passage of cur-

rent pin dislocations at their starting positions so strongly that the dislocations are unable to leave these positions under nondestructive stresses. Therefore, the passage of a current through the samples subjected to a special thermal treatment must increase the crystal rigidity as compared to the rigidity of samples carrying no current.

It should be noted, in conclusion, that the passage of a current through silicon crystals may lead to two opposite effects, depending on the experimental temperature and previous history of the samples. For $T < 973$ K, the samples not subjected to annealing ("initial" samples) exhibit a galvanoplasticization effect. In this case, the delay time of dislocation movement decreases (down to zero), and starting stresses are reduced (by a factor of several units). For $T \geq 973$ K, the galvanoplasticization effect is replaced by galvanostrenthening. Silicon crystals subjected to HTT exhibit a tendency to galvano-strengthening in the entire temperature range under investigation. This effect can be due to the pinning of dislocations at stoppers, which is manifested in the growth of starting stresses and in the increase in the starting delay time.

REFERENCES

1. Yu. A. Osip'yan and V. F. Petrenko, in *Physics of $A^{II}B^{IV}$ Compounds* (Mir, Moscow, 1986), p. 35.

2. N. Maeda, K. Kimura, and S. Takeuchi, Izv. Akad. Nauk SSSR, Ser. Fiz. **51** (4), 729 (1987).

3. T. Suzuki, H. Yoshinaga, and S. Takeuchi, *Dislocation Dynamics and Plasticity* (Syokabo, Tokyo, 1986; Mir, Moscow, 1989).

4. V. A. Makara, L. P. Steblenko, and E. G. Robur, Solid State Phenom. **32–33**, 619 (1993).

5. V. V. Lemeshko, V. A. Makara, V. V. Obukhovskiǐ, *et al.*, Fiz. Tverd. Tela **36** (9), 2618 (1994) [Phys. Solid State **36**, 1427 (1994)].

6. V. A. Makara, L. P. Steblenko, N. Ya. Gorid'ko, *et al.*, Dopovidi Akad. Nauk Ukr., No. 3, 78 (1994).

7. M. A. Aliev, Kh. O. Alieva, and V. V. Seleznev, Fiz. Tverd. Tela **37** (12), 3732 (1995) [Phys. Solid State **37**, 2057 (1995)].

8. N. Ya. Gorid'ko, V. A. Makara, N. N. Novikov, *et al.*, Fiz. Tverd. Tela **25** (9), 2598 (1983) [Sov. Phys. Solid State **25**, 1494 (1983)].

9. V. A. Makara, N. N. Novikov, L. P. Steblenko, *et al.*, Fiz. Tverd. Tela **31** (5), 31 (1989) [Sov. Phys. Solid State **31**, 738 (1989)].

10. V. S. Vavilov, V. F. Kiselev, and B. N. Mukashev, *Defects in the Bulk of Silicon and on Its Surface* (Nauka, Moscow, 1990).

11. K. Ravi, *Imperfections and Impurities in Semiconductor Silicon* (Wiley, New York, 1981; Mir, Moscow, 1984).

12. H. van Bueren, *Imperfections in Crystals* (Amsterdam, 1960; Foreign Languages Publ. House, Moscow, 1962).

13. B. V. Petukhov, Fiz. Metal. Metalloved. **56** (6), 1177 (1983).

14. J. Hirth and J. Lothe, *Theory of Dislocations* (McGraw-Hill, New York, 1968; Atomizdat, Moscow, 1972).

15. V. A. Makara, Preprint No. IMP-86-2 of IES (Paton Institute of Welding), Kiev (1986).

16. H. Matare, *Defect Electronics in Semiconductors* (Wiley, New York, 1971; Mir, Moscow, 1974).

17. I. E. Bondarenko and E. B. Yakimov, Phys. Status Solidi A **122** (1), 121 (1990).

18. F. Shimura, Electrochem. Soc. **128**, 1579 (1981).

Translated by N. Wadhwa

MAGNETISM
AND FERROELECTRICITY

Magnetostriction of Hexaferrites in the Region
of Spin–Reorientational Phase Transitions

A. G. Chesnokov and E. P. Naĭden

Siberian Physicotechnical Institute, pl. Revolyutsii 1, Tomsk, 634050 Russia
e-mail: naiden@elefot.tsu.ru
Received July 8, 1999

Abstract—The temperature dependence of magnetostriction of textured polycrystalline $Co_{0.72}Zn_{1.28}$–W hexaferrite has been studied by means of x-ray dilatometry and strain gauges. It is shown that the magnetostriction constants exhibit an anomalous behavior in the region of spin–reorientational phase transitions and reach as high as 10^{-5}–10^{-4}. © *2000 MAIK "Nauka/Interperiodica".*

In oxide ferrimagnets with the hexagonal structure (hexaferrites), which contain, besides trivalent iron, magnetoactive cations with strong spin-orbit coupling (for instance, Co^{2+} ions), variation of temperature can produce various magnetic structures, namely, the easy-cone, easy-plane, and easy-axis states. The role played by the magnetoelastic interaction in the formation of the magnetic states of magnets of this kind remains very poorly studied. The available data, obtained primarily at room temperature, provide no more than fragmentary information on the behavior of the magnetostriction constants of some simplest hexaferrites ($BaFe_{12}O_9$–BaM, $BaFe_{18}O_{27}$–Fe_2–W, etc.) [1–5]. Information on the temperature dependences of the magnetostriction constants and, hence, on those of the magnetoelastic coupling constants is extremely scant.

At the same time, it appears obvious that spin–reorientational phase transitions, i.e., the processes involving a change in direction of spin magnetic moments relative to the crystallographic axes, may be accompanied by a change in the crystal dimensions because of the anisotropic nature of the spin subsystem interaction with the lattice. In particular, x-ray dilatometric studies of the lattice parameter c made on a $BaCo_{2-x}Zn_x$–W sample, in which the whole variety of magnetic states can be realized, showed that in the spin–reorientation region one observes well-pronounced anomalies in $c(T)$, which may be interpreted as a manifestation of spontaneous magnetostriction ($\lambda_c \cong 10^{-4}$) [6, 7].

The measurement of the magnetostriction constants reduces to determining the relative change in the linear dimensions of a single-crystal sample along different crystallographic axes and different directions of the magnetizing field. Mason [8] derived general expressions for the magnetostriction constant in an arbitrary direction for a magnet of hexagonal symmetry for the following two cases:

(i) easy-axis anisotropy

$$
\begin{aligned}
\lambda = {} & \lambda_a[(\alpha_1\beta_1 + \alpha_2\beta_2)^2 - (\alpha_1\beta_1 + \alpha_2\beta_2)\alpha_3\beta_3] \\
& + \lambda_b[(1 - \alpha_3^2)(1 - \beta_3^2) - (\alpha_1\beta_1 + \alpha_2\beta_2)^2] \\
& + \lambda_c[(1 - \alpha_3^2)\beta_3^2 - (\alpha_1\beta_1 + \alpha_2\beta_2)\alpha_3\beta_3] \\
& + 4\lambda_d(\alpha_1\beta_1 + \alpha_2\beta_2)\alpha_3\beta_3;
\end{aligned}
\tag{1}
$$

(ii) easy-plane anisotropy

$$
\begin{aligned}
\lambda = {} & A[2\alpha_1\alpha_2\beta_1 + (\alpha_1^2 - \alpha_2^2)\beta_2]^2 \\
& + B\alpha_3^2[(\alpha_1\beta_1 + \alpha_2\beta_2)^2 - (\alpha_1\beta_1 - \alpha_2\beta_1)^2] \\
& + C[(\alpha_1\beta_1 + \alpha_2\beta_2)^2 - (\alpha_1\beta_2 - \alpha_2\beta_1)^2] \\
& + D(1 - \alpha_3^2)(1 - \beta_3^2) + E\alpha_3^2\beta_3^2(1 - \alpha_3^2) \\
& + F\alpha_3^2(1 - \alpha_3^2) + G\beta_3^2(1 - \alpha_3^2) \\
& + H\alpha_3\beta_3(\alpha_1\beta_1 + \alpha_2\beta_2) + I\alpha_3\beta_3(\alpha_1\beta_1 + \alpha_2\beta_2),
\end{aligned}
\tag{2}
$$

where α_i are the direction cosines of the magnetization vector relative to the crystallographic axes and β_i are the direction cosines of the direction in which the magnetostriction is measured.

It thus follows that in order to describe magnetostriction of a uniaxial magnet, it is sufficient to determine the four principal constants, whereas in the case of an easy-plane anisotropy, the number of independent constants increases to nine (because of the lowering of the magnetic symmetry). Experimental data should be treated with (2) for the easy-cone and easy-plane states and with (1) for the easy-axis magnetization.

This paper presents the results of magnetostriction measurements in the region of spin–reorientational phase transitions carried out on textured polycrystalline hexaferrite $BaCo_{0.72}Zn_{1.28}Fe_{16}O_{27}$–($Co_{0.72}Zn_{1.28}$–$W$), which undergoes easy-plane ⇔ easy-cone and easy-
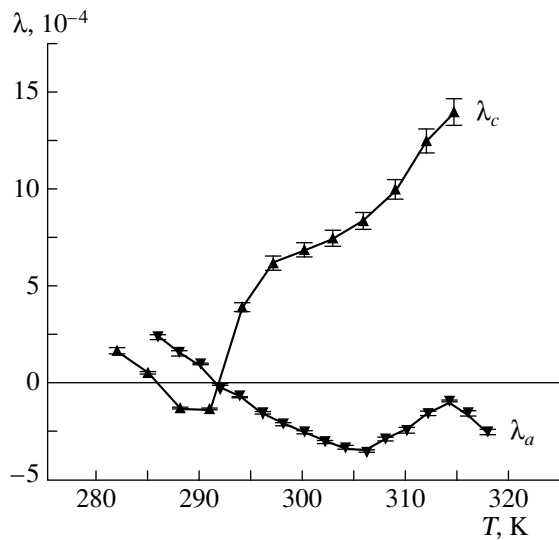
Fig. 1. Temperature dependence of the magnetostriction constants λ_a and λ_c of the $BaCo_{0.72}Zn_{1.28}Fe_{16}O_{27}$ hexaferrite.

cone $\Leftrightarrow$ easy-axis phase transitions near room temperature.

The magnetostriction constants of hexaferrites in the region of spin–reorientational transitions were determined by means of x-ray dilatometry and tensometry.

X-ray dilatometry permits one to study linear deformations of a crystal along certain crystallographic directions, i.e., to obtain information on the main magnetostriction constants of a single-crystal sample. The lattice parameters and their variation can be measured with high precision only on sufficiently perfect crystals, with rocking curves about $0.1°$ in a half-width, in which case the margin of error of determination of the relative elongation may be as small as $(2–3) \times 10^{-6}$. If the texture of a polycrystalline sample is perfect enough, the interplanar distances can be measured to within 10^{-5}. Figure 1 presents the magnetostriction constants λ_a and λ_c measured by this method on a textured polycrystalline sample ($f_t \cong 0.7$) of the above-mentioned hexaferrite. In the region of reorientational phase transitions one readily sees "giant" magnetostriction, which exceeds by at least two orders of magnitude the values quoted typically in the literature for ferrimagnets of this class [1–4, 9].

The polycrystalline sample used in the magnetostriction measurements by tensometric technique had a "sheet"-pattern texture in the basal planes, with the texture index $f_t \cong 0.35$. As strain transducers, we used GDT-type germanium dendrite strain sensors with a strain sensitivity coefficient $S = +55$ and a base length of 10 mm. The strain sensor was mounted on the sample surface in accordance with the averaged values of the directional cosines $\alpha_1 = \alpha_2 = \beta_1 = \beta_2 = 0.468$, $\alpha_3 =$
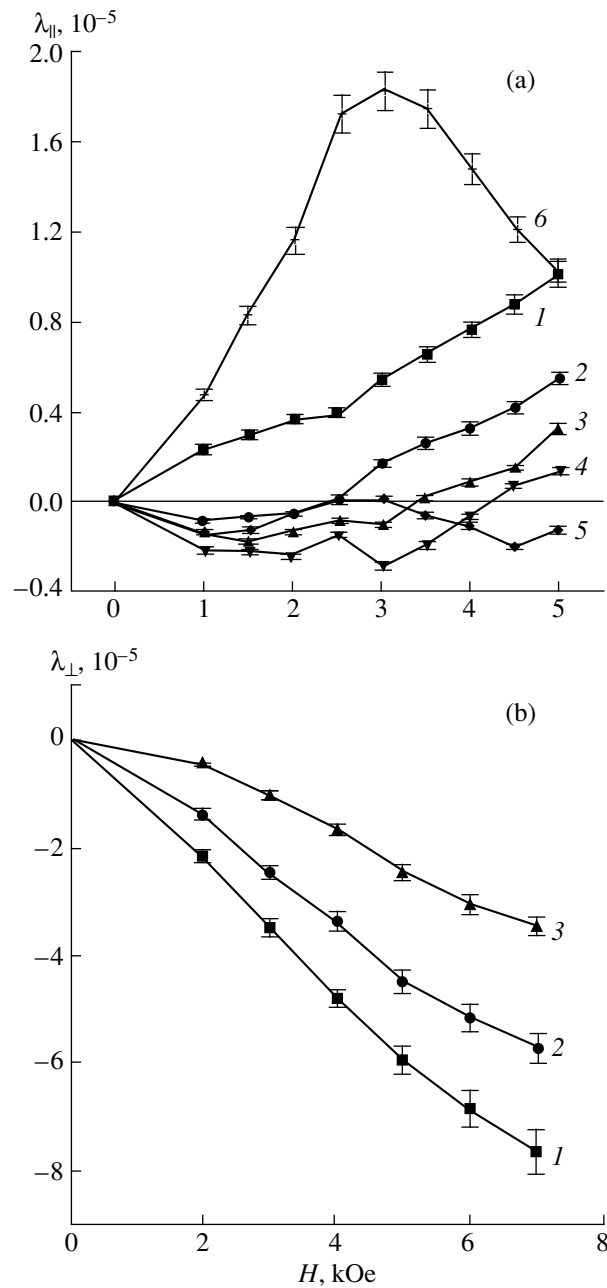

Fig. 2. Field dependences of (a) the longitudinal and (b) transverse magnetostriction of $BaCo_{0.72}Zn_{1.28}Fe_{16}O_{27}$ at different temperatures T(K): (a) (1) 178, (2) 308, (3) 323, (4) 333, (5) 363, (6) 389; and (b) (1) 317, (2) 367, (3) 388.

$\beta_3 = 0.352$ in the case of longitudinal magnetization, and with $\alpha_1 = \alpha_2 = 0.176$, $\alpha_3 = 0.936$, $\beta_1 = \beta_2 = 0.662$, $\beta_3 = 0.352$ for transverse magnetization.

Figure 2 displays the field dependences of the longitudinal and transverse magnetostriction obtained at different temperatures. In the case of transverse magnetostriction, the curves exhibit saturation, with the effect decreasing with increasing temperature. For longitudinal magnetostriction, the effect is small in the region
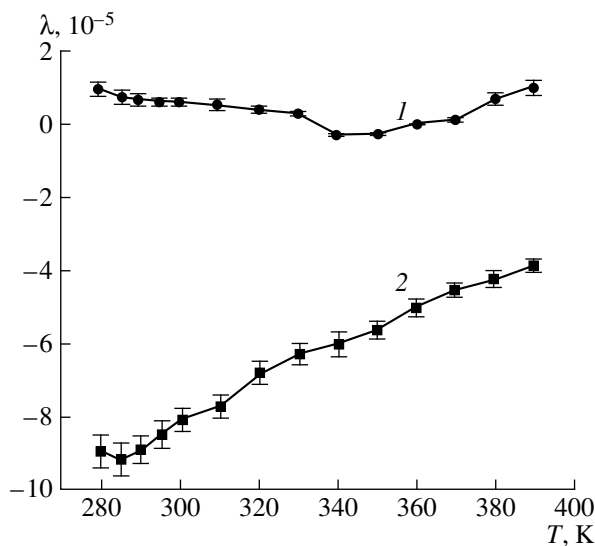
Fig. 3. Temperature dependences of (*1*) longitudinal and (*2*) transverse magnetostriction of the $BaCo_{0.72}Zn_{1.28}Fe_{16}O_{27}$ hexaferrite.

where easy-plane magnetization exists and is apparently due to domain-structure rearrangement. The dependence obtained at a temperature of 389 K, corresponding to the easy-axis state, has an anomalous shape with a maximum at a magnetizing field of 3–4 kOe.

Figure 3 presents the temperature dependences of the magnetostriction constants taken at a magnetizing field of 8 kOe. The maximum values of magnetostriction in the basal plane reached under magnetization along the *c* axis are reached at the temperatures of the easy-plane $\Leftrightarrow$ easy-cone spin–reorientational transition and are as high as 10^{-4}. Magnetostriction in the basal plane obtained under longitudinal magnetization is at least an order of magnitude smaller.

The analysis of the results of measurements, made using the relations (1) and (2) (derived for the magnetostriction of a magnet of hexagonal symmetry), took into account the real distribution of crystallographic axes in the textured sample under longitudinal and transverse magnetization. Substituting the magneto-

striction constants λ_a and λ_c, determined by the x-ray dilatometric method, and the directional cosines α_i and β_i into the expressions for magnetostriction under longitudinal and transverse magnetization yielded the following estimates for the main magnetostriction constants of this sample for 300 K:

$$\lambda_a = -(2.5 \pm 0.1) \times 10^{-4}, \quad \lambda_b = (2 \pm 0.5) \times 10^{-4},$$

$$\lambda_c = (7.5 \pm 0.2) \times 10^{-4}, \quad \lambda_d = -(5 \pm 1) \times 10^{-4}.$$

Thus, our study has shown that in the region of spin–reorientational transformations one observes anomalous magnetostriction effects. The maximum values of magnetostriction are found in the case where magnetization caused by an external field induces an orientational transition involving a maximum change of the orientation angle, for instance, at the induced easy-plane $\longleftrightarrow$ easy-axis phase transition. The results obtained in this work can be used advantageously to estimate magnetoelastic interactions in the region of spin reorientation.

REFERENCES

1. S. P. Kuntsevich, Yu. A. Mamaluĭ, and A. S. Mil'ner, Fiz. Met. Metalloved. **26**, 610 (1968).
2. S. P. Kuntsevich, Yu. A. Mamaluĭ, and V. P. Palekhin, Fiz. Tverd. Tela **22**, 2192 (1980) [Sov. Phys. Solid State **22**, 1278 (1980)].
3. S. P. Kuntsevich and V. P. Palekhin, Fiz. Tverd. Tela **15**, 3460 (1973) [Sov. Phys. Solid State **15**, 2314 (1973)].
4. S. P. Kuntsevich, Yu. A. Mamaluĭ, and A. S. Mil'ner, Ukr. Fiz. Zh. **16** (1), 67 (1971).
5. T. A. Elkin and K. M. Bol'shova, Vestnik MGU, No. 6, 72 (1969).
6. S. P. Kuntsevich and V. P. Palekhin, Fiz. Tverd. Tela **20**, 2869 (1978) [Sov. Phys. Solid State **20**, 1661 (1978)].
7. E. P. Naiden, V. I. Maltsev, and G. I. Ryabtsev, Phys. Status Solidi A **120**, 209 (1990).
8. W. P. Mason, Phys. Rev. **96**, 302 (1954).
9. S. S. Fonton and A. V. Zalesskiĭ, Zh. Éksp. Teor. Fiz. **17**, 1693 (1964).

Translated by G. Skrebtsov

MAGNETISM
AND FERROELECTRICITY

Investigation of Small-Scale Stray Magnetic Fields by Magnetooptical Methods

D. E. Balabanov* and S. A. Nikitov**

*Moscow Institute of Physics and Technology,
Institutskiĭ per. 9, Dolgoprudnyĭ, Moscow oblast, 141700 Russia
**Institute of Radio Engineering and Electronics, Russian Academy of Sciences,
ul. Mokhovaya 18, Moscow, 103907 Russia
Received July 22, 1999

Abstract—Domain structures with in-plane magnetization are investigated in magnetically hard films. A magnetooptical setup designed for studying stray magnetic fields combines the advantages of the vibrating-sample magnetometer and the magnetooptical method of signal detection. The sensitivity of measurements of the stray field normal component is ~0.1 Oe. The criteria for choosing the optimal parameters of magnetooptical media for information readout are established. © *2000 MAIK "Nauka/Interperiodica".*

The measurement of weak stray magnetic fields is important in connection with investigating the domain structure (DS) of magnetic films, with the magnetization vector lying in the film plane. The main problem of studying such objects is that the standard magnetooptical methods of DS observation cannot be used [1], since both the Faraday effect and the polar Kerr magnetooptical effect required for DS observations are considerably suppressed in the case of the magnetization in the plane of the film [1]. Other methods are either qualitative (e.g., the magnetic liquid method) or very complicated (e.g., the electron-optical method) and inapplicable for an express analysis [2]. A possible way of solving this problem is the application of an intermediate readout medium [1, 2] possessing high magnetooptical characteristics, on the one hand, and being coupled magnetostatically with the object under investigation, on the other hand.

The most promising media for detecting spatially nonuniform magnetic fields with a characteristic nonuniformity scale of the order of a micrometer or slightly larger are epitaxial films of Bi-containing garnet ferrites (EGFF) [1]. Besides, such films are the most suitable as magnetooptical heads for an information readout. Such heads are used when the magnetooptical parameters of an information-carrying medium do not permit a direct readout from the medium itself (e.g., due to the small value of the Kerr rotation).

The method of magnetic field visualization and topography using the configurations of domain structures of Bi-containing EGFF is known [2]. However, this method has limitations on the magnitude of the magnetic field under study and is characterized by a considerable error when the characteristic spatial scale of the field being measured is comparable with the DS period of the sensor.

In this communication, we describe a nonvisual magnetooptical method of recording weak magnetic fields and formulate the criteria for choosing the optimal parameters for EGFF to be used as a sensor. The main feature of the proposed method of measurements is the combination of a vibrating-sample magnetometer with the optical method of recording a useful signal.

1. EXPERIMENT

The setup for studying a nonuniform magnetic field was developed on the basis of a polarization microscope with a laser emitting $\lambda = 0.63$-μm-long waves as a light source (Fig. 1). The principle of operation is as follows: the laser beam is focused on a Bi-containing EGFF that serves as a readout medium; it has a light-reflecting aluminum layer of thickness 0.1 μm deposited on the back side of the film. A sample with a DS
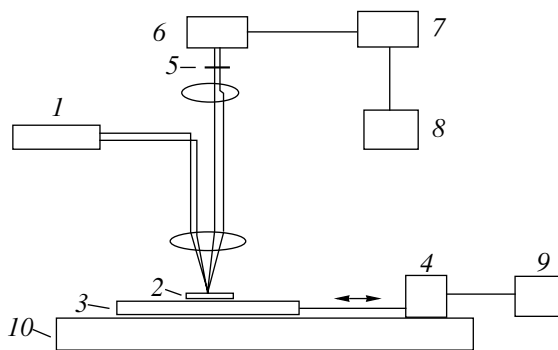

Fig. 1. Block diagram of the measuring setup: (*1*) laser, (*2*) EGFF, (*3*) sample, (*4*) sample displacement unit, (*5*) polarizer, (*6*) photodetector, (*7*) amplifier, (*8*) oscilloscope, (*9*) generator, (*10*) *x–y* desk.
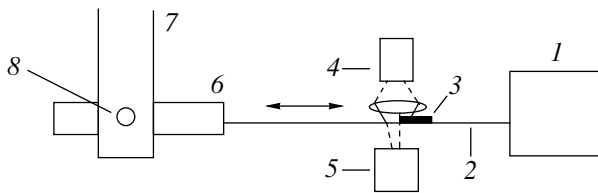
Fig. 2. Block diagram for measuring the sample vibration amplitude: (*1*) displacement unit, (*2*) rod, (*3*) opaque shutter, (*4*) light source, (*5*) photodetector, (*6*) sample, (*7*) sample holder, (*8*) EGFF.
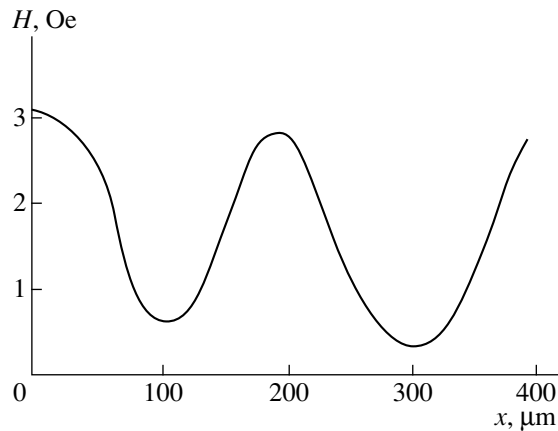

Fig. 3. Coordinate dependence of the normal component of the stray field.
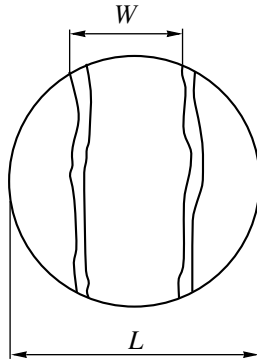

Fig. 4. Schematic diagram of a domain under illumination by a laser.

whose stray magnetic fields are to be measured is placed under the EGFF. The sample is mechanically set in motion parallel to the EGFF. As a result, the DS of the EGFF is under the action of variable stray fields of the sample under investigation, which leads to the emergence of Faraday rotation upon the reflection of the laser beam by the dielectric layer. The recording system measures the coordinate dependence of the magnetooptical signal amplitude proportional to the normal component of the stray field of the sample in the region of the laser spot.

In order to determine the normal component of the stray field, we use the comparison method applied for measuring the absolute value of saturation magnetization in vibrating-sample magnetometers. For this purpose, we arrange the calibrated coil so that the EGFF is located in a known variable magnetic field having the same frequency as the vibrational frequency of the vibrator. Comparing the amplitude of the magnetooptical signal from the DS of the vibrating sample with the amplitude of the magnetooptical signal induced by the magnetic field from the calibrated coil, one can determine the amplitude of the normal component of the stray field of the sample DS under investigation.

The recording system includes an FD-7 photodiode with a UPI-2 amplifier–transducer. The amplitude of sample vibrations is measured with the help of an optical system (Fig. 2) whose operation principle can be described as follows: an opaque shutter is fixed to the vibrator rod so that it partially covers the surface of the photodiode (*1*) when the latter is illuminated with a plane-parallel beam of light from the illuminant (*4*). The amplitude of photo-emf is proportional to the amplitude of the rod vibrations, provided that the latter is much smaller than the size of the photosensitive surface of the photodetector.

Figure 3 shows the results of experimental investigations of the normal component of the stray field as a function of the coordinate for a domain structure, with the magnetization vector lying in the plane of the film. The sample under investigation is a standard magnetic tape for audio recording, carrying a test signal of frequency 500 Hz. For the detecting medium, we have chosen the EGFF having the composition $(BiSmTm)_3(FeGa)_5O_{12}$ with the following parameters: film thickness $h = 6$ μm, domain size $P = 100$ μm, and saturation field $H_s = 6$ Oe.

2. CALCULATING THE OPTIMAL PARAMETERS OF A DETECTING MEDIUM

The most important parameters of the system intended for measuring weak magnetic fields are the sensitivity and spatial resolution. The sensitivity of this method is determined primarily by the magnetic parameters of the recording EGFF (saturation field, coercive force, and Faraday rotation), as well as by the sensitivity of the recording system of the magnetooptical signal.

Let us determine the parameters of the material to ensure the maximum sensitivity of the system, other conditions being equal. This can be done on the basis of the condition of the maximum of the magnetooptical signal amplitude under the action of an external magnetic field H. For the magnetooptical signal amplitude, we can write
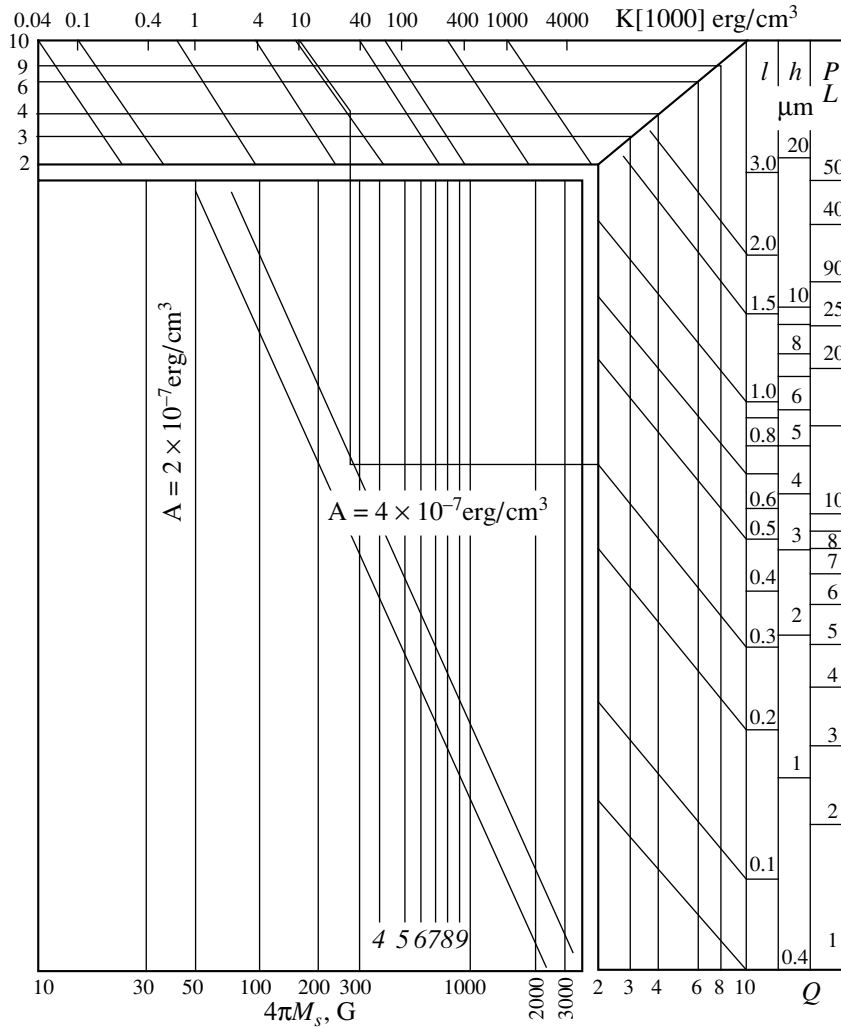
$$S = k\Psi_0 h\Delta W/Pn, \qquad (1)$$

Fig. 5. Nomogram for determining the optimal parameters of uniaxial materials for a magnetooptical readout of information.

where Ψ_0 is the specific value of Faraday rotation, h is the film thickness, P is the DS period, ΔW denotes the changes in the domain size under the action of the external magnetic field H, n is the number of domain walls in the region of the laser spot with a diameter L (Fig. 4) (L is the characteristic size of information bit), M is the magnetization of the material, M_s is the saturation magnetization, and k is a coefficient characterizing the sensitivity of the readout system. Besides, we can write

$$\Delta W/P = M/M. \qquad (2)$$

The magnetooptical susceptibility χ_{m0} can be written as

$$\chi_{m0} = dS/dH|_{H=0}. \qquad (3)$$

Obviously, χ_{m0} must have the maximum value. Substituting expressions (2) and (3) into formula (1), we obtain

$$\chi_{m0} = k\Psi_0 h/M_s(dM/dH|_{H=0})(2L/P - 1). \qquad (4)$$

The expression for $dM/dH|_{H=0}$ can be derived from the theory of a stripe DS [4] under the conditions $M/M_s \ll 1$ and $Q \gg 1$, where $Q = K_u/2\pi M_s^2$ is the quality factor of the material and K_u is the uniaxial anisotropy constant:

$$dM/dH|_{H=0} = \left[4\pi \left(1 + P/(\pi h) \right. \right.$$
$$\left. \left. \times \sum_n (-1)^n (1 - \exp(-2\pi h/P))/n \right) \right]^{-1}. \qquad (5)$$

In the region $1 < P/h < 5$, expression (5) can be approximated by the formula

$$dM/dH|_{H=0} = 0.053 + 0.047 P/h. \qquad (6)$$

Besides, the following relation holds in the same range of the ratio P/h [4]:

$$1/h = -0.05 + 0.083 P/h. \qquad (7)$$

For uniaxial magnetic materials, the following relations hold [3]:

$$M_s = (2QA/\pi)^{1/2}/l; \quad l = 4(AK_u)^{1/2}/(4\pi M_s^2),$$

where A is the exchange constant belonging to the range 2×10^{-7}–4×10^{-7} erg/cm^3 for an EGFF.

Substituting expressions (6) and (7) into (4), we obtain the following equation for the magnetooptical susceptibility:

$$\chi = k\Psi_0 h(-0.05h + 0.083P)$$
$$\times (0.053 + 0.047P/h)(2L/P - 1)(2QA/\pi)^{-1/2}.$$

We must find the values of P and h for which χ_{m0} has a maximum value, i.e., solve the system of equations

$$\begin{cases} \partial\chi_{m0}/\partial P = 0 \\ \partial\chi_{m0}/\partial h = 0, \end{cases} \quad \begin{cases} \partial^2\chi_{m0}/\partial P^2 = 0 \\ \partial^2\chi_{m0}/\partial h^2 = 0. \end{cases}$$

This condition is satisfied for the following relations: $P/h = 2.585$, $P = L$, and $l/h = 0.165$.

These relations determine the optimal parameters of the material used for measuring weak magnetic fields with the characteristic scale L by the magnetooptical method. Thus, if we must read out information with the characteristic size L of a recording bit by the magnetooptical method, the optimal parameters of the material serving as the readout medium are as follows: (1) a Bi-containing EGFF with the maximum possible concentration of Bi ions; (2) the DS period is equal to the size of an information bit, $P = L$; (3) the diameter of the laser spot is equal to the size of the information bit; (4) the characteristic length of the material is $l = 0.0637L$; (5) the film thickness is $h = 0.387L$, or $h = 6.07l$; (6) $4\pi M_s = 157(QA)^{0.5}/L$; and (7) $K_u = 1017Q^2A/L^2$.

It should be noted in addition that $\chi_{m0} \sim (QA)^{-1}$, and hence Q must have a minimum value. For the convenience of determining the required parameters of the film, Fig. 5 shows a nomogram which makes it possible to find the optimal magnetic parameters of EGFF. The principle of operation with such nomograms are described in detail in [3, 4]. The parameters should be determined in the following sequence. We assume that the characteristic size of a readout information bit is L. (1) Specify the Q-factor of the material (the value of Q normally belongs to the interval 1.5–10). (2) Choose the value of the exchange constant A, which usually varies from 2×10^{-7} to 4×10^{-7} erg/cm^3. (3) Mark the value of L on the diagram and find the values of film thickness h, domain size P, and characteristic length l of the material corresponding to it. (4) Knowing Q and A, draw a horizontal line to the intersection with the straight line on the nomogram. (5) Find the values of $4\pi M_s$ and K_u corresponding to this point (as shown in Fig. 5).

It should be observed that the film thickness h is bounded by the optical absorption of the material. If a laser with the wavelength $\lambda = 0.63$ μm is used, the maximum possible EGFF thickness is $h = 10$ μm. This means that if the characteristic size of the magnetic field under investigation is $L \geq h/0.346 = 26$ μm, the most optimal parameters of the EGFF can be determined from the condition $\partial\chi_{m0}/\partial P = 0$ for $h = 10$ μm and $P = L$. Besides, it should be borne in mind that the coercive force is $H_c \sim 1/h$ and can be as high as 4 Oe for $1/h \sim 1$–2 Oe [5]. Thus, the application of EGFF for studying weak magnetic fields with a characteristic period exceeding 50 μm is limited in view of the increase in coercive force. This difficulty can be overcome by increasing the EGFF thickness to the optimal value with the corresponding transition to the infrared spectral region, where the optical absorption coefficient is considerably smaller (e.g., a laser with the wavelength $\lambda = 0.8$ μm can be used). If, however, one has to operate in the visible spectral range, other magnetooptical materials (like orthoferrites) should be used as the sensor.

Thus, the setup we developed to measure the amplitude of the normal component of the stray field and using an intermediate recording medium in the form of Bi-containing garnet ferrite films makes it possible to determine the parameters of domain structure of magnetic materials with an in-plane magnetization vector. The theoretical analysis carried out here makes it possible to determine the optimal parameters of the recording medium material for magnetooptical readout of information as functions of the bit size (density of recording).

REFERENCES

1. A. K. Zvezdin and V. A. Kotov, *Magnetooptics of Thin Films* (Nauka, Moscow, 1988).

2. V. V. Randoshkin and A. Ya. Chervonenkis, *Applied Magnetooptics* (Énergoatomizdat, Moscow, 1990).

3. A. Eschenfelder, *Magnetic Bubble Technology* (Springer, Heidelberg, 1980; Mir, Moscow, 1983).

4. C. Kooy and U. Enz, Philos. Res. Rept. **15**, 7 (1960).

5. R. A. Aĭnetdinov, D. E. Balabanov, V. A. Kotov, *et al.*, *Abstracts of Papers to All-Union School–Seminar on Domain and Magnetooptical Storage* (Kobuleti, 1987).

Translated by N. Wadhwa

Dynamic Magnetic Susceptibility of a Two-Layer Film in a Strong Magnetic Field

A. L. Sukstanskiĭ and G. I. Yampol'skaya

Donetsk Physicotechnical Institute, Academy of Sciences of Ukraine, Donetsk, 340114 Ukraine
E-mail: yampolsk@kinetik.ac.donetsk.ua
Received July 29, 1999

Abstract—A theoretical study is reported of the effect of interlayer exchange coupling on the resonance properties of a two-layer magnetic film with "easy-axis" and "easy-plane" anisotropic layers in a strong tilted magnetic field. The dependence of the resonance fields on the tilting angle of the external magnetic field to the film has been obtained, the tensor of integrated high-frequency film susceptibility has been found, and its dependence on the strength and orientation of the external field, as well as on layer thickness, has been analyzed. The results obtained agree with the available experimental data. © *2000 MAIK "Nauka/Interperiodica".*

The continuing interest in the investigation of multilayer magnetic structures is stimulated by their fairly unusual properties, which in many cases turn out to be more complex and diverse than those of single-layer films. The current significant interest in multilayer films is due to their broad application potential in various devices.

Among the most important characteristics of magnetic systems are their high-frequency properties, in particular, the ferromagnetic resonance (FMR) frequencies, the dynamic magnetic susceptibility of a film, etc. Obviously enough, interlayer coupling in a multilayer film may strongly affect all its properties, including the FMR frequency spectrum, as well as give rise to features in energy absorption. For this reason, films made up of magnetic layers with different magnetic anisotropy types are of major interest among multilayer structures, both for theorists and for device applications.

Among the first theoretical approaches to the investigation of two-layer magnetic films was formulating the problem of magnetization distribution in a film consisting of two exchange-coupled ferromagnetic layers with differently oriented easy axes; a particular case was that of the easy axes lying in the film plane at an angle to one another [1, 2]. The strong exchange interaction between the layers accounts for the nonuniform distribution of magnetization across such a film, which was taken into account in [1, 2] by accepting the corresponding boundary conditions. Ion-implanted films consisting of layers differing in the nature of the magnetic anisotropy were considered in [3, 4].

Attempts to analytically solve the problem of magnetization distribution in the ground state meet with formidable mathematical difficulties, and therefore certain approximation are invoked (for example, by postulating a strong external magnetic field and infinite layer thickness [3]) or a numerical approach is used [2, 4].

This work reports a theoretical study of some features in FMR frequencies and a calculation of the high-frequency magnetic susceptibility tensor for a film made up of two layers with an easy-axis and an easy-plane magnetic anisotropy. Considerable attention is paid to the existence of a gap in the FMR frequency spectrum discovered experimentally in [5, 6]. Specific features in the absorption intensity described by the high-frequency susceptibility tensor were observed in [7]. The existence of a gap in the FMR spectrum was theoretically validated in [8], where this phenomenon was related to the finiteness of the interlayer exchange coupling. However, the model used in [8] only allows description of ultrathin films, where the interface is comparable in thickness to the layers themselves. At the same time, the layer thicknesses used in the experiment [5–7] far exceed (by an order of magnitude and more) the characteristic length. In the model proposed here, the limitation on the layer thickness is removed, and the small parameter allowing the analytical solution of the FMR frequency problem and the calculation of the susceptibility tensor is the small ratio of the layer anisotropy fields to the external magnetic field.

1. FORMULATION OF THE PROBLEM

Consider a two-layer film with the surface normal coinciding with the Z axis. One of the layers (layer 1) has an easy-axis anisotropy and extends in thickness through $0 < z < d_1$, and the second layer (layer 2), occupying the $-d_2 < z < 0$ region, is easy-plane anisotropic. We assume the easy axis in layer 1 and the hard axis in layer 2 to be parallel to the Z axis. A strong tilted magnetic field $\mathbf{H}^e$ exceeding the anisotropy field H_{an} in each

layer is applied to the film (here and subsequently, the subscript $n = 1, 2$ denotes the layer number).

The equilibrium distribution of the magnetization vector $\mathbf{M}$ in a constant external field $\mathbf{H}^e$ is determined by minimizing the energy W of the structure:

$$W = \sum_{n=1,2} \int_{V_n} dV \left\{ \frac{A_n}{M_n^2} \left(\frac{d\mathbf{M}_n}{dz} \right)^2 - \frac{K_n^*}{M_n^2} \mathbf{M}_{nz}^2 - \mathbf{M}_n \mathbf{H}^e \right\}$$

$$- \int_S dS \, 2J \mathbf{M}_1 \mathbf{M}_2, \tag{1}$$

where A_n are the exchange-coupling constants, M_n is the saturation magnetization of each layer, $K_n^* = K_n - 2\pi M_n^2$ are the effective magnetic-anisotropy constants, $\mathbf{H}^e$ is the external magnetic field, and J is the interlayer exchange-coupling constant. All the constants entering (1) (A_n, K_n^*, and M_n) are assumed to be constant within each layer. Integration in the first term is performed over the volumes of the corresponding layers, and in the second one, over the layer interface. In this work, we are going to restrict ourselves to analyzing the excitations uniform in the film plane (XY) and nonuniform across the film (i.e., along the Z axis); this actually makes the problem one-dimensional, and taking into account that the magnetostatic interaction reduces to a renormalization of the anisotropy constants, $K_n^* = K_n - 2\pi M_m^2$.

The equations of motion for the magnetization in each layer can be cast in the form

$$\frac{M_n \sin\theta}{g_n} \frac{\partial\varphi}{\partial t} - \frac{\delta W_n}{\delta\theta} = \frac{\lambda_n M_n}{g_n} \frac{\partial\theta}{\partial t}$$

$$-\frac{M_n \sin\theta}{g_n} \frac{\partial\theta}{\partial t} - \frac{\delta W_n}{\delta\varphi} = \frac{\lambda_n M_n}{g_n} \sin^2\theta \frac{\partial\varphi}{\partial t}, \tag{2}$$

where λ_n are the damping coefficients, g_n are the gyromagnetic ratios, and the angular variables θ and φ parametrize the magnetization vectors, $\mathbf{M}_n = M_n(\cos\theta, \sin\theta\sin\varphi, \sin\theta\cos\varphi)$.

The boundary conditions for the coupled equations (2) taking into account the interlayer exchange coupling can be written as [9–11]

$$\mathbf{M}'(d_1) = 0, \quad \mathbf{M}'(-d_2) = 0,$$

$$\mathbf{M}_1 \frac{A_1}{M_1^2} \mathbf{M}_1' = J\mathbf{M}_1\mathbf{M}_2, \quad \mathbf{M}_2 \frac{A_2}{M_2^2} \mathbf{M}_2' = J\mathbf{M}_1\mathbf{M}_2, \tag{3}$$

where the prime denotes the derivative with respect to the coordinate Z. This choice of boundary conditions corresponds to free spins at the film surface and takes into account the exchange interaction between the layers at their interface, which is described by the second term in (1).

Note that many works dealing with the analysis of linear and nonlinear excitations in layered structures [3–5] make use of simpler boundary conditions at the layer interface; i.e.,

$$\frac{A_1}{M_1^2}\mathbf{M}_1' = \frac{A_2}{M_2^2}\mathbf{M}_2', \quad \frac{\mathbf{M}_1}{M_1} = \frac{\mathbf{M}_2}{M_2}. \tag{4}$$

One readily sees that these boundary conditions are actually the limiting case of boundary conditions (3) and correspond to an infinitely strong interlayer exchange coupling ($J \longrightarrow \infty$). As we shall see later, in this limiting case, the two-layer film under study here has only one FMR frequency rather than two, which are found to exist at a finite exchange-coupling parameter J.

Because the film is assumed to be isotropic in the (XY) plane, we shall consider, without any loss of generality, that the external dc magnetic field $\mathbf{H}^e$ lies in the (YZ) plane, with its direction given by the φ_H and $\theta_H = \pi/2$ angles.

2. FMR AND RESONANCE FIELDS

In order to analyze the spectrum of linear excitations of the two-layer film under study, one has to linearize the equations of motion (2) and the boundary conditions (3) with respect to small deviations of the magnetization vector $\mathbf{M}$ from its equilibrium distribution, for which purpose we set $\theta = \theta_0 + \vartheta$, $\varphi = \varphi_0 + \psi$, and ϑ, $\psi \ll 1$, where the angles θ_0 and φ_0 correspond to the equilibrium distribution of the $\mathbf{M}$ vector. In the two-layer film under study with different magnetic anisotropies in the layers, this magnetization distribution is nonuniform across its thickness, even in a strong tilted magnetic field in excess of the layer anisotropy fields H_{an} [12]. The equilibrium magnetization in an infinite easy-axis magnet would be tilted at an angle $\varphi_{10} = \varphi_H - \sin 2\varphi_H/2h_1$, and in an easy-plane one, at $\varphi_{20} = \varphi_H + \sin 2\varphi_H/2h_2$. The interlayer exchange coupling in a two-layer film of a finite thickness makes the magnetization vector turn within the angular interval ($\tilde{\varphi}_{10}$, $\tilde{\varphi}_{20}$), where the $\tilde{\varphi}_{10}$ and $\tilde{\varphi}_{20}$ angles define the magnetization orientation at the film surfaces, $\varphi_{10} > \tilde{\varphi}_{10} > \tilde{\varphi}_{20} > \varphi_{20}$, to form a kind of a "domain wall." This nonuniformity in the magnetization distribution is, however, small because of the smallness of the ($\sim H_{an}/H$) parameter, and therefore in the equations linearized in the ϑ and ψ variables one can set $\theta_0 = \pi/2$, $\varphi_0 = \varphi_H$; i.e., assume the ground state to be uniform. In this case, interlayer exchange will become manifest only in the spin wave equations.

The equations describing the normal vibrations of

the system in this approximation have the form

$$\frac{1}{\omega_n}\frac{\partial \vartheta}{\partial t} - l_n^2 \psi'' + (h_n + \operatorname{sgn} K_n^* \cos 2\varphi_H)\psi$$

$$+ \lambda_n[-l_n \vartheta'' + (h_n + \operatorname{sgn} K_n^* \cos^2 \varphi_H)\vartheta] = 0,$$

$$-\frac{1}{\omega_n}\frac{\partial \psi}{\partial t} - l_n^2 \vartheta'' + (h_n + \operatorname{sgn} K_n^* \cos 2\varphi_H)\vartheta \tag{5}$$

$$- \lambda_n[-l_n \psi'' + (h_n + \operatorname{sgn} K_n^* \cos^2 \varphi_H)\psi] = 0.$$

Here $l_n = (A_n/|K_n^*|)^{1/2}$ is the characteristic length, $h_n = H^e M_n/2|K_n^*|$ is the normalized external field, and $\omega_n = 2g_n|K^*|/M_n$ is the frequency of uniform FMR in the nth layer in the absence of an external magnetic field.

The linearized boundary conditions can be written as

$$\vartheta'(d_1) = 0, \quad \psi'(d_1) = 0,$$

$$\vartheta'(d_2) = 0, \quad \psi'(d_2) = 0,$$

$$A_1 \vartheta'(+0) = A_2 \vartheta'(-0) = J[\vartheta'(-0) - \vartheta'(+0)], \tag{6}$$

$$A_1 \psi'(+0) = A_2 \psi'(-0) = J[\psi'(-0) - \psi'(+0)].$$

We shall look for the solution to linear homogeneous equations (5) in each layer in the form

$$\bar{\vartheta} = (\vartheta_{na}\cos k_n z + \vartheta_{nb}\sin k_n z)\exp(i\omega t),$$

$$\bar{\psi} = (\psi_{na}\cos k_n z + \psi_{nb}\sin k_n z)\exp(i\omega t). \tag{7}$$

Inserting (7) into equations (4) yields a homogeneous system of algebraic equations for the coefficients ϑ_{na}, ϑ_{nb}, ψ_{na}, ψ_{nb}; now, equating the determinant of this system to zero, we come to the spin-wave dispersion relation $\omega = \omega(k)$. The dissipative term in the equations of motion naturally results in the ω quantity being complex (while the wave vector k is real), $\omega = \omega' + i\omega''$, where ω' is the normal vibration frequency and ω'' characterizes the spin wave damping,

$$\omega'^2 = \omega_n^2(h_n + \operatorname{sgn} K_n^* \cos 2\varphi_H + l_n^2 k_n^2)$$

$$\times (h_n + \operatorname{sgn} K_n^* \cos^2 \varphi_H + l_n^2 k_n^2),$$

$$\omega'' = \lambda_n \omega_n(h_n \tag{8}$$

$$+ \operatorname{sgn} K_n^*(\cos 2\varphi_H + \cos^2 \varphi_H)/2 + l_n^2 k_n^2).$$

Obviously enough, the same frequency ω in different layers should be identified with different values of the wave vector $k = k_n$, namely,

$$k_n = \frac{1}{l_n}\left\{ \left(\frac{\omega^2}{\omega_n^2} + \frac{\sin^4 \varphi_H}{4} \right)^{1/2} - h_n \right.$$

$$\left. - \frac{\operatorname{sgn} K_n^*}{2}(\cos 2\varphi_H + \cos^2 \varphi_H) \right\}^{1/2} \tag{9}$$

(without loss of generality, we shall assume that $k_n > 0$).

Substituting (7) into the boundary conditions (6) yields an equation for resonance frequencies as functions of the external field $\mathbf{H}^e$, which can be cast in the form

$$(H_1 - H)(H_2 - H) + \frac{J}{M_1 d_1}(H_2 - H)$$

$$+ \frac{J}{M_2 d_2}(H_1 - H) = 0, \tag{10}$$

where

$$H_n = H_{an}[(\omega'^2/\omega_n^2 + \sin^4 \varphi_H/4)^{1/2}$$

$$- \operatorname{sgn} K_n^*(\cos 2\varphi_H + \cos^2 \varphi_H)/2].$$

One readily sees that the quantities H_n are actually the values of the external field at which the FMR occurs at a frequency ω for a fixed angle φ_H in individual layers; therefore, we shall call the H_n quantities in what follows the resonance fields of the nth layer.

Equation (10) gives the eigenfrequencies of a two-layer film as functions of parameters of the two-layer film and of the external magnetic field $\mathbf{H}^e$ in an implicit form. An explicit expression for the resonance frequencies generally cannot be derived from (10), and therefore one can conveniently consider this expression as representing the resonance field as a function of its tilt angle φ_H and of the frequency ω; i.e., $H = H(\omega, \varphi_H)$. Equation (10) can be solved for H in a trivial way by determining two values of the resonance field of a two-layer structure as a function of the frequency ω and of the tilt angle φ_H:

$$H_{\pm} = \frac{1}{2}\{H_1 + H_2 + J_1 + J_2 \pm D^{1/2}\},$$

$$D = (H_1 + H_2 + J_1 + J_2)^2 \tag{11}$$

$$- 4(H_1 H_2 + H_1 J_2 + H_2 J_1),$$

where we have introduced the notation $J_n = J/M_n d_n$.

As seen from (11), for any finite value of the J parameter, there exist two values of the resonance field given by expression (11) (and, hence, two FMR frequencies). In the limiting case of $J = 0$, which corresponds to noninteracting layers, the resonance fields H_+ and H_- coincide naturally with the corresponding values of the H_1 and H_2 fields for one-layer films. In the
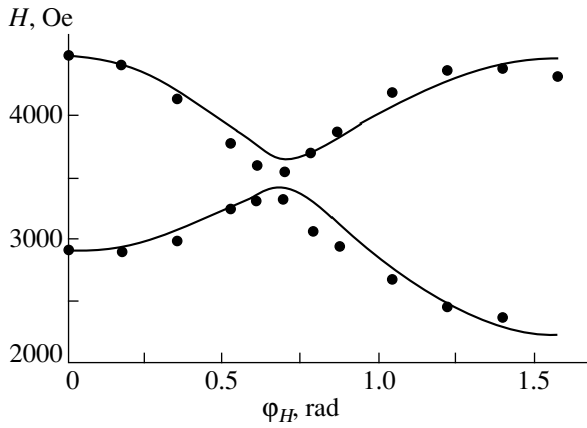
Fig. 1. Resonance fields $H_\pm$ plotted against the tilt angle φ_H of the external magnetic field with respect to the film normal. The points are experimental data.

opposite limiting case of $J \longrightarrow \infty$, which can be identified with the strongest possible exchange coupling between the layers, the resonance field H_+ also grows without limit, $H_+ \approx J_1 + J_2 \sim J \longrightarrow \infty$, which leaves only one hybrid resonance field for the film under study here (and, hence, only one FMR frequency)

$$H_- = H_1 \frac{J_2}{J_1 + J_2} + H_2 \frac{J_1}{J_1 + J_2}. \tag{12}$$

This behavior of the resonance fields (and FMR frequencies) allows a straightforward interpretation based on a simple mechanical analogy; indeed, a two-layer film may be considered conventionally as two coupled oscillators, with the normal frequency of each oscillator coinciding with the FMR frequencies of noninteracting layers. If the coupling between the oscillators is finite, the system will have two normal frequencies, while if the oscillators are rigidly connected, the system is characterized by a single resonance frequency.

Figure 1 presents plots of the two resonance fields vs. the tilt angle φ_H relative to the Z axis calculated for a fixed frequency ($\omega = 2\pi \times 7.92$ GHz) from (11) for several values of the two-layer parameters (solid

curves). Both branches are seen to depend nonmonotonically on the tilt angle φ_H, with the minimum resonance field on the upper branch, $(H_+)_{min}$, and the maximum field on the lower branch, $(H_-)_{max}$, occurring for different φ_H angles. It is essential that $(H_-)_{max} < (H_+)_{min}$ for any value of the film parameters. Hence, the upper branch is separated from the lower one by a gap; i.e., an interval of external fields within which FMR does not exist for any tilt angle φ_H. It goes without saying that the gap width depends on the parameter of interlayer exchange coupling.

The points in Fig. 1 show the experimental values of the resonance fields obtained in [13] for a two-layer film with known magnetic parameters (see the table). It is these parameters that were used in constructing the theoretical graphs in Fig. 1, with the interlayer exchange coupling constant J being the only fitting parameter; the best fit to the experiment was achieved for $J = 0.24$ cm. This film is characterized by a small value of the J parameter, such that $J_1, J_2 \ll H_1, H_2$; besides, the inequality $|J_1 - J_2| \gg |H_1 - H_2|$ holds. As can readily be seen from the general relation (11), for any value of the φ_H angle (excluding a narrow region near the gap), the resonance fields H_+ and H_- can be approximated for such parameters by the $H_1 + J_1$ and $H_1 - J_2$ expressions, respectively.

Generally, the analytic expressions for the extremal values of resonance fields, $(H_+)_{min}$ and $(H_-)_{max}$, and for the angles, $\varphi_+ = \varphi_H((H_+)_{min})$ and $\varphi_- = \varphi_H((H_-)_{max})$, at which these values are reached, are very cumbersome. However, if the angles φ_+ and φ_- are close to one another, the gap δH can be estimated approximately by the expression $\delta H \approx 2(J_1 J_2)^{1/2}$. For a two-layer film with the parameters listed in the table, one obtains 316 Oe, a value that agrees with the experiment.

In concluding to this section, we note that in the case of fairly "thick" magnetic layers making up a two-layer film, the effect of interlayer exchange coupling on the FMR frequencies of the film under consideration (or on the resonance fields) may be expected to be small. Indeed, for sufficiently large thicknesses, the parameters $J_n = J/M_n d_n$ become small; thus, we return to the limiting case $J_n \ll H_n$, where the second and third terms in (10) may be neglected, after which the resonance fields H_+ and H_- will coincide with the corresponding values of H_2 and H_1 characteristic of noninteracting layers. If one reduces the thickness of one of the layers (for instance, by gradually etching off the first layer), the second term in (10), which is proportional to J_1, will increase, while the third one, proportional to J_2, will remain small. As can be readily verified, the resonance fields in this case are equal to H_2 and $H_1 + J_1$ (except a region near the gap); i.e., one of the FMR frequencies of the two-layer film coincides with the resonance frequency of the thicker layer, and the second frequency differs from the FMR frequency of the thinner layer (in

Parameters of a two-layer YIG structure

Layer	1	2
Composition	$(YEuTmCa)_3(FeGe)_5O_{12}$	$(YGdLa)_3(FeGa)_5O_{12}$
A, erg/cm	2.9×10^7	3.5×10^7
M, Gs	36.53	70.06
K^*, erg/cm^3	18264	−70000
d	0.5×10^{-4}	0.18×10^{-4}
g, Oe^{-1} cm^{-1}	1.25×10^7	1.78×10^7
λ	2.5×10^{-3}	6×10^{-3}

the limit as $d_1 \longrightarrow 0$, the film only has one resonance frequency which coincides naturally with that of the second layer).

3. HIGH-FREQUENCY SUSCEPTIBILITY TENSOR FOR A TWO-LAYER FILM

To analyze forced linear vibrations of a two-layer film, consider linearized equations of motion that include not only a constant, but also a variable external magnetic field $\tilde{\mathbf{H}}(t) = \tilde{\mathbf{H}}_0 \exp(i\omega t)$ of frequency ω. These equations naturally differ from equations (5) only in the presence of a nonzero right-hand side, which is proportional to the external variable field $\tilde{\mathbf{H}}(t)$

$$\frac{1}{\omega_n}\frac{\partial \vartheta}{\partial t} - l_n^2 \psi'' + (h_n + \operatorname{sgn} K_n^* \cos 2\varphi_H)\psi$$

$$+ \lambda_n[-l_n \vartheta'' + (h_n + \operatorname{sgn} K_n^* \cos^2 \varphi_H)\vartheta]$$

$$= \tilde{h}_{ny} \cos \varphi_H - \tilde{h}_{nz} \sin \varphi_H, \qquad (13)$$

$$-\frac{1}{\omega_n}\frac{\partial \psi}{\partial t} - l_n^2 \vartheta'' + (h_n + \operatorname{sgn} K_n^* \cos 2\varphi_H)\vartheta$$

$$- \lambda_n[-l_n \psi'' + (h_n + \operatorname{sgn} K_n^* \cos^2 \varphi_H)\psi] = -\tilde{h}_{nx},$$

where $\tilde{\mathbf{h}}_n = \tilde{\mathbf{H}}/H_{an}$.

We shall look for the solution to the inhomogeneous linear equations (13) in the form of $\vartheta = \bar{\vartheta} + \tilde{\vartheta}$, $\psi = \bar{\psi} + \tilde{\psi}$, where $\bar{\vartheta}$, $\bar{\psi}$ is the general solution (7) of the homogeneous system found in the preceding section, and $\tilde{\vartheta}$, $\tilde{\psi}$ are particular solutions of the inhomogeneous system. We find from (13) that

$$\tilde{\vartheta}_n = \frac{-\tilde{H}_x F_n^{(2)} + (\tilde{H}_y \cos \varphi_H - \tilde{H}_z \sin \varphi_H)\left(\dfrac{i\omega}{\omega_n}H_{an} + \lambda_n F_n^{(2)}\right)}{(H_n + iR_n - H)(U_n - iR_n + H)},$$

$$\tilde{\psi}_n = \frac{\tilde{H}_x\left(\dfrac{i\omega}{\omega_n}H_{an} + \lambda_n F_n^{(1)}\right) + (\tilde{H}_y \cos \varphi_H - \tilde{H}_z \sin \varphi_H)F_n^{(1)}}{(H_n + iR_n - H)(U_n - iR_n + H)}. \qquad (14)$$

We have introduced here the notation $R_n = -\omega \lambda_n H_{an}/\omega_n$,

$$U_n = H_{an}\left[\left(\frac{\omega^2}{\omega_n^2} + \frac{\sin^4 \varphi_H}{4}\right)^{1/2}\right.$$

$$\left. - \frac{\operatorname{sgn} K_n^*}{2}(\cos 2\varphi_H + \cos^2 \varphi_H)\right],$$

$$F_n^{(1)} = H^e + \operatorname{sgn} K_n^* H_{an} \cos^2 \varphi_H,$$

$$F_n^{(2)} = H^e + \operatorname{sgn} K_n^* H_{an} \cos 2\varphi_H.$$

The coefficients ϑ_{na}, ϑ_{nb}, ψ_{na}, ψ_{nb} appearing in the general solution (7) of the homogeneous system of equations can be found by substituting the general solution of the inhomogeneous equation $\vartheta = \bar{\vartheta} + \tilde{\vartheta}$, $\psi = \bar{\psi} + \tilde{\psi}$ into the boundary conditions (6):

$$\vartheta_{1a} = (\tilde{\vartheta}_2 - \tilde{\vartheta}_1)\frac{J_1(H_2 + iR_2 - H)}{(H_+ + iR_+ - H)(H_- + iR_- - H)},$$

$$\vartheta_{1b} = (\tilde{\vartheta}_2 - \tilde{\vartheta}_1)\tan k_1 d_1,$$

$$\vartheta_{2a} = -(\tilde{\vartheta}_2 - \tilde{\vartheta}_1)\frac{J_2(H_1 + iR_1 - H)}{(H_+ + iR_+ - H)(H_- + iR_- - H)},$$

$$\vartheta_{2b} = (\tilde{\vartheta}_2 - \tilde{\vartheta}_1)\tan k_2 d_2,$$

$$\psi_{1a} = (\tilde{\psi}_2 - \tilde{\psi}_1)\frac{J_1(H_2 + iR_2 - H)}{(H_+ + iR_+ - H)(H_- + iR_- - H)}, \qquad (15)$$

$$\psi_{1b} = (\tilde{\psi}_2 - \tilde{\psi}_1)\tan k_1 d_1,$$

$$\psi_{2a} = -(\tilde{\psi}_2 - \tilde{\psi}_1)\frac{J_2(H_1 + iR_1 - H)}{(H_+ + iR_+ - H)(H_- + iR_- - H)},$$

$$\psi_{2b} = (\tilde{\psi}_2 - \tilde{\psi}_1)\tan k_2 d_2,$$

where the quantities $R_\pm = [R_1 + R_2 \pm (R_1 - R_2)(H_1 + J_1 - H_2 - J_2)/D^{1/2}]/2$ determine the height and width of the resonance peak.

Based on the expressions (7), (14), and (15) obtained for the magnetization distribution, one can readily find the tensor of the integrated high-frequency susceptibility $\hat{\tilde{\chi}}(\omega)$, which is defined as a coefficient of proportionality between the components of integrated magnetization and of the external variable magnetic field. The imaginary part $\hat{\tilde{\chi}}(\omega)$ is known to determine the energy absorption by a system:

$$Q = -\frac{\omega}{2}\sum_{i,j=1}^{2} \bar{\chi}_{ij}''(\omega)\tilde{H}_i\tilde{H}_j.$$

In the general case, we have

$$\hat{\bar{\chi}} = \frac{1}{(d_1 + d_2)} \frac{1}{(H_+ + iR_+ - H)(H_- + iR_- - H)}$$

$$\times \begin{pmatrix} P_1(2, 2) & -\cos\varphi_H P_2(2, 2) & \sin\varphi_H P_2(2, 2) \\ \cos\varphi_H P_2(1, 1) & \cos^2\varphi_H P_1(1, 1) & -\sin\varphi_H\cos\varphi_H P_1(1, 1) \\ -\sin\varphi_H P_2(1, 1) & -\sin\varphi_H\cos\varphi_H P_1(1, 1) & \sin^2\varphi_H P_1(1, 1) \end{pmatrix}. \tag{16}$$

The notation used here is as follows

$$P_1(k, j) = \frac{M_1 d_1(H_2 + J_1 + J_2 + iR_2 - H)F_1^{(k)}}{U_1 - iR_1 + H}$$

$$+ \frac{M_2 d_2(H_1 + J_1 + J_2 + iR_1 - H)F_2^{(j)}}{U_2 - iR_2 + H};$$

$$P_2(k, j) \tag{17}$$

$$= \frac{M_1 d_1(H_2 + J_1 + J_2 + iR_2 - H)\left(\dfrac{i\omega}{\omega_1}H_{a1} + \lambda_1 F_1^{(k)}\right)}{U_1 - iR_1 + H}$$

$$+ \frac{M_2 d_2(H_1 + J_1 + J_2 + iR_1 - H)\left(\dfrac{i\omega}{\omega_2}H_{a2} + \lambda_2 F_2^{(j)}\right)}{U_1 - iR_2 + H}.$$

It should be stressed that the components of the integrated susceptibility tensor $\hat{\bar{\chi}}(\omega)$, as expected, exhibit a resonance behavior at external fields H close to the resonance fields of a two-layer film, and H_+ and H_- [$P_n(k, j)$ are smooth functions of the external field, which do not contain resonance denominators], whereas the expressions (15) for the amplitudes ϑ_{na}, ϑ_{nb}, ψ_{na}, ψ_{nb} have resonance denominators not only in the fields $H_\pm$, but also in the fields $H_{1,2}$ characteristic of noninteracting layers.

Note also that all nine components of the integrated susceptibility tensor are usually different. The $\hat{\bar{\chi}}(\omega)$ tensor acquires a simpler form in the Cartesian frame $(X'Y'Z')$, in which the Cartesian axis Z' is directed along the external magnetic field $\mathbf{H}^e$, and the film surface normal lies in the $(Y'Z')$ plane. In this system, the integrated-susceptibility tensor can be written

$$\hat{\bar{\chi}} = \frac{1}{(d_1 + d_2)} \frac{1}{(H_+ + iR_+ - H)(H_- + iR_- - H)}$$

$$\times \begin{pmatrix} P_1(2, 2) & P_2(2, 2) & 0 \\ P_2(1, 1) & P_1(1, 1) & 0 \\ 0 & 0 & 0 \end{pmatrix}. \tag{18}$$

Figure 2 presents the dependences of the imaginary parts of the components of the susceptibility tensor $\hat{\bar{\chi}}''$ on the external field H^e calculated for different tilt angles φ_H of the external field with the two-layer film parameters given in the table. The diagonal components (Fig. 2a) exhibit a typical resonance behavior for fields close to H_+ and H_- [the difference is due to the presence of dissipative terms in the denominator of (18)], whereas the off-diagonal components of the $\hat{\bar{\chi}}''$ tensor follow a typical resonance-antiresonance pattern
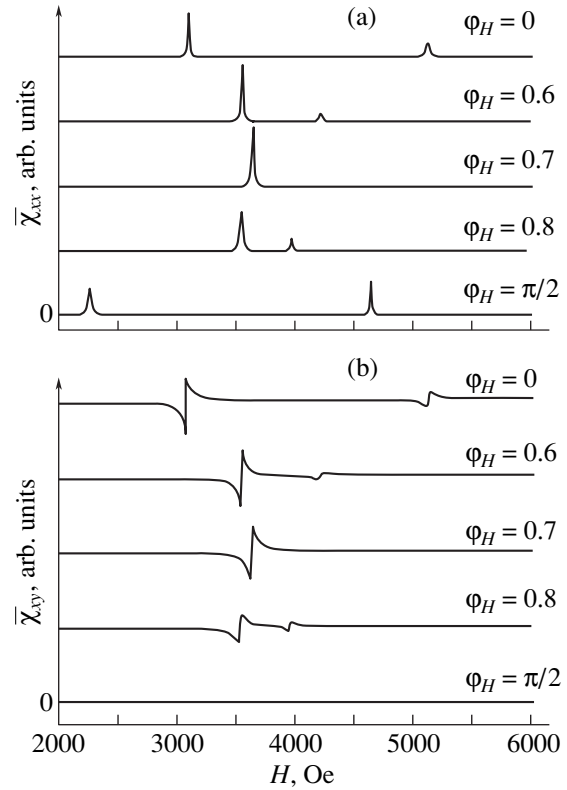

Fig. 2. Imaginary parts of the components of the integrated susceptibility $\hat{\bar{\chi}}$ plotted against the external magnetic field H^e for various angles φ_H (rad). (a) $\bar{\chi}''_{xx}$, (b) $\bar{\chi}''_{xy}$.
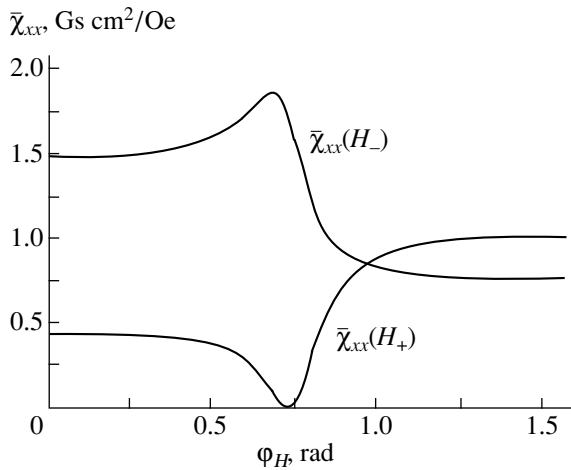
Fig. 3. Maximum values of the imaginary parts of the components of integrated susceptibility $\hat{\bar{\chi}}$ plotted against the angle φ_H.

Fig. 4. Dependence of the maximum values of $\bar{\chi}_{xx}''$ on thickness of the easy-axis layer (layer 1) plotted for $\varphi_H = 0$.

(Fig. 2b). The values of the resonance fields as functions of the tilt angle φ_H are naturally close to the corresponding dependences of the H_+ and H_- fields [see (11) and Fig. 1].

Note the substantial difference in the intensity of the peaks corresponding to the upper and lower resonance fields, and the strong dependence of these intensities on the angle φ_H. Figure 3 presents the extremal values of the imaginary parts of the integrated susceptibility tensor components as functions of the field tilt angle φ_H. The resonance peak corresponding to the upper resonance field H_+ decreases in intensity with the external magnetic field deviating from the film norm, and in the gap region, where the separation between the H_+ and H_- fields is small, this intensity becomes so low as to be practically indistinguishable against the background of the peak due to the lower resonance field H_-. A comparison of our theoretical dependence with the experimental plot [7] reveals a fairly good qualitative agreement between the theoretical and experimental curves, which proves the validity of the model proposed here.

The dependence of the peak intensity on the thickness d_1 of one of the layers making up a two-layer film was also studied experimentally [7]. Figure 4 plots a calculated dependence of the imaginary part of integrated susceptibility on the thickness of the easy-axis layer. For $H = H_+$, this dependence (the lower curve in Fig. 4) also exhibits a qualitatively good agreement with those presented in [7]. Unfortunately, the lack of reliable experimental data does not presently allow one to make a qualitative and a quantitative comparison of theoretical and experimental curves.

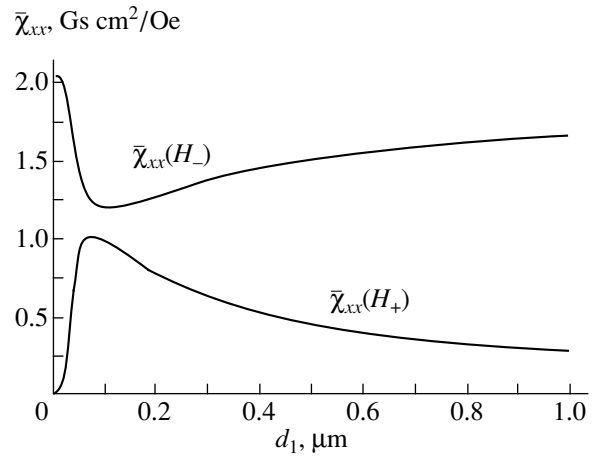We note, in conclusion, that the theoretical model put forward in this work permits a description of the main high-frequency properties of a two-layer exchange-coupled magnetic film. The above comparison was made with experimental data available for epitaxial YIG films, in which the interlayer exchange coupling parameter J is relatively small. However, the model adequately reproduces the properties of ion-implanted films as well, for which this parameter is fairly large [in some cases, one may consider it to be infinitely large and use approximate boundary conditions (4)]. Besides, by taking into account the eddy currents one can readily generalize the obtained results to cover metallic films.

ACKNOWLEDGMENTS

REFERENCES

1. E. Goto, N. Hayashi, T. Miyashita, *et al.*, J. Appl. Phys. **36**, 2951 (1951).
2. F. B. Hagedorn, J. Appl. Phys. **41**, 2491 (1970).
3. Yu. G. Lebedev, E. I. Raevskiĭ, Yu. K. Milyaev, *et al.*, Mikroélektronika **14**, 501 (1985).
4. V. B. Sadkov and G. A. Shmatov, Preprint no. 88/5, Sverdlovsk, 1988.
5. A. M. Grishin, V. S. Dellalov, V. F. Shkar, *et al.*, Phys. Lett. A **140**, 133 (1989).
6. N. K. Dan'shin, V. S. Dellalov, M. A. Kol'tsov, *et al.*, Zh. Éksp. Teor. Fiz. **110**, 938 (1996) [JETP **83**, 517 (1996)].
7. V. F. Shkar', I. M. Makmak, V. V. Petrenko, *et al.*, Pis'ma Zh. Éksp. Teor. Fiz. **56**, 251 (1992) [JETP Lett. **56**, 246 (1992)].

8. A. V. Kobelev and Ya. G. Smorodinskiĭ, Fiz. Tverd. Tela (Leningrad) **31** (10), 6 (1989) [Sov. Phys. Solid State **31**, 1656 (1989)].

9. V. A. Ignatchenko, Fiz. Met. Metalloved. **36**, 1219 (1973).

10. F. Hoffman, A. Stankoff, and H. Pascard, J. Appl. Phys. **41**, 1022 (1970).

11. G. Rado and J. Weertman, Phys. Rev. **94**, 1386 (1954).

12. A. L. Sukstanskiĭ and G. I. Yampol'skaya, Fiz. Tekh. Vys. Davl. **8** (3), 65 (1998).

13. A. L. Sukstanskiĭ and G. I. Yampol'skaya, Fiz. Tekh. Vys. Davl. **9** (2), 43 (1999).

Translated by G. Skrebtsov

MAGNETISM
AND FERROELECTRICITY

Depth-Selective Conversion-Electron Mössbauer Spectroscopy of the Surface of Ba–M Hexaferrite Single Crystals

A. Kamzin*, B. Stahl**, R. Gellert**, G. Klingelhofer**, E. Kankeleit**, L. G. Ol'khovik***, and D. Vcherashniĭ*

*Ioffe Physicotechnical Institute, Russian Academy of Sciences, Politekhnicheskaya ul. 26, St. Petersburg, 194021 Russia
**Institute of Nuclear Physics, Technical University, D-64289 Darmstadt, Germany
***Kharkov State University, pl. Svobody 4, Kharkov, 310077 Ukraine
Received August 20, 1999; in final form, October 5, 1999

Abstract—The magnetic properties of a 50- to 2-nm-thick surface layer in hexagonal ferrite $BaFe_{12}O_{19}$ single crystals are investigated for the first time. Measurements are made on a conversion-electron Mössbauer spectrometer constructed on the basis of a unique ultrahigh-vacuum magnetostatic electron analyzer of the "orange" type. An analysis of the experimental Mössbauer spectra obtained from the surface layer of $BaFe_{12}O_{19}$ 50- to 2-nm-thick single crystals reveals that (1) the spectral line widths are close to the natural widths of Mössbauer lines and neither changes nor a set of the values of effective magnetic fields, as well as a paramagnetic state of iron ions, could appear due to a defect such as the "surface," and (2) the experimental spectra are best described only under the assumption that the surface of a hexaferrite $BaFe_{12}O_{19}$ single crystal contains a 2-nm-thick layer, in which the magnetic moments of iron ions are deflected through ~20° from the crystallographic C axis along which the magnetic moments of ions located in the bulk of the crystal are oriented. © *2000 MAIK "Nauka/Interperiodica".*

Since the early 1970s, the number of publications devoted to peculiarities of the magnetic structure of the surface layer of crystals and the processes on the surface accompanying phase transitions has increased considerably. From the point of view of fundamental investigations, this is due to the need to explain the effect of surface on the properties of the surface layer of the crystal. The study of the formation of surface layer properties is also important from the viewpoint of applications, since fine powders and thin films, in which the effect of the surface is significant, are widely used in modern microelectronic devices.

The possibility that the properties of the surface layer and of the bulk of the crystal are different was first demonstrated by Neel [1], who theoretically substantiated the assumption of the existence of an anisotropic layer having a thickness of several tens of angströms on the surface of ferromagnetic crystals. The study of fine powders [2] revealed that the magnetic moments of iron ions in crystallites are not aligned collinearly to the magnetic field, even for its large values. This led to the conclusion on the existence of a thin layer on the surface, in which the orientation of magnetic moments differs from that in the bulk of the crystallite. Subsequently, the magnetic properties of fine powders were explained on the basis of a model according to which the magnetic moments of ions located in a thin surface layer are oriented not parallel to one another, but at a certain angle Θ, thus forming an angular, or a noncollinear, magnetic structure in this surface layer [3, 4].

The angle Θ in this model must vary smoothly as we move to the bulk of a crystallite.

Another approach to explaining the magnetic properties of a group of particles presumes the existence on the crystallite surface (or "magnetically dead," in the terminology of the authors of [5–7]) layer of a thin paramagnetic. In this case, the exchange interaction of surface ions is much weaker than for ions located in the bulk of the sample, in view of the absence of one or several nearest magnetic neighbors. The destruction of the magnetic ordering of ions located at the sample surface by thermal fluctuations results in the formation of a layer that makes no contribution to the magnetization of the crystallite. The estimated values of the thickness of the "magnetically dead" layer were ~20–25 Å for ferrite particles [5–8] and from 10 to 100 Å for other compounds [3, 9].

Other interpretations of the results of experiments described in [2, 3] also exist. For example, Parker *et al.* [10, 11] explained these results by the presence of a large fraction of smaller-size crystallites in the groups of particles under investigation. Thus, the existence of a thin layer with a noncollinear arrangement of magnetic moments on the surface of a crystallite did not receive unambiguous confirmation. This is due to the complexity of investigating the properties of the surface for fine powders due to relaxation processes intensified upon a decrease in the crystallite size, as well as to technological difficulties in obtaining a group of particles with a small size dispersion. Consequently, the properties of the surface should be investigated on the
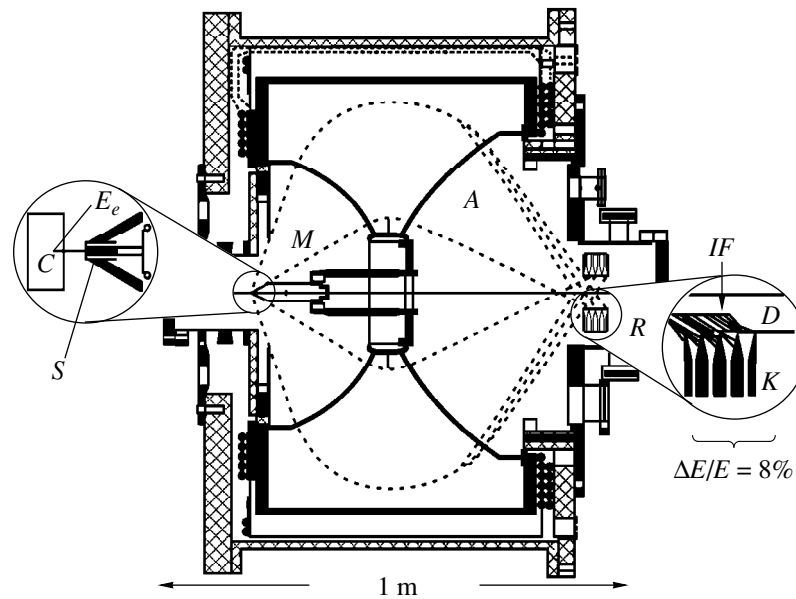
Fig. 1. Schematic diagram of the setup for depth-selective conversion-electron Mössbauer spectroscopy: (*A*) magnetic system of the electron analyzer, (*M*) Doppler modulator, (*S*) source of gamma quanta, (*C*) crystal under investigation, (*R*) electron counter, (*IF*) ideal focussing position, (*D*) diaphragm, and (*K*) electron recording channels.

cuts of macroscopic crystals. Such experiments were first made by Krinchik *et al*. [12, 13] assuming that the thickness of the anisotropic surface layer at the surface of antiferromagnets with weak ferromagnetism must be considerably larger than in ferromagnets. The experimental results allowed these authors to discover an anisotropic surface layer (called a "transition" layer) and to assume that the orientation of magnetic moments within this layer changes smoothly. Subsequently, a "transition" layer was observed for other macroscopic crystals exhibiting weak ferromagnetism [14–16]. The thickness of the "transition" layer obtained from theoretical calculations for $FeBO_3$ amounted to ~500 nm [15], which agrees well with the estimates based on the experimental data [14].

New prospects in the study of the properties of the surface of a macroscopic crystal were opened by the simultaneous gamma-resonance, x-ray, and electron Mössbauer spectroscopy (SGXES) methods, which makes it possible to simultaneously gain information about the surface layer and the bulk of the crystal [17, 18]. As a result, direct experimental evidence was obtained [19] on the existence of a ~400 nm-thick layer on the surface of single crystals with weak ferromagnetism, in which the orientation of magnetic moments differs from that in the bulk, this difference increasing as one approaches the surface.

The SGXES experiments with Ba–M, Sr–M, and Pb–M hexagonal ferrites [20] did not reveal the presence of a "transition" layer to within an experimental error in analyzing layers with thicknesses larger than 20 nm. According to estimates obtained in [1, 20], the thickness of the anisotropic surface layer in ferrites

amounts to a few nanometers. Thus, the magnetic structure of the surface of ferrites should be studied by using methods permitting an analysis of surface layers to within 1 nm. The results of investigating the surface layers of macroscopic crystals of Ba–M type hexagonal ferrite (with the chemical formula $BaFe_{12}O_{19}$) are described in the present paper.

1. METHOD OF DEPTH-SELECTIVE CONVERSION-ELECTRON MÖSSBAUER SPECTROSCOPY

In our measurements, we used the method of depth-selective conversion-electron Mössbauer spectroscopy (DSCEMS), first proposed in [21]. The schematic diagram of the spectrometer is shown in Fig. 1. The accuracy of the measurement of the layer thickness was elevated considerably by using computer technologies [22] for designing the shape of the magnetic separator for electrons. The information on the properties of the layer was obtained from calculations of energy losses for conversion or Auger electrons, whose yield function was determined on the basis of the Monte Carlo method [22, 23]. The magnetostatic system we developed has the following parameters: a transmittance of 21% of 4π, and an energy resolution of 0.2–2%, depending on the sample size.

2. DISCUSSION OF EXPERIMENTAL RESULTS

Single crystals of hexagonal barium ferrite $BaFe_{12}O_{19}$ were synthesized from a solution in melt. The concentration of the ^{57}Fe isotope in the compound
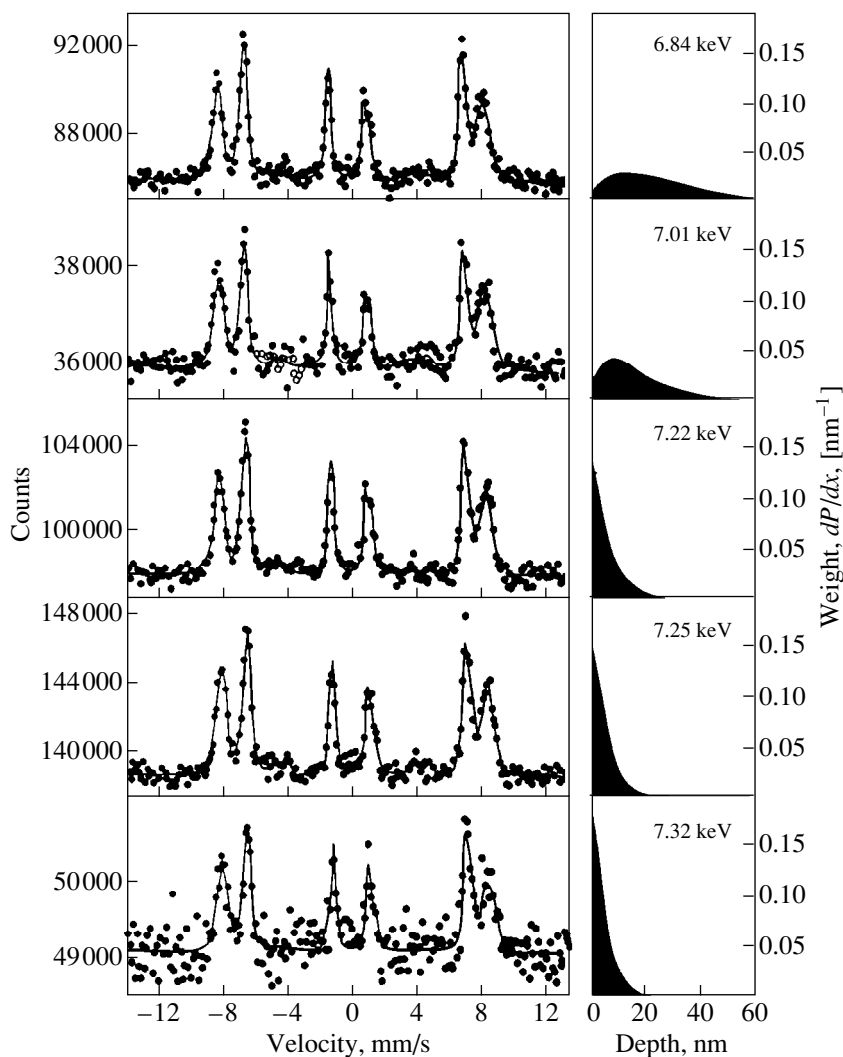
Fig. 2. Mössbauer spectra of $BaFe_{12}O_{19}$ single crystals obtained at 293 K by recording conversion electrons from surface layers. The wave vector of gamma quanta is parallel to the crystallographic C axis. The probabilities of an electron recording as functions of the depth of an atom's location at which the electron has been formed are shown on the right.

was natural, i.e., 2% of the iron content. The sample plates having a diameter of 9 nm and a thickness of ~120 μm were cut from single crystals. X-ray studies proved that the crystallographic C axis was perpendicular to the plane of the plates. In the sample preparation, special attention was paid to the quality of the crystal surface under investigation. Previous experiments proved that a high-quality surface can be obtained with a 1-min chemical polishing in the orthophosphoric acid at a temperature of 90°C.

The DSCEMS method was used to obtain experimental spectra in the energy range from 6.9 to 7.4 keV at room temperature (Fig. 2). The wave vector of gamma radiation was oriented parallel to the crystallographic C axis. The same figure (right part) shows the profiles of the weight functions of electrons for each Mössbauer spectrum. The correctness of the orientation of the crystallographic C axis relative to the cut plane

of the plate was controlled by recording the Mössbauer spectra in the gamma-radiation transmission geometry (Fig. 3). Figures 2 and 3 show that the spectral lines belonging to different sublattices are well resolved, which allows one to process experimental data more accurately.

Effective magnetic fields H_{eff}, isomeric shifts δ, and quadrupole splitting ΔE for $BaFe_{12}O_{19}$ at room temperature

Sublattices	H_{eff}, kOe	δ, mm s	ΔE, mm/s
$12k$	415 ± 1	0.25 ± 0.01	0.40 ± 0.02
$4f_{vi}$	493 ± 1	0.25 ± 0.01	0.18 ± 0.02
$4f_{vi} + 2a$	512 ± 2	0.16 ± 0.01	0.21 ± 0.02
$2b$	421 ± 4	0.23 ± 0.02	2.35 ± 0.04

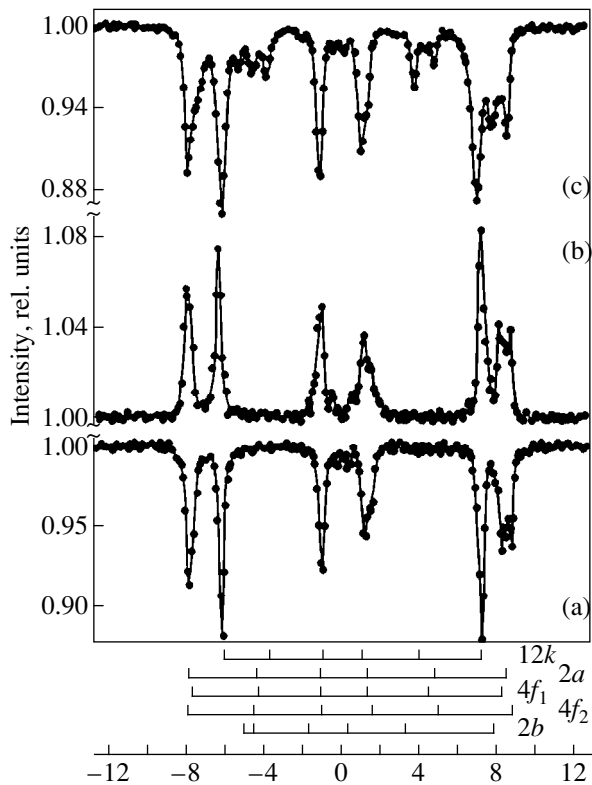Note: The isomeric shift δ is determined relative to α-Fe.

Fig. 3. Mössbauer spectra of a $BaFe_{12}O_{19}$ single crystal obtained at room temperature (a, c) by the recording of gamma quanta carrying information from the bulk of the crystal and (b) by the recording of secondary electrons from a surface layer of a thickness from 0 to 200 nm. The wave vector of gamma quanta is parallel to *C* for (a) and (b) and forms an angle of 28° with *C* for (c).

The experimental spectra were used to calculate the parameters of hyperfine interactions, which are presented in the table. The obtained values agree well with the available data (see [24] and the literature cited therein, as well as [20]).

Figure 3 shows that, in the recording of gamma quanta, no resonance lines are observed in the spectrum obtained for the orientation of the crystallographic *C* axis parallel to the wave vector of gamma radiation in the range from 4 to 5 mm/s, both for positive and negative values of the Doppler shift velocities of the gamma-quanta sources.

Using the formula

$$\Theta = \arccos\left(\frac{4A_{1.6} - 3A_{2.5}}{4A_{1.6} + 3A_{2.5}}\right)^{1/2}$$

$$= \arcsin\left(\frac{(3/2)A_{2.5}/A_{1.6}}{1 + (3/4)A_{2.5}/A_{1.6}}\right)^{1/2} \tag{1}$$

for the intensity ratio of first and second (and also fifth and sixth) lines of sextuplets (see, for example, [25]), we calculated the angles Θ determining the direction of

magnetic moments relative to the wave vector of gamma radiation.

The results of processing the spectra obtained during recording gamma quanta demonstrated that the intensities of the second and fifth lines, which correspond to transitions with $\Delta m = 0$ in the Zeeman sextuplets of each nonequivalent position, are equal to zero. This means that the angle Θ is zero, and hence the magnetic moments of iron ions located in the bulk of the crystal are collinear to the wave vector of gamma quanta and to the crystallographic *C* axis. This conclusion coincides with the results of the investigation of these crystals bulk properties (see, for example, [24]). The spectrum shown in Fig. 3 confirms the correctness of the orientation of the sample plate relative to the wave vector of gamma radiation in our experiments.

The Mössbauer spectra obtained with the recording of conversion electrons display low-intensity lines in the range from 4 to 5 mm/s for both positive and negative values of the velocities. An analysis of the results based on formula (1) proved that these lines correspond to transitions with $\Delta m = 0$.

The form of the spectrum obtained with the recording of gamma radiation (Fig. 3a) shows that these lines are not associated with disorientation of the crystallographic *C* axis relative to the gamma-quanta beam. The reasons behind the emergence of these lines in the spectra obtained with the recording of electrons can be formulated as follows. First, the source of gamma quanta and the samples under investigation are not pointlike, and the Mössbauer source was mounted as close as possible to the sample to intensify the electron beam. On account of a small separation between the source and the absorber (as compared to the diameter of the source), the experimental Mössbauer spectra display only the lines corresponding to transitions with $\Delta m = 0$. Second, the contribution to the intensities of these lines may come from the noncollinearity of the magnetic moments to the crystallographic *C* axis in the layer under investigation.

In the mathematical analysis of experimental spectra, both these factors were taken into account. In our experiments, we used the samples with a diameter of 8 mm mounted at a distance of 10.5 mm from the source of gamma quanta. The radioactive spot from the gamma-quanta emitter of the Mössbauer source was 4 mm in diameter. It should be noted that a positive factor of such a geometry is the elevation of the sensitivity of the experiments, owing to the employment of a steeper part of the function describing the dependence of the intensity of Mössbauer lines on the angle Θ.

The mathematical analysis of the experimental Mössbauer spectra for the $BaFe_{12}O_{19}$ hexaferrite was carried out on the basis of two different methods. In the first method, the shape of the lines and of the entire spectrum was analyzed by using the standard approach to Mössbauer spectra processing based on the least square technique. However, in contrast to the standard

procedure, all the spectra obtained during the recording of electrons with different energies were analyzed simultaneously. This means that the parameters of hyperfine interactions were determined from all the spectra in accordance with their statistical weight. The main goal of the given stage was to find out whether the intensities of the second and fifth lines (corresponding to transitions with $\Delta m = 0$) in the Mössbauer spectra obtained by recording electrons having different energies are different. Consequently, the intensities of the second and fifth lines, and accordingly, the angle Θ, were variable parameters. According to the results of our analysis, the angle Θ obtained from the spectra with the recording of electrons having an energy of 7.32 eV, i.e., from the thinnest surface layer, differs from zero. The error of calculations increases twofold if the value of the parameter Θ is fixed and equal to zero.

In the other method, we used the program developed specially for an analysis of the DSCEMS [23]. In the model used for data processing, the angle of inclination of magnetic moments to the C axis was fixed, i.e., was not a free parameter, while the thickness of the surface layer in which such a deviation could be observed was varied. It was found that for $\Theta = 25°$, the thickness of the surface layer in which the magnetic moments were not collinear to those in the bulk was 1.6 nm (the error of measurements varied from –0 to +1.6). In these calculations, the angle Θ was not a free parameter, but the thickness of the transition surface layer was varied. The analysis proved that the best agreement between the theoretical and experimental spectra is attained when assuming that there exists a 3-nm-thick layer on the crystal surface, in which the magnetic moments are deflected from the orientation in the bulk through 20°. The margin of error of the measurement of the layer thickness was +1 and –2 nm. Thus, a correct analysis of the Mössbauer spectra is possible only on the basis of the model presuming the existence of a thin layer on the crystal surface, where the magnetic moments are noncollinear to the directions of spins in the bulk of the sample.

The following experiments were made for control purposes. The single crystals under investigation were mounted so that the wave vector of gamma quanta was oriented at an angle α to the crystallographic C axis. Figure 3 shows an example of the Mössbauer spectrum obtained for $\alpha = 28 \pm 2°$. It can be seen from Fig. 3 that the deviation of the orientation of the magnetic moments from the direction of propagation of gamma quanta leads to the emergence in the spectra of a Zeeman sextuplet line corresponding to transitions with $\Delta m = 0$. The angle Θ determined by formula (1) amounts to $29 \pm 2°$ and coincides with the preset experimental conditions.

Thus, the DSCEMS method was first used to study the properties of the thin surface layer of single crystals of hexagonal ferrites $BaFe_{12}O_{19}$. It was found that a correct analysis of experimental data is possible only under the assumption that there exists a surface layer in ferrites $BaFe_{12}O_{19}$, having a thickness of 3 nm (the margin of error of measurements varying from –1 to +2 nm) and displaying a deviation of magnetic moments from their orientation in the bulk of the crystal through an angle of $20 \pm 3°$.

REFERENCES

1. L. Neel, J. Phys. Radium **15**, 225 (1954).
2. J. M. D. Coey, Phys. Rev. Lett. **27**, 1140 (1971).
3. A. H. Morrish, K. Haneda, and P. J. Schurer, J. Phys. Colloque **37** (C6), 301 (1976).
4. A. H. Morrish and K. Haneda, J. Magn. Magn. Mater. **35**, 105 (1983).
5. O. Kubo, T. Ido, and Y. Koike, J. Appl. Phys. **57**, 4280 (1985); S. Kuriso, T. Ido, and H. Yokayama, IEEE Trans. Magn. **23**, 3137 (1987).
6. P. Gornert, E. Sinn, W. Schuppel, *et al.*, IEEE Trans. Magn. **26**, 12 (1990).
7. M. Rosler, P. Gornert, and E. Sinn, Z. Phys. D **19**, 279 (1991); P. Gornert, H. Pfeiffer, E. Sinn, *et al.*, IEEE Trans. Magn. **30**, 714 (1994).
8. K. Haneda and A. H. Morrish, J. Appl. Phys. **63**, 4258 (1988); K. Haneda and A. H. Morrish, IEEE Trans. Magn. **25**, 2597 (1989).
9. K. Haneda, H. Kojima, A. H. Morrish, *et al.*, J. Appl. Phys. **53**, 2686 (1982).
10. F. T. Parker and A. E. Berkowitz, Phys. Rev. B **44**, 7437 (1991).
11. F. T. Parker, M. W. Foster, D. T. Margulis, *et al.*, Phys. Rev. B **47**, 7885 (1993).
12. G. S. Krinchik, A. P. Khrebtov, A. A. Askochenskiĭ, *et al.*, Pis'ma Zh. Éksp. Teor. Fiz. **17**, 466 (1973) [JETP Lett. **17**, 335 (1973)].
13. G. S. Krinchik and V. E. Zubov, Zh. Éksp. Teor. Fiz. **69**, 707 (1975) [Sov. Phys. JETP **42**, 359 (1975)].
14. V. G. Labushkin, V. V. Rudenko, É. R. Sarkisov, *et al.*, Pis'ma Zh. Éksp. Teor. Fiz. **34**, 568 (1981) [JETP Lett. **34**, 544 (1981)].
15. V. E. Zubov, G. S. Krinchik, V. N. Seleznev, *et al.*, Zh. Éksp. Teor. Fiz. **94**, 290 (1988) [Sov. Phys. JETP **67**, 2122 (1988)]; V. E. Zubov, G. S. Krinchik, V. N. Seleznev, *et al.*, J. Magn. Magn. Mater. **86**, 105 (1990).
16. E. A. Balykina, E. A. Gan'shina, and G. S. Krinchik, Zh. Éksp. Teor. Fiz. **93**, 1879 (1987) [Sov. Phys. JETP **66**, 1073 (1987)]; Fiz. Tverd. Tela (Leningrad) **30**, 570 (1988) [Sov. Phys. Solid State **30**, 326 (1988)].
17. A. S. Kamzin, V. P. Rusakov, and L. A. Grigoriev, in *Proc. Intern. Conf. on Physics of Transition Metals (USSR)* (1988), Part II.

18. A. S. Kamzin and L. A. Grigor'ev, Pis'ma Zh. Tekh. Fiz. **16**, 38 (1990) [Sov. Tech. Phys. Lett. **16** (1990)].

19. A. S. Kamzin and L. A. Grigor'ev, Pis'ma Zh. Éksp. Teor. Fiz. **57**, 543 (1993) [JETP Lett. **57**, 557 (1993)]; Zh. Éksp. Teor. Fiz. **104**, 3489 (1993) [JETP **77**, 658 (1993)].

20. A. S. Kamzin, L. P. Ol'khovik, and V. L. Rozenbaum, Pis'ma Zh. Éksp. Teor. Fiz. **61**, 916 (1995) [JETP Lett. **61**, 936 (1995)]; J. Magn. Magn. Mater. **161**, 139 (1996); Zh. Éksp. Teor. Fiz. **111**, 1426 (1997) [JETP **84**, 788 (1997)].

21. E. Moll and E. Kankeleit, Nukleonik **7**, 180 (1965).

22. B. Stahl, R. Gellert, O. Geiss, *et al.*, GSI Scientific Report, 180 (1994).

23. R. Gellert, O. Geiss, G. Klingelhofer, *et al.*, Nucl. Instrum. Methods Phys. Res. B **76**, 381 (1993).

24. Sh. Sh. Bashkirov, A. B. Liberman, and V. I. Sinyavskiĭ, *Magnetic Microstructure of Ferrites* (Kazan. Univ., Kazan, 1978).

25. *Chemical Applications of Mössbauer Spectroscopy*, Ed. by V. Gol'danskiĭ and R. Herber (New York, 1968; Mir, Moscow, 1970).

Translated by N. Wadhwa

MAGNETISM
AND FERROELECTRICITY

Effect of Electric Field on NMR Spectra
in Centroantisymmetric Antiferromagnets

V. V. Leskovets and E. A. Turov

Institute of Metal Physics, Ural Division, Russian Academy of Sciences, ul. S. Kovalevskoĭ 18, Yekaterinburg, 620219 Russia
e-mail: leskovez@imp.uran.ru

Received October 5, 1999

Abstract—A symmetry approach is used to study the influence of electric field $\mathbf{E}$ on the NMR frequency spectrum of antiferromagnets of the rhombohedral (Cr_2O_3) and tetragonal (e.g., the Fe_2TeO_6 trirutiles) systems exhibiting a linear magnetoelectric (ME) effect. The latter originates from the presence in their magnetic structure of an antisymmetry center $\bar{1}'$. It is shown that besides the trivial effect of $\mathbf{E}$ on the NMR frequency through the total magnetization induced by the ME phenomenon, there also exists an independent mechanism of a direct action of electric field on the local field at the nuclei, which can, in particular, produce an additional NMR frequency splitting. The dependence of this effect on the exchange magnetic structure and orientational state is considered.© *2000 MAIK "Nauka/Interperiodica".*

In crystals whose symmetry (the Fedorov group) includes the center of symmetry $\bar{1}$, antiferromagnetic (AF) ordering may transform the latter into an antisymmetry center, i.e., an element $\bar{1}' = \bar{1} \cdot 1'$ ($1'$ is the time inversion operation) from the viewpoint of magnetic symmetry, or an odd element $\bar{1}(-)$ if considered in terms of crystal-chemistry symmetry. The odd $g(-)$ and the even $g(+)$ elements relate in the lattice the magnetic moments belonging to magnetic sublattices with opposite and like magnetizations, respectively [1, 2]. Such centroantisymmetric (CAS) antiferromagnets exhibit the so-called magnetoelectric (ME) effect; i.e. they can be electrically polarized by a magnetic field $\mathbf{H}$ (the P_H effect) and magnetized by an electric field (the M_E effect):

$$\mathbf{P}_H = \hat{\alpha}\mathbf{H}, \quad \mathbf{M}_E = \hat{\alpha}^T\mathbf{E}, \tag{1}$$

where $\hat{\alpha}$ is the ME susceptibility tensor, and T is the transposition operation [3]. The form of the $\hat{\alpha}$ tensor is determined from the invariance of (1) under the magnetic point-symmetry group of the magnetic structure under study.

By inducing or changing the total magnetization $\mathbf{M}$ in accordance with (1), the electric field $\mathbf{E}$ affects the local magnetic fields at the nuclei and, hence, at the NMR frequencies. If this (actually trivial) effect of $\mathbf{E}$ on the NMR frequency had been the only one, our task could have been considered completed, because if one knows $\hat{\alpha}$, one can readily find $\mathbf{M}_E$ and, thus, calculate the corresponding contribution of $\mathbf{E}$ to the hyperfine field at the nuclei in each sublattice for a known AF structure.

In reality, however, there exists another, independent channel by which an electric field $\mathbf{E}$ can act on local magnetic fields and, hence, the NMR frequencies, which is determined directly by the AF vector $\mathbf{L}$ corresponding to the AF structure under study. Considered in terms of symmetry, this contribution of $\mathbf{E}$ to the local field $\mathbf{H}_\nu^E$ at the nuclei of the νth sublattice is given by the expression

$$\mathbf{H}_\nu^E = \hat{\lambda}_\nu \mathbf{L}\mathbf{E}, \tag{2}$$

where the form of the matrix $\hat{\lambda}_\nu = \lambda_{\alpha\beta\gamma}^\nu$ (here α, β, and γ take on the values $x \equiv 1$, $y \equiv 2$, $z \equiv 3$)[1] is found from the requirement of invariance of (2) under the local (island) symmetry group for the atoms of sublattice ν, and the relation between the $\hat{\lambda}_\nu$ belonging to different sublattices is determined by the elements of space crystal-chemistry symmetry transforming one sublattice into another. It is a theoretical analysis of this channel of the electric-field effect on the NMR frequency spectrum, which is performed for the specific example of CAS antiferromagnets of two types, i.e., the rhombohedral oxides Cr_2O_3 and the tetragonal trirutiles Fe_2TeO_6, that is the main purpose of this study.

There are factors that somewhat complicate this problem. We have in mind the possible (weak) noncollinearity of the four-sublattice magnetic structures of

---

[1] This double (alphanumeric) notation has the following meaning. The numerical indices are used to denote the expansion matrix constants that are not acted upon by symmetry transformations involved in finding the invariant form of this expansion. It is the variables in which the expansion is made and that transform under operation of the above symmetry elements that the literal indices (usually on the $\mathbf{L}$, $\mathbf{E}$, etc. vector components) belong to.

the above antiferromagnets [4]. It appears, however, more reasonable to touch on this point at the end of the paper when discussing the results obtained.

1. ON THE MAGNETIC STRUCTURE OF THE OXIDES AND TRIRUTILES

We understand by a magnetic structure the combination of the exchange magnetic structure (EMS) determined by the orientation of the magnetic moments with respect to one another as a result of their being exchange coupled and of the orientational state (OS), which depends on the directions of the moments relative to the crystallographic axes (magnetically isotropic relativistic interaction). A collinear EMS is identified by its code [1, 2], which specifies the parities of the elements acting as generators of the space crystal-chemistry group of the crystal. Because the chemical and magnetic cells for the antiferromagnets that are of interest to us here coincide, translations by integral periods may be considered to be identity elements.

The crystal-chemistry symmetry of the chromium oxide Cr_2O_3 is determined by space group $R\bar{3}c(D_{3d}^6)$, and its magnetic ions Cr^{3+} occupy the fourfold site $4c$ with the local symmetry {3}. As a result, crystals of this type (to which the hematite α-Fe_2O_3 belongs) allow the existence of collinear EMSs with the following codes [2]:

$$(a)\ \bar{1}(+)3_z(+)2_x(-),\quad \mathbf{L}_a = \mathbf{M}_1 - \mathbf{M}_2 - \mathbf{M}_3 + \mathbf{M}_4,$$

$$(b)\ \bar{1}(-)3_z(+)2_x(+),\quad \mathbf{L}_b = \mathbf{M}_1 + \mathbf{M}_2 - \mathbf{M}_3 - \mathbf{M}_4,$$

$$(c)\ \bar{1}(-)3_z(+)2_x(-),\quad \mathbf{L}_c = \mathbf{M}_1 - \mathbf{M}_2 + \mathbf{M}_3 - \mathbf{M}_4,$$

$$(f)\ \bar{1}(+)3_z(+)2_x(+),\quad \mathbf{M} = \mathbf{M}_1 + \mathbf{M}_2 + \mathbf{M}_3 + \mathbf{M}_4.$$

(3)

Shown on the right are the linear combinations of the sublattice magnetizations $\mathbf{M}_\nu$ ($\nu = 1, 2, 3, 4$), which represent vector order parameters of the corresponding EMSs (basis vectors). For the three AF structures (a, b, and c), these will be the antiferromagnetism vectors $\mathbf{L}_a$, $\mathbf{L}_b$, or $\mathbf{L}_c$, and for the fourth ferromagnetic (FM) structure, the ferromagnetism vector $\mathbf{M}$.

Each of these EMSs can be realized in pure form, depending on the actual character of the exchange interaction. However, relativistic interaction can give rise to a weak admixture of another structure to it. For instance, a structure (f) is admixed to a centrosymmetric (CS) structure (a) characteristic of the hematite (α-Fe_2O_3) to produce a weakly ferromagnetic structure with $M \ll L_a$. Also, to a CAS structure (c) with a vector $L_c \neq 0$ can, in principle, become admixed another CAS structure (b) with $L_b \ll L_c$ to yield a weakly noncollinear "cross"-type magnetic structure [5], whose vectors $\mathbf{M}_1$ and $\mathbf{M}_2$ ($\mathbf{M}_3$ and $\mathbf{M}_4$) deviate slightly from the strict parallelism characteristic of the pure structure (c).

We note immediately that in order to simplify as much as possible the problem of the effect of electric field $\mathbf{E}$ on an NMR spectrum, we shall neglect for the time being the latter noncollinearity, all the more so that no experimental data on its existence in the antiferromagnets under study are available. Thus, we actually set $\mathbf{L}_b = 0$ to reduce the case to a two-sublattice model in which $\mathbf{M}_1 = \mathbf{M}_2 = \frac{1}{2}\mathbf{M}_I$ and $\mathbf{M}_3 = \mathbf{M}_4 = \frac{1}{2}\mathbf{M}_{II}$, so that $\mathbf{M} = \mathbf{M}_I + \mathbf{M}_{II}$ and $\mathbf{L} \equiv \mathbf{L}_c = \mathbf{M}_I - \mathbf{M}_{II}$. This will be our first approximation. The question of what the abandoning of this approximation leads to is postponed until the end of the paper.

A similar consideration can be carried out for trirutiles with the $P4_2/mnm(D_{4h}^{16})$ crystal-chemistry symmetry. Their magnetic ions (Fe^{3+} or others) occupy the fourfold site $4e$ with the {mm} local symmetry. The EMSs possible for these ions are described by the following codes and basis vectors:

$$(a)\ \bar{1}(+)4_z(-)2_d(+),\quad \mathbf{L}_a = \mathbf{M}_1 + \mathbf{M}_2 - \mathbf{M}_3 - \mathbf{M}_4,$$

$$(b)\ \bar{1}(-)4_z(+)2_d(-),\quad \mathbf{L}_b = \mathbf{M}_1 - \mathbf{M}_2 + \mathbf{M}_3 - \mathbf{M}_4,$$

$$(c)\ \bar{1}(-)4_z(-)2_d(-),\quad \mathbf{L}_a = \mathbf{M}_1 - \mathbf{M}_2 - \mathbf{M}_3 + \mathbf{M}_4,$$

$$(f)\ \bar{1}(+)4_z(+)2_d(+),\quad \mathbf{M} = \mathbf{M}_1 + \mathbf{M}_2 + \mathbf{M}_3 + \mathbf{M}_4.$$

(4)

As in the preceding case, the $\mathbf{L}_a$ in a centrosymmetric EMS can be admixed with $\mathbf{M}$ to produce a weakly ferromagnetic structure, as this occurs with NiF_2. As for the two centroantisymmetric EMSs, (b) and (c), each of them can form the basis, either $\mathbf{L}_b$ with a relativistic admixture of $L_c \ll L_b$, or $\mathbf{L}_c$, with an admixture of $L_b \ll L_c$. Structure (b) is characteristic of Fe_2TeO_6 and Cr_2TeO_6, and structure (c) is realized in Cr_2WO_6 and V_2WO_6. The first and the last compounds have fairly high Néel points, $T_N = 210$ and 370 K, respectively. We also neglect for the time being this noncollinearity, and shall restrict ourselves to the two-sublattice model, namely, either with $\mathbf{L} \equiv \mathbf{L}_b$ (for $\mathbf{M}_1 = \mathbf{M}_3$ and $\mathbf{M}_2 = \mathbf{M}_4$) or with $\mathbf{L} \equiv \mathbf{L}_c$ (for $\mathbf{M}_1 = \mathbf{M}_4$ and $\mathbf{M}_2 = \mathbf{M}_3$).

To consider our problem, we should naturally know, besides the EMS, the orientational state as well. It can be found by minimizing the total thermodynamic potential, which consists of a magnetic part (exchange, magnetic anisotropy, Zeeman energy) and also, in the presence of an electric field $\mathbf{E}$, of the ME interaction [6–8], i.e.,

$$\Phi_{ME} = -\gamma_{\alpha\beta\gamma}L_\alpha P_\beta M_\gamma,\qquad (5)$$

as well as the energy associated with the polarizability P in this field. (Recall that summation is run over recurring dummy indices.) For the sufficiently low frequencies that are of interest to us here, $P_\alpha = \kappa_{\alpha\beta}E_\beta$, where $\kappa_{\alpha\beta}$ is the electrical susceptibility tensor [7, 8]. The form of the coefficients of the $\gamma_{\alpha\beta\gamma}$ matrix is found from the

requirements of invariance of (5) under the crystal-chemistry symmetry elements entering the code of the corresponding EMS, taken with due account of their parity. We shall not consider here the problem of the ground state, because in what follows, we intend to deal with the fairly simple situations where it is actually known, and we shall present some simple relations bearing primarily on the total magnetization, which includes both the magnetic and the electrical parts, i.e.,

$$M_\alpha = \chi_{\alpha\beta}H_\beta + \alpha_{\beta\alpha}E_\beta \equiv \mathbf{M}_H + \mathbf{M}_E, \qquad (6)$$

without proof.

2. LOCAL FIELDS AT NUCLEI AND THE NMR FREQUENCIES: GENERAL APPROACH

Thus, the local field at a nucleus ν is the sum of three vectors, namely, of the hyperfine field $\mathbf{H}_\nu^{hf}$, which is determined by the local magnetization at it, i.e., by the magnetization of the corresponding sublattice $\mathbf{M}_\nu$,

$$H_{\nu\alpha}^{hf} = 4A_\nu^{\alpha\beta}M_{\nu\beta}; \qquad (7)$$

of the external field $\mathbf{H}$; and of the ME field (2) introduced above. The actual form of $A_\nu^{\alpha\beta}$ is again found from the requirements of invariance (7) under the above local symmetry elements of site ν. On finding in this way the field $\mathbf{H}_\nu^{hf}$ for any concrete number ν, one can readily determine the field $\mathbf{H}_{\nu'}^{hf}$ at a nucleus ν' of any other sublattice from (7) by means of the symmetry operation transforming site ν into ν'. In this manner, one can obtain the hyperfine field for all four sublattices of chromium oxide or of trirutiles.

It appears reasonable now to transfer in (7), as was done in (2), to the antiferromagnetism vector $\mathbf{L}$, the basis vector representing the EMS of interest to us here. This is how one crosses over to the two-sublattice collinear model discussed above. For chromium oxide, we have the (c) structure, so that, in accordance with (3),

$\mathbf{L} \equiv \mathbf{L}_c \ (\mathbf{L}_a = \mathbf{L}_b = 0)$, with $\mathbf{M}_{1,3} = \frac{1}{4}(\mathbf{M} + \mathbf{L})$ and

$\mathbf{M}_{2,4} = \frac{1}{4}(\mathbf{M} - \mathbf{L})$. For the two possible CAS structures in trirutiles, (b) and (c), we have by (4), respectively,

$\mathbf{L} \equiv \mathbf{L}_b \ (\mathbf{L}_a = \mathbf{L}_c = 0)$, with $\mathbf{M}_{1,3} = \frac{1}{4}(\mathbf{M} + \mathbf{L})$ and

$\mathbf{M}_{2,4} = \frac{1}{4}(\mathbf{M} - \mathbf{L})$, or $\mathbf{L} \equiv \mathbf{L}_c \ (\mathbf{L}_a = \mathbf{L}_b = 0)$, so that

$\mathbf{M}_{1,4} = \frac{1}{4}(\mathbf{M} + \mathbf{L})$ and $\mathbf{M}_{2,3} = \frac{1}{4}(\mathbf{M} - \mathbf{L})$.

To present the effect of electric field $\mathbf{E}$ on NMR frequencies in the simplest way possible, we make here a second essential approximation, namely, we neglect in

(7) the anisotropic elements of matrix $A_\nu^{\alpha\beta}$ by assuming

$$A_\nu^{\alpha\beta} = A\delta_{\alpha\beta},$$

where $\delta_{\alpha\beta}$ is the Kronecker delta symbol. The role of the off-diagonal elements will be touched on later when discussing the results (together with the part played by the noncollinearity of magnetic structures in the four-sublattice model).

The NMR frequency for a nucleus ν of the sublattice is determined by the modulus of the total local field it sees [4]:

$$\Omega_\nu \equiv \frac{\omega_\nu}{\gamma_n} = \left| \mathbf{H}_\nu^{hf} + \mathbf{H} + \mathbf{H}_\nu^E \right| \qquad (8)$$

(γ_n is the nuclear gyromagnetic ratio). Rather than going through the entire procedure of Ω_ν calculation in its general form, we present here only the final results obtained for several simple particular cases of interest.

3. EASY-AXIS STATE FOR AN EMS WITH AN EVEN PRINCIPAL SYMMETRY AXIS: $\bar{1}(-)3_z(+)2_x(-)$ AND $\bar{1}(-)4_z(+)2_d(-)$

Let $\mathbf{E} \parallel \mathbf{H} \parallel \mathbf{L} \parallel \mathbf{Z}$.

For both structures, one obtains the same expressions:

$$\Omega_1 = \Omega_3 = |A(L_z + M_z) + H_z + \lambda_{333}L_zE_z|,$$
$$\Omega_2 = \Omega_4 = |A(L_z - M_z) - H_z - \lambda_{333}L_zE_z|, \qquad (9)$$

$$M_z = \chi_\parallel H_z + \alpha_{33}E_z(\alpha_{33} = \chi_\parallel\gamma_{333}\kappa_{33}L_z), \qquad (10)$$

where $\chi_\parallel$ and κ_{33} are the magnetic and dielectric susceptibilities for fields aligned with $\mathbf{L} \parallel Z$. The splitting of the NMR spectrum into two lines due to the sublattice magnetizations being oriented in opposite directions (along the $\mathbf{H}$ field and antiparallel to it) is retained here for $\mathbf{E} \neq 0$ as well. Both channels of the effect of electric field $\mathbf{E}$ on the spectrum via M_E (the M_E channel) and through $\mathbf{H}_\nu^E$ (2) (the LE channel) only shift these lines, similar to the H_z field. The only difference between these two channels probably lies in that the shift in the M_E channel vanishes as the temperature $T \longrightarrow 0$ K (together with the longitudinal magnetic susceptibility $\chi_\parallel$), whereas to the LE channel this statement, generally speaking, does not apply (it being an independent mechanism).

Equations (9) are valid for Cr_2O_3 and Fe_2TeO_6 for fields $H_z < H_{sf}$ (the spin-flop field).

4. EASY-AXIS STATE WITH $\mathbf{E} \parallel \mathbf{H} \parallel \mathbf{L} \parallel \mathbf{Z}$ FOR THE $\bar{1}(-)4_z(-)2_d(-)$ EMS STRUCTURE

Replacing the $4_z(+)$ even axis with the $4_z(-)$ odd one substantially changes the effect of the electric field on

the spectrum, which in this case will consist of four lines:

$$\Omega_{1,4} = |A(L_z + M_z) + H_z \pm \lambda_{333} L_z E_z|,$$
$$\Omega_{2,3} = |A(L_z - M_z) - H_z \mp \lambda_{333} L_z E_z|, \quad (11)$$
$$M_z = \chi_\parallel H_z$$

(here and subsequently, the first subscript on Ω corresponds to the upper sign on the right-hand side, and the second subscript, to the lower sign). Here $M_E = 0$, because for this structure $\alpha_{33} = 0$ and, hence, the M_E channel does not operate, and the above-mentioned additional splitting of the spectrum is due to the LE channel.

Unfortunately, the trirutiles with an odd $4_z(-)$ axis known to us (Cr_2WO_6 and V_2WO_6) are in the easy-plane state with $L \perp 4 \parallel Z$. Therefore, the antiferromagnets we are going to discuss will be in this state. The most probable ("easiest") directions of L in the XY plane correspond to the [100] (or [010]) axis, as well as to [110] (or $[\bar{1}10]$). These are the situations to be considered in what follows.

5. EASY-PLANE TRIRUTILES, $H \parallel [100] \parallel X$, $L \parallel [010] \parallel Y$, $E \parallel Z$

This orientational state is realized, even if it is not the easiest one, when the $H \parallel X$ field is strong enough to overcome the basal anisotropy and reach $L \perp H$.

A. $\bar{1}(-)4_z(+)2_d(-)$ Structure

In this case and in what follows, it is convenient to cast the expressions for squared NMR frequencies in the form

$$\Omega_{1,2}^2 = A^2 L_y(L_y + 2M_y)$$
$$+ 2AL_y^2 \lambda_{113} E_z \pm 2L_y \lambda_{123} E_z H_x,$$
$$\Omega_{3,4}^2 = A^2 L_y(L_y - 2M_y) \quad (12)$$
$$- 2AL_y^2 \lambda_{113} E_z \pm 2L_y \lambda_{123} E_z H_x,$$
$$M_y = \alpha_{32} E_z \quad (\alpha_{32} = \chi_\parallel \gamma_{223} \kappa_{33} L_y). \quad (13)$$

As seen from (12) and (13), the splitting into four lines is due in this case totally to the electric field E. However, in the absence of the LE channel, the spectrum would contain two lines only (as a result of $M_y \equiv M_E$). This splitting disappears (together with $\chi_\parallel$) for $T = 0$. The LE channel adds to the pair splitting the terms (the term with λ_{113}), which do not vanish for $T \longrightarrow 0$, and, besides, it splits each of these two lines in two (the term with λ_{123}). Significantly, the latter splitting occurs for both $E_z \neq 0$ and $H_x \neq 0$, because it is proportional to the $E_z H_x$ product.

B. $\bar{1}(-)4_z(-)2_d(-)$ Structure

In this case,

$$\Omega_1^2 = \Omega_3^2 = AL_y^2(A + 2\lambda_{113} E_z) + 2L_y \lambda_{123} E_z H_x,$$
$$\Omega_2^2 = \Omega_4^2 = AL_y^2(A - 2\lambda_{113} E_z) + 2L_y \lambda_{123} E_z H_x. \quad (14)$$

The splitting into two lines here is again associated with the LE channel (the term with λ_{113}), while the terms with λ_{123} are responsible for the line shift in the doublet, which varies linearly with H_x. There is no M_E channel (in this approximation).

6. EASY-PLANE TRIRUTILES, $H \parallel [110] \parallel 2_d$, $L \parallel [\bar{1}10]$, $E \parallel Z$

We are also presenting here the results for two EMS structures, $\bar{1}(-)4_z(+)2_d(-)$ and $\bar{1}(-)4_z(-)2_d(-)$.

A. $\bar{1}(-)4_z(+)2_d(-)$ Structure

$$\Omega_{1,3}^2 = A^2 L_{y'}(L_{y'} + 2M_{y'}) + 2AL_{y'}^2(\lambda_{113} \mp \lambda_{123})E_z,$$
$$\Omega_{2,4}^2 = A^2 L_{y'}(L_{y'} - 2M_{y'}) - 2AL_{y'}^2(\lambda_{113} \mp \lambda_{123})E_z. \quad (15)$$

Here, the $L \parallel [\bar{1}10]$ direction is taken as a new axis Y' of the coordinate frame $X'Y'Z$, which is obtained from XYZ by rotating it through 45° (by the rule of the right-hand screw) about the Z axis. Note that

$$M_{y'} = \alpha_{32'} E_z \quad (\alpha_{32'} = \chi_\parallel \gamma_{2'32'} \kappa_{33} L_{y'}); \quad (16)$$

i.e., it originates from the M_E channel. This channel is responsible for splitting into two lines only. An additional twofold splitting is due to the LE channel [the terms with λ_{123} in (15)]. Obviously enough, in the indices of (16), $2' \equiv y'$.

B. $\bar{1}(-)4_z(-)2_d(-)$ Structure

$$\Omega_{1,4}^2 = AL_{y'}[(AL_{y'} - 2M_{y'}) + (-\lambda_{123} \pm \lambda_{113})L_{y'}E_z],$$
$$\Omega_{2,3}^2 = AL_{y'}[(AL_{y'} + 2M_{y'}) + 2(\lambda_{123} \pm \lambda_{113})L_{y'}E_z]. \quad (17)$$

In this case, the M_E mechanism leads again to splitting into two lines only (the terms with $2M_{y'}$), with each of them being split in two due to the LE channel (this time, the terms with λ_{123}).

The authors believe the main and nontrivial results of this work consist in predicting an additional channel (mechanism) of the effect of an electric field on the NMR frequency spectrum, namely, not through the ME susceptibility (the M_E channel), but rather directly via the antiferromagnetism vector (the LE channel). Significantly, it is this second channel (the terms with $\lambda_{\alpha\beta\gamma}$) that is responsible for the additional spectral splitting, which is different for different EMSs and orientational states.

One could draw here an analogy with the ferromagnetic ($\propto M$) and antiferromagnetic (spontaneous, $\propto L$)

contributions to the Hall effect [9] and the Faraday effect [10] in centrosymmetric antiferromagnets. In these cases, the AF contribution is substantially larger than the FM one. It may be expected that, in this case, the *LE* channel in CAS antiferromagnets will likewise by far exceed the M_E channel in efficiency. This point is essential for experimental testing of the electric-field effect on the NMR spectrum, because an estimate of the frequency shift associated with the M_E channel yields too small a value. This estimate can be readily obtained; indeed, if one knows the ME susceptibility $\hat{\alpha}$, one can determine $\mathbf{M}_E$ and, hence, using the above expressions, the effect of electric field on NMR frequencies due to this channel. It turns out that such estimates of the shift yield, in the best case, figures of the order of the NMR line width. As for the *LE* channel, its efficiency can be derived quantitatively either directly from experiment or from calculations based on microscopic theory (the authors are presently trying to perform such calculations).

An obvious merit of the above results as applied to specific cases is, first, the possibility to refine or select an EMS by using the NMR technique with an applied electric field in the conditions where neutron diffraction (or other methods) cannot provide an unambiguous answer. The simplest realistic example can be obtained from a comparison of equations (11) and (12), which relate to the same experimental geometry ($\mathbf{E} \parallel \mathbf{H} \parallel \mathbf{L} \parallel \mathbf{4} \parallel Z$), but for EMSs differing only in the parity of the 4_z symmetry axis. In the first case, there are two, and in the second, four NMR lines.

Another possibility in the practical application of the relations presented in this work lies in establishing which of, orientational states is realized in an easy-plane antiferromagnet (for $\mathbf{H} = 0$), namely, with the $\mathbf{L}$ vector parallel to the edge of the basis square ([100] or [010]) or to its diagonal ([110] or [1$\bar{1}$0]). For instance, for the above-mentioned easy-plane tritrutiles Cr_2WO_6 and V_2WO_6, neutron diffraction measurements have thus far not provided an unambiguous answer to this question. To find it by the NMR technique in the presence of a $\mathbf{E} \parallel \mathbf{Z}$ field, one should apparently perform an experiment in two geometries, namely, with $\mathbf{H} \parallel [100]$ and $\mathbf{H} \parallel [110]$, which correspond to formulas (14) and (17) relating to the $\bar{1}(-)4_z(-)2_d(-)$ EMS. The $\mathbf{H}$ field should be strong enough to produce an orientational state with $\mathbf{L} \perp \mathbf{H}$ (irrespective of which of the two states is the easiest). Next, one should check for both situations which of the equations, (14) with two lines, or (17) yielding four lines, will fit the experiment if one reduces the $\mathbf{H}$ field down to the level at which the $\mathbf{L}$ vector changes the original orientational state, provided that it is not the easiest one.

Finally, we must now discuss the complicating circumstances mentioned in the beginning of the paper and which are associated with the possible lack of collinearity among the EMSs or, to be more precise, with

the presence of four sublattices. One can readily show that in easy-axis states with $\mathbf{L} \parallel 3$ or $\mathbf{L} \parallel 4$, whose NMR frequencies were considered in Sections 4 and 5, no collinearity and, thus, no admixture of other vectors to the ground basis vector can appear (similar to the case where no weak ferromagnetism appears in α-Fe_2O_3 below the Morin point, where $\mathbf{L} \parallel 3 \parallel Z$). As a result, the NMR frequency spectrum in nominally four-sublattice antiferromagnets residing in this orientational state will still be described by the corresponding expressions (9), for the $\bar{1}(-)3_z(+)2_x(-)$ and $\bar{1}(-)4_z(+)2_d(-)$ EMSs, or (11), for the $\bar{1}(-)4_z(-)2_d(-)$ EMS.

The situation is different for easy-plane antiferromagnets. In the magnetic structure discussed above (Cr_2WO_6 and V_2WO_6), we have an admixture to the ground basis vector $\mathbf{L} \equiv \mathbf{L}_c \perp Z$ of a vector $\mathbf{L}_b$ of another centroantisymmetric EMS, such that

$$L_{bx} = cL_{cy},$$
$$L_{by} = cL_{cx}, \qquad (18)$$

where c is a constant. (Similarly, in α-Fe_2O_3 above the Morin point and in $NiFe_2$, a weak ferromagnetism appears in the $\mathbf{L} \perp Z$ state.) Equations (18) imply that the relativistically induced vector $\mathbf{L}_b \perp \mathbf{L}_c$ (which accounts for the noncollinearity) if $\mathbf{L}_c \parallel [100]$ (or [010]), and $\mathbf{L}_b \parallel \mathbf{L}_c$ for $\mathbf{L}_c \parallel [110]$ (or [1$\bar{1}$0]). In both cases, there appears an anisotropic contribution to the hyperfine interaction tensor $A_\nu^{\alpha\beta}$ in (7). This affects the frequencies as well, namely, in formulas (14) one adds, respectively, the terms

$$-2cAL_yH_x \quad \text{and} \quad 2cAL_yH_x, \qquad (19)$$

and in formulas (17), the terms

$$-2cA^2L_{y'}^2 \quad \text{and} \quad 2cA^2L_{y'}^2. \qquad (20)$$

In both cases, the above factor does not produce any additional splitting, but the terms proportional to c affect the magnitude of the already existing splitting. Also, for $H_x \longrightarrow 0$, the shifts (19) in (14) vanish to leave only the splitting associated with the electric field $\mathbf{E}$ (the *LE* channel).

In the case of formula (17), the extra terms (20) affect only the twofold splitting (similar to the terms with $M_{y'}$), and the four lines observed will again be due to the electric field through the *LE* channel (the terms with λ_{113}).

Thus, the effects associated with taking into account a four-sublattice structure in the cases considered above cannot mask the effect of electric field on the NMR spectrum predicted in this work. Nevertheless, a rigorous theory should certainly study in more detail the part played by the anisotropy of the hyperfine tensor $A_\nu^{\alpha\beta}$, which can originate from a number of other reasons. Such a study was carried out for centrosymmetric anti-

ferromagnets in ([4], Section 3.8) and in [11]. Besides, in the case of nuclei with spins $I > 1/2$ (for ^{53}Cr, $I = 3/2$), one has also to take into account the quadrupole splitting of NMR spectra. It may be repeated that we chose here the simplest possible model to stress in a more revealing way the most essential aspect of the problem of the electric-field effect on NMR spectra in CAS antiferromagnets.

ACKNOWLEDGMENTS

REFERENCES

1. E. A. Turov, Usp. Fiz. Nauk **164** (3), 325 (1994).

2. E. A. Turov, *Kinetic, Optical, and Acoustical Properties of Antiferromagnets* (UrO RAN, Sverdlovsk, 1990).

3. L. D. Landau and E. M. Lifshits, *Electrodynamics of Continuous Media* (Nauka, Moscow, 1992; Pergamon, Oxford, 1960).

4. M. I. Kurkin and E. A. Turov, *NMR in Magnetically Ordered Substances and its Applications* (Nauka, Moscow, 1990).

5. E. A. Turov, *Physical Properties of Magnetically Ordered Crystals* (Akad. Nauk SSSR, Moscow, 1963), Ch. 10.

6. V. G. Shavrov, Zh. Éksp. Teor. Fiz. **48**, 1419 (1965) [Sov. Phys. JETP **21**, 948 (1965)].

7. E. A. Turov, Zh. Éksp. Teor. Fiz. **104**, 3886 (1993) [JETP **77**, 868 (1993)].

8. E. A. Turov, V. V. Men'shenin, and V. V. Nikolaev, Zh. Éksp. Teor. Fiz. **104**, 4157 (1993) [JETP **77**, 1014 (1993)].

9. K. B. Vlasov, E. A. Rozenberg, A. G. Titova, *et al.*, Fiz. Tverd. Tela (Leningrad) **22**, 1656 (1980) [Sov. Phys. Solid State **22**, 967 (1980)].

10. B. B. Kricheytsov, K. M. Mukimov, R. V. Pisarev, *et al.*, Pis'ma Zh. Éksp. Teor. Fiz. **34**, 399 (1981) [JETP Lett. **34**, 379 (1981)].

11. A. S. Moskvin, Zh. Éksp. Teor. Fiz. **90**, 1734 (1986) [Sov. Phys. JETP **63**, 1015 (1986)].

Translated by G. Skrebtsov

MAGNETISM
AND FERROELECTRICITY

Generation of Second Optical Harmonic and Magnetooptical Kerr Effect in Ferromagnet–Semiconductor Heterostructures CaF$_2$/MnAs/Si(111)

A. G. Banshchikov*, A. V. Kimel'*, V. V. Pavlov*,
R. V. Pisarev*, N. S. Sokolov*, and Th. Rasing**

*Ioffe Physicotechnical Institute, Russian Academy of Sciences, Politekhnicheskaya ul. 26, St. Petersburg, 194021 Russia
e-mail: pisarev@pop.ioffe.rssi.ru
**Research Institute for Materials, University of Nijmegen, 6525 ED Nijmegen, the Netherlands
e-mail: theoras@sci.kun.nl
Received October 11, 1999

Abstract—The second optical harmonic generation and magnetooptical Kerr effect are investigated for the light (λ = 800 nm) reflected by ferromagnet–semiconductor heterostructures CaF$_2$/MnAs/Si(111). The observed change in the second-harmonic intensity is odd in magnetization. A phenomenological analysis of possible contributions to the second harmonic is carried out, and the sources of optically nonlinear signals are determined from the experimental azimuthal dependences of the light intensity at double frequency. The difference in the field dependences of the second harmonic and the magnetooptical Kerr effect is observed. © *2000 MAIK "Nauka/Interperiodica"*.

The heterostructures obtained by growing ferromagnetic films directly on the surface of semiconductors such as silicon or gallium arsenide are promising for developing new magnetoelectronic devices [1]. Among potential applications of these structures, it is important to mention the possibility of creating devices combining the cells of energy-independent magnetic memory or magnetosensor cells and semiconducting readout elements in the same integrated circuit, as well as other devices based on galvanomagnetic phenomena. The characteristics of these devices will undoubtedly depend strongly not only on the bulk properties of a ferromagnetic film, but also on the magnetic state of the film near the surface and, especially, near the ferromagnet–semiconductor interface.

The traditional methods of studying the magnetic state of substances are based on the measurements of magnetization or the magnetooptical Kerr effect (KE) and are integral methods that do not possess the required spatial selectivity for probing several atomic layers near the surface or interface. The signal intensity in the inductive method depends on the magnetic state of the sample in the bulk, while the signal amplitude in KE measurements is determined by the characteristic depth of light penetration. One of the methods of studying the surface magnetism is associated with the spin-polarized diffraction of electrons. However, this method is inapplicable for studying interfaces at a depth of several tens or hundreds of nanometers in view of the small electron penetration depth. In recent years, the method of magnetically induced second optical harmonic generation (SHG) was proposed for studying the

surface and interface magnetic states of thin-film structures. For centrosymmetric media in the electric-dipole approximation, SHG is allowed only near interfaces where the spatial inversion is violated. The possibility of the influence of an external magnetic field and spontaneous magnetization on the nonlinear optical polarization was discussed in several theoretical publications [2–9]. The first attempt at experimental investigation of the SHG induced by magnetic ordering in the antiferromagnet BiFeO$_3$ was made by Agal'tsov *et al.* [10]. Aktsipetrov *et al.* [11] studied the SHG in magnetic films of garnet ferrites, but they attributed the observed variation in the optical signal at a double frequency to the manifestation of linear magnetooptical effects, and the existence of a magnetically induced contribution to SHG was not proved. Reif *et al.* [12,13] were the first to prove experimentally the influence of magnetization on the intensity of second harmonic. The method of magnetically induced SHG was successfully employed for studying the magnetic state near interfaces in various film-type structures [14]. Wierenga *et al.* [15] demonstrated that the source of magnetically induced SHG for multilayered films is confined to six atomic layers of the interface region. One can conclude that the method based on the measurement of the SHG intensity in a centrosymmetric magnetic medium is sensitive to the magnetic state of several atomic layers in the vicinity of the interface.

In contrast to SHG, the linear magnetooptical KE is formed by a region having the thickness of the order of the light penetration depth $d = \lambda/(4\pi k)$ [16], where λ is the wavelength of light and k is the absorption coeffi-

Table 1. Parameters of CaF_2/MnAs/Si(111) heterostructures

No.	CaF$_2$		MnAs		Si(111)
	Growth temperature, K	Thickness, nm	Growth temperature, K	Thickness, nm	Disorientation
1	613	5	613	40	5′
2	593	5	593	40	3°
3	593	5	593	70	13′

cient. Thus, the two magnetooptical methods based on the measurement of KE and the intensity of SHG and having different probing regions can provide mutually complementing information on the bulk magnetic properties and the magnetic state of the surface and the

Fig. 1. AFM images of the studied structures.

interface of the ferromagnet–semiconductor-type heterostructures.

This research aims at the investigation of magnetically induced SHG and the magnetooptical KE in CaF_2/MnAs/Si(111) heterostructures. The magnetic phase transition point close to room temperature, the large reflection coefficient, and relatively high values of magnetooptical KE in polycrystalline MnAs films [17] enable one to use this information for designing memory units with thermomagnetic recording and magnetooptical readout of information.

1. PHYSICAL PROPERTIES OF MNAS AND PREPARATION OF SAMPLES WITH CAF$_2$/MNAS/SI(111) HETEROSTRUCTURES

A decrease in temperature below 400 K in MnAs leads to a structural phase transition in which a centrosymmetric hexagonal crystal lattice of the NiAs type (point group 6/*mmm*) is transformed into a lattice of the MnP type (point group *mmm*) [18]. At a temperature of 318 K, the crystal structure is restored to the initial lattice, and a magnetic ordering is established with a collinear ferromagnetic structure and spins in the (0001) plane. The magnetic and magnetooptical properties of the MnAs/Si and MnAs/GaAs heterostructures were studied by the polarimetric and inductive methods in [19–22].

The CaF_2/MnAs/Si(111) heterostructures were grown in an ultrahigh-vacuum chamber by the molecular-beam epitaxy method. After the standard chemical cleaning [23], silicon substrates were loaded to the growth chamber and cleaned additionally by thermal annealing at 1520 K. This procedure allows one to obtain atomically clean silicon surface with a 7×7 superstructure. The crystal quality of the substrates and the growth of heterostructures were controlled *in situ* by the fast electron diffraction with an energy of 15 keV. The film thickness was estimated with the help of a surface roughness recorder. The MnAs film thickness was 40 nm in structures no. 1 and 2 and 70 nm in structure no. 3 (see Table 1). The MnAs films were grown on different buffer layers in the temperature range 320–340 K. The As buffer layer for structures no. 2 and 3 was deposited according to the technique described in [22]. An Mn buffer layer of thickness 3 nm for structure no. 1 was grown during the cooling of the substrate from 1000 to
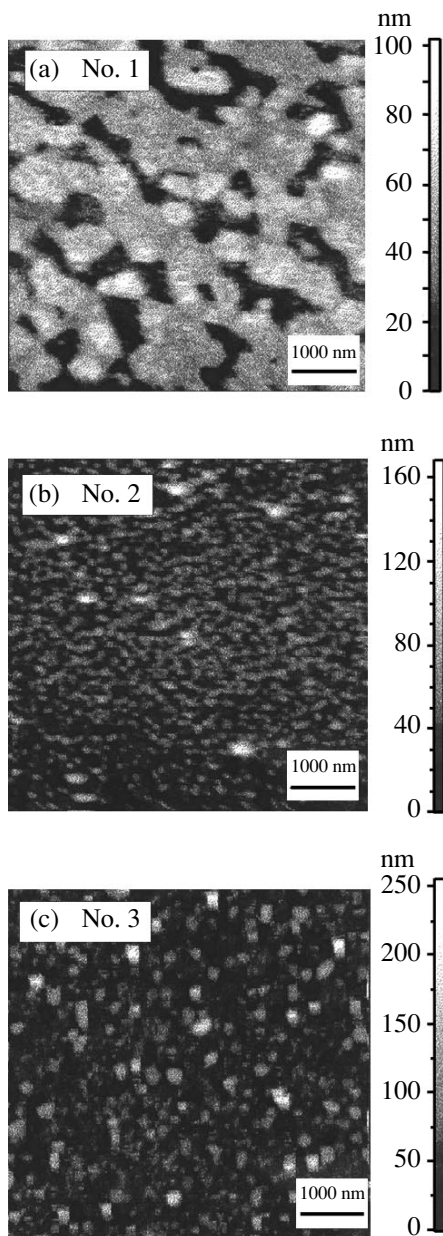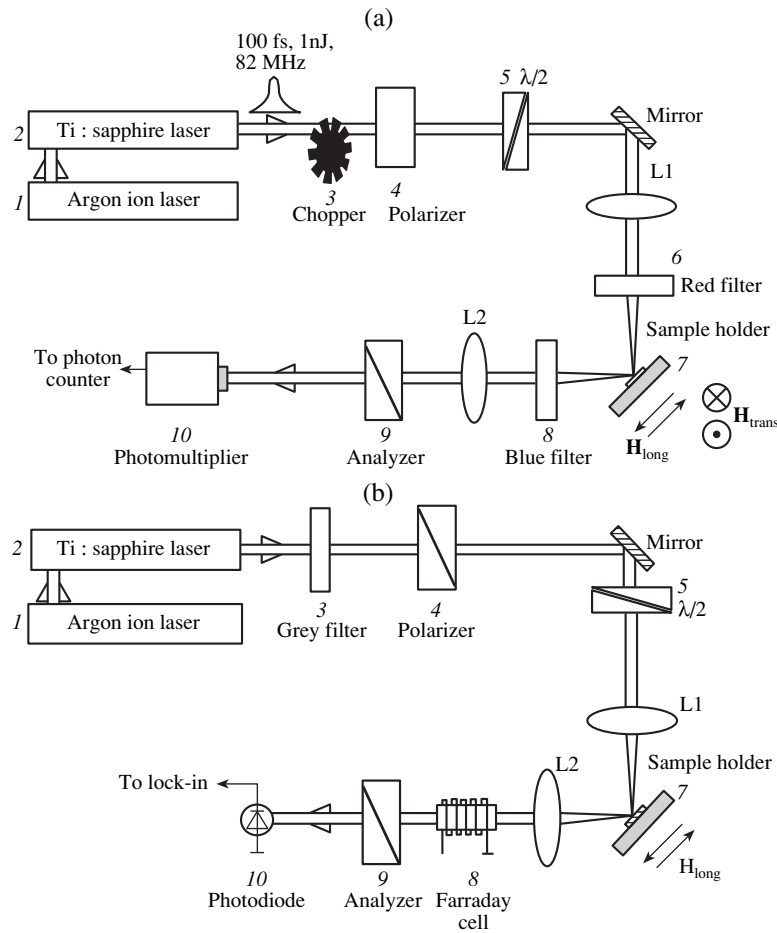
Fig. 2. Experimental setup for measuring (a) the generation of second optical harmonic and (b) meridional magnetooptical Kerr effect during light reflection at the magnetized sample.

750 K for 30 s. In order to prevent possible contamination from the atmosphere, the MnAs films were coated with several atomic layers of calcium fluoride CaF_2.

Morphological measurements on the surface of heterostructures were made on an atomic-force microscope. The obtained images (see Fig. 1) displayed a dependence of the surface morphology on the type of the buffer layer. The surfaces of MnAs layers grown on a Mn buffer layer display protrusions with a transverse size of 500–1000 nm and a height of 50–90 nm (Fig. 1a). The surface of the layers grown on an As buffer layer is formed by clusters having a size of several tens of nanometers (Figs. 1b and c).

2. EXPERIMENTAL SETUP

The intensities of SHG and KE were measured using the radiation emitted by a femtosecond-range Ti–sapphire $(Al_2O_3 : Ti)$ laser with a pulse duration of 100 fs and a pulse-repetition frequency of 82 MHz. The optical diagram of the experimental setup for measuring SHG signals is shown in Fig. 2a. The radiation of argon ion laser *1* having an average power of 8 W in the blue–green spectral region was used for pumping the Ti–sapphire laser *2*. In order to reduce the integrated intensity of radiation emitted by the Ti–sapphire laser without decreasing the peak intensity in the pulse, the light beam was passed through a mechanical modulator *3* of the chopper type and then through polarizer *4* and a Babinet–Soleil compensator *5* playing the role of a $\lambda/2$ phase plate. The polarization plane for light at the fundamental frequency ω was of the *P*- or *S*-type and was fixed by the rotation of compensator *5*. The red filter *6* was used for suppressing possible stray radiation from the optical elements at the double frequency 2ω. The beam of light passed through sample *7*, blue filter *8* absorbing the light of the fundamental frequency and transmitting the second harmonic, and through analyzer *9* and reached photomultiplier *10* operating in the photon counting mode.

In the setup intended for measuring the magnetooptical KE (Fig. 2b), the excess power of laser radiation was absorbed by the grey filter *3*. The Babinet–Soleil compensator *5* was tuned so that the beam of the light incident on sample *7* had *P*-type polarization. After the reflection at the sample, the light beam passed through
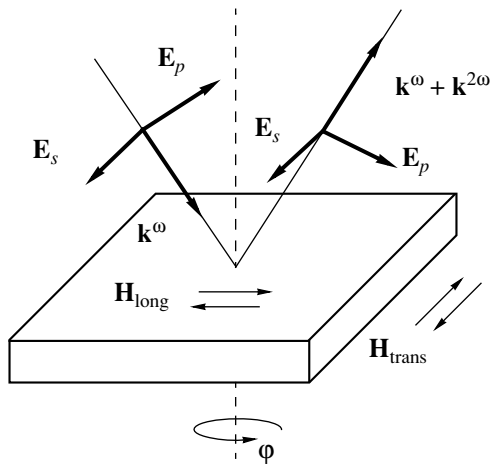
Fig. 3. Experimental geometry: $\mathbf{E}_P$ and $\mathbf{E}_S$ are the electric field strengths of a light wave of the *P*- and *S*-type, respectively; $\mathbf{k}^\omega$ and $\mathbf{k}^{2\omega}$ are the wave vectors of light for frequencies ω and 2ω, respectively; and $\mathbf{H}_{\text{long}}$ and $\mathbf{H}_{\text{trans}}$ are the magnetic field strengths in the meridional and equatorial geometries, respectively.

the Faraday cell *8* and analyzer *9* tuned for the maximum transmission of the *S*-type polarization and reached photodiode *10*. Electrical signal from the photodiode were fed to the synchronous detecting circuit.

All the measurements were made during reflection of the light of the fundamental frequency at a wavelength of 800 nm at an angle of incidence of 45°. The intensity of light incident on the sample was 40–60 mW. The possibility of sample rotation about the normal in the range of azimuthal angles $0 < \varphi < 340°$ was envisaged. The sample was in a magnetic field applied in the

Table 2. Independent components of tensors $\chi_{ijk}^{(2)}$ and $\chi_{ijkl}^{(3)}$ for point groups 3*m* and 6*mm* [24]

Point group	Tensor	Independent nonzero elements
3*m*	$\chi_{ijk}^{(2)}$	$-xxx = yyx = yxy = xyy$, $xxz = xzx = yyz = yzy$, $zxx = zyy$, zzz
6*mm*	$\chi_{ijk}^{(2)}$	$xxz = xzx = yyz = yzy$, $zxx = zyy$, zzz
6*mm*	$\chi_{ijkl}^{(3)}$	$yxxx = -xyyy,\ xzzy = -yzzx$, $xyxx = xxyx = -yxyy = -yyxy$, $zzxx = zxzy = -zzyx = -zyzx$, $xyzz = xzyx = -yxzz = -yzxz$, $xxxy = -yyyx = xyyy + 2yyxy$

equatorial ($\mathbf{H}_{\text{trans}}$) or meridional ($\mathbf{H}_{\text{long}}$) geometry as shown in Fig. 3.

3. PHENOMENOLOGICAL DESCRIPTION OF NONLINEAR OPTICAL EFFECTS

In the electric-dipole approximation, the nonlinear polarization $\mathbf{P}^{2\omega}$ induced in a medium with the magnetization $\mathbf{M}$ by the electric field $\mathbf{E}^\omega$ of an incident electromagnetic wave can be written as the sum of two terms

$$P_i^{2\omega} = \chi_{ijk}^{(2)} E_j^\omega E_k^\omega + \chi_{ijkl}^{(3)} E_j^\omega E_k^\omega M_l, \tag{1}$$

where $\chi_{ijk}^{(2)}$ and $\chi_{ijkl}^{(3)}$ are nonlinear tensors describing the crystallographic and magnetic contributions to the nonlinear polarization $P_i^{2\omega}$, respectively. The quantity $\chi_{ijk}^{(2)}$ is a polar rank-three tensor, and $\chi_{ijkl}^{(3)}$ is an axial tensor of rank four. Both tensors differ from zero only in noncentrosymmetrical media. Consequently, the generation of the second optical harmonic in the bulk of CaF_2, MnAs, and Si possessing a centrosymmetric structure is forbidden in the electric-dipole approximation. The nonlinear polarization can differ from zero only in the vicinity of interfaces such as air/CaF_2, CaF_2/MnAs, and MnAs/Si, where the space inversion is violated.

For the SHG intensity, we have

$$I^{2\omega} \propto \left|\chi^{(2)}\right|^2 + \left|\chi^{(3)} M\right|^2 \pm 2\chi^{(2)}\chi^{(3)} M. \tag{2}$$

In nondissipative media, the tensor $\chi_{ijk}^{(2)}$ is real-valued, while the tensor $\chi_{ijkl}^{(3)}$ is purely imaginary [2, 8]. Thus, the crystallographic and magnetic contributions to the nonlinear polarization of nonabsorbing media have a $\pi/2$ phase shift relative to one another and, hence, cannot interfere. In a dissipative medium, the nonlinear susceptibilities are complex-valued in the general case, and, hence, the interference of the crystallographic and magnetic contributions becomes possible, which leads to the emergence of the interference term $\pm 2\chi^{(2)}\chi^{(3)} M$ linear in magnetization $\mathbf{M}$ in the SHG intensity.

Table 2 lists the independent components of the tensors $\chi_{ijk}^{(2)}$ and $\chi_{ijkl}^{(3)}$ for the interfaces, where the second optical harmonic generation is allowed, i.e., for the MnAs/Si(111) interface (buffer layer/Si), whose symmetry can be described by the point group 3*m*, as well as for the CaF_2/MnAs(0001) interface, point group 6*mm*. Using equations for vector transformation from the laboratory reference frame to the crystallographic one and back, we can obtain the following dependences of nonlinear polarizations on the azimuthal rotational angle φ of the sample for the 45° angle of incidence.

The crystallographic contribution from the

MnAs/Si(111) interface is determined as

$$P_{PP}^{cr} = \left(\frac{\chi_{xxx}^{(2)}}{2}\cos 3\varphi - x_{xxz}^{(2)} + \frac{\chi_{zxx}^{(2)} + \chi_{zzz}^{(2)}}{2}\right)\frac{1}{\sqrt{2}},$$

$$P_{PS}^{cr} = \frac{\chi_{xxx}^{(2)}}{2}\sin 3\varphi,$$

$$(3)$$

$$P_{SP}^{cr} = (-\chi_{xxx}^{(2)}\cos 3\varphi + \chi_{zxx}^{(2)})\frac{1}{\sqrt{2}},$$

$$P_{SS}^{cr} = -\chi_{xxx}^{(2)}\sin 3\varphi.$$

The crystallographic contribution from the CaF$_2$/MnAs(0001) interface is given by

$$P_{PP}^{cr} = \left(-\chi_{xxz}^{(2)} + \frac{\chi_{zxx}^{(2)} + \chi_{zzz}^{(2)}}{2}\right)\frac{1}{\sqrt{2}}, \quad P_{PS}^{cr} = 0,$$

$$P_{SP}^{cr} = \frac{1}{\sqrt{2}}\chi_{zxx}^{(2)}, \quad P_{SS}^{cr} = 0.$$

$$(4)$$

The magnetic contribution from the CaF$_2$/MnAs(0001) interface for the meridional geometry can be written as

$$P_{PP}^{mag} = 0, \quad P_{PS}^{mag} = \frac{\chi_{yxxx}^{(3)} - \chi_{xzzy}^{(3)}}{2},$$

$$P_{SP}^{mag} = 0, \quad P_{SS}^{mag} = \chi_{yyyx}^{(3)}.$$

$$(5a)$$

The magnetic contribution from the CaF$_2$/MnAs(0001) interface for the equatorial geometry is as follows:

$$P_{PP}^{mag} = \frac{1}{\sqrt{2}}\chi_{yxxx}^{(3)}, \quad P_{PS}^{mag} = 0,$$

$$P_{SP}^{mag} = \frac{1}{\sqrt{2}}\left(-\frac{\chi_{yyyx}^{(3)}}{2} + \chi_{zzxy}^{(3)} + \frac{\chi_{xzzy}^{(3)}}{2}\right), \quad P_{SS}^{mag} = 0.$$

$$(5b)$$

The superscripts on the nonlinear polarization P_{IJ} indicate the states of input (I) and output (J) polarizations. All the nonlinear polarizations are normalized to the intensity of the incident wave. It should be noted that the isotropic component of the crystallographic contribution from the MnAs/Si(111) and CaF$_2$/MnAs(0001) interfaces and the magnetic contribution from the CaF$_2$/MnAs(0001) interface for the meridional geometry in each combination of polarizations are incompatible. Thus, the crystallographic and magnetic contributions to SHG can be separated using the rotational anisotropy method, in which the SHG intensity is measured as a function of the angle of crystal rotation about the normal. This method was used successfully in the experiments on SHG in garnet-ferrite epitaxial films [25, 26].

4. DISCUSSION OF RESULTS

Figure 4 shows the dependences of the SHG intensity on the azimuthal angle φ of sample rotation about the normal for the CaF$_2$/MnAs(40 nm)/Mn/Si(111) heterostructure. The dependences for CaF$_2$/MnAs (40 nm)/As/Si(111) have a similar form. The measurements were made for four combinations of the input–output light polarizations PP, PS, SP, and SS in the meridional geometry, when the magnetization ±$\mathbf{M}$ was in the plane of light incidence. The azimuthal dependences of the intensity for the PP and SP combinations of polarizations exhibit a 120° periodicity typical of a (111)-type plane in crystalline silicon. The magnetic contribution to SHG for these polarization combinations is not manifested; i.e., there is no difference between the SHG intensities corresponding to two directions of magnetization ±$\mathbf{M}$. The azimuthal dependences of the SHG intensities for the PS and SS polarization combinations exhibit a 60° periodicity for a demagnetized sample and a 120° periodicity for a magnetized sample. Thus, the application of an external magnetic field imparts the sample a single domain structure, resulting in nonequivalence of the SHG intensities for the two directions of magnetization for certain angles φ and, accordingly, in the change in the anisotropy type. The nonequivalence of the SHG intensities emerges as a result of the coexistence of the crystallographic and magnetic contributions to the nonlinear polarization and their interference.
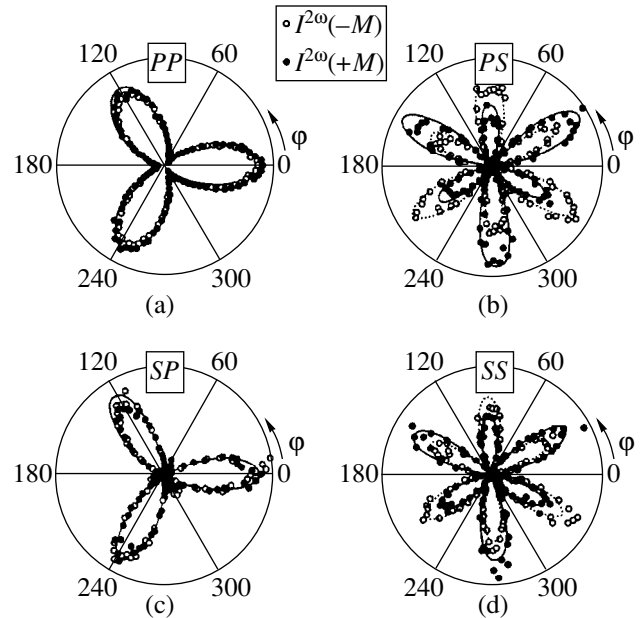

Fig. 4. Azimuthal dependences of the intensity of the second optical harmonic generation in the CaF$_2$/MnAs (40 nm)/Mn/Si(111) heterostructure for the meridional geometry and four combinations of the input–output polarizations of radiation: (a) PP, (b) PS, (c) SP, and (d) SS. Dark circles correspond to $I^{2\omega}(+M)$, and light circles, to $I^{2\omega}(-M)$.
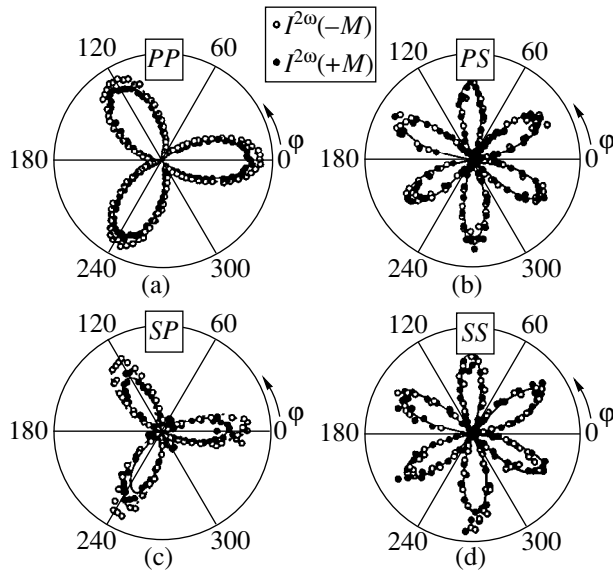
Fig. 5. Azimuthal dependences of the intensity of the second optical harmonic generation in the CaF$_2$/MnAs (40 nm)/As/Si(111) heterostructure for the equatorial geometry and four combinations of the input–output polarizations of radiation: (a) *PP*, (b) *PS*, (c) *SP*, and (d) *SS*. Dark circles correspond to $I^{2\omega}(+M)$, and light circles, to $I^{2\omega}(-M)$.

Figure 5 shows the azimuthal dependences of the SHG intensity in the CaF$_2$/MnAs(40 nm)/Mn/Si(111) heterostructure for four polarization combinations in the equatorial geometry when the magnetization $\pm\mathbf{M}$ is perpendicular to the plane of light incidence. In this

geometry, other combinations of the nonlinear suscep- tibilities differing from those in the meridional geome- try can operate [see expressions (5)]. In the given geometry, the magnetic contribution to SHG is mani- fested for the *PP* and *SP* polarization combinations and is not observed for the *PS* and *SS* combinations.

The experimental dependences shown in Figs. 4 and 5 are described correctly by the following expressions:

$$I^{2\omega}(\varphi) = (A\cos 3\varphi + B)^2 \qquad (6)$$

for the *PP* and *SP* polarization combinations and

$$I^{2\omega}(\varphi) = (A\sin 3\varphi + B)^2 \qquad (7)$$

for the *PS* and *SS* polarization combinations, where A and B are the coefficients characterizing the anisotropic and isotropic components of the SHG intensity, respec- tively. We can separate the crystallographic B^{cr} and the magnetically induced B^{mag} components of the B coeffi- cient as follows:

$$\begin{aligned} B^{cr} &= [B(+M) + B(-M)]/2, \\ B^{mag} &= [B(+M) - B(-M)]/2. \end{aligned} \qquad (8)$$

Tables 3 and 4 show the coefficients A, B^{cr}, and B^{mag} obtained as a result of the approximation of the experi- mental dependences on the basis of formulas (6) and (7). It can be seen that in the meridional geometry, $B^{mag} = 0$ for the *PP* and *SP* polarization combinations. This means that the isotropic contribution to SHG is purely crystallographic. On the contrary, in the case of the *PS* and *SS* combinations, $B^{mag} \neq 0$ and $B^{cr} = 0$, and

Table 3. Results of approximation of azimuthal dependences of SHG by formulas (6)–(8) for meridional and equatorial geometries and four combinations of polarizations in the CaF$_2$/MnAs(40 nm)/Mn/Si(111) heterostructure

	Coefficients	*PP*	*PS*	*SP*	*SS*
Meridional geometry	A, rel. units	16 ± 1	13.9 ± 0.2	10.9 ± 0.2	9.4 ± 0.1
	B^{cr}, rel. units	29.7 ± 0.2	0	5.3 ± 0.3	0
	B^{mag}, rel. units	0	4.7 ± 0.6	0	2.7 ± 0.4
Equatorial geometry	A, rel. units	16 ± 1	14.9 ± 0.1	11.2 ± 0.1	10.3 ± 0.1
	B^{cr}, rel. units	30 ± 0.1	0	6.0 ± 0.2	0
	B^{mag}, rel. units	1.2 ± 0.2	0	0.9 ± 0.2	0

Table 4. Results of approximation of azimuthal dependences of SHG by formulas (6)–(8) for meridional and equatorial geometries and three combinations of polarizations in the CaF$_2$/MnAs(40 nm)/As/Si(111) heterostructure

	Coefficients	*PP*	*PS*	*SP*
Meridional geometry	A, rel. units	6 ± 1	4.5 ± 0.1	2.9 ± 0.3
	B^{cr}, rel. units	24.5 ± 0.1	0	4.9 ± 0.1
	B^{mag}, rel. units	0	1.2 ± 0.3	0
Equatorial geometry	A, rel. units	4.5 ± 0.4	4.5 ± 0.1	1.9 ± 0.2
	B^{cr}, rel. units	25.3 ± 0.5	0	5.3 ± 0.2
	B^{mag}, rel. units	1.0 ± 0.3	0	0.7 ± 0.2

the isotropic contribution to SHG is purely magnetic. The phenomenological expressions (3)–(5) imply that the anisotropic contribution to SHG can only be the crystallographic contribution from the MnAs/Si(111) interface. In the case of equatorial magnetization, the isotropic crystallographic and magnetic contributions coexist in the *PP* and *SP* polarization combinations but are absent in the *SP* and *SS* combinations. This is in good agreement with the phenomenological expressions (3)–(5).

Figure 6 shows the azimuthal dependences for the CaF$_2$MnAs(70 nm)/As/Si(111) heterostructures with the *PP* polarization combination in the meridional (b) and equatorial (a) geometries. It can be seen that the azimuthal dependences of SHG for the given heterostructure are isotropic ($A = 0$), and the magnetic contribution to the SHG in the meridional geometry for the *PP* combination is absent ($B^{mag} = 0$). However, this contribution takes place for the *PP* and *SP* polarization combinations in the equatorial experimental geometry. Table 5 contains the results of approximating the azimuthal dependences of SHG by formula (6).

Expressions (3)–(5) show that anisotropy in the SHG can be due to the interfaces (buffer layer)/Si and MnAs/Si) or open Si regions (see Fig. 1a). It should be noted that in view of the strong absorption of the light at frequency ω in the MnAs film, we can expect that the largest contribution to the anisotropic component of SHG comes from open regions in Si. The fact that heterostructures are characterized by the different amplitudes A can also be attributed to strong absorption of the light at frequency ω in MnAs films (the absorption coefficient $k = 2.8$ for light with the wavelength $\lambda = 800$ nm [17]).

The dependence of the SHG intensity on the magnetization **M** can be used for determining the magnetic contrast ρ:

$$\rho = \frac{I^{2\omega}(+M) - I^{2\omega}(-M)}{I^{2\omega}(+M) + I^{2\omega}(-M)} = \frac{2\chi^{(2)}\chi^{(3)}M}{\left|\chi^{(2)}\right|^2 + \left|\chi^{(3)}M\right|^2}. \quad (9)$$

Figure 7 shows the magnetic contrast ρ of the SHG as a function of the analyzer rotational angle α for the *P*-type polarized light incident on the sample of the CaF$_2$/MnAs(70 nm)/As/Si(111) structure in the meridional geometry. This experimental dependence was approximated by the function [27]

$$\rho = \frac{2C\cos\delta\tan\alpha}{1 + C\tan\alpha^2}, \quad (10)$$

where δ is the phase difference between the crystallographic and magnetic contributions and C is the ratio between the amplitudes of the magnetic and crystallographic contributions. As a result of approximation, we obtain $\delta = 146°$ and $C = 0.12$. Thus, analyzing the SHG in the meridional geometry as a function of the analyzer rotational angle, one can obtain important information
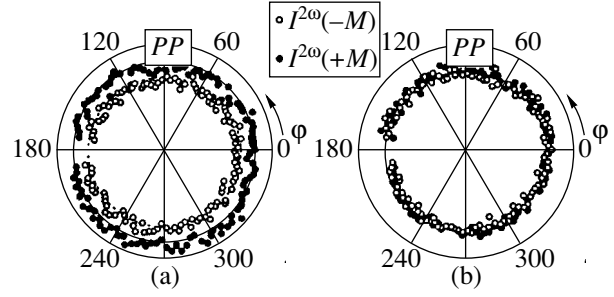

Fig. 6. Azimuthal dependences of the intensity of the second optical harmonic generation in the CaF$_2$/MnAs (70 nm)/As/Si(111) heterostructure for (a) equatorial and (b) meridional geometries and the *PP*-combinations of the input–output polarizations of radiation. Dark circles correspond to $I^{2\omega}(+M)$, and light circles, to $I^{2\omega}(-M)$.
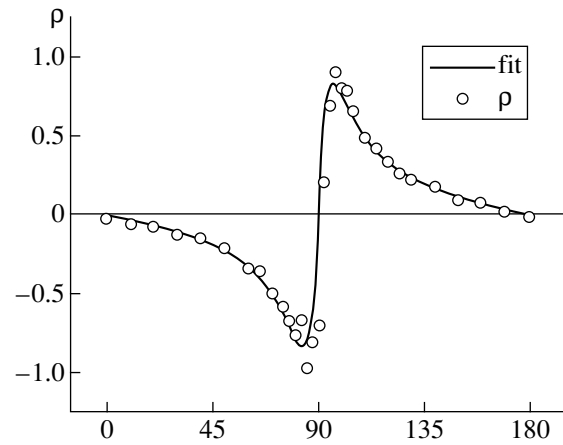

Fig. 7. Dependence of the magnetic contrast ρ of the second optical harmonic on the analyzer rotational angle α. Light circles correspond to experimental points, and the solid curve described the approximation by formula (14).

concerning the relation and phase difference between the crystallographic and magnetic contributions.

Figure 8 presents the field dependences of SHG and magnetooptical Kerr effect in the heterostructures CaF$_2$/MnAs(70 nm)/As/Si(111) and CaF$_2$/MnAs (40 nm)/Mn/Si(111) in the meridional geometry for the analyzer angle $\alpha = 80°$, which corresponds to a high magnetic contrast and a favorable signal-to-noise ratio.

Table 5. Results of approximation of azimuthal dependences of SHG by formula (6) for meridional and equatorial geometries and two combinations of polarizations in the CaF$_2$/MnAs(70 nm)/As/Si(111) heterostructure

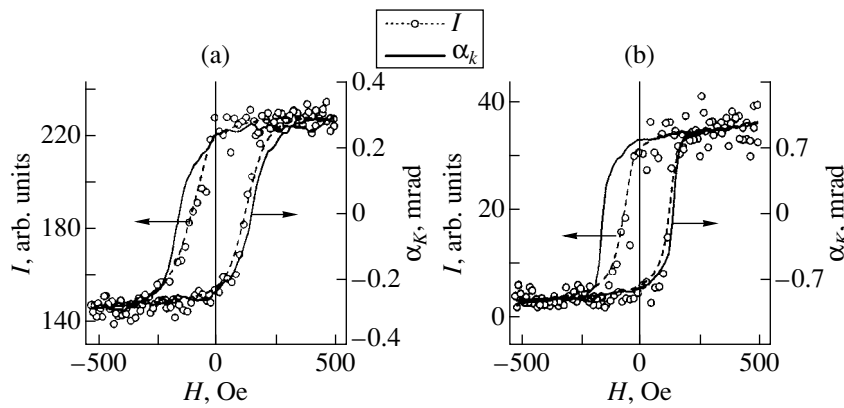| Coefficients	*PP* (merid.)	*PS* (equat.)	*SP* (equat.)
A, rel. units	0	0	0
B^{cr}, rel. units	23.1 ± 0.1	23.3 ± 0.2	3.6 ± 0.2
B^{mag}, rel. units	0	1.2 ± 0.2	0.7 ± 0.2

Fig. 8. Field dependences of the intensity $I^{2\omega}$ of the second optical harmonic and the angle of rotation of polarization plane (Kerr effect) for the (a) CaF$_2$/MnAs(40 nm)/Mn/Si(111) and (b) CaF$_2$/MnAs(70 nm)/As/Si(111) heterostructures.

It can be seen that the hysteresis loop for SHG is narrower than that for the Kerr effect. This result can be interpreted as follows. In the electric-dipole approximation, a SHG signal is formed in defective noncentrosymmetric regions such as the surface and the interface. The formation of a domain wall is most probable at a defect. Since the motion of domain walls takes place at the first stage of technical magnetization [28], the magnetization reversal can be carried out more easily in the region of nonlinear-optic probing, and hence, the hysteresis loop for SHG can become narrower. The field dependences of SHG show that the hysteresis loop is asymmetric relative to the ordinate axis and is displaced toward positive fields. This effect can be observed at the interface between a ferromagnet and an antiferromagnet [29]. The emergence of the antiferromagnetic state in a MnAs crystal under the effect of applied pressure was studied in [30]. It can be proposed that some interfacial regions of the MnAs film were transformed from the ferromagnetic state to the antiferromagnetic state due to stresses emerging as a result of mismatching of the unit cell parameters of MnAs and Si crystals. The effect of hysteresis loop asymmetry forms the basis of operation of magnetic valves, and hence, MnAs films can find application in such devices.

CONCLUSION

Thus, we have studied the ferromagnet–semiconductor heterostructures CaF$_2$/MnAs/Si(111) by using two mutually complementing magnetooptical methods. On the basis of symmetry analysis of the azimuthal dependences of the second optical harmonic generation, we proved that the nonlinearity of the optical signal is accounted for by the interference of the anisotropic contribution and the isotropic crystallographic and isotropic magnetic contributions. These contributions were separated by using the azimuthal and field dependences. It was found that the field dependences of the two magnetooptical phenomena are different due to the sensitivity of the second optical harmonic and the mag-netooptical Kerr effect to the interfaces and the bulk of the film, respectively, which are characterized by different magnetic properties.

REFERENCES

1. G. A. Prinz, Science **250**, 1092 (1990); Physics Today **48** (4), 58 (1995).
2. P. S. Pershan, Phys. Rev. **130**, 919 (1963).
3. E. Adler, Phys. Rev. **134**, A728 (1964).
4. S. Kielich, Acta Phys. Pol. **29**, 875 (1966).
5. S. Kielich and R. Zawodny, Opt. Commun. **4**, 132 (1971); Optica Acta **20**, 867 (1973).
6. N. N. Akhmediev, S. B. Borisov, A. K. Zvezdin, *et al.*, Fiz. Tverd. Tela (Leningrad) **27**, 106 (1985) [Sov. Phys. Solid State **27**, 650 (1985)].
7. S. S. Girgel' and T. V. Demidova, Opt. Spektrosk. **62**, 101 (1987) [Opt. Spectrosc. **62**, 63 (1987)].
8. Ru-Pin Pan, H. D. Wei, and Y. R. Shen, Phys. Rev. B **39**, 1229 (1989).
9. W. Hübner and K. H. Bennemann, Phys. Rev. B **40**, 5973 (1989).
10. A. M. Agal'tsov, V. S. Gorelik, A. K. Zvezdin, *et al.*, Tr. Inst. im. Lebedeva, Akad. Nauk **5**, 37 (1989).
11. O. A. Aktsipetrov, O. V. Braginskiǐ, and D. A. Esikov, Kvantovaya Élektron. (Moscow) **17**, 320 (1990) [Sov. J. Quantum Electron. **20**, 259 (1990)].

12. J. Reif, J. C. Zink, C.-M. Schneider, *et al.*, Phys. Rev. Lett. **67**, 2878 (1991).

13. J. Reif, C. Rau, and E. Matthias, Phys. Rev. Lett. **71**, 1931 (1993).

14. *Nonlinear Optics in Metals*, Ed. by K. H. Bennemann (Oxford Univ. Press, Oxford, 1998).

15. H. A. Wierenga, W. de Jong, M. W. J. Prins, *et al.*, Phys. Rev. Lett. **74**, 1462 (1995).

16. V. E. Zubov and A. D. Modestov, Opt. Spektrosk. **82**, 64 (1997) [Opt. Spectrosc. **82**, 56 (1997)].

17. A. M. Stoffel and J. Schneider, J. Appl. Phys. **41**, 1405 (1970).

18. Yu. A. Izyumov and V. N. Syromyatnikov, *Phase Transitions and Crystal Symmetry* (Nauka, Moscow, 1984).

19. M. Tanaka, Mater. Sci. Eng. B **31**, 117 (1995).

20. Y. Morishita, K. Iida, J. Abe, *et al.*, Jpn. J. Appl. Phys. **36**, L1100 (1997).

21. A. G. Banshchikov, A. V. Kimel', B. B. Krichevtsov, *et al.*, Fiz. Tverd. Tela (S.-Peterburg) **41**, 110 (1999) [Phys. Solid State **41**, 97 (1999)].

22. K. Akeura, M. Tanaka, T. Nashinaga, *et al.*, J. Appl. Phys. **79**, 4957 (1996).

23. A. Ishizaka and Y. Shiraki, J. Electrochem. Soc. **133**, 666 (1986).

24. R. R. Birss, *Symmetry and Magnetism* (North-Holland, Amsterdam, 1966).

25. R. V. Pisarev, V. V. Pavlov, A. Kirilyuk, *et al.*, J. Magn. Soc. Jpn. **20** (S1), 23 (1996).

26. V. V. Pavlov, R. V. Pisarev, A. Kirilyuk, *et al.*, Phys. Rev. Lett. **78**, 2004 (1997).

27. M. Straub, R. Vollmer, and J. Kirschner, Phys. Rev. Lett. **77**, 743 (1996).

28. S. Chikasumi, *Physics of Ferromagnetism. Magnetic Characteristics and Engineering Application* (Syokabo, Tokyo, 1984; Mir, Moscow, 1987).

29. W. H. Meiklejohn and C. P. Bean, Phys. Rev. **102**, 1413 (1956).

30. N. Menyuk, J. A. Kafalas, K. Dwight, and J. B. Goodenough, Phys. Rev. **177**, 942 (1963).

Translated by N. Wadhwa

MAGNETISM
AND FERROELECTRICITY

Nonlinear Response of Superparamagnetic Particles
to a Sudden Change of a High Constant Magnetic Field

Yu. P. Kalmykov and S. V. Titov

Institute of Radio Engineering and Electronics (Fryazino Branch), Russian Academy of Sciences, pl. Vvedenskogo 1,
Fryazino, Moscow oblast, 141120 Russia
e-mail: kalmykov@univ-perp.fr
e-mail: svt245@ire216.msk.su
Received October 20, 1999

Abstract—For a system of superparamagnetic particles in a high external constant magnetic field, a technique for calculating the nonlinear response to a sudden change in the field direction and magnitude is proposed. A set of momentary equations for the averaged spherical harmonics, which is derived from the Fokker–Planck equation for the magnetization-orientation distribution function is the basis of this technique. As an example, the nonlinear response of a system of particles with anisotropy of the easy-axis type is examined. For this case, a solution to the momentary equations is obtained by using matrix continued fractions. The magnetization relaxation time and the spectrum of the relaxation function are calculated for typical values of anisotropy, dissipation, and nonlinearity parameters. It is shown that the magnetization kinetics is essentially dependent on these parameters. © 2000 MAIK "Nauka/Interperiodica".

1. Single-domain ferromagnetic particles are characterized by internal anisotropy magnetostatic potential, which may have several local minima separated by potential barriers. If particles are small (~10 nm) and, hence, the potential barriers are low, the magnetization vector $\mathbf{M}(t)$ may be reoriented from one equilibrium portion to another, overcoming the potential barriers owing to thermal fluctuations [1]. The magnetization thermal instability gives rise to a so-called superparamagnetism [2], because each particle is similar to a paramagnetic atom with a magnetic moment equal to about 10^4–10^5 Bohr magnetons. Presently, studying thermal fluctuations and the relaxation of single-domain particle magnetization comes to the attention in the context of getting better characteristics of magnetic recording media [3].

The kinetics of the magnetization of superparamagnetic particles (SPs) is described by the Fokker–Planck equation for the probability density W of the magnetization $\mathbf{M}$. This equation was first obtained by Brown [4] from the Gilbert equation with a fluctuating field [5] that takes into account thermal fluctuations in the magnetization of an individual particle. On the basis of the Gilbert and Fokker–Planck equations, a theory of magnetic relaxation in a system of SPs was elaborated (see, for example, [6–8]). The similar Fokker–Planck equations, describing the Brownian rotation of particles, are often used in studies of dielectric relaxation in molecular and liquid crystals [9, 10], of birefringence kinetics in liquids [11], etc.

In an external magnetic field $\mathbf{H}_0$ of a moderate magnitude, due to the large magnetic dipole moment of a particle, the particle energy becomes comparable to kT (k is Boltzmann's constant, T is the temperature). In view of the magnetization relaxation time being essentially dependent on the external field intensity [12–14], it is necessary to consider nonlinear effects in analyzing the magnetization kinetics in an external field changing in both magnitude and direction (e.g., in the case where $\mathbf{H}_0$ is reversed). If the field variation is faster than the process of relaxation, such a variation may be considered sudden. Therefore, the problem may be formulated as a usual problem of calculating a nonlinear response (NR) to a sudden change in the external field. However, until now, the appropriate theory was elaborated only for the case of the linear response (LR) of superparamagnetic particles, i.e., when the particle energy change due to the external field variation is far smaller than kT. The theory of the response to high magnetic fields has barely been developed. It is very difficult to calculate the response to the strong external action, because the response depends on the type of an external action, and there is no universal response function being able to describe all types of action, as it takes place in the case of a linear response. For nonlinear problems, the main results were obtained by using the perturbation theory (see, for example, [15–17]), which implies that they are applicable only in the range of weak fields.

The primary aim of this work is to investigate the kinetics of the SP magnetization after a sudden change

in both the intensity and direction of the high constant magnetic field. The results of the examination of the nonlinear response of superparamagnetics to a high varying field shall be described in another paper.

2. Let the system of noninteracting SPs to be located in an external uniform magnetic field $\mathbf{H}_I$, which is suddenly changed in magnitude, as well as in direction into $\mathbf{H}_{II}$ at the instant $t = 0$. Up to the instant of the field change, the system was in the equilibrium state, which is characterized by the distribution function

$$W_I = Z_I^{-1} e^{-\beta[U - (\mathbf{MH}_I)]}. \tag{1}$$

After the field change, the system relaxes to the new equilibrium state II, characterized by the distribution function

$$W_{II} = Z_{II}^{-1} e^{-\beta[U - (\mathbf{MH}_{II})]}. \tag{2}$$

In (1) and (2), U is the particle free energy density in the absence of any external field, $\beta = v/kT$, v is the volume of the particle, and Z_N ($N = I, II$) is the normalization constant. This problem is essentially nonlinear, because it is assumed that the field change, in both magnitude and direction, may be considerable. The kinetics of the magnetization nonlinear response (MNR) is described by the normalized relaxation function

$$f(t) = \frac{\langle M_r \rangle(t) - \langle M_r \rangle_{II}}{\langle M_r \rangle_I - \langle M_r \rangle_{II}} = \frac{\langle \mathbf{ru} \rangle(t) - \langle \mathbf{ru} \rangle_{II}}{\langle \mathbf{ru} \rangle_I - \langle \mathbf{ru} \rangle_{II}}, \tag{3}$$

where M_r is the projection of the magnetization on the direction of the unit vector $\mathbf{r} = \mathbf{i}v_X^r + \mathbf{j}v_Y^r + \mathbf{k}v_Z^r$,

$$\mathbf{M} = M_S\mathbf{u} = M_S(\mathbf{i}u_X + \mathbf{j}u_Y + \mathbf{k}u_Z); \tag{4}$$

M_S is the spontaneous magnetization; $u_X = \sin\theta\cos\varphi$, $u_Y = \sin\theta\sin\varphi$, $u_Z = \cos\theta$; θ and φ are the polar and azimuthal angles, respectively; and the angle brackets denote averaging with respect to the function W_N,

$$\langle \mathbf{ru} \rangle_N = \int_0^{2\pi} d\varphi \int_0^{\pi} \sin\theta d\theta (\mathbf{ru}) W_N. \tag{5}$$

For the diffusion model, the kinetics of the magnetization vector $\mathbf{M}(t)$ of a single-domain particle is similar to the Brownian rotation of a macromolecule in liquid and described by the Fokker–Planck equation for the distribution function $W(\vartheta, \varphi, t)$ [6, 8]

$$\frac{\partial}{\partial t} W = b[\alpha^{-1}\mathbf{u}(\operatorname{grad}V_{II} \times \operatorname{grad}W)$$
$$+ \operatorname{div}(W\operatorname{grad}V_{II}) + \beta^{-1}\Delta W] \quad (t > 0) \tag{6}$$

with the initial condition $W(\vartheta, \varphi, 0) = W_1$. Here, Δ is the angular part of the Laplace operator, $V_{II} = U - (\mathbf{MH}_{II})$ is the particle density free energy in the state II, $\alpha = \eta\gamma M_S$ is the dimensionless dissipation coefficient, γ is the gyromagnetic ratio, η is the coefficient of friction, $b = \beta/2\tau_N$, and

$$\tau_N = \beta M_S(1 + \alpha^2)/2\gamma\alpha \tag{7}$$

is the characteristic time of thermal fluctuations of the magnetization. Equation (6) was derived under the assumption that the random field causing the magnetization fluctuations possesses white noise properties. Therefore, the possible effects of "memory" are also not taken into account in (6). The surface effects are not taken into account here, and, furthermore, it is assumed that the magnetization is uniform inside the particle. These assumptions are discussed in detail, for example, in [18].

From (6), using the results of [19, 20], the following equations can be obtained for the relaxation functions $c_{l,m}(t) = \langle Y_{l,m} \rangle(t) - \langle Y_{l,m} \rangle_{II}$:

$$\tau_N \frac{d}{dt} c_{l,m}(t) = \sum_{l'} \sum_s d_{l', m \pm s, l, m} c_{l', m \pm s}(t) \tag{8}$$

with the initial conditions

$$c_{l,m}(0) = \langle Y_{l,m} \rangle_I - \langle Y_{l,m} \rangle_{II}, \tag{9}$$

where $Y_{l,m}(\theta, \varphi)$ are the spherical harmonics [21]. Explicit expressions for $d_{l', m \pm s, l, m}$ in terms of the Clebsch–Gordon coefficients and the expansion of the free energy V in terms of spherical harmonics are given in [19, 20]. Thus, in (3), the nonlinear response function $f(t)$ may be expressed in terms of $c_{l,m}(t)$ as

$$f(t) = \frac{\sqrt{2}v_Z^r c_{1,0}(t) + (v_X^r + iv_Y^r)c_{1,-1}(t) - (v_X^r - iv_Y^r)c_{1,1}(t)}{\sqrt{2}v_Z^r c_{1,0}(0) + (v_X^r + iv_Y^r)c_{1,-1}(0) - (v_X^r - iv_Y^r)c_{1,1}(0)}. \tag{10}$$

3. Equations (8)–(10) are applicable for particles with arbitrary anisotropy: of the easy-axis type, cubic, etc. In this work, we will consider, for simplicity's sake, only the particles with uniaxial anisotropy, whose free energy takes the form [8]

$$V = -K\cos^2\theta - (\mathbf{MH}_N)$$

$$= -H_N M_S \sqrt{\frac{2\pi}{3}} [(\nu_X^N + i\nu_Y^N)Y_{1,-1} + \sqrt{2}\nu_Z^N Y_{1,0} \quad (11)$$

$$- (\nu_X^N - i\nu_Y^N)Y_{1,1}] - \frac{4K}{3}\sqrt{\frac{\pi}{5}}Y_{2,0} - \frac{K}{3},$$

where K is the anisotropy constant and ν_X^N, ν_Y^N, and ν_Z^N are the direction cosines of the vectors $\mathbf{H}_N$. In this case, equation (8) for $c_{l,m}(t)$ takes the recurrent form

$$\tau_N \frac{d}{dt} c_{l,m}(t) = \sum_{l'=-2}^{2} \sum_{s=-1}^{1} d_{l',m\pm s,l,m} c_{l',m\pm s}(t) \quad (12)$$

$$(t > 0),$$

where $d_{n\pm 2,m\pm 1,n,m} \equiv 0$; explicit expressions for the eleven nonzero coefficients $d_{l',m',l,m}$ are given in the Appendix.

From the mathematical point of view, solving (12) is reduced to solving an infinite set of linear differential equations. In [22–24], it was shown that the solution of this problem may be simplified significantly by using matrix-continued fractions (MCFs) [25, 26]. To do this, equation (12) should be transformed to a matrix equation with the following form:

$$\tau_N \frac{d}{dt} C_n(t) = Q_n^- C_{n-1}(t) + Q_n C_n(t) + Q_n^+ C_{n+1}(t), \quad (13)$$

$$n = 1, 2, 3, \dots.$$

Here, the vectors $C_n(t)$ can be represented in the same form as in [23]; the matrices Q_n, Q_n^+, and Q_n^- are given in the Appendix. The expect solution of (13) for the spectrum $\tilde{C}_1(\omega)$ has the form [25, 26]

$$\tilde{C}_1(\omega) = \tau_N \Delta_1(\omega)$$

$$\times \left\{ C_1(0) + \sum_{n=2}^{\infty} \left(\prod_{k=2}^{n} Q_{k-1}^+ \Delta_k(\omega) \right) C_n(0) \right\}, \quad (14)$$

where

$$\Delta_n(\omega) = \cfrac{I}{i\omega\tau_N I - Q_n - Q_n^+ \cfrac{I}{i\omega\tau_N I - Q_{n+1} - Q_{n+1}^+ \cfrac{I}{i\omega\tau_N I - \dots} Q_{n+2}^-} Q_{n+1}^-} \quad (15)$$

is an MCF, and tilde denotes the Fourier transform

$$\tilde{F}(\omega) = \int_0^{\infty} F(t)e^{-i\omega t}dt. \quad (16)$$

The initial values $C_n(0)$ in (14) are also calculated using MCFs (see Appendix). With $\tilde{C}_1(\omega)$ determined from (14), it becomes possible to calculate the spectrum of the RF and the relaxation time from (10):

$$\tau = \int_0^{\infty} f(t)dt = \frac{\sqrt{2}\nu_Z^r \tilde{c}_{1,0}(0) + (\nu_X^r + i\nu_Y^r)\tilde{c}_{1,-1}(0) - (\nu_X^r - i\nu_Y^r)\tilde{c}_{1,1}(0)}{\sqrt{2}\nu_Z^r c_{1,0}(0) + (\nu_X^r + i\nu_Y^r)c_{1,-1}(0) - (\nu_X^r - i\nu_Y^r)c_{1,1}(0)}. \quad (17)$$

The above results are true for a system of particles whose easy axes are oriented along the OZ axis. If the easy axes of the particles are randomly distributed in space, then, in order to calculate the spectrum and the relaxation time, they must be probably averaged. Moreover, in the above consideration, it was assumed that all particles are identical. To take the poly-dispersion of the particles into account, averaging with the corresponding distribution functions must be performed (e.g., over the volumes of the particles).

4. For uniaxial particles, there is a certain geometry of the problem in which the relaxation time τ may be calculated with quadratures. It corresponds to the case when, in both states I and II, the constant magnetic field coincides with the easy axis of the particle. In this case, due to the symmetry of the problem, the Fokker–Planck equation (6) becomes one-dimensional, and, therefore, we can use the results of [27], where the problem of time relaxation was solved in the general form for the nonlinear response of one-dimensional systems, whose dynamics may be described with the one-dimensional
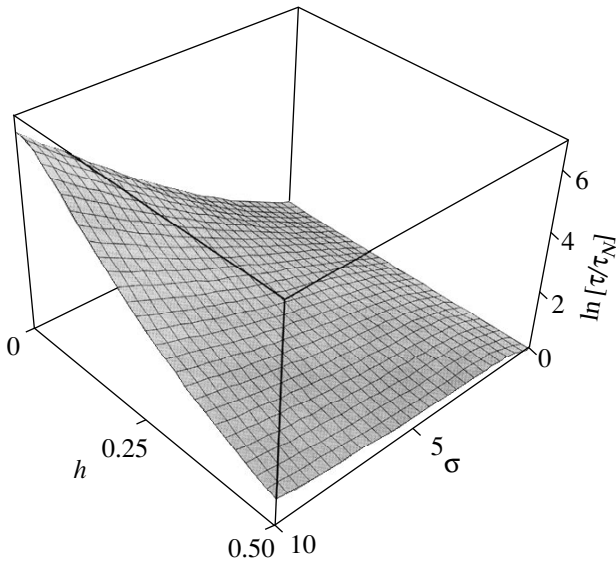
Fig. 1. Logarithm $\ln(\tau/\tau_N)$ as a function of σ and $h = |h_{\mathrm{I}}| = |h_{\mathrm{II}}|$ for the case of the sudden reverse of the field direction $(\mathbf{H}_{\mathrm{I}} = -\mathbf{H}_{\mathrm{II}})$.

Fokker–Planck equation. Applying the results of [27] to our problem, it can be shown that the relaxation time τ is defined by the quadrature

$$\tau = \frac{2\tau_N}{\langle\cos\theta\rangle_{\mathrm{II}} - \langle\cos\theta\rangle_{\mathrm{I}-1}}$$
$$\times \int_{-1}^{1} \frac{\Phi(z)\Psi(z)e^{-\sigma(z^2 + 2h_{\mathrm{II}}z)}dz}{1 - z^2}, \quad n = 1, 2, \tag{18}$$

where

$$\Phi(z) = \int_{-1}^{z} [W_{\mathrm{II}}(z') - W_{\mathrm{I}}(z')]dz', \tag{19}$$

$$\Psi_1(z) = \int_{-1}^{z} [z' - \langle\cos\theta\rangle_{\mathrm{II}}]e^{-\sigma(z'^2 + 2h_{\mathrm{II}}z')}dz', \tag{20}$$

$$\sigma = \beta K, \quad h_N = H_N M_S/2K.$$

In (18)–(20), $h_{\mathrm{II}} > 0$ or $h_{\mathrm{II}} < 0$ when $\mathbf{H}_{\mathrm{II}}$ is parallel or antiparallel to $\mathbf{H}_{\mathrm{I}}$, respectively.

5. In our calculations, for simplicity's sake, we limited ourselves to the case when the field $\mathbf{H}_{\mathrm{I}}$ is directed along the easy axis of the particle, and the response is calculated in the direction of the field $\mathbf{H}_{\mathrm{II}}$. In this case, it can be assumed without loss of generality that the direction cosines of the vector $\mathbf{H}_{\mathrm{II}}$ are $\nu_X^{\mathrm{II}} = \sin\Theta$, $\nu_Y^{\mathrm{II}} = 0$, and $\nu_Z^{\mathrm{II}} = \cos\Theta$, since the response does not depend on the azimuthal angle because of the symmetry of the problem. At $\Theta \neq 0$, the nonlinear response depends on the dissipation parameter α because the longitudinal and transverse modes are coupled. However, qualitatively, this dependence is similar to that of the linear response, which was examined in detail in [23, 28]. The experimental and theoretical methods of estimating α were discussed, for example, in [7, 19, 29]. The estimations assign its value to the range of ~0.01–0.1. For definiteness, we carried out our calculations at $\alpha = 0.1$.

Figure 1 shows the relaxation time τ as a function of anisotropy parameter σ and of field $h = |h_{\mathrm{I}}| = |h_{\mathrm{II}}|$ for the case of the field direction being reversed suddenly
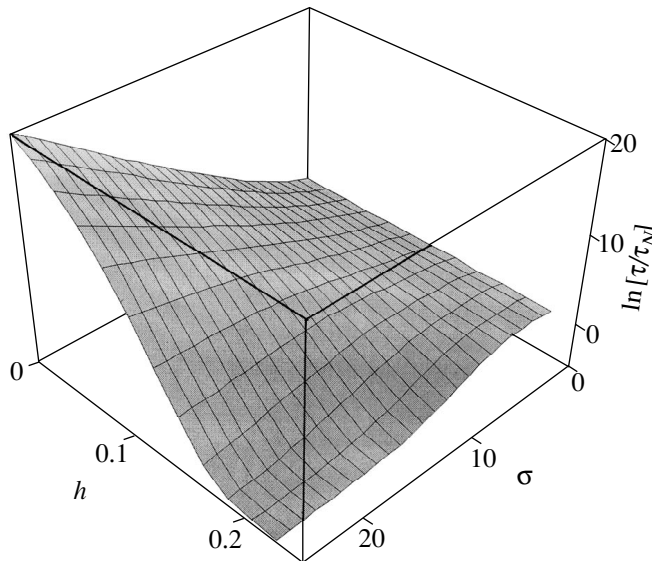
Fig. 2. Logarithm $\ln(\tau/\tau_N)$ as a function of σ and $h = h_{\mathrm{II}}/2 = h_{\mathrm{I}}$ for when the external field intensity is suddenly doubled.
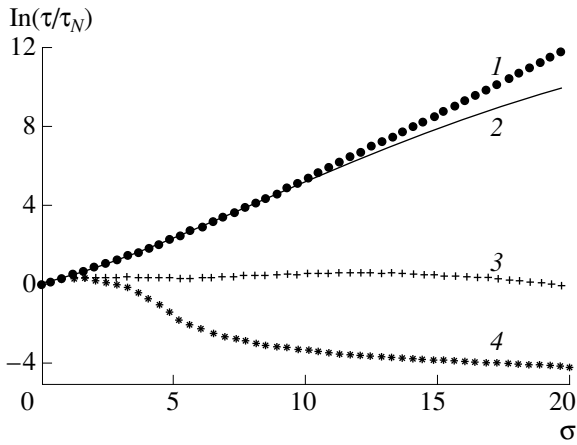
Fig. 3. Logarithm $\ln(\tau/\tau_N)$ as a function of σ: (*1* and *4*) correspond to the linear response, (*2* and *3*) to the nonlinear one. (*1*) $h_{II} = h_I - \varepsilon = 0.1$ ($\varepsilon \longrightarrow 0$)); (*4*) $h_{II} = h_I - \varepsilon = 0.5$ ($\varepsilon \longrightarrow 0$); (*2*) $h_I = 0.5 \longrightarrow h_{II} = 0.1$; and (*3*) $h_I = 0.1 \longrightarrow h_{II} = 0.5$.
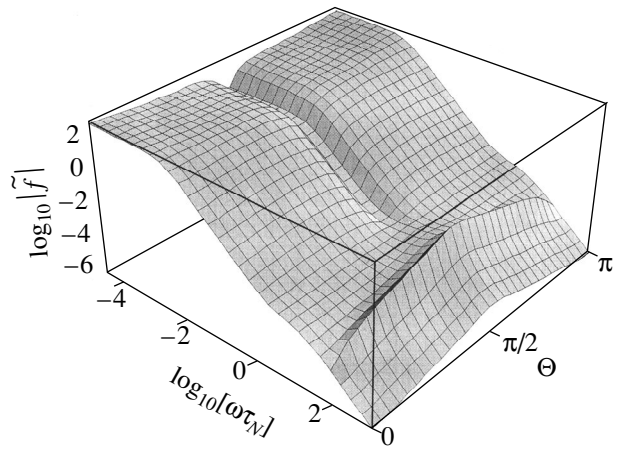

Fig. 4. Logarithm $\log_{10}|\tilde{f}|$ as a function of $\log_{10}(\omega\tau_N)$ and Θ at the sudden switch-on of the constant magnetic field ($h_I = 0$; $h_{II} = 0.1$; $\sigma = 10$; and $\alpha = 0.1$).

($\mathbf{H}_I = -\mathbf{H}_{II}$). Figure 2 exhibits the behavior of τ in the case where the external field intensity is suddenly doubled, i.e., $h_{II} = 2h_I$. In these cases, τ does not depend on α and can be determined from (18)–(20). In a low external field, τ is mainly determined by the lower-frequency relaxation mode, which characterizes transitions of the magnetization vector through the potential barrier of the double-well potential (11), from one potential well to the other. In this case, the dependence of τ on the anisotropy parameter σ is of an activation character, namely, it increases exponentially with σ growth. However, when the field $\mathbf{H}_{II}$ is fairly high, the time τ decreases with σ growth (see Fig. 2). This effect, first discovered in [14] by analyzing the linear response (LR) of a system of uniaxial particles in the low-temperature limit, is due to the depletion of the population of the higher well. The last circumstance, in particular, explains the fact that the relaxation time τ ceases to be of the activation type when values of h are larger than a certain critical value h_c (for potential (14), $h_c \approx 0.17$ at $\Theta = 0$ [30]). This means that the relaxation time τ decreases, rather than increases, with σ growth. The absolute value of the NR time τ may differ substantially (see Fig. 3) from the magnetization relaxation times τ_I and τ_{II} characterizing the LR of the particle to a weak external probe field in states I and II (τ_I and τ_{II} are determined by the eigenvalues of the Fokker–Planck operator[1] (6) in states I and II, respectively [7, 14, 28]).

In Fig. 4, the results of calculations of the modulus of the Fourier transform f of the relaxation function are presented for the case of the sudden switch of the high field (i.e., for $h_I = 0$ and $h_{II} = h$) forming an arbitrary

---

[1] With the matrix continued fraction method used in this work, the eigenvalues λ of the Fokker–Planck operator are determined from the equation $\det|\lambda I + Q_1 + Q_I^- \Delta_2(-\lambda) Q_2^-| = 0$.

angle Θ with the particle axis. In all these figures, three bands are seen in the f spectrum. The characteristic frequency and half-width of the lower-frequency band are defined by the reciprocal value of the mean lifetime of the magnetization vector in the less deep potential well. The significantly weaker relaxation band associated with intrawell modes manifests itself at high frequencies (at $\Theta = 0$ and $\sigma \gg 1$, and the characteristic frequency of this band is $\omega_{well} \approx 2\sigma(1 + h)/\tau_N$ [30]). Moreover, in Figs. 3 and 4, in the high-frequency range of the spectrum, the resonance band is seen, which is due to the contribution of the transverse modes at the frequencies of the magnetization vector precession. With a decrease in α, this high-frequency band is narrowed down and displaced to the high-frequency region. At $\Theta = 0$, this band completely disappears, because, in this case, the transverse modes do not take part in the relaxation process. In Fig. 5, the results of the calculations of $|\tilde{f}|$ are presented for the cases of the sudden change in the field direction, with $|\mathbf{H}_I| = |\mathbf{H}_{II}|$. As in Fig. 4, three typical bands, which are associated with long-lived, intrawell, and transverse modes, respectively, are seen here. Besides, in Fig. 5, the effect of a low-frequency mode suppressed by a constant field, when the field vector rotates through the angle $\Theta < \pi/2$, is clearly demonstrated.

6. So, in this work, the method of calculating the spectrum $\tilde{f}(\omega)$ and relaxation time τ for the nonlinear relaxation function $\tilde{f}(\omega)$ describing the kinetics of the SP magnetization after a sudden change of the constant magnetic field is proposed. For uniaxial particles, $\tilde{f}(\omega)$ and τ can be calculated from (14) using MCSs for all ranges of nonlinearity, anisotropy, and dissipation parameters. In this way, the cubic anisotropy particles may be examined, for which a similar technique of LR

characteristics calculations was developed in [24]. It is hoped that our approach will be useful in setting and interpreting experiments in the nonlinear response investigation.

APPENDIX

In (13), the matrices Q_n, Q_n^+, Q_n^- are of the form

$$Q_n = \begin{pmatrix} X_{2n} & W_{2n} \\ Y_{2n-1} & X_{2n-1} \end{pmatrix}, \quad Q_n^+ = \begin{pmatrix} Z_{2n} & Y_{2n} \\ 0 & Z_{2n-1} \end{pmatrix},$$

$$Q_n^- = \begin{pmatrix} -\dfrac{2n+1}{2n-2}Z_{2n-2}^T & 0 \\ W_{2n-1} & -\dfrac{2n}{2n-3}Z_{2n-3}^T \end{pmatrix}. \tag{A1}$$

Here, the index T denotes the transposition of the matrix. The dimensions of Q_n, Q_n^+, Q_n^- matrices are $8n \times 8n$, $8n \times 8(n+1)$, $8n \times 8(n-1)$, respectively. The explicit forms of the tridiagonal submatrices X_l, Y_l, W_l, Z_l of formula (A1) are given in [23]. However, their elements, used in our work, differ from those presented in [23] and are as follows:

$$x_{n,m} = d_{n,m,n,m} = \frac{\sigma(n(n+1)-3m^2)}{(2n-1)(2n+3)}$$
$$- \frac{n(n+1)}{2} - i\frac{m\sigma h_{\mathrm{II}}\gamma_Z^{\mathrm{II}}}{\alpha},$$

$$x_{n,m}^+ = -(x_{n,-m}^-)^* = d_{n,m+1,n,m}$$
$$= -i\frac{\sigma h_{\mathrm{II}}(\gamma_X^{\mathrm{II}} - i\gamma_Y^{\mathrm{II}})}{2\alpha}\sqrt{(n+m+1)(n-m)},$$

$$y_{n,m} = d_{n+1,m,n,m}$$
$$= -\sigma\left(h_{\mathrm{II}}n + i\frac{m}{\alpha}\right)\sqrt{\frac{(n+1)^2 - m^2}{(2n+1)(2n+3)}},$$

$$y_{n,m}^+ = -(y_{n,-m}^-)^* = d_{n+1,m+1,n,m}$$
$$= \frac{n\sigma h_{\mathrm{II}}(\gamma_X^{\mathrm{II}} - i\gamma_Y^{\mathrm{II}})}{2}\sqrt{\frac{(n+m+1)(n+m+2)}{(2n+1)(2n+3)}},$$

$$w_{l,m} = d_{n-1,m,n,m}$$
$$= \sigma\left(h_{\mathrm{II}}\gamma_Z^{\mathrm{II}}(n+1) - i\frac{m}{\alpha}\right)\sqrt{\frac{n^2 - m^2}{(2n+1)(2n-1)}},$$

$$w_{n,m}^+ = -(w_{n,-m}^-)^* = d_{n-1,m+1,n,m}$$
$$= \frac{(n+1)\sigma h_{\mathrm{II}}(\gamma_X^{\mathrm{II}} - i\gamma_Y^{\mathrm{II}})}{2}\sqrt{\frac{(n-m)(n-m-1)}{(2n+1)(2n-1)}},$$

$$z_{n,m} = d_{n+2,m,n,m}$$
$$= -\frac{\sigma n}{2n+3}\sqrt{\frac{[(n+2)^2 - m^2][(n+1)^2 - m^2]}{(2n+1)(2n+5)}}.$$

The calculation of the initial values $C_n(0)$ in (14) is carried out in the following way. Let us introduce the vector

$$R_n^N = \begin{pmatrix} \langle Y_{2n,-2n}\rangle_N \\ \langle Y_{2n,-2n+1}\rangle_N \\ \vdots \\ \langle Y_{2n,2n}\rangle_N \\ \langle Y_{2n-1,-2n+1}\rangle_N \\ \langle Y_{2n-1,-2n+2}\rangle_N \\ \vdots \\ \langle Y_{2n-1,2n-1}\rangle_N \end{pmatrix}. \tag{A2}$$

Then, in accordance with (12), for R_n^N, the following matrix recurrent relation is true:

$$Q_n^- R_{n-1}^N + Q_n R_n^N + Q_n^+ R_{n+1}^N = 0, \quad n = 1, 2, 3, \dots \tag{A3}$$

Its solution is

$$R_n^N = \Delta_n^N(0)Q_n^- R_{n-1}^N = \frac{1}{\sqrt{4\pi}}\prod_{k=1}^{n}[\Delta_k^N(0)Q_k^-]. \tag{A4}$$

Here, it is taken into account that $R_0^N = 1/\sqrt{4\pi}$. Thus,
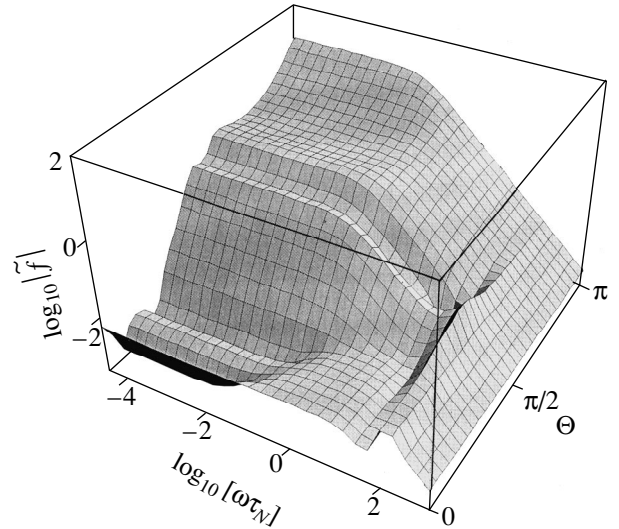

Fig. 5 Logarithm $\log_{10}|\tilde{f}|$ as a function of $\log_{10}(\omega\tau_N)$ and Θ for the case of the sudden rotation of the constant magnetic field ($h = |h_{\mathrm{I}}| = |h_{\mathrm{II}}| = 0.3$; $\sigma = 10$, and $\alpha = 0.1$).

for $C_n(0)$, we have

$$C_n(0) = R_n^{\mathrm{I}} - R_n^{\mathrm{II}}.$$

REFERENCES

1. L. Néel, Ann. Geophys. **5**, 99 (1949).
2. H. B. Braun and H. N. Bertram, J. Appl. Phys. **75**, 4609 (1994).
3. C. P. Bean and J. D. Livingston, Suppl. J. Appl. Phys. **30**, 1205 (1959).
4. W. F. Brown, Jr., Phys. Rev. **130**, 1677 (1963).
5. T. L. Gilbert, Phys. Rev. **100**, 1243 (1956).
6. W. F. Brown, Jr., IEEE Trans. Mag. **15**, 1196 (1979).
7. Yu. L. Raikher and M. I. Shliomis, Adv. Chem. Phys. **87**, 595 (1994).
8. L. J. Geoghegan, W. T. Coffey, and B. Mulligan, Adv. Chem. Phys. **100**, 475 (1997).
9. L. M. Blinov, *Electro- and Magnetooptics of Liquid Crystals* (Nauka, Moscow, 1982).
10. G. Moro and P. L. Nordio, Z. Phys. B.: Condens. Matter **64**, 217 (1986).
11. J. L. Dejardin, *Dynamic Kerr Effect* (World Scientific, Singapour, 1996).
12. A. Aharoni, Phys. Rev. **177**, 763 (1969).
13. D. A. Garanin, V. V. Ishchenko, and L. V. Panina, Zh. Teor. Mat. Fiz. **82**, 242 (1990).
14. W. T. Coffey, D. S. F. Crothers, Yu. P. Kalmykov, *et al.*, Phys. Rev. B **51**, 15947 (1995).
15. É. K. Sadykov and A. G. Isavnin, Fiz. Tverd. Tela **38**, 2104 (1996) [Phys. Solid State **38**, 1160 (1996)].
16. Yu. L. Raikher and V. I. Stepanov, Phys. Rev. **B 55**, 15005 (1997).
17. Yu. L. Raikher, V. I. Stepanov, A. N. Grigirenko, *et al.*, Phys. Rev. E **56**, 6400 (1997).
18. I. Klik and L. Gunther, J. Stat. Phys. **60**, 473 (1990).
19. Yu. P. Kalmykov and S. V. Titov, Fiz. Tverd. Tela **41**, 2020 (1999) [Phys. Solid State **41**, 1854 (1999)].
20. Yu. P. Kalmykov and S. V. Titov, Phys. Rev. Lett. **82**, 2967 (1999).
21. R. N. Zare, *Angular Momentum: Understanding Spacial Aspects in Chemistry and Physics* (Wiley, New York, 1988; Mir, Moscow, 1993).
22. Yu. P. Kalmykov, S. V. Titov, and W. T. Coffey, Phys. Rev. B **58**, 3267 (1998).
23. Yu. P. Kalmykov and S. V. Titov, Fiz. Tverd. Tela **40**, 1642 (1998) [Phys. Solid State **40**, 1492 (1998)].
24. Yu. P. Kalmykov and S. V. Titov, Zh. Éksp. Teor. Fiz. **115**, 101 (1999) [JETP **88**, 58 (1999)].
25. H. Risken, *The Fokker–Planck Equation* (Springer, Berlin, 1989).
26. W. T. Coffey, Yu. P. Kalmykov, and J. T. Waldron, *The Langevin Equation* (World Scientific, Singapore, 1996).
27. Yu. P. Kalmykov, J. L. Dejardin, and W. T. Coffey, Phys. Rev. E **55**, 2509 (1997).
28. W. T. Coffey, D. S. F. Crothers, J. L. Dormann, *et al.*, Phys. Rev. B **58**, 3249 (1998).
29. W. T. Coffey, D. S. F. Crothers, J. L. Dormann, *et al.*, Phys. Rev. Lett. **80**, 5655 (1998).
30. D. A. Garanin, Phys. Rev. **E 54**, 3250 (1996).

Translated by N. Ostrovskaya

Interface Phenomena and Microwave Magnetoresistance in Polycrystalline La$_{1-x}$Ca$_x$MnO$_3$ Lanthanum Manganites

N. I. Solin, S. V. Naumov, and A. A. Samokhvalov

Institute of Metal Physics, Ural Division, Russian Academy of Sciences, ul. S. Kovalevskoĭ 18, Yekaterinburg, 620219 Russia
e-mail: magsemi@ifm.e-burg.su
Received October 20, 1999

Abstract—A study is reported of the dc and 9.2-GHz electrical and magnetoresistance (ρ_0, MR_0, ρ_{mw}, and MR_{mw}) in La$_{1-x}$Ca$_x$MnO$_3$ polycrystals ($x = 0$–0.3) in the 77–300 K temperature interval. The microwave magnetoresistance exhibits a sharp peak within a narrow interval near the Curie temperature T_C, while $MR_{mw} \approx 0$ is far from T_C. The microwave absorption in low magnetic fields is shown to be due to a variation of the microwave magnetic, rather than electrical losses. The peaks of ρ_0, ρ_{mw}, MR_0, and MR_{mw} do not coincide in temperature. The specific features in the behavior of ρ_0, MR_0, ρ_{mw}, and MR_{mw} are explained as being due to an inhomogeneity of the grains, which generates in the grain close to the interface a magnetic-field-dependent contact potential difference. The origin of the inhomogeneities can either be traced to the formation on a grain of a surface layer with properties differing from those in the grain bulk, or understood in terms of the model postulating grain separation into a conducting and a nonconducting phase. © 2000 MAIK "Nauka/Interperiodica".

We pointed out that the current flowing through a structure of two different contacting substances whose Fermi level positions depend on magnetic field should be also magnetic-field dependent [1]. We hypothesized that, in view of the observed sensitivity of the band structure of the manganites to magnetic ordering and magnetic field [2], a colossal magnetoresistance (CMR) in polycrystalline manganites can be realized due to the presence of a surface layer, whose properties differ from those of the grain bulk. Such a layer forms, e.g., in ferrites [3] as a result of the sample not being in equilibrium with the atmosphere in the course of its preparation (for instance, during cooling). Our study of the microwave surface resistance R_s and of the electrical properties as functions of the electric field E permitted an estimate of the surface layer thickness and the height of the potential barrier between the surface layer and the manganite grain.

This work reports on a study of the electrical resistivity ρ_0, ρ_{mw}, and magnetoresistance MR_0 ($\equiv [\rho(H) - \rho(H = 0)]/\rho(H = 0)$), MR_{mw}, both in the dc mode and at a frequency of 9.2 GHz, as well as of the microwave complex permeability $\mu^* = \mu' + i\mu''$ of La$_{1-x}$Ca$_x$MnO$_3$ polycrystalline manganites ($x = 0$–0.3), performed at temperatures from 77 to 300 K in magnetic fields of up to 1.8 T. The results of the study indicate that the grains are not homogeneous, and this can be explained in terms of the model proposed in [1]. Besides, some publications [4–6] maintained that in polycrystalline manganites $MR_{mw} > MR_0$. We show that at low temperatures $T \ll T_C$, a reverse relation, $MR_{mw} \ll MR_0$, holds for these substances, and that the substantial microwave absorption observed in low magnetic fields is due to the contribution of the natural ferromagnetic resonance to the permeability μ^*.

1. EXPERIMENTAL TECHNIQUES AND SAMPLES

The samples, prepared by solid-state reaction among the starting powders of La$_2$O$_3$, CaCO$_3$, and Mn$_3$O$_4$ at $T = 1300°$C, were shown by x-ray diffraction to be single phase. The unit cell was found to be orthorhombic for LaMnO$_3$ and cubic for the other compounds. The dc measurements of ρ_0 were performed by the standard four-probe method. To determine R_s, a polished plate of thickness t and with surface area S was placed at the center, at the antinode of the microwave magnetic field h of a rectangular reentrant resonator [7]. The resonance frequency ω and the passband $\delta\omega$ of the resonator with the magnetic material inside are also determined [8], in addition to the electrical resistance [7], by the complex permeability $\mu = \mu' + i\mu''$. Following [7–9], it can be shown that for $\tau = t/\delta \gg 1$, we have

$$(\delta\omega^L - \delta\omega^0)/\omega^0 = R_s S C_1/V_r + \mu'' 2\delta S C_2/V_r, \quad (1)$$

$$(\omega^L - \omega^0)/\omega^0$$
$$= (V_s - 2\delta S)C_3/V_r - (\mu' - 1)2\delta S C_4/V_r. \quad (2)$$

For an arbitrary τ, including $\tau \leq 1$, the first term of equation (1) can be written as [1]

$$(\delta\omega^L - \delta\omega^0)/\omega^0$$
$$= 2V_s(\sinh\tau - \sin\tau)/(\cosh\tau + \cos\tau)\tau V_r. \quad (3)$$

Here $R_s = \rho_{mw}/\delta$, $\delta = \sqrt{2\rho_{mw}/\omega\mu}$ is the skin depth, V_s and V_r are the volumes of the sample and of the resonator, respectively, $(\mu)^2 = (\mu')^2 + (\mu'')^2$, C_1–C_4 are some known constants, and the superscripts L and 0 identify

Activation energies ΔE_0 and ΔE_{mw} of polycrystalline lanthanum manganites in a magnetic field

Compound	ΔE_0, eV		ΔE_{mw}, eV	
	$H = 0$	$H = 16$ kOe	$H = 0$	$H = 9$ kOe
$La_{0.7}Ca_{0.3}MnO_3$	0.150	0.140	0.074	0.072
$La_{0.9}Ca_{0.1}MnO_3$	0.144	0.135	0.074	0.073
$LaMnO_3$	0.157	0.154	0.100	0.100

the parameters of the resonator with and without the sample inside.

Solving the coupled equations (1)–(3) for two samples of different thicknesses, $t_1 \gg \delta$ and $t_2 < \delta$, yields the three unknowns, μ', μ'', and ρ_{mw}. However, because of the large values of μ' and μ'', their contribution to the resonator parameters may far exceed that due to the electrical resistance of the sample. Therefore, preliminary measurements of the temperature dependences of μ' and μ'' were carried out on very thin samples, with $t \ll \delta$ (sometimes down to $t \approx 25$ µm), which, in accordance with (3), provide a small contribution to ρ_{mw} compared to those due to the magnetic losses. The studies of ρ_{mw} and MR_{mw} in a magnetic field were performed for $H \parallel h$, because in this case the transverse ac magnetization in a ferromagnet magnetized to saturation is zero, and $\mu' \approx 1$ and $\mu'' \approx 0$ [10]. The microwave electrical resistivity ρ_{mw} was derived from R_s (1) and refined in measurements on samples with different thicknesses using (3). Equation (2) was used to estimate the skin depth and, thus, to provide an additional check on the results of ρ_{mw} measurements.

The dc and 9.2-GHz measurements were performed on a computer-controlled setup. The dc current, temperature, microwave transmission, and sweep generator signals were fed into the computer, and the values of the resonator $\delta\omega$ and ω were obtained by a least-squares fitting of the absorption line shape. The measurements were made in steps of approximately 2 K, and the Q-factor of the silver-coated measuring resonator was about 7000.

2. RESULTS

Figure 1 presents temperature dependences of the dc and 9.2-GHz electrical and magnetoresistance, and ac magnetic susceptibility χ_{ac} at 1 kHz obtained in a zero magnetic field on a series of $La_{1-x}Ca_xMnO_3$ samples with $x = 0$, 0.1, and 0.3. Measurements of the χ_{ac} (curve 5 in Fig. 1) show that the $La_{1-x}Ca_xMnO_3$ compounds we studied ($x = 0$–0.3) are magnetically ordered and have a Curie temperature $T_C = 160$–215 K, depending on the calcium concentration x. Phase diagrams plotted for the stoichiometric composition suggest that $LaMnO_3$ should be an antiferromagnetic dielectric. It is known, however, that ferromagnetic manganites can

also be prepared quite often without any doping by making them nonstoichiometric in lanthanum and oxygen [11]. The polycrystals studied in the dc mode exhibited properties typical of manganites (curves 1 and 2 in Fig. 1), namely, a maximum in ρ_0 and a peak of the negative magnetoresistance MR_0 near T_C. The temperature dependences of ρ_0 and ρ_{mw} are approximately the same; indeed, they show a semiconducting behavior at high temperatures and a metallic one in the low-temperature domain. Note that $\rho_{mw} \ll \rho_0$ throughout the temperature range covered, with the variation of ρ_{mw} being strongest at the temperatures where $\rho_{mw}(T)$ reaches its maximum value.

One readily sees (Fig. 1) that in samples with high $T_C = 205$–215 K ($x = 0$ and 0.3), ρ_{mw}, MR_{mw}, ρ_0, and MR_0 pass through a maximum at about the same temperatures close to T_C. The maxima of $\rho_{mw}(T)$ and $MR_{mw}(T)$ in the sample with a low $T_C \approx 160$ K ($x = 0.1$), which also exhibited the largest dc and ac resistivity, differ from those of $\rho_0(T)$ and $MR_0(T)$ by about 70–80 K. Interestingly, the values of ρ_{mw} and MR_{mw} for all samples reach a maximum near $T \cong 190$–225 K.

Note that the field dependences $MR_0(H)$ are also typical of polycrystalline manganites; indeed, in the paramagnetic region, $MR_0 \sim H^2$, while in the ferromagnetic region, up to the demagnetizing field, one observes a strong growth (up to $MR_0 \cong -0.1$ at $T = 77$ K in all samples), followed by a weak, approximately linear rise of $|MR_0|$ with the increasing magnetic field H.

The table lists the activation energies ΔE_0 and ΔE_{mw} derived from the temperature dependences of ρ_0 and ρ_{mw} in the paramagnetic region. The dc activation energy ΔE_0 is less than the microwave one, ΔE_{mw}, and, unlike the latter, it depends noticeably on the magnetic field.

Some publications [4–6] maintained that when measured in the ac mode, $MR_{mw} > MR_0$. To check this point, we studied R_s in a magnetic field $H \parallel h$ on two samples of the same composition but with different thicknesses, $t_1 \gg \delta$ and $t_2 \ll \delta$. As follows from (3), for $\tau \gg 1$, $R_s \sim (\delta\omega^L - \delta\omega^0)$, while for $\tau \ll 1$, $R_s \sim (\delta\omega^L - \delta\omega^0)^{-1/2}$. Therefore, a negative magnetoresistance MR_{mw} should bring about a decrease of $\delta\omega$ in the thick sample, and an increase of $\delta\omega$ in the thin one, with an increasing magnetic field. The experiment (Fig. 2) showed both samples to follow about the same pattern; indeed, $\delta\omega$ and ω decrease with the increasing magnetic field up to about the demagnetizing field $H_d \approx 4\pi M$, after which they remain practically constant. The variation of $\delta\omega(H)$ and $\omega(H)$ does not correlate with that of ρ. If the decrease of $\delta\omega(H)$ (curves 1 and 2 in Fig. 2) were connected with that of ρ_{mw}, this should have resulted in a decrease of the skin depth and, according to (2), in an increase, rather than decrease, of ω (curves 3 and 4 in Fig. 2). This shows that the variations in microwave absorption in manganites observed to occur in a magnetic field are

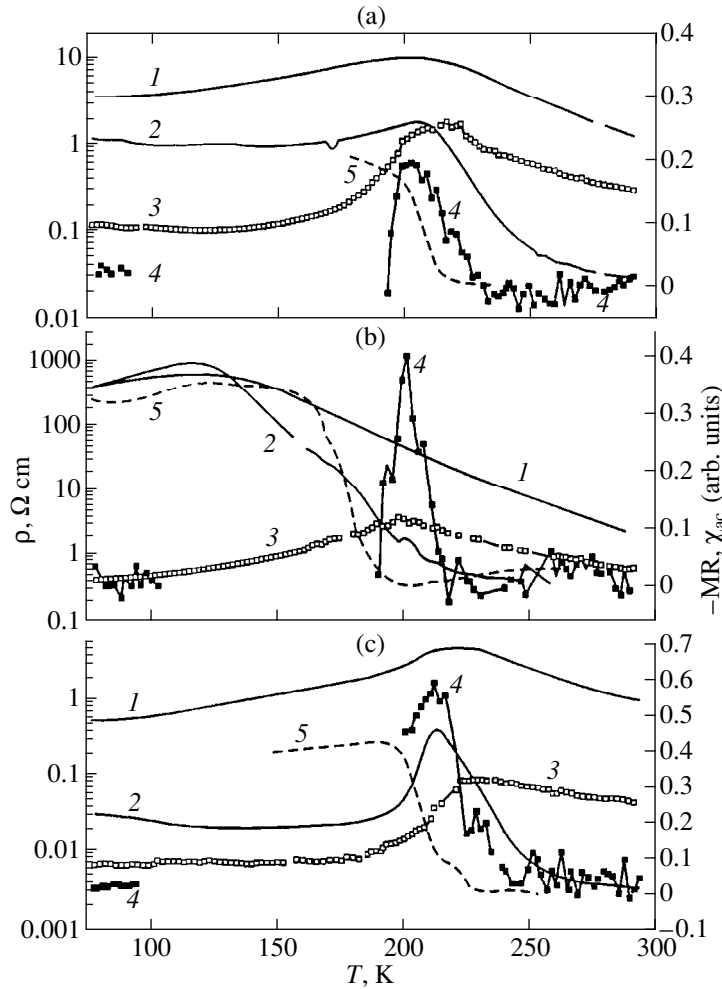**Fig. 1.** Temperature dependences of the dc and 9.2-GHz electrical and magnetoresistance (ρ_0, MR_0, ρ_{mw}, MR_{mw}), and of the magnetic susceptibility χ_{ac} at 1 kHz of $La_{1-x}Ca_xMnO_3$ polycrystals (a, b, and c for $x = 0$, 0.1, and 0.3, respectively). (Curves *1*) ρ_0, (curves *2*) MR_0, (curves *3*) ρ_{mw}, (curves *4*) MR_{mw}, (curves *5*) χ_{ac}.

due primarily to variations in the permeability μ^*, rather than in the electrical resistivity ρ_{mw} of the manganites. One readily sees that as the magnetic field increases up to saturation, $\mu' \longrightarrow 1$, and $\mu'' \longrightarrow 0$ (curves *5* and *6* in Fig. 2).

Both experiments and calculations show that at low temperatures ($T \approx 77$ K), the microwave magnetoresistance of other $La_{1-x}Ca_xMnO_3$ manganites is also small, $|MR_{mw}| \leq 0.02$–0.03 (curves *4* in Fig. 1). The high values of μ' and μ'' (Fig. 3) result in a large error in MR_{mw} determination. The most reliable values of MR_{mw} can be obtained for $T \geq T_C$, where both μ' and μ'' are small. The sharp peak of MR_{mw} is seen to occur in the samples studied (curves *4* in Fig. 1) in the temperature region where the behavior of the microwave electrical resistivity crosses over from semiconducting to metallic. Although we have not been able to determine MR_{mw} with a high enough accuracy within a certain temperature interval because of the effect of μ^*, additional

studies and calculations give one grounds to suggest that MR_{mw} decreases here from the high values near T_C to low MR_{mw} at $T = 77$ K. Note that MR_{mw} increases near T_C with increasing calcium concentration, and was also found to reach a maximum at $x = 0.3$.

Figure 3 displays temperature dependences of μ' and μ'' for $La_{1-x}Ca_xMnO_3$ samples. The largest and strongest variations of μ' and μ'' near T_C are seen to occur in $La_{0.7}Ca_{0.3}MnO_3$.

3. DISCUSSION

Thus, microwave experiments confirm that polycrystalline samples consist of a conducting grain [1, 4, 5], whose T_C, derived from the maximum of MR_{mw} for different calcium concentrations, is about the same, $T_C \approx 190$–225 K. Because the microwave response is dominated by the contributions due to single-crystal grains, the temperature dependence of MR_{mw} in this
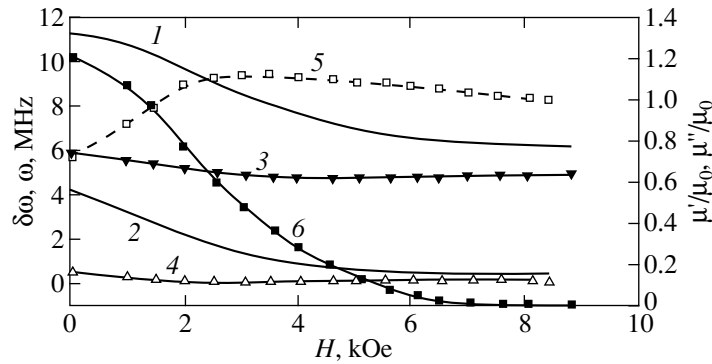
Fig. 2. Magnetic-field dependences of the resonator passband $\delta\omega$ (curves *1* and *2*), resonance frequency ω (curves *3* and *4*) for samples with thickness $t = 1.12$ mm $\gg \delta$ (curves *1* and *3*) and $t = 0.23$ mm $< \delta$ (curves *2* and *4*), and microwave permeabilities μ' (curves *5*) and μ'' (curves *6*) for polycrystalline $La_{0.9}Ca_{0.1}MnO_3$ obtained at 77 K.
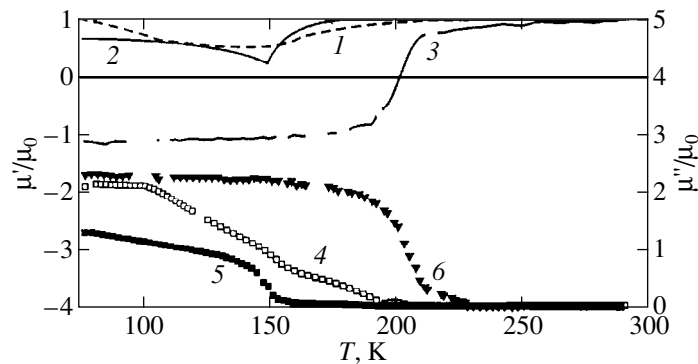

Fig. 3. Temperature dependences of the microwave permeabilities μ' (curves *1–3*) and μ'' (curves *4–6*) for polycrystalline $La_{1-x}Ca_xMnO_3$ with $x = 0$ (curves *1, 4*), $x = 0.1$ (curves *2, 5*), and $x = 0.3$ (curves *3, 6*).

region should have a pattern typical of single crystals measured in the dc mode [12], namely, a sharp peak of MR_0 near T_C and a small MR_0 far from T_C, exactly what we observe experimentally for MR_{mw} (curves *4* in Fig. 1).

The high values of ρ_0 in polycrystals can be accounted for by surface phenomena [12, 13]. However, the simplest model, by which the high ρ_0 values for polycrystals are due to high values of ρ_0 in the grain surface layer, cannot explain, for instance, why substantially below the ferromagnetic transition the values of MR_0 for polycrystals are higher than those for single crystals [12]. Since below T_C the conduction electrons in manganites are completely polarized, carrier tunneling between grains with different magnetization directions gives rise to additional scattering, which results in negative MR when the sample reaches saturation magnetization [13]. This model cannot, however, account for the linear decrease of $\rho_0(H)$ above the demagnetizing field, observed to occur in polycrystalline manganites for $T \ll T_C$.

We suggested [1] that polycrystals could have, besides the intergrain barrier, an additional barrier inside a grain because of the formation of a surface layer on the former. An analysis of the energy diagram of the contact between two different substances [14, 15] (metal–semiconductor, *p–n* junction) reveals the formation in such a structure of a space charge generating a contact potential difference. This contact potential difference $U_c = E_F^1 = E_F^2$ is determined by the difference between the thermionic work functions, or Fermi energies E_F^1 and E_F^2, of these substances. If the contact potential difference depends on the magnetic field, one should also expect ρ_0 to vary with the magnetic field. One could also expect the band structure of the manganites undergoing magnetic ordering to depend on the magnetic field. This is indicated by the optical properties of manganites being sensitive to magnetic ordering and to the magnetic field in the ferromagnetic region (the redshift effect) [2]. As follows from studies of magnetic semiconductors of the type of EuO and $HgCr_2Se_4$ [16–18], the sensitivity of their band structure to the magnetic field is maximal near T_C, while also being quite large above and below it. This may account for the peak in the magnetoresistance of polycrystalline manganites near T_C, and for MR_0 remaining fairly high both above and below T_C.

To transfer from one region to another, carriers have to overcome the potential barrier U_c due to their thermal energy kT. The exponential nature of the electrical conductivity gives one grounds to expect that small changes in U_c can give rise to large values of MR_0 in a magnetic field. The existence of a surface layer is argued for by the comparatively slow decay of the magnetic susceptibility χ_{ac} within a 30-K interval near T_C (curve 5 in Fig. 1) and by the strong effect of the electric field on ρ_0 [1]. The thickness of this surface layer, estimated by us [1] as $\approx 10^3$ Å, may reach a few percent of the grain size and can depend on the temperature, sample composition, and magnetic field.

This model allows interpretation of some features in the behavior of MR_0 and ρ_0 in the samples studied. The samples with $x = 0$ and 0.3 have $T_C \cong 205$–215 K (Fig. 1), which is close to the maximum value $T_C \approx 230$ K in the $La_{1-x}Ca_xMnO_3$ system, and this apparently accounts for the properties of the surface layers not differing much from those of the grain bulk (core). The sample with $x = 0.1$ has a lower value $T_C \cong 160$ K (as follows from χ_{ac} data in Fig. 1), and so one can expect that the properties of its surface layer (for instance, T_C) should differ substantially from those of the core, whose Curie temperature $T_C \cong 200$ K estimated from the maximum of MR_{mw} (see Fig. 1) is also high. In this case, the values of U_c may be higher and vary within a broader temperature range than those in the samples with $x = 0$ and 0.3. The behavior of U_c can account for the higher value of ρ_0, the difference between the temperatures of the maxima in ρ_0 and ρ_{mw}, MR_0 and MR_{mw}, the smoother growth of MR_0 within a broad temperature range $T = 225$–125 K, and the higher value of MR_0 at 77 K in the sample with $x = 0.1$ compared to those in the samples with $x = 0$ and 0.3 (Fig. 1).

The part played by the contact potential difference U_c and the effect of the magnetic field on the band structure of manganites are also evidenced by the variation in the activation energy ΔE_0, and by the independence of ΔE_{mw} on the magnetic field (see the table). Besides, when considered in terms of this model, carriers excited in the dc mode should overcome an additional potential barrier compared with those involved in microwave measurements of ρ_{mw} by the induction technique [7]. As seen from the table, in the paramagnetic region, ΔE_{mw} is smaller than ΔE_0 by 0.05–0.07 eV. This value of the additional potential barrier coincides with the potential barrier derived from the breakdown voltage in a strong electric field for the samples with $x = 0$ and 0.1 [1].

The nature of the CMR in manganites still remains unclear, with the double exchange [19] or phase separation [11] models being most popular. In the case of phase separation, space charge and a contact potential difference U_c may appear at the boundaries of inhomogeneities, and one may observe approximately the same temperature and field dependences of ρ_0, MR_0, ρ_{mw}, and MR_{mw} as in the sample with $x = 0.1$ (Fig. 1b). It may be conjectured that the conducting grain is divided by nonconducting (for instance, antiferromagnetic) layers with a thickness $d \approx 10^2$ Å. Such estimates of d are obtained when adapting the calculations of $\rho_0(E)$ [1] to the phase-separation model. The small layer thickness d could account for the stronger effect of the electric field on the electrical properties of the sample with $x = 0.1$ compared to those with other x; indeed, in the sample with $x = 0.1$, deviations from Ohm's law start from very low fields $E \approx 1$ V/cm, with ρ_0 decreasing by nearly two orders of magnitude at $E \approx 10^2$ V/cm (Fig. 2 in [1]). Note that the results obtained in the optical studies of these samples also agree with the phase-separation model.

In ferrites, the nature of the dispersion in permeability has largely been established long ago [3, 10]. Because the manganites are "poor" metals, the skin-layer thickness ($\delta \geq 10^{-3}$ cm) in the highest conductivity samples ($\rho \approx 10^{-3}$–10^{-4} Ω cm) at 10 GHz is larger or of the order of the equilibrium linear domain size (10^{-3}–10^{-4}) cm [21], with the result that the electromagnetic field acts on the domain as a whole. Therefore, the conventional concepts of the quasistatic magnetization mechanism used to explain the dispersion of μ in ferrites should also be applicable in most cases to the manganites. Polycrystalline materials actually represent aggregates of small, arbitrarily oriented single crystals. In nonsaturated samples, the tiny magnets break down into domains magnetized in various directions. In the regions where an magnetic field has a component perpendicular to the domain walls, one will observe the so-called "natural ferromagnetic resonance" (NFMR). The dependences of μ' and μ'' of ferrites at low frequencies (below 300 MHz) are usually related to domain wall vibrations, and the higher-frequency losses, to the NFMR, whose extreme frequencies in polycrystals are determined by the Polder–Smith relations $\omega_{min} = \gamma H_a$, and $\omega_{max} = \gamma(H_a + 4\pi M)$ [10]. Because in manganites the anisotropy field is small ($H_a \approx 10^2$ Oe) and the saturation magnetization $4\pi M \approx 5$ kG, the NFMR-induced dispersion of μ^* should be observed within a broad frequency region extending from 10^2 MHz to 15–20 GHz. The field and temperature dependences of μ' and μ'' in $La_{1-x}Ca_xMnO_3$ (Figs. 2 and 3) generally follow behavior typical of ferrites at NFMR, namely, $\mu' = 1$, $\mu'' = 0$ in the paramagnetic region; in the ferromagnetic region, they depend on temperature and the magnetic field; and $\mu' = 1$, $\mu'' = 0$ in a sample magnetized to saturation at $H \parallel h$. Note [3, 10] that the values of μ' and μ'' are governed by many factors, primarily by the size and shape of the grains, pores, and specific features of the domain structure, which could be the subject of a dedicated study. A new aspect of the problem of CMR in the manganites is the finding that the variation of microwave

absorption in magnetic fields at low temperatures, $T \ll T_C$, is associated with the change in the magnetic rather than electrical losses.

Thus, intergranular surface phenomena in inhomogeneous structures (interface layers) may lie at the origin of the colossal magnetoresistance.

ACKNOWLEDGMENTS

REFERENCES

1. N. I. Solin, A. A. Samokhvalov, and S. V. Naumov, Fiz. Tverd. Tela (S.-Peterburg) **40**, 1881 (1998) [Phys. Solid State **40**, 1706 (1998)].

2. N. N. Loshkareva, Yu. P. Sukhorukov, B. A. Gizhevskii, *et al.*, Phys. Status Solidi A **164** (2), 863 (1997).

3. J. Smith and H. P. J. Wijn, *Ferrites* (Philips Technical Library, Eindhoven, 1959; Inostrannaya Literatura, Moscow, 1962).

4. M. Domínguez, S. M. Bhagat, S. E. Lofland, *et al.*, Europhysics Lett. **32**, 349 (1995).

5. S. E. Lofland, P. H. Kim, P. Dahiroc, *et al.*, J. Phys.: Condens. Matter **9**, 6697 (1997).

6. F. J. Owens, J. Appl. Phys. **82**, 3054 (1997).

7. N. I. Solin, A. B. Davydov, and G. L. Shtrapenin, Defektoskopiya, No. 2, 77 (1991) [Sov. J. Nondestruct. Test. **27**, 146 (1991)].

8. S. A. Shmulevich, Prib. Tekh. Éksp., No. 2, 170 (1971).

9. L. D. Landau and E. M. Lifshits, *Electrodynamics of Continuous Media* (Pergamon, Oxford, 1960; Gostekhizdat, Moscow, 1957).

10. A. G. Gurevich and G. A. Melkov, *Magnetic Vibrations and Waves* (Nauka, Moscow, 1994).

11. É. L. Nagaev, Usp. Fiz. Nauk **165**, 529 (1995); *ibid.* **166**, 833 (1996); Fiz. Tverd. Tela (S.-Peterburg) **40**, 2069 (1998) [Phys. Solid State **40**, 1873 (1998)].

12. A. Gupta, G. Q. Gong, Gang Xiao, *et al.*, Phys. Rev. B **54**, R15629 (1996).

13. H. Y. Hwang, S.-W. Cheong, N. P. Ong, *et al.*, Phys. Rev. Lett. **77**, 2041 (1996).

14. R. A. Smith, *Semiconductors* (University Press, Cambridge, 1959; Inostrannaya Literatura, Moscow, 1962).

15. V. L. Bonch-Bruevich and S. G. Kalashnikov, *Physics of Semiconductors* (Nauka, Moscow, 1977).

16. É. L. Nagaev, *Physics of Magnetic Semiconductors* (Nauka, Moscow, 1979).

17. A. Selmi, A. Mauger, and M. Heritier, J. Magn. Magn. Mater. **66**, 295 (1987).

18. I. K. Bol'nykh and G. N. Sever, Fiz. Tverd. Tela (S.-Peterburg) **37**, 570 (1995) [Phys. Solid State **37**, 312 (1995)].

19. P. G. de Gennes, Phys. Rev. **118**, 141 (1960).

20. N. N. Loshkareva, Yu. P. Sukhorukov, S. V. Naumov, *et al.*, Pis'ma Zh. Éksp. Teor. Fiz. **68**, 89 (1998) [JETP Lett. **68**, 97 (1998)].

21. S. V. Vonsovskiĭ, *Magnetism* (Halsted, New York, 1975; Nauka, Moscow, 1971), Ch. 24.

Translated by G. Skrebtsov

Polarization Interaction and Phase Transitions in Crystals with Two Interacting Subsystems

V. A. Sanina and E. I. Golovenchits

Ioffe Physicotechnical Institute, Russian Academy of Sciences, Politekhnicheskaya ul. 26, St. Petersburg, 194021 Russia
e-mail: e.golovenchits@shuvpop.ioffe.rssi.ru

Abstract—The influence of the polarization interactions on the state and phase transitions in magnetic-ordered and dielectric crystals with two interacting order parameters has been investigated. Consideration is given to the case when the interaction in one of the subsystems is considerably weaker than that in the other subsystem. It is demonstrated that the polarization interactions in the weak subsystem can substantially affect the state and the character of phase transitions in the strong subsystem. These interactions can bring about the disordering (formation of the random-field state or the state of spin glass) in the critical region near the second-order phase transition in the main subsystem and also the smearing of the phase transition. At the same time, the polarization interactions can give rise to the ordered and disordered states in the weak subsystem. © *2000 MAIK "Nauka/Interperiodica"*.

1. INTRODUCTION

In this paper, the polarization interaction will be taken to mean the interaction between polaron states (polarons) in crystals. It is the effective interaction due to the mutual polarization of interacting subsystems and manifests itself in the second-order approximation of the perturbation theory.

In the solid-state physics, the polarization interactions have been most extensively investigated for semiconductors. There are works dealing with the polaron effect caused by the self-consistent action of free electrons and anionic lattice skeleton. The study was also given to the decrease in energy of the ground level of a system due to the electron–phonon interaction, the renormalization of effective masses of electrons and excitons, the polaron mobility, etc. (see, for example, the review [1]).

However, the polaron effects and polarization interactions in crystals should be taken into account not only in consideration of the electron–phonon interaction for charge carriers. Similar effects and polarization interactions are observed in dielectric crystals and other systems involving at least two interacting subsystems. In the present work, we analyzed how the exchange polarization interactions affect the properties of magnetodielectric crystals and how the polarization interactions associated with the mutual influence of ionic displacements in dielectric crystals affect the structure of these crystals.

The situation when the unit cell contains several different-type magnetic ions that form interacting subsystems with their own order parameters is characteristic of many magnetic crystals. In this case, the states of subsystems produce a mutual effect on each other, which depends on the character of interactions within the subsystems and between them. It is clear that the phase transitions (their temperature and character) in these magnetic crystals also depend on the interaction between the subsystems.

Note that, in the case when a magnetic crystal contains magnetic ions of only one type, there also exist nonmagnetic subsystems in this crystal that can interact with the magnetic subsystem. Examples of such subsystems can be provided by the orbital subsystem of the magnetic ions or ionic displacements in the lattice. This gives rise to the spin–orbit and magnetoelastic interactions, respectively, which, in turn, can lead to the polarization effects.

A situation completely similar to that observed for two interacting magnetic subsystems arises in the case when the nonmagnetic order parameter is described within the pseudospin formalism and the corresponding interactions can be represented by the exchange Hamiltonians. The most characteristic example of this situation is the order–disorder structural second-order phase transition (see, for example, [2]).

2. POLARIZATION EXCHANGE INTERACTION

Let us consider the case of a magnetic-ordered dielectric in which the unit cell involves magnetic ions of two types (*A* and *B*) with the spins S^A and S^B, respectively. The Hamiltonian of exchange interactions can be written in the following form:

$$H = \Sigma_{ij} J_{ij}^{AA} \mathbf{S}_i^A \mathbf{S}_j^A + \Sigma_{ij} J_{ij}^{BB} \mathbf{S}_i^B \mathbf{S}_j^B + \Sigma_{ij} J_{ij}^{AB} \mathbf{S}_i^A \mathbf{S}_j^B. \quad (1)$$

Here, the quantities J_{ij}^{AA}, J_{ij}^{BB}, and J_{ij}^{AB} are nonzero for the *i*th and *j*th nearest neighbor ions and characterize

the exchange interactions in a subsystem of the S^A and S^B spins and between the S^A and S^B spins, respectively. Now, we assume that the exchange interactions obey the following hierarchy, which is often realized in magnetic crystals: $J_{ij}^{AA} \gg J_{ij}^{AB} \gg J_{ij}^{BB}$. For example, this hierarchy of exchange interactions is observed in magnetic crystals of rare-earth garnets, rare-earth orthoferrites, and rare-earth orthochromites [3] containing both the $3d$ (S^A spins) and $4f$ (S^B spins) ions.

In the framework of perturbation theory, the effective Hamiltonian describing the spin states in the B subsystem can be written to the second order in the small parameter $J_{ij}^{AB} / J_{ij}^{AA}$ as follows:

$$H_{eff}^{B} = \Sigma_{ij} J_{ij}^{AB} \langle \mathbf{S}_i^A \rangle \mathbf{S}_j^B$$
$$- \Sigma_{ij,kl} (J_{ik}^{BA} K_{kl}^{AA} J_{lj}^{AB}) 1/J^{AA} \mathbf{S}_i^B \mathbf{S}_j^B + \Sigma_{ij} J_{ij}^{BB} \mathbf{S}_i^B \mathbf{S}_j^B \quad (2)$$
$$\equiv \Sigma_j H_{mfj}^B \mathbf{S}_j^B + \Sigma_{ij} V_{ij}^{BB} \mathbf{S}_i^B \mathbf{S}_j^B + \Sigma_{ij} J_{ij}^{BB} \mathbf{S}_i^B \mathbf{S}_j^B.$$

The quantity $\langle S_i^A \rangle$ characterizes the spin averaged over the states in the A subsystem. This quantity is nonzero when the A subsystem possesses a homogeneous long-range magnetic order and is equal to zero in the paramagnetic phase. Moreover, this quantity is also equal to zero at any temperature if the A subsystem involves a cooperative, but disordered state (for example, the random-field state or the state of spin glass [4]).

The quantity $K_{kl}^{AA} = \langle S_k^A S_l^A \rangle - \langle S_k^A \rangle \langle S_l^A \rangle$ characterizes the correlation function of spin fluctuations in the A subsystem, which is nonzero at any temperature and for any state of the crystal.

The first sum in the effective Hamiltonian (2) accounts for the magnetic biasing of the S^B spins by the mean field of the A ordered subsystem, that is, $H_{mfj}^B = \Sigma_i J_{ij}^{AB} \langle S_i^A \rangle$.

The second sum in Hamiltonian (2) describes the effective exchange interaction between the S^B spins through the correlations in the spin orientation in the A subsystem. This polarization exchange interaction is represented in the form

$$V_{ij}^{BB} = -\Sigma_{kl} (J_{ik}^{BA} K_{kl}^{AA} J_{lj}^{AB}) 1/J^{AA}. \quad (3)$$

The summation in the second term in expression (2) [and, correspondingly, in formula (3)] is carried out over all sites of the lattice. In this case, the polaron effect (exchange polaron) is described by the self-action, i.e., the exchange interaction between one ion B at the ith site with the spin S_i^B and the whole matrix of the A ions with the spins S_j^A. The polarization exchange interaction (3) describes the interaction between the exchange polarons. The polarization exchange V_{ij}^{BB} is efficient when the direct exchange interaction of spins

in the B subsystem is weaker than the polarization exchange interaction ($J_{ij}^{BB} \ll V_{ij}^{BB}$) or when the role of the mean field H_{mfj}^B is considerably weakened (by virtue of the crystal symmetry in the critical region near the phase transition in the A subsystem or when the A subsystem is disordered).

Note that the effective exchange interaction between impurity atoms in interstitial sites of a metamagnet lattice due to the polarization of spins in the main sublattice was originally treated by Ivanov and Shender [5]. Earlier [6], we considered the f–d–f polarization exchange in rare-earth magnets and wrote the Hamiltonian in the explicit form (2) in order to interpret the magnetic phase transition induced by high-power optical pumping in EuCrO$_3$. The polarization (fluctuation) exchange was studied in antiferromagnetic garnets [7] and in rare-earth orthoferrites and orthochromites [8].

It should be emphasized that, unlike the orienting action of the mean field H_{mfj}^B on spins in the B subsystem, the polarization exchange V_{ij}^{BB} can result in the ordering of the S^B spins characterized by the specific temperature of ordering and the proper symmetry. Such an ordering of the optically excited Eu^{3+} ions, which was brought about by the polarization interaction through spin excitations in the main magnetic subsystem of Cr^{3+} ions, was first found in EuCrO$_3$ crystals in our earlier works [6, 9].

Unlike the mean field H_{mfj}^B, which is equal to zero in the disordered state, the polarization exchange is nonzero at any temperature. At the same time, the polarization exchange depends on the temperature and state of the crystal, which determine the correlation function K_{ij}^{AA}.

It is important to note that, when the J_{ij}^{AA}, J_{ij}^{BB}, and J_{ij}^{AB} exchange interaction constants are nonzero only for the nearest neighbors, the range of the polarization exchange interaction V_{ij}^{BB} [see expression (3)] is determined by the correlation radius of spin fluctuations in the A subsystem. This means that the polarization interaction is, by definition, the long-range interaction, and, therefore, the corresponding molecular field $H_{MF}^P = V_{ij}^{BB} \langle S_i^B \rangle$ is enhanced by this long-range interaction. As a result, the temperature of the ordering of spins of the B ions at the expense of the polarization exchange interaction V_{ij}^{BB} can be considerably higher than the temperature of the ordering of the S^B spins through the exchange interaction J_{ij}^{BB}.

In the case when appreciable spin fluctuations with large correlation radii take place in the A subsystem, the

contribution of the V_{ij}^{BB} interaction becomes especially noticeable. This situation arises either in the vicinity of the second-order phase transition in the A subsystem or in the cases when this subsystem is low-dimensional and disordered.

Apart from the ordering of the B subsystem, the polarization interaction V_{ij}^{BB} in a number of cases can substantially affect the state and phase transitions in the main magnetic subsystem A. Let us now consider these situations in more detail.

3. EFFECT OF POLARIZATION INTERACTIONS ON THE CHARACTER OF MAGNETIC PHASE TRANSITIONS IN CRYSTALS WITH TWO ORDER PARAMETERS

As mentioned above, the polarization interaction V_{ij}^{BB} can induce the ordering of the B subsystem with the specific temperature of ordering and the proper symmetry. In this case, the polarization interaction V_{ij}^{BB} and the direct short-range exchange interaction J_{ij}^{BB} can be opposite in sign. This leads to frustrations in the B subsystem, provided that the J_{ij}^{BB} interaction is not negligibly small compared to the V_{ij}^{BB} interaction. As a consequence, the frustrations due to the presence of exchange interactions with opposite signs can arise in the B ordered subsystem containing no impurities of other ions (i.e., in the subsystem without ionic disorder). In some cases, the effect of these frustrations can be quite significant.

(A) If the magnetic bias field $H_{mfj}^{B} = \Sigma_i J_{ij}^{AB} \langle S_i^A \rangle$ considerably exceeds the molecular field $H_{MF}^{P} = V_{ij}^{BB} \langle S_i^B \rangle$ (and, especially, $J_{ij}^{BB} \langle S_i^B \rangle$), then, at temperatures below the ordering temperature of the A subsystem, the state of the B subsystem is homogeneous and will be determined by the magnetic bias field H_{mfj}^{B} of the A ordered subsystem. However, the situation can radically change in the vicinity of the magnetic phase transition in the A subsystem (in the critical range of temperatures). Actually, in the critical range, the effect of the mean field H_{mfj}^{B} weakens (the order parameter $\langle S_i^A \rangle$ decreases in accord with the Brillouin function), whereas the correlation radius of critical fluctuations in the A subsystem and, correspondingly, the V_{ij}^{BB} interaction increase. Taking into account the competition between the interactions V_{ij}^{BB} and J_{ij}^{BB}, which leads to frustrations in the B subsystem, the random-field state or the state of spin glass [4] can arise in this subsystem. As a result, the mean molecular field in the B subsystem, which is determined by the V_{ij}^{BB} and J_{ij}^{BB} interactions [the last

two terms in Hamiltonian (2)], proves to be random. Then, the $\langle S_i^B \rangle$ quantity characterizes the frozen random local spin in the B subsystem [4]. Owing to the interaction between the A and B subsystems, the random field $H_{RF}^A = J_{ij}^{AB} \langle S_i^B \rangle$ arises in the A subsystem, too. Furthermore, in the critical region near the phase transition, the random-field state or the state of spin glass also arises in the A subsystem. Indeed, according to the Imre–Ma theorem [10], the state with a homogeneous long-range order is unstable toward the formation of bounded regions with the same order in the presence of random field.

Therefore, the polarization interaction in the B subsystem and the competition with its own exchange interaction in the same subsystem give rise to the disordered state in the critical region near the phase transition in the A subsystem and lead to the smearing of the phase transition in this state.

(B) A similar situation always arises in the critical region near the second-order phase transition in the A subsystem with allowance made only for the polarization interaction (even without regard for the competition with the exchange interaction J_{ij}^{BB}), provided that the A subsystem is an antiferromagnetic subsystem. In this case, in the critical temperature range of the A subsystem, when the correlation radius of antiferromagnetic spin fluctuations $\xi \gg a$ (where a is the lattice spacing), the polarization exchange interaction V_{ij}^{BB} [see expression (3)] appears to be both long-range (on the ξ scale) and alternating-sign simultaneously for every lattice spacing (because the antiferromagnetic correlation function K_{ij}^{AA} changes sign every lattice spacing). The interaction of this type brings about the stochastization of the spin state in the B subsystem and the formation of glass state, even though there is no frozen random disorder in the ion arrangement of the B subsystem in the crystal. The reverse effect of the B disordered subsystem on the A subsystem also gives rise to a random-field (or glass) state in the critical region in the A subsystem. A similar situation was considered in studying the mechanism of the formation of orbital glass in Eu_2CuO_4 crystals in our earlier work [11].

4. THE CASE OF LOW-DIMENSIONAL OR DISORDERED A SUBSYSTEM

A specific situation occurs when the A subsystem originally exhibits a cooperative, but disordered state, for example, the random-field state or the state of spin glass. In this case, the mean molecular field H_{mfj}^{B} biasing the B subsystem is equal to zero at all temperatures, and the polarization interaction (3) becomes predominant for the B subsystem. If the A subsystem involves sufficiently large regions of spin correlations, the polar-

ization interaction V_{ij}^{BB} is rather strong. Under these conditions, both ordered (order from disorder) and disordered states can arise in the B subsystem not only in the critical region, but over the entire range of temperatures.

In the quasi-two-dimensional Heisenberg antiferromagnets R_2CuO_4 (R = Eu, Pr, and Gd) studied in [12, 13], we experimentally observed the random-field state over a wide range of temperatures (at both $T \ll T_N$ and $T \gg T_N$, where T_N is the Néel temperature). In our opinion, this state stems from the random anisotropy in the A subsystem due to the polarization interactions in the B subsystem [14]. In this case, the A subsystem is the quasi-two-dimensional Heisenberg antiferromagnetic subsystem of spins of the Cu^{2+} ions (in the CuO_2 layers), and the B subsystem at different temperatures can be either the magnetic orbital subsystem of Cu^{2+} ions or the subsystem of magnetic rare-earth ions R^{3+}.

As an illustration, let us consider the effect of magnetic rare-earth ions on the state of the quasi-two-dimensional Heisenberg antiferromagnetic subsystem of Cu^{2+} ions in the CuO_2 layers. In analyzing Hamiltonian (2), we will take into account the first two terms and disregard the exchange interaction between rare-earth ions.

(A) Assume that, at $T < T_N$, the quasi-two-dimensional antiferromagnetic subsystem possesses the long-range order and the mean molecular field H_{mfj}^B is non-zero. Under the action of this field, the moments of rare-earth ions (the S^B spins in our model) should be antiferromagnetically biased; i.e., the staggered field should occur in the B subsystem. Then, the V_{ij}^{BB} polarization exchange interaction is determined by the interaction between the S^B spins through the spin waves in the A ordered subsystem. Note that, as was shown in [7, 8], the polarization interaction tends to ferromagnetically order the S^B spins. As a result, in the case of the homogeneous antiferromagnetic long-range order in the A subsystem, the polarization interactions bring about the emergence of competing interactions, which result in the frustrations and the disordering of the B subsystem. In turn, this gives rise to a random anisotropy for the A subsystem (H_{RF}^A) and a random-field state in the A subsystem. Therefore, in the antiferromagnetic A subsystem, the homogeneous antiferromagnetic long-range order cannot be realized, and a state of the random-field type arises if the polarization interaction in the B subsystem is not negligibly small compared to the mean field H_{mfj}^B.

(B) If the A subsystem originally (without considering the influence of the B subsystem) exhibit spin fluctuations with large correlation radii (for example, the quantum two-dimensional Heisenberg antiferromagnetic spin fluctuations in the CuO_2 layers in quasi-two-

dimensional crystals R_2CuO_4), the role of the polarization exchange becomes quite significant beginning with the lowest temperatures—the long-range and alternating-sign (frustrating) polarization interaction takes place in the B subsystem. This interaction can result in both the disordering of the B subsystem and the formation of the random-field state in the A subsystem.

5. EFFECT OF POLARIZATION INTERACTION ON THE STRUCTURAL PHASE TRANSITION IN CRYSTALS WITH TWO ORDER PARAMETERS

The manifestation of polarization interactions upon the second-order structural phase transitions can be illustrated by the isostructural phase transition in $EuCrO_3$, which was observed with a change in the concentration of thermally excited ions Eu^{3+} ($^7F_1$) [15, 16]. This transition was revealed at temperature $T \sim 280$–290 K in studies of the dielectric susceptibility and X-ray diffraction analysis. The transition was accompanied by strong anomalies in the dielectric properties, which is usually typical of smeared ferroelectric phase transitions [2]. According to the X-ray diffraction data, the transition leads to the uniform displacement of the Eu^{3+} ions by ~0.0076 Å, all the other lattice parameters being the same [16].

The $EuCrO_3$ crystals belong to the rare-earth orthochromite class and have the symmetry of orthorhombically distorted perovskite with the space group D_{2h}^{16} (*Pbnm*). The Eu^{3+} ions in the ground state ($^7F_0$) are nonmagnetic. The first excited state ($^7F_1$) differs in energy from the ground state ($^7F_0$) by ~300 cm^{-1}. The first excited state is magnetic and degenerate (triplet $J = 0$, ± 1), so that the thermal filling of the excited level gives rise to the magnetic moment and local lattice distortions (the local Jahn–Teller pseudoeffect [17]). In the temperature range $T > 200$ K, the thermal filling of the excited levels of Eu^{3+} ions rapidly increases, and the possibility exists of forming the metastable clusters consisting of the structurally correlated, thermally excited ions. A further increase in the concentration of thermally excited ions results in the isostructural phase transition, which is attended by the correlated displacements of all the Eu^{3+} ions in the crystal [16].

In the case under consideration, two interacting subsystems take place: the Eu^{3+} ions in the ground state and the thermally excited ions. There are two interacting order parameters—the displacements of the Eu^{3+} ions in the ground state and the displacements of the Eu^{3+} thermally excited ions in the lattice with respect to the central position in the cubic praphase. The local ionic displacements in the lattice are described by the pseudospins, and the Hamiltonian of the corresponding interactions within the subsystems and between them is similar to the exchange Hamiltonian (2). Moreover, the

following condition is met: additional displacements of the thermally excited ions are small in comparison with the initial displacements of ions in the ground state. The antiferroelectric ordering is realized in the original subsystem of the Eu^{3+} ions (in the ground state). The polarization interaction between the excited ions has a ferroelectric nature and leads to an increase in the concentration of the ferroelectric clusters and also to the structural phase transition in the whole crystal. This is accompanied by the antiferroelectric ordering of the europium ions in the ground state and the thermally excited europium ions throughout the crystal [16].

Thus, in the present work, we demonstrated that the polarization interactions play an important role in the crystals with two interacting order parameters. The polarization interactions can bring about changes in the state of crystals and affect the character of phase transitions in these crystals.

REFERENCES

1. J. Appel, Solid State Phys. **21**, 193 (1968).

2. B. A. Strukov and A. P. Levanyuk, *Physical Principles of Ferroelectric Crystals* (Nauka, Moscow, 1983).

3. A. K. Zvezdin, V. M. Matveev, A. A. Mukhin, and A. I. Popov, *Rare-Earth Ions in Magnetically Ordered Crystals* (Nauka, Moscow, 1985).

4. S. L. Ginzburg, *Irreversible Phenomena in Spin Glasses* (Nauka, Moscow, 1989).

5. M. A. Ivanov and E. F. Shender, Zh. Éksp. Teor. Fiz. **69**, 350 (1975) [Sov. Phys. JETP **42**, 179 (1975)].

6. E. I. Golovenchits, B. D. Laĭkhtman, and V. A. Sanina, Pis'ma Zh. Éksp. Teor. Fiz. **31**, 243 (1980) [JETP Lett. **31**, 223 (1980)].

7. E. F. Shender, Zh. Éksp. Teor. Fiz. **83**, 326 (1982) [Sov. Phys. JETP **56**, 178 (1982)].

8. E. I. Golovenchits and V. A. Sanina, Fiz. Tverd. Tela (Leningrad) **26**, 1640 (1984) [Sov. Phys. Solid State **26**, 996 (1984)].

9. E. I. Golovenchits, V. A. Sanina, and T. A. Shaplygina, Zh. Éksp. Teor. Fiz. **80**, 1911 (1981) [Sov. Phys. JETP **53**, 992 (1981)].

10. Y. Imry and S. Ma, Phys. Rev. Lett. **35**, 1399 (1975).

11. A. V. Babinskiĭ, S. L. Ginzburg, E. I. Golovenchits, *et al.*, Pis'ma Zh. Éksp. Teor. Fiz. **57**, 289 (1993) [JETP Lett. **57**, 299 (1993)].

12. E. I. Golovenchits, V. A. Sanina, and A. V. Babinskiĭ, Zh. Éksp. Teor. Fiz. **110**, 714 (1996) [JETP **63**, 674 (1996)].

13. E. I. Golovenchits and V. A. Sanina, Fiz. Tverd. Tela (S.-Peterburg) **41**, 1437 (1999) [Phys. Solid State **41**, 1315 (1999)].

14. E. I. Golovenchits and V. A. Sanina, Fiz. Tverd. Tela (S.-Peterburg) **41**, 1259 (1999) [Phys. Solid State **41**, 1149 (1999)].

15. E. I. Golovenchits, V. A. Sanina, and G. A. Smolenskiĭ, Pis'ma Zh. Éksp. Teor. Fiz. **40**, 110 (1984) [JETP Lett. **40**, 857 (1984)].

16. E. I. Golovenchits, V. A. Sanina, A. A. Levin, *et al.*, Fiz. Tverd. Tela (Leningrad) **29**, 3553 (1987) [Sov. Phys. Solid State **29**, 2036 (1987)].

17. I. B. Bersuker, *The Jahn–Teller Effect and Vibronic Interactions in Modern Chemistry* (Nauka, Moscow, 1987).

Translated by O. Borovik-Romanova

Dielectric and Electromechanical Properties of (1 – x)PMN–xPZT Ferroelectric Ceramics

A. I. Burkhanov, A. V. Shil'nikov, A. V. Sopit, and A. G. Luchaninov

Volgograd State Architecture and Building Academy, Akademicheskaya ul. 1, Volgograd, 400074 Russia

Received in final form, October 21, 1999

Abstract—The dielectric and electromechanical characteristics of the $(1 - x)$PMN–xPZT ferroelectric ceramics have been obtained at different temperatures, amplitudes, and frequencies of the measuring field and at different bias field strengths. It is shown that this ferroelectric ceramics at low and infralow frequencies possesses pronounced relaxor properties in a certain temperature range and ferroelectric properties in other temperature range. The temperature and amplitude ranges have been determined, in which the permittivity ε' either only decreases or first increases and then decreases with an increase in the measuring field amplitude E_0. The temperature ranges of existing the phases similar to the superparaelectric phase, dipole glass phase, and ferroelectric phase are evaluated from the temperature dependences of the coercive field $E_c(T)$ and the remanent polarization $P_r(T)$ and also from the reverse dependences of ε^* and the electromechanical characteristics. The PZT concentration in the PMN–PZT system is determined, at which the electrostrictive constant M_{11} is maximum. It is demonstrated that, in the neighborhood of the temperature at a maximum of ε', the strain S_3 is quadratic in the field $E_=$; that is, $S_3 = M_{11}E^2$. © 2000 MAIK "Nauka/Interperiodica".

1. INTRODUCTION

It is known that ferroelectric ceramics based on lead magnesium niobate (PMN) is one of the most promising materials for the use as micropositioners, adaptive mirrors, actuators, etc. In addition to their technical applications, these materials are very attractive from the viewpoint of basic research, because they are convenient (model) objects in studies of various nonequilibrium processes proceeding in disordered systems. In particular, these materials belong to the class of the so-called relaxor ferroelectrics [1].

Despite a considerable amount of available experimental information regarding relaxors, there has been no unified interpretation of the physics of processes occurring in these materials under different experimental conditions. For example, a number of properties are explained in the framework of the superparaelectric model [1, 2]. Within this model, it is assumed that, in the temperature range $T \geq T_m$ (where T_m is the temperature at a maximum of the permittivity ε'), there exist thermally activated polar nanoregions that can be switched (reoriented) in an external (even weak) field and, thus, contribute to the dielectric response of a system. At the same time, the behavior of the dielectric properties in the temperature range $T < T_m$ under the action of a dc electric field $E_=$ [3] and without field (when very prolonged processes of polarization relaxation—aging [4] and different memory effects [5, 6]—are observed) can be more adequately described either within the model of spin or dipole glass [7], in the framework of the random field model [8], or in the context of concepts developed by Isupov [9, 10]. In these works, Isupov has attached much importance to the influence of paraelectric interlayers on the time dependences of different processes occurring in the course of smeared phase transitions, specifically on the possibility of forming a macrodomain state in relaxors.

However, recent works published by Tagantsev and Glazounov [11–13] cast some doubt on the above approaches (for example, for lead magnesium niobate materials). Particularly, in order to describe the properties of ceramics and crystals of lead magnesium niobate, they proposed the model based on the statement that the contribution to the permittivity ε' in the ergodic phase is determined by the interphase boundary oscillations (irreversible hysteresis motion of interphase boundaries [14]); i.e., in the authors' opinion [11–13], the depinning of phase boundary is more probable than the reorientation of polar nanoregions under the action of an ac electric field at temperatures above 200 K. Note that, in principle, there is no considerable difference between the notion of the polar nanoregion reorientation and the notion of the interphase boundary vibration, particularly where the activation by electric field is concerned [14]. The matter is that the "vibration" of interphase boundary can be reversible (thermally activated) and irreversible (activated by the ac measuring field [14]). The former case is virtually not considered [11–13], even though it is completely analogous in physical nature to the reorientation of thermally activated polar nanoregions. It should be emphasized that, in the recent work [15] concerned with the investigation of lead magnesium niobate by high-reso-

lution electron microscopy, Yoshida and coworkers conclusively proved that, in the "nonergic phase" of lead magnesium niobate, the formation of domain boundaries does not require external action, as it was earlier assumed in discussions of the results obtained for this material. According to [15], the noninduced (spontaneous) formation of domains occurs upon cooling of the crystal at very low temperatures corresponding to the reversible phase transition from the relaxor phase (on the average, with a cubic symmetry) to the rhombohedral ferroelectric phase. Yoshida *et al.* [15] demonstrated that, upon cooling of the lead magnesium niobate crystal, this phase transition begins only at a temperature of 200 K and ceases at $T_{pht} = 135$ K. Therefore, the temperature $T_{pht} = 135$ K can be considered the average (most probable) temperature of the structural ferroelectric phase transition, at which a larger part of the phase becomes rhombohedral.

It should be mentioned that the occurrence of a similar reversible phase transition not induced by the electric field was earlier established by Heike and William [16], reasoning from the Raman scattering when a sharp change in the wavenumber and the width of the 227-cm^{-1} band attributed to the bending mode was observed in the spectra in the range of $T \sim 200$ K. Still earlier, Kuznetsova *et al.* [17] reported that the extrapolation of the temperatures of field-induced phase transitions to zero field amplitude resulted in $T_{pht} \approx 100$–120 K for lead magnesium niobate, which is in good agreement with the data obtained by the high-resolution electron microscopy [15]. On the other hand, the results presented by Koroleva [18] and Vakhrushev [19] do not agree with the data obtained in [15–17] and are not quite consistent with the conclusions made in [11–13]. Note also that the approach developed in [11–13] was applied to relaxors even in our earlier works [5, 6] in the interpretation of memory effects in the PLZT and PMN relaxor ceramics within the model of pinning and depinning of interphase boundaries at mobile point defects. Furthermore, Nadolinskaya *et al.* [20] emphasized that the dispersion of ε* in the lead magnesium niobate crystal at low and infralow frequencies in different temperature ranges is determined by the contribution of domain walls, interphase boundaries, and (or) polar nanoregions to ε*; in other words, these authors considered the thermally activated reversible motion (oscillation or vibration) of the domain and interphase boundaries.

A very large body of experimental data accumulated up to now for different relaxors and their rather contradictory interpretation mentioned above gave impetus to the complex investigations into the dielectric response at low and infralow frequencies over wide ranges of temperatures, measuring field amplitudes, and bias field strengths, as well as the studies of the electromechanical parameters and pyroelectric current [21] in the $(1 - x)$PMN–xPZT relaxor ceramic system similar in properties to the lead magnesium niobate ceramics. In the present work, we made a further attempt to give insight into the mechanisms of polarization, repolarization, and electromechanical response in typical relaxors.

2. SAMPLE PREPARATION AND EXPERIMENTAL TECHNIQUE

The dielectric parameters—the real (ε') and imaginary (ε") parts of the permittivity ε*—were measured at low (10–10^3 Hz) and infralow (0.1–10 Hz) frequencies in the dynamic mode upon cooling at a rate of 1 K/min from 353 to 90 K by using the bridge method [22] and in the quasi-static mode with the use of a modified Sawyer–Tower hysteresis scheme involving an S9-8 digital storage oscilloscope equipped with a computer.

In the former case (in the ultraweak measuring fields at amplitude $E_0 \approx 1$ V/cm), we determined the initial values of the real (ε'_0) and imaginary (ε''_0) parts of the complex permittivity ε^*_0. In the latter case (in the medium and strong fields E_0), we obtained the effective quantities ε'_{eff} and ε''_{eff} and evaluated the contributions from the hysteresis and relaxation mechanisms of domain and interphase boundary motions [14]. Moreover, the maximum (P) and remanent (P_r) polarizations and the coercive fields E_c were obtained from the analysis of the polarization loops. The latter parameters were also evaluated from the reverse dielectric and reverse piezoelectric characteristics obtained by the resonance and antiresonance methods. The induced strain S_3 in ferroelectric ceramics was measured with an instrument based on a capacitance-type transducer [23]. These measurements were carried out above the T_m temperature in the range from 298 to 318 K.

The samples of the $(1 - x)$Pb[Mg$_{1/3}$Nb$_{2/3}$]O$_3$-xPb[Zr$_{0.53}$Ti$_{0.47}$]O$_3$ (where $0 \le x \le 0.3$) ferroelectric ceramics were prepared according to the usual ceramic technology. The dielectric measurements were performed using the samples with size $S = 5 \times 5$ mm and thickness from 0.2 to 0.5 mm. The ceramic discs with diameter $D = 10$ mm and thickness from 0.5 to 3 mm were used for measuring of the electromechanical parameters. Electrodes were applied by burning-in silver solder paste.

3. RESULTS AND DISCUSSION

3.1. Characterization of the phase state of the material. Figure 1 demonstrates the temperature–field dependences $\varepsilon'_{eff}(T, E_0)$ and $\varepsilon''_{eff}(T, E_0)$ for the 0.89PMN–0.11PZT ferroelectric ceramics at the measuring field frequency $\nu = 1$ Hz. It is clearly seen from Fig. 1 that, as the measuring field amplitude E_0 increases, the maximum values of $\varepsilon'_{eff}(T)$ and, especially, $\varepsilon''_{eff}(T)$ first increase and then decrease, shifting
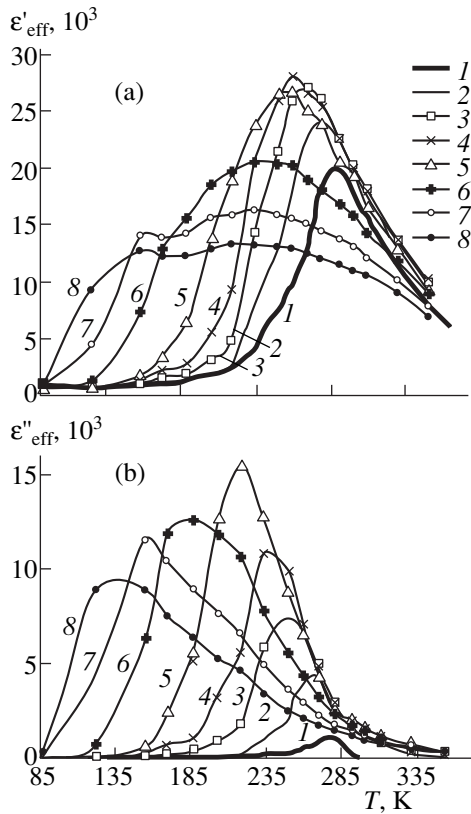
Fig. 1. Temperature–field dependences $\varepsilon'_{\text{eff}}(T, E_0)$ and $\varepsilon''_{\text{eff}}(T, E_0)$ of the 0.89PMN–0.11PZT ferroelectric ceramics at frequency $\nu = 1$ Hz. Measuring field amplitude E_0 [kV/cm]: (*1*) 0.001, (*2*) 0.6, (*3*) 1.8, (*4*) 3, (*5*) 5.4, (*6*) 10.8, (*7*) 16.2, and (*8*) 21.7.
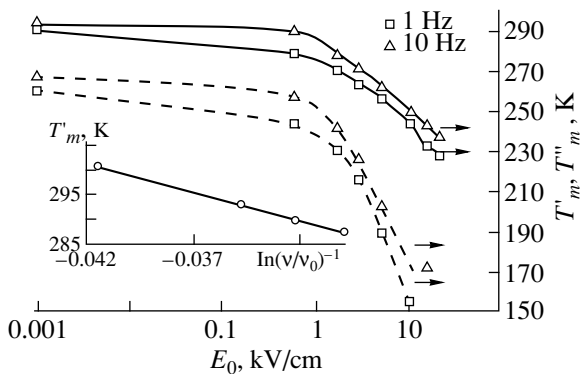

Fig. 2. Field dependences of the temperatures at a maximum of the real $T'_m(E_0)$ (solid line) and imaginary $T''_m(E_0)$ (dashed line) parts of the permittivity at frequencies of 1 and 10 Hz. The inset shows the frequency dependence $T_m([\ln(\nu/\nu_0)]^{-1})$ at $\nu_0 = 3 \times 10^{13}$ Hz [11] for ultraweak measuring fields ($E_0 = 0.001$ kV/cm).

toward the low-temperature range. It is worth noting that, at the measuring field amplitude $E_0 \geq 15$ kV/cm, the temperature dependences $\varepsilon'_{\text{eff}}(T)$ exhibit new anomalies in the form of small additional maxima at temperatures of about 155 K.

The field dependences of the temperatures at a maximum of the effective permittivity $\varepsilon'_{\text{eff}}$ ($T'_m(E_0)$) and the effective dielectric losses $\varepsilon''_{\text{eff}}$ ($T''_m(E_0)$) at two measuring field frequencies of 1 and 10 Hz for the 0.89PMN–0.11PZT ferroelectric ceramics are depicted in Fig. 2. The frequency dependence $T'_m(\nu)$ of the temperature at a maximum of the permittivity ε'_0 measured in ultraweak fields for the same sample is displayed in the inset of Fig. 2.

As can be seen from Fig. 2, a substantial decrease in temperatures T'_m and T''_m is observed only at a measuring field amplitude exceeding a certain threshold field (in our case, $E_0 = E_{threshold} \sim 600$–700 V/cm).

An increase in the values of $\varepsilon'_{\text{eff}}$ and $\varepsilon''_{\text{eff}}$ at measuring fields less than $E_{threshold}$ (Fig. 1) and a shift of temperatures T'_m and T''_m toward the low-temperature range with an increase in the field amplitude, on the whole, agree with the data reported in [11–13] for the lead magnesium niobate crystal. However, there are certain differences. For example, the $T'_m(E_0)$ dependence given in [11] shows a linear behavior. In our case, one can see two field ranges in Fig. 2: in the first range (at the relatively low prethreshold field amplitudes E_0), the T'_m temperature very weakly depends on E_0, and, in the second range (at the relatively strong fields when $E_0 > E_{threshold}$), the $T'_m(E_0)$ dependence is sufficiently well approximated by the logarithmic relationship $T'_m \sim f(\log(E_0))$. Moreover, in [11], the value of ε' in the temperature range $T \leq T_m$ always increases with an increase in the field. By contrast, according to our data (Fig. 3), at the temperatures $T \leq T_m$ and frequencies of 0.1–10 Hz, an increase in the values of $\varepsilon'_{\text{eff}}(E_0)$ and $\varepsilon''_{\text{eff}}(E_0)$ gives way to their decrease (Fig. 3, curves *1*, *2*).

On the other hand, at a sufficiently high temperature when $(T - T'_m) \approx 60$ K (Fig. 3, curves *3*), there is a portion of the curve in which the value of $\varepsilon'_{\text{eff}}$ is independent of E_0, and also a portion in which $\varepsilon'_{\text{eff}}$ noticeably decreases with an increase in the measuring field amplitude E_0.

Therefore, it can be argued that an increase in the measuring field amplitude leads to a decrease in the real and imaginary parts of the effective complex permittivity at the temperatures T_i above T_m; i.e., in the temperature range where the interaction between elements con-
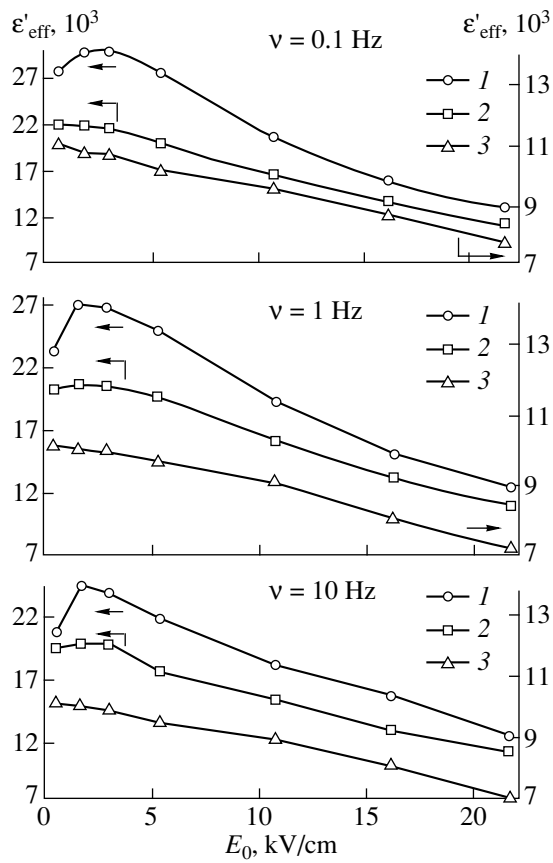
Fig. 3. Amplitude dependences $\varepsilon'_{eff}(E_0)$ of the 0.89PMN–0.11PZT ferroelectric ceramics at frequencies of 0.1, 1, and 10 Hz and temperatures of (*1*) 271, (*2*) 303, and (*3*) 355 K.
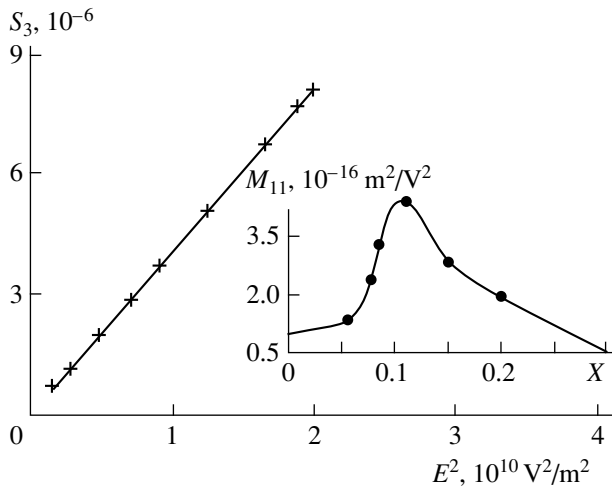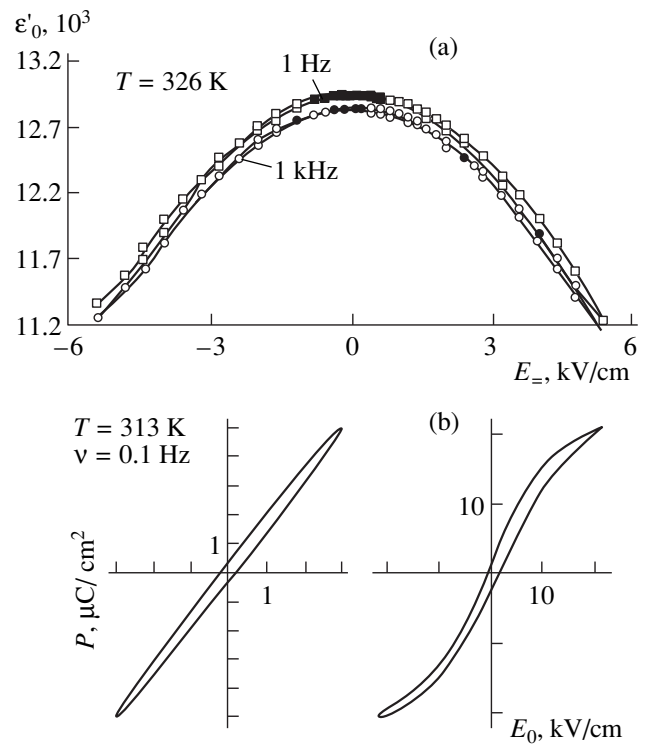

Fig. 4. (a) Reverse dependences of the permittivity $\varepsilon'(E_=)$ and (b) polarization loops $P(E_0)$ in weak and strong fields for the 0.89PMN–0.11PZT ferroelectric ceramics at temperatures above T'_m.
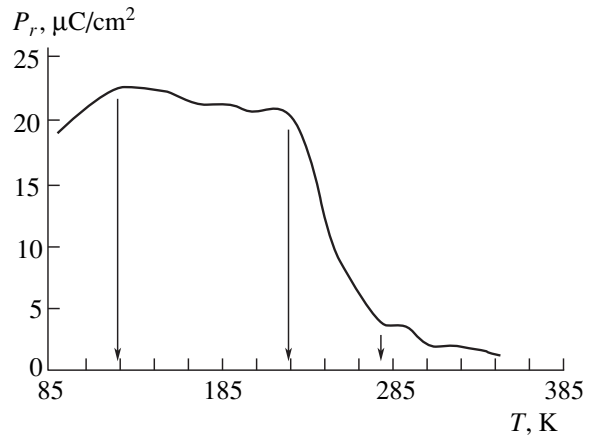

Fig. 5. Dependence of the induced strain $S_3(E^2)$ for the 0.89PMN–0.11PZT ferroelectric ceramics at temperature $T = 328$ K $> T'_m$. The inset shows the concentration dependence of the electrostrictive constant $M_{11}(x)$ for the $(1 - x)$PMN–xPZT ferroelectric ceramics at $T = 298$ K.

Fig. 6. Temperature dependence of the remanent polarization $P_r(T)$ at the measuring field amplitude $E_0 \approx$ 21.7 kV/cm.
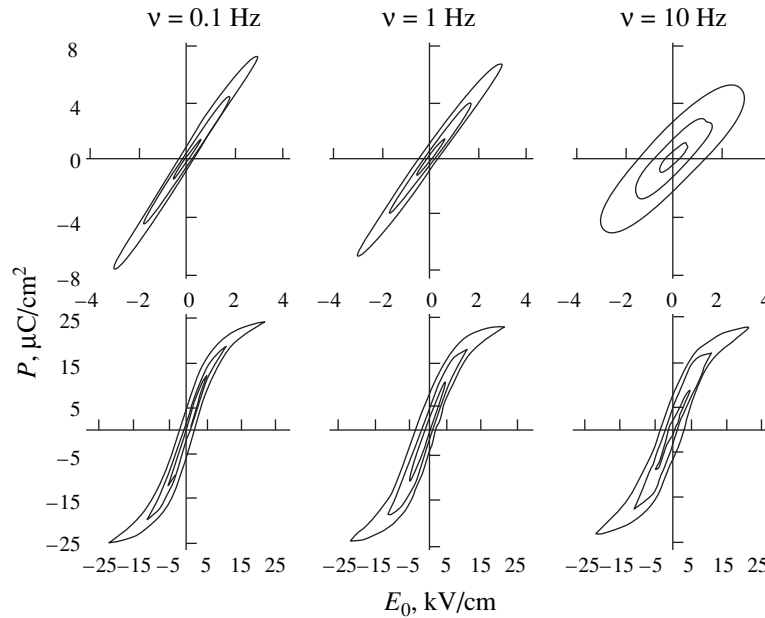
Fig. 7. Polarization loops $P(E_0)$ in the 0.89PMN–0.11PZT ferroelectric ceramics at temperature $T = 283$ K for frequencies of 0.1, 1, and 10 Hz.

tributing to the dielectric response is actually absent (ergodic phase). To put it differently, the polarization is saturated, and the assumption can be made that the sample exhibits a superparaelectric behavior in the repolarizing field.

The above inference is conclusively supported by analysis of the reverse dependence $\varepsilon_0' (E_=)$ obtained at $T = 326$ K when $T > T_m$, and the difference $\Delta T = T - T_m$ is sufficiently large (Fig. 4a). Actually, the dependence shown in Fig. 4a [$\varepsilon'(E_=) = b - dE_=^2$, where b and d are the approximate constants for a given temperature] is similar to the curve of the dielectric nonlinearity of the paraelectric phase in ferroelectrics when (at $T = $ const) we have restricted ourselves to two terms of the rapidly convergent series $\varepsilon(E)$ [24].

The fact that this phase state is identical to the super-paraelectric state is corroborated by the following facts: (a) the strong dependence $\varepsilon_0' (E_=)$ (Fig. 4a), (b) the occurrence of nonzero spontaneous polarization ($P_s \neq 0$) detected by the pyroelectric current [21] at the above temperature, (c) the shape of the polarization loops in strong fields (Fig. 4b), and (d) the character of the field dependence of the induced strain $S_3(E^2)$ (Fig. 5). The concentration dependence $M_{11}(x)$ is depicted in the inset of Fig. 5. This dependence shows a maximum at $x = 0.11$, which has motivated a more detailed investigation of the material with the given concentration. Likely, we can believe with a fair degree of confidence that the aforementioned polar state stems from the pres-

ence of the polar nanoregions—polar clusters—in the bulk of the sample [19].

Analysis of the dependence $P_r(T)$ represented in Fig. 6 allows us to conventionally separate the studied range of temperatures into three portions. In the first temperature range from ~350 to ~285 K, the rate of increase in the remanent polarization ($-dP_r/dT$) with a decrease in the temperature is relatively low. In the second range from ~285 to ~230 K, the magnitude $|dP_r/dT|$ is appreciably larger than that in the first portion. Finally, in the third portion from ~230 to ~150 K, the magnitude $|dP_r/dT|$ is somewhat less than that in the first portion.

Therefore, taking into account the foregoing, it can be concluded that the superparaelectric phase being ergodic exists at temperatures above ~285 K.

The fact that a phase similar to the dipole glass phase exists in the second temperature range is supported, in particular, by a virtual coincidence between the "glass" transition temperature calculated by the Vogel–Fulcher formula and $T_f \approx 285$ K. Moreover, the polarization loops obtained in very weak electric fields at a frequency of 10 Hz take the shape of concentric ellipses at a temperature close to T_f (Fig. 7), which indicates the polarization relaxation at infralow frequencies. Furthermore, in the same temperature range, the minimum dispersion of ε_{eff}^* at infralow frequencies is observed in relatively weak fields, which also is characteristic of the dipole glass.

The third portion in the $P_r(T)$ dependence (Fig. 6) corresponds to the polar phase. This is evidenced by the
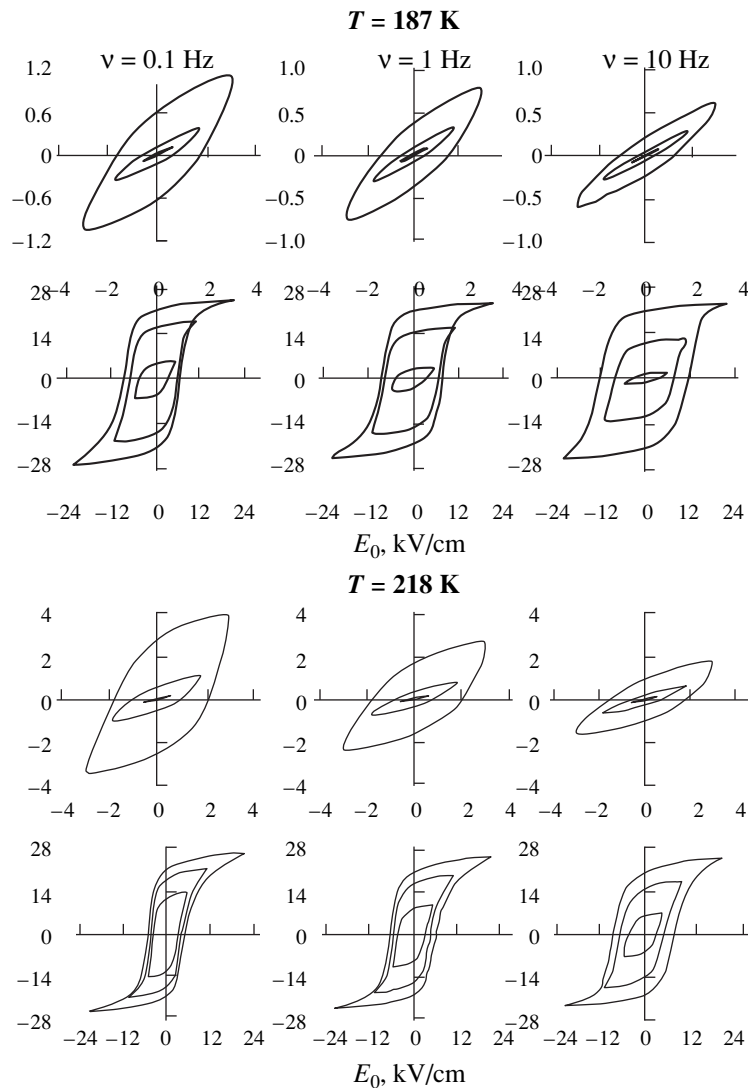
Fig. 8. Evolution of the polarization loops in the 0.89PMN–0.11PZT ferroelectric ceramics at temperatures of 187 and 218 K, frequencies of 0.1, 1, and 10 Hz, and different amplitudes E_0.

polarization loop family (Fig. 8) typical of ferroelectrics, the character of the reverse dependences $\varepsilon'(E_=)$ and $s_{11}^{*E}(E_=)$ (Figs. 9a, 9b), and the temperature dependence of the piezoelectric coefficient $g_{31}(T) \sim P_s(T)$ whose extrapolation leads to the phase transition temperature $T \approx 230$ K (Fig. 9c).

It should be remarked that, within the polar phase, there is one more ferroelectric transition, which, as follows from the maximum in the $\varepsilon_0'(T)$ dependence [25] and the behavior of P_r (Fig. 6), occurs in the vicinity of $T \approx 113$ K. Note that this phase transition in strong fields is observed at $T \approx 123$ K (Fig. 1a) and at higher temperatures according to the data on the piezoelectric coefficient (Fig. 9c). However, no structural investigations were performed in this work.

3.2. On the mechanisms of polarization and repolarization. Analysis of the polarization loops (Figs. 4b, 7, 8) and the reverse dependences $\varepsilon_0'(E_=)$ (Fig. 9a), $s_{11}^{*E}(E_=)$ (Fig. 9b), and the piezoelectric characteristics [$d_{31}(E_=)$, $g_{31}(E_=)$, and $k_p(E_=)$] indicates that different mechanisms of the interphase and domain boundary motions contribute significantly to the corresponding dielectric and electromechanical characteristics of the material in all three temperature ranges studied (Fig. 6).

In the first temperature range, the reversible elastic and reversible relaxation motions of interphase boundaries in relatively weak fields make the contributions to the permittivities ε_0^* and ε_{eff}^* and also to the piezoelectric characteristics (d_{31}, g_{31}, k_p, and s_{11}^{*E}). In the relatively strong fields characterized by the depinning of
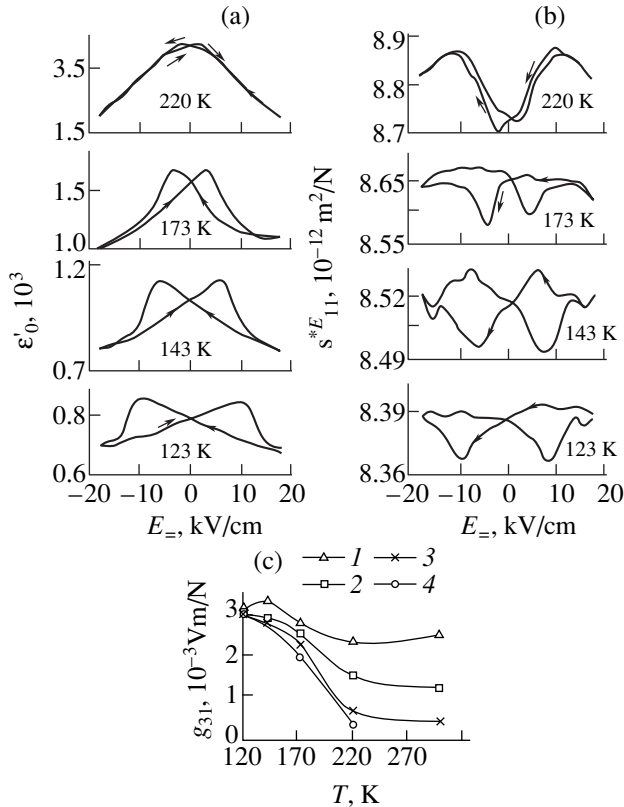
Fig. 9. Reverse dependences of (a) the permittivity $\varepsilon'(E_=)$ and (b) the compliance $s_{11}^{*E}(E_=)$ at temperatures of 220, 173, 143, and 123 K and (c) temperature dependences of the piezoelectric coefficient $g_{31}(T)$ at bias field strengths of (*1*) 17.84, (*2*) 5.88, (*3*) 1.98, and (*4*) 0 kV/cm for the 0.89PMN–0.11PZT ferroelectric ceramics.

interphase boundaries, these quantities are contributed by the irreversible hysteresis (jumpwise) motion of interphase boundaries. Therefore, the statement made in [11–13] is valid only for this (last) case.

In the second temperature range, unlike the first range, the reversible elastic motion of interphase boundaries is not observed; however, the interphase boundaries execute an irreversible relaxation motion (in addition to all the other types).

The mechanisms of the domain boundary motion in the course of the polarization and repolarization in the ferroelectric phase do not radically differ from those considered earlier for ferroelectrics [26, 27].

Thus, the results obtained in the present work can be summarized as follows:

(1) The phase transitions in the $(1 - x)$PMN–xPZT ferroelectric ceramics are characterized. It is demonstrated that compounds in this system undergo at least three phase transitions, namely, the transition from the superparaelectric phase to a phase similar to the dipole glass, transition from the glasslike phase to the "first" ferroelectric phase, and transition from the "first" ferroelectric phase to the "second" ferroelectric phase.

(2) It is established that different mechanisms of interphase and domain boundary motions contribute to the dielectric and piezoelectric properties.

REFERENCES

1. L. E. Cross, Ferroelectrics **76**, 241 (1987).
2. G. A. Rossetti, T. Nishimura, and L. E. Cross, J. Appl. Phys. **70**, 1630 (1991).
3. Z.-G. Ye and H. Schmid, Ferroelectrics **145**, 83 (1993).
4. W. Pan, F. Furmann, G. O. Daytan, *et al.*, J. Mater. Sci. Lett. **5**, 647 (1986).
5. A. V. Shil'nikov, A. I. Burkhanov, and E. Kh. Birks, Fiz. Tverd. Tela (Leningrad) **29**, 809 (1987) [Sov. Phys. Solid State **29**, 520 (1987)].
6. A. V. Shil'nikov, A. I. Burkhanov, E. H. Birks, *et al.*, Ferroelectrics **81**, 317 (1988).
7. D. Viehland, S. J. Jang, L. E. Cross, *et al.*, Phys. Rev. B **46**, 8003 (1992).
8. M. D. Glinchuk, R. Farhi, and V. A. Stephanovich, Ferroelectrics **199**, 11 (1997).
9. V. A. Isupov, Fiz. Tverd. Tela (S.-Peterburg) **38**, 1326 (1996) [Phys. Solid State **38**, 734 (1996)].
10. V. A. Isupov, Phys. Status Solidi B **213**, 211 (1999).
11. A. E. Glazounov, A. K. Tagantsev, and A. J. Bell, Phys. Rev. B **53**, 11281 (1996).
12. A. K. Tagantsev and A. E. Glazounov, Phys. Rev. B **57**, 18 (1998).
13. A. K. Tagantsev and A. E. Glazounov, J. Korean Phys. Soc. **32**, S951 (1998).
14. A. B. Shil'nikov, N. M. Galiyarova, S. V. Gorin, *et al.*, Izv. Akad. Nauk SSSR, Ser. Fiz. **55**, 578 (1991).
15. M. Yoshida, S. Mori, N. Yanamoto, *et al.*, J. Korean Phys. Soc. **32**, S993 (1998).
16. I. Heike and W. William, J. Appl. Phys. **76**, 1789 (1994).
17. L. A. Kuznetsova, L. S. Kamzina, and N. N. Kraĭnik, in *Proceedings of the 1981 USSR Academy of Sciences* (Physicotechnical Institute, Leningrad, 1981), p. 103.
18. E. Yu. Koroleva, Candidate's Dissertation in Mathematical Physics (St. Petersburg, 1998).
19. S. B. Vakhrushev, Doctoral Dissertation in Mathematical Physics (St. Petersburg, 1998).
20. E. G. Nadolinskaya, N. N. Kraĭnik, A. V. Shil'nikov, *et al.*, Fiz. Tverd. Tela (Leningrad) **30**, 149 (1988) [Sov. Phys. Solid State **30**, 82 (1988)].
21. A. V. Shil'nikov, A. V. Sopit, A. I. Burkhanov, *et al.*, J. Eur. Ceram. Soc. **19**, 1295 (1999).

22. *AS TM-D 150-70. Methods for Determination of Dielectric Constants and Dielectric Losses of Solid Electroinsulating Materials at an Alternating Current: US Standards* (Moscow, 1979), p. 108.

23. A. G. Luchaninov, A. V. Vladimtsev, B. N. Chernykh, *et al.*, Prib. Tekh. Éksp., No. 1, 213 (1990).

24. Yu. M. Poplavko, *Physics of Dielectrics* (Vishcha Shkola, Kiev, 1980).

25. A. V. Sopit, A. I. Burkhanov, A. V. Shil'nikov, *et al.*, in *Proceedings of International Conference on Phase Transitions and Critical Phenomena in Condensed Matters, Makhachkala, Dagestan, Russia, 1999* (Inst. of Physics, Dagestan Scientific Center, Russian Academy of Sciences, Makhachkala, 1999), p. 251.

26. A. V. Shil'nikov, Izv. Akad. Nauk SSSR, Ser. Fiz. **51**, 1726 (1987).

27. A. V. Shil'nikov, V. N. Nesterov, and A. I. Burkhanov, Ferroelectrics **175** (14) (1995).

Translated by O. Borovik-Romanova

Hysteresis Phenomena in the Course of Polarization Evolution in a Sinusoidal Electric Field in Lead Magnesium Niobate Crystals

N. N. Kraĭnik*, L. S. Kamzina*, and S. A. Flerova**

* Ioffe Physicotechnical Institute, Russian Academy of Sciences, Politekhnicheskaya ul. 26, St. Petersburg, 194021 Russia
** Dnepropetrovsk State University, pr. Gagarina 72, Dnepropetrovsk 10, 320625 Ukraine
Received August 5, 1999; in final form, November 10, 1999

Abstract—The processes of polarization evolution in single crystals of the $PbMg_{1/3}Nb_{2/3}O_3$ model ferroelectric relaxor in a sinusoidal electric field are investigated at temperatures near and above the temperature T_{d0} of destruction of the induced ferroelectric state upon heating in zero electric field. The polarization switching current loops are measured in the ac electric field applied along the $\langle 111 \rangle$ and $\langle 110 \rangle$ pseudocubic directions. The electroluminescence intensity loops are obtained under the combined action of ac and dc electric fields applied along the $\langle 100 \rangle$ direction. In a certain temperature range above T_{d0} and the freezing temperature T_f in lead magnesium niobate, there are electric current anomalies, that correspond to the dynamic formation and subsequent destruction of the ferroelectric macroregions throughout each half-cycle of the ac electric field. The measurements of electroluminescence hysteresis loops demonstrate that the observed depolarization delay (related to the ac electric field amplitude) increases with an increase in the dc electric field and decreases as the ac field amplitude increases. The nature of the observed phenomena is discussed. © 2000 MAIK "Nauka/Interperiodica".

INTRODUCTION

Research in disordered materials is a rapidly progressing direction in solid-state physics. An example of ferroelectric disordered materials is provided by the ferroelectrics with a smeared phase transition or ferroelectric relaxors, which were first discovered by Smolenskiĭ and coworkers (see, for example, [1]). In these materials, there exists only a short-range order in the distribution of different ions over single-type crystallographic sites, and considerable random fields can arise at the boundaries of ordered regions. Despite a large number of works dealing with these materials, even for a model relaxor such as the lead magnesium niobate crystal, there is no generally accepted concept regarding the nature of induced dielectric polarization and its evolution with variations in the temperature and the electric filed applied to the crystal. In particular, the question as to whether the low-temperature state in the absence of electric field is a state similar to a dipole glass or a state of frozen polar regions remains open [2–7]. The hysteresis phenomena observed in strong electric fields near the temperature of phase transition between the field-induced macrodomain ferroelectric state and the higher temperature nonpolar state also have not been adequately investigated. [Upon cooling in zero electric field, the phase transition occurs at temperature $T_{d0} \simeq 210$ K (see, for example, [8–12])]. A further accumulation of information about the processes associated with the polarization evolution in lead magnesium niobate crystals at different temperatures and in various electric fields can contribute to the development of concepts on the nature of relaxor properties and changes in the correlation interactions between polar regions in an inhomogeneous medium. Moreover, these data can be useful in expanding practical applications of relaxors. Specifically, it is of interest to investigate the hysteresis phenomena in the course of polarization and depolarization at temperatures near and above the T_{d0} temperature. It is also instructive to reveal the possibility of observing the induced phase transition to the ferroelectric state in lead magnesium niobate crystals in the ac electric field at these temperatures.

EXPERIMENTAL RESULTS AND DISCUSSION

In this paper, we report the results of investigations into the processes of polarization switching and the attendant hysteresis phenomena. The presented data were obtained by measurements of the current loops in the ac electric field E and the electroluminescence hysteresis loops in the ac and dc electric fields applied simultaneously. The lead magnesium niobate crystals were grown by a modified method of spontaneous crystallization [13].

The current loops $i(E)$ were measured in the ac electric field with a frequency of 50 Hz upon heating (see also [14]). The electric field E was applied along the $\langle 111 \rangle$ and $\langle 110 \rangle$ pseudocubic directions at temperatures near (and above) the T_{d0} temperature. The electric field was switched off between measurements.
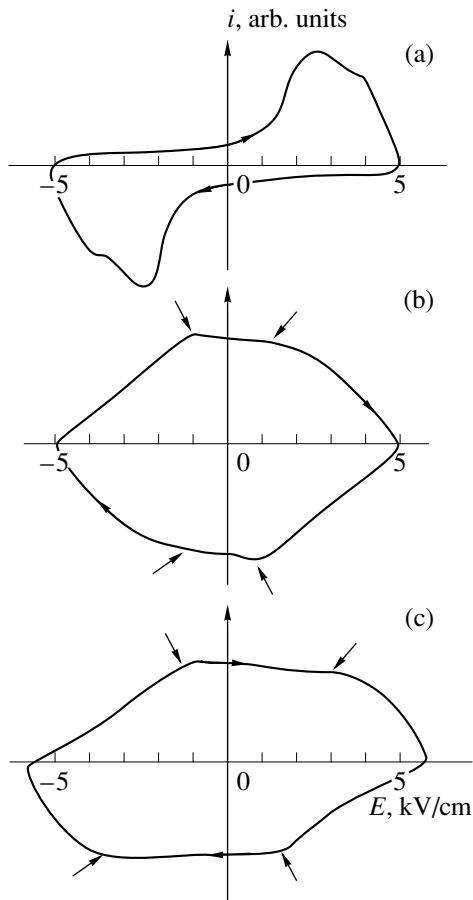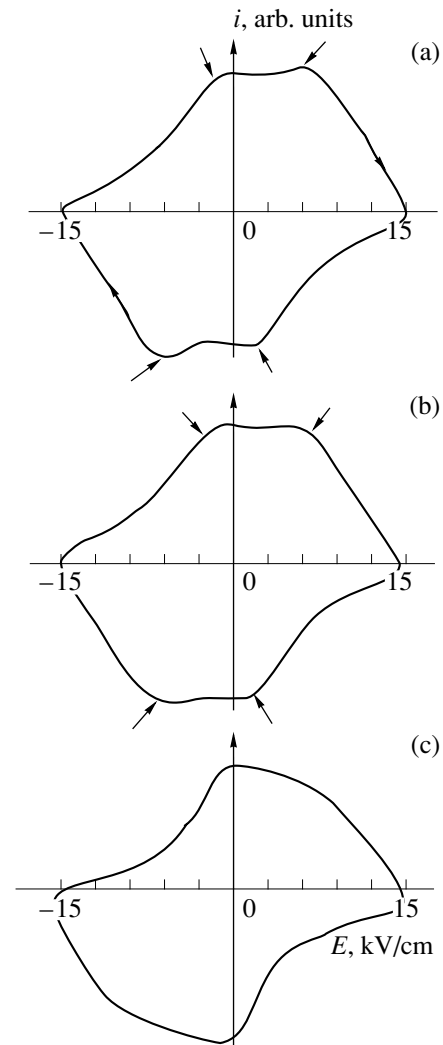
Fig. 1. Schematic representation of the polarization switching current loops $i(E)$ measured at different temperatures in lead magnesium niobate crystals in ac electric field E applied along the $\langle 111 \rangle$ pseudocubic direction. T, K: (a) 176, (b) 236, and (c) 239. Arrows indicate the current anomalies arising upon the induced ferroelectric phase transition.

Fig. 2. Schematic representation of the polarization switching current loops $i(E)$ measured at different temperatures in lead magnesium niobate crystals in ac electric field E applied along the $\langle 110 \rangle$ pseudocubic direction. T, K: (a) 235, (b) 237, and (c) 247. Arrows indicate the current anomalies arising upon the induced ferroelectric phase transition.

The electroluminescence in ferroelectrics is a sensitive tool for studying the processes of polarization evolution. The luminescence is usually observed upon radiative recombination of nonequilibrium current carriers formed during the transformations of domain and heterophase structures, which are accompanied by the appearance of strong local electric fields [15]. The electroluminescence hysteresis loops are the dependences of the electroluminescence intensity on the applied electric field $I(E)$ [16]. The sinusoidal field and the dc electric bias field E were simultaneously applied along the $\langle 100 \rangle$ direction (see also [17]). The technique based on the electroluminescence hysteresis loops provides more illustrative information on the evolution of polarization and depolarization processes as compared to the

oscillograms of the electroluminescence intensity as a function of time [12].

It is well known that, in the case when the dc electric field is applied to the depolarized lead magnesium niobate crystal at temperatures below T_{d0}, the time it takes for the stationary ferroelectric state to be attained is equal to tens of minutes (see, for example, [8, 18, 19]). Analysis of the current loops measured in the present work shows that, at temperatures above ~230 K, the collective processes of formation and destruction of the ferroelectric regions can be observed in the sinusoidal electric field. This is clearly seen from the current loops displayed as an example in Figs. 1 and 2.

For the ferroelectric phase of lead magnesium niobate, the polarization branches of the current loops measured in electric fields applied along the $\langle 111 \rangle$ and
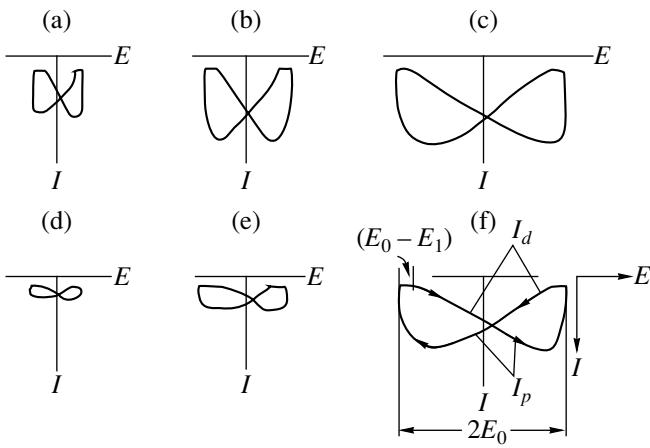
Fig. 3. Schematic representation of the electroluminescence intensity loops $I(E)$ measured in ac electric field $E = E_0\sin(2\pi\nu t)$ with frequency $\nu = 6$ kHz at a temperature of ~293 K. The ac electric field E and dc electric bias field $E_=$ are jointly applied along the $\langle 100\rangle$ pseudocubic direction. E_0 (kV/cm): (a, d) 6.45, (b, e) 9.7, and (c, f) 19.4. $E_=$ (kV/cm): (a, b, c) 8.3 and (d, e, f) 23.5. Electroluminescence intensity I is given in arbitrary units. The scale of the ordinate axis in (c and f) is half as much as that in (a, b, d, and e).

$\langle 110\rangle$ directions are characterized by two current maxima (with different coercive forces) associated with the domain reorientations. At a temperature of ~230 K, the coercive force of the low-field maximum reduces to zero [14]. Above ~230 K, the polarization branches of the current loops exhibit a smeared maximum of the current, and a maximum of the current appears in the depolarization branches. These maxima are shown by arrows in Figs. 1b, 1c, 2a, and 2b. An increase in the temperature leads to the shift of the maxima toward the high-field range.

The presence of current maxima in the polarization and depolarization branches of the current loops at temperatures above 230 K and their shift toward the high-field range with an increase in the temperature suggest the dynamic formation and the subsequent suppression of the ferroelectric state in macroregions with a change in the instantaneous electric field. The polarization current maximum corresponding to the formation of ferroelectric regions is superposed on the high-field maximum associated with the domain reorientations. This superposition leads to an additional smearing of the maximum of electric current.

The collective processes of formation and destruction of the ferroelectric regions manifest themselves only in the limited range of temperatures from ~230 to 240 K. This is not contradictory to the inference about the smearing of the ferroelectric phase transition with an increase in the electric field and its possible transformation to the second-order transition [18, 19]. It can be seen from Fig. 2c that, at higher temperatures, the polarization and depolarization branches of the current loop show spread-out inflections instead of current

maxima. In this case, small currents of the depolarization branches that indicate the delay of the development of depolarization are observed in a narrower range of the decreasing electric field.

It can be assumed that two maxima in the polarization branches of the current loops at temperatures below 230 K in the electric fields applied along the $\langle 111\rangle$ and $\langle 110\rangle$ directions (see Fig. 1a and [14]) are caused by the domain reorientations in different local regions of the crystal. Then, the induced ferroelectric phase transition occurs only in macrovolumes of the studied crystals where the domain reorientations with a smaller coercive force corresponding to the low-field maximum of the current are observed at temperatures below ~230 K. It should be noted that the current maxima associated with the domain reorientations, rather than with the induced ferroelectric phase transition, are also observed at temperatures above the transition temperature T_{d0}; moreover, the coercive force becomes zero only at ~230 K. These findings demonstrate that, at temperatures immediately above T_{d0}, the crystal in the ac electric field is in the metastable state. At these temperatures, the fluctuation times of ionic displacements and dielectric relaxation are rather large, because the temperature T_f of freezing the local correlated polarization states in the lead magnesium niobate crystal falls just in the range of ~230 K [20–22]. The observation of the collective processes of forming and destroying the ferroelectric regions at temperatures above ~230 K reveals that the rates of these processes and, hence, the rates of formation and motion of the heterophase boundaries are higher than those in the experiments with the dc electric field [8, 19]. The breakdown of interlayers of the glasslike phase and also changes in random fields under the action of applied electric field facilitate the liberation of defects pinning the boundaries. These factors can be responsible for the decrease in the duration of the formation and destruction of the ferroelectric regions at temperatures above 230 K.

The coexistence of the local ferroelectric regions, which earlier possessed a large coercive force, and the regions of the crystal, in which the ferroelectric phase transition occurs in the electric field, apparently persists over the entire temperature range from ~230 to 240 K. A further increase in the temperature brings about a weakening of the correlation interactions within and between the local ferroelectric regions and a decrease in the concentration of the ferroelectric regions. This manifests itself in a change in the character of the field dependences of the current and in a decrease of the current magnitude.

Now, let us consider the results obtained in the study of the electroluminescence hysteresis loops $I(E)$ and analyze the combined effect of ac and dc electric fields on the polarization in the lead magnesium niobate crystal at a temperature of ~293 K.

Figure 3 clearly demonstrates the difference between the electroluminescence intensity I_p upon polarization with an increase in the electric field magnitude E and the electroluminescence intensity I_d upon depolarization with a decrease in the electric field (see designations in Fig. 3f). The $I_d(E)$ dependences are similar to the dependences of the depolarization current $i_d(E)$, which are observed at temperatures above 240 K (cf., for example, Figs. 2c and 3). As the instantaneous magnitude of the ac electric field E approaches zero, the magnitudes of I_d and i_d rapidly increase. The field range that corresponds to the decreased magnitudes of I_d and i_d characterizes the delay of depolarization evolution. In the electroluminescence loops, the depolarization delay more clearly manifests itself under the combined action of the alternating E and constant $E_=$ electric fields, especially when $E_= > E_0$. The electric fields were applied along the $\langle 100 \rangle$ pseudocubic direction (Fig. 3). The field range of the depolarization delay can be evaluated from the difference $E_0 - E_1$, where E_0 is the ac field amplitude and E_1 is the field below which a decrease in the electric field leads to a more rapid increase in I_d (see Fig. 3f). In addition to the range of depolarization delay, we also estimated the relative delay $(E_0 - E_1)/E_0$.

The field dependence of the depolarization delay can qualitatively characterize how the applied electric fields affect the correlation interactions between polar regions. Moreover, the depolarization delay can depend on the kinetic processes of motion of the domain and heterophase boundaries, which are associated with the transformations in a system of defects pinning the boundaries.

In the case when the dc electric field $E_=$ and the ac field E exciting the electroluminescence are jointly applied along the same crystallographic direction $\langle 100 \rangle$, the depolarization delay increases at the constant amplitude E_0. We consider the depolarization delay for a half-cycle of the ac field when the directions of the electric fields E and $E_=$ coincide with each other (Figs. 4a, 4b). An increase in the dc electric field $E_=$ brings about an extension of the field range of the delay and an increase in the relative delay of depolarization, which suggests an increase in the correlation interactions. At the same time, it was found that an increase in the ac field amplitude E_0 at a constant value of $E_=$ leads to a decrease in the relative depolarization delay (Fig. 4b). This decrease can be explained by a more intense formation of new local polar regions at large instantaneous fields and the subsequent destruction of these regions when the field decreases. The destruction of the arisen regions is reflected by an increase in the electroluminescence intensity I_d beginning with electric fields that are higher than E_1 and close to the field amplitude E_0. This suggests a continuous distribution of local critical fields inducing the formation of different polar regions and the absence of a common collec-
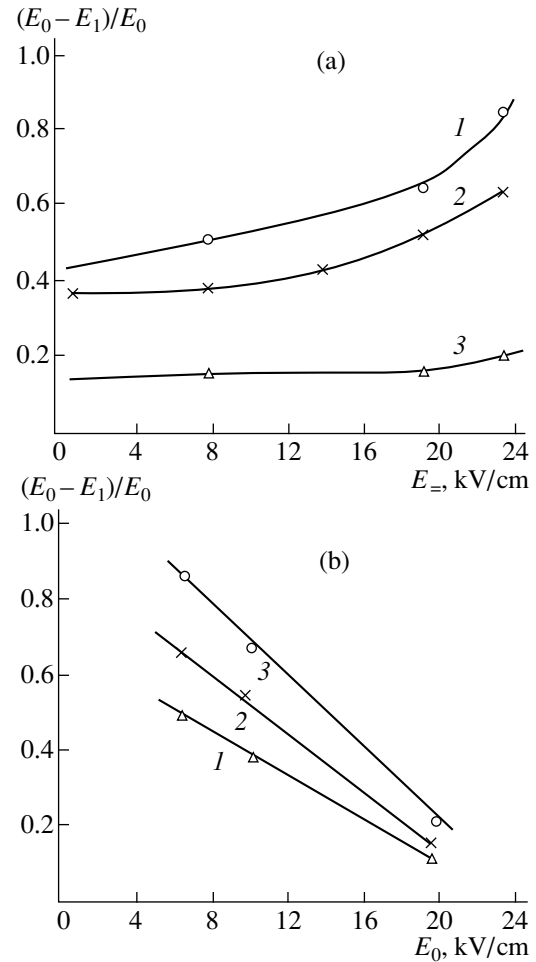

Fig. 4. Relative depolarization delay $(E_0 - E_1)/E_0$ in the lead magnesium niobate crystal at a temperature of ~293 K under the combined action of ac electric field with amplitude E_0 and dc electric field $E_=$ applied along the $\langle 100 \rangle$ pseudocubic direction as a function of (a) the dc field $E_=$ at constant values of $E_0 = $ (*1*) 6.45, (*2*) 9.7, and (*3*) 19.4 kV/cm and (b) the ac field amplitude E_0 at constant values of $E_= = $ (*1*) 8.3, (*2*) 19.5, and (*3*) 23.5 kV/cm.

tive process of formation. In order to elucidate how the increase in the field amplitude E_0 affects the depolarization delay, allowance should be made for the increase in the number and the mobility of domain and heterophase boundaries, which, during the course of the increase in the electric field, have no time to be pinned on defects and be shielded. It is this motion of more mobile boundaries that is responsible for a jumpwise, rapider increase in the electroluminescence intensity I with an increase in E_0. This motion was observed in lead magnesium niobate crystals in our earlier work [16]. The effect of incompleteness of changes in the polarization on the rate of development of these changes also showed itself in lead magnesium niobate in pulsed electric fields when the current pulse duration was shorter than, and of the order of, the probable time taken to accomplish the polarization [12].

The above changes in the delay of depolarization in lead magnesium niobate can also depend on changes in the distribution of random fields under the action of applied electric fields.

Therefore, the analysis of the current loops in single crystals of the lead magnesium niobate ferroelectric relaxor demonstrates that the heating in the ac electric field applied along the $\langle 111 \rangle$ and $\langle 110 \rangle$ pseudocubic directions gives rise to collective processes of the formation and subsequent destruction of the ferroelectric phase in the temperature range ~230–240 K. These processes are observed throughout each half-cycle of the ac electric field in certain regions of the crystal. Note that the collective processes under consideration are observed only beginning with temperatures above the freezing point of lead magnesium niobate ($T_f \simeq 230$ K) and not with the temperature of destroying the ferroelectric state ($T_{d0} \simeq 210$ K). It can be assumed that, in strong ac fields, the ferroelectric regions with two different effective coercive forces coexist in lead magnesium niobate crystals at temperatures above the T_{d0} point. The coercive force in the regions characterized by its smaller value reduces to zero at $T \simeq 230$ K. An increase in the temperature leads to a decrease in the relaxation times in these regions, because they are apparently more homogeneous, possess weaker random fields, and involve smaller volumes of glasslike interlayers. Therefore, although the stationary state is not attained in the applied ac field, it is possible to observe the processes of forming and destroying the ferroelectric phase in the temperature range ~230–240 K until the correlation interactions between the polar regions remain sufficiently strong. Upon further increase in temperature, the current maxima corresponding to these processes become almost completely smeared. The origin of this smearing calls for further investigation. At temperatures above 240 K, the correlation interactions between the persistent polar regions, as well as the correlation interactions between the polar regions whose formation is induced by sufficiently strong instantaneous fields, manifest themselves in the delay of depolarization processes with a decrease in the instantaneous magnitudes of the applied electric field. During the course of the depolarization delay, the depolarization current has decreased magnitudes.

Consideration of the loops of the electroluminescence intensity as a function of the strength of the sinusoidal electric field applied simultaneously with the dc bias field shows that, at a temperature of ~293 K, the depolarization delay is observed in electric fields in the range from several kV/cm to a total field of ~40 kV/cm. The luminescence intensity remains low and virtually constant in the ac electric field range corresponding to the depolarization delay. This made it possible to examine the character of the field dependences of the depolarization delay. The delay increases with an increase in the dc electric field. At the same time, it was found that an increase in the ac field amplitude brings about a decrease in the ratio between the field range of depolarization delay and the field amplitude. The found decrease in the relative depolarization delay can be explained by more intense local processes of the formation and subsequent destruction of new polar regions. The observed change in the kinetics of depolarization processes depending on the electric field can be caused either by changes in the concentration of polar regions or by changes in the rate of motion of the heterophase boundaries due to the incompleteness of the processes of pinning the boundaries by defects and their shielding. The effect of changes in the distribution of random fields under the action of the applied electric fields is also possible.

The hysteresis phenomena observed in lead magnesium niobate in sufficiently strong electric fields indicate that the motion of heterophase and domain boundaries plays an important role in the processes of polarization evolution over a wide range of temperatures above the temperature of phase transition between the ferroelectric state and the high-temperature nonpolar state.

ACKNOWLEDGMENTS

REFERENCES

1. G. A. Smolenskiĭ, V. A. Isupov, and A. I. Agranovskaya, Fiz. Tverd. Tela (Leningrad) **1**, 170 (1959) [Sov. Phys. Solid State **1** (1959)].

2. D. Viehland, S. J. Jang, L. E. Cross, et al., J. Appl. Phys. **68**, 2916 (1990).

3. E. V. Colla, S. B. Vakhrushev, E. Yu. Koroleva, et al., Fiz. Tverd. Tela (S.-Peterburg) **38**, 2183 (1996) [Phys. Solid State **38**, 1202 (1996)].

4. L. A. Markova, N. N. Kraĭnik, and R. N. Kyutt, Fiz. Tverd. Tela (Leningrad) **33**, 35 (1991) [Sov. Phys. Solid State **33**, 18 (1991)].

5. M. D. Glinchuk, R. Farhi, and V. A. Stephanovich, Ferroelectrics **199**, 11 (1997).

6. W. Kleemann and R. Lindner, Ferroelectrics **199**, 1 (1997).

7. A. K. Tagantsev and A. E. Glazounov, Appl. Phys. Lett. **74**, 1910 (1999).

8. G. Calvarin, E. Husson, and Z. G. Ye, Ferroelectrics **165**, 349 (1995).

9. G. A. Smolenskiĭ, N. N. Kraĭnik, L. A. Kuznetsova, et al., Fiz. Tverd. Tela (Leningrad) **23**, 1341 (1981) [Sov. Phys. Solid State **23**, 784 (1981)].

10. G. Schmidt, H. Arndt, G. Borchardt, et al., Phys. Status Solidi A **63,** 501 (1981).

11. A. K. Tagantsev and A. E. Glazounov, Phys. Rev. B **57**, 18 (1998).

12. N. N. Kraĭnik, L. S. Kamzina, and S. A. Flerova, Ferroelectrics **208–209**, 363 (1998).

13. I. E. Myl'nikova and V. A. Bokov, in *Growth of Crystals* (Akad. Nauk. SSSR, Moscow, 1961), Vol. 3, p. 438.

14. N. N. Kraĭnik and L. S. Kamzina, Fiz. Tverd. Tela (S.-Peterburg) **37**, 999 (1995) [Phys. Solid State **37**, 542 (1995)].

15. A. S. Sidorkin, B. M. Darinskiĭ, and T. N. Pankova, Izv. Akad. Nauk SSSR, Ser. Fiz. **48**, 1135 (1984).

16. S. A. Flerova, N. N. Kraĭnik, and A. Yu. Kudzin, Ferroelectrics **90**, 135 (1989).

17. E. O. Bochkov, N. N. Kraĭnik, A. Yu. Kudzin, *et al.*, Izv. Akad. Nauk, Ser. Fiz. **57**, 36 (1993).

18. E. V. Colla, E. Yu. Koroleva, N. M. Okuneva, *et al.*, Phys. Rev. Lett. **74**, 1681 (1995).

19. Z. G. Ye and H. Schmidt, Ferroelectrics **145**, 83 (1993).

20. S. B. Vakhrushev, B. E. Kvjatkovsky, A. A. Nabereznov, *et al.*, Physica B (Amsterdam) **156–157**, 90 (1989).

21. A. E. Glazounov and A. K. Tagantsev, Appl. Phys. Lett. **73**, 856 (1998).

22. A. Levstik, Z. Kutnjak, C. Filipic, *et al.*, Phys. Rev. B: Condens. Matter **57**, 11 204 (1998).

Translated by O. Borovik-Romanova

MAGNETISM
AND FERROELECTRICITY

Effect of γ Irradiation on the Heat Capacity of $(CH_3)_2NH_2Al(SO_4)_2 \cdot 6H_2O$ Crystals near the Ferroelectric Phase Transition

A. U. Sheleg, T. I. Dekola, and N. P. Tekhanovich

Institute of Solid State and Semiconductor Physics, Belarus Academy of Sciences, Minsk, 220072 Belarus

Received, in final form, November 15, 1999

Abstract—The heat capacity of dimethyl ammonium-aluminum sulfate crystals (DMAAS), both nonirradiated and γ-irradiated to fluences of 10^7, 5×10^7, and 10^8 R, has been measured by the adiabatic method near the ferroelectric phase transition (PT) within the 80–300 K temperature range. The $C_p = f(T)$ curve exhibits a λ-shaped anomaly near the phase-transition point $T_C = 152$ K. The PT temperature and the magnitude of the anomaly are shown to decrease with increasing γ-irradiation fluence. It has been established that the ferroelectric PT at $T_C = 152$ K, which lies close to the tricritical point, shifts progressively more under γ irradiation toward the second-order PT, and that the behavior of the anomalous part of the heat capacity in the ferroelectric phase is described by the thermodynamic theory of Landau. The experimental heat-capacity data have been used to calculate the variation of the thermodynamic functions of the DMAAS crystal. © *2000 MAIK "Nauka/Interperiodica".*

DMAAS crystals, which are representatives of a new family of ferroelectrics–ferroelastics, have been synthesized fairly recently and are presently widely studied by a variety of methods. It is known [1] that at $T_C = 152$ K the DMAAS crystals undergo phase transition (PT) from the $2/m$ paraelectric-ferroelastic to the m ferroelectric phase. Below $T_C = 152$ K, the crystals exhibit ferroelectric properties and are ferroelastics throughout the temperature range covered. Besides, as shown in [2, 3], one observes near $T \approx 75$ K a second low-temperature PT, whose nature still remains unknown and whose low-temperature phase symmetry has not been established.

This paper presents the results of a study of the heat capacity of crystalline DMAAS within the 80–300 K temperature range, as well as of the effect of γ irradiation on the heat capacity in the vicinity of the ferroelectric PT at $T_C = 152$ K.
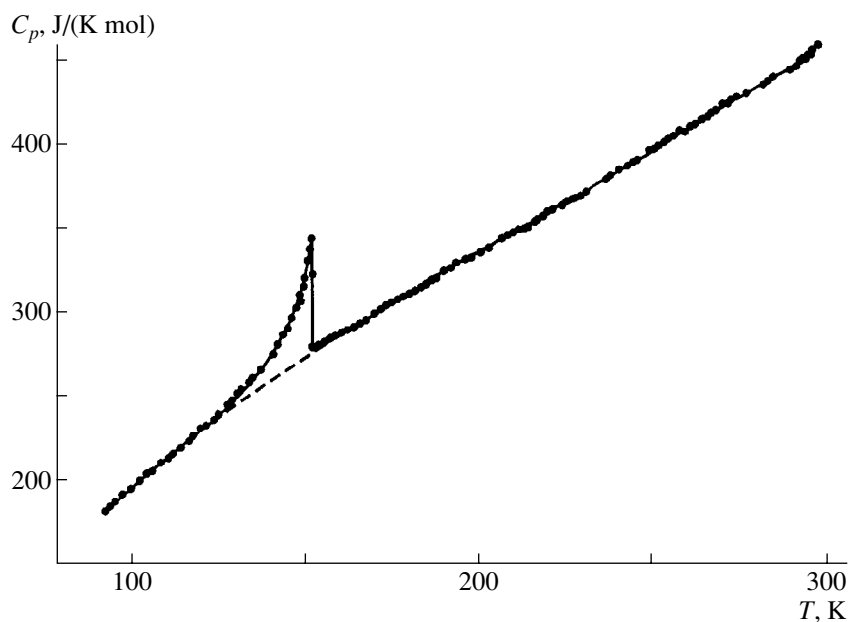

Fig. 1. Temperature dependence of the heat capacity of crystalline DMAAS.

EXPERIMENTAL TECHNIQUES AND THE RESULTS OF THE STUDY

The heat capacity measurements were carried out on an UNTO setup with automatic temperature control in a vacuum adiabatic calorimeter providing discrete heat supply to the sample ($m = 7.67$ g). The sample was heated with a heating rate of 0.04–0.09 K/min. The sample temperature was monitored by a platinum resistance thermometer capable of temperature determination to within ±0.01 K. The heat capacity was measured in steps of 0.8–1.8 K to within 0.3%. The sample was irradiated with Co^{60} γ rays, with a dose rate of ≈ 300 R/s in the irradiation zone. The fluence was accumulated in successive exposures of the same sample to 10^7, 5×10^7, and 10^8 R.

Figure 1 plots the temperature dependence of the heat capacity of DMAAS crystals in the range from 80 to 300 K. At the phase-transition point $T_C = 152$ K, one clearly sees a λ-shaped anomaly in the heat capacity characteristic of second-order phase transitions. The dashed line represents the lattice component of the heat capacity determined by interpolation with a $C = \sum_{i=0}^{3} A_i T^i$ polynomial. Numerical integration yielded for the changes in the enthalpy and entropy at the transition 702 J/mol and 4.8 J/(K mol), respectively. The smoothened values of the heat capacity of DMAAS and the calculated changes in the relevant thermodynamic functions, namely, the entropy, enthalpy, and Gibbs free energy, are listed in Table 1.

Figure 2 presents a $C_p(T)$ dependence for a DMAAS sample irradiated to various γ-ray fluences. The phase-transition point is seen to shift toward lower temperatures with increasing fluence, but the transition itself does not become diffuse. Also, the anomaly peak noticeably decreases in amplitude. As pointed out in [1], the transformation occurring in DMAAS at $T_C = 152$ K is a proper, order–disorder-type ferroelectric PT, which is close to the tricritical point. This has stimulated our investigation of the evolution of the heat capacity anomaly with γ-irradiation fluence.

For transitions close to the tricritical point, the dependence of the thermodynamic potential on a one-component order parameter η has the form [4]

$$\Phi(P, T, \eta) = \Phi_0 + A\eta^2 + B\eta^4 + C\eta^6,$$

where $A = A_T(T - T_C)$, T_C is the transition temperature, $C > 0$, and the sign of B depends on the type of the transition ($B < 0$ for a first-order PT, and $B > 0$ for a PT of the second kind). The excess heat capacity below T_C is given in this case by [4]

$$\Delta C_p^{-2} = \frac{4B^2}{A_T^4 T_C^2} + \frac{12C}{A_T^3 T_C^2}(T_C - T). \quad (1)$$

Table 1. Smoothened values of the heat capacity and of the changes in the DMAAS thermodynamic functions

T, K	$C_p(T)$	$S(T)$–S(80 K)	$\Phi(T)$–Φ(80 K)	$H(T)$–H(80 K), J/mol
		J/(K mol)		
80	154.1	0.000	0.000	0.0
100	196.1	38.87	8.974	3502
120	230.8	77.71	22.14	7771
140	260.3	115.5	37.42	12680
160	286.7	152.1	53.77	18150
180	311.4	187.3	70.65	24130
200	335.5	221.4	87.74	30600
220	359.8	254.5	104.9	37560
240	384.7	286.9	122.0	45000
260	410.0	318.7	139.0	52950
280	435.6	350.0	155.9	61400
300	460.5	380.9	172.7	70370

Table 2. Thermodynamic parameters of the phase transition in DMAAS

Irradiation fluence, R	T_C, K	$A_T \times 10^3$, K^{-1}	$B \times 10^8$, J^{-1} mol	$C \times 10^{11}$, J^{-2} mol^2	$N \times 10^4$
0	152.16	5.4	0.31	0.46	6.20
10^7	151.25	5.4	0.33	0.87	7.14
5×10^7	149.85	5.4	0.38	0.95	7.91
10^8	148.68	5.4	0.46	1.29	8.25

Using the $(\Delta C_p)^{-2} \sim T_C - T$ plot (Fig. 3), one can determine the coefficients of the thermodynamic potential for the pure and irradiated DMAAS samples. One can readily verify that function (1) remains linear in the vicinity of the PT point for all fluences. Table 2 lists the expansion coefficients A_T, B, and C in the SI system. The value of A_T was derived from the measurements of the permittivity made in [1] and was assumed not to change under irradiation. By Landau's theory, in the case of the tricritical point, the behavior of the heat capacity in the ferroelectric phase near the transition point obeys a power law with an exponent of 0.5 [4]. An analysis of the experimental data obtained on the DMAAS crystal showed the $\Delta C_p \sim \left| \dfrac{T_C - T}{T_C} \right|^{-\alpha}$ relation to hold for $\alpha = 0.47 \pm 0.06$. This observation, as well as the positive sign of the B coefficient, provides supportive evidence for the existence in DMAAS of a second-order phase transition close to the tricritical point. The B and C coefficients increase with increasing fluence. The increase of coefficient B indicates that the phase transition moves gradually away from the tricritical point along the phase-transition line for this crystal.
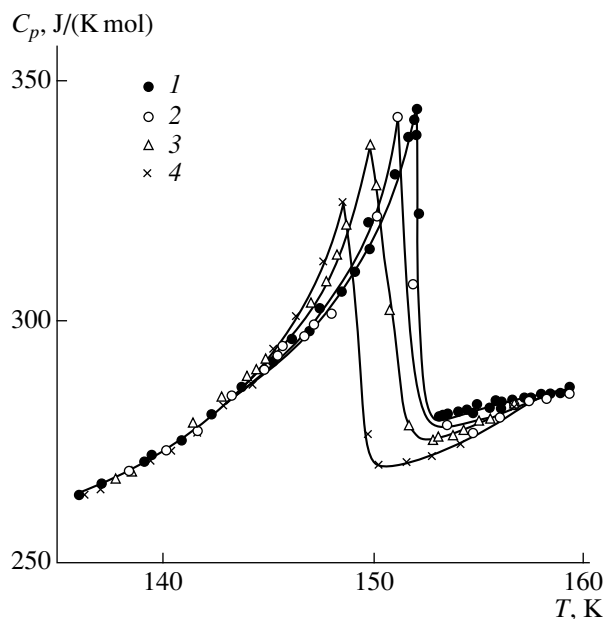
C_p, J/(K mol)

Fig. 2. Temperature dependence of the heat capacity of crystalline DMAAS subjected to various irradiation fluences (R): (*1*) 0, (*2*) 10^7, (*3*) 5×10^7, and (*4*) 10^8.

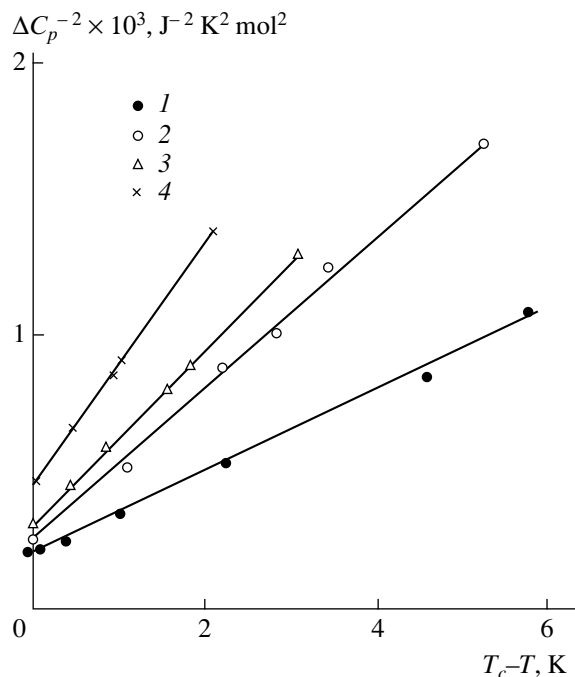$\Delta C_p^{-2} \times 10^3$, J^{-2} K^2 mol^2

Fig. 3. $(\Delta Cp)^{-2}$ *vs* $T_{CT}-T$ plot. Notation same as in Fig. 2.

The degree of closeness to this point can be characterized by a dimensionless quantity $N = \sqrt{\dfrac{B^2}{2A_TCT_C}}$ [4]. As seen from Table 2, N increases in magnitude, which suggests that γ irradiation changes the nature of the PT in DMAAS from close to the tricritical point to a second-order phase transition. A similar effect was found earlier in TGSel and DTGSel crystals [5, 6].

An analysis of the origin of ferroelectricity in DMAAS, i.e., of the PT at $T = 152$ K, made in [7, 8], gave preference to the mechanism associated with orientational ordering of the dimethyl ammonium (DMA) ion in the crystal lattice. However, a Raman scattering study [9] suggests the existence of strong hydrogen bonding between the $[Al(H_2O)_6]^{3+}$ complex and the sulfate sublattice in DMAAS and that the order–disorder-type PT can be driven by orientational ordering of water molecules on the Al–O–H–…–O–S bonds. As follows from experimental studies of the dimethyl ammonium-gallium sulfate crystal (DMAGS), which is isomorphous with the DMAAS, such a PT of the second kind occurs in the former at 135 K. Substitution of Ga^{3+} for Al^{3+} lowers the PT temperature, and the interatomic distances in the lattice increase. It is also known that the $[Ga–6H_2O]$ cations are looser than the $[Al–6H_2O]$ ones, because the (Ga–OH) distance is 1.91–1.98 Å, whereas the (Al–OH) one is 1.86–1.91 Å [10]. It was shown earlier [11] that the PT point in DMAGS also shifts toward lower temperatures under γ irradiation. Thus, the experimentally observed dis-

placement of the PT point in DMAAS to low temperatures permits one to suggest preferential effect of γ irradiation on the Al–O–H–…–O–S chains, which causes bond deformation in these links. The above reasoning permits one to maintain that the mechanism of the ferroelectric PT proposed in [9], as well as the DMA orientational ordering, plays a certain role in the phase transition in DMAAS.

REFERENCES

1. L. F. Kirpichnikova, E. F. Andreev, N. R. Ivanov, *et al.*, Kristallografiya **33**, 1437 (1988) [Sov. Phys. Crystallogr. **33**, 855 (1988)].

2. A. Petrashko, L. F. Kirpichnikova, and L. A. Shuvalov, Kristallografiya **40**, 569 (1995) [Crystallogr. Rep. **40**, 523 (1995)].

3. L. F. Kirpichnikova, I. Bendarskiĭ, S. Vaplyak, *et al.*, Kristallografiya **44**, 111 (1999) [Crystallogr. Rep. **44**, 106 (1999)].

4. K. S. Aleksandrov and I. N. Flerov, Fiz. Tverd. Tela **21**, 327 (1979) [Sov. Phys. Solid State **21**, 195 (1979)].

5. B. A. Strukov, S. A. Taraskin, and A. B. Suvkhanov, Ferroelectrics **124**, 189 (1991).

6. B. A. Strukov, S. A. Taraskin, Song-Yong Von, *et al.*, Izv. RAN, Ser. Fiz. **57** (6), 12 (1993).

7. G. A. Kiosse, I. M. Razdobreev, L. F. Kirpichnikova, *et al.*, Kristallografiya **39**, 34 (1994) [Crystallogr. Rep. **39**, 27 (1994)].

8. V. Yu. Kazimirov, V. A. Sarin, K. Ritter, *et al.*, Kristallografiya **44**, 61 (1999) [Crystallogr. Rep. **44**, 56 (1999)].

9. V. I. Torgashev, Yu. I. Yuzyuk, L. F. Kirpichnikova, *et al.*, Kristallografiya **36**, 677 (1991) [Sov. Phys. Crystallogr. **36**, 376 (1991)].

10. L. F. Kirpichnikova, A. Petrashko, M. Polomska, *et al.*, Kristallografiya **41**, 722 (1996) [Crystallogr. Rep. **41**, 685 (1996)].

11. A. U. Sheleg, T. I. Dekola, N. P. Tekhanovich, *et al.*, Neorg. Mater. **36**, 4 (2000).

Translated by G. Skrebtsov

LATTICE DYNAMICS
AND PHASE TRANSITIONS

Effects of the Phase Transition in $Hg_2(Br,I)_2$ Crystals

Yu. F. Markov*, K. Knorr**, and E. M. Roginskiĭ***

* *Ioffe Physicotechnical Institute, Russian Academy of Sciences, Politekhnicheskaya ul. 26, St. Petersburg, 194021 Russia*
** *Universität des Saarlandes, Saarbrücken, Germany*
*** *St. Petersburg State Technical University, Politekhnicheskaya ul. 29, St. Petersburg, 195251 Russia*
Received October 29, 1999

Abstract—The effects of the phase transition in $Hg_2(Br,I)_2$ crystals have been investigated over a wide range of temperatures by the Raman scattering spectroscopy and X-ray diffraction analysis. The overtones (at the X point of the Brillouin zone boundary) and the fundamental tones (at the center of Brillouin zone) of soft modes are found in the Raman spectra of these crystals and studied in detail. The density of one-phonon states of the soft TA branch manifests itself in the Raman spectra of mixed crystals. The potentialities of the soft-mode spectroscopy are realized in full measure. Analysis of the ratio between intensities of overtones and fundamental tones of the soft modes has demonstrated the applicability of the Landau phenomenological theory of phase transitions. The orthorhombic splitting of the reflections corresponding to the basal plane is revealed in the X-ray diffraction patterns and thoroughly explored. The temperature dependences of the isotropic and shear spontaneous strains are obtained. It is shown that the shear spontaneous strain plays a decisive role. The critical indices are determined and the model of the improper ferroelastic phase transition $D_{4h}^{17} \longrightarrow D_{2h}^{17}$ in the vicinity of the tricritical point is corroborated. © 2000 MAIK "Nauka/Interperiodica".

1. INTRODUCTION

Crystals of the univalent mercury halides Hg_2Hal_2 (Hal = Cl, Br, and I) at room temperature form the tetragonal body-centered lattice D_{4h}^{17} with two linear molecules (formula units) in the unit cell [1]. They possess unique physical properties, in particular, the highest birefringence, the lowest sound velocity, and high acoustooptical constants [2]. In technology, these crystals have found a wide use as basic elements of polarizers, acoustic delay lines, acoustooptical filters, etc.

Considerable attention drawn to these objects is explained by the fact that they can be regarded as model crystalline systems in studies of general problems concerning structural phase transitions. The improper ferroelastic phase transitions $D_{4h}^{17} \longrightarrow D_{2h}^{17}$ from a tetragonal phase to the orthorhombic phase were found in these crystals upon their cooling down to the temperature T_c equal to 186 K for Hg_2Cl_2 and 144 K for Hg_2Br_2 [3]. These transitions are induced by the condensation of the slowest soft TA branch at the X point of the Brillouin zone boundary and accompanied by the doubling of the unit cell and the $X \longrightarrow \Gamma$ "crossover" in the Brillouin zone. The phase transition in the Hg_2I_2 crystals was observed only under a high hydrostatic pressure (P_c = 9 kbar at T = 293 K) [4].

In recent years, particular interest has been expressed by researchers in the lattice dynamics and phase transitions in mixed crystals. The $Hg_2(Cl,Br)_2$ crystals were investigated in our earlier work [5]. Moreover, the $Hg_2(Cl,I)_2$ [6] and $Hg_2(Br,I)_2$ [7] crystals

have come under the study. In the present work, the phase transitions in a system of the mixed $Hg_2(Br,I)_2$ crystals were studied for the first time by the X-ray diffraction and optical (Raman light scattering) techniques. We investigated the mixed $Hg_2(Br_{0.88},I_{0.12})_2$ single crystals and, for comparison, the iodine-free crystals Hg_2Br_2—the last component in the $Hg_2(Br,I)_2$ system. Consideration was also given to the soft modes in the paraphase (overtones at the X point of the Brillouin zone boundary), which are responsible for the phase transitions, the soft modes in the ferroelastic phase (the fundamental tones at the center of Brillouin zone—the Γ point), the orthorhombic splitting of the fundamental Bragg reflections, spontaneous strains, critical indices, etc.

2. EXPERIMENTAL TECHNIQUE

The optical spectra were measured on a Dilor-Z24 triple Raman spectrometer with the use of argon (λ = 5145 Å) and helium–neon (λ = 6328 Å) lasers whose powers were varied from tens to hundreds of mW. The X-ray diffraction patterns were recorded on a two-circle diffractometer ($CuK_{\alpha_1-\alpha_2}$ radiation). The low-temperature (optical and X-ray structural) measurements were carried out using Cryogenics closed-cycle helium cryostats with a good temperature stabilization (~0.1 K). For these measurements, samples of the $Hg_2(Br,I)_2$ single crystals 5 × 5 × 5 mm in size were split along the cleavage planes (110) and ($1\bar{1}0$), cut along the (001) plane, ground, and polished. Moreover,

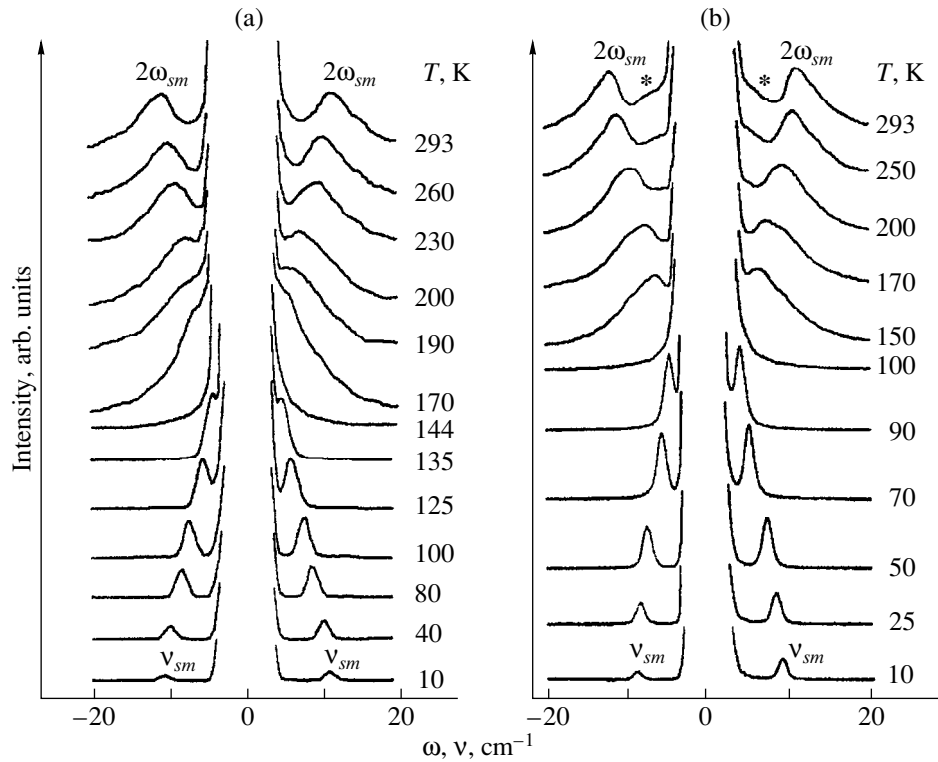**Fig. 1.** Low-frequency Raman spectra (Stokes and anti-Stokes regions) for crystals (a) Hg_2Br_2 and (b) $Hg_2(Br_{0.88},I_{0.12})_2$ at different temperatures. The second-order spectra ($2\omega_{sm}$) are shown on a scale enlarged by a factor of ~20. The maxima corresponding to the density of one-phonon states of the soft *TA* branch at the *X* point of the Brillouin zone are marked by asterisks.

in order to perform the X-ray diffraction experiments, the samples were additionally treated by an etching agent—a solution of aqua regia in distilled water.

3. LOW-FREQUENCY RAMAN SPECTRA

The Raman spectra of the mixed $Hg_2(Br,I)_2$ crystals at room temperature were studied earlier in [7]. In the present work, most attention was focused on the investigation into the effects of phase transitions, i.e., on the observation and exploration of soft modes in the paraphase (at the *X* point of the Brillouin zone boundary) and in the ferroelastic phase (at the Γ point—the center of Brillouin zone).

Figure 1 displays a number of the most characteristic low-frequency Raman spectra of the $Hg_2(Br,I)_2$ crystals in the $Z(XX)Y$ geometry at different temperatures above and below T_c. It can be seen from Fig. 1a that the Stokes and anti-Stokes spectral regions at temperatures $T > T_c = 144$ K (Hg_2Br_2) are characterized by the clearly defined broad $2\omega_{sm}$ maxima at about 12 cm^{-1} (293 K) and the narrow intense ν_{sm} lines at $T \le T_c$, whose frequencies tend to zero as the phase transition temperature is approached ($T \longrightarrow T_c$). The above maxima correspond to the $2\omega_{sm}$ overtone of the soft *TA* branch (primarily, at the *X* point of the Brillouin zone boundary), and the lines, to the ν_{sm} fundamental tone of

the soft mode at the center of Brillouin zone. This tone is excited at temperatures $T \le T_c$ due to the phase transition or, in other words, the doubling of the unit cell and the $X \longrightarrow \Gamma$ crossover in the Brillouin zone.

Typical low-frequency Raman spectra of the mixed $Hg_2(Br_{0.88},I_{0.12})_2$ crystals are depicted in Fig. 1b. As can be seen from this figure, all the soft-mode spectra are similar to the spectra of pure Hg_2Br_2; however, the lines (maxima) are somewhat broadened, which is associated with the inhomogeneous broadening caused by the disordering of anionic sublattice. Moreover, the spectra exhibit new broad maxima (marked by asterisks), which most clearly manifest themselves at temperatures near room temperature in the frequency range of ~6 cm^{-1}. The nature of these maxima stems from the density of one-phonon states of the soft *TA* branch. The excitation of the fundamental tone of the soft mode (the Γ point of the Brillouin zone) is observed at the lower temperature $T_c = 100$ K; i.e., the introduction of a small amount of Hg_2I_2 (12%) into pure Hg_2Br_2 results in an anomalously large shift (decrease) of the transition temperature T_c. In this case, as for pure Hg_2Br_2, the intensity of the $2\omega_{sm}$ overtone of the soft mode is considerably (approximately twenty times) less than the intensity of the ν_{sm} fundamental tone of the soft mode.

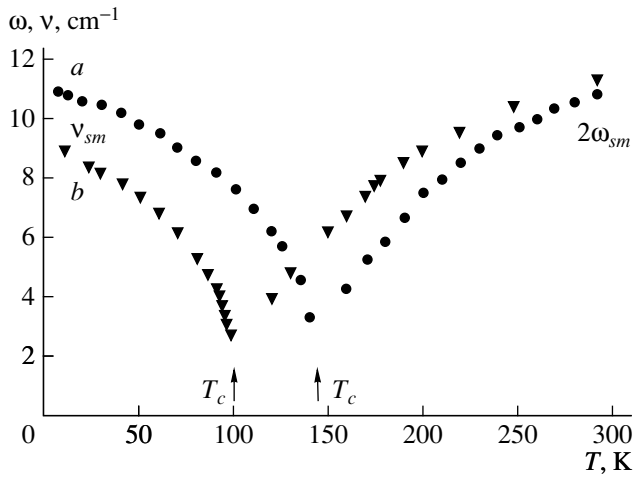The temperature dependences of the frequency of soft modes for the studied crystals are constructed in

Fig. 2. Temperature dependences of the frequency of the $2\omega_{sm}$ overtone and the ν_{sm} fundamental tone of the soft mode for crystals (*a*) Hg_2Br_2 (circles) and (*b*) $Hg_2(Br_{0.88},I_{0.12})_2$ (triangles).
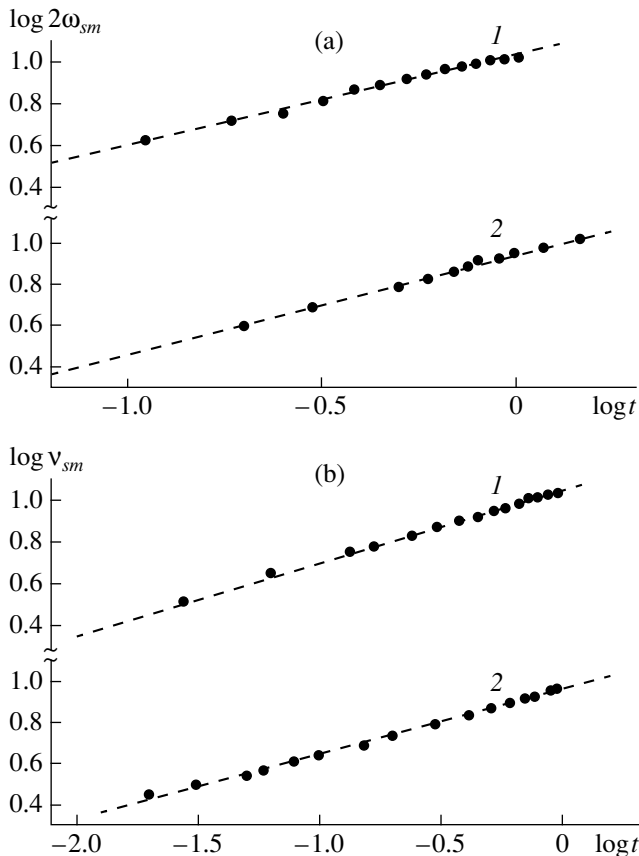

Fig. 3. Dependences of the frequency of (a) $2\omega_{sm}$ overtone and (b) ν_{sm} fundamental tone of the soft mode on the reduced temperature *t* on the log–log scale for crystals (*1*) Hg_2Br_2 and (*2*) $Hg_2(Br_{0.88},I_{0.12})_2$. Dashed lines represent the linear approximation.

Fig. 2. It is clearly seen that the fundamental tone and the overtone of the soft mode are substantially softened as the temperature approaches the T_c point. Figure 3 demonstrates similar dependences on the reduced temperature $t = (T - T_c) / T_c$ on the log–log scale. As can be seen from Fig. 3, at $T > T_c$, the dependences of the logarithm of the $2\omega_{sm}$ overtone frequency of the soft mode on the logarithm of the reduced temperature *t* for pure and mixed crystals are described well by straight lines. Therefore, the dependence of the overtone frequency of the soft mode can be approximated by the formula

$$2\omega_{sm} = gt^{\beta'}, \qquad (1)$$

where *g* is a constant, and β' is the critical index.

The critical indices β' determined from this formula are equal to 0.50 ± 0.02 for Hg_2Br_2 and 0.51 ± 0.02 for $Hg_2(Br_{0.88},I_{0.12})_2$. These indices are completely consistent with the Landau phenomenological theory of second-order phase transitions ($\beta' = 0.5$). An analysis of the plots in Fig. 3 (the logarithmic dependences of the ν_{sm} fundamental tone frequency of soft modes on the reduced temperature *t* at $T \le T_c$) shows that these dependences over a wide range of temperatures are approximated by nearly straight lines and, as for the overtones of the soft mode, can be described by the simple power law

$$\nu_{sm} = \delta t^{\beta''}, \qquad (2)$$

where δ is a constant, and β'' is the critical index.

This formula enabled us to evaluate the critical indices β'' (at $T \le T_c$). Their values were found to be equal to 0.34 ± 0.02 for the pure Hg_2Br_2 crystal and 0.33 ± 0.02 for the mixed $Hg_2(Br_{0.88},I_{0.12})_2$ crystal.

4. X-RAY DIFFRACTION MEASUREMENTS

The temperature dependences of the basal plane parameters for the aforementioned crystals $Hg_2(Br,I)_2$ were examined down to helium temperatures. Specifically, we studied the orthorhombic splitting of the fundamental (440) reflections of the D_{4h}^{17} tetragonal paraphase due to the phase transition (Fig. 4). The splitting of these reflections at $T \le T_c$ is brought about by the formation of orthorhombic domains rotated through 90° with respect to each other around the tetragonal axis; i.e., the reflections of the (110) plane are superimposed on the reflections of the ($1\bar{1}0$) plane. In the low-temperature phase, the parameters (sizes) of a new unit cell along the [110] and [$1\bar{1}0$] directions become non-equivalent, and the Bragg peaks along these directions are split below the T_c temperature. A further decrease in the temperature leads to an increase in the orthorhombic splitting. The temperature corresponding to the appearance of this splitting (Fig. 4), as well as the instant of the excitation of the ν_{sm} fundamental tone of

the soft mode at the Brillouin zone center (the Γ point), serves as a reference point of the phase transition temperature T_c, which is equal to 144 K for Hg$_2$Br$_2$ and 100 K for Hg$_2$(Br$_{0.88}$,I$_{0.12}$)$_2$. The orthorhombic splitting was measured upon both cooling and heating; however, within the limits of experimental error, no hysteresis was observed for these crystals. In both cases, the orthorhombic splitting occurs without jumps, which suggests a continuous character of the phase transitions. For the mixed crystals ($T \leq T_c$), the orthorhombic splitting has a somewhat lesser value at the same difference in temperatures T and T_c, which can be reasonably explained by the disordering of the anionic sublattice. The aforementioned anomalous temperature dependences of the lattice parameters are associated with the appearance of spontaneous ferroelastic strains at temperatures $T \leq T_c$. According to [3], the spontaneous strains ε_i^0 (i = 1, 2, 3, and 6) in the basal plane of the Hg$_2$(Br,I)$_2$ crystals are characterized by the following nonzero components (in terms of tetragonal phase): $\varepsilon_1^0 = \varepsilon_{xx} = \varepsilon_2^0 = \varepsilon_{yy}$, $\varepsilon_3^0 = \varepsilon_{zz}$, and $\varepsilon_6^0 = \varepsilon_{xy}$, where x, y, and z are the tetragonal crystal axes. The shear spontaneous strain is defined as

$$\varepsilon_6^0 = \frac{d_{110} - d_{1\bar{1}0}}{d_{110}^0}. \qquad (3)$$

The isotropic strain in the basal plane is represented in the form

$$\varepsilon_1^0 = \frac{d_{110} + d_{1\bar{1}0}}{2d_{110}^0} - 1, \qquad (4)$$

where d_{110}^0 is the crystal lattice parameter corresponding to a temperature of 0°C, at which the spontaneous strains are equal to zero.

Figure 5 demonstrates the temperature dependences of the spontaneous strains calculated from the experimental data for the studied crystals Hg$_2$(Br,I)$_2$ according to relationships (3) and (4). It is clear that, above the phase transition temperature, the shear spontaneous strain is equal to zero [see formula (3)], whereas the isotropic strain in this temperature range varies linearly with temperature. At $T \leq T_c$, the temperature dependences of the strains for both the pure Hg$_2$Br$_2$ and mixed Hg$_2$(Br$_{0.88}$,I$_{0.12}$)$_2$ crystals are typical of structural phase transitions. The share ε_6^0 and isotropic ε_1^0 spontaneous strains ($T \leq T_c$) were determined as the difference between the experimental values and the background strains obtained by the extrapolation of the high-temperature dependence of ε toward the low-temperature range. In the case of the shear spontaneous strain ε_6^0, the background strain is equal to zero at any temperature [see formula (3)]. The temperature dependence of the
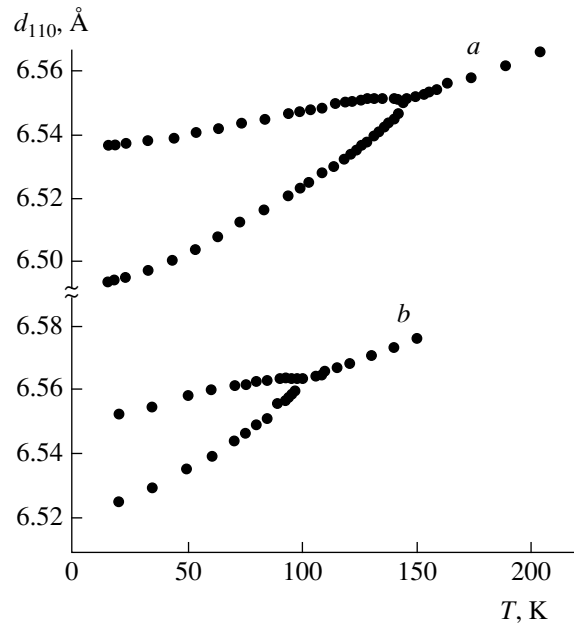

Fig. 4. Temperature dependences of the basal plane parameter d_{110} for crystals (*a*) Hg$_2$Br$_2$ and (*b*) Hg$_2$(Br$_{0.88}$,I$_{0.12}$)$_2$.
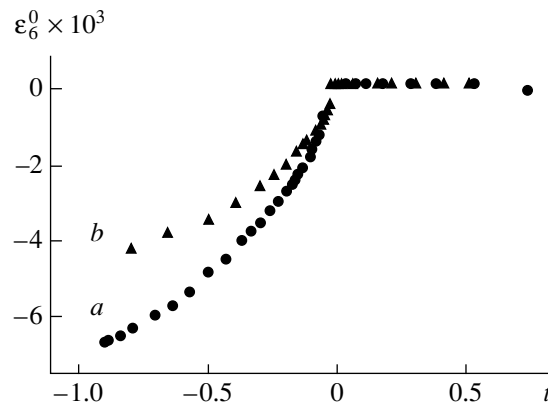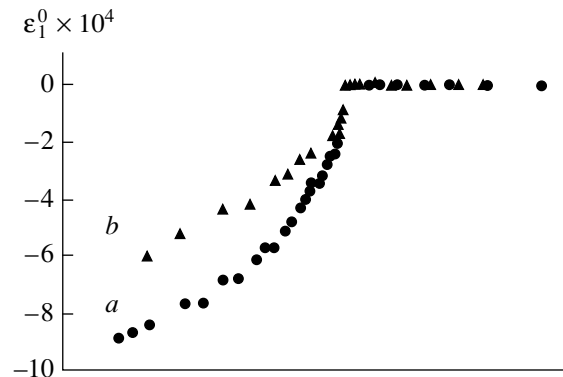

Fig. 5. Dependences of the isotropic ε_1^0 and share ε_6^0 spontaneous strains on the reduced temperature t for crystals (*a*) Hg$_2$Br$_2$ and (*b*) Hg$_2$(Br$_{0.88}$,I$_{0.12}$)$_2$.
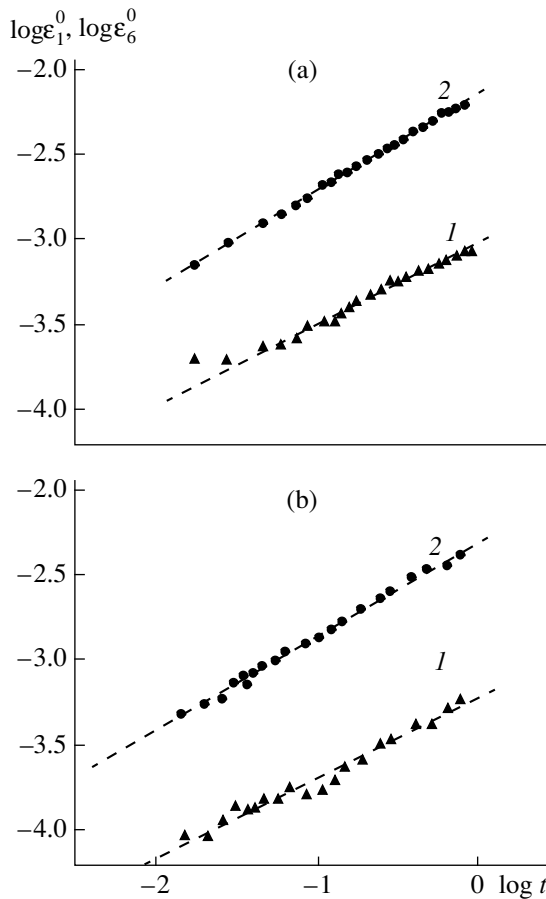
Fig. 6. Dependences of (*1*) isotropic ε_1^0 and (*2*) share ε_6^0 spontaneous strains on the reduced temperature *t* on the log–log scale for crystals (a) Hg_2Br_2 and (b) $Hg_2(Br_{0.88},I_{0.12})_2$. Dashed lines represent the linear approximation.

spontaneous strain ε_i^0 (*i* = 1 and 6) at $T \le T_c$ can be described by the following expression:

$$\varepsilon_i^0 = a_i t^{2\beta}, \tag{5}$$

where a_i is the constant multiplier, and 2β is the critical index.

Similar dependences on the log–log scale are displayed in Fig. 6. The experimental data for the studied crystals $Hg_2(Br,I)_2$ are described by the linear dependences (dashed lines in Fig. 6). The critical indices 2β determined from the slopes of the linear dependences are equal to 0.48 ± 0.08 (ε_1^0), 0.56 ± 0.05 (ε_6^0) and 0.46 ± 0.08 (ε_1^0), 0.55 ± 0.05 (ε_6^0) for the Hg_2Br_2 and $Hg_2(Br_{0.88},I_{0.12})_2$ crystals, respectively. It should be mentioned here that the critical indices describing the temperature dependences of the shear spontaneous strain ε_6^0 can be more precisely determined, because, in this case, there is no problem with the background (the background strain is absent), and the absolute values of ε_6^0 are almost one order of magnitude larger than those of the isotropic spontaneous strain ε_1^0.

5. RESULTS AND DISCUSSION

The investigations into the effects of phase transitions in the $Hg_2(Br,I)_2$ crystals demonstrate that the soft modes are observed in the Raman scattering spectra of the paraphase and the ferroelastic phase in both crystals under study. The $2\omega_{sm}$ overtone of the slowest soft *TA* branch at the *X* point of the Brillouin zone boundary predominantly manifests itself in the low-frequency spectra of the paraphase. The spectra of the ferroelastic phase are characterized by the ν_{sm} fundamental tone of the soft mode at the Brillouin zone center (the Γ point). The appearance of this overtone is associated with the phase transition or, in other words, with the doubling of the unit cell and the $X \longrightarrow \Gamma$ crossover in the Brillouin zone. The low-frequency spectra of the pure Hg_2Br_2 and mixed $Hg_2(Br_{0.88},I_{0.12})_2$ crystals are similar to each other. However, there are certain differences. Specifically, the spectra of the mixed $Hg_2(Br,I)_2$ crystals even at small degrees of doping show maxima (in both Stokes and anti-Stokes regions) marked by asterisks in Fig. 1, which are likely accounted for by the density of one-phonon states of the soft *TA* branch. Note that the main contribution is made by the vibrational states at the *X* point of the Brillouin zone. As should be expected, the frequencies of these maxima are approximately two times less than the frequencies of the corresponding overtones ($2\omega_{sm}$) of soft modes; they anomalously depend on the temperature and, similar to the overtone, are softened at $T \longrightarrow T_c$. The effect associated with the density of one-phonon states is caused by the disturbance of translational symmetry due to a random distribution of the bromine and iodine atoms in the anionic sublattice of mixed crystals. This disturbance is rather large and arises from a considerable difference in the ionic radii of bromine and iodine, which, upon replacement of bromine ions by iodine ions, can give rise to large local elastic stresses and produce conditions favorable for the nucleation of clusters of the low-temperature orthorhombic phase in the high-temperature tetragonal paraphase matrix. [Recall here that the ratio between the change in the phase transition temperature and the change in the external hydrostatic pressure for the Hg_2Br_2 crystals is equal to 46.8 K / kbar [8]. A similar strong dependence of the T_c temperature on the elastic stresses can also be expected for the mixed $Hg_2(Br,I)_2$ crystals at small degrees of substitution.]

A comparison of the intensity of the $2\omega_{sm}$ overtone of the soft mode (the *X* point of the Brillouin zone boundary) at temperatures $T > T_c$ and the intensity of the ν_{sm} fundamental tone (the Brillouin zone center) at $T < T_c$ in the Raman scattering spectra of the $Hg_2(Br,I)_2$ crystals demonstrates that the former intensity is approximately twenty times less than the latter intensity. This implies that the Landau phenomenological theory of phase transitions [9] is applicable over the entire temperature range under consideration. The crit-

ical indices characterizing the temperature behavior of soft modes at temperatures above and below T_c are also consistent with the Landau theory of second-order phase transitions. In the paraphase, the critical indices for the pure Hg_2Br_2 (0.50) and mixed $Hg_2(Br,I)_2$ (0.51) crystals are in complete agreement with the predicted value ($\beta' = 0.5$) given by the Landau theory in the case of the second-order phase transitions and weak first-order transitions close to the second-order structural transitions. However, at $T \leq T_c$, the β'' indices, which are equal to 0.34 and 0.33 for the pure Hg_2Br_2 and mixed $Hg_2(Br,I)_2$ crystals, respectively, can be interpreted only by invoking the model of phase transitions in the vicinity of the tricritical point, which we successfully applied earlier for the pure Hg_2Cl_2 and Hg_2Br_2 crystals [10].

Analysis of the experimental data on the orthorhombic splitting for the studied crystals $Hg_2(Br,I)_2$ (Fig. 4) shows that, at the same difference in temperatures T and T_c ($T \leq T_c$), the splitting brought about by the phase transition in the mixed $Hg_2(Br_{0.88},I_{0.12})_2$ crystal is less than that for the pure Hg_2Br_2 crystal. Since the spontaneous strains ε_i^0 are related to this splitting and the temperature dependence of the basal plane parameters for the ferroelastic phase, it can be expected that, over the entire temperature range covered, the values of ε_i^0 for the mixed $Hg_2(Br_{0.88},I_{0.12})_2$ crystals are less than those for the pure Hg_2Br_2 crystals (see Fig. 5). The smaller spontaneous strains ε_i^0 for the mixed $Hg_2(Br_{0.88},I_{0.12})_2$ crystals are explained by the disordering of anionic sublattice and the appearance of substantial random elastic stresses and strains upon substitution of iodine ions for bromine ions. It should be noted here that the mechanism of the phase transition in the $Hg_2(Br,I)_2$ crystals is primarily determined by the shear spontaneous strain ε_6^0, which is almost one order of magnitude larger than the isotropic spontaneous strain ε_1^0 over the entire temperature range studied ($T \leq T_c$), including helium temperatures. Let us dwell briefly on the critical indices 2β obtained by analyzing the temperature dependences of the spontaneous strains ε_i^0. As can be seen, their values are close to 0.5, which is characteristic of the phase transitions occurring near the tricritical

point. It should be recalled that the temperature behavior of the soft modes in these crystals and the relevant critical indices can be interpreted only by invoking the model of phase transitions in the vicinity of the tricritical point.

REFERENCES

1. H. Mark and J. Steinbach, Z. Kristallogr. **64**, 78 (1926).

2. *Proceedings of the Second International Symposium on Univalent Mercury Halides, Trutrov, CSFR, 1989* (Trutrov, 1989).

3. A. A. Kaplyanskiĭ, Yu. F. Markov, and Ch. Barta, Izv. Akad. Nauk SSSR, Ser. Fiz. **43**, 1641 (1979); Ch. Barta, A. A. Kaplyanskiĭ, V. V. Kulakov, *et al.*, Zh. Éksp. Teor. Fiz. **70**, 1429 (1976) [Sov. Phys. JETP **43**, 744 (1976)].

4. Ch. Barta, A. A. Kaplyanskiĭ, Yu. F. Markov, *et al.*, Fiz. Tverd. Tela (Leningrad) **27**, 2500 (1985) [Sov. Phys. Solid State **27**, 1497 (1985)].

5. G. F. Dobrzhanskii, A. A. Kaplyanskii, M. F. Limonov, *et al.*, Ferroelectrics **48**, 69 (1983).

6. G. M. Zinger, Yu. F. Markov, and V. V. Shabalin, Fiz. Tverd. Tela (Leningrad) **29**, 3620 (1987) [Sov. Phys. Solid State **29**, 2073 (1987)].

7. Yu. F. Markov and A. Sh. Turaev, Fiz. Tverd. Tela (S.-Peterburg) **37**, 2133 (1995) [Phys. Solid State **37**, 1160 (1995)].

8. A. A. Kaplyanskiĭ, Yu. F. Markov, V. Yu. Mirovitskiĭ, *et al.*, Fiz. Tverd. Tela (Leningrad) **27**, 223 (1985) [Sov. Phys. Solid State **27**, 133 (1985)].

9. *Light Scattering near the Phase Transition Points*, Ed. by G. Kamminz and A. P. Levanyuk (Nauka, Moscow, 1990).

10. M. E. Boiko, Yu. F. Markov, V. S. Vikhnin, *et al.*, Ferroelectrics **130**, 263 (1992).

Translated by O. Borovik-Romanova

LOW-DIMENSIONAL SYSTEMS AND SURFACE PHYSICS

Two-Particle States in the 2D Hubbard model

A. S. Saakyan

Armenian State Engineering University, 375009 Yerevan, Armenia
e-mail: root@yeriac.arminco.com

Abstract—An exact solution is proposed for the problem of two singlet electrons (zero-spin bosons) interacting through a Hubbard-type potential on a bounded quadratic lattice. Exact two-particle states and the energy spectrum are constructed. © 2000 MAIK "Nauka/Interperiodica".

1. Interest in the two-particle problem on a low-dimensional bounded lattice is provoked by the search for mechanisms of high-temperature superconductivity [1], the study of magnetic properties of strongly correlated electron systems [2], and the problem of zero-point defectons in adsorbed He^3–He^4 monolayers on the graphite surface [3]. The properties of these systems are investigated on the basis of lattice models with δ-interaction (Hubbard-type models, the model of zero-spin lattice bosons, etc.) [4, 5]. The knowledge of exact two-particle states in these models allows us to investigate the effective two-particle interaction in a many-particle system and a possible rearrangement of the ground state of the system associated with this interaction [6]. Exact two-particle states are known only for a 1D bounded lattice [7], while exact results for a 2D lattice have not been obtained. Chen and Mei [8] studied two-particle states on 1D and 2D bounded Hubbard lattices by using the variational method, while Dong and Yang [9] investigated bound states on 2D and 3D lattices; however, the Lifshitz approach used does not lead to exact results in the case of high dimensions.

In this paper, we consider the problem of two Hubbard electrons (δ-interacting zero-spin bosons) on a quadratic $N \times N$ lattice. Exact two-particle states and the energy spectrum are constructed. The lattice is assumed to coil into a torus, ensuring the fulfillment of the cyclic boundary conditions.

2. In the center-of-mass system, the Schrödinger equation for two particles on a quadratic lattice has the form

$$-t(\Delta_x^2 + \Delta_y^2)\Psi(x, y) + U\delta_{x0}\delta_{y0}\Psi(x, y) = E\Psi(x, y), \tag{1}$$

where t is the tunneling amplitude, U is the δ-interaction amplitude, $\Delta_{x,y}^2$ are the second-order finite-difference operators, and x and y are the components of the 2D discrete position vector describing the relative motion.

Henceforth, we shall assume that the eigenvalues are parametrized as follows:

$$E = -4t(\cos p_1 + \cos p_2). \tag{2}$$

We divide the coordinate plane into the four regions: I ($x < 0, y < 0$), II ($x > 0, y > 0$), III ($x < 0, y > 0$), and IV ($x > 0, y < 0$) and seek the wave function in the form of a superposition of plane waves in each of the four regions:

$$\Psi_{\mathrm{I}}(x, y) = A_1 e^{i(p_1 x + p_2 y)} + A_2 e^{-i(p_1 x + p_2 y)}$$
$$+ A_3 e^{i(p_1 x - p_2 y)} + A_4 e^{-i(p_1 x - p_2 y)},$$

$$\Psi_{\mathrm{II}}(x, y) = B_1 e^{i(p_1 x + p_2 y)} + B_2 e^{-i(p_1 x + p_2 y)}$$
$$+ B_3 e^{i(p_1 x - p_2 y)} + B_4 e^{-i(p_1 x - p_2 y)},$$

$$\Psi_{\mathrm{III}}(x, y) = C_1 e^{i(p_1 x + p_2 y)} + C_2 e^{-i(p_1 x + p_2 y)}$$
$$+ C_3 e^{i(p_1 x - p_2 y)} + C_4 e^{-i(p_1 x - p_2 y)}, \tag{3}$$

$$\Psi_{\mathrm{IV}}(x, y) = D_1 e^{i(p_1 x + p_2 y)} + D_2 e^{-i(p_1 x + p_2 y)}$$
$$+ D_3 e^{i(p_1 x - p_2 y)} + D_4 e^{-i(p_1 x - p_2 y)}.$$

We must impose the following conditions on wave functions (3):

$$\Psi_{\mathrm{I}}(-x, -y) = \Psi_{\mathrm{II}}(x, y),$$
$$\Psi_{\mathrm{III}}(-x, -y) = \Psi_{\mathrm{IV}}(x, y), \tag{4}$$

because the states Ψ are also eigenfunctions of the parity operator.

Conditions (4) and expressions (3) imply that

$$B_2 = A_1, \quad B_1 = A_2, \quad B_4 = A_3, \quad B_3 = A_4,$$
$$D_2 = C_1, \quad D_1 = C_2, \quad D_4 = C_3, \quad D_3 = C_4. \tag{5}$$

We also take into account the fact that the wave functions must coincide at the boundaries of the regions, i.e.,

$$\Psi_I(0, y) = \Psi_{IV}(0, y); \quad \Psi_{III}(0, y) = \Psi_{IV}(0, y);$$
$$\Psi_I(x, 0) = \Psi_{III}(x, 0); \quad \Psi_{II}(x, 0) = \Psi_{IV}(x, 0), \tag{6}$$

so that we ultimately have

$$A_1 + A_4 = C_2 + C_3, \quad A_1 + A_3 = C_1 + C_3,$$
$$A_2 + A_3 = C_1 + C_4, \quad A_2 + A_4 = C_2 + C_4. \tag{7}$$

Among other things, these conditions imply that the wave functions (3) coincide at zero.

Substituting expressions (3) into equation (1) and taking into account the parametrization (2), we obtain the following equations:

$$\left[-\frac{\eta}{2} - i(\sin p_1 + \sin p_2)\right]A_1$$

$$+ \left[-\frac{\eta}{2} + i(\sin p_1 + \sin p_2)\right]A_2$$

$$\hspace{5cm} (8)$$

$$+ \left[-\frac{\eta}{2} - i(\sin p_1 - \sin p_2)\right]A_3$$

$$+ \left[-\frac{\eta}{2} + i(\sin p_1 - \sin p_2)\right]A_4 = 0,$$

$$\left[-\frac{\eta}{2} - i(\sin p_1 - \sin p_2)\right]C_1$$

$$+ \left[-\frac{\eta}{2} + i(\sin p_1 - \sin p_2)\right]C_2$$

$$+ \left[-\frac{\eta}{2} - i(\sin p_1 + \sin p_2)\right]C_3 \hspace{1.5cm} (9)$$

$$+ \left[-\frac{\eta}{2} + i(\sin p_1 + \sin p_2)\right]C_4 = 0,$$

$$\eta = \frac{U}{2t}.$$

We introduce vectors

$$n_i\left(-\frac{\eta}{2} - i(\sin p_1 + \sin p_2), \; -\frac{\eta}{2} + i(\sin p_1 + \sin p_2),\right.$$

$$\left. -\frac{\eta}{2} - i(\sin p_1 - \sin p_2), \; -\frac{\eta}{2} + i(\sin p_1 - \sin p_2)\right),$$

$$a_i(A_1, A_2, A_3, A_4), \quad c_i(C_3, C_4, C_1, C_2).$$

In this case, equations (8) and (9) assume the form

$$n_i a_i = 0, \quad n_i c_i = 0, \tag{10}$$

implying that the vectors a_i and c_i are linearly dependent:

$$c_i = \lambda a_i. \tag{11}$$

Supplementing this relation with the condition of the equality of the wave functions (3) at zero, we find that $\lambda = 1$, and, hence, conditions (7) are satisfied automatically.

Carrying out complex conjugation in equations (8) and (9), we can easily see that

$$A_2^* = \mu A_1, \quad A_1^* = \mu A_2,$$
$$A_3^* = \mu A_4, \quad A_4^* = \mu A_3, \tag{12}$$

whence

$$|A_1|^2 = |A_2|^2, \quad |A_3|^2 = |A_4|^2, \quad |\mu|^2 = 1. \tag{13}$$

We write these relations in the form

$$A_1 = |A_1|e^{i\varphi_1}, \quad A_2 = |A_1|e^{i\varphi_2}, \quad A_3 = |A_3|e^{i\varphi_3},$$
$$A_4 = |A_3|e^{i\varphi_4}, \quad \mu = e^{i\varphi_0}. \tag{14}$$

In this case, equations (8) and (9) can be written in the form

$$\alpha|A_1|\cos\left(\delta_1 + \varphi_1 + \frac{\varphi_0}{2}\right)$$
$$+ \beta|A_2|\cos\left(\delta_2 + \varphi_2 + \frac{\varphi_0}{2}\right) = 0, \tag{15}$$

where

$$\alpha, \beta = \left[\frac{\eta^2}{4} + (\sin p_1 \pm \sin p_2)^2\right]^{1/2},$$
$$\delta_{1,2} = -\arctan\frac{\eta}{2}(\sin p_1 \pm \sin p_2). \tag{16}$$

Equation (15) holds if we put

$$\varphi_{1,2} = -\delta_{1,2} - \frac{\varphi_0}{2} + \frac{\pi}{2} \tag{17}$$

and choose $\varphi_0 = \pi$ to satisfy the boundary condition

$$\lim_{\substack{U \to \infty \\ x, y \to 0}} \Psi(x, y) = 0, \tag{18}$$

according to which, two particles cannot get to the same lattice site in the case of infinitely strong repulsion.

Then the wave functions (3) assume the form

$$\Psi_{I, II} = |A_1|\cos(p_1 x + p_2 y \mp \delta_1)$$
$$+ |A_3|\cos(p_1 x - p_2 y \mp \delta_2),$$
$$\Psi_{III, IV} = |A_1|\cos(p_1 x - p_2 y \mp \delta_1) \quad (19)$$
$$+ |A_3|\cos(p_1 x + p_2 y \mp \delta_2).$$

Here, we have changed the notation of the products $\alpha|A_1|$ and $\beta|A_3|$ for $|A_{1, 3}|$.

It should be observed that the transposition of the parameters p_1 and p_2 leads to new two-particle states corresponding to the same eigenvalues, i.e.,

$$\Psi'_{I, II} = |A'_1|\cos(p_2 x + p_1 y \mp \delta_1)$$
$$+ |A'_3|\cos(p_2 x - p_1 y \pm \delta_2),$$
$$\Psi'_{III, IV} = |A'_1|\cos(p_2 x - p_1 y \mp \delta_1) \quad (20)$$
$$+ |A'_3|\cos(p_2 x + p_1 y \pm \delta_2),$$

where we have taken into account that

$$\delta_1(p_2, p_1) = \delta_1(p_1, p_2),$$
$$\delta_2(p_2, p_1) = -\delta_2(p_1, p_2). \quad (21)$$

Consequently, the general solution of equation (1) should be presented as a superposition of the two-particle states (19) and (20):

$$\Psi(x, y) = \Psi(p_1 x; p_2 y) + \Psi(p_2 x; p_1 y). \quad (22)$$

We impose on the wave function (21) the constraints

$$\Psi_I(y, -x) = \Psi_{IV}(x, y), \quad \Psi_{II}(y, -x) = \Psi_{III}(x, y),$$
$$\Psi_{III}(y, -x) = \Psi_I(x, y), \quad \Psi_{IV}(y, -x) = \Psi_{II}(x, y). \quad (23)$$

These relations are accounted for by the following circumstance: the rotation of the coordinate axes through the angle $\theta = \pi/2$ should not change the state of the system, while the rotation through $2\theta = \pi$ leads to (4) (in view of the symmetry of a quadratic lattice).

A direct verification shows that $|A_1| = |A'_1|$ and $|A_3| = |A'_3|$. Moreover, the transformation $p_1 \longrightarrow -p_1$ or $p_2 \longrightarrow -p_2$ must transform the wave function into itself. This constraint is due to the fact that the wave function is single-valued in each of the four quadrants. It gives $|A_1| = |A_3|$, and hence we obtain the following expressions for $\Psi(x, y)$ correct to an arbitrary factor:

$$\Psi_{I, II} = \cos(p_1 x + p_2 y \mp \delta_1)$$
$$+ \cos(p_1 x - p_2 y \mp \delta_2) + \cos(p_2 x + p_1 y \mp \delta_1)$$
$$+ \cos(p_2 x - p_1 y \pm \delta_2),$$
$$\Psi_{III, IV} = \cos(p_1 x - p_2 y \mp \delta_1) \quad (24)$$
$$+ \cos(p_1 x + p_2 y \mp \delta_2) + \cos(p_2 x - p_1 y \mp \delta_1)$$
$$+ \cos(p_2 x + p_1 y \pm \delta_2).$$

Thus, two-particle states can be presented as a superposition of standing waves, while on an infinite lattice they can be expressed in terms of Bessel's functions [10]. In our opinion, it would be interesting to relate the states (24), derived here, to expressions (16) from [10] for the lattice constant tending to zero or the lattice size tending to infinity.

We must impose cyclic boundary conditions on the states (24). For this purpose, note that (24) can be written in the form

$$\Psi = \Psi_I\theta(-x)\theta(-y) + \Psi_{II}\theta(x)\theta(y)$$
$$+ \Psi_{III}\theta(-x)\theta(y) + \Psi_{IV}\theta(x)\theta(-y), \quad (25)$$

where $\theta(x)$ is a Heaviside function.

This obviously leads to

$$\Psi_I(x + N, y + N) + \Psi_{II}(x + N, y + N)$$
$$+ \Psi_{III}(x + N, y + N) + \Psi_{IV}(x + N, y + N) \quad (26)$$
$$= \Psi_{II}(x, y),$$

and relations (24) and (26) can be used to derive the following equations for $p_{1, 2}$:

$$p_1 = \frac{\delta_1 + \delta_2}{2N} + \frac{\pi(n + m)}{2N},$$
$$p_2 = \frac{\delta_1 - \delta_2}{2N} + \frac{\pi(n - m)}{2N}, \quad (27)$$

where $n, m = 0, 1, ..., N - 1$.

Thus, the energy spectrum is defined completely by relations (2) and (27).

The ground-state energy of the system is

$$E_0 = -8t\cos\frac{\delta_1}{2N}\cos\frac{\delta_2}{2N} \quad (n = m = 0). \quad (28)$$

In particular, for $U = +\infty$, we have

$$E_0 = -8t\cos^2\frac{\pi}{4N} \quad (29)$$

or, for an asymptotically large N,

$$E_0 = -8t\left(1 - \frac{\pi^2}{16N^2}\right). \quad (30)$$

The variational calculations made by Chen and Mei [8] prove that, for $N \gg 1$, the ground-state energy can be written in the form

$$E_0 = -8t\left(1 - \frac{\alpha}{N^2}\right), \quad (31)$$

where, in particular, for $U/t = 10$, the parameter α varies from 0.618 to 0.682 depending on the size of the lattice, and it increases slowly with U/t. The results (29) and (30), obtained here, prove that the energy of the true ground state is lower than the variational value; besides, the parameter α is independent of the lattice size in the limit $U = +\infty$.

REFERENCES

1. J. C. Bednorz and K. A. Müller, Z. Phys. B **64**, 189 (1986).
2. Y. Nagaoka, Phys. Rev. B **141**, 392 (1966).
3. M. Bretz, Phys. Rev. Lett. **38**, 501 (1977).
4. J. Hubbard, Proc. R. Soc. London A **276**, 238 (1963); *ibid.* **277**, 237 (1964).
5. C. N. Yang, Phys. Rev. Lett. **19**, 1312 (1967).
6. A. N. Kocharyan and A. S. Saakyan, Fiz. Tverd. Tela (S.-Peterburg) **40**, 761 (1998) [Phys. Solid State **40**, 701 (1998)].
7. A. N. Kocharyan and A. S. Saakyan, Fiz. Tverd. Tela (S.-Peterburg) **40**, 366 (1998) [Phys. Solid State **40**, 336 (1998)].
8. L. Chen and C. Mei, Phys. Rev. B **39**, 9006 (1989).
9. Sh. Dong and Ch. N. Yang, Rev. Math. Phys. **146**, 139 (1989).
10. G. A. Vardanyan and A. S. Saakyan, Zh. Éksp. Teor. Fiz. **88**, 1079 (1985) [Sov. Phys. JETP **61**, 634 (1985)].

Translated by N. Wadhwa

LOW-DIMENSIONAL SYSTEMS
AND SURFACE PHYSICS

Two-Particle Correlations on a 1D Lattice
in a Constant Magnetic Field

A. S. Saakyan

Armenian State Engineering University, 375009 Yerevan, Armenia
e-mail: root@yeriac.arminco.com
Received in final form November 4, 1999

Abstract—The problem of two particles interacting through the Hubbard potential on a 1D finite lattice in a constant uniform magnetic field is solved. Exact wave functions are determined, and an equation for the energy spectrum is constructed and analyzed. The possibility of a field-induced singlet–triplet transition is demonstrated. © 2000 MAIK "Nauka/Interperiodica".

1. Correlations between particles are important in explaining various effects in many-particle systems. Some models taking these correlations into account can be exactly solved in the thermodynamic limit in the 1D case [1–3]. However, in certain cases, the transition to the thermodynamic limit is incorrect (as for a finite number of particles), and the problem should be solved on a bounded lattice. This problem is of importance, for example, in relation to the recent discovery of atomic clusters of rhodium possessing strong ferromagnetism, which is not observed in bulk samples [4]. The analysis of the two-particle problem on a bounded lattice is also important for determining the mechanisms of high-temperature superconductivity, for elucidating the effective two-particle interactions in a many-particle system, and for analyzing magnetic properties of strongly correlated systems [5–8].

In this communication, we consider the behavior of two interacting particles ($U > 0$) on a finite 1D lattice in a constant uniform magnetic field. A simple model used here allows us to obtain exact solutions for two-particle states and to analyze the energy spectrum as a function of the magnetic field strength.

2. We choose the Hamiltonian of the system in the form

$$H = \sum_{n\sigma} \varepsilon_{0\sigma} a_{n\sigma}^+ a_{n\sigma} - \gamma H \sum_n (a_{n\uparrow}^+ a_{n\uparrow} - a_{n\downarrow}^+ a_{n\downarrow})$$

$$- t \sum_{nl\sigma} a_{n+l\sigma}^+ a_{n\sigma} + \frac{U}{2} \sum_{\substack{nn' \\ \sigma\sigma'}} \delta_{nn'} \delta_{\sigma,-\sigma'} a_{n\sigma}^+ a_{n\sigma} a_{n'\sigma'}^+ a_{n'\sigma'}. \tag{1}$$

Here, σ is the spin index; $\varepsilon_{0\sigma}$ are the centers of the bands; $2t$ is the width of the energy bands, which is the same for the two particles; and U is the amplitude of the Hubbard interaction. Henceforth, we shall assume that the term corresponding to the spin–magnetic-field interaction is included in the first addend in (1), and the

same notation will be used: $\varepsilon_{0\sigma} \mp \gamma H \longrightarrow \varepsilon_{0\sigma}$. Thus, the energy bands are separated, the separation between the band centers being $\varepsilon_{01} - \varepsilon_{02}$. Carrying out the transformation

$$b_{n1,2} = \frac{1}{\sqrt{2}}(a_{n\uparrow} \pm a_{n\downarrow}) \tag{2}$$

in the Hamiltonian (1), we obtain

$$H = -t \sum_{nls} b_{n+ls}^+ b_{ns} + g \sum_{ss'n} \delta_{s,-s'} b_{ns}^+ b_{ns'}$$

$$+ \frac{U}{2} \sum b_{ns}^+ b_{ns} b_{ns'}^+ b_{ns'} \delta_{s,-s'}, \tag{3}$$

where s, s' are the pseudospin indices, the energy is measured from the value $\varepsilon = (1/2)(\varepsilon_{01} + \varepsilon_{02})$, and $g = (1/4)(\varepsilon_{01} - \varepsilon_{02})$.

Thus, we arrive at the pattern of two mutually scattering pseudosinglet fermions in the band; the system displays a sort of hybridization at a lattice site, which is dependent on the magnetic field.

We present two-particle states of the Hamiltonian (3) in the form of the following expansion in terms of the occupation-number states:

$$|2\rangle = \sum_{\substack{ss' \\ nn'}} \Psi(s, n; s', n') b_{n,s}^+ b_{n',s'}^+ |0\rangle, \tag{4}$$

where Ψ is the first-quantized two-particle wave function. Applying the operator (3) to the state (4), we arrive at the Schrödinger equation

$$-t(\Delta_1^2 + \Delta_2^2)\Psi(n_1, s_1; n_2, s_2)$$

$$+ g \sum_s [\Psi(n_1, s; n_2, s_2)\delta_{s,-s_1} + \Psi(n_1, s_1; n_2, s)\delta_{s,-s_2}]$$

$$+ U\delta_{n_1,n_2}\delta_{s_1,-s_2}\Psi(n_1, s_1; n_2, s_2) = E\Psi(n_1, s_1; n_2, s_2), \tag{5}$$

where $\Delta_{1,2}^2$ are second-order finite-difference operators

with respect to the variables $n_{1,2}$. We write equations (5) in an explicit form:

$$-t(\Delta_1^2 + \Delta_2^2)\Psi_1(n_1, n_2) + U\delta_{n_1, n_2}\Psi_1(n_1, n_2)$$
$$+ g[\Psi_3(n_1, n_2) + \Psi_4(n_1, n_2)] = E\Psi_1(n_1, n_2),$$

$$-t(\Delta_1^2 + \Delta_2^2)\Psi_2(n_1, n_2) + U\delta_{n_1, n_2}\Psi_2(n_1, n_2)$$
$$+ g[\Psi_3(n_1, n_2) + \Psi_4(n_1, n_2)] = E\Psi_2(n_1, n_2),$$
$$\quad (6)$$
$$-t(\Delta_1^2 + \Delta_2^2)\Psi_3(n_1, n_2)$$
$$+ g[\Psi_1(n_1, n_2) + \Psi_2(n_1, n_2)] = E\Psi_3(n_1, n_2),$$

$$-t(\Delta_1^2 + \Delta_2^2)\Psi_4(n_1, n_2)$$
$$+ g[\Psi_1(n_1, n_2) + \Psi_2(n_1, n_2)] = E\Psi_4(n_1, n_2).$$

Here, $\Psi_{1,2}(n_1, n_2)$ and $\Psi_{3,4}(n_1, n_2)$ are the wave functions corresponding to the pseudosinglet and pseudotriplet states, respectively.

Equations (6) can be written in the matrix form:

$$-t\hat{\Delta}^2\hat{\Psi} + \hat{g}\hat{\Psi} + \hat{U}\Psi = \hat{E}\hat{\Psi}, \qquad (7)$$

where $\hat{\Delta}^2 = (\Delta_1^2 + \Delta_2^2)\hat{I}$, $\hat{I}$ is a 4×4 unit matrix, $\hat{U} = U\delta_{n_1, n_2}\hat{I}$, $\hat{E} = E\hat{I}$, and

$$\hat{g} = \begin{pmatrix} 0 & 0 & g & g \\ 0 & 0 & g & g \\ g & g & 0 & 0 \\ g & g & 0 & 0 \end{pmatrix}, \quad \Psi = \begin{pmatrix} \Psi_1 \\ \Psi_2 \\ \Psi_3 \\ \Psi_4 \end{pmatrix}. \qquad (8)$$

We write a solution of equation (7) in the form

$$\hat{\Psi} = e^{iQ/2(n_1 + n_2)}\sum_k \hat{\Psi}(k, Q)e^{ik(n_1 - n_2)}, \qquad (9)$$

where Q is the quasi-momentum of the center of mass of two particles, k is the "bare" quasi-momentum of the relative motion, and $\hat{\Psi}(k, Q)$ is the Fourier transform of the column vector (8). Here and below, we assume that cyclic boundary conditions are satisfied, so that $k = 2\pi n/N$, $n = 0, 1, ..., N - 1$.

Substituting (9) into (7) and carrying out transformations, we obtain

$$\hat{\Psi}(k, Q) = -(\hat{L} + \hat{g} - \hat{E})\hat{\tau},$$

$$\hat{L}(k, Q) = L(k, Q)\hat{I}, \qquad (10)$$

$$L(k, Q) = -2t[\cos(k + Q/2) + \cos(k - Q/2)],$$

and the column vector $\hat{\tau}$ can be determined from the self-consistency condition

$$\hat{\tau} = -\sum_k (\hat{L} + \hat{g} - \hat{E})^{-1}\hat{U}\hat{\tau}. \qquad (11)$$

The condition for the existence of a nonzero solution of system (11) is the equality of the determinant to zero:

$$\det \left\| \hat{I} + \sum_k (\hat{L} + \hat{g} - \hat{E})^{-1}\hat{U} \right\| = 0. \qquad (12)$$

This condition leads to the following equations for determining the eigenvalues of the problem (Lifshitz–Yang equations):

$$\frac{1}{N}\sum_k \left[\frac{1}{L(k, Q) - E - 2g} + \frac{1}{L(k, Q) - E + 2g} \right]$$
$$= -\frac{2}{U}, \qquad (13)$$

$$\frac{1}{N}\sum_k \frac{1}{L(k, Q) - E} = -\frac{1}{U}. \qquad (14)$$

Solving the system of the homogeneous equations (11), we obtain

$$\tau_2 = \frac{1 + UA}{UB}\tau_1, \quad \tau_{3,4} = UC(\tau_1 + \tau_2), \qquad (15)$$

where

$$A = \frac{1}{N}\sum_k \frac{1}{L(k, Q) - E}\left\{ 1 + \frac{2\eta^2}{[L(k, Q) - E]^2 - 4g^2} \right\},$$

$$B = \frac{1}{N}\sum_k \frac{1}{L(k, Q) - E}\frac{2\eta^2}{[L(k, Q) - E]^2 - 4g^2}, \qquad (16)$$

$$C = \frac{1}{N}\sum_k \frac{\eta}{[L(k, Q) - E]^2 - 4g^2}.$$

It can be easily seen that the condition (12) for the existence of nonzero solutions or, what is the same, the condition for the solubility of equations (13) and (14) has the form

$$U(A \pm B) = -1. \qquad (17)$$

Taking into account (15) and (16), we can write the

wave functions $\Psi_{1,2}(n_1, n_2)$ in the form

$$\Psi_{1,2}(n_1, n_2)$$

$$= e^{iQ/2(n_1+n_2)} \left\{ \mp \frac{U}{2N}(\tau_1 - \tau_2) \sum_k \frac{e^{ikn}}{L(k, Q) - E} \right.$$

$$- \frac{U}{4N}(\tau_1 + \tau_2) \sum_k \left[\frac{e^{ikn}}{L(k, Q) - E - 2g} \right. \qquad (18)$$

$$\left. \left. + \frac{e^{ikn}}{L(k, Q) - E + 2g} \right] \right\}.$$

For the solutions of equation (17), we obtain

$$\tau_2 = -\tau_1, \quad \tau_{3,4} = 0, \qquad (19)$$

and, finally,

$$\Psi_{1,2}(n_1, n_2) = \mp \frac{U\tau}{N} \sum_k \frac{e^{ikn}}{L(k, Q) - E} e^{iQ/2(n_1 + n_2)}, \qquad (20)$$

$$\Psi_{3,4}(n_1, n_2) = 0.$$

The constant τ can be determined from the self-consistency condition defined by equation (8) from [6] and has the form

$$\tau = U \left(1 + \frac{U}{N} \sum_k \frac{1}{L(k, Q) - E} \right)^{-1}. \qquad (21)$$

Thus, the wave functions of two-particle states coincide in form with those obtained in [6], but the eigenvalues E are determined from (13).

If we try to determine the eigenvalues from (14), we will find that the t-matrix $U\tau_3$ diverges for $U = +\infty$; i.e., the states defined by (14) are deprived of any physical meaning.

Parametrizing the eigenvalues of the problem in accordance with

$$E = -4t \cos Q/2 \cos p, \qquad (22)$$

we obtain

$$\Psi(n_1, n_2)$$

$$= e^{iQ/2(n_1+n_2)} \begin{cases} \cos[p(n_1 - n_2) - \delta], & n_1 < n_2 \\ \cos[p(n_1 - n_2) + \delta], & n_1 > n_2, \end{cases} \qquad (23)$$

and the scattering phase is given by

$$\delta = \arctan \frac{U}{2t \sin p \cos Q/2}. \qquad (24)$$

Analyzing equation (13), we note, in particular, that, in the region $|\cos p| < 1 - \eta$ ($\eta < 1$), it can be reduced to

the form

$$\frac{\cot \frac{Np_1}{2}}{\sin p_1} + \frac{\cot \frac{Np_2}{2}}{\sin p_2} = \frac{2t}{U} \cos Q/2, \qquad (25)$$

$$\cos p_{1,2} = \cos p \pm \eta, \quad \eta = \frac{g}{2t \cos Q/2}$$

by using a method similar to that described in [6].

The denominator $\sin p_1$ in the expression on the left-hand side of equation (25) vanishes for $p_0 = \arcsin \sqrt{\eta(2 - \eta)}$; expanding it into a power series in $p - p_0$, we obtain

$$p = \frac{2\pi n}{N} + \frac{2}{N} \arctan \frac{U}{2^{11/3} t \sqrt{p - p_0}}. \qquad (26)$$

Henceforth, we assume the parameter η to be small ($\eta \ll 1$). Taking into account the fact that expression (26) is transformed into

$$p_0 = \frac{2\pi n}{N} + \frac{\pi}{N} \qquad (27)$$

under the substitution $p = p_0$ and that (26) holds in the neighborhood of p_0, we can write it, to a fairly high degree of accuracy, in the form

$$p = \frac{2\pi n}{N} + \frac{\pi}{N} - \frac{2^{11/3} t}{\pi N U} \sqrt{\pi^2/N^2 - 2\eta}. \qquad (28)$$

Expression (27) implies that, for the value of the parameter $\eta = \pi^2/2N^2$, the particles acquire a rigid core; i.e., the scattering phase becomes $\delta = \pi/N$, and the wave function $\Psi_{1,2}$ assumes the form

$$\Psi_{1,2}(n_1, n_2) \sim \sin \frac{\pi}{N}(n_1 - n_2). \qquad (29)$$

The values (28) of the parameter p correspond to the following ground-state energy of the two-particle system:

$$E = -4t \cos \frac{\pi}{N} - \frac{32}{N^2} \frac{t^2}{U} \sqrt{\pi^2/N^2 - 2\eta}. \qquad (30)$$

In the region $\eta \gg 1$, the sum (13) immediately leads to $E = \varepsilon_0 - 2\gamma H$, and the magnetization of the system is $M = 2\gamma$. Thus, the transition described by (28) and (30) obviously corresponds to a transition to the triplet state.

It should be noted that the singlet–triplet transition described here occurs for any finite value of the Hubbard interaction potential. The case when $U = +\infty$ should be analyzed separately.

It should also be noted that the canonical transformation (2) does not mix up even and odd solutions; this follows from the commutativity of the Hamiltonians (1) and (3) with the parity operator, which enables us to speak not of pseudo-, but of true singlet and triplet states.

REFERENCES

1. T. D. Lee and C. N. Yang, Phys. Rev. **113**, 1406 (1959).

2. C. N. Yang, Phys. Rev. Lett. **19**, 1312 (1967).

3. E. H. Lieb and F. Y. Wu, Phys. Rev. Lett. **64**, 1445 (1968).

4. L. Chen and Ch. Mei, Phys. Rev. B **39**, 9006 (1989).

5. L. A. Bloomfield, A. I. Cox, and I. C. Louderback, Bull. Am. Phys. Soc. **39**, 540 (1994).

6. A. N. Kocharyan and A. S. Saakyan, Fiz. Tverd. Tela (St. Petersburg) **40**, 366 (1998) [Phys. Solid State **40**, 336 (1998)].

7. A. N. Kocharyan and A. S. Saakyan, Fiz. Tverd. Tela (St. Petersburg) **40**, 761 (1998) [Phys. Solid State **40**, **701** (1998)].

8. A. N. Kocharian, G. R. Reich, and A. S. Saakian, Physica B **206–207**, 732 (1995).

Translated by N. Wadhwa

LOW-DIMENSIONAL SYSTEMS
AND SURFACE PHYSICS

Self-Propagating High-Temperature Synthesis in Pt/Co/MgO(001) Epitaxial Thin Films

V. G. Myagkov*, L. A. Li*, L. E. Bykova*, I. A. Turpanov*, P. D. Kim*, G. V. Bondarenko*, and G. N. Bondarenko**

* Kirenskiǐ Institute of Physics, Siberian Division, Russian Academy of Sciences,
Akademgorodok, Krasnoyarsk, 660036 Russia
** Institute of Chemistry and Chemical Technology, Siberian Division, Russian Academy of Sciences,
Akademgorodok, Krasnoyarsk, 660036 Russia
e-mail: kim@post.krascience.rssi.ru
e-mail: kim@iph.krasnoyarsk.su
Received July 9, 1999

Abstract—The self-propagating high-temperature synthesis in the two-layer and multilayer Pt/Co(001) thin films has been investigated. It is shown that the initiation of the synthesis occurs at temperatures of 770–820 K. After the synthesis in the two-layer film samples, the PtCo(001) disordered phase exhibits an epitaxial growth at the interface between cobalt and platinum layers. In the multilayer Pt/Co(001) thin films, the self-propagating high-temperature synthesis also brings about the formation of the PtCo(001) disordered phase on the MgO(001) surface. Further annealing at a temperature of 870 K for 4 h results in the transition of the PtCo(001) disordered phase to the ordered phase. Rapid thermal annealing of the Pt/Co(001) multilayer films at a temperature of 1000 K leads to the formation of the $CoPt_3$ phase. The magnetic characteristics change in accord with the structural transformations in Pt/Co film samples. © 2000 MAIK "Nauka/Interperiodica".

1. INTRODUCTION

In recent years, intensive studies of the Pt/Co multilayer films have been caused by their possible use as a medium for high-fidelity magnetooptical recording [1–7]. The Pt/Co multilayers deposited onto glass substrates are characterized by the (111) texture and a considerable perpendicular magnetic anisotropy whose nature remains unclear. In the Pt/Co/MgO(001) epitaxial multilayer films, the easy magnetization axis either can be aligned perpendicular [8] or within the plane of the film [9, 10], or can form an angle with the sample plane [11]. In the course of annealing [8, 12] or ionic bombardment [13], the structural and magnetic properties of the Pt/Co multilayer films exhibit substantial changes. Actually, the Pt/Co/MgO(001) multilayer films due to annealing in the temperature range 475–675°C for 14 h undergo a transformation into the CoPt ordered tetragonal phase with the c axis perpendicular to the surface of the sample [8, 12].

However, in analyzing the results of heat treatments or the action of ionic bombardment, it is usual practice to ignore the possibility of initiating the self-propagating high-temperature synthesis between cobalt and platinum layers. Unlike the self-propagating high-temperature synthesis occurring in powders, which is rather well understood [14], this process in thin films has come under the scrutiny of science only in the very recent years [15, 16]. Upon fast heating of the two-layer film samples above the initiation temperature T_0 at a rate of higher than 20 K/s, the self-propagating

high-temperature synthesis in thin films proceeds in the form of a surface combustion wave. Since the velocity of the front of self-propagating high-temperature synthesis at temperatures close to the initiation temperature T_0 is equal to $\sim(0.2–0.5) \times 10^{-2}$ m/s, its propagation can be observed visually. The temperature of the front is considerably higher than the temperature of the rest of the film, and, hence, most of the mass transfer and the formation of reaction products take place solely at the front of self-propagating high-temperature synthesis. As a result, upon fast cooling at the rear of the front, the metastable, quasicrystalline, and amorphous phases, apart from the equilibrium compounds, can be formed in the reaction products [15–17].

The purpose of the present work was to investigate the self-propagating high-temperature synthesis and its influence on the structural and magnetic properties of the epitaxial two-layer and multilayer Pt/Co/MgO(001) films.

2. SAMPLE PREPARATION AND EXPERIMENTAL TECHNIQUE

The two-layer and multilayer Pt/Co film samples were prepared by the ion–plasma sputtering onto glass substrates and onto the freshly cleaved MgO(001) surfaces. The total thickness of cobalt was equal to 30–50 nm, and the total thickness of platinum was 50–70 nm. In the experiments, their ratio was taken to be close to the atomic ratio 1 : 1. The character of the

propagation of high-temperature synthesis essentially depends on the thermal properties and substrate thickness. In order to decrease the heat transfer into the substrates, their thicknesses were taken to be minimum as far as possible. The glass substrates used in the experiments were 0.18 mm thick, and the thickness of the MgO substrates was varied in the range from 0.35 to 0.40 mm. The Pt/Co two-layer film samples were produced by the sequential evaporation of cobalt and platinum layers onto a substrate in the following way: the cobalt film was first evaporated at a temperature of 550 K, and then, the platinum layer was applied at a temperature of 300 K. The Pt/Co epitaxial multilayers were deposited at a temperature of 550 K onto the MgO(001) substrates and contained from 60 to 90 pairs of the cobalt and platinum layers. The thicknesses of cobalt and platinum layers in each pair fell in the ranges 0.40–0.44 and 0.51–0.55 nm for cobalt and platinum, respectively.

The phase composition of the samples was determined on a DRON-4-07 instrument (K_α-radiation). The X-ray fluorescence analysis was employed to determine the chemical composition and thickness of the studied films. The magnetic properties of samples were examined with the use of vibrating-sample and torsional magnetometers. The biaxial anisotropy constant was determined as $2l_{max}$, where l_{max} is the maximum torque moment per unit volume of the sample. To initiate the self-propagating high-temperature synthesis, the samples prepared were placed on a tungsten heater to produce a uniform temperature field in the sample plane. The heating was performed under a vacuum of $\sim 1 \times 10^{-3}$ Pa at a rate of no less than 20 K/s up to the temperature T_0 of the initiation of self-propagating high-temperature synthesis followed by cooling at a rate of ~10 K/s.

3. EXPERIMENTAL RESULTS AND DISCUSSION

The self-propagating high-temperature synthesis in the Pt/Co two-layer films deposited onto glass substrates was initiated at temperature $T_0 = 770$–820 K. The front of the propagation of high-temperature synthesis was observed visually (Fig. 1). A visual observation showed that the self-propagating high-temperature synthesis proceeded across the whole width of the film sample.

Figure 1 demonstrates the autowave motion of the front of self-propagating high-temperature synthesis, which is typical of the two-layer film samples [15, 16]. The temperature profile of the front and the mechanism of its autowave propagation were described in [15, 16]. However, in the case of the two-layer and multilayer Pt/Co films deposited onto the MgO(001) substrates, the motion of the front of self-propagating high-temperature synthesis was not visually observed. This can be due to the fact that the heat transfer from the front to the substrate is quite significant even if the thickness of the MgO substrate is equal to ~0.35 mm. As a conse-
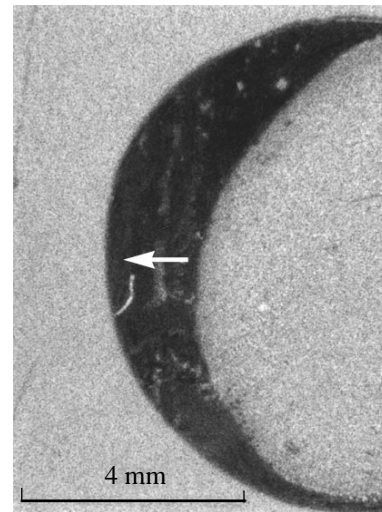

Fig. 1. A micrograph of the self-propagating high-temperature synthesis in the Pt(50 nm)/Co(40 nm) film on a glass substrate 0.18 mm thick. The arrow indicates the direction of the front of self-propagating high-temperature synthesis.

quence, the temperature of the front decreases, and the wave of self-propagating high-temperature synthesis covers only the thin boundary layer between platinum and cobalt, which is invisible to the eye. An alternative explanation resides in the fact that, upon reaching the initiation temperature T_0, the self-propagating high-temperature synthesis proceeds throughout the phase boundary rather than in the form of a surface combustion wave. Hence, the cycle of the self-propagating high-temperature synthesis consisted in heating the two-layer and multilayer Pt/Co/MgO(001) film samples at a rate of higher than 20 K/s up to a temperature of 870 K, which exceeded the initiation temperature T_0. Thereafter, the samples were allowed to stand at this temperature for 30 s, followed by cooling at a rate of ~10 K/s. This time is large enough for the self-propagating high-temperature synthesis to extend over the whole sample, including the induction period.

The heat treatment similar to the above cycle of self-propagating high-temperature synthesis is often employed in thin films and is referred to as the rapid thermal annealing [18]. The rapid thermal annealing was also used in studies of the Fe/Pt nanoscale multilayers [19].

The X-ray diffraction patterns of the Pt/Co/MgO(001) two-layer film samples prior to the initiation of the self-propagating high-temperature synthesis indicated that the β-Co film grew up with the (001) orientation on the MgO(001) surface at the substrate temperature $T_s = 470$ K. The upper platinum layer, which was deposited onto the β-Co(001) film at the temperature $T_s = 300$ K, grew up with the predominant (001) orientation. However, in this case, the (111) orientation of the platinum phase is also observed, but to a lesser degree (Fig. 2a). According to the magnetic measurements, the
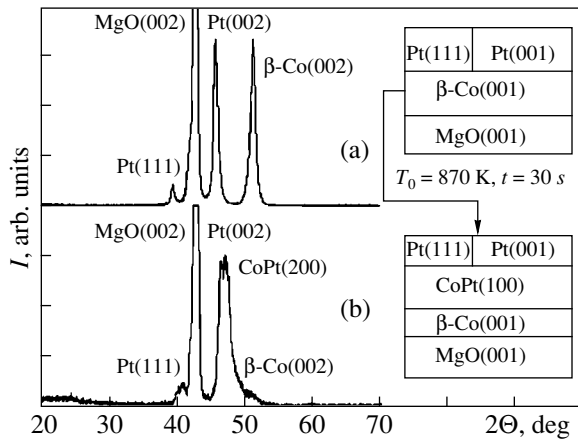
Fig. 2. X-ray diffraction patterns and schematic diagrams of the phase composition and phase orientation in the Pt(50 nm)/Co(40 nm)/MgO(001) two-layer films: (a) initial sample and (b) sample after the cycle of self-propagating high-temperature synthesis.
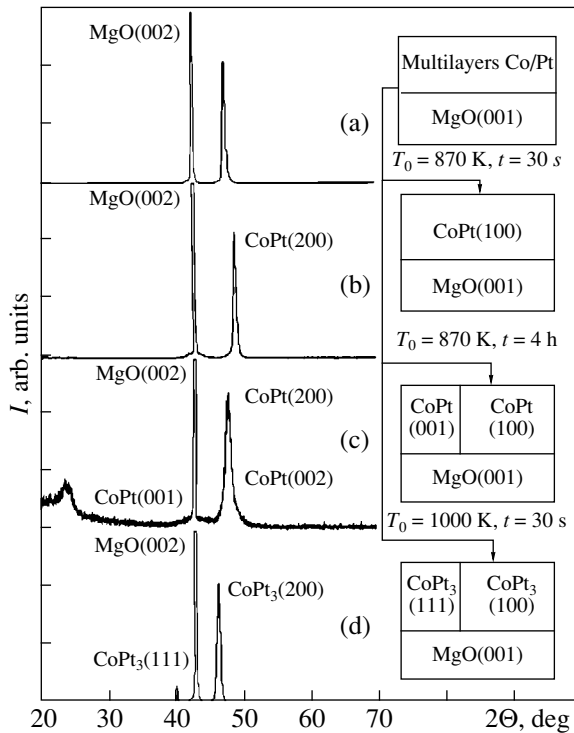

Fig. 3. X-ray diffraction patterns and schematic diagrams of the phase composition and phase orientation in the Pt(5.3 nm)/Co(4.2 nm)/MgO(001) multilayer films: (a) initial sample and samples after (b) the cycle of self-propagating high-temperature synthesis, (c) annealing at a temperature of 870 K for 4 h, and (d) annealing at a temperature of 1000 K for 30 s.

saturation magnetization I_s and the first constant of magnetocrystalline anisotropy K_1 for these samples (per unit volume of the cobalt film) correspond, respectively, to the values of I_s and K_1 for the β-Co phase.

An analysis of the X-ray diffraction patterns and magnetic measurements demonstrate that the β-Co film and the MgO substrate are characterized by the epitaxial relationships (001), Co[100] ∥ (001), MgO[100], which were observed earlier in [20]. The X-ray diffraction patterns of samples after the cycle of self-propagating high-temperature synthesis indicate that, in addition to the residual layers of cobalt and platinum, the reaction products contain a layer of the CoPt disordered phase with a coherent orientation with respect to the (001) plane. As follows from the magnetic measurements, the self-propagating high-temperature synthesis between cobalt and platinum layers proceeds not across the whole width of the film sample, but extends for a depth of no more than 25–30 nm (Fig. 2b). The biaxial anisotropy in the plane of the sample increases by a factor of 1.5–2 after the cycle of self-propagating high-temperature synthesis, whereas the easy magnetization axes do not change their directions.

The discrepancy between the lattice parameters of the β-Co and CoPt phases has a minimum value when the CoPt disordered phase grows in an epitaxial fashion and, in the case of the β-Co matrix phase, follows the orientational relationships (100), CoPt[100] ∥ (100), Co[100]. This implies that the CoPt disordered phase, like the β-Co matrix phase, possesses the negative magnetocrystalline anisotropy. Similar epitaxial relationships are observed upon self-propagating high-temperature synthesis in the Al/Fe/MgO(001) two-layer films [21]. It seems likely that the cooling at high rates makes impossible the formation of the CoPt equilibrium tetragonal ordered phase.

The X-ray diffraction patterns of the Pt/Co/MgO(001) multilayer film samples prior to the initiation of the self-propagating high-temperature synthesis exhibit a peak corresponding to the lattice parameter intermediate between the unit cell parameters of cobalt and platinum (Fig. 3a). The absence of large-angle and small-angle satellite reflections suggests a partial mixing between the cobalt and platinum layers. The magnetic measurements show that the easy axes of the Pt/Co/MgO(001) multilayers coincide with the MgO[111]-type directions rather than lie in the plane of the film. As follows from the curves of torque moments measured in the (100), (010), (001), (110), and MgO($1\bar{1}0$) planes, the magnetocrystalline anisotropy of the Pt/Co/MgO(001) multilayer films is adequately described by the anisotropy constant $K_1 = 1 \times 10^6$ erg/cm³, which considerably exceeds the shape anisotropy of the sample $2\pi I_S^2$ ($K_1 \gg 2\pi I_S^2$). The measured values of the saturation magnetization of these samples ($I_s = 200$–220 emu/cm³) satisfy this inequality. This gives grounds to believe that the multilayers under consideration are not a superposition of cobalt and platinum layers, but represent a weakly modulated phase that consists of mutually penetrating layers of cobalt and platinum.

After the cycle of self-propagating high-temperature synthesis, the diffraction peak shifts and, thus, corresponds to the reflection from the (200) plane of the CoPt disordered phase (Fig. 3b). The magnetic properties of the samples upon self-propagating high-temperature synthesis exhibit radical changes. The plane of the film becomes the easy magnetic plane. The easy axes of magnetization in the plane of the film do not change their directions; however, the biaxial anisotropy in the film plane and the saturation magnetization increase up to the values of $2l_{max} = (2.5–2.0) \times 10^6$ erg/cm³ and $I_s = 560–580$ emu/cm³, respectively. From the foregoing, it is evident that the CoPt disordered phase epitaxially grows on the MgO(001) surface in the same manner as in the course of growth in the Pt/Co two-layer films, follows the orientational relationships (100), CoPt[100] ∥ (100), MgO[100], and has the first magnetocrystalline anisotropy constant $K_1 = –(2.5–2.0) \times 10^6$ erg/cm³.

In the experiments, we also used the thermal annealing of the Pt/Co/MgO(001) multilayer films at a temperature of 870 K for 4 h. After the annealing, the easy magnetization axes are located at an angle of 10–15 deg with the plane of the film, rather than lie within this plane. The biaxial magnetic anisotropy in the plane of the sample retains the directions of easy magnetization axes. However, the magnetic anisotropy and the coercive force along the direction of easy magnetization drastically increase and become equal to $(10–12) \times 10^6$ erg/cm³ and 10 kOe, respectively. That large values of the magnetic anisotropy and coercive force correspond to the formation of the CoPt tetragonal ordered phase [8, 12]. This is corroborated by the diffraction data. The X-ray diffraction patterns of these samples display the (002) reflections and also the (001) superstructure reflections from crystallites of the CoPt tetragonal ordered phase, which is oriented by the c axis perpendicular to the film plane (Fig. 3c). The presence of reflections from the CoPt(200) phase suggests that crystallites of the CoPt tetragonal phase are ordered by the c axis along three mutually perpendicular axes of the MgO phase. The magnetocrystalline anisotropy energy E_K of the tetragonal crystal per unit volume of the sample without regard for anisotropy in the basal plane can be written in the following form: $E_K = E_0 + K_1\sin^2\theta + K_2\sin^4\theta$, where θ is the angle between the magnetization I_s and the c axis. Under the assumption that crystallites of the CoPt ordered phase equiprobably grow with the c axes along three mutually perpendicular axes of the MgO phase, the magnetocrystalline anisotropy energy of this film system can be represented as $E_K = E_0 + 1/6 K_2(\sin^2 2\psi \sin^4\psi \sin^2 2\phi)$, where φ is the angle between the projection of the magnetization I_s onto the film plane and the MgO[100] axis, and ψ is the angle between the magnetization I_s and the normal to the film. The torque moment curve $L = –dE_K/d\phi$ in the plane of the sample ($\psi = \pi/2$) has a maximum that can be determined as $2l_{max} = K_2/3$; the experimental value of this maximum is equal to $(1.0–1.2) \times 10^7$ erg/cm³. From

this, one can obtain the second constant of magnetocrystalline anisotropy $K_2 = (3.0–3.6) \times 10^7$ erg/cm³ for the PtCo ordered phase. The CoPt ordered phase of the bulk alloy is characterized by the values $K_1 = 5 \times 10^7$ [22] and $K_1 + K_2 = 2 \times 10^7$ erg/cm³ [23]. The found value of the second magnetocrystalline anisotropy constant $K_2 = (3.6–4.2) \times 10^7$ erg/cm³ for the PtCo ordered phase on the films is inconsistent in sign with the K_2 value for the bulk samples.

The magnetic measurements of the Pt/Co/MgO(001) multilayer films after the cycle of self-propagating high-temperature synthesis carried out at a temperature of 1000 K demonstrate that no anisotropy is observed in the plane of the sample. In this case, the samples exhibit a low saturation magnetization (~100 emu/cm³) with the easy magnetic plane coinciding with the plane of the film. The diffraction patterns indicate that crystallites of only the $CoPt_3$ phase with the predominant orientation of the (001) plane parallel to the MgO(001) plane are formed in the samples. There exists also a small amount of the $CoPt_3$ phase with an orientation of the (111) plane parallel to the MgO(001) plane (Fig. 3d). The $CoPt_3$ ordered phase is nonferromagnetic at room temperature, whereas the $CoPt_3$ disordered phase possesses the magnetization equal to 500 emu/cm³ [24]. Hence, it follows that the $CoPt_3$ phase formed during the self-propagating high-temperature synthesis exhibits a larger degree of ordering. The sequences of the phase formation with an increase in the annealing temperature, which are similar to the sequence Pt/Co ⟶ CoPt ⟶ $CoPt_3$, can be frequently observed in the solid-phase reactions. As mentioned above, the Pt/Co/MgO(001) multilayer films, as well as the CoPt phase formed upon the heat treatment, have the larger negative magnetocrystalline anisotropy constant K_1. Therefore, in the Pt/Co multilayer films with the (111) texture, the easy magnetization axis is perpendicular to the plane of the sample, and the perpendicular magnetic anisotropy constant is primarily determined by the magnetocrystalline anisotropy constant K_1. It is important to keep in mind that the temperature of the initiation of self-propagating high-temperature synthesis $T_0 = 770–820$ K for the Pt/Co film samples coincides with the ordering temperature for the CoPt alloy [25]. This gives grounds to assume that there is a certain interrelation between the chemical mechanisms of the synthesis and ordering. The FePt phase is formed as the result of annealing in the Fe/Pt multilayer films [8, 12, 19, 26]. Hence, it can be expected that the self-propagating high-temperature synthesis should be initiated in the two-layer and multilayer Fe/Pt film samples with the formation of the FePt phase in the reaction products.

Therefore, in the Pt/Co two-layer films deposited onto glass substrates, the self-propagating high-temperature synthesis in the form of a surface combustion wave is initiated between the cobalt and platinum layers at temperatures $T_0 = 770–820$ K and proceeds across the whole width of the film sample provided that

the total thickness of the films does not exceed 100 nm. In the same film samples, but deposited onto the MgO substrates, the self-propagating high-temperature synthesis covers an interphase boundary between cobalt and platinum whose thickness is equal to 20–30 nm. After the cycle of self-propagating high-temperature synthesis at temperatures $T_0 = 770$–820 K, the reaction products contain a layer of the CoPt disordered phase, which epitaxially grows on the surfaces of cobalt and platinum. Upon annealing at a temperature of 870 K for 4 h, the CoPt disordered phase undergoes a transformation into the ordered phase. It is assumed that crystallites of the CoPt ordered tetragonal phase equiprobably grow with the *c* axes, which coincide with the crystallographic directions of the MgO[100] type. This assumption made it possible to determine the constant $K_2 = (3.0$–3.6$) \times 10^7$ erg/cm^3 in the expression of the magnetocrystalline anisotropy energy for the CoPt ordered tetragonal phase. The cycle of self-propagating high-temperature synthesis in the Pt/Co/MgO(001) multilayer films at a temperature of 1000 K results in the formation of the CoPt$_3$ phase, which grows with the predominant (100) orientation on the MgO(100) surface.

ACKNOWLEDGMENTS

REFERENCES

1. F. P. Carcía, A. D. Meinhaldt, and A. Suna, Appl. Phys. Lett. **47**, 178 (1985).
2. F. P. Carcía, J. Appl. Phys. **63**, 5066 (1988).
3. Y. Ochiai, S. Hashimoto, and K. Aso, IEEE Trans. Magn. **25**, 3755 (1989).
4. W. B. Zeper, F. J. A. M. Greidanus, and F. P. Carcía, IEEE Trans. Magn. **25**, 3764 (1989).
5. S. Sumi, K. Tanase, Y. Teragaki, *et al.*, Jpn. J. Appl. Phys. **31**, 3328 (1992).
6. W. B. Zeper, H. W. van Kesteren, B. A. J. Jacobs, *et al.*, J. Appl. Phys. **70**, 2264 (1991).
7. F. P. Carcía, D. Coulman, R. S. McLean, *et al.*, J. Magn. Magn. Mater. **164**, 411 (1996).
8. B. M. Lairson, M. R. Visokay, R. Sinclair, *et al.*, J. Magn. Magn. Mater. **126**, 577 (1993).
9. C. H. Lee, R. F. C. Farrow, C. H. Lin, *et al.*, Phys. Rev. B **42**, 11 384 (1990).
10. C. L. Canedy, X. W. Li, and G. Xiao, J. Appl. Phys. **81**, 5367 (1997).
11. R. L. Stamps, L. Louail, M. Hehn, *et al.*, J. Appl. Phys. **81**, 4751 (1997).
12. B. M. Lairson and B. M. Clemens, Appl. Phys. Lett. **63**, 1438 (1993).
13. C. Chappert, H. Bernas, J. Ferre, *et al.*, Science (Washington, D.C.) **280**, 1919 (1998).
14. A. G. Merzhanov, in *Physical Chemistry*, Ed. by Ya. M. Kolotyrkin (Khimiya, Moscow, 1983), p. 6.
15. V. G. Myagkov and L. E. Bykova, Dokl. Akad. Nauk **354**, 777 (1997).
16. V. G. Myagkov, V. S. Zhigalov, L. E. Bykova, *et al.*, Zh. Tekh. Fiz. **68**, 58 (1998) [Tech. Phys. **43**, 1189 (1998)].
17. V. G. Myagkov, L. E. Bykova, and G. N. Bondarenko, Pis'ma Zh. Éksp. Teor. Fiz. **68**, 121 (1998) [JETP Lett. **68**, 131 (1998)].
18. R. Singh, J. Appl. Phys. **63**, R59 (1988).
19. J. P. Liu, C. P. Lio, Y. Liu, *et al.*, Appl. Phys. Lett. **72**, 483 (1998).
20. V. G. Pyn'ko, A. S. Komalov, M. A. Ovsyannikov, *et al.*, Izv. Akad. Nauk SSSR, Ser. Fiz. **31**, 485 (1967).
21. V. G. Myagkov, L. E. Bykova, and G. N. Bondarenko, Dokl. Akad. Nauk **368**, 615 (1999).
22. P. Brissonne, A. U. Ablanchard, and H. Bartholin, IEEE Trans. Magn. **2**, 479 (1966).
23. R. A. McCurrie and P. Gaund, Philos. Mag. **13**, 567 (1966).
24. T. Taoka, K. Yasukochi, R. Honda, *et al.*, J. Phys. Soc. Jpn. **14**, 888 (1959).
25. K. Barmak, R. A. Ristau, K. R. Coffey, *et al.*, J. Appl. Phys. **79**, 5330 (1996).
26. B. M. Lairson, M. R. Visokay, R. Sinclair, *et al.*, Appl. Phys. Lett. **62**, 639 (1993).

Translated by O. Borovik-Romanova

LOW-DIMENSIONAL SYSTEMS
AND SURFACE PHYSICS

Interaction of Thin Silicon Layers with the (0001) Surface of Rare-Earth Metals

**A. M. Shikin, A. Yu. Grigor'ev, G. V. Prudnikova,
D. V. Vyalykh, S. L. Molodtsov, and V. K. Adamchuk**

Institute of Physics (Petrodvorets Branch), St. Petersburg State University, Petrodvorets, 198904 Russia
e-mail: shikin@snoopy.phys.spbu.ru

Received September 15, 1999

Abstract—The electronic and crystalline structures of the systems formed upon deposition of silicon layers onto the Gd(0001) and Dy(0001) surfaces of single-crystal films annealed subsequently at $T = 450–500°C$ have been studied by low-energy electron diffraction (LEED) and also by the Auger electron and angle-resolved photoelectron spectroscopy of the valence band and the Si(2p) core level. It is shown that the systems thus produced can be described as starting single-crystal films of Gd and Dy, with 3D islands of the silicides of these metals on the surface of the corresponding metal films. © 2000 MAIK "Nauka/Interperiodica".

1. INTRODUCTION

At present, there is a wealth of publications on the interaction of rare-earth metals (REM) with silicon surface. It is reliably established that the REM deposition onto the Si(111) surface followed by annealing at a temperature of ~400–500°C gives rise to a strong interaction of Si with the rare-earth metals and epitaxial growth on the surface of ordered layers of REM disilicides with an AlB_2-type structure and a stoichiometry close to $MeSi_{1.7}$ [1–9]. These disilicides have a layered Si–REM–Si structure with a hexagonal arrangement of Si and REM atoms inside the corresponding layers [1, 5–9]. Note that if rare-earth metal atoms form centered hexagons (i.e., with an atom at the hexagon center) with a lattice constant of ~3.8 Å, the silicon atoms inside the corresponding layers build noncentered graphite-like hexagons with one additional vacancy in each hexagon [1, 2, 6–8]. These vacancies form, in turn, an ordered structure of a larger size whose diffraction patterns are of the $(\sqrt{3} \times \sqrt{3})R30°$ type with respect to the principal structure. These vacancies account for the silicon hexagon matching to the corresponding basal lattice constant of the system (~3.8 Å). It is this that stimulates the growth of epitaxial layers of nonstoichiometric REM disilicides on the Si(111) surface with a good lattice match between the disilicide film and the silicon substrate. This work was aimed at studying the interaction between silicon and rare-earth metals (Gd, Dy) in a Si/REM system obtained by deposition of silicon onto an REM surface, which can be called "reverse" with respect to the system formed by REM deposition on the silicon surface.

We studied the electronic and crystalline structure of the systems produced by deposition of thin silicon

films onto the (0001) surface of the gadolinium and dysprosium single-crystal films grown on a W(110) single-crystal surface. The basal constants of the crystal structure of these rare-earth metals are smaller than those of the epitaxial silicides in the "direct" system: 3.63 Å for Gd and 3.59 Å for Dy [10]. On the one hand, this removes the requirement of lattice matching between the silicide phases and the REM substrate. On the other, these metals readily form silicide-like structures in the direct system; i.e., when a rare-earth metal is deposited onto the Si(111) surface with its subsequent thermal annealing [3, 4, 11, 12].

In this work, the studies were carried out by the methods of Auger electron and photoelectron spectroscopy of the valence band and the Si(2p) core level in the course of deposition of thin Si layers on the (0001) surface of Gd and Dy single-crystal films, followed by thermal annealing at ~450–500°C. Low-energy electron diffraction (LEED) spectroscopy was employed to characterize the crystal structure of the systems.

It was shown that the systems formed by deposition of silicon thin layers on the (0001) surface of the gadolinium and dysprosium single-crystal films annealed subsequently at ~450–500°C can be described as single-crystal films of rare-earth metals (Gd, Dy) with 3D islands of the silicides of these rare-earth metals created on the surface of the system.

2. EXPERIMENTAL TECHNIQUE

The photoelectron studies were carried out at the Synchrotron Radiation Center (BESSY I, Berlin) on the TGM-3 channel with the use of a WSW-ARIES-type electron spectrometer capable of angular resolu-
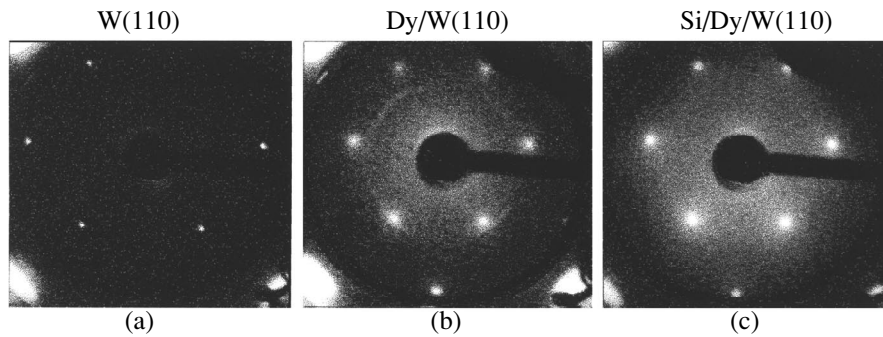
Fig. 1. LEED patterns ($E_p \sim 83$ eV) for (a) clean W(110) surface, (b) Dy(0001) single-crystal film on the W(110) surface, and (c) Si(12 Å)/Dy(0001)/W(110) system after annealing at 450–500°C.
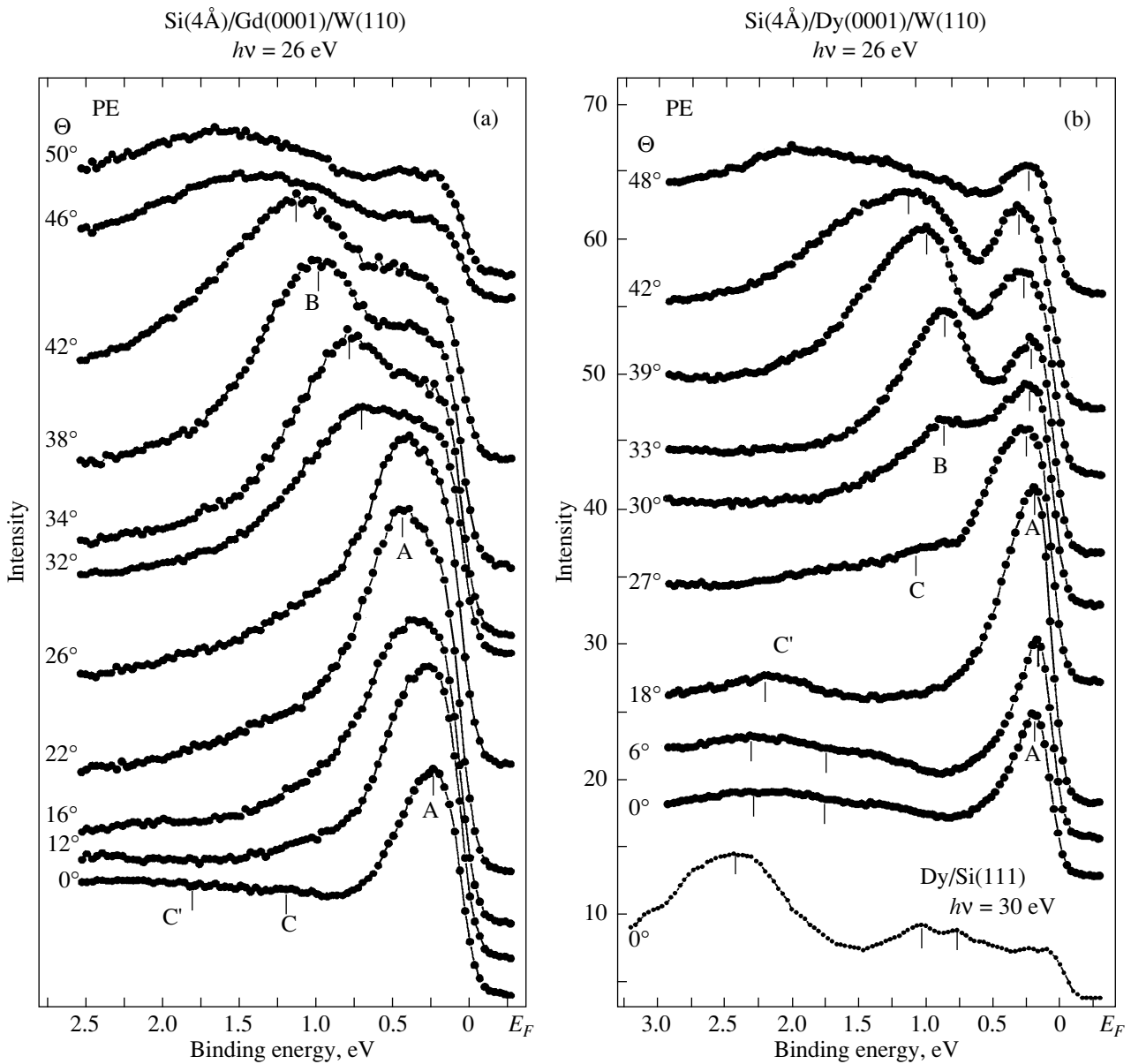

Fig. 2. Valence-band photoelectron spectra for different photoelectron polar takeoff angles (Θ) measured for the systems (a) Si(4 Å)/Gd(0001)/W(110) and (b) Si(4 Å)/Dy(0001)/W(110) after annealing at 450–500°C. Shown in the bottom of Fig. 2b is the photoelectron spectrum of the Dy/Si(111) system after annealing at 400–500°C.

tion and provided with a LEED diffractometer. The total energy resolution of the system during experiments was no worse than 0.2 eV. We measured the photoelectron spectra of the valence band and the Si(2p) core level in the course of deposition of silicon thin films of different thicknesses onto the (0001) surface of the gadolinium and dysprosium single-crystal films, followed by warming the systems up to temperatures of 450–500°C. The exciting photon energy was chosen so as to reduce the contribution of the REM 4f and 5d states to the valence-band photoelectron spectra and was equal to 26 eV. The Si(2p) photoelectron spectra were measured at an incident energy of 130 eV, which provided the maximum possible surface sensitivity of the experiment. The Auger electron spectra of the Si/REM systems studied during the Si deposition and thermal annealing were measured by means of a four-grid retarding-field energy analyzer at a primary-electron energy of ~1 keV.

The gadolinium and dysprosium single-crystal films were grown on the (110) surface of a tungsten single crystal according to the standard procedure [13, 14] by depositing these metals to a thickness of ~150–200 Å, followed by thermal annealing at a temperature of ~400–500°C. The films thus prepared had a hexagonal structure characteristic of the REM(0001) surfaces. The diffraction patterns obtained from a clean W(110) surface and a dysprosium single-crystal film grown on the W(110) surface are compared in Figs. 1a and 1b, respectively. The LEED patterns of a gadolinium single-crystal film were similar. Silicon was deposited onto the REM films from a silicon plate heated directly by passing through it electric current. The thickness of the deposited Si and REM layers was determined from the frequency shift of a quartz resonator placed inside the chamber so as to be at the same conditions as the sample. The base pressure in the chamber during the experiment was no higher than 1×10^{-10} Torr. After the silicon deposition, the Si/Gd(0001) and Si/Dy(0001) systems were annealed at 450–500°C. As a result of this treatment, both systems recovered the hexagonal-structure LEED patterns characteristic of the original surfaces of the gadolinium and dysprosium single-crystal films. Figure 1c shows a typical LEED pattern for the Si/Dy(0001) system after its annealing at 450–500°C. Similar patterns were observed for the Si/Gd(0001) system.

3. RESULTS AND DISCUSSION

Figures 2a and 2b present the photoelectron spectra of the valence band near the Fermi level at different polar photoelectron takeoff angles for the Si(4 Å)/Gd(0001) and Si(4 Å)/Dy(0001) systems after annealing at 450–500°C. [The spectra of thicker (up to 12 Å) predeposited Si layers measured after thermal annealing had the same pattern.] The photoelectron spectra of both systems were measured along the Γ–M–Γ direction of the surface Brillouin zone of the rare-earth metal. As is seen from Figs. 2a and 2b, the photoelectron spectra obtained for polar angles below 30° relative to the normal to the surface for both systems have a strong feature (A) in the range of binding energies near the Fermi level (0–0.5 eV). The structure of the spectra changes with an increase in the polar angle. The A feature first shifts toward higher binding energies and, at polar angles above 30°, splits into two features (A and B), one of which (B) strongly disperses toward higher binding energies. The A structure near the Fermi level is more complex. However, one can likewise isolate here features dispersing with a variation in the polar angle and reaching a maximum binding energy at polar angles of ~25 and 50°. The above variations in the binding energy within the main electron groups (features) in the valence band of the Si/Gd(0001) and Si/Dy(0001) systems after annealing are shown graphically in more detail in Figs. 3a and 3b, which display the dispersion relations $E(k_\parallel)$ derived from the photoemission spectra with the use of the standard expression

$$k_\parallel \sim 0.51 \sqrt{E_{kin}} \sin\Theta,$$

where $k_\parallel$ is the parallel component of the quasi-momentum in the Brillouin zone, E_{kin} is the photoelectron kinetic energy, and Θ is the photoelectron polar takeoff angle relative to the surface normal.

The features corresponding to different thicknesses of the predeposited silicon layers (2, 4, and 12 Å) are identified in Figs. 3a and 3b by different symbols. For comparison, crosses in Fig. 3a show the corresponding dispersion relations for the original Gd(0001) single-crystal film, which were measured in this work also for $h\nu = 26$ eV.

For comparison, Fig. 2b presents a photoelectron spectrum of epitaxial Dy disilicide obtained in the direct system by depositing Dy onto the Si(111) surface, with its subsequent annealing at ~500°C. This spectrum exhibits a clearly pronounced silicide-like structure with the main features at binding energies of 0.8, 1.1, and about 2.5 eV—a pattern similar to that of the valence band of the disilicides of other rare-earth metals, including Gd [3–8]. As is seen from comparison with the spectrum of dysprosium silicide, the Si/Dy(0001) system does not exhibit distinct spectral features characteristic of epitaxial bulk phases of REM disilicides. One can distinguish only very weak features near the binding energies of 2–2.5 and 1–1.5 eV (C and C'), which are identified in the figure by dashes.

The photoelectron spectra of the Si/Gd and Si/Dy systems presented in Figs. 2a and 2b resemble more closely those of the valence band, which are characteristic of the original Gd(0001) and Dy(0001) single-crystal films. A comparison with the dispersion relations obtained for a clean Gd(0001) surface shows that
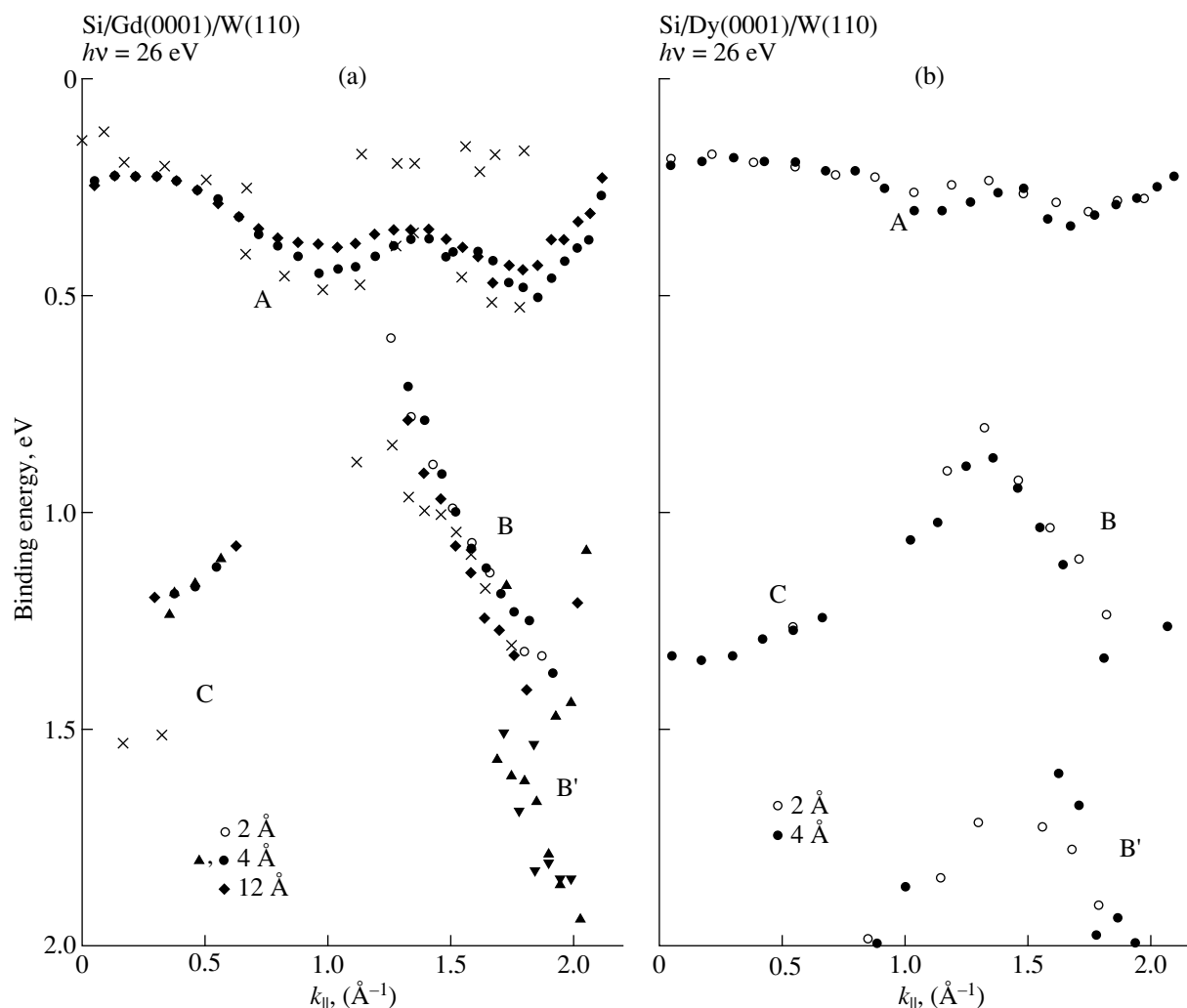
Si/Gd(0001)/W(110)
$h\nu = 26$ eV

Si/Dy(0001)/W(110)
$h\nu = 26$ eV

Fig. 3. Dispersion relations of the main valence-band features in the Γ–M–Γ direction of the surface Brillouin zone of rare-earth metals for the systems (a) Si/Gd(0001)/W(110) and (b) Si/Dy(0001)/W(110) after annealing at 450–500°C. The different symbols identify the Si layer thicknesses. For comparison, crosses in Fig. 3a show the dispersion relations of the ground electronic states for a clean Gd(0001)/W(110) film.

the main features in the electronic structure of the Gd(0001) film and the Si/Gd(0001) system after annealing are clearly similar to each other. This relates primarily to the *B* feature, which disperses strongly toward higher binding energy for polar angles $\Theta > 25$–$30°$ ($k_\parallel > 1$–1.2 Å^{-1}). The pattern of the variation and the binding energies of the main features (*A* and *B*) in the valence band of the original Gd(0001) film and the Si/Gd(0001) system after annealing practically coincide.

The variations in the photoelectron spectra and in the binding energies for the main valence-band features (*A*, *B*, and *C*) of the Si/Gd and Si/Dy systems presented here correlate with the theoretical and experimental studies made for the Gd(0001) and Dy(0001) surfaces in the Γ–M–Γ direction [13–17]. This provides support for the above assumption that the main features in the

photoelectron spectra characteristic of the starting Gd(0001) and Dy(0001) single-crystal films are retained after deposition of thin silicon layers, which are subsequently annealed at 450–500°C.

Figure 4 displays the Si(2p) core-level photoelectron spectra measured for the Si(12 Å)/Gd(0001) and Si(4 Å)/Dy(0001) systems after annealing at ~450–500°C. Also shown for comparison is a photoelectron spectrum for a ~20-Å-thick silicon layer deposited onto a Gd film and measured directly after a room-temperature deposition of silicon. An analysis of the spectra permits the following conclusion. If a spectrum obtained before the annealing of the system has a single broad peak with a maximum at a kinetic energy of ~27.2 eV, the annealing leads to the formation of a distinct Si(2p) doublet and a shift of the spectrum as a whole toward higher kinetic energies (and, hence, toward lower binding energies). After the annealing of

the Si/Dy system, one can observe a similar Si($2p$) doublet at the same energies (with one peak at about 27.3 eV, and another, at ~27.8 eV). The energies of the peaks in the doublet do not depend on the thickness of the predeposited silicon layer. At the same time, the location of the maximum of the Si($2p$) peak before the annealing of the system does depend on the thickness of the Si layer deposited preliminarily and varies from 27.5 to 26.8 eV for the thicknesses studied in the work (from 2 to 20 and 50 Å). Following the annealing of the Si/Gd and Si/Dy systems, the intensity of the Si($2p$) peak decreases substantially.

Figures 5a and 5b demonstrate the variations in the silicon and rare-earth metal (Gd, Dy) Auger spectra obtained after the deposition of silicon layers with the different thicknesses (3, 12, and 15 Å) on the Gd(0001) and Dy(0001) surface and annealing of the Si/REM systems with the different thicknesses of the deposited Si layer at a temperature of 450–500°C. Analysis of the spectra shows that the Si(LVV) Auger peaks before and after the annealing differ substantially in shape. While before the annealing (particularly in the case of the 50-Å-thick silicon layer), the Si(LVV) Auger peak is close in structure to that characteristic of pure noninteracting silicon, after the annealing, this peak has a structure observed in direct systems upon formation of the bulk REM silicides [12, 18], particularly the Gd silicide [12].

Thus, analysis of the Si($2p$) photoelectron spectra and the Si(LVV) Auger electron spectra evidences the presence of silicon on the surface of REM films after the silicon deposition and following their heating despite the fact that the valence band manifests itself primarily in the features typical of REM films. The location of the Si($2p$) doublet and its structure are similar to those of the features in the Si($2p$) spectra of REM silicides [3–6]. The Si(LVV) Auger electron spectra obtained after the annealing of the Si/Gd and Si/Dy systems also have a structure characteristic of REM silicides in direct systems. All this evidences a silicide-like nature of the interaction between surface silicon and the underlying REM film and the formation of the corresponding Gd and Dy silicides on the surface of these systems.

We believe that the totality of the features observed in the photoelectron and Auger spectra can be accounted for by an intense interaction of deposited silicon with a part of surface atoms in the REM film, which occurs during annealing of the Si/REM systems at 450–500°C and leads to the formation of silicide-like bonds between Si and the rare-earth metal. The silicide thus formed, rather than producing a uniform coating, grows in three-dimensional islands on the surface of the starting REM films. This can be due, on the one hand, to the fact that this silicide is a chemically saturated phase and is not bonded to the surface of the REM film. On the other hand, the fairly large lattice mismatch
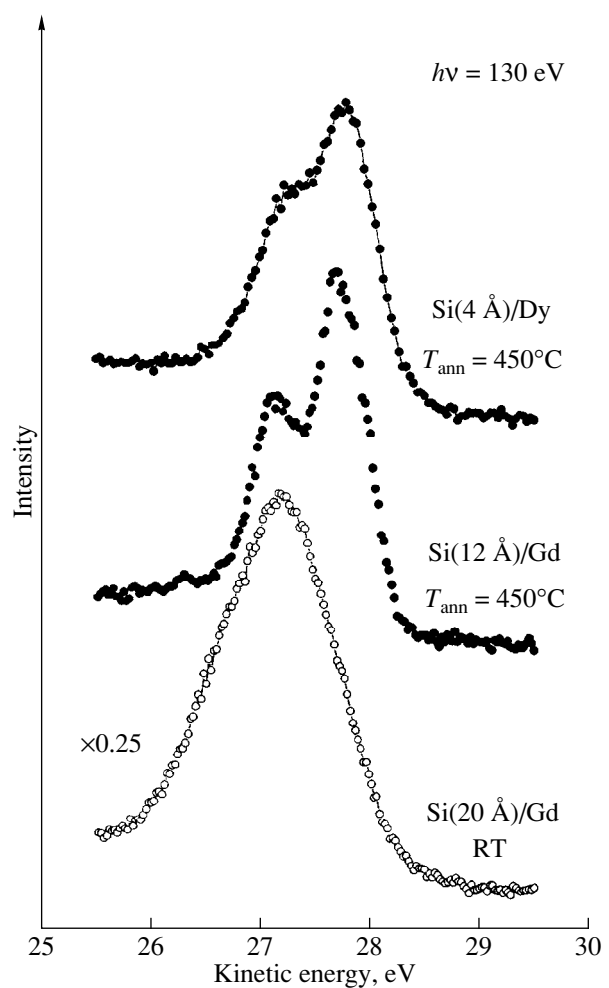

Fig. 4. The Si($2p$) core-level photoelectron spectra measured for the Si(4 Å)/Gd(0001)/W(110) systems after annealing at 450°C. Shown in the bottom is a Si($2p$) photoelectron spectrum obtained immediately after deposition of a 20-Å-thick Si layer onto the Gd(0001) surface.

between the silicide and the metal precludes formation of epitaxial silicide phases on the REM surface. The REM silicide islands occupy a small fraction of the surface (they grow apparently primarily near defect clusters in the starting REM films) and, hence, do not affect appreciably the photoelectron spectra and the LEED patterns. As a result, the photoelectron spectra and the LEED patterns generally have a structure and symmetry similar to those observed in the original REM films. The 3D silicide islands become manifest in the valence-band spectra as weak features at binding energies of 1–1.5 and 2–2.5 eV (Fig. 2), as well as in the form of a clearly pronounced silicide-like doublet in the photoelectron spectra of the Si($2p$) level and a modified Si(LVV) Auger peak in the Auger spectra of the final systems. Experiments involving layer-by-layer Ar-ion etching of the Si/Gd and Si/Dy systems bear out the
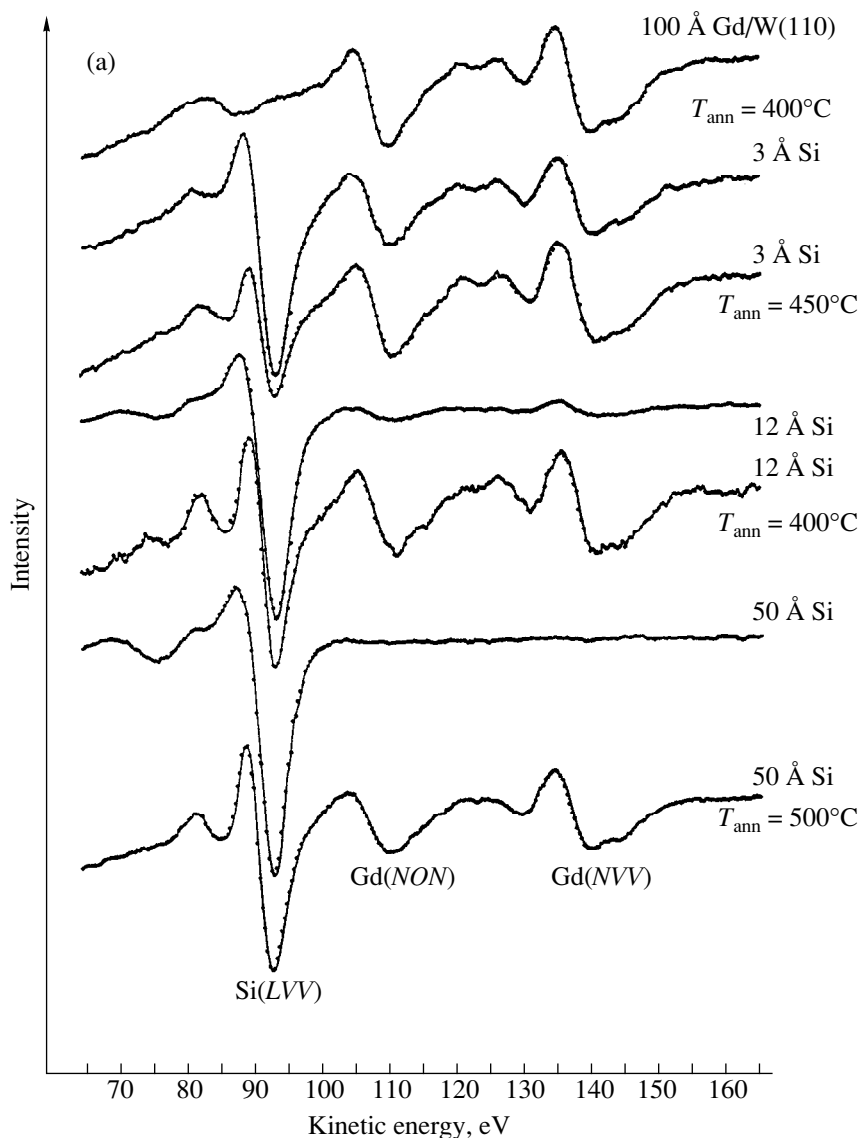
Fig. 5. Variations in the Auger electron spectra during the deposition of silicon layers with different thicknesses (3, 12, and 50 Å) onto the single-crystal films (a) Gd(0001)/W(110) and (b) Dy(0001)/W(110) measured at room temperature and after annealing at 450–500°C.

above assumptions of the bulk of the REM films remaining unaffected after the interaction with thin Si layers and the accumulation of the reacted silicon on the surface of the REM films. The experiments showed that silicon (in the form of silicide) is distributed directly on the surface of the system, so that etching it off leaves a film of a pure rare-earth metal down to the REM/W(110) interface.

In conclusion, we note that silicide-like bonds between the deposited silicon and an REM start to form already at room temperature. As is seen from Figs. 5a and 5b, the Si(*LVV*) Auger spectra measured after the deposition of ~3 Å Si have a nearly silicide-like struc-

ture. Heating the system to 450–500°C only makes the process more intense, which permits all deposited silicon to react with the rare-earth metal and, thus, to form a thermodynamically stable system.

Thus, the above analysis of the experimental photoelectron spectra [of the valence band and of the Si(2*p*) core level] and the Auger electron spectra of the Si/REM systems studied permits the conclusion that the deposition of thin silicon layers on the surface of the Gd(0001) and Dy(0001) single-crystal films, followed by their annealing at 450–500°C, favors the formation of 3D island films of the silicides of the corresponding REM on the REM surface. After the annealing, the sili-
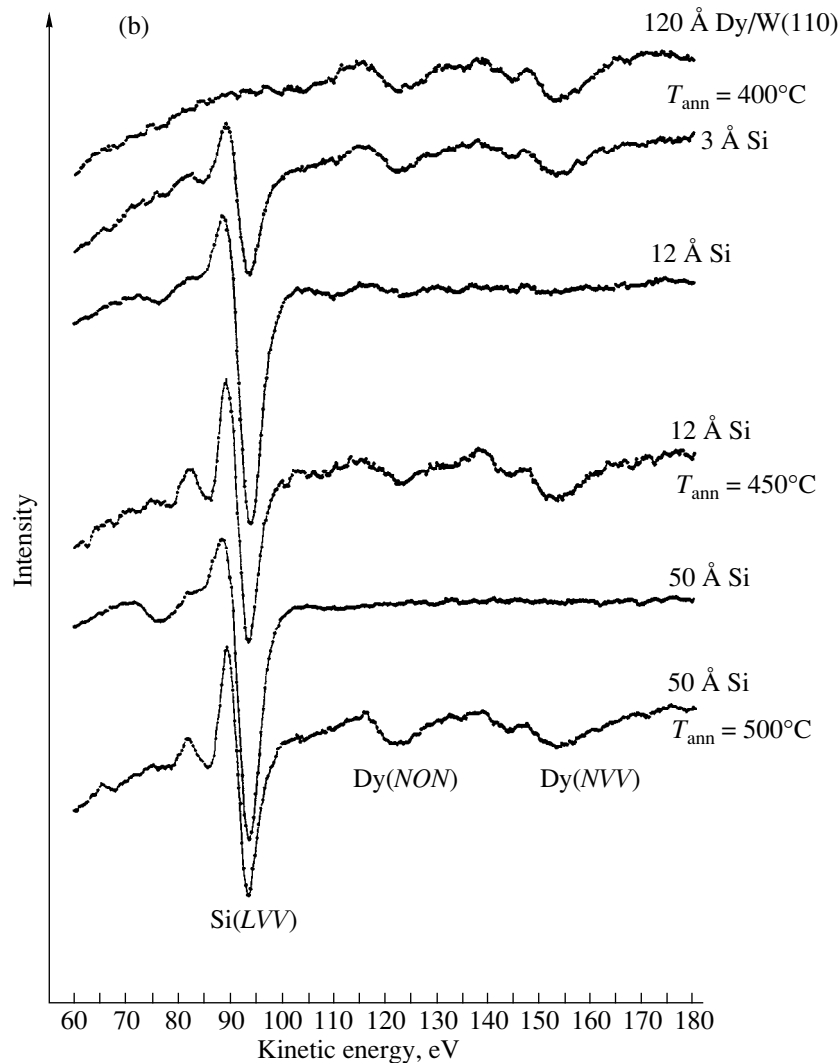
Fig. 5. (Contd.).

cide islands occupy a small fraction of the surface. The island-free surface represents the Gd and Dy single-crystal surfaces with a valence-band structure and a symmetry similar to those of the starting REM films.

REFERENCES

1. B. Baptist, S. Ferrer, G. Grenet, *et al.*, Phys. Rev. Lett. **64**, 311 (1990).
2. G. V. Samsonov and I. M. Vinitskii, *Handbook of Refractory Compounds* (IFI Plenum Data Company, 1980).
3. F. P. Netzer, J. Phys. **7**, 991 (1995).
4. S. Vandre, T. Kalka, C. Preinesberger, *et al.*, Appl. Surf. Sci. **123/124**, 100 (1998).
5. J.-Y. Veuillen, L. Magaud, D. B. B. Lollman, *et al.*, Surf. Sci. **269/270**, 964 (1992).
6. J.-Y. Veuillen, D. B. B. Lollman, T. A. Nguyen Tan, *et al.*, Appl. Surf. Sci. **65/66**, 712 (1993).
7. P. Wetzel, C. Pirri, D. Bolmont, *et al.*, Appl. Surf. Sci. **65/66**, 718 (1993).

8. L. Stauffer, A. Mharchi, A. Saintenoy, *et al.*, Phys. Rev. B **52**, 11932 (1995).

9. A. Mharchi, L. Stauffer, S. Saintenoy, *et al.*, Solid State Commun. **97**, 249 (1996).

10. S. D. Barret, Surf. Sci. Rep. **14**, 271 (1992).

11. G. Molnar, G. Petö, and E. Zsoldos, Appl. Surf. Sci. **70/71**, 466 (1993).

12. M. Sancrotti, A. Iandelli, G. L. Olcese, *et al.*, Phys. Rev. B **44**, 3328 (1991).

13. G. Kaindl, J. Alloys Compd. **223**, 265 (1995).

14. G. Kaindl, A. Höhr, E. Weschke, *et al.*, Phys. Rev. B **51**, 7920 (1995).

15. R. Wu, C. Li, A. J. Freeman, *et al.*, Phys. Rev. B **44**, 9400 (1991).

16. J. O. Dimmock and A. J. Freeman, Phys. Rev. Lett. **13**, 750 (1964).

17. S. H. Liu, in *Handbook on the Physics and Chemistry of Rare Earths*, Ed. by K. A. Gschneidner, Jr., and L. Eyring (North Holland, Amsterdam, 1978), Vol. 1.

18. W. A. Henle, M. G. Ramsey, F. P. Netzer, *et al.*, Surf. Sci. **254**, 182 (1991).

Translated by G. Skrebtsov

LOW-DIMENSIONAL SYSTEMS
AND SURFACE PHYSICS

Optical Anisotropy of the (100) Surfaces in $Al_xGa_{1-x}As$ Ternary Compounds

V. L. Berkovits, A. B. Gordeeva, V. M. Lantratov, and T. V. L'vova

Ioffe Physicotechnical Institute, Russian Academy of Sciences, Politekhnicheskaya ul. 26, St. Petersburg, 194021 Russia
e-mail: berkovits@pop.ioffe.rssi.ru
Received November 16, 1999

Abstract—The reflectance anisotropy spectra of the clean (100) surfaces of the $Al_xGa_{1-x}As$ ternary compounds at aluminum concentrations $0 \le x \le 0.5$ have been measured and thoroughly studied. In the spectral range from 1.6 to 3.5 eV, the signal caused by the optical transitions in the arsenic dimers dominates in the spectra of the clean arsenic-terminated GaAs surfaces. For the ternary compounds, an increase in the aluminum concentration brings about the broadening of this signal and its shift toward the low-energy range. This is explained by the appearance of additional signals associated with the optical transitions in the nonequivalent arsenic dimers, in which a part of the Ga atoms in the bulklike bonds is replaced by the Al atoms. An increase in the number of the substituted gallium atoms leads to a decrease in the energy of optical transition in the dimer. The fundamental optical transition energies are determined for the nonequivalent dimers. © *2000 MAIK "Nauka/Interperiodica".*

1. INTRODUCTION

In recent years, an optical modulation technique—reflectance anisotropy spectroscopy—has been widely used in studies of electronic states on the surfaces of semiconductors [1]. For cubic semiconductors, this method provides a means for separating weak signals of optical transitions on the surface from much stronger signals of the optical transitions in the bulk of a material due to the difference in the polarization properties. The (100) surfaces of A_3B_5 semiconductors, unlike their bulk, possess a pronounced optical anisotropy. In particular, the clean surface becomes anisotropic owing to the reconstruction, which leads to the lowering of its symmetry. This brings about the polarization of optical transitions on the surface, as a result of which the reflectances for the light linearly polarized along two principal axes of the surface appear to be different. For the (100) surface, the signal in the reflectance anisotropy spectrum is defined as

$$\Delta R/R = 2(R_{1\bar{1}0} - R_{110})/(R_{1\bar{1}0} + R_{110}),$$

where $R_{1\bar{1}0}$ and R_{110} are the reflectances for the normally incident light linearly polarized along the $\langle 1\bar{1}0 \rangle$ and $\langle 110 \rangle$ axes, respectively. Since the bulk of the A_3B_5 semiconductors, to a first approximation, can be regarded as an optically isotropic medium, the reflectance anisotropy signal from the bulk is equal to zero. Nonzero signal can be formed only in the reconstructed layer of atoms on the surface.

The clean GaAs(100) surfaces have been extensively investigated in recent years by the reflectance anisotropy spectroscopy under growth conditions of

molecular beam epitaxy [2], MOS hydride epitaxy [3], and upon annealing of samples passivated by sulfide solutions [4]. These studies made it possible to obtain the characteristic spectra corresponding to the known reconstructions of the (100) surface. However, the interpretation of these spectra involves considerable difficulties, because, apart from the signals of optical transitions between surface states, the spectra can exhibit signals brought about by the transitions in the adjacent bulk region perturbed by the surface of the crystal. Specifically, the spectrum of the As-rich GaAs(100) surface with the $(2 \times 4)/C(2 \times 8)$ reconstruction [2] shows a similarity to the spectrum of the imaginary part of the permittivity for GaAs and consists of two broad lines lying in the range of the bulklike transitions E_1, $E_1 + \Delta_1$ (3 eV), and E_0' (4.5 eV). Reasoning from this coincidence, the spectral features observed were assigned to the transitions in the subsurface layer of the bulk [5].

According to another viewpoint [6–8], the reflectance anisotropy spectrum of the GaAs(100) surface with the $(2 \times 4)/C(2 \times 8)$ reconstruction can be directly connected with the transitions between electronic states of the arsenic dimers, which represent the basic units of the given reconstruction. The dimer is formed by the two nearest-neighbor arsenic atoms on the (100) surface and linked to four gallium atoms of the underlying layer of the crystal. The optical transitions can occur between orbitals of the dimer that are predominantly oriented along the $[1\bar{1}0]$ axis of the surface. The tight binding calculations have assigned the spectral feature at an energy of 3 eV to the transition of an electron from
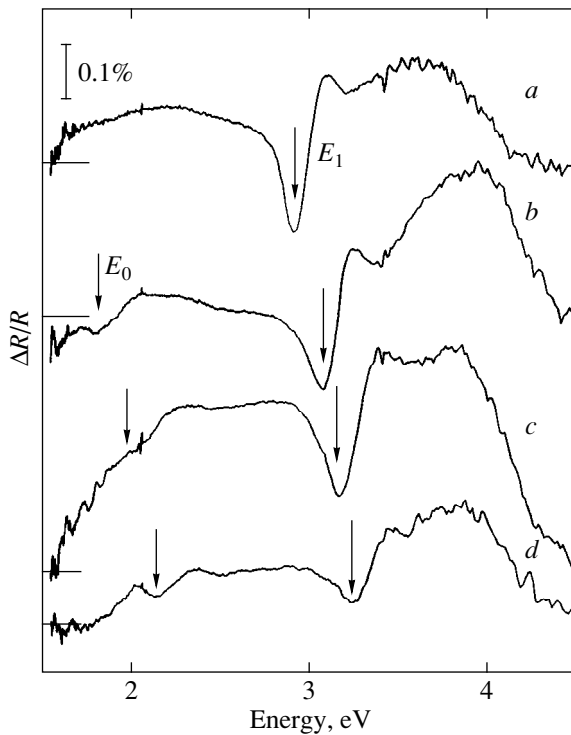
Fig. 1. Reflectance anisotropy spectra of the $Al_xGa_{1-x}As(100)$ oxidized surfaces at different aluminum concentrations x: (*a*) 0, (*b*) 0.27, (*c*) 0.35, and (*d*) 0.5. Arrows show the energies of the bulklike transitions E_0 and E_1. Horizontal straight-line segments at the left indicate the levels of zero signals.

the occupied dangling orbital to the antibonding orbital of the arsenic dimer [7, 8].

It is obvious that, in the former case, the anisotropy of the GaAs(100) surface is associated with the transitions between the electronic states delocalized in the subsurface region, and, in the latter case, it is caused by the transitions between the localized states on the surface.

The validity of these viewpoints can be experimentally verified by the investigation of solid solutions of the $Al_xGa_{1-x}As$ ternary compounds. The lattice parameter of these compounds does not depend on the aluminum concentration. Consequently, it can be expected that the configuration of arsenic dimers formed on the As-terminated $Al_xGa_{1-x}As(100)$ surface is identical to that on the GaAs(100) surface. However, the nonequivalent arsenic dimers should be formed in the ternary compound due to the substitution of the Al atoms for the Ga atoms in the nearest environment of the dimer. It can be assumed that the spectral feature at an energy of 3 eV stems from the transitions between the delocalized states in the subsurface layer. Then, an increase in the aluminum concentration in the composition of the solid solution should lead to the shift of this feature toward the high-energy range, as it was observed in the

permittivity spectrum of the bulk of a material [9]. If the spectral feature results from the transitions between the electronic states of the arsenic dimer, one can expect its broadening and even splitting due to the formation of dimers with other energies of the optical transition.

In the present work, we measured and investigated the reflectance anisotropy spectra of the clean As-terminated $Al_xGa_{1-x}As(100)$ surfaces. The main purpose of our investigation was to reveal the extent to which these spectra are contributed by the optical transitions localized at the arsenic dimers on the surface.

2. EXPERIMENTAL RESULTS

An experimental setup for recording the reflectance anisotropy spectra was described in detail in [10]. The experiments were performed using the $Al_xGa_{1-x}As$ liquid-phase epitaxial layers 6 μm thick with compositions $x = 0$ and 0.27; moreover, we used the MOS hydride epitaxial samples 2.3 μm thick with $x = 0.35$ and 0.5. The compositions of the solid solutions of ternary compounds were refined from the reflectance anisotropy spectra of the oxidized surfaces of samples.

Figures 1*a*–1*d* demonstrate the reflectance anisotropy spectra of the oxidized (100) surfaces of the p-$Al_xGa_{1-x}As$ layers at several concentrations x in the range from 0 to 0.5. In the spectrum of GaAs, the spectral feature most clearly manifests itself in the energy range of the bulklike transitions E_1 and $E_1 + \Delta_1$. This feature is associated with the anisotropy of the linear electrooptical effect induced by the space-charge electric field in the subsurface layer [10, 11]. As the aluminum concentration in the $Al_xGa_{1-x}As$ solid solution increases, the spectral feature shifts toward the high-energy range, thus reflecting an increase in the energy of the E_1 and $E_1 + \Delta_1$ transitions [9]. The compositions of the solid solutions were refined from the location of a minimum that corresponds to the energy of the E_1 transition. It should be noted that a broad structureless signal is also observed in the reflectance anisotropy spectra over the entire energy range studied. A possible reason for this signal is the shielding effect at the semiconductor–oxide interface [12]. In the energy range below the absorption edge, the spectrum shown in Fig. 1c exhibits oscillations caused by the interference in the solid solution layer.

At present, there has been no technique for preparing clean $Al_xGa_{1-x}As(100)$ surfaces by annealing of the samples under ultrahigh vacuum. Earlier [13], it was shown that the reconstructed GaAs(100) surface can be obtained when the sample is *in situ* treated in a passivating sulfide solution. The experimental procedure devised in [13] was applied in the present work to the ternary compounds. This procedure was as follows. A sample was fixed in a quartz cell. The quartz cell was filled with a 1 M $Na_2S \cdot 9H_2O$ solution, and immediately afterward the reflectance anisotropy spectrum of

the sample in the solution was recorded. Then, the sample was isolated from the external lighting and left to stand in the solution for 90–120 min. In this time interval, the natural oxide was removed, instead of which the passivating coating was formed on the sample surface to prevent a further contact between the surface and the solution. Then, the spectrum was recorded again. The difference between the spectra obtained characterizes the anisotropy due to the formation of a passivating coating on the surface. Thereafter, the sample was exposed for a short time (several minutes) to light with a quantum energy higher than the band gap of the semiconductor, and the reflectance anisotropy spectrum was recorded again. As was shown for the GaAs(100) surface, exposure to the light brings about the breaking of the As–S chemisorption bonds, which are formed in the course of the "dark" treatment and dominate on the crystal surface. As a result, the arsenic dimers are formed on the surface under the passivating coating. Note that the difference spectrum obtained from the spectra prior to and after the exposure to light appears to be identical to the spectrum of the clean (100) surface with the (2×4) reconstruction [14].

The spectra of the GaAs(100) surfaces obtained according to the above experimental procedure are depicted in Fig. 2 (curves *a–c*). In all the spectra, the signal decreases down to zero at energies above 3.5 eV due to the absorption of light by the solution. Spectrum *d* in Fig. 2 (the difference between spectra *b* and *a*) characterizes changes observed in the reflectance anisotropy spectra due to the dark treatment of the surface in the solution. At energies below 3.5 eV, this spectrum is the sum of the monotonically increasing signal caused by the formation of passivating coating on the surface [13] and the narrow spectral feature near 3 eV, which reflects the change in the subsurface electric field [10]. Spectrum *e* (the difference between spectra *c* and *b*) is associated with the anisotropy induced by the illumination of the passivated surface by the light. This spectrum is represented by the spectral line with a maximum at about 3 eV and coincides with the characteristic spectrum of the clean GaAs(100) surface with the (2×4) reconstruction (spectrum *f*) [14].

Figure 3 displays the reflectance anisotropy spectra of the clean As-terminated $Al_xGa_{1-x}As(100)$ surfaces, which were obtained in the same manner as spectrum *e* in Fig. 2. It can be seen that, in the spectra of ternary compounds, an increase in the aluminum concentration leads to a considerable broadening of the line observed in the spectrum of GaAs(100) at about 3 eV toward the low-energy range, and, at $x = 0.5$, the signal maximum is also shifted toward the low-energy range.

3. DISCUSSION

It is evident that the reflectance anisotropy spectra of the $Al_xGa_{1-x}As$ ternary compounds (Fig. 3) do not follow the behavior observed in the spectra of the imag-
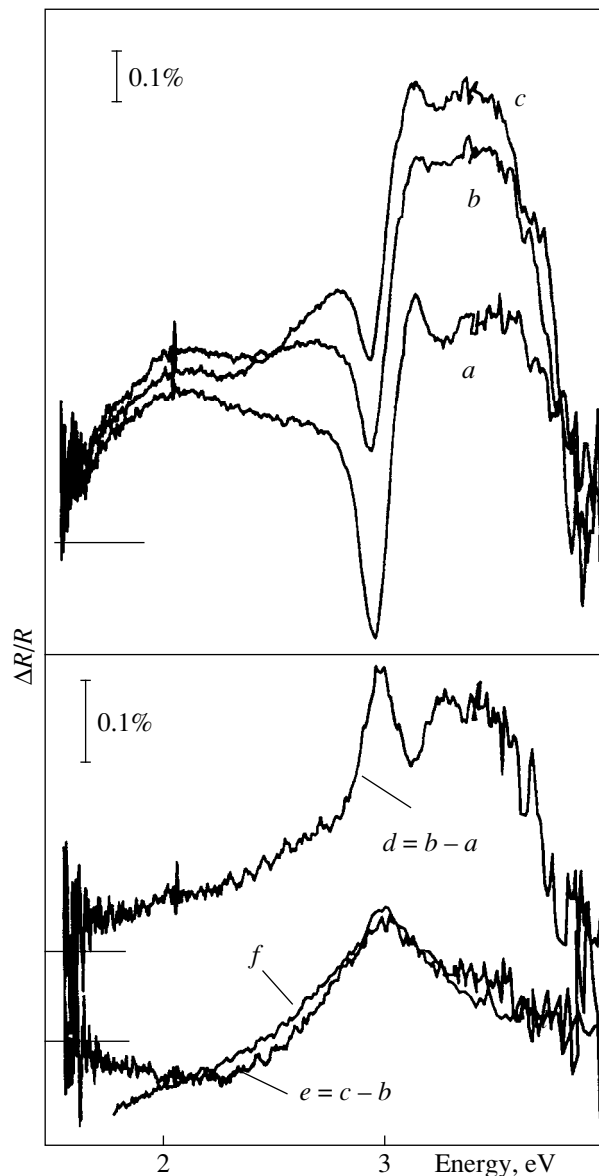

Fig. 2. Reflectance anisotropy spectra of the (100) surface of the GaAs sample *in situ* treated in a Na_2S solution: (*a*) immediately after the pouring of the solution, (*b*) after the treatment in the solution without lighting for 120 min, and (*c*) after exposure of the surface to the light. (*d*, *e*) Difference spectra characterizing the anisotropy induced at the corresponding stage of treatment. (*f*) The characteristic spectrum (obtained under ultrahigh vacuum [10]) of a clean (100) surface with the (2×4) reconstruction. Horizontal straight-line segments at the left indicate the levels of zero signals.

inary part of the permittivity for these compounds, which are displaced toward the high-energy range with an increase in *x*. At the same time, the aforementioned spectral changes can be easily explained under the assumption that the reflectance anisotropy spectra in the range 1.6–3.5 eV are predominantly contributed by the optical transitions localized at the arsenic dimers on
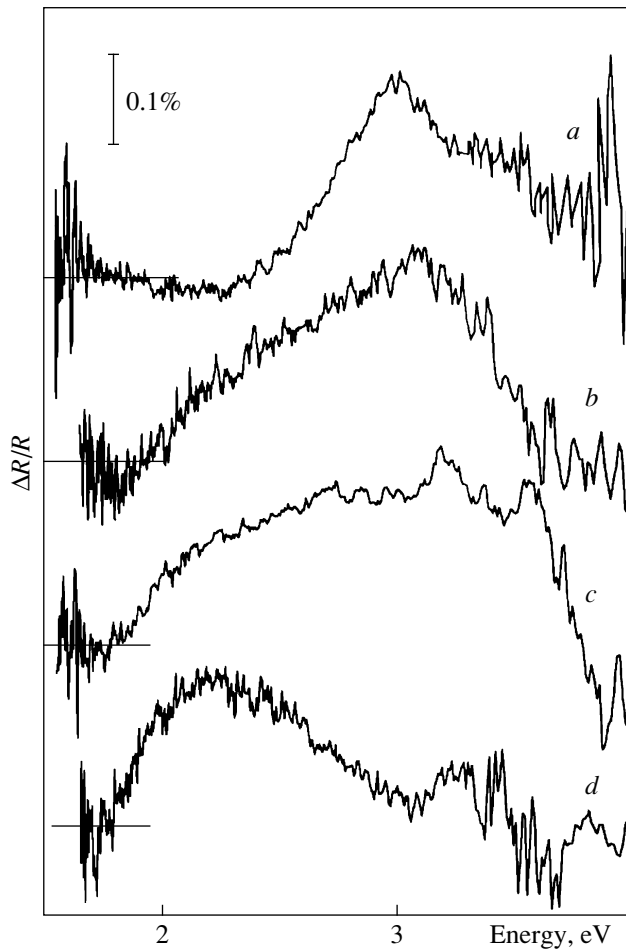
Fig. 3. Reflectance anisotropy spectra of the clean As-terminated $Al_xGa_{1-x}As(100)$ surfaces at different aluminum concentrations x: (*a*) 0, (*b*) 0.27, (*c*) 0.35, and (*d*) 0.5. Horizontal straight-line segments at the left indicate the levels of zero signals.

Fig. 4. Decomposition of the reflectance anisotropy spectra of the clean surfaces: (a) GaAs and (b) $Al_{0.5}Ga_{0.5}As$. Dotted lines show the spectral lines corresponding to the optical transitions in the nonequivalent As dimers. Dashed lines represent the contributions of the bulk to the reflectance anisotropy signal.

the surface. In the spectrum of GaAs, this contribution is reflected by a single line at an energy of 3 eV. The broadening and shifting of the reflectance anisotropy spectra of the ternary compounds toward the low-energy range with an increase in x are reasonably explained by the splitting of this line due to the formation of nonequivalent arsenic dimers when the Al atoms substitute for the Ga atoms in the bulklike bonds of the dimer. In this case, as can be seen from the spectra, the energy of optical transition in the nonequivalent dimers should decrease with an increase in the number of the substituted gallium atoms. This decrease can be qualitatively explained in the following way. The replacement of the Ga atom by the more electropositive Al atom leads to an increase in the electron density on the As atom in the dimer. Then, the energy level of an electron in the dangling orbital of the dimer, from which the optical transition occurs, is shifted toward the energy
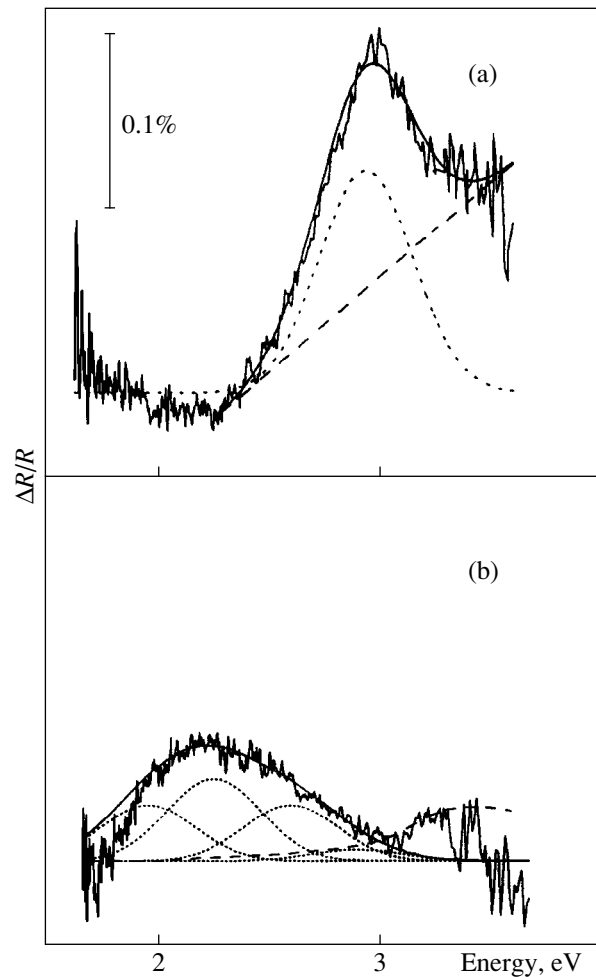
level of the electron in vacuum. The level of the antibonding state of the dimer is also shifted upward; however, since this state is more delocalized, the shift is smaller. As a consequence, the energy of the optical transition contributing to the reflectance anisotropy spectrum is shifted toward the low-energy range. The energies of optical transitions in arsenic dimers of different types can be exactly calculated within the tight binding approximation.

The decomposition of the reflectance anisotropy spectrum of the GaAs(100) surface with the (2×4) reconstruction (see Fig. 3, spectrum *a*) is demonstrated in Fig. 4. According to [14], in the spectral range from 1.6 to 3.5 eV, this spectrum can be represented as the sum of the spectral line described by the Gaussian contour with a maximum at 3 eV and the monotonically increasing structureless signal. As follows from the experimental data [15], the latter signal persists after

Spectral parameters of optical transitions in the nonequivalent As dimers on the $Al_{0.5}Ga_{0.5}As(100)$ surface

Atoms in bulklike bonds of As dimers	4Ga	3Ga + 1Al	2Ga + 2Al	1Ga + 3Al	4Al
Energy location of lines of optical transitions, eV	2.9	2.6	2.25	1.95	(1.6–1.65)?
Normalized integrated intensity (experiment)	0.06	0.255	0.38	0.255	
Relative concentration of As dimers (calculation)	0.0625	0.25	0.375	0.25	0.0625

the complete oxidation of the surface. Therefore, it can be assumed according to [16] that this signal reflects the contribution of the subsurface bulk region to the reflectance anisotropy spectrum.

The spectrum of the clean $Al_{0.5}Ga_{0.5}As(100)$ surface (Fig. 3, spectrum d) can be decomposed in a similar way as the spectrum shown in Fig. 4a on the basis of the following simple considerations. First, the broad structureless signal arising from the bulk anisotropy should be strongly shifted toward the high-energy range owing to an increase in the energy of the bulklike transitions in the ternary compound and virtually should not overlap with the spectral feature attributed to the optical transitions in the arsenic dimers. Second, it can be assumed that the half-width of the decomposition components corresponding to the optical transitions in the nonequivalent dimers is identical to that of the Gaussian contour in Fig. 4a. Since, at $x = 0.5$, the percentage of the Ga and Al atoms is the same, the As dimers with two Ga atoms and two Al atoms in the nearest environment are most probably formed on the clean $Al_{0.5}Ga_{0.5}As(100)$ surface. Consequently, the energy of the appropriate optical transition should coincide with the location of a maximum in the reflectance anisotropy spectrum of the $Al_{0.5}Ga_{0.5}As(100)$ surface. The total number of the splitting components for the line associated with the arsenic dimers is equal to five, provided that the energy of optical transition depends only on the number of substituted gallium atoms. In Fig. 4b, a part of the spectrum associated with the optical transitions in dimers is represented as the sum of four components corresponding to nonequivalent dimers of four types. The neighboring components of the decomposition are separated in energy by 0.3–0.35 eV. This allows us to assume that the fifth component of decomposition associated with the transitions in the As dimers with four Al atoms in the nearest environment should lie in the energy range 1.6–1.65 eV, which corresponds to the boundary of the operating range of the experimental setup. The energies and the normalized integrated intensities of the decomposition components are listed in the table.

It is clear that the intensity of each component of the decomposition should be proportional to the concentration of dimers of a particular type on the surface. The relative concentrations of nonequivalent arsenic dimers of each type on the $Al_{0.5}Ga_{0.5}As$ surface can be estimated from probability considerations. If the total concentration of dimers is equal to unity, the sought concentrations are equal to $C_4^k x^k (1 - x)^{4-k}$, where k is the number of Al atoms in the nearest environment, and x is the Al concentration in the solid solution. The table presents the concentrations of nonequivalent dimers at $x = 0.5$, which were calculated using this relationship. It is seen from the table that the calculated concentrations correlate well with the normalized integrated intensities of the spectral lines corresponding to the nonequivalent dimers.

Thus, in the present work, we obtained and examined the reflectance anisotropy spectra of the (100) surfaces of the $Al_xGa_{1-x}As$ ternary semiconductors. It is revealed that the spectra of the oxidized surfaces of the ternary compounds are similar to the spectrum of GaAs. This enables us to draw the inference that the reflectance anisotropy in the ternary compounds, as in GaAs, can be represented as the sum of two contributions, one of which is associated with the subsurface electric field, and the other contribution is due to the shielding effect at the semiconductor–oxide interface. The spectra of the clean As-rich $Al_xGa_{1-x}As$ surfaces were obtained using non-vacuum technique under conditions when the samples were in the sodium sulfide solutions. It is found that, in the spectral range 1.6–3.5 eV, the reflectance anisotropy signals are primarily brought about by the localized optical transitions in the nonequivalent arsenic dimers differing in the number of Al atoms in the bulklike bonds (from 0 to 4). As the number of Al atoms increases by one atom, the energy of optical transition in the dimer decreases by approximately 0.3 eV. The fundamental optical transition energies are determined for the nonequivalent dimers of four types.

Moreover, it was found that the spectra of the clean $Al_xGa_{1-x}As$ surfaces, like the spectra of GaAs, exhibit a structureless monotonically increasing signal attributed to the transitions in the subsurface perturbed layer in the bulk of the semiconductor. With an increase in x, the signal shifts toward the high-energy range in much the same manner as the spectrum of the imaginary part of the permittivity for ternary compounds.

REFERENCES

1. P. Chiaradia and G. Charotti, in *Photonic Probes of Surface*, Ed. by P. Halevi (Elsevier Science, Amsterdam, 1995), Chap. 3, p. 98.

2. M. Wassermeier, I. Kamiya, D. E. Aspnes, *et al.*, J. Vac. Sci. Technol. B **9**, 2263 (1991).

3. I. Kamiya, D. E. Aspnes, H. Tanaka, *et al.*, Phys. Rev. Lett. **68** (5), 627 (1992); O. Acher, S. M. Koch, F. Omnes, *et al.*, J. Appl. Phys. **68**, 3564 (1990).

4. V. L. Berkovits and D. Paget, Thin Solid Films **233**, 9 (1993).

5. R. Eryigit and I. P. Herman, Phys. Rev. B **56**, 9263 (1997).

6. I. Kamiya, D. E. Aspnes, L. T. Flórez, *et al.*, Phys. Rev. B **46**, 15894 (1992).

7. M. Murayama, K. Shirashi, and T. Nakayama, Jpn. J. Appl. Phys., Part 1 **37**, 4109 (1998).

8. Yia-Chung Chang, Shang-Fen Ren, and D. E. Aspnes, J. Vac. Sci. Technol. A **10**, 1856 (1992); Shang-Fen Ren and Yia-Chung Chang, Phys. Rev. B **44**, 13573 (1991).

9. D. E. Aspnes, S. M. Kelso, R. A. Logan, *et al.*, J. Appl. Phys. **60**, 754 (1986).

10. V. L. Berkovits, V. N. Bessolov, T. V. L'vova, *et al.*, Fiz. Tekh. Poluprovodn. (Leningrad) **25**, 1406 (1991) [Sov. Phys. Semicond. **25**, 847 (1991)].

11. S. E. Acosta-Órtiz and A. Lastras-Martínez, Phys. Rev. B **40**, 1426 (1989).

12. U. Rossow, L. Mantese, and D. E. Aspnes, Appl. Surf. Sci. **123/124**, 237 (1998).

13. V. L. Berkovits, A. O. Gusev, V. M. Lantratov, *et al.*, Phys. Rev. B **54**, R8369 (1996).

14. D. Paget, V. L. Berkovits, and A. O. Gusev, J. Vac. Sci. Technol. A **13**, 2368 (1995).

15. V. L. Berkovits, P. Chiaradia, D. Paget, *et al.*, Surf. Sci. 1999 (in press).

16. T. Nakayama, Phys. Status Solidi B **202**, 741 (1997).

Translated by O. Borovik-Romanova

Permittivity of Liquid Crystals of the Alkylcyanobiphenyl Group in a Decimeter Wavelength Range

B. A. Belyaev, N. A Drokin, V. F. Shabanov, and V. N. Shepov

Kirenskiĭ Institute of Physics, Siberian Division, Russian Academy of Sciences, Akademgorodok, Krasnoyarsk, 660036 Russia
e-mail: belyaev@post.krascience.rssi.ru
Received November 16, 1999

Abstract—The high-frequency dielectric spectra of liquid crystals of the alkylcyanobiphenyl group with various length of the mobile alkyl chain C_nH_{2n+1} ($n = 5$–8) are experimentally studied. It is established that a resonance feature is observed in the frequency range of 300 MHz for all the crystals on the high-frequency branch of the orientational part of dielectric spectra. It is shown that the position of the dielectric resonance is virtually independent of the temperature and the degree of crystal dilution by benzene, but its intensity essentially depends on both factors. The nature of the dielectric resonance found is probably caused by the intramolecular motion of methylene fragments, which are strongly bound with a rigid core of molecules. © *2000 MAIK "Nauka/Interperiodica".*

For a number of mesomorphic phases of liquid crystals, the dielectric spectra often involve portions with a significant deviation from the Debye dispersion law. As a rule, the spectra are characterized by high- and low-frequency distortions depending on the molecule structure, magnitude, and type of the liquid-crystal order. The low-frequency part of the dispersion (radio-frequency range) is usually associated with the features of the orientational collective motion of molecules and mobile ionic charges [1, 2]. The high-frequency part of the spectrum is the least understood, and additional mechanisms of dielectric relaxation related to the intramolecular mobility are currently only assumed to take effect in a decimeter wavelength range [3, 4]. In our earlier detailed study [5] of the dielectric spectra of the 4-*n*-pentyl-4'-cyanobiphenyl (5CB) liquid crystal in the frequency range 50–1000 MHz, we found that, in the vicinity of 300 MHz (and at higher frequencies with an increase in the temperature), there is a rather strong deviation of the spectrum from the Debye monotonic dependence.

The present work is devoted to the study of the dielectric spectra in a decimeter wavelength range on the samples of liquid crystals from the series of 4-*n*-alkyl-4'-cyanobiphenyls with a various length of the mobile alkyl chain C_nH_{2n+1} ($n = 5$–8). As is known, the rigid core of molecules in the cyanobiphenyl compounds of liquid crystals is formed by two benzene rings, along the axis of which the strongly polar group C≡N is situated on one side of the core (this group has a large dipole moment oriented along the long axis of the molecule) and the flexible hydrocarbon chains ("tails"), which consist of –CH$_2$– groups, are located on the other side of the core. All the samples under study are nematic liquid crystals by type of liquid-crystal

ordering, and only for the 8CB crystal, there is also the smectic phase in the temperature range $20.9 \leq t \leq 33.5°C$. The dielectric spectrum of each sample was taken twice for two states of the crystal. For measurements in the nematic phase, the temperature was set 5 K below the temperature t_{ni} of transition from the nematic state to the isotropic state, and in the case of the isotropic phase, the temperature was set 2 K above t_{ni}.

The dielectric properties of liquid-crystal mesophases were investigated in the frequency range 50–500 MHz, which corresponds to the most pronounced resonance feature in the spectrum [5]. This range of decimeter wavelengths is rather difficult to carry out reliable measurements. For this reason, we used specially devised miniature tunable microwave sensors based on the ring-shaped microstrip resonators. The sensors and techniques of resonance measurements were described in [5, 6]. A liquid crystal was placed inside an UHF measuring cell in the antinode of a high-frequency electric field between two gold-coated surfaces 2×2 mm in size with a spacing of 100 μm. The parallel orientation of long axes of the liquid crystal molecules with respect to the high-frequency field was achieved with the help of the uniform constant magnetic field $H = 2.5$ kOe. The temperature of the measuring cell was stabilized with an accuracy of 0.1°C and could be varied from 0 to 60°C.

The spectra of the real part of the permittivity for 5CB, 7CB, and 8CB liquid crystal samples, which were taken in the nematic phase under the molecular director orientation parallel to the polarization of the high-frequency field $\varepsilon'_\parallel(f)$, are given in Fig. 1 (curves *1*, *2*, and *3*, respectively). In order not to overload the figure, the spectrum for a 6CB liquid crystal is not shown, because it almost coincides with the spectrum of the 5CB liquid
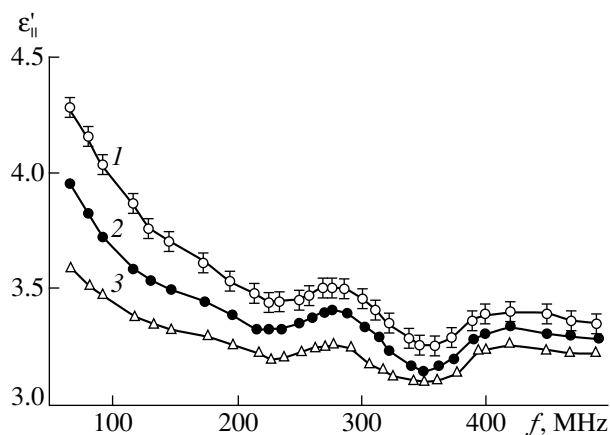
Fig. 1. Frequency dependences of the real part of the permittivity for (*1*) 5CB, (*2*) 7CB, and (*3*) 8CB liquid crystals in the nematic phase.

Fig. 2. Frequency dependences of the real part of the permittivity for 8CB liquid crystal in (*1*) smectic phase, (*2*) nematic phase, and (*3*) isotropic state.

crystal sample. The absolute precision of the $\varepsilon'_\parallel(f)$ measurements is shown in curve *1*. This precision was observed in all the experimental curves and was equal to ± 0.02. It can be seen that all the curves are qualitatively similar to each other, and the main feature of each dielectric spectrum is a clearly revealed maximum near 280 MHz (ε'_{max}) and a minimum near 350 MHz (ε'_{min}). The behavior of $\varepsilon'_\parallel(f)$ in the range under consideration indicates the existence of dielectric resonance, which is observed at about the same frequency for all the samples under study.

To put it differently, the resonance location is independent on the length of the alkyl chain in cyanobiphenyls. However, as is known, this length rather strongly affects the Debye relaxation frequencies f_D. Actually, the f_D frequencies measured for 5CB, 7CB, and 8CB liquid crystals at temperatures 5 K below t_{ni} are equal 7.2, 6.2, and 5.45 MHz, respectively [7]. As the length of alkyl "tails" increases, i.e., when passing from the less "inertial" composition to the more "inertial" (Fig. 1), one can observe not only a decrease in the permittivity of the liquid crystal samples at high frequencies, but also a significant decrease in the dielectric resonance intensity, which can be evaluated from the difference ($\varepsilon'_{max} - \varepsilon'_{min}$).

Note that the intensity of the resonance observed monotonically increases with an increase in the temperature. It follows from the experiment that, upon transition from the nematic phase to the isotropic phase, the resonance intensity increases for all the samples studied more than three times. However, in this case, the characteristic frequencies corresponding to ε'_{max} and ε'_{min} virtually do not change, and, hence, the location of the dielectric resonance does not change as well. It is of interest to note that the resonance observed rather well manifests itself in the smectic phase, which exists in the 8CB liquid crystal. The dielectric spectra of this liquid crystal are shown in Fig. 2. These spectra were mea-
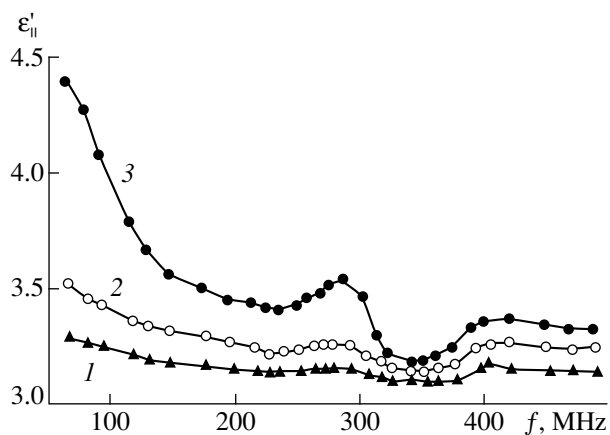
sured for three different phases, namely, the smectic ($t = 28.5°C$), nematic ($t = 35.8°C$), and isotropic liquid ($t = 42.2°C$) phases. It is seen that, upon transition from the nematic phase to the smectic phase, the intensity of resonance decreases approximately three times, but its location on the frequency axis remains as before.

It is known that the Debye relaxation frequency of liquid crystals increases with an increase in the temperature. As a result, the orientational part of the dielectric spectrum shifts to the right toward the high-frequency range. It is also known that, as the length of alkyl chain in a liquid crystal molecule increases, the f_D frequency, on the contrary, decreases, and, as a consequence, the orientational part of the dielectric spectrum shifts toward the low-frequency range. Therefore, taking into account the results of experiments presented in Figs. 1 and 2, we can conclude that the intensity of the dielectric resonance observed increases in any cases when the relaxation region of the spectrum (induced by the polarization of liquid crystal molecules) approaches this resonance.

The degree of deviation of the experimentally observed dielectric spectra from the Debye frequency dependences of the permittivity for liquid crystals from the series of alkylcyanobiphenyls was evaluated in [1–4] according to the Cole–Cole diagrams. The high-frequency distortions in the diagrams, as a rule, are described by a set of internal relaxation regions of the Debye type. In this case, the frequency dependence of the real part of the permittivity $\varepsilon'_D(\omega)$ is represented in the form

$$\varepsilon'_D(\omega) - \varepsilon'_\infty = \sum_k \frac{\varepsilon'_k - \varepsilon'_\infty}{1 + \omega^2 \tau_k^2}, \qquad (1)$$

where ε'_k and τ_k are the *k*th components of the static permittivity and relaxation time, respectively; and ε'_∞ is
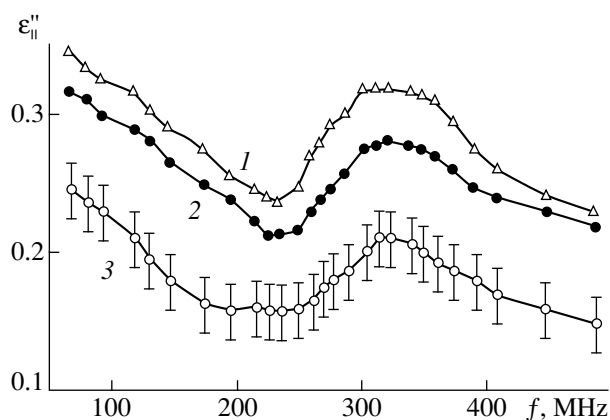
Fig. 3. Frequency dependences of the imaginary part of the permittivity for (*1*) 5CB, (*2*) 7CB, and (*3*) 8CB liquid crystals in the nematic phase.

the rf permittivity. Because of the limited number of experimental points presented in the papers, the spectral components of these regions and, first of all, the reasons for their appearance still remain unclear.

However, in the present work, we established that the deviation from the Debye dependence in the high-frequency part of the dielectric spectrum most likely can be connected with the resonance behavior of alkyl-cyanobiphenyls at high frequencies rather than with their relaxation behavior. Evidence for this conclusion is the absence of the characteristic frequency shift in the dispersion region of the dielectric spectrum with a change in the temperature of samples, which is certainly not typical of the relaxation processes. The location of a maximum in the frequency dependence of the imaginary part of the permittivity (Fig. 3) determines the resonance vibrational frequency, which turned out to be approximately identical (about 320 MHz) for all the samples studied.

The experiments performed demonstrate that the origin of the dielectric resonance found is brought about by the excitation of intramolecular vibrations. This is confirmed by the following findings. First, the resonance intensity increases with an increase in the temperature of samples, which especially clearly manifests itself in the nematic–isotropic liquid phase transition. Second, upon dilution of liquid crystals by benzene (up to 50% benzene content in the sample volume), the resonance intensity first significantly increases and then monotonically decreases, the resonance frequency being unchanged.

The vibrations of flexible alkyl groups can be the most probable intramolecular motions connected with the dielectric resonance. However, the fact that the frequency of the resonance found is virtually independent of the length of the alkyl chain suggests that only certain methylene fragments can contribute to the vibrational process. This assumption is well justified with the data obtained by the NMR method [8, 9]. According to these data [8, 9], the order parameter is strongly non-uniform along the length of alkyl chain. Its value drastically decreases toward the chain end and remains almost the same for the three first fragments in all alkyl-cyanobiphenyl compounds. It is quite probable that it is these vibrations of the first alkyl chain fragments strongly bound with the rigid core that manifest themselves as the dielectric resonance found at the end of the Debye dispersion region. The natural frequencies of vibrations of the next alkyl chain fragments are significantly higher, and, probably, the resonances observed at frequencies of 450–1000 MHz in the isotropic phase of a 5CB liquid crystal are caused by these fragments [15].

REFERENCES

1. H. Mada and A. Nishikawa, Jpn. J. Appl. Phys. **32**, 1009 (1993).
2. J. P. Parneix, A. Chapoton, and E. Constant, J. Phys. (Paris) **36**, 1143 (1975).
3. C. Druon and J. M. Wacrenier, J. Phys.(Paris) **38**, 47 (1977).
4. D. Lippens, J. P. Parneix, and A. Chapoton, J. Phys. (Paris) **38**, 1465 (1977).
5. B. A. Belyaev, N. A. Drokin, V. F. Shabanov, *et al.*, Pis'ma Zh. Éksp. Teor. Fiz. **66**, 251 (1997) [JETP Lett. **66**, 271 (1997)].
6. B. A. Belyaev, N. A. Drokin, and V. N. Shepov, Zh. Tekh. Fiz. **65**, 189 (1995) [Tech. Phys. **40**, 216 (1995)].
7. J. M. Wacrenier, C. Druon, and D. Lippens, Mol. Phys. **43**, 97 (1981).
8. J. W. Emsley, B. M. Fung, N. J. Heaton, *et al.*, J. Chem. Phys. **87**, 3099 (1987).
9. K. Akasaka, M. Kimura, A. Natio, *et al.*, J. Phys. Chem. **99**, 9523 (1995).

Translated by T. Galkina